MINERALOGY, METAL ZONING, AND GENESIS OF THE CAMBRIAN Zn-Pb-Cu-Ag-Au LEMARCHANT VOLCANOGENIC MASSIVE SULFIDE (VMS) DEPOSIT

By Shannon Gill

A Thesis submitted to the School of Graduate Studies

in partial fulfillment of the requirements for the degree of

Master of Science, Department of Earth Sciences

Memorial University of Newfoundland

February 2015

St. John's, Newfoundland and Labrador

Abstract

The Lemarchant deposit is a Cambrian bimodal felsic Zn-Pb-Cu-Ag-Au volcanogenic massive sulfide (VMS) deposit that is hosted in the Newfoundland Appalachians. The mineralogy consists of barite and normal VMS sulfides (e.g., sphalerite, galena, pyrite, chalcopyrite), as well as minerals common to epithermal deposits (e.g., tetrahedrite, bornite, electrum) and enrichments in epithermal suite elements. Sulfur isotope analyses of sulfides range from $\delta^{34}S$ -6.4 to +15.1‰ and indicate sulfur was derived from thermochemically reduced seawater sulfate, igneous leaching and magmatic SO_2. Lead isotope data are restricted, and indicate Pb-sourcing from Neoproterozoic basement rocks and more juvenile sources.

The occurrence of epithermal suite minerals and element enrichments with bladed suggest that precious metals were derived from magmatic fluid additions to the VMS hydrothermal system. Precious metal enrichment of the Lemarchant deposit was caused by low temperature, oxidized, near neutral fluids that boiled upon seafloor discharge in a shallow water (<1500 mbsl) setting.

Acknowledgments

My thanks are first and foremost directed to my dedicated supervisor, Dr. Steve Piercey. I am extremely appreciative of his honesty, integrity, advice, and support in the name of good science. Thank you also to my committee member Dr. Graham Layne and undergraduate supervisor Dr. Dan Layton-Matthews, for their guidance and insight throughout the analytical and written aspects of this project. The following are mentioned for their support, advice, contrasting points of view, inspiration, and always stimulating conversation: Jonathan Cloutier, Christine Devine, Mary Devine, Mike Gadd, Stefanie Lode, Tiffany Miller, Jean-Luc Pilote, Lindsay Waffle. Lastly, from the bottom of my heart I thank my family, especially my parents Dave and Kim, my sister Lindsay, and my grandmother Rishwantreet, and my poleaxed boyfriend Mack for their unwavering confidence in my ability.

Funding for this project comes primarily from the Geological Survey of Canada (GSC) Targeted Geoscience Initiative 4 (TGI4) Program, and the Research Affiliate Program (RAP) of Natural Resources Canada (NRCan). Secondary financial support comes from grants to Dr. Stephen J. Piercey, including a Natural Sciences and Engineering Research Council (NSERC) Discovery Grant and the NSERC-Altius Industrial Research Chair in Mineral Deposits supported by NSERC, Altius Resources Inc., and the Research and Development Corporation of Newfoundland and Labrador. Thank you to Canadian Zinc Corporation and Paragon Minerals Corporation (a 100% owned subsidiary of Canadian Zinc Corporation) for access to the Lemarchant drill core

and core shack facilities. Prior publication of two manuscripts through the GSC's annual Current Research is acknowledged in this manuscript, and both are included as Appendices to the main text.

Table of Contents

Abstract……ii
Acknowledgements……iii
Table of Contents……v
List of Tables……vii
List of Figures……viii
List of Abbreviations……x
List of Appendices……xii
Chapter 1: Introduction……1
1.1 – Exploration history……2
1.2 – Regional geology……2
1.3 – Deposit geology……4
1.4 – VMS deposits: Setting, classification and characteristics……6
1.4.1 – Mechanisms of massive sulfide deposition……8
1.4.2 – Gold enrichment in the VMS environment……10
1.5 – Thesis objectives……12
1.6 – Methods……13
1.6.1 – Core logging……13
1.6.2 – Petrography……14
1.6.3 – Ore mineral chemistry……15
1.6.4 – *In situ* sulfur and lead isotope geochemistry……15
1.7 – Presentation……16
1.8 – Co-authorship statement……16
Chapter 2: Mineralogy, metal zoning, and genesis of the Cambrian Zn-Pb-Cu-Ag-Au Lemarchant volcanogenic massive sulfide (VMS) deposit, Newfoundland……25
2.1 – Abstract……25
2.2 – Introduction……26
2.3 – Geological setting……29
2.3.1 – Regional geology……29
2.3.2 – Deposit geology and host rock lithology……30
2.4 – Mineralization……33
2.4.1 – Sulfide mineralogy……34
2.4.1.1 – Type 1 mineral assemblage……35
2.4.1.2 – Type 2A mineral assemblage……35
2.4.1.3 – Type 2B mineral assemblage……36
2.4.1.4 – Type 3 mineral assemblage……37
2.4.1.5 – Type 4 mineral assemblage……37
2.5 – Sulfide mineral chemistry……38
2.5.1 – Analytical methods……39
2.5.2 – Results: Major and minor element geochemistry……40
2.5.3 – Results: Trace element geochemistry……45
2.5.3.1 – Type 1 mineral assemblage……45

2.5.3.2 – Type 2A mineral assemblage……..…….....46
2.5.3.3 – Type 2B mineral assemblage……..…….....47
2.5.3.4 – Type 3 mineral assemblage……..…….....48
2.5.3.5 – Type 4 mineral assemblage……..…….....48
2.6 – Discussion……..…….....49
2.6.1 – Deposit type and sulfide mineral paragenesis……..…….....49
2.6.2 – Physicochemical and geological conditions of metal transport and deposition……..…….....51
2.6.3 – Magmatic contribution to the hydrothermal fluid..…..…….....57
2.7 – Conclusion ……..…….....60
2.8 – Acknowledgements……..……61
2.9 – References…….....61
Chapter 3: Sulfur and lead isotope geochemistry of sulfides from the Cambrian Zn-Pb-Cu-Ag-Au Lemarchant volcanogenic massive sulfide (VMS) deposit, Newfoundland……...88
3.1 – Abstract……..…….....88
3.2 – Introduction……..…….....89
3.3 – Regional geology……..……....91
3.4 – Deposit geology……..…….....93
3.5 – Mineralization……..…….....95
3.6 – Isotope geochemistry of sulfides……..……...97
3.6.1 – Analytical methods……..……..97
3.6.2 – Results: Lead isotopes……..…….99
3.6.3 – Results: Sulfur isotopes……..……101
3.7 – Discussion……...…102
3.7.1 – Source(s) of metals……...……102
3.7.2 – Source(s) of sulfur……105
3.7.3 – Sulfur isotope geothermomtetry……...109
3.8 – Conclusion……...111
3.9 – Acknowledgements……112
3.10 – References……112
Chapter 4: Summary……136
4.1 – Directions for Future Research……..…….....138
References……..140
Appendices…….....(included electronically)

List of Tables

Chapter 2

Table 2.1. Sulfides and sulfosalts identified from the Lemarchant deposit.

Table 2.2. Trace element contents of sulfides and sulfosalts at Lemarchant.

Chapter 3

Table 3.1. Lead isotope ratios, model lead ages and μ-values of galena at Lemarchant.

Table 3.2. Sulfur isotope ratios in pyrite, galena and chalcopyrite at Lemarchant.

List of Figures

Chapter 1

Figure 1.1. Tectonostratigraphic zones of Newfoundland.
Figure 1.2. Geological map of the Exploits subzone, Newfoundland Central Mobile Belt.
Figure 1.3. Geological map of the Lemarchant deposit.
Figure 1.4. Long section of the Lemarchant deposit, looking east.
Figure 1.5. Essential components in the volcanogenic massive sulfide-forming environment.
Figure 1.6. Stratigraphic sections representing the five types of lithotectonic settings for volcanogenic massive sulfide districts.
Figure 1.7. Schematic diagrams of bimodal felsic-type and hybrid bimodal felsic-type volcanogenic massive sulfide deposits.

Chapter 2

Figure 2.1. Geological map of the Exploits subzone, Newfoundland Central Mobile Belt.
Figure 2.2. Geological map of the Lemarchant deposit.
Figure 2.3. Cross section diagrams of: A) long section A-A'; B) section B-B' (L10300N); and C) section C-C' (L10100N) at Lemarchant.
Figure 2.4. Fence diagrams of: A) section L10300N; B) section L10100N highlighting mineralization at Lemarchant.
Figure 2.5. Drill core photographs of the 5 types of mineralization at Lemarchant.
Figure 2.6. Thin section and backscatter electron (BSE) images of mineralogy and textures at Lemarchant.
Figure 2.7. Thin section reflected light and BSE images of mineralogy and textures at Lemarchant (cont'd).
Figure 2.8. Compositional variation in select phases at Lemarchant (data from electron microprobe analyses).
Figure 2.9. Down hole variation of select element contents in sphalerite and pyrite from Lemarchant (Drill hole LM11-59).
Figure 2.10. Arsenic zonation in pyrite from Lemarchant.
Figure 2.11. Along-strike variation in trace element contents in tetrahedrite, pyrite and electrum from the Lemarchant depoist.
Figure 2.12. Bivariate plots of trace element contents in sulfide phases from the five types of mineralization at Lemarchant.
Figure 2.13. Paragenetic sequence of sulfide and gangue phases at Lemarchant.
Figure 2.14. αS_2 vs. temperature phase diagram depoicting areas of stability for Lemarchant paragenetic stages, with contours of mole% FeS in sphalerite and solubility of $Au(HS)_2^-$ at pH 5.
Figure 2.15. Schematic diagram of Lemarchant genesis. A) Stage 1; B) Stage 2; and C) Stage 3.

Chapter 3

Figure 3.1. Geological map of the Exploits subzone, Newfoundland Central Mobile Belt.
Figure 3.2. Geology of the Lemarchant deposit. A) Geological plan map of Lemarchant. B) Long section of Lemarchant, looking east.
Figure 3.3. Photomicrographs of representative mineral textures in pyrite, galena and chalcopyrite at Lemarchant; sulfur isotope values and Pb isotope ratios at spot analyses locations.
Figure 3.4. Paragenetic sequence of sulfide phases and mineral assemblages at Lemarchant.
Figure 3.5. Plots of Pb isotope variation in galena in the Lemarchant deposit. A) $^{208}Pb/^{204}Pb$ vs. $^{206}Pb/^{204}Pb$. B) $^{207}Pb/^{204}Pb$ vs. $^{206}Pb/^{204}Pb$.
Figure 3.6. Comparison of uranogenic lead isotope data in Appalachian VMS deposits.
Figure 3.7. Notched box and whisker plot of $\delta^{34}S$ variation in Lemarchant sulfides.
Figure 3.8. Frequency distribution of $\delta^{34}S$ values in Lemarchant sulfides according to mineral assemblage.
Figure 3.9. Range of $\delta^{34}S$ values from Lemarchant, with respect to modern black smoker deposits and ancient VMS deposits.

List of Abbreviations

Alb	Albite
Ant	Anatase
Avg	Average
BDL	Below detection limit
Bn	Bornite
Bnn	Bournonite
BSR	Bacterial sulfate reduction
Cal	Calcite
Ccp	Chalcopyrite
c.f.	Compare
Clf.	Colloform
Col	Colusite
CPS	Counts per second
CREAIT	Core Research Equipment and Instrument Training Network
Cv	Covellite
EDX	Energy dispersive X-ray
e.g.	For example
Elec	Electrum
EMPA	Electron microprobe analysis
Euh.	Euhedral
Fig(s)	Figure(s)
Gn	Galena
GSC	Geological Survey of Canada
g/t	Grams per tonne
i.e.	That is
LA-ICP-MS	Laser ablation inductively-coupled plasma mass spectrometry
LFB	Lower felsic block
MAF-IIC	Micro-Analysis Facility, Inco Innovation Centre
mbsl	Metres below sea level
MLA	Mineral liberation analysis
Mrc	Marcasite
NRCan	Natural Resources Canada
NSERC	Natural Sciences and Engineering Research Council
per mil	Parts per thousand
Plb	Polybasite

ppm	Parts per million
Py	Pyrite
Pyx	Pyroxene
QFIR	Queen's Facility for Isotope Research
RAP	Research Affiliate Program
sec	Seconds
SEDEX	Sedimentary exhalative
SEM	Scanning electron microscope
SIMS	Secondary ion mass spectrometry
Sp	Sphalerite
SPO	Siliceous pyrite ore
Stm	Stromeyerite
Sub.	Subhedral
TERRA	The Earth Resources Research and Analysis Facility
TGI4	Targeted Geoscience Initiative 4 Program
Tnn	Tennantite
TPB	Tally Pond volcanic belt
Trt	Tetrahedrite
TSR	Thermochemical sulfate reduction
VMS	Volcanogenic massive sulfide
WDS	Wavelength dispersive spectrometry
wt %	Weight percent

List of Appendices

Appendix A: Graphic Logs
A.1 – Graphic Logs
A.2 –Abbreviation Key and Legend for Graphic Logs
Table A.2.1. Abbreviation Key for Graphic Logs
Table A.2.2. Legend for Graphic Logs
A.3 – Compilation of Graphic Logs
Appendix B: Current Research 2013
Appendix C: Current Research 2014
Appendix D: Electron Microprobe Results
D.1 – Supplementary Electron Microprobe Methods
D.2 – Compiled Electron Microprobe Analyses
Table D.2.1. Electron Microprobe Analyses for sphalerite
Table D.2.2. Electron Microprobe Analyses for pyrite
Table D.2.3. Electron Microprobe Analyses for galena
Table D.2.4. Electron Microprobe Analyses for chalcopyrite
Table D.2.5. Electron Microprobe Analyses for tetrahedrite
Table D.2.6. Electron Microprobe Analyses for bornite
Table D.2.7. Electron Microprobe Analyses for colusite, sulvanite, reinerite
Table D.2.8. Electron Microprobe Analyses for electrum
Table D.2.9. Electron Microprobe Analyses for stromeyerite, polybasite, miargyrite
Table D.2.10. Electron Microprobe Analyses for bournonite
Table D.2.11. Electron Microprobe Analyses for unknowns
Table D.2.12. Electron Microprobe Analyses for barite
D.3 – Methods for Mineral Formula Calculations
D.3.1 – Mineral Formula Calculation for sulfides and sulfosalts
Table D.3.1. Example Mineral Formula Calculation for sphalerite
D.3.2 – Mineral Formula Calculation for non-sulfides
Table D.3.2. Example Mineral Formula Calculation for electrum
D.3.3 – Mineral Formula Calculation for sulfates
Table D.3.3. Example Mineral Formula Calculation for barite
Appendix E: Laser Ablation ICP-MS Results
E.1 – Supplementary Laser Ablation ICPMS Methods
Table E.1.1. List of Standard Reference Materials
E.2 – Compiled Laser Ablation ICP-MS Analyses
Table E.2.1. Laser Ablation Spot Analyses for the type 1 mineral assemblage
Table E.2.2. Laser Ablation Spot Analyses for the type 2A mineral assemblage

Table E.2.3. Laser Ablation Spot Analyses for the type 2B mineral assemblage
Table E.2.4. Laser Ablation Spot Analyses for the type 3 mineral assemblage
Table E.2.5. Laser Ablation Spot Analyses for the type 4 mineral assemblage
E.3 – Methods for Laser Ablation Correction Calculations
E.3.1 – Calibration Curve Correction
E.3.2 – Element Ionization Correction
Table E.3.2.1. Example Element Ionization Correction for sphalerite
E.3.3 – Laser Yield Correction
Table E.3.3.1. Example Laser Yield Correction for sphalerite
Appendix F: Secondary Ion Mass Spectrometry Results
F.1 – Analytical Methods for Pb isotopes in SIMS
F.2 – Analytical Methods for S isotopes in SIMS
F.3 – Methods for TSR-derived $\delta^{34}S$ Calculations
Table F.3.1. TSR-derived $\delta^{34}S$ calculation for sulfides
F.4 – Methods for Temperature Calculations from $\delta^{34}S$ in sulfide mineral pairs
Table F.4.1. Geothermometry calculations with sulfide mineral pairs

Chapter 1: Introduction

The Cambrian-Ordovician Central Mobile Belt of the Newfoundland Appalachians is composed of multiple arc, rifted arc, back-arc basin, and ophiolitic assemblages that host volcanogenic massive sulfide (VMS) deposits (Swinden and Thorpe, 1984; Swinden, 1991; Piercey and Hinchey, 2012). These VMS deposits have variable settings and styles (Swinden and Thorpe, 1984; Swinden, 1991; Thurlow, 1996; Squires and Moore, 2004; Hinchey, 2007). The Tally Pond volcanic belt, host to the Lemarchant deposit, is a district of bimodal felsic-type VMS deposits, including two producing deposits (Duck Pond and Boundary), defined mineral resources (including Lemarchant), and numerous prospects (Evans and Kean, 2002; Squires et al., 2001; Squires and Moore, 2004). The Zn-Pb-Cu-Ag-Au Lemarchant deposit is hosted within the same ~513-509 Ma felsic volcanic horizon as the Cu-Zn Duck Pond mine and Boundary deposit (Dunning et al., 1991; Squires and Moore, 2004; McNicoll et al., 2010). The Lemarchant deposit is a bimodal felsic VMS deposit with polymetallic mineralization; however, the deposit contains mineral assemblages that are atypical of normal polymetallic VMS deposits, and has anomalous precious metal contents. The objective of this project is to better constrain the mineralogical and metallogenic evolution of the Zn-Pb-Cu-Ag-Au Lemarchant VMS deposit through detailed petrography, *in-situ* mineral chemical analyses and sulfur and lead isotope determinations of sulfides in drill core. The scientific goal is to provide insight into the mechanisms of precious metal enrichment in the Lemarchant deposit, and in similar VMS deposits at a regional and global scale.

1.1 – Exploration History

Newfoundland is host to numerous past and present producing VMS deposits, and has been the focus of massive sulfide exploration and development for over a century. The Lemarchant deposit is hosted within the Tally Pond group of the Victoria Lake Supergroup and is part of the 45 km by 8 km South Tally Pond property in the Tally Pond group, which was initially discovered by Noranda Incorporated (Copeland et al., 2008a and 2008b; Squires and Moore, 2004). From 2007-2011, Paragon Minerals Corporation discovered the bulk of the deposit and developed a National Instrument 43-101 compliant resource (Fraser et al., 2012). Canadian Zinc Corporation, the current owner of the property, purchased Paragon Minerals Corporation in August 2012, and has continued to drill throughout 2013 and 2014. The Lemarchant deposit has an Indicated Mineral Resource of 1.24 million tonnes grading 5.38% Zn, 0.58% Cu, 1.19% Pb, 1.01 g/t Au and 59.17 g/t Ag and an Inferred Mineral Resource of 1.34 million tonnes grading 3.70% Zn, 0.41% Cu, 0.86% Pb, 1.00 g/t Au and 50.41 g/t Ag (Fraser et al., 2012); this does not yet include additional resources intersected by Canadian Zinc Corporation during 2013 and 2014.

1.2 – Regional Geology

The Appalachian Orogen in Newfoundland consists of four tectonostratigraphic units from east to west: Avalon, Gander, Dunnage and Humber zones (Fig. 1.1). The Dunnage Zone is divided by the Red Indian Line into the Notre Dame and Exploits subzones, which are arc and back-arc rocks that formed along the edges of Laurentia (peri-Laurentian) and Gondwana (peri-Gondwanan), respectively (Williams, 1979; van

Staal et al., 1998; Evans and Kean, 2002). These subzones accreted to Laurentian and Gondwanan fragments during the closure of the Iapetus Ocean associated with the Late Cambrian-early Ordovician Taconic and Penobscot orogenies, respective, and then later to each other at the Red Indian Line during the Silurian Salinic Orogeny (van Staal, 2007; Zagorevski et al., 2007; van Staal and Barr, 2012).

The Dunnage Zone is composed of ophiolite sequences, island-arc and back-arc assemblages intercalated with marine sedimentary rocks, and an Upper Ordovician shale unit (Williams, 1979; Evans and Kean, 2002; Rogers and van Staal, 2002). There is a generalized upward gradation from tholeiitic to calc-alkalic volcanic rocks in the Exploits subzone, representing the transition from a nascent island arc environment through a rifted arc, back-arc and finally mature arc setting (Evans and Kean, 2002; Rogers et al., 2006; Zagorevski et al., 2007).

The Exploits Subzone is composed of a sequence of volcanic belts collectively termed the Victoria Lake Supergroup (Fig. 1.2), which are underlain by Neoproterozoic (~563 Ma) volcanic rocks of the Sandy Lake group and the plutonic Cripplebacк intrusive suite (Rogers et al., 2006; McNicoll et al., 2010). The Victoria Lake Supergroup is bound to the west and east by the Red Indian Line and the Noel Paul's Line, respectively (Zagorevski et al., 2007). The Red Indian Line demarcates the Iapetus suture zone (see above) and the Noel Paul's Line represents an unconformity between the Neoproterozoic, Cambrian, and Ordovician rocks of the Exploits subzone, and the Silurian sedimentary rocks of the Botwood group (Rogers and van Staal, 2002; Rogers et al., 2006). The Victoria Lake Supergroup consists of a series of fault-bounded, Cambrian to Ordovician,

volcanic arc and back-arc belts (Rogers and van Staal, 2002; Zagorevski et al., 2007). From east to west these units are termed the Tally Pond group (~513-509 Ma), the Long Lake group (~505 Ma), the Tulks group (~498 Ma), the Pats Pond group (~488 Ma), the Sutherlands Pond group (~462-457 Ma) and the Wigwam Brook group (~453 Ma) (Dunning et al., 1991; Evans and Kean, 2002; Rogers and van Staal, 2002; Pollock, 2004; Rogers et al., 2006; Zagorevski et al., 2007; McNicoll et al., 2010).

1.3 – Deposit Geology

The Victoria Lake Supergroup hosts VMS deposits in the Tally Pond and Tulks groups (Fig. 1.2; Swinden and Thorpe, 1984; Squires and Moore, 2004; Hinchey, 2007). These deposits are generally associated with bimodal, predominantly felsic-dominated sequences with variable amounts of sedimentary rocks (Swinden and Thorpe, 1984; Swinden et al., 2001; Squires and Moore, 2004; van Staal et al., 2007; Piercey and Hinchey, 2012).

The Tally Pond group contains two informal formations: the mafic dominated Lake Ambrose formation (~Lake Ambrose basalts of Dunning et al., 1991 and Evans and Kean, 2002), and the felsic-dominated Bindons Pond formation (~Boundary Brook formation of Dunning et al., 1991 and Evans and Kean, 2002). These rocks are crosscut by the Lemarchant microgranite, a fine- to medium-grained quartz-feldspar porphyritic intrusion that is considered to be syngenetic with the Lake Ambrose and Bindons Pond formations (Squires and Moore, 2004; Piercey and Hinchey, 2012). The generally underlying Lake Ambrose formation is considered the older of the two volcanic sequences (Copeland et al., 2008a, 2008b; Squires and Moore, 2004; McNicoll et al.,

2010). Overlying the Lake Ambrose and Bindons Pond formations are Caradocian black shales and Ordovician marine turbidites (Swinden and Thorpe, 1984; Evans and Kean, 2002). Middle Ordovician Harpoon Hill Gabbro sills and dykes cross cut the Tally Pond group and have ages of ~465 Ma (Pollock, 2004; Squires and Moore, 2004). Deformation of the Tally Pond group by an east-northeast striking antiform was accompanied by thrust faulting and greenschist facies metamorphism (Evans and Kean, 2002; Rogers and van Staal, 2002). Despite the regional deformation, most deposits in this belt show remarkably good preservation of volcanic rock and sulphide mineral textures (Squires et al., 2001; Evans and Kean, 2002; Squires and Moore, 2004; Piercey and Hinchey, 2012).

The Lemarchant VMS deposit is located in the southern part of the Tally Pond group, approximately 10 km southwest of the Duck Pond mine (Fig. 1.2). The deposit is hosted in a bimodal volcanic sequence, but the immediate host to mineralization is rhyolite; both units are minimally offset by several upright, east-west striking faults (Fig. 1.3; Copeland et al., 2008a; Fraser et al., 2012). The deposit was most recently displaced by the Lemarchant fault, an east-vergent, north-south-striking and west-dipping thrust fault that may have transported a portion of the mineralized zone northwest of the deposit (Fig. 1.3; Copeland et al., 2008a; Fraser et al., 2012). This "Northwest Zone" has been targeted by recent magnetic surveys and may be a structural repetition of the main mineralized zone (Fraser et al., 2012).

The Lemarchant deposit itself is hosted within a 4 km by 0.7 km upright anticline that consists of an unaltered felsic volcanic base overlain successively by ~40 m of moderate to strongly altered barite-rich pyroclastic volcanic rocks, <30 m of massive to

stringer sulfides in massive barite, and capped by a thin layer (generally <1m) pyritic mudstones (Fig. 1.4; Copeland et al., 2008a; Fraser et al., 2012). Felsic rocks, mineralization, and mudstones are overlain by variably magnetic mafic volcanic rocks (Fig. 1.4). The bimodal-felsic Lemarchant deposit consists of a barite-rich Zn-Pb semi-massive to massive sulfide mound and an underlying Cu-Zn stringer stockwork zone (Fraser et al., 2012).

1.4 – VMS deposits: Setting, classification and characteristics

Volcanogenic massive sulfide deposits are found in settings dominated by volcanic and volcaniclastic rocks, with or without abundant sedimentary and intrusive rocks, and form at or just below the seafloor from the venting of hydrothermal fluids (Franklin et al., 1981, 2005; Gibson et al., 2007; Galley et al., 2007). They are distinguished from other massive sulfide deposit types (i.e., sedimentary exhalative, or SEDEX) in that they form from high temperature fluid circulation and commonly contain abundant copper mineralization (Lydon, 1984, 1996; Franklin et al., 2005), unlike SEDEX deposits, which only contain Zn-Pb mineralization.

The VMS deposit model is generally well accepted and consists of six integral parts (Franklin et al., 1981, 2005): 1) a source of heat (i.e., subvolcanic intrusions) to initiate and drive the hydrothermal convection cell; 2) a reaction zone capped by a semi-permeable barrier in which metals are leached from country rock by hot hydrothermal fluids; 3) conduits, generally synvolcanic faults, through which fluids can escape from the reaction zone; 4) alteration zones formed in the footwall, and to a lesser extent in the hanging wall, as a result of fluid-rock interaction; 5) a massive sulfide ore body emplaced

at the footwall-hanging wall contact; and 6) hydrothermal sediment or exhalites, emplaced above and distal to the massive sulfide body (Fig. 1.5).

Districts that host volcanogenic massive sulfides occur in extensional tectonic regimes, in many cases associated with subduction zones, arc rifts, and back-arc basins in the ancient record (Lydon, 1996; Franklin et al., 2005; Galley et al., 2007; Piercey, 2011). Extensional activity caused thinning of the crust, magma upwelling beneath the rift, and provided the heat flow required to drive hydrothermal circulation (e.g., Swinden, 1991; Gibson et al., 2007; Piercey, 2011). Extensional environments also generated the deep structural conduits necessary for initiating large, long-lived hydrothermal convection systems (Lydon, 1996; Gibson et al., 2007). Bimodal volcanism is typical of some these tectonic settings (see below; Lydon, 1996; Galley et al., 2007; Piercey, 2011). Volcanogenic massive sulfide deposits rarely occur as singular deposits within a district; instead, they commonly form clusters of deposits along a well-defined stratigraphic horizon (e.g., Sangster, 1980; Lydon, 1996).

Volcanogenic massive sulfide deposits have been variously classified (e.g., Franklin et al., 1981; Large, 1992); however, the most commonly used classification scheme is the lithotectonic classification Barrie and Hannington (1999) that was later modified by Franklin et al. (2005) and Galley et al. (2007). The five lithotectonic classes include: 1) mafic; 2) mafic-siliciclastic; 3) bimodal-mafic; 4) bimodal-felsic; and 5) felsic-siliciclastic (Fig. 1.6; Franklin et al., 2005; Gibson et al., 2007; Piercey, 2011). The first three classes are primarily associated with mafic-dominated footwall assemblages and are distinguished by lesser amounts of sedimentary, felsic volcanic, or mafic-

ultramafic intrusive rocks, whereas the latter two classes are hosted by felsic-dominated footwall rocks with varying amounts of sedimentary and mafic volcanic rocks (Piercey, 2011). A further division of the bimodal-felsic deposit class was established by Galley et al. (2007) to include a hybrid bimodal-felsic class, which are deposits characterized by features found in both VMS and intermediate to high sulfidation epithermal Au-Ag deposits.

Regardless of the classification scheme, most VMS deposits are composed of two distinct parts: 1) the massive sulfide mound or lens, situated atop (2) a siliceous, stringer-sulfide-bearing stockwork (Lydon, 1984; Lydon, 1996). Generally, mineralization displays distinctive zoning from lower temperature, earlier formed Zn-Pb mineralization in the outer portions of the mound/lens, to higher temperature, later formed Cu-rich mineralization at the core of the mound/lens and in the stringer zone (Eldridge et al., 1983; Lydon, 1984, 1988; Large, 1992; Ohmoto, 1996; Franklin et al., 2005). This zonation is interpreted to be a consequence of temperature gradient and subsequent zone refinement within the sulfide mound (e.g., Eldridge et al., 1983; Lydon, 1988; Large, 1992; Ohmoto, 1996). There is also a general zonation observed in the hydrothermal alteration associated with mineralization, from distal, lower temperature sericitic alteration (~Zn-Pb association) to more proximal chloritic alteration (~Cu association) (e.g., Riverin and Hodgson, 1980; Gemmell and Large, 1992; Franklin et al., 1981, 2005).

1.4.1 – Mechanisms of massive sulfide deposition

The formation of volcanogenic massive sulfide deposits is dependent on the evolution and venting behaviour of the hydrothermal fluid. Shallowly emplaced plutons

heated seawater entrained in the overlying, semi-permeable volcanic sequence and initiated a convection cell as the heated fluid rose and was replaced with ambient seawater (Lydon, 1988, 1996). The circulating hot fluid stripped base and precious metals from the country rock reservoir, and became metal-enriched as it rose along structurally controlled boundaries (Fig. 1.5). Upon reaching the seafloor, mixing with seawater resulted in a decrease in temperature and oxidation of the metal- and sulfur-rich hydrothermal fluid (Hannington and Scott, 1989; Huston and Large, 1989; Lydon, 1996; Franklin et al., 2005). As venting continued, sulfates, namely anhydrite, precipitate and formed a porous column (chimney) surrounding the orifice, which was subsequently replaced with sulfides (Lydon, 1988, 1996). The retrograde solubility of anhydrite causeed mechanical collapse of the porous column as the system cooled, and a mound began to form from the rubble of collapsed hydrothermal chimneys. Continued escape of the fluid through this pile caused reworking and zone refinement of the sulfides precipitated. Enlargement of the insulating mound subsequently retarded fluid flow and a stockwork was formed from the hydrothermal reservoir below the mineralized mound.

As discussed above, primary mineralization in VMS deposits is predominantly derived from a hydrothermal fluid formed by recirculated seawater that has reacted with the surrounding, generally mafic, ocean floor rocks (up to 2 km depth) (Franklin et al., 2005; Galley et al., 2007; Gibson et al., 2007). However, some VMS deposits contain sulfide mineral assemblages with unusual enrichments in precious and/or trace metals similar to some epithermal-type ore deposits. This strongly implies the additional presence of magmatic fluids derived from associated intrusions, or that these elements

were derived from the leaching of more felsic volcanic rocks (Stanton, 1991; Lydon, 1988, 1996; Sillitoe et al., 1996; Galley et al., 2007). Hydrothermal fluids with magmatic fluid input that are vented at relatively shallow seafloor depths (less than 1500 m; Butterfield et al., 1990; Hannington et al., 1995; Hannington and Monecke, 2009) can boil, effectively precipitating precious and/or trace elements in sulfide mineral assemblages characteristic of some epithermal-type deposits (i.e., bornite, tennantite, enargite, electrum, covellite; Lydon, 1996; Sillitoe et al., 1996).

Anomalous alteration mineral assemblages can also exist in cases where magmatic fluids have made a significant contribution to the hydrothermal fluid, mostly as advanced argillic alteration with phases such as alunite, kaolinite, pyrophyllite and quartz (Fig. 1.7; Sillitoe et al., 1996; Huston and Kamprad, 2001; Galley et al., 2007). Furthermore, polymetallic massive sulfides commonly contain enrichments of "epithermal suite" elements, especially Au, Ag, Sb, As, Hg, Bi, and Te. Consequently, the ore mineral assemblage may contain minerals such as tennantite, tetrahedrite, enargite, luzonite, bornite and covellite, tellurides, orpiment and realgar (e.g. Sillitoe et al., 1996; Roth et al., 1999; Hannington et al., 1999; Galley et al., 2007). These minerals are indicative of acidic, oxidized, and sulfur-rich hydrothermal fluids that are considered by Sillitoe et al. (1996) to represent transitional, intermediate to high sulfidation epithermal-type VMS environments (Fig. 1.7).

1.4.2 – Gold enrichment in the VMS environment

The occurrence of gold in volcanogenic massive sulfide deposits is not uncommon, but has historically been of secondary economic significance in deposits with an

abundance of base metal ore (Huston, 2000). Recent compilations of Au content in VMS deposits (e.g., Huston and Large, 1989, Hannington et al., 1999; Huston, 2000; Mercier-Langevin et al., 2011) have revealed that certain deposits have gold as a secondary product, or produce gold as the primary commodity. The polymetallic Lemarchant VMS deposit contains anomalous silver and gold associated with the barite-rich sulfide mound mineralization (Fraser et al., 2012). A detailed understanding of the process(es) that cause Au-enrichment in this and other VMS deposits is therefore critical to designing an effective model for exploring and developing Au-rich VMS deposits.

Because gold is a relatively inert precious metal, specific physicochemical conditions permit Au to form complexes with various ligands, become solvated and then mobilized by a fluid. Extremely oxidizing, acidic conditions at ambient temperatures, or temperatures greater than 350°C, favour the transport of gold in solution as a chloride complex (Stefánsson and Seward, 2004; Williams-Jones et al., 2009). However, in shallow, slightly alkaline submarine environments with hydrothermal fluid temperatures below 350°C, Au is transported in solution predominantly as a bisulfide complex (Seward, 1973; Huston and Large, 1989; Williams-Jones et al., 2009).

When solute complexes become unstable, Au precipitates from the hydrothermal fluid. In the case of the Au-bisulfide complex, mechanisms such as cooling, sulfidation and boiling will cause precipitation, due to decreased HS^- activity and increased pH of the transport fluid (Seward, 1973; Huston and Large, 1989; Williams-Jones et al., 2009). If chloride complexes are facilitating Au transport in the VMS environment, mixing with a more dilute fluid is considered the most efficient mechanism for deposition from the

carrier hydrothermal fluid. Later supergene transport and deposition of gold is possible in shallowly exhumed deposits, but this is entirely dependent upon ambient climate, and occurs within organic solutions (i.e., acidic groundwater, petroleum) or supersaturated fluids (Williams-Jones et al., 2009).

Hydrothermal fluids associated with the formation of VMS and epithermal-Au deposits are relatively sulfur-rich and sufficiently hot enough to promote bisulfide complexation of gold (Hannington and Scott, 1989; Huston and Large, 1989; Sillitoe et al., 1996; Hannington et al., 1999). Some Au-rich VMS deposits show evidence of deposition in water depths of less than 1500 m, at confining pressures that may have permitted boiling of fluids venting at or near the seafloor, and consequent de-stabilization of the Au-bisulfide complex to precipiate Au (Butterfield et al., 1990; Hannington et al., 1993; Sillitoe et al., 1996; Lydon, 1996; Roth et al., 1999; Huston, 2000; Hannington et al., 2009).

1.5 – Thesis objectives

Despite exploration of the Lemarchant property since the 1980s there has been very little research undertaken on the mineralization at Lemarchant. In particular, there has been no documentation of the style of mineralization, zoning of base and precious metals, or a clear understanding of the origin of high-grade base and precious metal enrichment. This thesis addresses these issues to provide a comprehensive descriptive and genetic model for the Lemarchant VMS deposit. The general goals of the thesis are two-fold: (1) to create a physical deposit model, and (2) to propose a genetic model of deposit genesis, based on the characteristics of the deposit model. Detailed documentation of the

setting and styles of mineralization, zonation of base and trace metals, and deportment of precious metals (Ag, Au) are used to define the deposit model. The physicochemical characteristics defined by the deposit model, and related isotope geochemistry, provide a basis for understanding the conditions of enrichment, transportation and deposition of precious metals at Lemarchant. This model of deposit genesis is then compared to other VMS deposits in the Appalachians, and precious metal enriched VMS deposits globally.

1.6 – Methods

A deposit model and a genetic model for Lemarchant are defined using: (1) documentation of styles of mineralization from drill core logging, thin section petrography and scanning electron microprobe (SEM) analyses; (2) major and trace element mineral compositions from electron microprobe analyses (EMPA) and laser ablation inductively coupled plasma mass spectrometry (LA-ICP-MS); and 3) sulfur and lead isotope compositions of sulfide minerals from *in situ* secondary ion mass spectrometry (SIMS) of polished section. Detailed descriptions of each type of analysis are documented below.

1.6.1 – Core logging

Detailed drill core logging was undertaken on NQ-sized and BQ-sized core from the Lemarchant deposit in June-August 2012 and 2013 using core previously drilled by Canadian Zinc Corp., Paragon Minerals Corp., Noranda Inc. and Altius Minerals Corp. Core was logged in the immediate mineralized zones and ~50 m up- and down-hole from mineralization, in order to document host rock stratigraphy and alteration associated with mineralization. Unmineralized holes along and perpendicular to strike of the main drilling

trend (NNW; Fig. 1.4) were logged for comparison. Stratigraphic sections were created in the field, with supplementary notes, photos and sample numbers recorded in a field journal. Photographs were taken of all samples, along with supplementary photographs of the mineralization or alteration. A total of 154 samples of halved core were taken, which varied from 5 cm to 10 cm in length. Stratigraphic sections were digitized using Adobe Illustrator software (Appendix A). Lithological layers and mineralogical facies were extrapolated between drill holes, and 2-dimensional fence diagrams of mineralization were created to further constrain ore facies zonation within the Lemarchant VMS deposit.

1.6.2 – Petrography

All core samples were cut down to standard microscope slide size (4.5cm x 2.5cm) using a water-cooled rock saw in the Core Research Equipment and Instrument Training Network (CREAIT)-TERRA facility at Memorial University. Quartered drill core was retained and archived. A total of 143 cut samples were sent to Vancouver Petrographics and prepared as polished thin sections. Preliminary petrographic work was undertaken with a Nikon LV100POL polarizing microscope at Memorial University; reflected and transmitted light microscopy were used to document the petrography, mineral assemblages, textures and paragenesis. A subset of thin sections was analyzed with the FEI MLA 650F SEM at the CREAIT-Micro-Analysis Facility, Inco Innovation Centre (MAF-IIC). Relevant micro-textures were identified using backscatter electron imaging. Semi-quantitative element maps, line scans, and individual mineral spectra were also utilized to characterize the mineralogy. Mineral Liberation Analysis (MLA) coupled with SEM was performed on each type of mineralization to identify small mineral phases

not readly discerned using standard petrography, primarily due to the similar colouration of some phases and the difficulty in distinguishing between barite, galena and tetrahedrite, which are very common phases in the Lemarchant deposit. The SEM analyses were particularly important for the identification of microscopic precious metal associations in the thin sections.

1.6.3 – Ore mineral chemistry

Major and trace element contents of sulfide minerals were determined in 22 thin sections using the JEOL JXA-8230 electron microprobe at the Queen's University Facility for Isotope Research (QFIR) in Kingston, Ontario. Trace element compositions, where appropriate, were obtained from 19 of the above 22 thin sections previously analyzed by EMPA, using LA-ICP-MS with an ESI NWR-193nm Excimer laser coupled to a ThermoFisher X-Series 2 Quadrupole ICP-MS at QFIR. Major and trace element data were used to examine possible sources of metals, and the physicochemical conditions of the hydrothermal fluids that resulted in precious metal enrichment at Lemarchant (see Chapter 2).

1.6.4 – *In situ* sulfur and lead isotope geochemistry

Sulfur and lead isotope compositions were measured in the offcuts of eight thin sections via SIMS at CREAIT-MAF-IIC. *In situ* stable and radiogenic isotope data supplemented major and trace element chemical data by providing further insight into the possible sources of sulfur and lead in the Lemarchant VMS deposit (see Chapter 3).

1.7 – Presentation

The contents of this thesis are presented in manuscript format and is comprised of two chapters based on articles that will be submitted for publication in peer-reviewed journals. The introduction to this project (this chapter) is followed by an article outlining the mineralogy, mineral chemistry, and base and precious metal zonation of the Lemarchant deposit (Chapter 2), and a second article describing the results of in situ stable and radiogenic isotope analyses of Lemarchant sulfides (Chapter 3). A summary of these results, and a concluding statement on a unified genetic model for the Lemarchant VMS deposit are presented in Chapter 4. Appendices include compiled graphic logs (Appendix A), two previously published government reports (Appendices B and C), and extended methods for analyses and reduction of data via EMPA (Appendix D), LA-ICP-MS (Appendix E), and SIMS (Appendix F).

1.8 – Co-authorship statement

The construction and design of this research project is attributed to Dr. Stephen J. Piercey, along with contributions from Dr. Graham D. Layne, Christine A. Devine and Dave A. Copeland. The author conducted primary research, including core logging and optical microscopy. Scanning electron microscopy was conducted by the author, and supervised by Michael Schaffer; Brian Joy and the author conducted electron microprobe analyses; laser ablation ICP-MS was conducted by the author in conjunction with Dr. Dan Layton-Matthews and Michael Gadd; and SIMS was conducted by Glenn Piercey and the author. Reduction and interpretation of data are attributed primarily to the author. The

primary editor of this manuscript is Dr. Stephen J. Piercey, with secondary editing performed by Dr. Graham D. Layne and Dr. Dan Layton-Matthews.

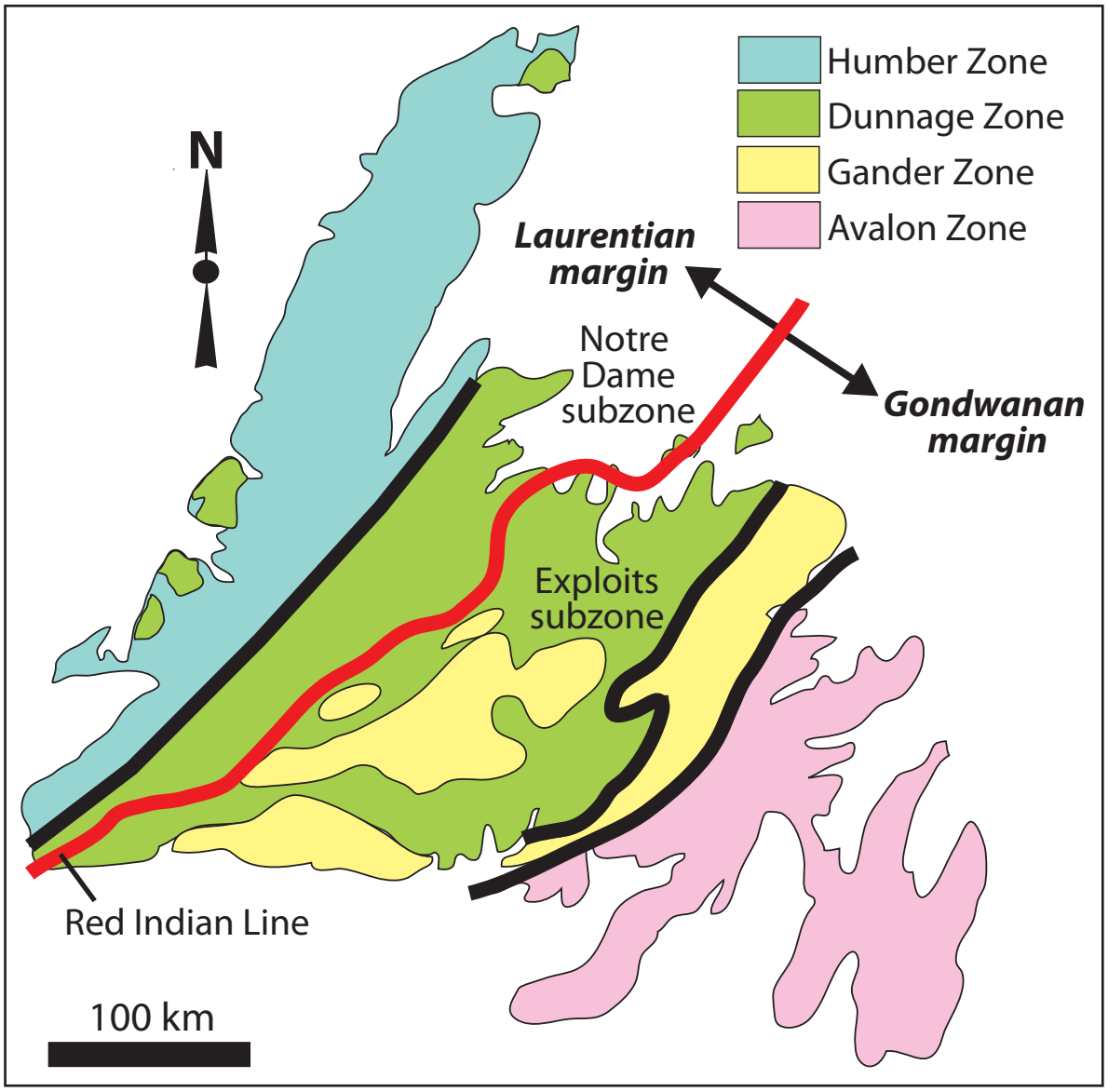

Figure 1.1. Tectonostratigraphic map of Newfoundland (modified from Rogers et al., 2006).

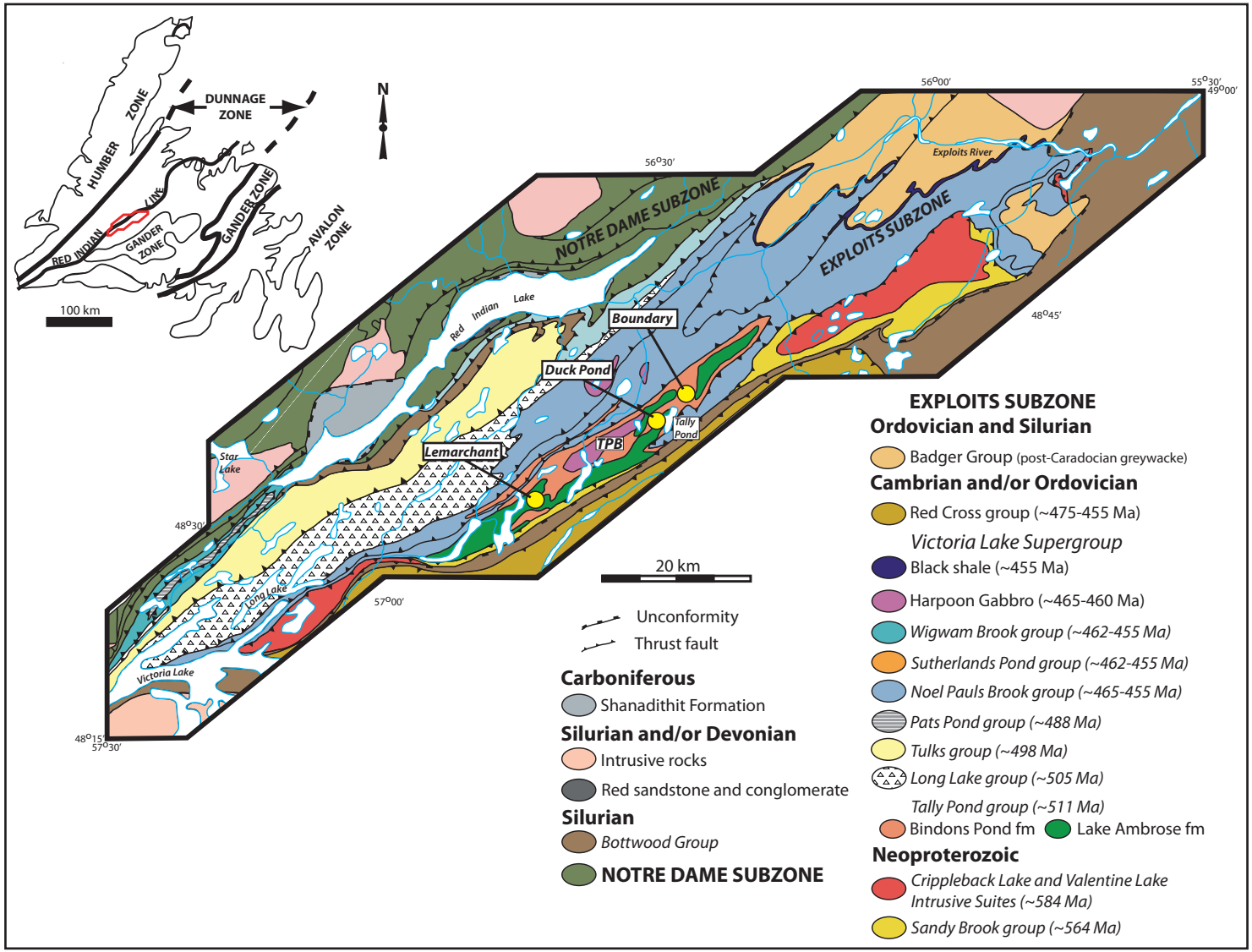

Figure 1.2. Geological map of the central Exploits subzone, highlighting the Tally Pond group of the Victoria Lake Supergroup (after Rogers et al., 2006; McNicoll et al., 2010; Piercey and Hinchey, 2012). TPB = Tally Pond belt.

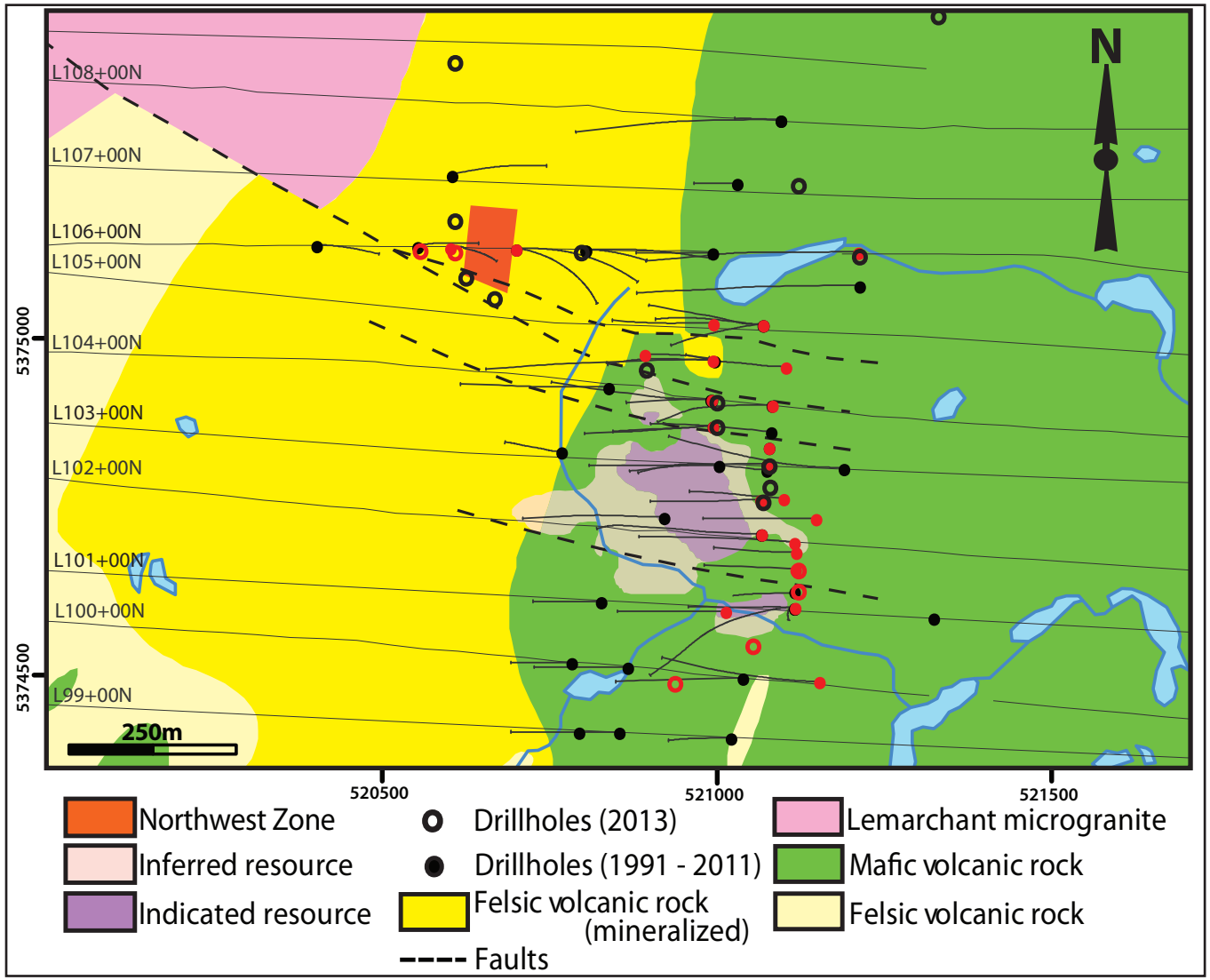

Figure 1.3. Geological map of the Lemarchant deposit displaying the bimodal volcanic character of the district (modified from Fraser et al., 2012). Inferred and indicated resources, and Northwest Zone are projected to surface. East-west sections of the deposit are indicated on left-hand side, and logged drill holes are indicated by red markers.

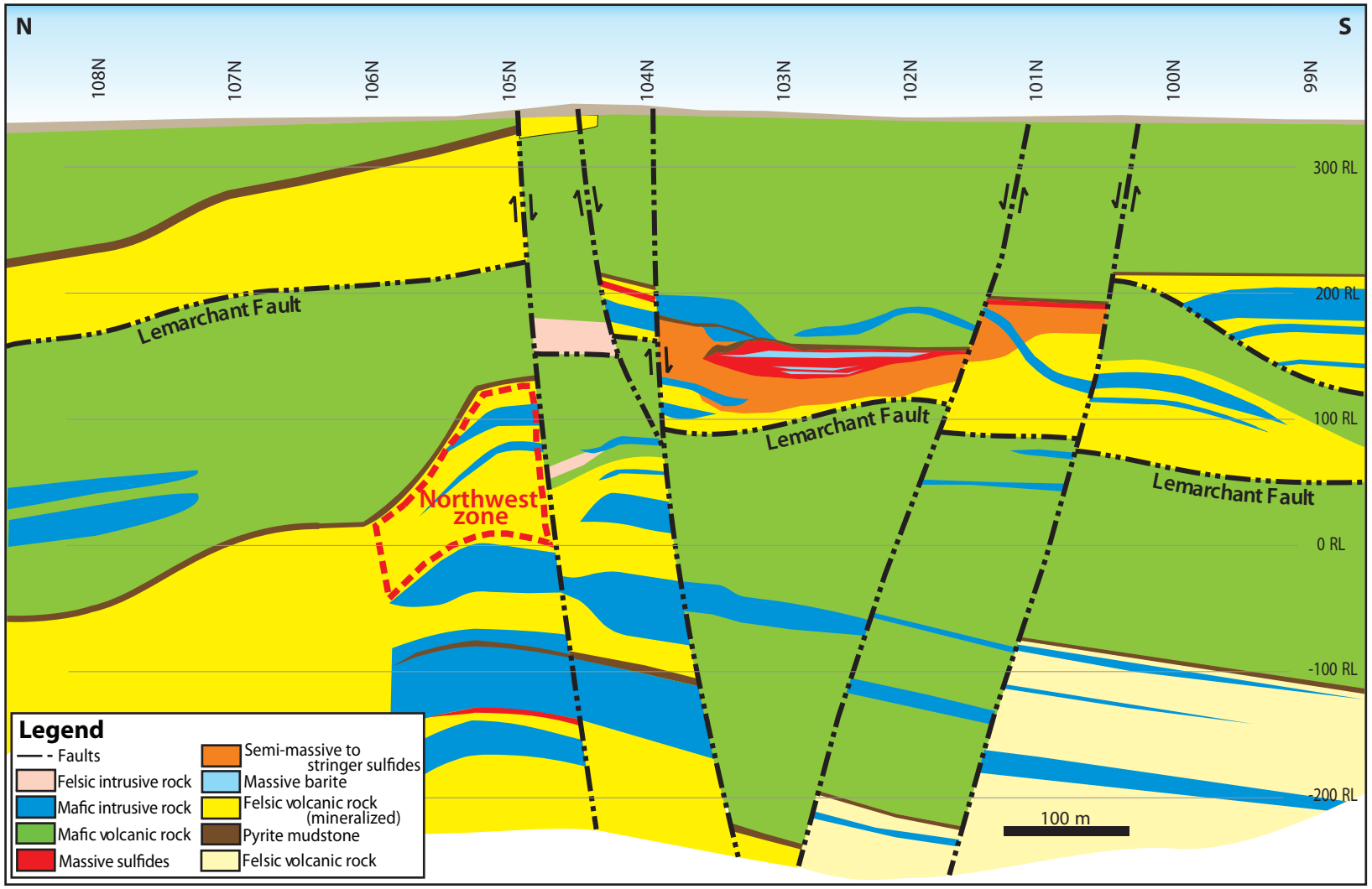

Figure 1.4. Long section, looking east, of the Lemarchant deposit through the main mineralized zone at the 521000 Easting (see Fig. 1.3); the Northwest zone has been projected onto the section from the west (modified from Fraser et al., 2012).

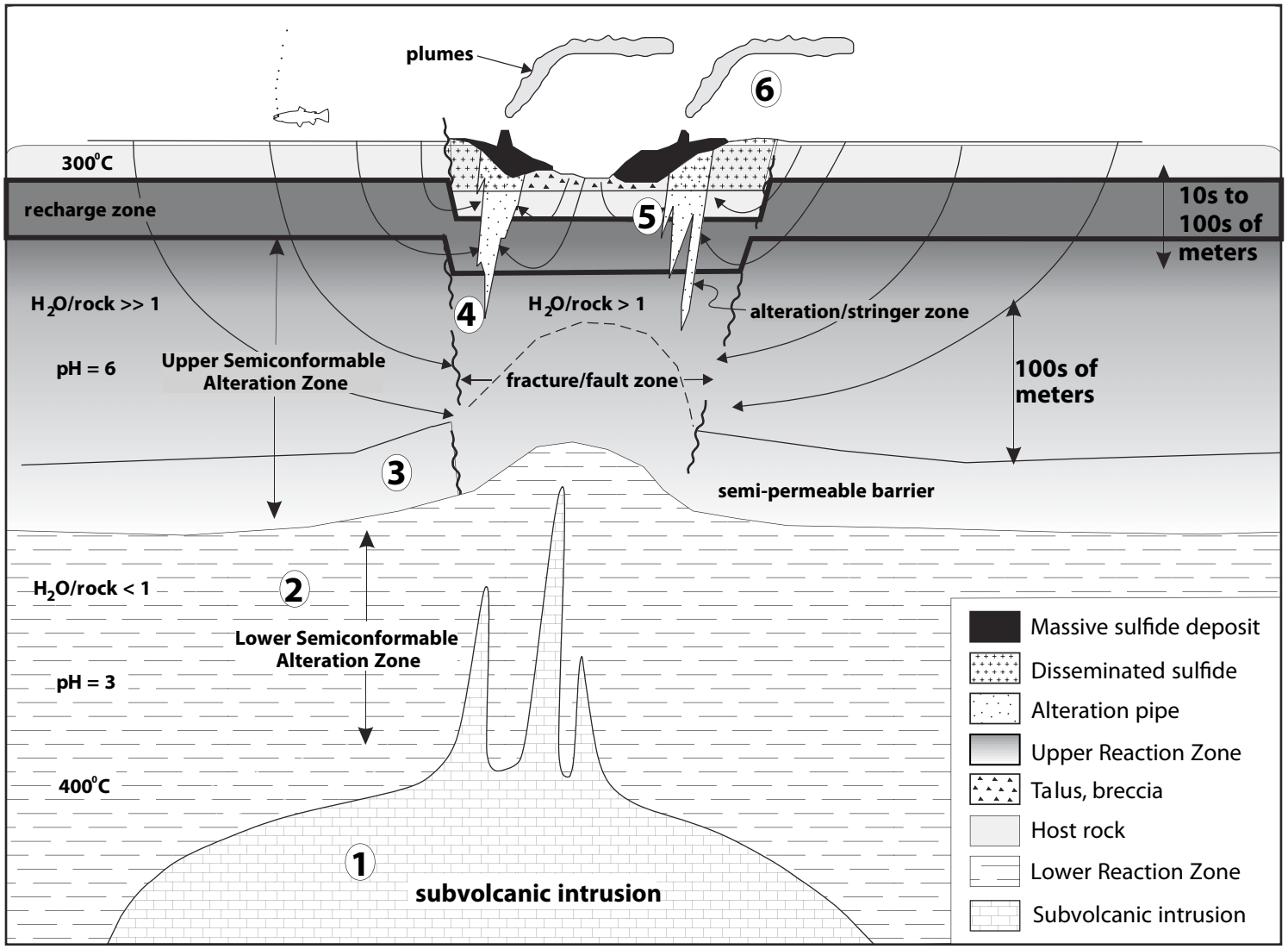

Figure 1.5. Idealized diagram of essential components in the volcanogenic massive sulfide-forming environment (after Galley et al., 2003; Franklin et al., 2005; Gibson et al., 2007).

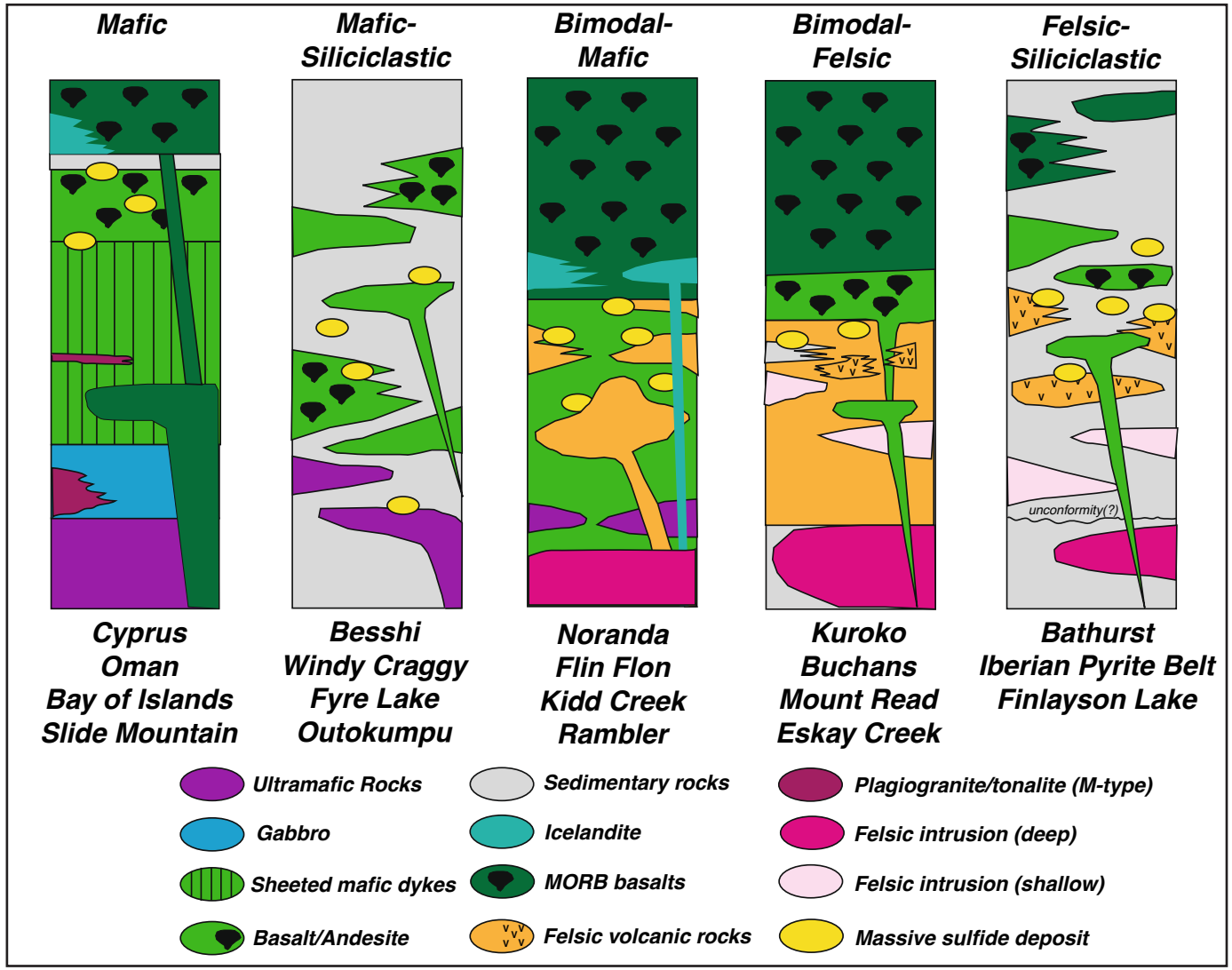

Figure 1.6. Generalized stratigraphic sections representing the five types of lithotectonic settings for VMS districts as outlined by Franklin et al. (2005) (diagram after Piercey, 2011).

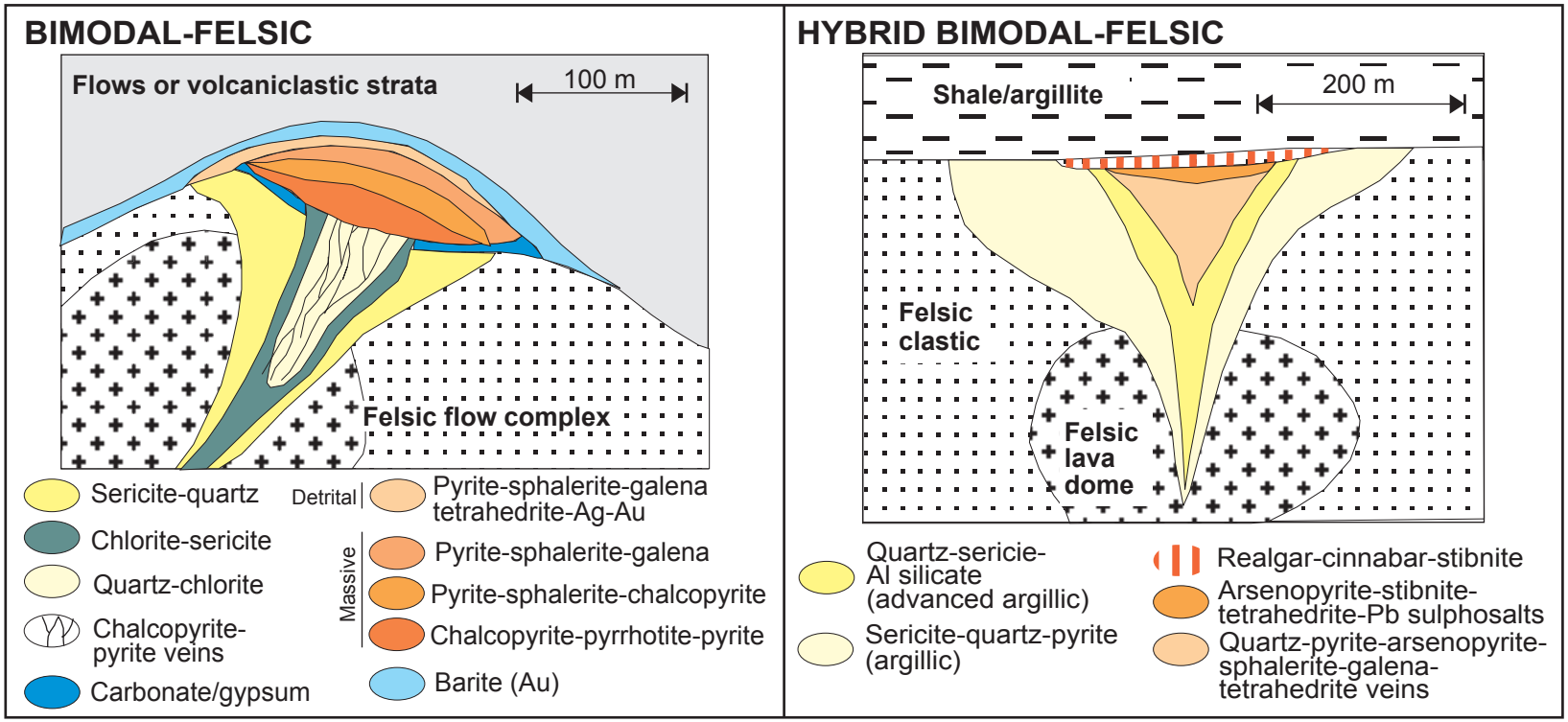

Figure 1.7. General lithostratigraphic representations of bimodal felsic-type VMS deposits. Hybrid bimodal felsic-type added by Galley et al. (2007) after the description by Franklin et al. (2005) to include transitional, high sulfidation epithermal-analogue VMS deposits (after Galley et al., 2007).

Chapter 2: Mineralogy, metal zoning, and genesis of the Cambrian Zn-Pb-Cu-Ag-Au Lemarchant volcanogenic massive sulfide (VMS) deposit, Newfoundland

2.1 – Abstract

The Lemarchant deposit is a Cambrian bimodal felsic Zn-Pb-Cu-Ag-Au volcanogenic massive sulfide (VMS) deposit located in the Central Mobile Belt, Newfoundland. Despite regional greenschist metamorphism and faulting, primary mineralogy and mineral textures are well preserved, and the deposit is a type example of an Appalachian precious metal-enriched VMS deposit. Mineralization consists of a stratiform massive sulfide zone that lies at the contact between a rhyolitic footwall and a mafic hanging wall. A stringer sulfide zone that is hosted in footwall rhyolite breccia underlies the massive sulfide lens. The stratiform zone contains massive barite that is heterogeneously replaced by sphalerite and pyrite, lesser galena, and trace chalcopyrite. The stringer zone contains chalcopyrite, pyrite, and lesser sphalerite and galena. Sphalerite ranges in colour from white (low-Fe) to red (high-Fe). The palest sphalerite (<1 wt‰ Fe) occurs in the barite-rich startiform zone and is associated with early stage exhalative mineralization, intermediate sulfidation epithermal suite minerals (tetrahedrite, bornite, colusite, electrum, covellite) and sulfide minerals enriched in the epithermal trace element suite (Au, As, Bi, Co, Cr, In, Mo, Ni, Sb, Se, Te). Darker sphalerite (2.7-8 wt‰

Fe) in the stratiform zone overprints early stage mineralization and occurs with chalcopyrite; high Fe sphalerite is also present in the stringer zone.

Early exhalative/epithermal-type VMS mineralization was deposited from low temperature (150-250°C), oxidized, acidic to near neutral hydrothermal fluids with high sulfur activity, likely in relatively shallow water (<1500 mbsl) that intermittently boiled and deposited Au in the stratiform zone. Late stage polymetallic, Cu-rich VMS mineralization was likely deposited from higher temperature (>300°C), less oxidized, near neutral hydrothermal fluids likely in deeper water (>1500 mbsl). Abundant epithermal suite minerals and epithermal trace element suite-enriched sulfides at Lemarchant are evidence for a direct magmatic contribution to the hydrothermal fluid.

2.2 – Introduction

Precious metal-bearing volcanogenic massive sulfide (VMS) deposits are a sub-type of VMS deposit (Sillitoe et al., 1996; Hannington et al., 1999; Huston, 2000; Dubé et al., 2007a; Mercier-Langevin et al., 2011). However, the distribution of precious metals within VMS deposits, and the processes of precious metal enrichment, are have not been adequately described and are not clearly understood. Many precious metal-enriched VMS deposits also display enrichments in epithermal suite elements (e.g., As, Sb, Sn, In, Hg, Mo; Sillitoe et al., 1996; Hannington et al., 1999; Cooke and Simmons, 2000), have anomalous aluminous alteration (e.g., Mount Lyell, Tasmania; Huston and Kamprad, 2001; LaRonde Penna, Canada; Mercier-Langevin et al., 2007), and show evidence for deposition in shallow water volcanic environments (e.g., Nurukawa, Japan; Yamada et al., 1988; LaRonde-Penna and Bousquet 2, Canada; Dubé et al., 2007b). This sub-type of

VMS deposit commonly occurs in bimodal felsic lithostratigraphic sequences associated with rifted arc/back-arc basin environments (Franklin et al., 2005; Hannington et al., 2005; Hannington and Monecke, 2009). Modern precious metal-enriched seafloor massive sulfide (SMS) deposits generally posess the above features, but are also characterized by sulfur and helium isotope signatures that provide strong evidence for magmatic fluid involvement during their genesis (de Ronde et al., 2001; de Ronde et al., 2005). Magmatic fluid involvement is also considered important in the enrichment of Au, Ag and epithermal suite elements in ancient precious metal-rich VMS deposits (Herzig et al., 1993; Sillitoe et al., 1996; Hannington et al., 1999; Scotney et al., 2005; Hannington et al., 2005; Dubé et al., 2007a).

Numerous studies have suggested that the formation of precious metal-enriched VMS deposits is due to a unique combination of the fluid chemical conditions and geological setting. Hannington and Scott (1989) and Hannington and Monecke (2009) showed that low temperature (<250°C), oxidized hydrothermal fluids with high sulfur content (fS_2) are ideal for the transport of substantial gold in the VMS environment. Similarly, Huston and Large (1989) demonstrate that near neutral, oxidized, low salinity, 150°-275°C fluids with high fS_2 are highly efficent transporting significant gold in solution. Huston and Large (1989) also define two element associations with Au in VMS deposits: 1) Cu-Au; and 2) Zn-Pb-Ag-Au, which are interpreted to reflect gold transport in fluids by $AuCl_2^-$ and by $Au(HS)_2^-$, respectively (c.f., Seward, 1973). Deposition of gold in the SMS and VMS environments is strongly controlled by boiling and the depth-to-boiling curve for seawater (Bischoff and Rosenbauer, 1983; Bischoff and Rosenbauer,

1984; Butterfield et al., 1990). Boiling of the hydrothermal fluid in shallow seafloor environments (<1500 mbsl) is especially effective at inducing gold precipitation from solution (Huston, 2000; Hannington et al., 2009).

Despite the general understanding of precious metal-enrichment processes in modern SMS and some ancient VMS deposits, precious metal-enrichments in Appalachian VMS deposits are not well understood, with some exceptions (Bathurst, New Brunswick; McClenaghan et al., 2009; Ming Mine, Newfoundland; Brueckner et al., 2014). In particular, the styles of mineralization, mineralogy, precious metal associations, mineral chemistry and physicochemical conditions deposit formation are poorly understood.

The Lemarchant VMS deposit is a well-preserved example of an Appalachian precious metal-bearing massive sulfide deposit that is hosted by the Cambrian Tally Pond group, central Newfoundland, Canada. The deposit has a combined geological resource of 2.58 Mt grading 54.62g/t Ag and 1.00 g/t Au, yet is located in the same volcanic belt as the precious metal-poor Duck Pond and Boundary deposits (Fraser et al., 2012). Gold- and Ag-bearing massive sulfides at Lemarchant are characterized by Zn-Pb-Ba-rich mineralization with abundant sulfosalts and epithermal suite element enrichment. The Lemarchant deposit represents a type example of precious metal-enriched Zn-Pb-Cu VMS mineralization within the Appalachians that has similarities with precious metal-rich VMS globally (e.g., Wetar, Indonesia; Scotney et al., 2005; La Plata, Ecuador; Chiaradia et al., 2008).

Herein, a documentation of the mineralization styles and mineralogy of the Lemarchant deposit is provided through drill core analysis, petrography and scanning electron microscopy (SEM). The sulfide mineral assemblages, precious metal associations, and their compositional variations, are described using SEM, electron microprobe analysis (EMPA) and laser ablation inductively coupled plasma mass spectrometry (LA-ICP-MS). These data provide detailed documentation of the Lemarchant VMS deposit and insights into the setting of mineralization, physicochemical conditions of formation and genesis of the deposit. The results have implications for precious metal-enriched VMS deposits in the Appalachians and globally.

2.3 – Geological setting

2.3.1 – Regional geology

The Lemarchant deposit is located in the Dunnage Zone of the Newfoundland Appalachians, which is host to the majority of volcanogenic massive sulfide occurrences in Newfoundland (Swinden et al., 1988; Piercey, 2007; Piercey and Hinchey, 2012). The Exploits subzone comprises the southeastern section of the Dunnage Zone, and is composed of volcanic arc, back-arc and sedimentary rocks (Kean and Evans, 1988; Swinden, 1991; Rogers et al., 2006; McNicoll et al., 2010). The oldest sequence in the Exploits subzone is composed of a succession of Cambrian to Pre-Caradocian volcanic arc, back-arc and nascent to rifted arc rocks termed the Victoria Lake Supergroup (Fig. 2.1; Swinden, 1991; Dunning et al., 1991; Evans and Kean, 2002; Rogers et al., 2006; McNicoll et al., 2010). The Cambrian Tally Pond group forms the base of the Victoria Lake Supergroup and is overlain by the younger successions in the Tulks Volcanic belt,

which was further divided by Rogers et al. (2006) and Zagorevski et al. (2007) into discrete stratigraphic packages (Fig. 2.1).

The Tally Pond group, host to the Lemarchant deposit, is a bimodal succession of ~513-509 Ma (Pollock, 2004; McNicoll et al, 2010) tholeiitic mafic and mostly calc-alkaline felsic with minor mafic volcanic rocks, respectively called the Lake Ambrose and Bindons Pond formations (~Lake Ambrose basalts and Boundary Brook formation of Dunning et al., 1991 and Evans and Kean, 2002). Mineralization is concentrated in the felsic volcanic-dominated Bindons Pond formation (McNicoll et al., 2010). The Tally Pond group is crosscut by Ordovician diabase to gabbroic intrusions, sourced from the Harpoon Hill Gabbro intrusion to the north-east, and by the likely synvolcanic Lemarchant microgranite that outcrops ~400m northwest of the Lemarchant deposit (Fig. 2.2; Squires and Moore, 2004; McNicoll et al., 2010; Fraser et al., 2012). Neoproterozoic volcanic (Sandy Brook group) and intrusive (Cripplebback Lake Suite) rocks occur below the Tally Pond group and are not considered part of the Victoria Lake Supergroup; rather, the Sandy Brook group and Cripplebback Lake Suite form the basement through which the Tally Pond group was erupted (McNicoll et al., 2010; Piercey and Hinchey, 2012). The Tally Pond group is interpreted to have formed as a peri-Gondwanan nascent to rifted arc (Evans and Kean, 2002; Rogers et al., 2006; van Staal and Barr, 2012; Piercey et al., 2014).

2.3.2 – Deposit geology and host rock lithology

The Lemarchant deposit consists of a stratiform massive to semi-massive sulfide zone and a thin, possibly truncated, underlying stringer sulfide zone. The upper massive

sulfide zone strikes north-northwest for 350m and is ~20m thick (Figs. 2.2 and 2.3a). Massive to semi-massive mineralization is hosted at the contact between hanging wall mafic volcanic rocks and footwall rhyolitic volcanic rocks of the Lake Ambrose formation and Bindons Pond formation, respectively (Fig. 2.3a-c). The massive sulfides and hanging wall-footwall contact are marked by a thin, pyrite-rich mudstone layer that is laterally extensive and locally present in the hanging wall basalts overlying mineralization (Fig. 2.3 and 2.4a-b).

The felsic volcanic footwall consists of calc-alkaline, aphyric rhyolite breccia and rhyolite flows that contain devitrified glass fragments and are interbedded with rhyolite lapilli tuff, tuff breccia and polylithic lapilli tuffs (Squires and Moore, 2004; Copeland et al., 2008a; Copeland et al., 2008b). Massive granular, and locally bladed, barite immediately overlies the felsic footwall in the stratiform zone, and is intergrown with and replaced by sulfide mineralization. Barite and sulfides in the lower stratiform zone occur interstitial to rhyolite breccia and lapilli tuff breccia, and variably replace the felsic lapilli tuff. The stringer zone crosscuts the felsic footwall below the stratiform zone, and is devoid of barite mineralization. A pyritic and variably graphitic mudstone layer conformably overlies the deposit and is interpreted to be an exhalative (chemical sedimentary) unit (Copeland et al., 2008b; Lode et al., 2012). Minor base and precious metal mineralization (i.e., chalcopyrite, galena, electrum) crosscuts the fine-grained pyrite-bearing mudstone, suggesting the exhalative unit was deposited prior to the massive and semi-massive sulfide mineralization (Lode et al., 2014). However, as noted above, hanging wall mafic flows proximal to the felsic footwall are locally intercalated

with mudstone and hematitic chert, and are weakly hydrothermally altered, indicating hydrothermal activity persisted after initial eruption of the hanging wall mafic rocks (Copeland et al., 2008a; Copeland et al., 2008b; Lode et al., 2014). The mafic hanging wall is composed of dark green, variably magnetite-bearing, pillowed, vesicular to massive, transitional to calc-alkaline, basalt and basaltic andesite flows (Copeland et al., 2008a; Copeland et al., 2008b; Piercey and Hinchey, 2012).

Light brown, pyroxene-phyric mafic dykes crosscut both mineralization and the hanging wall and footwall rocks. The dykes have wispy, peperitic contacts with variable amygdule content and, based on these characteristics, are likely synvolcanic (e.g., Gibson et al., 1999). Greenish-brown, medium-grained gabbro to diabase dykes and pink to white, aphyric to quartz-phyric felsic intrusions are less abundant; they have sharp contacts and crosscut both mineralized footwall rocks and pyroxene-phyric synvolcanic dykes (Pollock , 2004; Squires and Moore, 2004; Copeland et al., 2008a).

Alteration in the felsic footwall is dominated by quartz and sericite, with minor chlorite and albite (Squires and Moore, 2004; Copeland et al., 2008a; Copeland et al., 2008b). However, chlorite alteration is locally pervasive in footwall rhyolite and felsic volcaniclastic rock; intensely chlorite-altered fragments (relict volcanic glass?) occur locally in rhyolite breccia and lapilli tuffs. Mafic flows proximal to the footwall have weak silica-chlorite-epidote alteration (Squires and Moore, 2004; Copeland et al., 2008a; Copeland et al., 2008b). Post-depositional carbonate alteration is present in all lithologies and includes disseminated rhombic calcite and ankerite, and crosscutting quartz-carbonate

veinlets. Deformed synvolcanic dykes have carbonate bleaching and are variably fuchsite-bearing.

The Lemarchant deposit and other VMS occurrences within the Tally Pond group are thrust imbricated and have experienced lower greenschist grade regional metamorphism during Silurian-Devonian tectonism. However, despite post-depositional faulting, the stratigraphy and deposit features are exceptionally well preserved (Dunning et al., 1991; Squires and Moore, 2004; Rogers et al., 2006). Post-mineralization deformation created and/or reactivated a number of east-west-trending, upright faults that slightly offset portions of the Lemarchant deposit vertically and horizontally (Fig. 2.3a) and created a north-trending, gently west-dipping thrust fault (the Lemarchant fault; Squires and Moore, 2004; Copeland et al., 2008a; Fraser et al., 2012). Section L10600N is down-dip of the main Lemarchant deposit, 200m north-northwest of the Main Zone, and contains the "Northwest Zone" (Fig. 2.2 and 2.3a; Fraser et al., 2012). Sulfide layers observed in L10600N are texturally and geochemically similar to the single mineralized horizon in the Main Zone, and may indicate stacking of thrust sequences due to the Lemarchant fault.

2.4 – Mineralization

The Lemarchant deposit displays five distinct styles of mineralization; four mineral assemblages compose the stratiform zone and one mineral assemblage composes the underlying stringer zone (Fig. 2.4a-b). Type 1 consists of granular barite and semi-massive sulfides that include white to honey sphalerite, subordinate fine-grained pyrite, galena, and minor chalcopyrite and tetrahedrite-tennantite (Fig. 2.5a). The type 2 mineral

assemblages crosscut the type 1 mineral assemblage (Fig. 2.5b-d). Type 2A consists of bornite, galena and minor chalcopyrite stringers (Fig. 2.5b-c) and type 2B consists of tetrahedrite-tennantite, galena, bladed barite, pyrite and visible gold (Fig. 2.5b, d-e)Type 2A is situated in the centre of the stratiform zone (proximal), whereas the type 1 and type 2B assemblages extend from the proximal to the distal regions of the stratiform zone (Fig. 2.4a and 2.4b, respectively). Type 3 partially replaces the type 1 assemblage in the upper portion of the stratiform sulfide zone and is composed of massive to stringer, honey brown to red sphalerite, with lesser pyrite, galena and chalcopyrite (Fig. 2.5f).

The stringer zone stratigraphically underlies the stratiform zone, and comprises type 4 mineralization consisting of chalcopyrite, disseminated to coarse-grained pyrite, honey brown to orange sphalerite, and minor galena stringers (Fig. 2.5g-h). Sphalerite and galena content in type 4 stringers decreases with increasing depth below the stratiform zone (Fig. 2.5h). A well-developed stockwork zone has not been documented beneath the Lemarchant deposit; the stringer zone is devoid of basal pyrite-dominated stringers and there is minimal evidence of a discordant alteration zone. The base of the stringer zone is abrupt, and it is possible that a discordant alteration zone was removed due to thrust faulting associated with the Lemarchant fault.

2.4.1 – Sulfide mineralogy

Despite local faulting and regional metamorphism, the Lemarchant deposit contains exceptionally well-preserved primary textures in most sulfides, with only local structural remobilization. The Lemarchant deposit is dominated by sphalerite, pyrite, chalcopyrite, and galena, as well as numerous other sulfides and sulfosalts that occur in 5

mineral assemblages (Table 2.1). Detailed mineralogy of each type assemblage is outlined below.

2.4.1.1 – Type 1 mineral assemblage

The type 1 assemblage contains primary and recrystallized textures. Sphalerite is semi-massive, anhedral, honey to white-coloured and contains microscopic blebs of chalcopyrite (Table 2.1; Fig. 2.6a and inset). Pyrite occurs in various forms reflecting multiple stages of growth. Fine-grained, colloform to reniform pyrite (Fig. 2.6b) is partly to completely recrystallized and forms annealed, fine-grained clusters. Euhedral pyrite is present but rare. Medium-grained subhedral to euhedral atoll pyrite contains minor inclusions of sphalerite and galena; zoned pyrite crystals are inclusion-rich (Figs. 2.6a, c). Galena generally occurs as medium- to coarse-grained anhedral grains in type 1 sphalerite and pyrite; discrete, subhedral tetrahedrite grains are commonly present with galena. Minor, very fine-grained chalcopyrite blebs are disseminated throughout type 1 sphalerite (Fig. 2.6a, inset) and fine- to medium-grained chalcopyrite blebs occur at sphalerite-pyrite and sphalerite-galena grain boundaries.

2.4.1.2 – Type 2A mineral assemblage

The type 2A mineral assemblage crosscuts the type 1 assemblage as thin sulfide veinlets composed of bornite, galena and chalcopyrite with lesser stromeyerite, covellite, unknown Cu-Ag phases and trace Ni-S phases (Table 2.1).

Bornite grains are blebby to sheeted, and occur in sphalerite and barite gangue (Figs. 2.6d-f). Anhedral galena is abundant in type 2A sulfides (Figs. 2.6d-e).

Chalcopyrite occurs at the grain boundaries of type 2A bornite and galena with type 1 sphalerite, pyrite and gangue (Figs. 2.6d-f). Minor, irregular to acicular stromeyerite occurs at bornite, galena and chalcopyrite grain boundaries (Fig. 2.6d) and bright blue covellite overprints bornite, stromeyerite and chalcopyrite (Figs. 2.6d-e). Type 2A bornite, galena and chalcopyrite locally infill cracks in other sulfides and gangue (Figs. 2.6e-f), or form composite wires in thin section (not pictured).

2.4.1.3 – Type 2B mineral assemblage

The type 2B mineral assemblage crosscuts and is disseminated throughout the type 1 assemblage. It is variably intergrown with sulfides from the type 2A assemblage. The major minerals in the type 2B assemblage are tetrahedrite-tennantite, galena, and bladed barite, with lesser white sphalerite and minor chalcopyrite. Trace minerals in the type 2B assemblage include marcasite, colusite-germanocolusite, electrum, bournonite, polybasite, miargyrite, and unidentified V-Ge-Cu and Ag-Te phases (see Table 2.1). Galena is angular to anhedral, medium- to coarse-grained and intergrown with sphalerite, tetrahedrite, barite (Figs. 2.6g-h, 2.7a-e), and trace sulfides and sulfosalts (Figs. 2.6h, 2.7a-c). Tetrahedrite-tennantite (hereafter referred to as tetrahedrite) occurs with galena and sphalerite, and is variably associated with electrum, colusite, and chalcopyrite (Figs. 2.6g, 2.7c-d). Compositionally zoned tetrahedrite occurs toward the outer edges of the deposit (Fig. 2.7d). Electrum occurs in contact with galena and is spatially associated with sphalerite, pyrite and tetrahedrite in a barite-rich matrix (Figs. 2.7c-e). Sulfosalts of the colusite-germanocolusite (hereafter refereed to as colusite), sulvanite, and reinerite group form anhedral, <50 μm light brown-pink grains and occur in the central portion of the

deposit, intergrown with the type 2A assemblage (Figs. 2.6e-f; symplectitic galena-colusite; Fig. 2.6h). Pyrite associated with the type 2B assemblage is recrystallized and forms irregular, subhedral and lesser euhedral atolls (Figs. 2.6h and 2.7e). In rare cases, crystalline pyrite occurs in vuggy quartz-barite veins crosscutting massive sulfide mineralization.

2.4.1.4 – Type 3 mineral assemblage

The type 3 assemblage is hosted in the uppermost stratiform zone and is composed of massive sphalerite, pyrite, chalcopyrite and galena. Type 3 honey brown to red sphalerite is generally free of inclusions and replaces type 1 white to honey sphalerite, galena and barite (Fig. 2.7f and inset). Pyrite from the type 3 mineral assemblage consists of fine- to coarse-grained euhedral crystals, but relict colloform to recrystallized subhedral pyrite of the type 1 and type 2B assemblages is also present. Galena occurs with recrystallized pyrite, at sulfide grain boundaries or as wiry strands in type 3 sphalerite. Amorphous chalcopyrite is present at sulfide grain boundaries. Blebby pyrrhotite and rhombic arsenopyrite are locally present with type 3 chalcopyrite near the stratiform zone-pyritic mudstone contact at the top of the deposit.

2.4.1.5 – Type 4 mineral assemblage

The type 4 stringer sulfide assemblage is hosted exclusively in the altered footwall rhyolite breccia and lapilli tuffs that are stratigraphically below massive sulfide mineralization. The type 4 assemblage is composed of chalcopyrite, pyrite, sphalerite and minor galena stringers; sphalerite and galena decrease markedly in abundance with increased distance below the massive sulfide lens. Chalcopyrite is blebby and crosscuts

gangue, sphalerite and galena, and is associated with rare dendritic marcasite (Figs. 2.7g-h). Type 4 sphalerite is honey brown to orange and contains microscopic acicular chalcopyrite inclusions (Fig. 2.7g). Pyrite forms rounded to euhedral coarse-grained atolls that are host to anhedral grains of galena, sphalerite and chalcopyrite (Figs. 2.7g-h). Fine- to medium-grained euhedral pyrite is also disseminated throughout footwall gangue.

2.5 – Sulfide mineral chemistry

2.5.1 – Analytical methods

Stratigraphic sections from 44 diamond drill holes were constructed to document the mineralized zones at the Lemarchant deposit. Drill core samples were made into 143 polished 30 μm thin sections for petrographic analysis. Forty-five representative samples of mineral assemblage types were analyzed using a FEI™ MLA 650F scanning electron microscope (SEM) at the CREAIT MAF-IIC facility, Memorial University of Newfoundland. Energy dispersive X-ray (EDX) analyses (predominantly back-scatter electron images) were conducted to identify free gold (electrum) occurring with sulfides, sulfosalts, and gangue in the type mineral assemblages. Of these representative samples, 22 thin sections were selected and analyzed by electron microprobe analysis (EMPA) at the Queen's Facility for Isotope Research (QFIR), Queen's University. Quantitative analyses of major and minor element compositions of sulfides and sulfosalts were determined using wavelength dispersive spectrometry (WDS) on a JEOL™ JXA-8230 instrument. Operating conditions were an accelerating voltage of 20 kV, a beam diameter of 1μm and a beam current of 50 nA for galena and pyrite, 30 nA for sphalerite and barite, and 20 nA for all other sulfides and sulfosalts. The X-ray takeoff angle was 40 degrees.

Count times for elements varied from 10-120 sec depending on the relative abundance of the element in the mineral phase (e.g., S and Au in pyrite, respectively); off-peak (background) count times were set equal to peak count times. Element abundances were determined using large-area and high-intensity LIF and PET crystals, and TAP crystals. Natural and synthetic mineral phases, and pure elements were used as internal standards for instrument calibration to monitor background conditions, element interferences and peak quality, and to correct for instrumental drift. The data were processed using the CITZAF V3.5 online software program for JEOL™ written by J. T. Armstrong (California Institute of Technology). Standard and unknown intensities were corrected for dead time. Major element precision in analyses of unknowns was generally better than 1% (1σ), with reduced precision for minor (<1 wt%) elements. Lower detection limits for minor elements were better than 100-500 ppm (3σ). Analyses with totals outside of 100±1.5 wt%, and quantities below calculated detection limits (3σ) were discarded. Interference corrections were made for Au Mα interference with Pb Mα in galena. More detailed EMPA procedures are described in Appendix A.

Trace element (Ag, As, Au, Bi, Cd, Co, Cr, In, Ge, Mn, Mo, Ni, Sb, Se, Sn, Ti, Tl, V) analyses were conducted by laser ablation ICP-MS at QFIR on 19 of the 22 samples analyzed by EMPA. Ablation techniques and data reduction methods used in this study are outlined by Longerich et al. (1996) and Eggins et al. (1998). An ESI™ NWR-193nm Excimer laser coupled to a ThermoFisher™ X-Series 2 Quadrapole ICP-MS was used to ablate 50 μm diameter spots, using 70% total power and a pulse rate of 10 Hz to minimize elemental fractionation, with a gas blank of 30s. Daily setup of the LA-ICP-MS was

conducted on a USGS glass standard (GSD) to optimize He and Ar flow through the ablation cell and the plasma torch to yield >300 kCPS on ^{238}U, <0.5% doubly charged species and <0.5% oxides. Sets of 20 spots were bracketed by calibrations using the USGS glass standards (GSC-1G, GSD-1G and GSE-1G) and an external standard (BHVO-2G) to monitor instrument drift and correct for changes in element ionization. Trace element contents in Lemarchant sulfides and sulfosalts were quantified by comparison to a sulfide matrix standard (MASS-1). Standard data are included in Appendix B.1. Minor elements measured by EMPA were used as internal standards to correct for variability in laser yield, and included: Cd for sphalerite, Zn for tetrahedrite and Ag for bornite. Major element abundances for Fe, Cu, Pb and Zn in pyrite, galena and chalcopyrite were either beyond the calibration curves for the GS-series glasses or not constrained by microprobe data (below detection), and not suitable for laser yield correction. Supplementary methods for LA-ICP-MS analyses are included in Appendix B.

2.5.2 – Results: Major and minor element geochemistry

The complete set of electron microprobe data for the 15 analyzed mineral phases and unknown phases are included in Appendix A.2. Example mineral formula calculations for sulfides, electrum and sulfate are found in Appendix A.3. Notable trends in compositional variation, down-hole compositional variation and compositional variation along strike are highlighted in Figures 2.8-2.11.

Compositions of galena, chalcopyrite and barite are generally stoichiometric and show little variation in major and minor element composition. Lead and S in galena range from 84.57-87.98 wt% and 13.11-13.67 wt%, respectively. Minor Zn and Fe (<10.00

wt%) and trace Ag and Sb (<0.10 wt%) are present in some galena. Sulfur, Cu and Fe in chalcopyrite range from 34.43-35.53 wt%, 33.43-35.4 wt% and 28.91-30.69 wt%, respectively. Zinc in chalcopyrite ranges as high as 12780 ppm, whereas Ag is <1500 ppm. Near-stoichiometric chalcopyrite has higher contents of minor and trace elements. Barium and S in barite range from 63.56-67.23 wt% and 33.44-35.28 wt%, respectively. Minor Sr (<15700 ppm) and trace Ca (<1703 ppm) are common.

Sphalerite is stoichiometric but contains variable Zn and Fe. Major elements Zn and S range from 57.03-67.00 wt% and 32.10-33.69 wt%, respectively. Sphalerite commonly contains minor Cd (1950-4890 ppm; avg. 2882 ppm). Iron content is up to 8.41 wt% (13.65 mol% FeS), and Fe contents are antipathetic with Zn, consistent with Fe substitution in the Zn site in sphalerite (Wright, 2009). Type 1 sphalerite is white- to honey-coloured and contains a maximum of 2.60 wt% Fe (4.54 mol% FeS), with most grains having <1.87 wt% Fe (3.27 mol% FeS; Fig. 2.8a). White type 2B sphalerite contains <0.18 wt% Fe (0.32 mol% FeS). Type 3 and 4 honey brown to red sphalerite contains >2.72 wt% Fe (4.72 mol% FeS), with Fe in type 3 sphalerite >2.84 wt% (5.06 mol% FeS). Sphalerite Fe content is lowest in the stratigraphic middle portion of the deposit, whereas the highest Fe-contents occur at the top and bottom (Fig. 2.9).

Pyrite is stoichiometric to near-stoichiometric. Sulfur and Fe ranges from 51.56-54.38 wt% and 43.43-46.66 wt%, respectively. Arsenic substitution at the expense of S can be up to 3.60 wt% (Fig. 2.8b), which is consistent with the incorporation of As as AsS dianon groups within the pyrite crystal lattice (Blanchard et al., 2007; Reich and Becker, 2006). Zoned pyrite is common, with As ranging from below detection limit (BDL) to ~3 wt% within a single grain (Fig. 2.10). The highest As values occur in

recrystallized colloform and subhedral atoll pyrite in the middle section of the deposit, and proximal to the centre of the deposit along strike (Figs. 2.9 and 2.11, respectively).

The tetrahedrite group has a range of stoichiometric and non-stoichiometric compositions between end member tetrahedrite (1.0 Sb/(Sb+As)) and end member tennantite (0.97 As/(Sb+As)). Major elements Cu and S range from 17.44-42.01 wt% and 21.42-28.32 wt%, respectively. Minor elements Sb, As, Zn and Fe range from 1.03-27.24 wt%, 0.06-19.35 wt%, 0.09-8.77 wt%, and up to 7.87 wt%, respectively. Silver contents range up to 27.78 wt% and correlate positively with Sb contents (Fig. 2.8c). Substitution of Ag and Sb at Cu and As sites, respectively, increases along strike in type 2B tetrahedrite distal to the central portion of the deposit (Fig. 2.11). This is consistent with the fractional crystallization model by Hackbarth and Petersen (1984) and Huston et al. (1996), in which Cu and As are preferentially incorporated into the tetrahedrite crystal lattice over Ag and Sb, until Cu and As contents in the mineralizing fluid are sufficiently depleted and Ag-Sb-bearing tetrahedrite can be precipitated. Silver-rich tetrahedrite (Ag >15.00 wt%) is generally Zn-poor (<0.60 Zn/(Zn+Fe)); however, some Zn-rich tetrahedrite contains up to 15.00 wt% Ag (Fig. 2.8d). Tellurium contents are up to 2.70 wt% in Zn-rich (>6.00 wt% Zn) tennantite (Fig. 2.8e), and increase along strike toward the centre of the deposit (Fig. 2.11).

Bornite is near-stoichiometric and has a major element composition of 60.85-63.70 wt% Cu, 25.23-25.99 wt% S and 11.00-11.57 wt% Fe. Silver in bornite ranges from 1720-14720 ppm; minor Zn is present and ranges up to 13220 ppm in bornite.

Colusite and other V-bearing phases are stoichiometric to non-stoichiometric. Major elements in the colusite group of minerals include Cu, S, V and Ge, which range from 41.80-51.11 wt%, 31.47-33.20 wt%, 3.05-3.28 wt% and up to 11.63 wt%, respectively. Zinc ranges from 330-72680 ppm. Minor elements As, Fe, Sb and Sn range up to 92180 ppm, 38810 ppm, 12500 ppm and 19500 ppm, respectively. Coupled substitution of As and Sb with Ge and Sn is consistent with the presence of Ge-bearing colusite according to Spry et al. (1994) and Wagner and Monecke (2005) (Fig. 2.8f); however, more complex substitution mechanisms may contribute to the composition of colusite at Lemarchant. Three distinct compositions of colusite are recognized: (1) arsenian colusite with Ge+Sn <5.00 wt%, As+Sb >8.00 wt%, Cu >49.00 wt% and Zn <1.50 wt%; (2) germanium-rich colusite with Ge+Sn >11.00 wt%, As+Sb <1.00 wt%, Cu <43.00 wt% and Zn >5.50 wt%; and (3) intermediate colusite with Ge+Sn, As+Sb, Cu and Zn ranging from 8.00-11.00 wt%, 2.00-5.00 wt%, 44.00-47.00 wt% and 3.00-5.50 wt%, respectively (Figs. 2.8f-h). Arsenian colusite occurs along strike at the edges and central portions of the deposit with type 2B mineralization, whereas Ge-rich and intermediate colusite occur only in the centre of the deposit with type 2B mineralization. Minor sulvanite and reinerite also occur with type 2B mineralization in the centre of the deposit (Table 2.1). Sulvanite is stoichiometric and contains 50.30-50.43 wt% Cu, 34.80-34.93 wt% S and 13.55-13.78 wt% V. Minor Fe, Zn and Ag range from 14600-6732 ppm, 12500-3097 ppm and 727-401 ppm respectively. A single analysis below the total cutoff (<98.5%) is included because it is typical of reinerite composition and is near stoichiometric. An unknown Cu-V-Ge-S phase rims germanium-rich colusite in the central portion of the deposit (Gill and Piercey, 2014).

Gold at Lemarchant primarily occurs as electrum. The composition of electrum ranges from 57.26-86.36 wt% Au and 10.97-41.19 wt% Ag. Trace Cu, Fe and Zn are locally present in electrum, but comprise <0.50 wt%. The highest ratios of Au:Ag (>0.70) occur in electrum at the centre of the deposit, whereas these ratios drop to 0.4-0.7 along the north and south edges of the deposit (Fig. 2.11). Five of the 14 accepted electrum analyses are below the lower total cutoff (>95%); this error is attributed to small grain size effects and the analyses are considered relevant to the understanding of the deposit. An unidentified Hg-rich (11.98 wt%) Au-Ag phase occurs with the high-Au electrum in the central portion of the deposit (Appendix A.2).

The Ag-bearing minor phases include stromeyerite, polybasite and miargyrite. In general, these phases are near stoichiometric to non-stoichiometric; miargyrite is stoichiometric. Stromeyerite contains 42.99-58.55 wt% Ag, 26.05-38.00 wt% Cu, 14.17-18.53 wt% S and 810-1540 ppm Te. Polybasite contains 6.05 wt% Cu, 66.05 wt% Ag, 16.40 wt% S, 2.50 wt% As, 6.70 wt% Sb and 1910 ppm Te. Miargyrite contains 40.97-41.90 wt% Sb, 35.14-35.42 wt% Ag and 12.45-21.66 wt% S, with up to 1.30 wt% Pb. All Ag-bearing minor phases display variable trace Fe, Zn, Pb and Cu, which is likely due to their small grain size and contamination by proximal major phases (i.e., pyrite, sphalerite, galena and chalcopyrite). Stromeyerite occurs with the type 2A assemblage, whereas miargyrite and polybasite occur with the type 2B assemblage. At least two unknown Ag-Cu-S phases are present in the centre of the deposit and occur with stromeyerite (see Appendix A.2).

Bournonite is near-stoichiometric and only occurs as rims on type 2B galena at the outer edges of the Lemarchant deposit (Fig. 2.7b). Lead, Sb, S and Cu range from 42.46-43.11 wt%, 23.92-24.69 wt%, 19.23-19.88 wt% and 13.42-13.57 wt%, respectively. Bournonite contains trace As up to 3460 ppm and Zn up to 2720 ppm.

Silver-telluride and Ni-sulfide analyses are mostly below the total cutoff (<98.5%) as the analyses were conducted on very small grains (<10 μm). Analyses above or close to the cutoff that yielded unknown compositions occur in the Northwest Zone with type 2A and type 2B mineralization (Appendix A.2).

2.5.3 – Results: Trace element geochemistry

Average values for analyzed phases from each type mineral assemblage are listed in Table 2.2. Figure 2.12 displays the complete set of semi-quantitiative laser ablation ICP-MS data for the 6 analyzed mineral phases in the 5 mineral assemblages types, which are also tabulated in Appendix B.2. Example calculations for element ionization and laser yield corrections are in Appendix B.3.

2.5.3.1 – Type 1 mineral assemblage

A total of 32 analyses were performed on sphalerite and pyrite from the type 1 assemblage. The type 1 assemblage is enriched in Mn, Mo, Tl and As relative to the type 2A, 2B, 3 and 4 assemblages (Fig. 2.12). All five assemblages have similar Cd, Sn and Ge content in sphalerite and pyrite. Cobalt contents of pyrite in the type 1 and type 2B mineral assemblages are comparable (Fig. 2.12). The type 1 assemblage has lower Cr, In, Ti, Sb, Ni and Au relative to other mineral assemblages.

Type 1 sphalerite contains Mn, Cd, Sn and Ge up to 806 ppm, 2306-3450 ppm, <24 ppm and <16 ppm, respectively (Table 2.2). Colloform to reniform type 1 pyrite contains Mn, Mo, Tl, As, Ge and Co <1189 ppm, 4-2610 ppm, <2566 ppm, 744-45600 ppm, <7 ppm and 6-69 ppm, respectively (Table 2.2). Ni and Au in pyrite range from 151-2961 ppm and 1540-15250 ppm, respectively; however, colloform pyrite has lower Ni and Au relative to type 3 pyrite and type 2B pyrite, respectively (Fig. 2.12). Type 1 pyrite contains atypically high Se (up to 17740 ppm) relative to all other phases in the deposit (Fig. 2.12).

2.5.3.2 – Type 2A mineral assemblage

There are twenty-nine galena, chalcopyrite and bornite analyses for the type 2A mineral assemblage. The type 2A mineral assemblage has higher Ge, Ag and Sn contents relative to the others (Fig. 2.12). Titanium, Bi, In, Co, Ni and Cr contents are also higher in the type 2A and 2B mineral assemblages (Fig. 2.12).

Galena in the type 2A assemblage contains Ge, Sn, Ti, Bi, In, Co, Ni and Cr from 22-42 ppm, 26-72 ppm, 428-681 ppm, 40-82 ppm, <8 ppm, 13-22 ppm, 1292-2032 ppm and 20-35 ppm, respectively (Table 2.2); Se contents are erratic and range up to 9192 ppm (Fig. 2.12). Significant Ag enrichment occurs only in bornite (1867-7012 ppm), which also contains Ge, Sn, Ti, Bi, In, Mo, Co, Ni and Cr from 6-54ppm, 8-75 ppm, <380 ppm, <45 ppm, <13 ppm, <1385 ppm, <37 ppm, <1050 ppm and <19 ppm, respectively (Table 2.2). Chalcopyrite in the type 2A assemblage contains Ge, In and Mo ranging from 8-62 ppm, <14 ppm and <1604 ppm, respectively (Table 2.2).

2.5.3.3 – Type 2B mineral assemblage

Ninety-four analyses were conducted on sphalerite, recrystallized pyrite, galena, chalcopyrite and tetrahedrite from the type 2B mineral assemblage. The type 2B assemblage has higher V, In, Au and Sb relative to other assemblages (Fig. 2.12). Chromium, Co, BI, Ti, Ge and Ni are similar to the type 2A assemblage, whereas Mo, Ag, Tl and As are lower than in other mineral assemblages (Fig. 2.12). Silver, As and Sb are elevated in type 2B tetrahedrite relative to the other assemblages (Figs. 2.8c,d and 2.11).

White sphalerite in the type 2B assemblage contains V, In, Mn, Sn and Cd up to 274 ppm, <30 ppm, 156-333 ppm, <156 ppm and 2297-3892 ppm, respectively (Table 2.2). Type 2B recrystallized to subhedral atoll pyrite contains V, Au, Sb, Cr, Mn, Co and Ti up to 762 ppm, <133000 ppm, <6804 ppm, <110 ppm, <1390 ppm and <56 ppm, respectively (Table 2.2). Thallium, Ni and As contents in pyrite are up to 1781 ppm, <2341 ppm and <37160 ppm, respectively (Table 2.2); however, Tl, Ni and As are lower in subhedral pyrite relative to pyrite in the other assemblages (Fig. 2.12). Type 2B galena contains In, Au, Sb, Cr, Co, Ge, Se, Bi, Ni and Ti up to 10 ppm, 773-8552 ppm, 56-3735 ppm, 8-46 ppm, 7-26 ppm, 7-225 ppm, <1955 ppm, 12-105 ppm, 159-2563 ppm and 174-782 ppm, respectively (Table 2.2). The Ag-content of galena at Lemarchant is highest in type 2B assemblage (52-6549 ppm) and is associated with high Sb and Bi contents, which is consistent with the coupled substitution of Ag with Sb and/or Bi in galena (Fig. 2.12; Amcoff, 1984; Huston et al., 1996). Tin in type 2B galena ranges from 5-45 ppm, but is lower than type 2A galena (Fig. 2.12). Chalcopyrite in the type 2B assemblage contains In, Ge, Ti and Sn up to 5ppm, 3-40 ppm, <260 ppm and 5-111 ppm, respectively (Table

2.2). Type 2B tetrahedrite contains Mn, Ge, Se and Cd up to 857 ppm, <23 ppm, <382 ppm and 375-6088 ppm, respectively (Table 2.2).

2.5.3.4 – Type 3 mineral assemblage

Ten analyses of sphalerite, pyrite and chalcopyrite from the type 3 mineral assemblage contain lower trace element contents than those minerals in the type 1 and 2 assemblages. However, Ni is higher in the type 3 assemblage relative to the other mineral assemblages (Fig. 2.12). Cadmium and Sn contents in type 3 sphalerite are similar to those in type 1 and in type 2B white sphalerite (Fig. 2.12). Molybdenum contents in pyrite and high Sn in chalcopyrite from the type 3 mineral assemblage are similar to type 1 pyrite and type 2B chalcopyrite, respectively (Fig. 2.12). The type 3 assemblage has lower In, V, Mn, Ge and Ti relative to other mineral assemblages.

Type 3 sphalerite contains Cd and Sn from 3047-3880 ppm and 8-25 ppm, respectively (Table 2.2). Euhedral atoll pyrite in the type 3 assemblage contains Ni and Mo from 1258-3429 ppm and <2714 ppm, respectively (Table 2.2); however, extreme variability in Mo is likely due to the presence of inclusions (Fig. 2.12). Type 3 chalcopyrite contains 55-62 ppm Sn (Table 2.2).

2.5.3.5 – Type 4 mineral assemblage

Type 4 chalcopyrite has very low trace element contents relative to other mineral assemblages (Fig. 2.12). Trace Se, In and Sn in chalcopyrite range from 84-107 ppm, 16-18 ppm and 19-20 ppm, respectively (Table 2.2).

2.6 – Discussion

2.6.1 – Deposit type and sulfide mineral paragenesis

In many respects, the Lemarchant deposit resembles a typical polymetallic volcanogenic massive sulfide deposit (i.e., Kuroko- or bimodal felsic-type; Eldridge et al., 1983; Large, 1992; Poulsen and Hannington, 1995; Franklin et al., 2005; Galley et al., 2007). The stratiform sulfide zone at Lemarchant (~concordant massive sulfide zone; after Lydon, 1984 and Gibson et al., 2007) is barite-rich with Zn+Pb> Cu, and is underlain by a discordant Cu-rich stringer zone (e.g., Riverin and Hodgson, 1980; Lydon, 1984a; Large, 1992; Franklin et al., 2005; Galley et al., 2007). The felsic volcanic host rocks contain mostly quartz-sericite alteration with localized chlorite-rich alteration proximal to mineralization. These metal zoning, mineralogical and alteration features are common to bimodal felsic VMS deposits (e.g., Eldridge et al., 1983; Large, 1992; Ohmoto, 1996).

There are features in the Lemarchant deposit, however, that are atypical of VMS deposits. For example, the type 2A and type 2B assemblages contain sulfides and sulfosalts (e.g., tetrahedrite, bornite, electrum, covellite and tellurides) that are more characteristic of intermediate to high sulfidation epithermal gold deposits (White and Hedenquist, 1995; Cooke and Simmons, 2000; Taylor, 2007). The type 2 assemblages also contain epithermal suite elements (e.g., Au, Ag, As, Sb, Bi, Te, Sn and Mo; White and Hedenquist, 1995; Sillitoe et al., 1996; Cooke and Simmons, 2000). Gold contents at Lemarchant are elevated relative to typically barren polymetallic VMS deposits, and both free gold (electrum) and Ag-bearing phases occur with barite and type 2B bladed barite,

which are atypical characteristics in VMS deposits. Collectively, the above features suggest that there was likely a substantial contribution of magmatic fluid to the Lemarchant deposit (e.g., Sillitoe et al., 1996; Hannington et al., 1999; Dubé et al., 2007a; Mercier-Langevin et al., 2011).

The mineral textures and crosscutting relationships of sulfides and sulfosalts in the Lemarchant deposit suggest that an early VMS- epithermal event (stages 1 and 2) was overprinted by a later VMS event (Fig. 2.13). There are three paragenetic stages of formation of the Lemarchant deposit:

Stage 1 – low temperature (100-300°C), polymetallic VMS- (to epithermal?) style type 1 barite-honey to white sphalerite-colloform pyrite-galena±tetrahedrite-tennantite assemblage deposited at or near the seafloor;

Stage 2 – low temperature (150-275°C), epithermal-style mineralization and overprinting of stage 1 mineralization, resulting in the deposition of intermediate to high sulfidation epithermal-type assemblages including type 2A bornite-galena-chalcopyrite-stromeyerite±Ni-sulfide stringers and the type 2B assemblage of bladed barite-tetrahedrite-galena-pyrite±colusite-electrum-bournonite-miargyrite-polybasite-Ag-telluride;

Stage 3 – higher temperature (>300°C), Cu-rich VMS related mineralization. This included deposition of the type 3 assemblage of honey brown to red sphalerite-pyrite-chalcopyrite±galena that crosscut and variably replaced the type 1, type 2A and type 2B

assemblages, and type 4 chalcopyrite-pyrite±orange sphalerite-galena stringers that crosscut the felsic footwall underlying the stratiform mineralized zone.

The mineral zonation, spatial features of sulfide phases, and paragenesis at Lemarchant indicate a complex depositional history and varying physicochemical conditions of formation for each stage of mineralization.

2.6.2 – Physicochemical and geological conditions of metal transport and deposition

The paragenesis, textures, mineral assemblages, and mineral compositions that define Lemarchant provide key insights into the physicochemical conditions of metal transport, deposition and evolution of the deposit. Paragenetic relationships imply three stages of evolution, which likely had distinctive physicochemical conditions of formation (Fig. 2.13).

Stage 1. The textures of the dominant phases in the type 1 mineral assemblage (i.e., granular barite, fine-grained, colloform-reniform pyrite) are indicative of rapid precipitation of sulfide minerals by mixing of the hydrothermal fluid with colder seawater at or near the seafloor (Barton and Skinner, 1979; Ohmoto, 1996). Additionally, the relative lack of chalcopyrite suggests that initial deposition occured at lower temperatures because Cu solubility is very low at temperatures less than 300°C (Ohmoto et al., 1983; Pisutha-Arnond and Ohmoto, 1983). Low temperature (~100-275°C) deposition is also supported by the presence of Fe-poor (<2.6 wt%), honey to white sphalerite in this assemblage (Fig. 2.14; Scott and Barnes, 1971; Czamanske, 1974; Hannington and Scott,

1989; Huston and Large, 1989) and the high Mn, Tl and As contents in colloform pyrite (Fleischer, 1955; Ballantine and Moore, 1988; Hannington et al., 1995). Sulfate (barite)-Zn-Pb-rich mineralization and associated low-Fe contents of type 1 sphalerite indicate low Fe solubility in relatively oxidized, acidic to near-neutral pH hydrothermal fluids (Large, 1977; Ohmoto et al., 1983; Hannington and Scott, 1989; Huston and Large, 1989; Seyfried and Ding, 1995).

Stage 2. The complex textural intergrowth of type 2A and type 2B sulfides and sulfosalts (Figs. 2.6d-h, 7a-e) implies synchronous deposition of these two assemblages. The very low Fe-contents in type 2B sphalerite (<0.2 wt%) and associated Zn-Pb-Ag, barite-rich and Ag-Au-bearing mineralogy indicate that stage 2 hydrothermal fluid temperatures were also likely low (150-275°C; Scott and Barnes, 1971; Czamanske, 1974; Hannington and Scott, 1989; Huston and Large, 1989). Silver-enrichment of tetrahedrite relative to galena and chalcopyrite, and coupled substitution of Bi and Sb with Ag in galena also suggest hydrothermal fluid temperatures below 275°C (Amcoff, 1984; Huston et al., 1996). The low-Fe sphalerite and associated Au-enrichment, barite- and bornite-pyrite-chalcopyrite mineral assemblages, and Ag-rich tetrahedrite further suggest that type 2A and type 2B assemblages were deposited from relatively oxidized (high fO_2) and high fS_2 hydrothermal fluids (Fig. 2.13; Barton and Skinner, 1979; Pisutha-Arnond and Ohmoto, 1983; Hannington and Scott, 1989; Huston and Large, 1989; Ohmoto, 1996; Hannington et al., 1999; Lusk and Calder, 2004). High fS_2-fO_2 conditions are also consistent with the pentavalent As and V, and tetravalent Ge, present in colusite and reinerite, which require highly oxidized conditions for transportation and deposition

(Kase et al., 1994; Spry et al., 1994; Wagner and Monecke, 2005). The mineralogy of the type 2 assemblages are indicative of acidic to near-neutral fluid conditions during stage 2 mineralization (pH ~5; Ohmoto et al., 1983; Hannington and Scott, 1989; Hannington et al., 1999; Wagner and Monecke, 2005).

Precious metal enrichment of the Lemarchant deposit occurred almost entirely during stage 2 paragenesis. Although deposition of silver and gold were contemporaneous at Lemarchant, the mechanisms of Au- and Ag-precipitation were distinct. Silver occurs mostly in tetrahedrite, with subordinate enrichment in electrum, galena, bornite and trace Ag-Sb-sulfosalts (Table 2.1; Fig. 2.8c-d and 2.12). The dominance of tetrahedrite as a Ag-host, and the close association of tetrahedrite with barite in the type 2B assemblage, suggests that fractional crystallization of tetrahedrite from the hydrothermal fluid was the main mechanism for Ag enrichment in the Lemarchant deposit (Hackbarth and Petersen, 1984; Huston et al., 1996). This is reflected by the distribution of Cu-As- and Ag-Sb-tetrahedrite compositions along the strike length of the Lemarchant deposit (Fig. 2.11); near end-member tennantite (Cu-As>Ag-Sb) occurs primarily in the centre of the deposit, whereas end-member tetrahedrite (Sb/(As+Sb) >0.6) occurs in the more distal parts of the deposit. Furthermore, the presence of very Ag-rich tetrahedrite, minor Ag-rich tennantite (>15 wt% Ag) and high-Ag electrum (<40 wt% Ag) in the type 2B assemblage, and Ag-bearing bornite (<0.7 wt% Ag) in the type 2A assemblage suggest that Ag was significantly enriched in the hydrothermal fluid relative to normal polymetallic VMS-forming fluids (Hackbarth and Petersen, 1984; Petersen et al., 1990). Furthermore, given that the assemblages were deposited from fluids with temperatures <275°C (Fig. 2.14), it

is likely that the Ag was transported as $AgCl_2$ (Seward, 1976; Huston et al., 1996). Gold also occurs in these lower temperature assemblages, primarily as electrum, indicating gold was transported as $Au(HS)_2^-$, likely at high fS_2 and fO_2 (Fig. 2.14; Seward, 1973; Hannington and Scott, 1989; Huston and Large, 1989; Williams-Jones et al., 2009).

The type 2 assemblages, including Au-Ag-bearing phases that occur with bladed barite (i.e., electrum, Ag-rich tetrahedrite) and euhedral feldspar (albite) within the ore (see Appendix C), suggest that hydrothermal fluid boiling was important during stage 2 mineralization for the precipitation and sedimentation of crystalline gangue minerals (Drummond and Ohmoto, 1985; Hannington and Scott, 1989; Huston and Large, 1989; Sillitoe et al., 1996; Roth et al., 1999; Huston et al., 2000; Dubé et al., 2007a; Hannington and Monecke, 2009). Furthermore, the observation of fluid boiling imparts limitations on the depth of emplacement of the massive sulfide deposit in seawater. In particular, the depth to boiling curve for seawater (Bischoff and Rosenbauer, 1984; Butterfield et al., 1990) requires relatively shallow emplacement of the deposit (<1500 mbsl at <275 ^oC) to permit boiling of the hydrothermal solution at or near the seafloor (Sillitoe et al., 1996; Hannington et al., 1999; Hannington and Monecke, 2009). Although many polymetallic black smoker deposits at mid-ocean ridges form at depths >2000 mbsl (Hannington et al., 1995, 1999; Hannington and Monecke, 2009), precious metal-enriched black and white smokers venting fluids with a magmatic fluid component (in addition to modified seawater) are common in shallow back-arc basins (e.g., Lau Basin; Herzig et al., 1993; Okinawa Trough; Glasby and Notsu, 2003), calderas in submarine arcs (e.g., Brothers volcano; de Ronde et al., 2001, 2005), and ancient analogies in back-arc (e.g., Eskay

Creek; Roth et al., 1999; Sherlock et al., 1999) to rifted arc (e.g., Kuroko-type deposits; Cathles et al., 1983; Boundary deposit; Piercey et al., 2014) settings – the latter environment most closely resembling that of the Lemarchant deposit.

Stage 3. The type 3 and type 4 mineral assemblages were deposited under typical VMS conditions. The abundance of chalcopyrite and euhedral pyrite, relatively coarse-grained sulfides, and chalcopyrite disease in type 1 sphalerite suggest that hydrothermal fluid temperatures were greater than 300°C, and that previously deposited ores were partially recrystallized via zone refining (Eldridge et al., 1983; Pisutha-Arnond and Ohmoto, 1983; Ohmoto, 1996). Type 3 honey brown to red sphalerite and type 4 orange sphalerite contain the highest Fe at Lemarchant (<8.4 wt%), consistent with higher temperature fluids (>300°C; Scott and Barnes, 1971; Barton and Skinner, 1979; Hannington and Scott, 1989). The absence of sulfur-rich phases (i.e., bornite-pyrite; Scott and Barnes, 1971; Barton and Skinner, 1979) associated with the high temperature, high-Fe sphalerite type 3 and type 4 assemblages further suggests a change to lower fS_2 (and likely lower fO_2) conditions (Fig. 2.14).

The abrupt transition from stage 2 to stage 3 in the paragenetic sequence is accompanied by notable Fe enrichment in sphalerite, an abundance of chalcopyrite, and a coarsening of sulfide mineral textures, which collectively indicate an increase in the temperature of the system to greater than 300°C. A prolonged temperature increase is not likely in this case because sustained heating associated with chalcopyrite formation within the hanging wall rocks would likely have produced well developed alteration in the overlying (insulating) hanging wall (Franklin et al., 2005; and references therein);

such a feature is not manifested in the poorly altered hanging wall mafic flows at Lemarchant (e.g., Copeland et al., 2008a; Copeland et al., 2008b; Fraser et al., 2012). Additionally, any increase in temperature above 250°C in a shallow water system (<1500 m) would necessitate an increase in confining pressure of the system (Bischoff and Rosenbauer, 1984; Butterfield et al., 1990; Hannington et al., 1995; Hannington et al., 2005), suggesting that the >300°C increase in temperature at Lemarchant during stage 3 mineralization was accompanied by an increase in seawater depth of the deposit (to >1500 mbsl) to prevent boiling. Variation in mineralization styles between the at Lemarchant, Duck Pond and Boundary deposits within the Tally Pond group provide evidence for an increase in water depth accompanying the increase in temperature of the hydrothermal fluid and deposition of high temperature (Cu-rich) mineralization. The Duck Pond and Boundary deposits have normal polymetallic VMS mineralization (deep water VMS; Hannington et al., 2005; Hannington and Monecke, 2009), and are relatively younger than the Lemarchant deposit (~509Ma vs. ~513Ma, respectively), but are hosted in a stratigraphic sequence with rifted arc geochemical signatures, similar to those of the Lemarchant host rocks (Squires and Moore, 2004; Copeland et al., 2008a; McNicoll et al., 2010; Piercey et al., 2014). This suggests that formation of the Lemarchant deposit began during arc rifting around ~1500 m seawater depth, but deposition continued at an increased water depth during the final stages of mineralization, due to basin subsidence in an extensional environment.

Although the mineralization at Lemarchant has been zone refined, this is not well-developed in the stratiform zone, and there is no typical ‘stockwork’ sulfide zone like

many VMS deposits (Fig. 2.3a-c; Riverin and Hodgson, 1980; Eldridge et al., 1983; Lydon, 1984; Large, 1992; Ohmoto, 1996). In the stratiform zone, early deposited mineralization (i.e., type 1 white to honey sphalerite and colloform-reniform pyrite, Fig. 2.6a-c) is moderately chalcopyrite diseased (i.e., formed at a reaction front; Eldridge et al., 1983; Barton and Bethke, 1987) and are only partially replaced by the type 3 mineral assemblage. The type 4 mineral assemblage is mostly chalcopyrite-dominated and does not extend far below the stratiform zone (<50 m; Fig. 2.3 and 2.4). The incomplete zone refining of the stratiform zone and absence of "siliceous pyrite ore" (SPO; Eldridge et al., 1983) in type 4 sulfides suggests this stage of mineralization was relatively short-lived. Alternatively, and consistent with field relationships, part of the stockwork zone may have been removed by the Lemarchant Fault. In this case, it is possible that stage 3 mineralization was much more long-lived than suggested above, or that another stage of low temperature mineralization persisted after the stockwork zone was formed. This latter possibility is supported by the presence of minor interpillow mudstone and hematitic chert in the hanging wall basalt flows (up to 200m above mineralization), which indicate hydrothermal activity at Lemarchant persisted even after the massive sulfides were capped (Copeland et al., 2008a; Copeland et al., 2008b; Lode et al., 2014).

2.6.3 – Magmatic contribution to the hydrothermal fluid

The stage 1 polymetallic sulfide mineralization at Lemarchant is likely precipitated entirely from evolved seawater containing metals (i.e., Zn, Pb, Cu, Ge) leached from the felsic host rocks and from the greater mass of surrounding volcano-sedimentary basement rocks (Lydon, 1988; Kase et al., 1994; James et al., 2003; Franklin,

2005). In contrast, the type 2A and type 2B assemblages contain mineral phases and elemental enrichments that cannot be derived solely from evolved seawater (e.g., Lydon, 1996). High fS_2, highly oxidized mineralizing fluids, as indicated by the Cu-rich bornite-, tetrahedrite-, colusite-, covellite- and electrum-bearing assemblages (Fig. 2.14; Barton and Skinner, 1979; Hannington and Scott, 1989; Huston and Large, 1989), are characteristic of magmatic fluid contributions to VMS hydrothermal systems (Poulsen and Hannington, 1995; Hannington et al., 1999; Dubé et al., 2007a). Furthermore, the enrichment of many trace elements in type 2A and 2B ore mineral phases (i.e., Au, As, Bi, Co, Cr, In, Mo, Ni, Sb, Se, Te) are likely not present in sufficient quantity in the volcanic host rock to contribute to the composition of the hydrothermal fluid solely by leaching (Poulsen and Hannington, 1995; Lydon, 1996; Franklin et al., 2005). However, these elements could be readily transferred to the hydrothermal fluid episodically from a contemporaneous magma via magmatic fluids and/or volatiles (Hedenquist and Lowenstern, 1994; White and Hedenquist, 1995; Hannington et al., 1999; Sillitoe et al., 1996). Evidence for pulsed magmatic fluid contributions is provided by zoned, subhedral pyrite associated with the type 2 assemblages that contains As-rich bands and As-poor bands (Fig. 2.9), indicating significant periodic As addition to the hydrothermal fluid during deposit formation (Rye, 1993; Hedenquist and Lowenstern, 1994; Cathles et al., 1997).

Although sulfide mineral associations in the type 2A and type 2B assemblages (i.e., bornite+pyrite-chalcopyrite, low-Fe sphalerite) indicate an elevated sulfidation state for low temperature stage 2 hydrothermal fluids (Fig. 2.14), the Lemarchant deposit lacks

the acidic, advanced argillic alteration assemblage (e.g., vuggy silica, alunite-dickite) that is typically a diagnostic feature of high-sulfidation epithermal-style mineralization (Rye, 1993; Hedenquist and Lowenstern, 1994; White and Hedenquist, 1995; Poulsen and Hannington, 1995; Sillitoe et al., 1996). Rather, the quartz-sericite±chlorite-albite alteration assemblage present at Lemarchant (Copeland et al., 2008a; Copeland et al., 2008b; Fraser et al., 2012) suggests that stage 2 fluids were near-neutral (Hedenquist et al., 2000; Franklin et al., 2005). Similarly, despite convincing evidence for a magmatic contribution to the hydrothermal fluid during deposit genesis, alteration at Eskay Creek deposit consists of sericite±K-feldspar (Roth et al., 1999) and the Ming deposit has quartz- and sericite-dominant alteration (Brueckner et al., 2014). Hedenquist et al. (2000) and Sillitoe and Hedenquist (2003) define deposits such as these, with low-sulfidation alteration and low- to high-sulfidation sulfide mineral assemblages, as "intermediate-sulfidation" epithermal-style deposits. The absence of low-pH, highly aluminous alteration at Lemarchant can be attributed either to the contribution of magmatic liquid-phase fluids (c.f., Hedenquist and Lowenstern, 1994; Einaudi et al., 2003) or to the prolonged mixing of seawater-dominated hydrothermal fluids with magmatic fluids (vapour or liquid) prior to sulfide precipitation. Both mechanisms of magmatic fluid contribution, contemporaneous with the shallow seafloor setting (<1500 mbsl) and the presence of the proximal, synvolcanic Lemarchant microgranite intrusion, are compatible with the precious metal-enrichment of stage 2 hydrothermal fluids and precipitation of intermediate-sulfidation epithermal-style mineralization (Sillitoe and Hedenquist, 2003; Taylor, 2007).

2.7 – Conclusion

The extremely well preserved mineralization at Lemarchant exhibits two styles of massive sulfide deposition: 1) bimodal felsic (Kuroko)-style polymetallic VMS mineralization; and 2) intermediate sulfidation epithermal-style mineralization. Distinctly different mineral assemblages and crosscutting relationships define three stages of deposition at Lemarchant (Fig. 2.15). Stage 1 was initially submarine exhalative, with deposition of massive barite and precipitation of semi-massive low-Fe sphalerite and fine-grained colloform pyrite at or near the seafloor due to a relatively lower temperature "VMS-type" hydrothermal fluid cooling and mixing with seawater (Fig. 2.15a). Stage 2 was characterized by the deposition of epithermal suite minerals (i.e., bornite, tetrahedrite, colusite, covellite, and electrum) and sulfide mineralization with magmatic trace element signatures (i.e., Au, As, Bi, Co, Cr, In, Mo, Ni, Sb, Se, Te) from a low temperature, oxidized, intermediate sulfidation and near neutral magma-derived hydrothermal fluid (Fig. 2.15b). Gold enrichment occurred during stage 2 paragenesis, due to intermittent boiling of the hydrothermal fluid at shallow depth; however, Ag was mostly deposited in tetrahedrite due to fractional crystallization of the mineral from the hydrothermal fluid with increasing distance from the centre of the deposit, as the fluid mixed with seawater and cooled. Stage 3 deposition formed a chalcopyrite-pyrite-dominated basal stringer zone and Zn-Pb-Cu mineralization that partially overprinted the stratiform sulfide zone (Fig. 2.15c). This limited zone refinement is typical of Kuroko-type VMS deposits, and occurred below the boiling point (at >1500 mbsl) for higher temperature hydrothermal fluids.

A direct magmatic contribution of precious and trace metals to the hydrothermal fluid is thus inferred from the intermediate sulfidation epithermal mineral assemblages and epithermal element suite of the type 2A and type 2B mineral assemblages at Lemarchant. The combination of a shallow seawater environment and the extremely close spatial association of a magmatic body, within a VMS-forming environment, enabled precious metal enrichment of polymetallic massive sulfides at the Lemarchant deposit, in the absence of acidic (advanced argillic) alteration. Precious metal enrichment in the polymetallic Lemarchant VMS deposit has implications for similar VMS deposits in the Appalachians and globally.

2.8 – Acknowledgements

Funding for this project is principally supported by the GSC Targeted Geoscience Initiative 4 Program and the Research Affiliate Program of NRCan. Additional grants to Dr. Stephen J. Piercey, including an NSERC Discovery Grant and the NSERC-Altius Industrial Research Chair in Mineral Deposits supported by NSERC, Altius Resources Inc., and the Research and Development Corporation of Newfoundland and Labrador contribute to the funding of this project. Access to the Lemarchant drill core and core logs was provided by the Canadian Zinc Corporation and the Paragon Minerals Corporation (a wholly owned subsidiary of Canadian Zinc Corporation). Many thanks to the following people for their technological help and interpretive guidance: Dr. Patrick Mercier-Langevin at NRCan; Stefanie Lode, Jean-Luc Pilote and Jonathan Cloutier at the Memorial University of Newfoundland; Diane Fost and Christine Devine at Canadian Zinc Corporation; Michael Schaeffer and David Grant at CREAIT MAF-IIC; and Brian

Joy, Dr. Dan Layton-Matthews and Michael Gadd at QFIR. Thanks to editors Dr. Piercey, Stefanie Lode and Dr. Layton-Matthews for their constructive and insightful comments, and to Jan Peter and Aphrodite Indares for their reviews.

2.9 – References

Amcoff, Ö., 1984. Distribution of silver in massive sulfide ores: Mineralium Deposita, v. 19, p. 63-69.

Ballantyne, J.M., and Moore, J.N., 1988. Arsenic geochemistry in geothermal systems: Geochimica et Cosmochimica Acta, v. 52, p. 475-483.

Barton Jr, P., and Skinner, B., 1979. Sulfide mineral stabilities: *in* Barnes, H.L., ed., Geochemistry of Hydrothermal Ore Deposits, 2nd Edition, p. 278-403.

Bischoff, J.L., and Rosenbauer, R.J., 1983. A note on the chemistry of seawater in the range 350°–500°C: Geochimica et Cosmochimica Acta, v. 47, p. 139-144.

Bischoff, J.L., and Rosenbauer, R.J., 1984. The critical point and two-phase boundary of seawater, 200–500°C: Earth and Planetary Science Letters, v. 68, p. 172-180.

Blanchard, M., Alfredsson, M., Brodholt, J., Wright, K., and Catlow, C.R.A., 2007. Arsenic incorporation into FeS_2 pyrite and its influence on dissolution: A DFT study: Geochimica et Cosmochimica Acta, v. 71, p. 624-630.

Brueckner, S.M., Piercey, S.J., Sylvester, P.J., Maloney, S., and Pilgrim, L., 2014. Evidence for syngenetic precious metal enrichment in an Appalachian volcanogenic massive sulfide system: the 1806 Zone, Ming Mine, Newfoundland, Canada: Economic Geology, v. 109, p. 1611-1642.

Butterfield, D.A., Massoth, G.J., McDuff, R.E., Lupton, J.E., and Lilley, M.D., 1990. Geochemistry of hydrothermal fluids from Axial Seamount hydrothermal emissions study vent field, Juan de Fuca Ridge: Subseafloor boiling and subsequent fluid−rock interaction: Journal of Geophysical Research: Solid Earth, v. 95, p. 12895-12921.

Cathles, L.M., Guber, A., Lenagh, T.C., and Dudas, F., 1983. Kuroko-type massive sulfide deposits of Japan: Products of an aborted island arc rift: Economic Geology Monograph, v. 5, p. 96-114.

Cathles, L.M., Erendi, A., and Barrie, T., 1997. How long can a hydrothermal system be sustained by a single intrusive event?: Economic Geology, v. 92, p. 766-771.

Chiaradia, M., Tripodi, D., Fontboté, L., and Reza, B., 2008. Geologic Setting, Mineralogy, and Geochemistry of the Early Tertiary Au-Rich Volcanic-Hosted Massive Sulfide Deposit of La Plata, Western Cordillera, Ecuador: Economic Geology, v. 103, p. 161-183.

Cooke, D.R., and Simmons, S.F., 2000. Characteristics and genesis of epithermal gold deposits: Reviews in Economic Geology, v. 13, p. 221-244.

Copeland, D.A., Toole, R.M.S., and Piercey, S.J., 2008a. Assessment report on diamond drilling and soil sampling, License 8183M (10th Year) and 9569M (5th Year) South Tally Pond property, Rogerson Lake area, Newfoundland and Labrador, NTS 12A/10 and 12A/07. Newfoundland and Labrador Geological Survey, Assessment Report, 956 p. [for Paragon Minerals and Altius Minerals].

Copeland, D.A., McClenaghan, S.M., and Piercey, S.J., 2008b. Ninth year assessment report on diamond drilling, lithogeochemistry, pulse EM surveying and linecutting on license 8183M, South Tally Pond Property, Rogerson Lake area, Newfoundland and Labrador NTS 12A/10 and 12A/07. Newfoundland and Labrador Geological Survey, Assessment Report, 91 p. [for Paragon Minerals and Altius Minerals].

Czamanske, G.K., 1974. The FeS content of sphalerite along the chalcopyrite-pyrite-bornite sulfur fugacity buffer: Economic Geology, v. 69, p. 1328-1334.

de Ronde, C.E.J., Baker, E.T., Massoth, G.J., Lupton, J.E., Wright, I.C., Feely, R.A., and Greene, R.R., 2001. Intra-oceanic subduction-related hydrothermal venting, Kermadec volcanic arc, New Zealand: Earth and Planetary Science Letters, v. 193, p. 359-369.

de Ronde, C.E.J., Hannington, M.D., Stoffers, P., Wright, I.C., Ditchburn, R.G., Reyes, A.G., Baker, E.T., Massoth, G.J., Lupton, J.E., Walker, S.L., Greene, R.R., Soong, C.W.R., Ishibashi, J., Lebon, G.T., Bray, C.J., and Resing, J.A., 2005. Evolution of a submarine magmatic-hydrothermal system: Brothers Volcano, Southern Kermadec Arc, New Zealand: Economic Geology, v. 100, p. 1097-1133.

Drummond, S., and Ohmoto, H., 1985. Chemical evolution and mineral deposition in boiling hydrothermal systems: Economic Geology, v. 80, p. 126-147.

Dubé, B., Gosselin, P., Mercier-Langevin, P., Hannington, M., and Galley, A., 2007a. Gold-rich volcanogenic massive sulfide deposits: *in* Goodfellow, W.D., ed., Mineral deposits of Canada: A synthesis of major deposit-types, district metallogeny, the evolution of geological provinces, and exploration methods: Geological Association of Canada, Mineral Deposits Division, Special Publication, v. 5, p. 75-94.

Dubé, B., Mercier-Langevin, P., Hannington, M., Lafrance, B., Gosselin, G., and Gosselin, P., 2007b. The LaRonde Penna world-class Au-rich volcanogenic massive

sulfide deposit, Abitibi, Québec: mineralogy and geochemistry of alteration and implications for genesis and exploration: Economic Geology, v. 102, p. 633-666.

Dunning, G.R., Swinden, H.S., Kean, B.F., Evans, D.T.W., and Jenner, G.A., 1991. A Cambrian island arc in Iapetus; geochronology and geochemistry of the Lake Ambrose volcanic belt, Newfoundland Appalachians: Geological Magazine, v. 128, p. 1-17.

Eggins, S., Rudnick, R., and McDonough, W., 1998. The composition of peridotites and their minerals: a laser-ablation ICP–MS study: Earth and Planetary Science Letters, v. 154, p. 53-71.

Eldridge, C.S., Barton, P.B., Jr., and Ohmoto, H., 1983. Mineral textures and their bearing on formation of the Kuroko orebodies: Economic Geology Monograph, v. 5, p. 241-281.

Einaudi, M.T., Hedenquist, J.W., and Inan, E.E., 2003. Sulfidation state of fluids in active and extinct hydrothermal systems; transitions from porphyry to epithermal environments: Society of Economic Geologists, Special Publication, v. 10, p. 285-313.

Evans, D., and Kean, B., 2002. The Victoria Lake Supergroup, central Newfoundland – its definition, setting and volcanogenic massive sulfide mineralization: Newfoundland Department of Mines and Energy, Geological Survey, Open File NFLD/2790, 68 p.

Fleischer, M., 1955. Minor elements in some sulfide minerals: Economic Geology, v. 50, p. 1024.

Franklin, J., Gibson, H., Jonasson, I., and Galley, A., 2005. Volcanogenic massive sulfides: Economic Geology 100th Anniversary Volume, p. 523-560.

Fraser, D., Giroux, G.H., Copeland, D.A., and Devine, C.A., 2012. Technical report and resource minerals estimate on the Lemarchant deposit, South Tally Pond VMS project, Central Newfoundland, Canada – NI 43-101 Technical Report prepared for Paragon Minerals Corporation, 132 p.

Galley, A., Hannington, M., and Jonasson, I., 2007. Volcanogenic massive sulfide deposits: *in* Goodfellow, W.D., ed., Mineral deposits of Canada: A synthesis of major deposit-types, district metallogeny, the evolution of geological provinces, and exploration methods: Geological Association of Canada, Mineral Deposits Division, Special Publication, v. 5, p. 141-161.

Gibson, H., Morton, R., and Hudak, G., 1999. Submarine volcanic processes, deposits, and environments favorable for the location of volcanic-associated massive sulfide deposits: Reviews in Economic Geology, v. 8, p. 13-51.

Gibson, H.L., Allen, R.L., Riverin, G., and Lane, T.E., 2007. The VMS model; advances and application to exploration: Abstracts, Decennial International Conference on Mineral Exploration, v. 5, p. 713-730.

Gill, S.B. and Piercey, S.J., 2014. Preliminary observations on styles of mineralization and sulphide mineral zonation in the Cambrian Zn-Pb-Cu-Ag-Au Lemarchant volcanogenic massive sulphide (VMS) deposit, Newfoundland and Labrador; Geological Survey of Canada, Current Research 2014-5, 17 p

Glasby, G., and Notsu, K., 2003. Submarine hydrothermal mineralization in the Okinawa Trough, SW of Japan: an overview: Ore Geology Reviews, v. 23, p. 299-339.

Goldfarb, R.J., Baker, T., Dubé, B., Groves, D.I., Hart, C.J., and Gosselin, P., 2005. Distribution, character, and genesis of gold deposits in metamorphic terranes: Economic Geology 100th Anniversary Volume, p. 407-450.

Hackbarth, C.J., and Petersen, U., 1984. A fractional crystallization model for the deposition of argentian tetrahedrite: Economic Geology, v. 79, p. 448-460.

Hannington, M.D., and Scott, S.D., 1989. Sulfidation equilibria as guides to gold mineralization in volcanogenic massive sulfides; evidence from sulfide mineralogy and the composition of sphalerite: Economic Geology, v. 84, p. 1978-1995.

Hannington, M.D., Jonasson, I.R., Herzig, P.M., and Petersen, S., 1995. Physical and chemical processes of seafloor mineralization at mid-ocean ridges; *in* Humphris, S.E., Zierenberg, R.A., Mullineaux, L.S., Thomson, R.E., eds., Seafloor hydrothermal systems: Physical, chemical, biological, and geological interactions: Geophysical Monograph, v. 91, p. 115-157.

Hannington, M.D., Poulsen, K.H., Thompson, J.F.H., and Sillitoe, R.H., 1999. Volcanogenic gold in the massive sulfide environment: Reviews in Economic Geology, v. 8, p. 325-356.

Hannington, M.D., de Ronde, C.D., and Petersen, S., 2005. Sea-floor tectonics and submarine hydrothermal systems: Economic Geology 100th Anniversary Volume, p. 111–141.

Hannington, M., and Monecke, T., 2009. Modern submarine hydrothermal systems - A global perspective on distribution, size and tectonic settings: *in* Cousens, B., and Piercey, S.J., eds., Submarine Volcanism and mineralization: modern through ancient: Geological Association of Canada, Mineral Deposits Division, Short Course Notes, v. 19, p. 91-146.

Hedenquist, J.W., Arribas R, A., and Gonzalez-Urien, E., 2000. Exploration for epithermal gold deposits: Reviews in Economic Geology, v. 13, p. 245-277.

Hedenquist, J.W., and Lowenstern, J.B., 1994. The role of magmas in the formation of hydrothermal ore deposits: Nature, v. 370, p. 519-527.

Herzig, P.M., Hannington, M.D., Fouquet, Y., von Stackelberg, U., and Petersen, S., 1993. Gold-rich polymetallic sulfides from the Lau back arc and implications for the geochemistry of gold in sea-floor hydrothermal systems of the Southwest Pacific: Economic Geology, v. 88, p. 2182-2209.

Huston, D.L., 2000. Gold in volcanic-hosted massive sulfide deposits; distribution, genesis, and exploration: Reviews in Economic Geology, v. 13, p. 401-426.

Huston, D.L., and Large, R.R., 1989. A chemical model for the concentration of gold in volcanogenic massive sulfide deposits: Ore Geology Reviews, v. 4, p. 171-200.

Huston, D.L., and Kamprad, J., 2001. Zonation of alteration facies at western Tharsis: implications for the genesis of Cu-Au deposits, Mount Lyell field, western Tasmania: Economic Geology, v. 96, p. 1123-1132.

Huston, D.L., Jablonski, W., and Sie, S., 1996. The distribution and mineral hosts of silver in eastern Australian volcanogenic massive sulfide deposits: The Canadian Mineralogist, v. 34, p. 529-546.

James, R.H., Allen, D.E., and Seyfried Jr, W.E., 2003. An experimental study of alteration of oceanic crust and terrigenous sediments at moderate temperatures (51 to 350°C): insights as to chemical processes in near-shore ridge-flank hydrothermal systems: Geochimica et Cosmochimica Acta, v. 67, p. 681-691.

Kase, K., Yamamoto, M., and Mitsuno, C., 1994. Germanium-bearing colusite from the Yanahara mine, Japan, and its significance to ore genesis: Journal of the Society of Resource Geology, v. 44, p. 33-38.

Kean, B., and Evans, D., 1988. Regional metallogeny of the Victoria Lake Group, central Newfoundland: Newfoundland Department of Mines and Energy, Mineral Development Division, Current Research Report 88-1, p. 319-330.

Large, R.R., 1977. Chemical evolution and zonation of massive sulfide deposits in volcanic terrains: Economic Geology, v. 72, p. 549-572.

Large, R.R., 1992. Australian volcanic-hosted massive sulfide deposits; features, styles, and genetic models: Economic Geology, v. 87, p. 471-510.

Lode, S., Piercey, S.J.P., Copeland, D.A., Devine, C.A., and Sparrow, B., 2012. Setting and styles of hydrothermal mudstones near the Lemarchant volcanogenic massive sulfide (VMS) deposit, Central Mobile Belt, Newfoundland: *in* Abstracts, Geological Association of Canada-Mineralogical Association of Canada, Joint Annual Meeting, v. 35, p. 79.

Lode, S., Piercey, S. J., Devine, C. A., Layne, G. D., Piercey, G., and Hewa, L., 2014. Lithogeochemistry and sulfur isotopic composition of hydrothermal mudstones associated with the Lemarchant volcanogenic massive sulfide (VMS) deposit, Tally

Pond Belt, Central Newfoundland: *in* Abstracts, Geological Association of Canada, Newfoundland Spring Technical Meeting, v. 40, p. 20.

Longerich, H.P., Jackson, S.E., and Gunther, D., 1996. Inter-laboratory note – Laser ablation inductively coupled plasma mass spectrometric transient signal data acquisition and analyte concentration calculation: Journal of Analytical Atomic Spectrometry, v. 11, p. 899-904.

Lusk, J., and Calder, B.O.E., 2004. The composition of sphalerite and associated sulfides in reactions of the Cu–Fe–Zn–S, Fe–Zn–S and Cu–Fe–S systems at 1 bar and temperatures between 250 and 535°C: Chemical Geology, v. 203, p. 319-345.

Lydon, J.W., 1984. Volcanogenic massive sulfide deposits, Part 1: A descriptive model: Geoscience Canada, v. 11, p. 145-181.

Lydon, J.W., 1988. Volcanogenic massive sulfide deposits, Part 2: Genetic models: Geoscience Canada, v. 15, p. 155-181.

Lydon, J.W., 1996. Characteristics of volcanogenic massive sulfide deposits; interpretations in terms of hydrothermal convection systems and magmatic hydrothermal systems: Boletin Geologico y Minero, v. 107, p. 215-264.

McClenaghan, S.H., Lentz, D.R., Martin, J., and Diegor, W.G., 2009. Gold in the Brunswick No. 12 volcanogenic massive sulfide deposit, Bathurst Mining Camp, Canada: Evidence from bulk ore analysis and laser ablation ICP-MS data on sulfide phases: Mineralium Deposita, v. 44, p. 523-557.

McNicoll, V., Squires, G., Kerr, A., and Moore, P., 2010. The Duck Pond and Boundary Cu-Zn deposits, Newfoundland; new insights into the ages of host rocks and the timing of VHMS mineralization: Canadian Journal of Earth Sciences, v. 47, p. 1481-1506.

Mercier-Langevin, P., Dubé, B., Hannington, M.D., Davis, D.W., Lafrance, B., and Gosselin, G., 2007. The LaRonde Penna Au-rich volcanogenic massive sulfide deposit, Abitibi Greenstone belt, Quebec: Part I. Geology and geochronology: Economic Geology, v. 102, p. 585-609.

Mercier-Langevin, P., Hannington, M., Dubé, B., and Bécu, V., 2011. The gold content of volcanogenic massive sulfide deposits: Mineralium Deposita, v. 46, p. 509-539.

Ohmoto, H., Mizukami, M., Drummond, S., Eldridge, C., Pisutha-Arnond, V., and Lenagh, T., 1983. Chemical processes of Kuroko formation: Economic Geology Monograph, v. 5, p. 570-604.

Ohmoto, H., 1996. Formation of volcanogenic massive sulfide deposits; the Kuroko perspective: Ore Geology Reviews, v. 10, p. 135-177.

Petersen, E.U., Petersen, U., and Hackbarth, C., 1990. Ore zoning and tetrahedrite compositional variation at Orcopampa, Peru: Economic Geology, v. 85, p. 1491-1503.

Piercey, S., 2007. Volcanogenic massive sulfide (VMS) deposits of the Newfoundland Appalachians: an overview of their setting, classification, grade-tonnage data, and unresolved questions: Newfoundland and Labrador Department of Natural Resources, Geological Survey, Report 07-1, p. 169-178.

Piercey, S.J., Chaloux, E.C., Péloquin, A.S., Hamilton, M.A., and Creaser, R.A., 2008. Synvolcanic and younger plutonic rocks from the Blake River Group: implications for regional metallogenesis: Economic Geology, v. 103, p. 1243-1268.

Piercey, S.J. and Hinchey, J., 2012. Volcanogenic massive sulfide (VMS) deposits of the Central Mineral Belt, Newfoundland: Geological Association of Canada–Mineralogical Association of Canada Joint Annual Meeting, Field Trip Guidebook B, Newfoundland and Labrador Department of Natural Resources, Geological Survey, Open File NFLD/3173, 56 p.

Piercey, S.J., Squires, G.C., and Brace, T.D., 2014. Lithostratigraphic, hydrothermal, and tectonic setting of the Boundary volcanogenic massive sulfide deposit, Newfoundland Appalachians, Canada: Formation by subseafloor replacement in a Cambrian rifted arc: Economic Geology, v. 109, p. 661-687.

Pisutha-Arnond, V., and Ohmoto, H., 1983. Thermal history, and chemical and isotopic compositions of the ore-forming fluids responsible for the Kuroko massive sulfide deposits in the Hokuroku District of Japan: Economic Geology Monograph, v. 5, p. 523-558.

Pollock, J., 2004, Geology and paleotectonic history of the Tally Pond Group, Dunnage zone, Newfoundland Appalachians: An integrated geochemical, geochronological, metallogenic and isotopic study of a Cambrian island arc along the Peri-Gondwanan margin of Iapetus: Unpublished M.Sc. thesis, St. John's, Newfoundland, Memorial University, 420 p.

Poulsen, K.H., and Hannington, M.D., 1995. Volcanic-associated massive sulfide gold: *in* Eckstrand, O.R., Sinclair, W.D., and Thorpe, R.I., eds., Geology of Canadian mineral deposit types, Geology of Canada No. 8, Decade of North American Geology (DNAG): Geological Society of America, Part 1, p. 183-196.

Reich, M., and Becker, U., 2006. First-principles calculations of the thermodynamic mixing properties of arsenic incorporation into pyrite and marcasite: Chemical Geology, v. 225, p. 278-290.

Riverin, G., and Hodgson, C., 1980. Wall-rock alteration at the Millenbach Cu-Zn mine, Noranda, Quebec: Economic Geology, v. 75, p. 424-444.

Rogers, N., van Staal, C.R., McNicoll, V., Pollock, J., Zagorevski, A., and Whalen, J., 2006. Neoproterozoic and Cambrian arc magmatism along the eastern margin of the Victoria Lake Supergroup: A remnant of Ganderian basement in central Newfoundland?: Precambrian Research, v. 147, p. 320-341.

Roth, T., Thompson, J.F.H., and Barrett, T.J., 1999. The precious metal-rich Eskay Creek Deposit, northwestern British Columbia: Reviews in Economic Geology, v. 8, p. 357-373.

Rye, R.O., 1993. The evolution of magmatic fluids in the epithermal environment; the stable isotope perspective: Economic Geology, v. 88, p. 733-752.

Scotney, P.M., Roberts, S., Herrington, R.J., Boyce, A.J., and Burgess, R., 2005. The development of volcanic hosted massive sulfide and barite-gold orebodies on Wetar Island, Indonesia: Mineralium Deposita, v. 40, p. 76-99.

Scott, S., and Barnes, H., 1971. Sphalerite geothermometry and geobarometry: Economic Geology, v. 66, p. 653-669.

Seward, T.M., 1973. Thio-complexes of gold and the transport of gold in hydrothermal ore solutions: Geochimica et Cosmochimica Acta, v. 37, p. 379-399.

Seward, T.M., 1976. The stability of chloride complexes of silver in hydrothermal solutions up to 350°C: Geochimica et Cosmochimica Acta, v. 40, p. 1329-1341.

Seyfried, W., and Ding, K., 1995. Phase equilibria in subseafloor hydrothermal systems: A review of the role of redox, temperature, pH and dissolved Cl on the chemistry of hot spring fluids at mid-ocean ridges: *in* Seafloor hydrothermal systems: Physical, chemical, biological, and geological interactions: Geophysical Monograph, v. 91, p. 248-272.

Sherlock, R.L., Roth, T., Spooner, E.T.C., and Bray, C.J., 1999. Origin of the Eskay Creek precious metal-rich volcanogenic massive sulfide deposit; fluid inclusion and stable isotope evidence: Economic Geology, v. 94, p. 803-824.

Sillitoe, R.H., and Hedenquist, J.W., 2003. Linkages between volcanotectonic settings, ore-fluid compositions, and epithermal precious metal deposits: Society of Economic Geologists, Special Publication, v. 10, p. 315-343.

Sillitoe, R.H., Hannington, M.D., and Thompson, J.F.H., 1996. High sulfidation deposits in the volcanogenic massive sulfide environment: Economic Geology, v. 91, p. 204-212.

Spry, P.G., Merlino, S., Wang, S., Zhang, X., and Buseck, P.R., 1994. New occurrences and refined crystal chemistry of colusite, with comparisons to arsenosulvanite: American Mineralogist, v. 79, p. 750-762.

Squires, G., and Moore, P., 2004. Volcanogenic massive sulfide environments of the Tally Pond Volcanics and adjacent area: Geological, lithogeochemical and geochronological results *in* Current Research, Newfoundland and Labrador Department of Natural Resources, Geological Survey, Report 04-1, p. 63-91.

Swinden, H.S., 1991. Paleotectonic settings of volcanogenic massive sulfide deposits in the Dunnage Zone, Newfoundland Appalachians, Canadian Institute of Mining and Metallurgy Bulletin, Volume 84, p. 59-89.

Swinden, H., Kean, B., and Dunning, G., 1988. Geological and paleotectonic settings of volcanogenic massive sulfide mineralization in Central Newfoundland: The Volcanogenic Sulfide Districts of Newfoundland, Geological Association of Canada, Mineral Deposits Division, p. 2-27.

Taylor, B.E., 2007. Epithermal gold deposits: *in* Goodfellow, W.D., ed., Mineral deposits of Canada: a synthesis of major deposit-types, district metallogeny, the evolution of geological provinces, and exploration methods: Geological Association of Canada, Mineral Deposits Division, Special Publication, v. 5, p. 113-139.

van Staal, C., and Barr, S., 2012. Lithospheric architecture and tectonic evolution of the Canadian Appalachians and associated Atlantic margin, Chapter 2: *in* Percival, J.A., Cook, F.A., and Clowes, R.M., eds., Tectonic Styles in Canada Revisited: the LITHOPROBE perspective, Geological Association of Canada, Special Paper, v. 49, p. 41-95.

Wagner, T., and Monecke, T., 2005. Germanium-bearing colusite from the Waterloo volcanic-rock-hosted massive sulfide deposit, Australia: Crystal chemistry and formation of colusite group minerals: The Canadian Mineralogist, v. 43, p. 655-669.

White, N.C., and Hedenquist, J.W., 1995. Epithermal gold deposits: styles, characteristics and exploration: SEG newsletter, v. 23, p. 9-13.

Williams-Jones, A.E., Bowell, R.J., and Migdisov, A.A., 2009. Gold in solution: Elements, v. 5, p. 281-287.

Wright, K., 2009. The incorporation of cadmium, manganese and ferrous iron in sphalerite: Insights from computer simulations: The Canadian Mineralogist, v. 47, p. 615-623.

Yamada, R., Nishitani, Y., Tanimura, S., and Konishi, N., 1988. Recent development and geologic characteristics of the Nurukawa Kuroko deposit: Mining Geology, v. 38, p. 309-322.

Zagorevski, A., Van Staal, C.R., McNicoll, V., and Rogers, N., 2007. Upper Cambrian to Upper Ordovician peri-Gondwanan Island arc activity in the Victoria Lake Supergroup, Central Newfoundland: Tectonic development of the northern Ganderian margin: American Journal of Science, v. 307, p. 339-370.

Table 2.1. Sulfide minerals identified from the Lemarchant deposit along strike (proximal to distal stratiform stringer zone) and with depth (stratiform to stringer sulfide zones). Relative abundance indicated from high (xxx) to low (x), and absent (----).

	Mineral phase	Formula	Stratiform sulfide zone	Proximal	Distal	Stringer sulfide zone
Identified	Barite	$BaSO_4$	xxx	xxx	x	-----
phases	White to honey sphalerite	(Zn,Fe)S	xxx	xxx	xx	-----
	Honey brown to red sphalerite	(Zn,Fe)S	xx	xx	x	x
	Colloform to reniform pyrite	FeS_2	x	x	x	-----
	Recrystallized subhedral pyrite	FeS_2	xx	xx	xx	xx
	Euhedral pyrite	FeS_2	x	x	x	xxx
	Galena	PbS	xx	xx	xx	x
	Tetrahedrite	$(Cu,Ag)_{10}(Fe,Zn)_2(As,Sb)_4S_{13}$	xx	x	xx	-----
	Tennantite	$(Cu,Ag)_{10}(Fe,Zn)_2(As,Sb)_4S_{13}$	xx	xx	x	-----
	Silver-tetrahedrite	$(Cu,Ag)_{10}(Fe,Zn)_2(As,Sb)_4S_{13}$	x	-----	xx	-----
	Chalcopyrite	$CuFeS_2$	x	x	x	xxx
	Bornite	Cu_5FeS_4	xx	xx	-----	-----
	Arsenian colusite	$Cu_{26}V_2(As,Ge,Sb,Sn)_6S_{32}$	x	x	x	-----
	Intermediate colusite	$Cu_{26}V_2(As,Ge,Sb,Sn)_6S_{32}$	x	x	-----	-----
	Germanium-rich colusite	$Cu_{26}V_2(As,Ge,Sb,Sn)_6S_{32}$	x	x	-----	-----
	Sulvanite	$Cu_3(V,Fe)S_4$	x	x	-----	-----
	Reinerite	$(Cu,Fe)_{22}(Ge_{4-x}As_x)Fe_8S_{32}$	x	x	-----	-----
	Stromeyerite	AgCuS	x	x	-----	-----
	Bournonite	$PbCuSbS_3$	x	-----	x	-----
	Polybasite	$[(Ag,Cu)_6(Sb,As)_2S_7][Ag_9CuS_4]$	x	-----	x	-----
	Miargyrite	$AgSbS_2$	x	-----	x	-----
	Electrum, high Au	(Au,Ag)	x	x	-----	-----
	Electrum, high Ag	(Au,Ag)	x	-----	x	-----
	Marcasite	FeS_2	x	x	x	x
	Pyrrhotite	$Fe_{1-x}S$	x	x	x	-----
	Arsenopyrite	FeAsS	x	x	x	-----
	Covellite	CuS	x	x	x	-----
Unidentified	Silver telluride		x	-----	x	-----
phases	Nickel sulphide		x	x	-----	-----
	Cu-Ag sulfosalts		x	x	x	-----
	Cu-V-Ge sulfosalts		x	x	-----	-----

Table 2.2. Average trace element contents and standard deviation (3σ) of sulfide phases in type assemblages at the Lemarchant deposit. Dataset is semi-quantitative. All values are above detection limit (LOD) or indicated BDL = below detection limit.

Type Mineralogy	Phase	Number of analyses		Ti (ppm)	V (ppm)	Cr (ppm)	Mn (ppm)	Co (ppm)	Ni (ppm)	Ge (ppm)	As (ppm)	Se (ppm)	Mo (ppm)	Ag (ppm)	Cd (ppm)	In (ppm)	Sn (ppm)	Sb (ppm)	Au (ppb)	Tl (ppm)	Pb (ppm)	Bi (ppm)
Type 1	**Sphalerite**	24	**Avg**	BDL	BDL	BDL	267	BDL	BDL	5	131	BDL	65	20	2680	BDL	10	52	BDL	19	121	BDL
			StDev	0	1	0	268	4	34	5	458	17	88	36	645	0	5	180	189	87	338	0
	Pyrite	8	**Avg**	BDL	49	BDL	491	27	1609	6	20347	7660	1170	715	118	BDL	BDL	1616	9230	1355	19951	8
			StDev	119	49	1	360	24	1116	1	19830	8384	1031	420	211	0	2	1171	5223	860	15063	9
Type 2A	**Galena**	7	**Avg**	578	BDL	28	BDL	18	1682	34	BDL	2532	24	372	70	BDL	48	409	2746	8	1220788	61
			StDev	99	0	5	16	3	327	8	79	4329	9	837	36	3	15	952	589	2	147987	17
	Chalcopyrite	9	**Avg**	BDL	BDL	BDL	BDL	BDL	30	22	BDL	BDL	230	132	4	8	10	3	BDL	2	4928	BDL
			StDev	0	6	3	25	2	36	21	0	0	524	228	2	5	8	5	0	4	14481	3
	Bornite	13	**Avg**	183	12	6	40	7	181	25	BDL	BDL	331	4818	12	6	27	12	833	3	80078	9
			StDev	159	15	5	50	10	348	14	12	100	455	1931	14	5	20	21	1337	3	200968	12
Type 2B	**Sphalerite**	8	**Avg**	BDL	97	BDL	205	BDL	BDL	102	7384	BDL	39	65	3032	14	33	2283	BDL	2	177	BDL
			StDev	0	118	4	55	0	14	259	20238	46	43	65	728	15	50	6401	0	1	419	0
	Pyrite	24	**Avg**	1182	58	7	208	13	635	8	6421	BDL	121	57	12	BDL	BDL	981	15439	211	1428	BDL
			StDev	5336	166	23	442	15	749	13	12736	115	275	89	47	1	2	2075	36488	524	4654	6
	Galena	25	**Avg**	373	BDL	18	44	13	892	27	111	219	71	1442	143	BDL	19	6986	1909	35	769021	39
			StDev	163	14	10	40	5	683	43	377	510	109	1431	433	4	10	27817	1785	64	451672	26
	Chalcopyrite	12	**Avg**	BDL	BDL	BDL	146	BDL	BDL	11	BDL	BDL	23	214	58	BDL	28	15	BDL	0	516	BDL
			StDev	114	4	2	429	4	17	12	0	16	73	324	191	2	38	45	0	0	1188	0
	Tetrahedrite	25	**Avg**	BDL	BDL	BDL	281	BDL	25	10	113279	86	159	10216	2128	BDL	8	81495	BDL	1	2199	BDL
			StDev	57	4	1	247	2	32	5	37131	105	630	23683	1629	7	7	64086	441	2	9767	2
Type 3	**Sphalerite**	4	**Avg**	BDL	38	4	278	BDL	BDL	5	BDL	BDL	112	52	3463	BDL	18	43	BDL	0	534	BDL
			StDev	0	60	8	158	0	0	1	0	0	148	37	481	4	7	48	0	0	407	0
	Pyrite	4	**Avg**	BDL	7	BDL	BDL	BDL	2627	4	302	BDL	711	19	4	BDL	BDL	37	BDL	BDL	4287	BDL
			StDev	93	9	0	17	3	1005	1	136	0	1337	38	7	0	2	72	0	0	8496	3
	Chalcopyrite	2	**Avg**	BDL	7	BDL	BDL	BDL	BDL	BDL	BDL	BDL	60	234	9	BDL	59	13	BDL	0	443	BDL
			StDev	0	10	4	0	0	22	4	0	0	85	15	1	0	5	15	0	0	619	0
Type 4	**Chalcopyrite**	2	**Avg**	BDL	BDL	BDL	BDL	BDL	BDL	4	BDL	95	BDL	170	4	17	21	0	BDL	0	BDL	BDL
			StDev	0	0	0	0	0	0	0	0	16	0	11	1	2	2	0	0	0	0	0

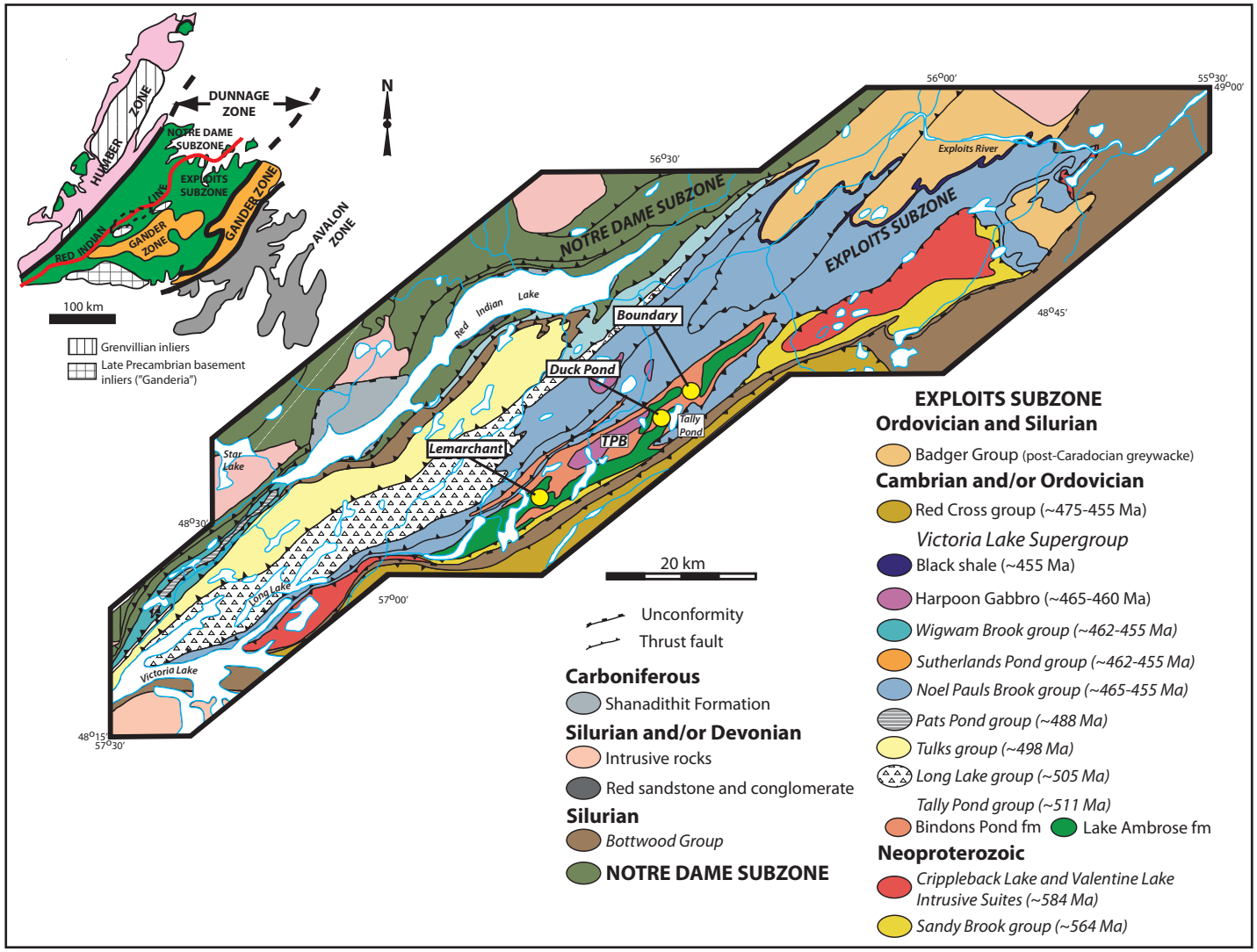

Figure 2.1. Geological map of the Victoria Lake Supergroup in the Newfoundland Central Mobile Belt (Dunnage Zone, inset). Locations of the Tally Pond belt (TPB) and the Lemarchant, Duck Pond and Boundary VMS deposits are highlighted (modified after Rogers et al., 2006; McNicoll et al., 2010; Piercey and Hinchey, 2012).

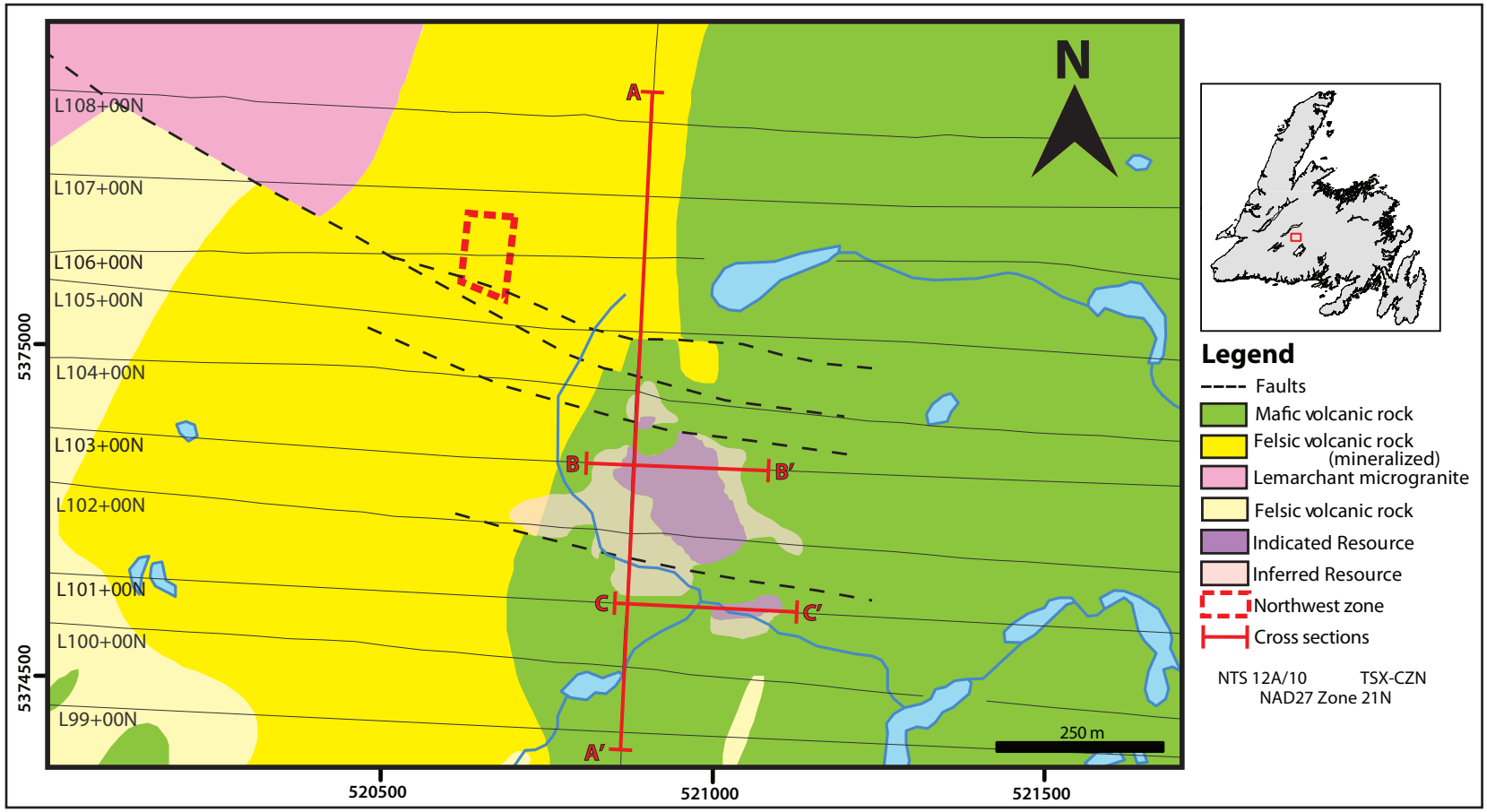

Figure 2.2. Schematic geological map of the Lemarchant deposit in the Tally Pond volcanic belt (modified from Fraser et al., 2012). Indicated and inferred calculated resources (Fraser et al., 2012), and Northwest zone projected to surface. Northing grid is superimposed to show locations of Fig. 2.3 cross-sections (Long section A-A'; L10300N B-B'; and L10100N C-C'), which are also highlighted in red.

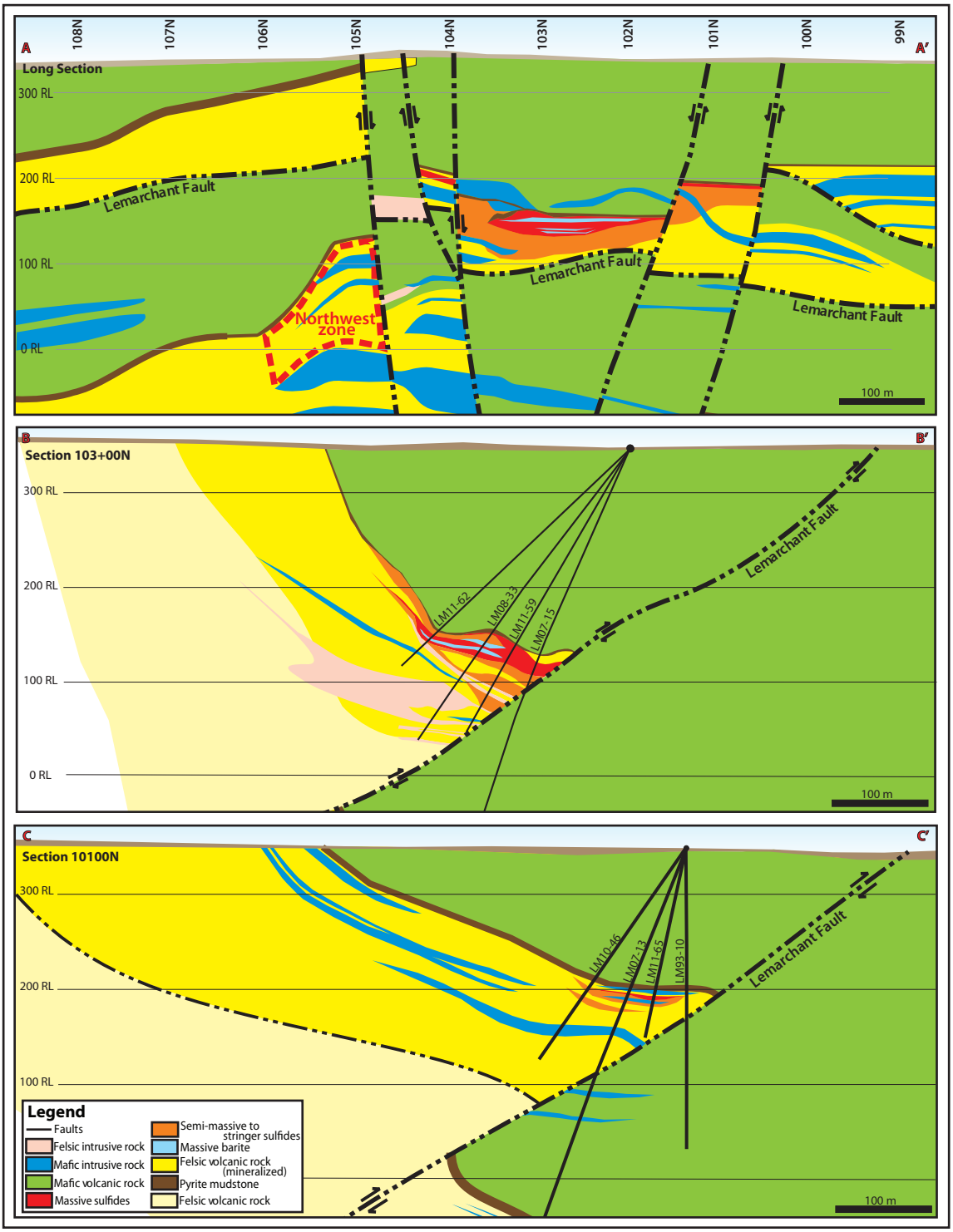

Figure 2.3. Section diagrams of selected portions of the Lemarchant deposit (modified from Fraser et al., 2012). A) Long section A-A', looking east, bisecting the main mineralized zone; Northwest Zone projected onto section. B) Cross section B-B' of L10300N, looking north, highlighting the centre portion of main mineralized zone. C) Cross section C-C' of L10100N, looking north, highlighting the outer edge of main mineralized zone.

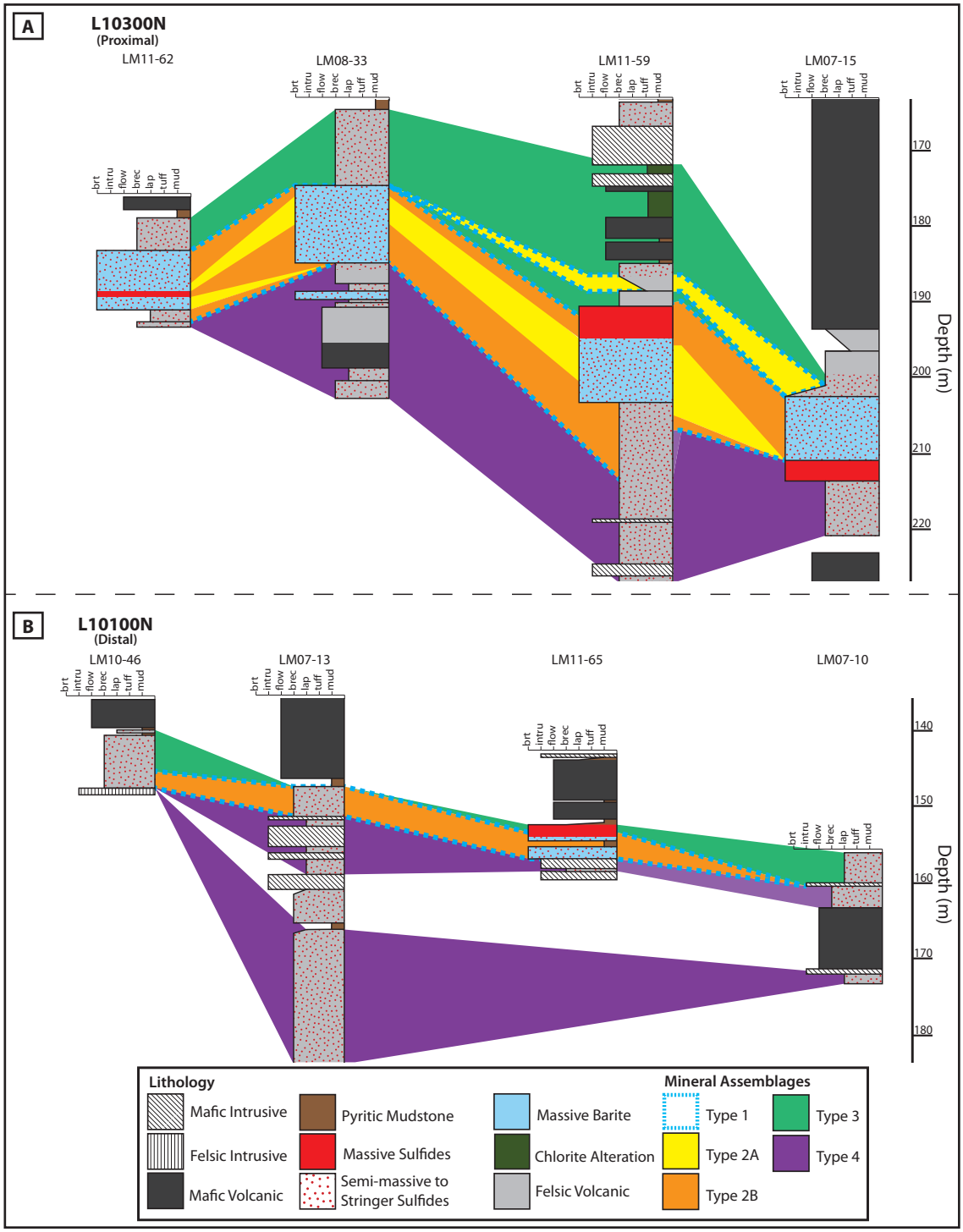

Figure 2.4. Fence diagrams of representative, mineralized sections within the Lemarchant deposit. A) Proximal section L10300N contains the complete set of (5) mineral assemblage types. B) Distal section L10100N contains only the type 1, 2B, 3 and 4 mineral assemblages. Section locations are shown as red traces in Fig. 2.2, and represented in cross-section in Fig. 2.3. Lithology colour coding has been altered from Fig. 2.2 and 2.3 to highlight type mineral assemblage relationships.

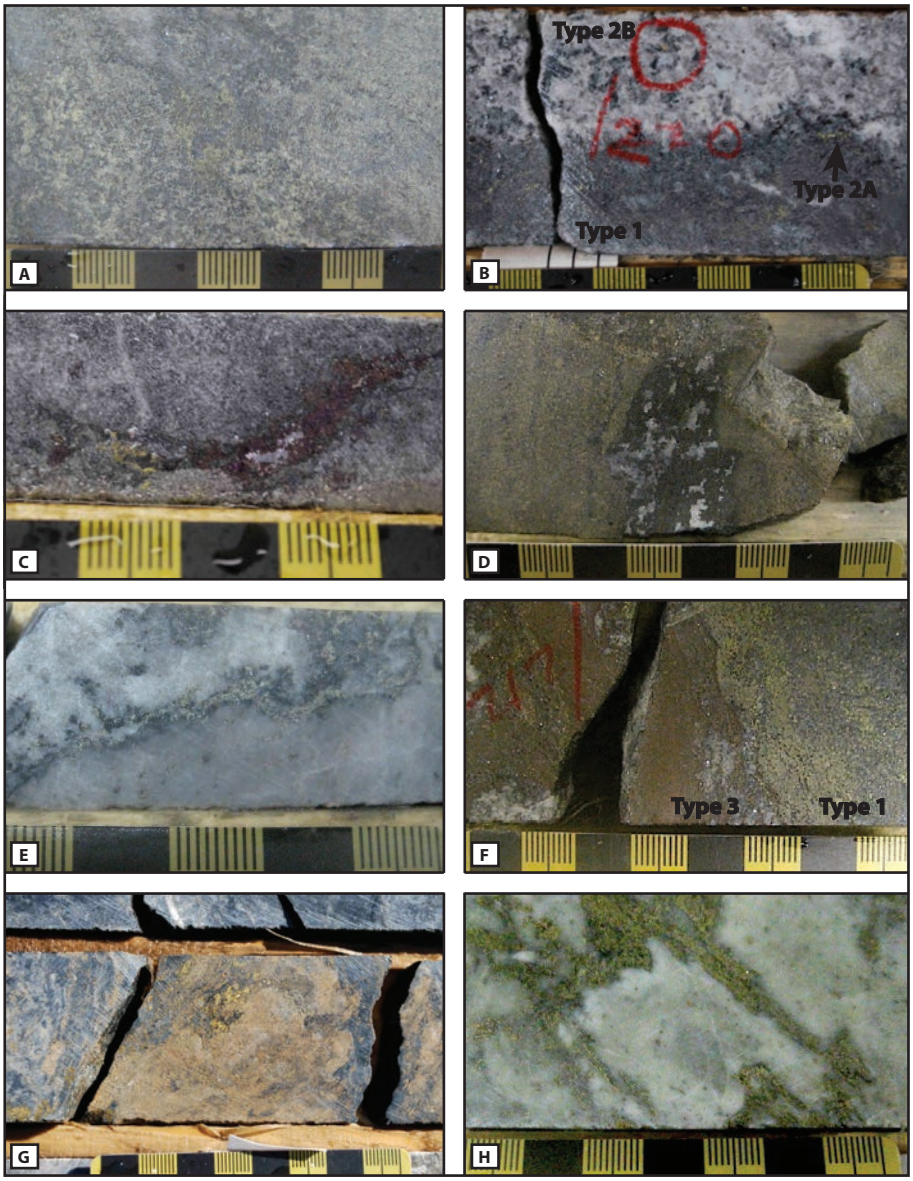

Figure 2.5. Representative drill core photographs of the 5 types of mineralization comprising the Lemarchant deposit. Black Squares = 1 cm. A) Type 1 semi-massive pale honey sphalerite, fine-grained pyrite and galena, with minor chalcopyrite in massive barite (Drill hole LM11-64 at 218.85m depth). B) Visible gold (in red) in type 2B massive to bladed barite-tetrahedrite-sphalerite-galena, with type 2A purple bornite-chalcopyrite stringers and type 1 semi-massive pale honey sphalerite-galena-pyrite (LM10-43 at 220.05m). C) Type 2A red-purple bornite-tetrahedrite-galena and late chalcopyrite stringers cross-cut type 1 barite-white sphalerite-pyrite-galena mineralization (LM11-62 at 259.6m). D) Type 2B coarse-grained barite and dark grey tetrahedrite with lesser galena and white sphalerite cross-cut type 1 massive honey coloured sphalerite-pyrite-galena (LM11-52 at 212.3m). E) Type 2B barite and tetrahedrite, lesser white sphalerite-galena and late chalcopyrite interstitial to rhyolite breccia (LM11-61 at 237.4m). F) Type 3 massive red sphalerite-pyrite-chalcopyrite replacing type 1 massive honey sphalerite, fine-grained pyrite, minor galena and chalcopyrite (LM11-52 at 212.0m). G) Type 4 orange sphalerite-chalcopyrite-pyrite stringers cross-cutting heavily chlorite altered matrix (LM11-59 at 251.22m). H) Type 4 chalcopyrite-pyrite stringers replacing matrix of concentrically-altered rhyolite breccia (LM11-52 at 228.54m).

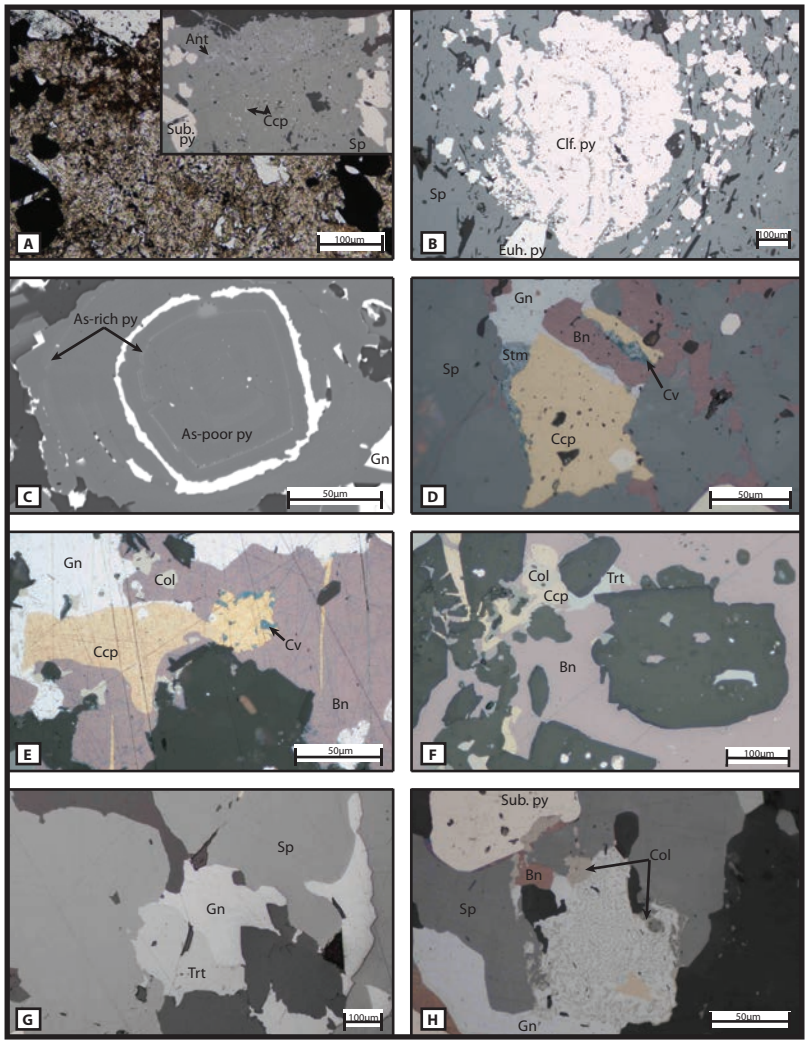

Figure 2.6. Thin section and backscatter electron (BSE) image compilation of mineralogy and textures in the type 1, type 2A and type2B mineral assemblages at the Lemarchant deposit. A) Transmitted light image of type 1 massive pale honey-coloured sphalerite; inset reflected light image shows chalcopyrite disease in sphalerite, subhedral pyrite and anatase lathes (Sample CNF29959 in drill hole LM11-59 at 207.72m depth). B) Reflected light image of colloform pyrite in sphalerite (CNF29960 in LM11-59 at 216.0m). C) Backscatter image of zoned subhedral to fine-grained pyrite; lighter grey growth rings have higher As-content (CNF25120 in LM11-52 at 212.0m). D) Type 2A bornite, galena and sphalerite with rounded pyrite and type 3 chalcopyrite replacement; irregular stromeyerite hosts late blue covellite (CNF29967 in LM07-17 at 247.63m). E) Type 3 chalcopyrite replacing and infilling cracks in type 2A bornite, galena and type 2B colusite; chalcopyrite is host to late blue covellite (CNF14279 in LM08-33 at 230.75m). F) Type 2A bornite overprinted by type 2B colusite and tetrahedrite, and replaced by type 3 chalcopyrite (CNF14299 in LM13-73 at 327.95m). G) Type 2B galena and tetrahedrite; galena shows resorbing by pale honey sphalerite (CNF25146 in LM10-46 at 182.56m). H) Myrmekitic growth of type 2B galena-colusite-sphalerite and replacement of type 2A bornite at the pyrite atoll-sphalerite interface; type 3 chalcopyrite is also present replacing galena-colusite intergrowth (CNF14279 in LM08-33 at 230.75m). Abbreviations as follows: Ant = anatase; Sub. py = subhedral pyrite; Ccp = chalcopyrite; Sp = sphalerite; Clf. py = colloform pyrite; Euh. py = euhedral pyrite; Py = pyrite; Gn = galena; Stm = stromeyerite; Bn = bornite; Cv = covellite; Col = colusite; Trt = tetrahedrite.

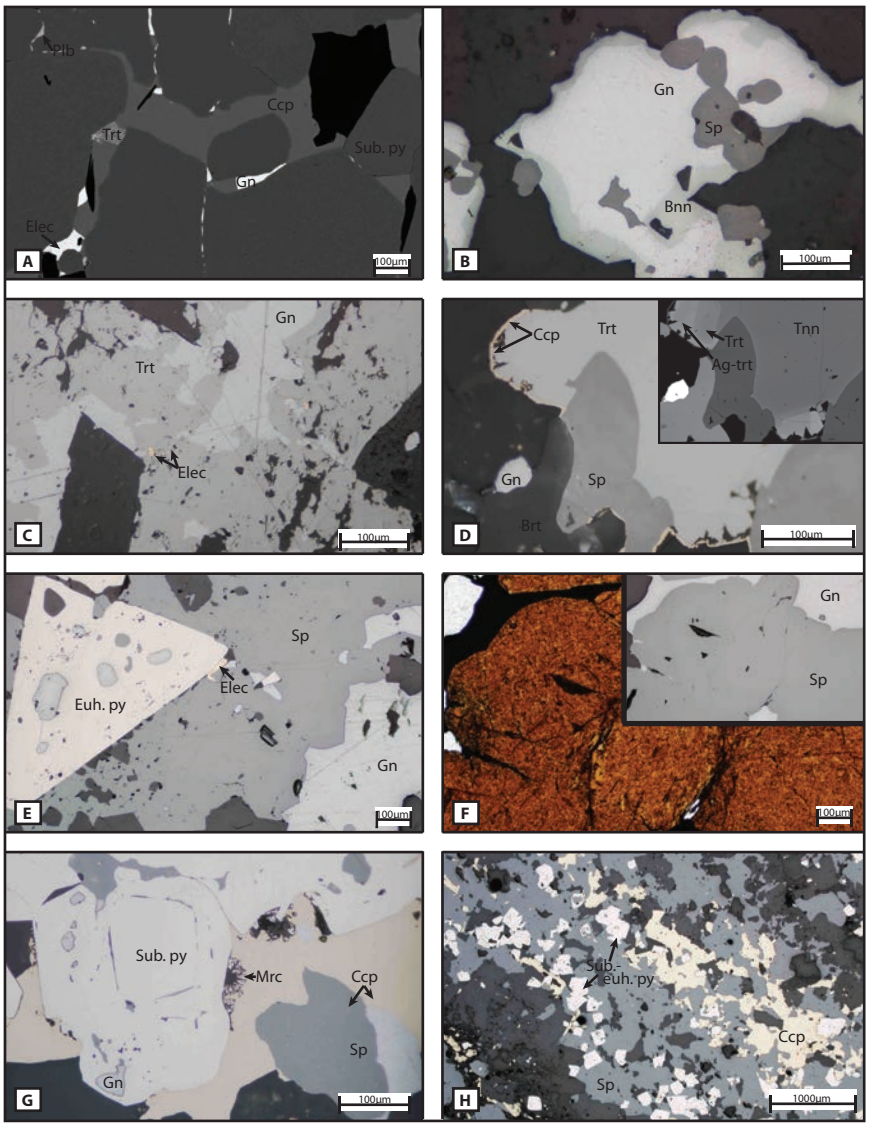

Figure 2.7. Thin section reflected light and BSE image compilation of mineralogy and textures in the type 2b, type 3 and type 4 mineral assemblages at the Lemarchant deposit. A) Backscatter image of type 2B assemblage of rounded pyrite-galena-tetrahedrite-electrum-polybasite and type 3 chalcopyrite (Sample CNF29986 in drill hole LM08-19 at 97.63m depth). B) Reflected light image of type 2B bournonite rimming galena and sphalerite (CNF14291 in LM11-65 at 159.3m). C) Type 2B galena-electrum in tetrahedrite (CNF25121 in LM11-52 at 212.3m). D) Reflected light image of type 2B tetrahedrite, galena, sphalerite, rounded pyrite and rimming chalcopyrite; inset BSE silver zonation map highlighting gradational Ag-rich rims in tetrahedrite (CNF14293 in LM11-65 at 161.75m). E) Type 2B galena-electrum at euhedral pyrite atoll boundary in massive sphalerite (CNF14291 in LM11-65 at 159.3m). F) Transmitted light image of type 3 massive red sphalerite; inset reflected light image shows scalloped sphalerite replacing galena (CNF29959 in LM11-59 at 207.72m). G) Type 3 recrystallized atoll pyrite with entrained sphlalerite and galena, dendritic marcasite in chalcopyrite and chalcopyrite-diseased sphalerite with galena (CNF14257 in LM11-62 at 266.84m). H) Type 3 subhedral to euhedral atoll pyrite and chalcopyrite with honey brown sphalerite (CNF29971 in LM11-63 at 224.7m). Additional abbreviations as follows: Plb = polybasite; Elec = electrum; Bnn = bournonite; Tnn = tennantite; Ag-trt = silver-rich tetrahedrite; Mrc = marcasite.

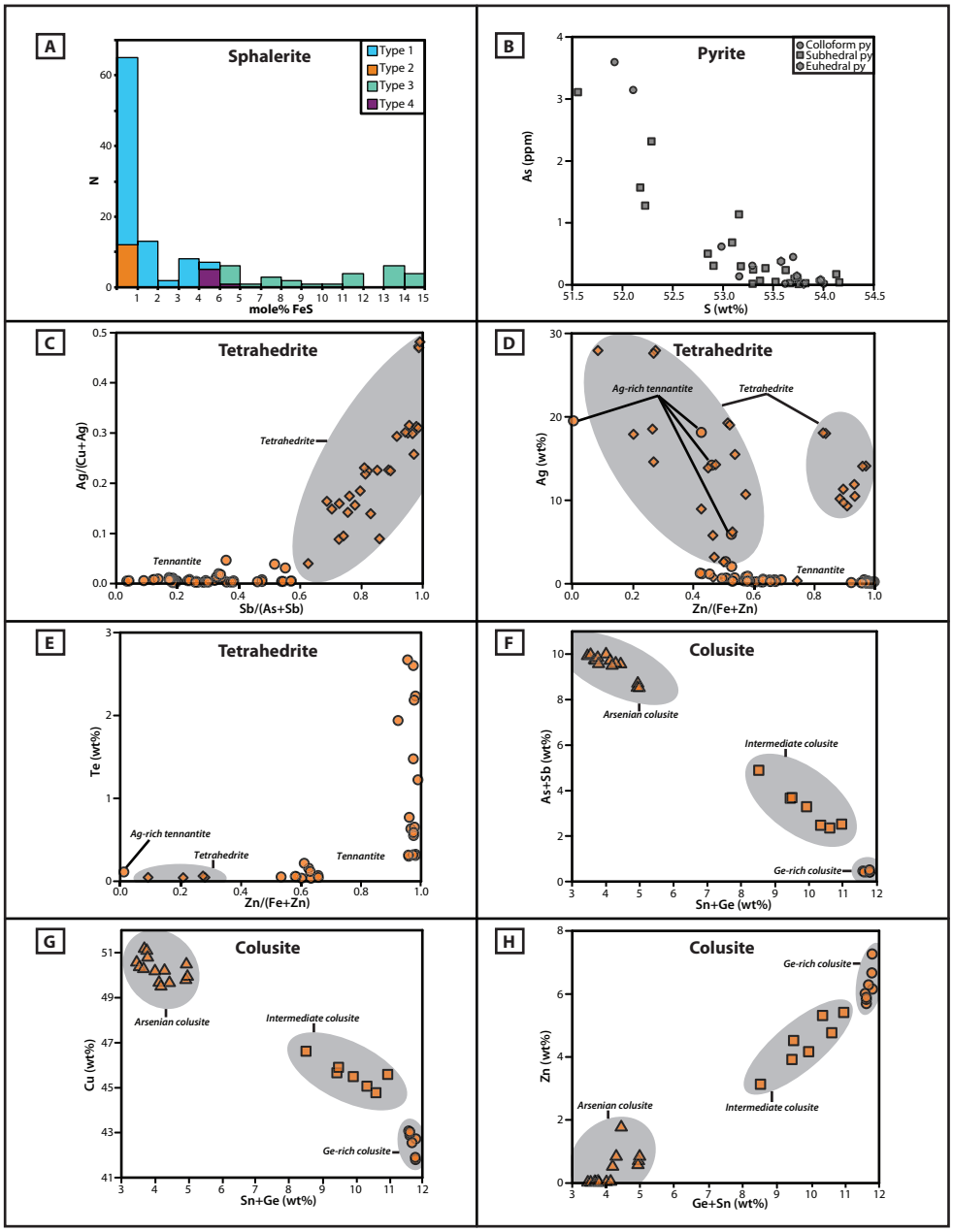

Figure 2.8. Compositional variation in select sulfide and sulfosalt phases from the Lemarchant deposit via electron microprobe analyses. A) Iron-content (mole% FeS) in sphalerite by mineral assemblage type. B) Arsenic (ppm) vs. S (wt%) conntents in pyrite. C) Normalized silver (Ag/(Ag+Cu)) vs. antimony (Sb/(As+Sb)) ratios in tetrahedrite-tennantite; shaded area distinguishes compositions with more tetrahedrite affinity (Sb/(As+Sb) >0.6). D) Silver (wt%) vs. the normalized zinc (Zn/(Fe+Zn)) ratio in tetrahedrite-tennantite; shaded area as above with Ag-rich tennantite samples are indicated (Ag >5 wt%). E) Tellurium (wt%) vs. the normalized zinc (Zn/(Fe+Zn)) ratio in tetrahedrite-tennantite; shaded area as above with Ag-rich tennantite samples are indicated. F) Sums of As+Sb (wt%) vs. Sn+Ge (wt%) in colusite-germanocolusite; shaded areas highlight populations with distinct As-Ge compositions. G) Copper (wt%) vs. the sum of Sn+Ge (wt%) in colusite-germanocolusite; shaded areas as above. H) Zinc (ppm) vs. the sum of Sn+Ge in colusite-germanocolusite; shaded areas as above.

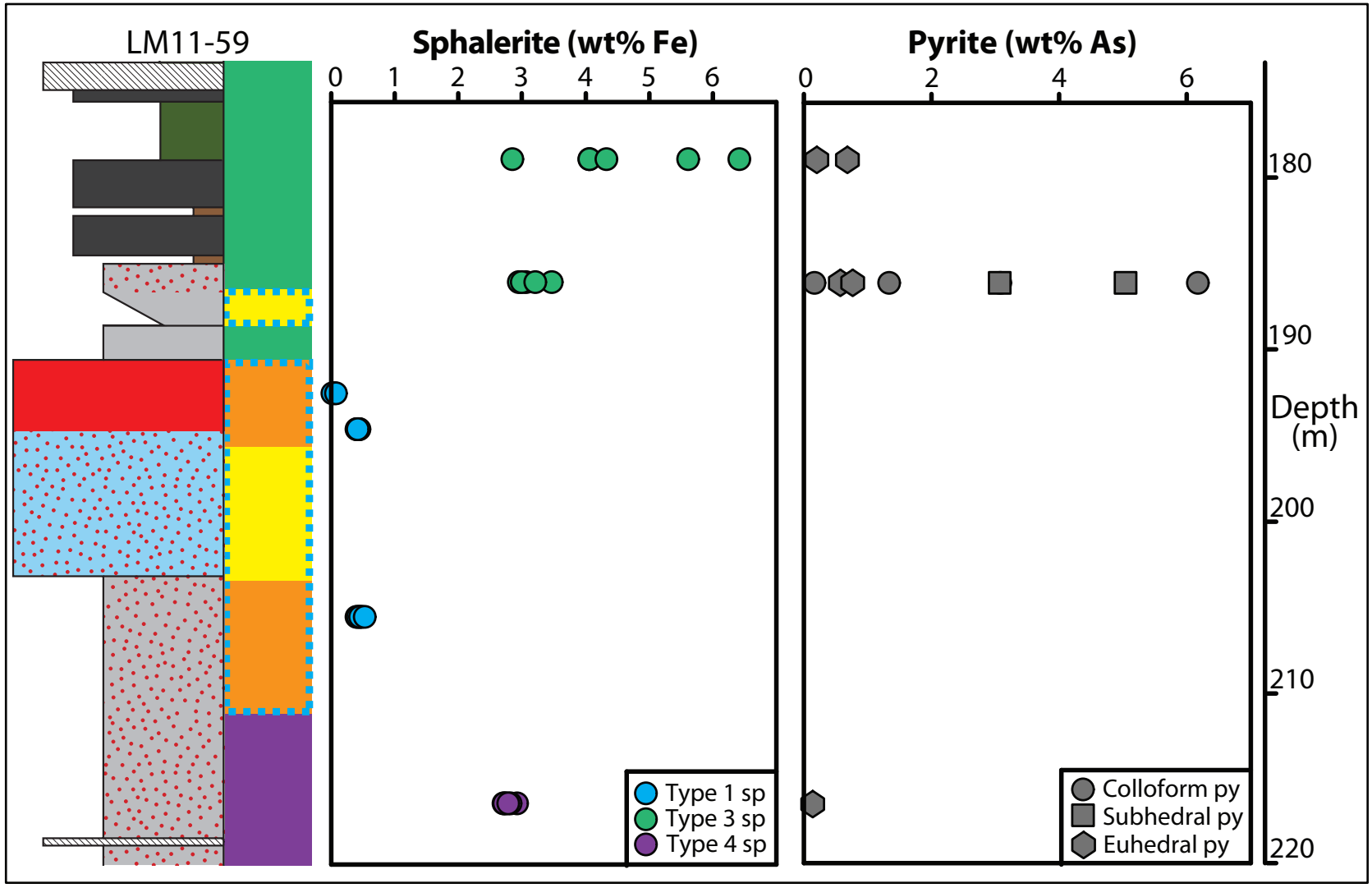

Figure 2.9. Down hole variation in minor element contents of Fe and As in sphalerite and pyrite, respectively, in the central portion of the Lemarchant deposit (drill hole LM11-59 at section L10300N). Legend for drill hole lithofacies and mineral assemblages as in Fig. 2.4. Drill hole and sample depths have been corrected to true depth.

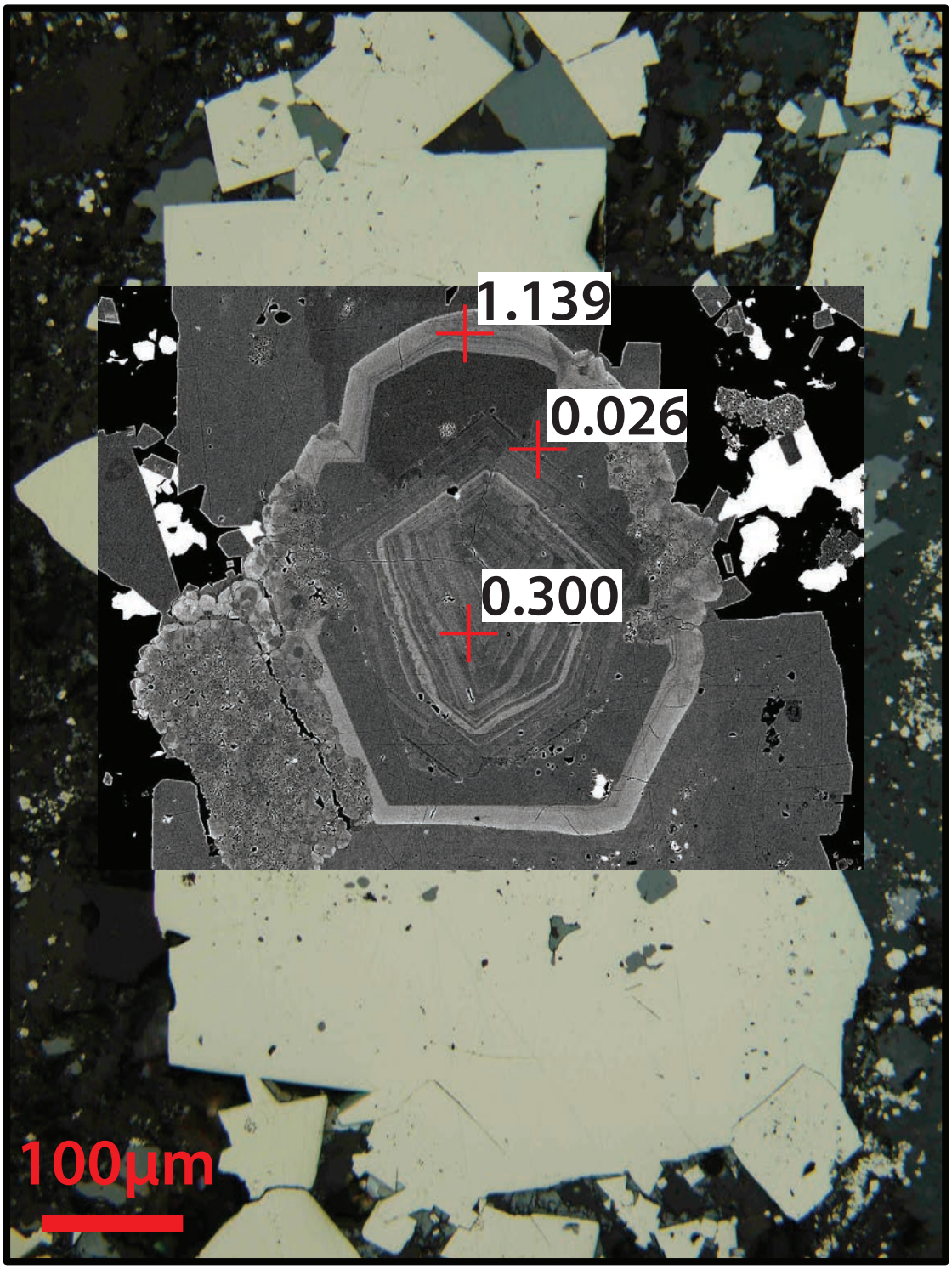

Figure 2.10. Arsenic zonation in pyrite. Reflected light image of variably recrystallized colloform, subhedral and minor euhedral pyrite (Sample CNF25134 in drill hole LM11-56 at 158.7m depth); overlying backscatter electron image shows arsenic content (wt% As) in pyrite from EMPA.

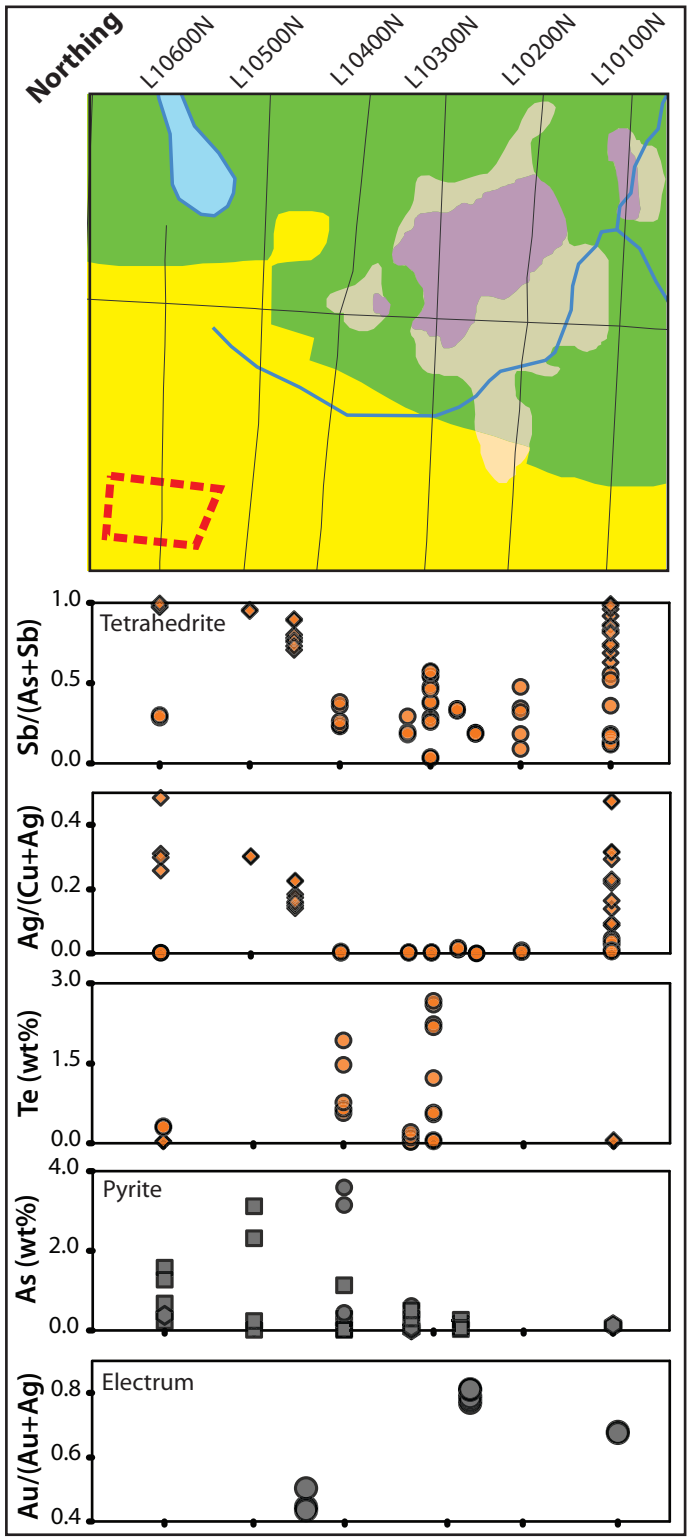

Figure 2.11. Along-strike variation in major to trace element contents and ratios in tetrahedrite (circles = tennantite; diamonds = tetrahedrite), pyrite (circles = colloform pyrite; squares = subhedral pyrite; hexagons = euhedral pyrite) and electrum. Legend for plan map lithofacies and phase symbols above as in Figs. 2.4 and 2.8).

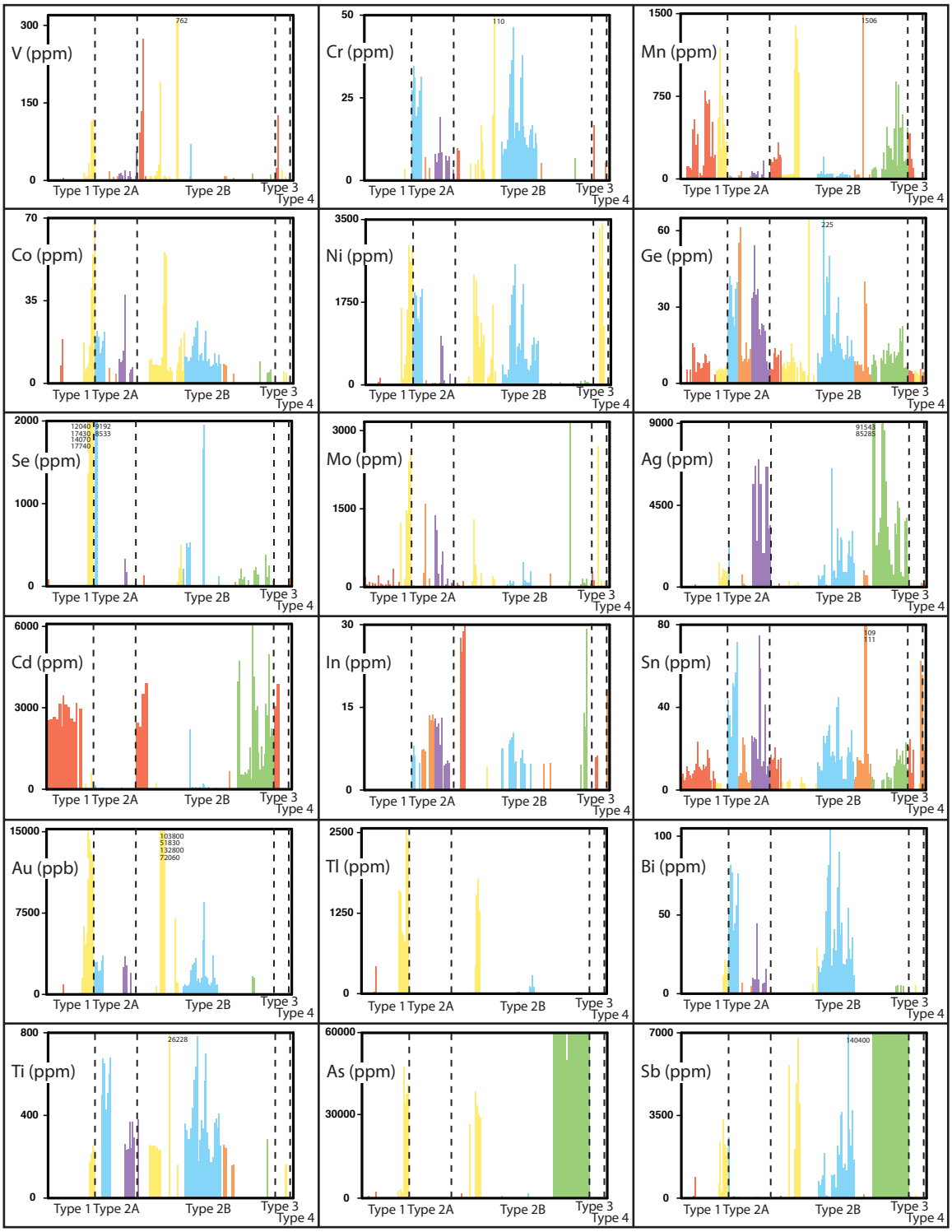

Figure 2.12. Trace element variation between sulfide phases composing the five types of mineralization. Sulfide phases represented: sphalerite (red), pyrite (yellow), chalcopyrite (orange), galena (blue), tetrahedrite (green) and bornite (purple). Elements highlighted: Ag, As, Au, Bi, Cd, Co, Cr, In, Ge, Mn, Mo, Ni, Sb, Se, Sn, Ti, Tl, V.

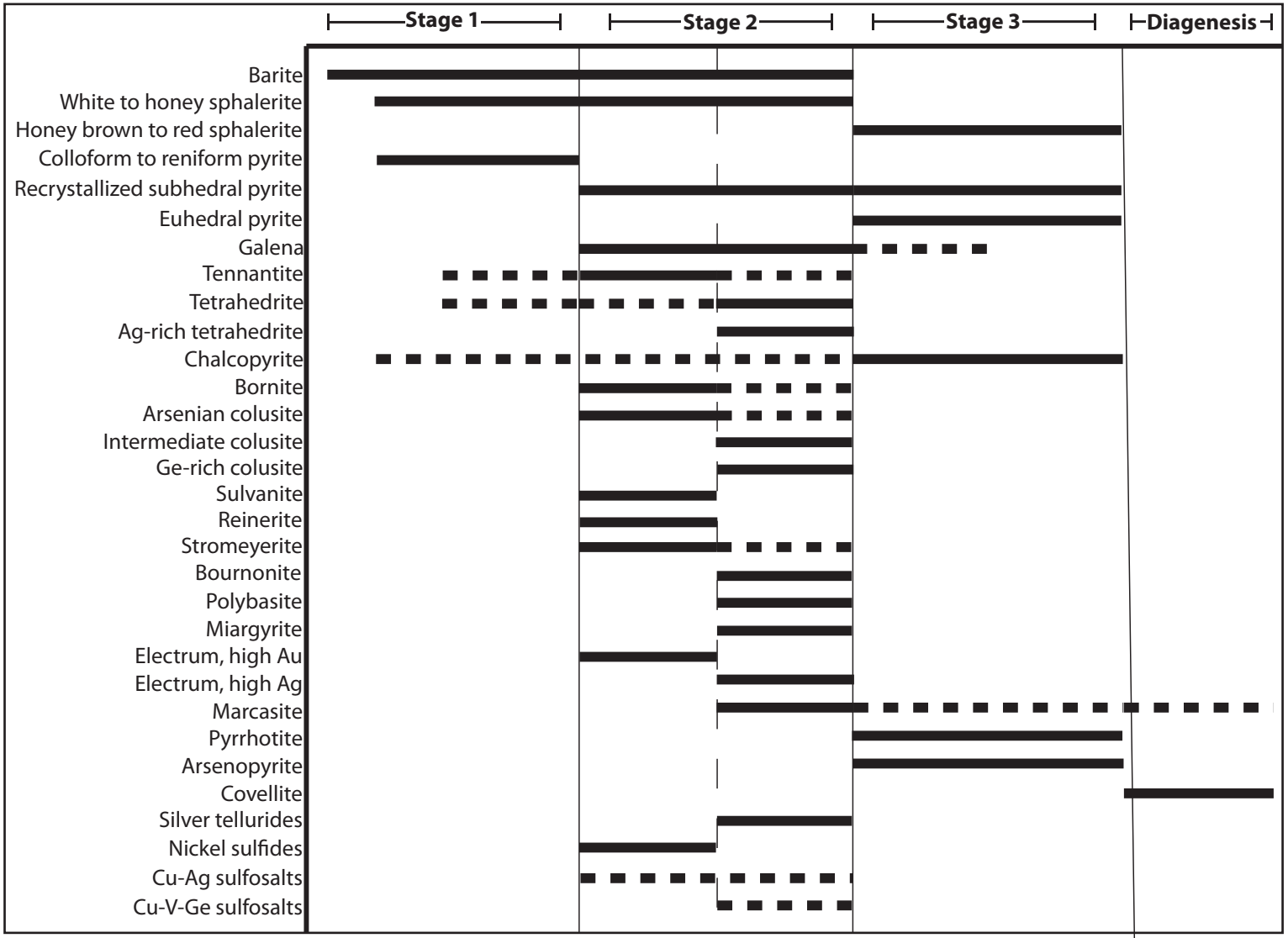

Figure 2.13. Paragenetic sequence of all mineral phases that compose the Lemarchant stratiform and stringer sulfide zones.

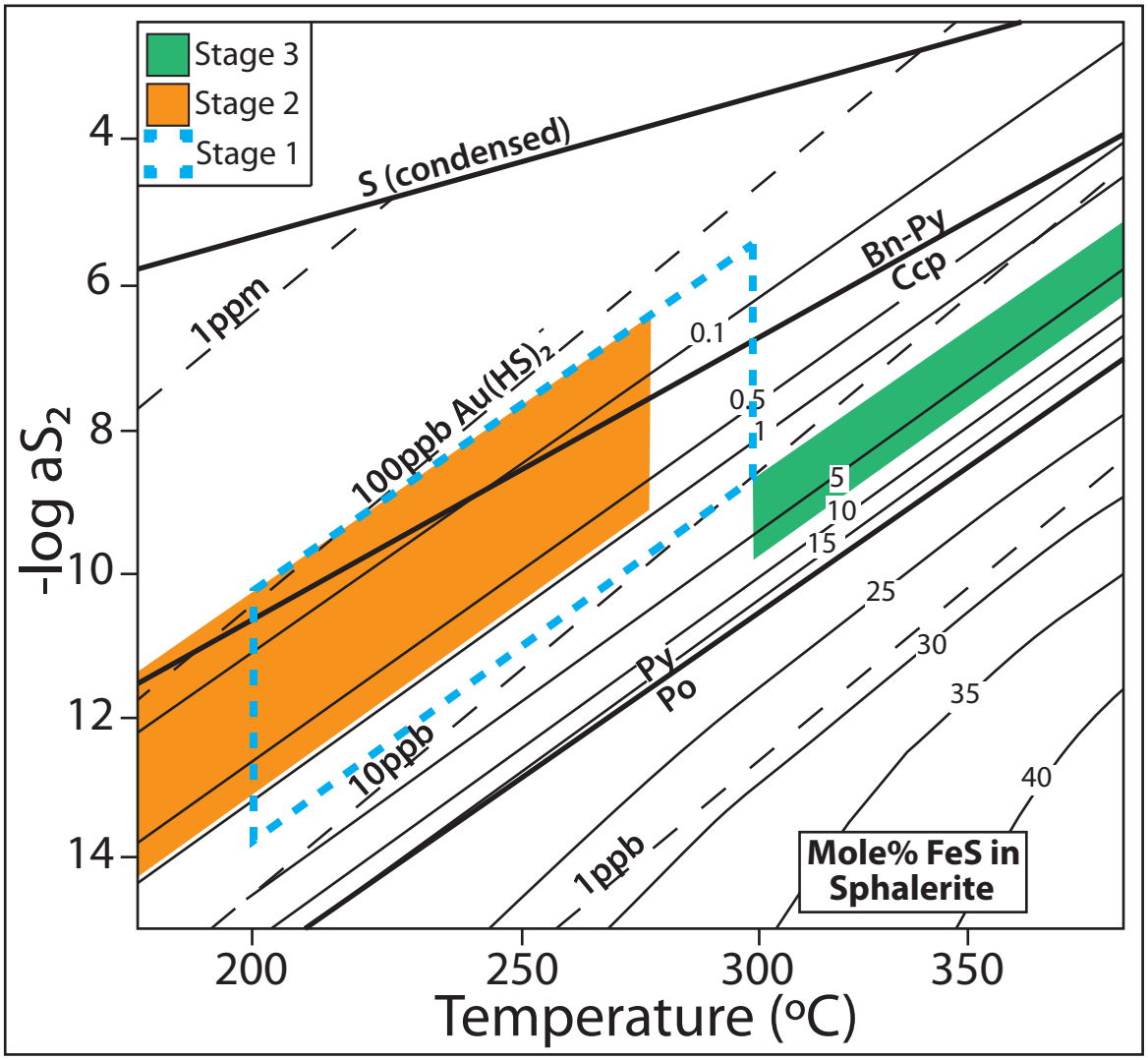

Figure 2.14. Log αS2 (Fig. 3; Hannington &Scott, 1989) vs. temperature phase diagrams showing the contours of mole% FeS in sphalerite and of gold solubility as Au(HS)2- at pH 5. Shaded areas represent fluid conditions during stages of paragenesis at Lemarchant based on FeS in sphalerite, sulfide mineral assemblage and the average range of hydrothermal fluid temperatures for VMS deposits.

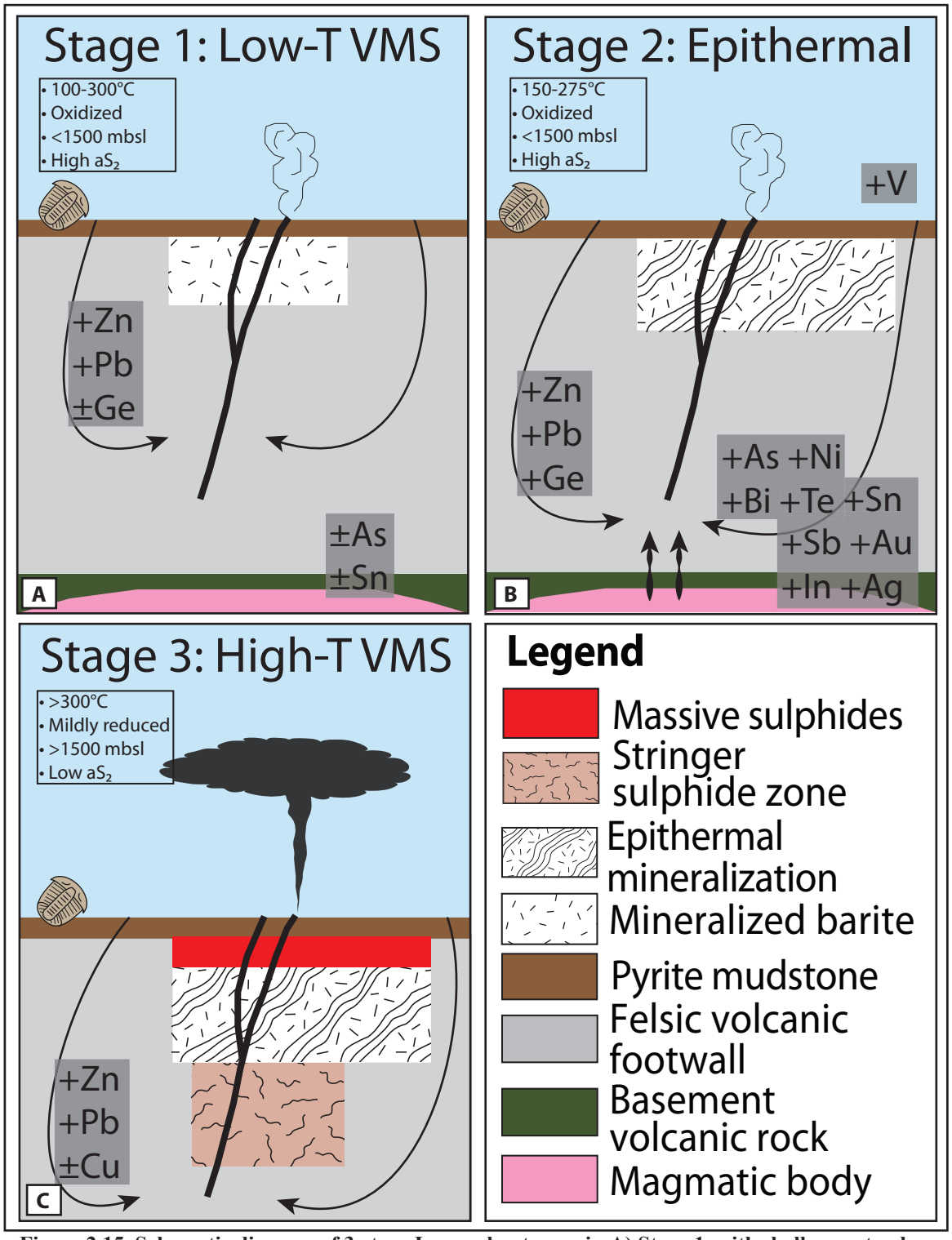

Figure 2.15. Schematic diagram of 3-stage Lemarchant genesis. A) Stage 1, with shallow water, low temperature polymetallic VMS mineralization. B) Stage 2, with intermediate sulfidation epithermal-style mineralization, including boiling and addition of magmatic fluid, in a shallow water volcanic setting. C) Stage 3, with deep water, high temperature Cu-rich VMS mineralization, zone refinement and formation of a stringer sulfide zone.

Chapter 3: Sulfur and lead isotope geochemistry of sulfides from the Cambrian Zn-Pb-Cu-Ag-Au Lemarchant volcanogenic massive sulfide (VMS) deposit, Newfoundland

3.1 – Abstract

The Lemarchant deposit is a bimodal felsic Zn-Pb-Cu-Ag-Au volcanogenic massive sulfide deposit, and a type example of a precious metal-enriched VMS deposit in the Newfoundland Appalachians. The deposit contains paragenetically distinct VMS and epithermal-style mineralization. Initial epithermal-style mineralization was deposited from low temperature (<250°C), oxidized, near-neutral fluids with a high sulfur activity. Later Cu-rich polymetallic mineralization was deposited from higher temperature (>300°C), less oxidized hydrothermal fluids with lower sulfur activity. *In situ* microanalyses of pyrite, chalcopyrite and galena yield a wide range of δ^{34}S values (-6.4 to +15.1‰). Analyses of sulfides from early low temperature assemblages have the lowest average δ^{34}S values (+4.6‰) and the highest δ^{34}S values occur in sulfides from late-stage, high temperature assemblages; however, there is significant overlap of galena δ^{34}S values from all mineral assemblages. Variability in the sulfur isotopic range occurs in all styles of mineralization, and this is consistent with the complex paragenetic history and open system environment of the deposit during its formation. Sulfur isotope ratios indicate that thermochemical reduction of seawater sulfate, igneous leaching, and disproportionated magmatic SO_2 all contributed reduced sulfur to the Lemarchant sulfides. Although it is

commonly difficult to distinguish between leached igneous and magmatic sources, mineralogical and geochemical data from Lemarchant suggest some contribution of magmatic SO_2, at least during the deposition of intermediate sulfidation epithermal mineralization.

Lead isotope compositions of galena show little variability between styles of mineralization, suggesting continual mixing Pb sources throughout deposition. Most Pb at Lemarchant is derived from the underlying Neoproterozoic Sandy Brook group volcanic rocks, with input of possible juvenile Pb from the basaltic rocks of the Lake Ambrose formation of the Tally Pond group, and/or from more juvenile mafic Neoproterozoic basement rocks.

3.2 – Introduction

Lead and sulfur isotopes are critical tools for understanding the source of metals and sulfur in volcanogenic massive sulfide (VMS) and seafloor massive sulfide (SMS) deposits (Ohmoto, 1972; Sato et al., 1981; Janecky and Shanks, 1988; Huston, 1999; Tosdal et al., 1999; Shanks, 2001; Franklin et al., 2005; Seal, 2006). In ancient VMS deposits, circulating hydrothermal fluids transported metals and sulfur that were derived from the interaction of the fluids with a variety of sources between the seafloor and up to 2 km below the site of deposition (Franklin et al., 2005; Galley et al., 2007; Gibson et al., 2007; Hannington and Monecke, 2009). Lead isotope compositions of sulfides from VMS and SMS deposits record the integrated source of metals, and in most studied examples these data indicated that lead was leached from underlying basement rocks (Stacey and Kramers, 1975; Zartman and Doe, 1981; Fouquet and Marcoux, 1995; Kramers and

Tolstikhin, 1997; Tosdal, 1999; Franklin et al., 2005; Mortensen et al., 2006). In contrast, S isotope systematics are much more complex due to the variety of sources and processes that can contribute to the sulfur isotope composition of sulfide minerals (Jensen, 1967; Huston, 1999; Marini et al., 2011). The S isotope signature of sulfides in most VMS deposits is generally attributed to seawater sulfate and/or sulfur leached from basement rocks (Janecky and Shanks, 1988; Ohmoto and Rye, 1979; Sakai et al., 1984; Halbach et al., 1989; Rye, 1993; Herzig et al., 1998; Shanks, 2001; Seal 2006). In rarer cases, sulfur may have been derived from bacteriogenic sources (Jensen, 1967; Janecky and Shanks, 1988; Huston, 1999; Shanks 2001) or magmatic fluids (de Ronde, 1995; Hannington et al., 1995; Herzig et al., 1998; de Ronde et al., 2005). The latter source has been inferred for certain ancient VMS environments, especially those with syngenetic precious metal enrichment (i.e., Herzig et al., 1993; Hannington et al., 1999; Roth et al., 1999; Ulrich et al., 2002; Chiaradia et al., 2008). Additionally, because S isotopes are strongly fractionated by variation in physicochemical characteristics of the hydrothermal fluid, compositions of sulfides can change with fluid evolution during the formation of the deposit – particularly if redox reactions acted to change the speciation of sulfur (e.g., Ohmoto, 1972; Ohmoto and Lasaga, 1982; Ohmoto and Goldhaber, 1997, and references therein).

Although stable and radiogenic isotope systematics in VMS systems can prove very useful tools for understanding deposit genesis, only limited Pb and S isotope data are available for Appalachian VMS deposits (e.g., Swinden and Thorpe, 1984; Goodfellow and Peter, 1996; Pollock and Wilton, 2001; Pollock, 2004). There are even fewer in situ

Pb and S isotope data for Appalachian and global VMS deposits, and their application to global precious metal enriched VMS deposits has not been fully tested. The bimodal felsic Zn-Pb-Cu-Ag-Au Lemarchant VMS deposit in central Newfoundland is composed of five distinct styles of mineralization, which were deposited in three sequential stages from an evolving hydrothermal system (see Chapter 2; Gill et al., 2013; Gill and Piercey, 2014). Correspondingly, the Lemarchant deposit provides an excellent opportunity to investigate Pb and S isotope evolution, and study a type example of Ag-Au-bearing Appalachian VMS deposit. Herein, paragenetically controlled *in situ* Pb and S isotope data for the major sulfides is presented, providing insight into the sources of base and precious metals and sulfur in the deposit and the hydrothermal fluid evolution at Lemarchant. These data may elucidate sources of Pb and S in similar precious metal enriched VMS deposits in the Appalachians and globally.

3.3 – Regional geology

The Lemarchant deposit is located in the Dunnage Zone of the Newfoundland Appalachians, which is composed of nascent to mature volcanic arc, arc-rift and back arc basin sequences (Swinden et al., 1988; Rogers et al., 2006; McNicoll et al., 2010; Piercey and Hinchey, 2012). The Dunnage Zone is divided into the western Notre Dame and eastern Exploits subzones, which represent the respective peri-Laurentian and peri-Gondwanan realms located on opposite sides of the Iapetus suture zone (Red Indian Line; Fig. 3.1, inset; Williams et al., 1988; Evans and Kean, 2002; Rogers et al., 2006; McNicoll et al., 2010). The volcanic and sedimentary sequences within Exploits subzone were accreted to the Ganderian subcontinent during the mid-Ordovician Penobscot

Orogeny, and were subsequently accreted to composite Laurentia along the Red Indian Line during the Late Ordovician (Rogers and van Staal, 2002; Rogers et al., 2006; van Staal and Barr, 2012; Piercey et al., 2014). The Lemarchant deposit is hosted in the Victoria Lake Supergroup, which consists of six discrete volcanic assemblages (e.g., Rogers and van Staal, 2002; Rogers et al., 2006; Zagorevski et al., 2007) and is underlain by Neoproterozoic metavolcanic and metaplutonic basement rocks (Sandy Brook group and Cripplebacк/Valentine Lake intrusive suites, respectively; Rogers et al., 2006; McNicoll et al., 2010).

The oldest and lowermost volcanic assemblage in the Victoria Lake Supergroup is the Cambrian Tally Pond group (~513-509 Ma; Pollock, 2004; McNicoll et al., 2010), which forms part of the eastern margin of the Exploits subzone (Fig. 3.1). The Tally Pond group is informally divided into the Bindons Pond and Lake Ambrose formations (Rogers et al., 2006; ~Boundary Brook formation and Lake Ambrose basalts, respectively, of Dunning et al, 1991). The Bindons Pond formation is composed of transitional to calc-alkaline island arc volcanic rocks that are dominated by rhyolite to dacite flows and volcaniclastic rocks, and carbonaceous rocks (Evans and Kean, 2002; Rogers et al., 2006; Copeland et al., 2008; Piercey and Hinchey, 2012; Piercey et al, 2014). The Lake Ambrose formation is generally interlayered with the Bindons Pond formation, and is composed predominantly of mafic sub-alkalic to depleted tholeiitic island arc volcanic rocks (Evans and Kean, 2002; Rogers et al., 2006; Copeland et al., 2008; Piercey and Hinchey, 2012). The felsic dominated Bindons Pond formation is host to the majority of massive sulfide mineralization in the Tally Pond group, including the producing Duck

Pond and Boundary VMS deposits, and the Lemarchant VMS deposit (McNicoll et al., 2010; Piercey and Hinchey, 2012). The Lemarchant deposit occurs at a contact between the Bindons Pond felsic volcanic rocks and overlying Lake Ambrose mafic volcanic rocks, and formed during a hiatus in effusive volcanism in an extensional, arc-rift setting (Evans and Kean, 2002; Rogers and van Staal, 2002; Rogers et al., 2006; van Staal and Barr, 2012; Piercey et al., 2014).

3.4 – Deposit geology

The Lemarchant deposit is hosted in a bimodal felsic volcanic assemblage, and is broadly divided into a semi-conformable massive to semi-massive sulfide component ("stratiform zone"), and a discordant stringer sulfide component ("stringer zone"). The stratiform zone strikes 350 m northwest, is ≤20 m thick, barite-rich, and occurs at the contact between the felsic footwall and the mafic hanging wall (Fig. 3.2a). A thin, pyritic mudstone layer occurs immediately above the stratiform zone, at the footwall-hanging wall contact (Fig. 3.2b). The stringer zone is situated below the stratiform zone within footwall felsic rocks. Stringer sulfide mineralization does not extend far below the stratiform zone and is abruptly truncated, possibly indicating removal of the lower stringer zone by thrust faulting. A portion of the deposit (the "Northwest Zone") has been displaced 200 m to the northwest at >100 m below the main mineralized zone (Fig. 3.2), and is mineralogically and geochemically similar to the main mineralized zone (see Chapter 2).

The footwall is composed of aphyric rhyolite flows/domes, breccia, lapilli tuffs and tuff breccia, polylithic lapilli tuffs and minor tuffs (Squires and Moore, 2004;

Copeland et al., 2008). Massive granular barite and interstitial granular barite occur at the top of the felsic footwall, and are variably replaced by sulfide mineralization. The thin, pyritic and variably graphitic mudstone layer contains minor sulfide stringers and is interpreted to be, in part, an exhalative sedimentary rock (Copeland et al., 2008b; Lode et al., 2012). The pyritic mudstone is commonly intercalated with the overlying mafic hanging wall proximal to mineralization, and is considered to have formed prior to and during mineralization at Lemarchant (Lode et al., 2014). Hanging wall mafic rocks are composed of massive basalt to basaltic andesite, vesicular pillow basalt and hyaloclastite breccia, which are variably magnetic (Squires and Moore, 2004; Copeland et al., 2008; Piercey and Hinchey, 2012). Three types of intrusions crosscut mineralized lithologies at Lemarchant, including two types of mafic dykes and a less common type of felsic dyke: (1) light brown to green, pyroxene phyric synvolcanic mafic dykes, commonly with peperitic and vesicular margins (Pollock, 2004; Squires and Moore, 2004; Copeland et al., 2008); (2) grey-green medium-grained diabase to gabbroic dykes with sharp contacts; and (3) pink to white, aphyric to minor quartz-phyric felsic dykes.

The felsic volcanic footwall is quartz and sericite altered, with lesser chlorite and albite. However, sections of chlorite-dominated alteration occur locally in the stringer zone, and devitrified glass fragments in brecciated rhyolite are heavily chlorite altered. The mafic hanging wall is weakly altered to quartz, chlorite and minor epidote. Rare fuchsite occurs in synvolcanic dykes. Carbonate alteration is abundant in the form of carbonate stringers, with lesser quartz, that crosscut all lithologies at Lemarchant;

carbonate bleaching occurs at mafic dyke contacts; and trace ankerite is disseminated throughout the mafic lithologies.

Repetition of the volcanic stratigraphy in the Lemarchant deposit suggests thrust imbricated stacking of the footwall host rock, particularly along the Lemarchant Fault, and the deposit has been disrupted by a number of (possibly reactivated?) upright normal faults (Fig. 3.2b; Squires and Moore, 2004; Copeland et al., 2008a; Fraser et al., 2012). Low-grade greenschist metamorphism accompanied deformation during Silurian-Devonian tectonic activity (Dunning et al., 1991; Squires and Moore, 2004; Rogers et al., 2006). Although the deposit has been variably deformed, there is exceptional preservation of sulfide textures in the mineralized footwall and only minor local remobilization of sulfide mineralization.

3.5 – Mineralization

The sulfide mineralogy at Lemarchant is dominated by sphalerite and pyrite, with lesser galena, chalcopyrite, tetrahedrite-tennantite and bornite (Fig 3.3). Minor minerals include pyrrhotite, arsenopyrite, marcasite and visible electrum. Trace minerals are colusite-germanocolusite, stromeyerite, covellite, polybasite, miargyrite and bournonite, with unidentified silver tellurides, nickel sulfides, Cu-Sb-Ag- and Cu-V-bearing sulfosalts. Electrum is the only described deportment of gold at Lemarchant; however, electron microprobe and laser ablation analyses reveal Au is also resident in pyrite, either as lattice substitutions or micro-inclusions of Au (see Chapter 2). Silver is hosted in the tetrahedrite-tennantite series of minerals (mostly Ag-tetrahedrite and tetrahedrite), in electrum, and in the Ag bearing sulfosalts; trace Ag is also present in galena. Gold

contents in electrum are higher in the centre of the deposit, whereas silver-rich electrum and silver bearing minerals are more abundant at the outer edges of the deposit.

Most sulfide mineralization at Lemarchant is hosted in the barite-rich stratiform zone, with lesser sulfides in the underlying stringer zone. Sulfide mineral associations and textures can be used to define five mineral assemblage types (see Chapter 2): (1) semi-massive granular barite-pale sphalerite-colloform pyrite-galena (±chalcopyrite-tetrahedrite-tennantite) (Figs. 3.3a and 3.4); (2A) bornite-galena-chalcopyrite (±stromeyerite-covellite-Ni-sulfide) stringers (Figs. 3.3b and 3.4); (2B) disseminated tetrahedrite-tennantite-galena-bladed barite-white sphalerite-recrystallized pyrite (±electrum-colusite-germanocolusite-polybasite-miargyrite-bournonite-Ag-tellurides) (Figs. 3.3b-d and 3.4); (3) massive dark sphalerite-subhedral to euhedral pyrite-galena-chalcopyrite(±pyrrhotite-arsenopyrite) (Figs. 3.3e-f and 3.4); and (4) chalcopyrite-medium-grained euhedral pyrite (±orange sphalerite-galena) stringers (Figs. 3.3g-h and 3.4).

In the stratiform zone, the type 1 assemblage is intergrown with massive barite mineralization, and is partially replaced and infilled by type 2A stringers, and the type 2B assemblage. Type 3 mineralization overlies and partially replaces the upper portion of the type 1, 2A and 2B assemblages in the stratiform zone. The stringer zone lies stratigraphically below the stratiform zone, is composed of type 4 stringers, and is devoid of barite.

The 5 mineral assemblages were deposited in 3 paragenetic stages, each with distinct pyrite textures (Fig. 3.4; see Chapter 2). In the first stage of paragenesis, barite and low-Fe sphalerite-rich type 1 mineralization was deposited with fine-grained colloform pyrite from a low temperature (150-275°C), likely oxidized and mildly acidic hydrothermal fluid. The second stage encompassed partial replacement and infill of stage 1 sulfides by intermediate sulfidation epithermal type 2A and type 2B mineral assemblages, and resulted in recrystallization of type 1 pyrite to form rounded to subhedral fine-medium sized grains of pyrite. Replacement and minor zone refinement of the stratiform zone by barite poor, high-Fe sphalerite-rich type 3 sulfides, and formation of the basal stringer zone with chalcopyrite dominated type 4 sulfides both occurred during the final stage of mineralization, and are consistent with formation from a higher temperature (>300°C), relatively less oxidized hydrothermal fluid.

3.6 – Isotope geochemistry of sulfides

3.6.1 – Analytical methods

A subset of samples was selected as representative of each of the 5 types of mineralization described above. Offcuts of 8 thin section samples, from 5 drill holes, that were previously analyzed by scanning electron microscopy (SEM), electron microprobe and laser ablation ICPMS (see Chapter 2), were epoxy mounted in one inch diameter Al ring mounts. These mounts were then polished using standard lapidary procedures and sputter coated with Au (~300 Å). *In situ* isotope microanalyses were performed using a Cameca IMS 4f^{TM} secondary ion mass spectrometer (SIMS) at the MAF-IIC facility, Memorial University of Newfoundland. Procedures for analyses of Pb and S isotopes are

outlined below. Appendix F.1 and F.2 contain the details of the analytical methods for Pb and S isotopes, respectively.

Lead isotope analyses were performed exclusively on galena due to the absence of U, and therefor absence of radiogenic Pb, in the mineral. Where possible, galena was selected to represent each of the 5 types of mineralization, but some bias was introduced based on relative abundance of mineral grains of appropriate size (>25 μm in diameter) in the various mineralization types. Three grains were selected per sample, and two spots were analyzed per grain to monitor possible zonal variation in Pb isotope values. An O^- primary ion beam with a 14-16 nA current at a nominal 10 keV potential was focused into a 15-20 μm beam diameter. The spot to be analyzed was first rastered for 120 s over 25 μm^2, and then pre-sputtered for 75 s over 10 μm^2 prior to measurement of 15 cycles of peak switching (1.0 s at background, 8.0 s on $^{204}Pb^+$, and 4.0 s on $^{206}Pb^+$, $^{207}Pb^+$ and $^{208}Pb^+$, with 0.4 s waiting time between each isotope to allow for magnet settling (0.5 s on background)). Total analysis time for a single spot was 9.0 minutes. Correction for instrumental mass fractionation was performed using standard reference material F19 (galena); the secondary reference material, JMBH (galena), was analyzed periodically to monitor accuracy and reproducibility. Internal precision (standard error of the mean) on individual spot measurements of $^{204}Pb/^{206}Pb$, $^{207}Pb/^{206}Pb$ and $^{208}Pb/^{206}Pb$, were routinely better than 0.05-0.10% (1σ). External reproducibility of replicate standard analyses was typically better than 0.10-0.15% for these same ratios.

Sulfur isotope analyses were performed on pyrite, chalcopyrite and galena grains >25 μm in diameter. Where possible, sulfide minerals were selected to represent each of

the 5 types of mineralization but, as for Pb isotope microanalysis of galena, some bias was introduced based on relative abundance of mineral grains of appropriate size in the sample. Three grains were selected per sample, and two spots were analyzed per grain to monitor possible zonal variation in S isotope values. A Cs^+ primary ion beam with a 0.6-0.8 nA current for pyrite and chalcopyrite, and a 0.9-1.0 nA current for galena, at a nominal 10 keV potential was focused into a 5-15 μm beam diameter. The spot to be analyzed was first rastered for 120 s over 25 μm^2, and then pre-sputtered for 200s over 10 μm^2 prior to measurement of 80 cycles of peak switching (0.5 s at background, 2.0 s on $^{32}S^-$ and 6.0 s on $^{34}S^-$, with 0.25 s waiting time between each peak to allow for magnet settling). Analysis time for a single spot was ~15 minutes in total. Correction for instrumental mass fractionation was performed using standard reference materials UL9B (pyrite; $\delta^{34}S$: 15.8‰ VCDT), Norilsk (chalcopyrite; $\delta^{34}S$: 8.3‰ VCDT) and HT10 (galena; $\delta^{34}S$: 14.2‰ VCDT). Results are expressed as $\delta^{34}S$ relative to Vienna Canyon Diablo troilite (VCDT). Internal precision (standard error of the mean) on measured $\delta^{34}S$ values of the standards, were routinely better than ±0.3‰ (1σ). External reproducibility of replicate standard analyses was routinely better than ±0.35-0.45‰ (1σ).

3.6.2 – Results: Lead isotopes

A total of 42 *in situ* SIMS analyses were performed on galena from the stratiform zone of the Lemarchant deposit (Table 3.1). Overall, lead isotope ratios are clustered and range from 18.04 to 18.21 (average 18.12±0.04 (1σ)), 15.48 to 15.69 (average 15.57±0.06) and 37.35 to 38.33 (average 37.80±0.20) for $^{206}Pb/^{204}Pb$, $^{207}Pb/^{204}Pb$ and $^{208}Pb/^{204}Pb$, respectively (Table 3.1; Fig. 3.5). Three outliers exist in the Lemarchant data

that deviate from the overall $^{206}Pb/^{204}Pb$ trend, and these are discussed below. Galena in type 1 and type 4 sulfides were not analyzed due to their extremely small grain sizes; however, Pb isotope ratios from the type 2A, type 2B and type 3 assemblages have significant overlap and are considered to originate from the same source(s) (Fig. 3.5).

Certain features are evident when Pb isotope ratios are plotted in uranogenic ($^{207}Pb/^{204}Pb$ vs. $^{206}Pb/^{204}Pb$) and thorogenic ($^{208}Pb/^{204}Pb$ vs. $^{206}Pb/^{204}Pb$) space, and compared to the Pb isotope growth curves for various reservoirs from Kramers and Tolstikhin (1997) (Fig. 3.5). The data for Lemarchant have $^{206}Pb/^{204}Pb$ ratios that are very close to expected values for young upper crust at ~500 Ma, but with varying $^{208}Pb/^{204}Pb$ and $^{207}Pb/^{204}Pb$ (Fig. 3.5). With the exception of the three anomalous values, most samples have Stacey and Kramers (1975) model ages of 163-578 Ma and μ values that range from 9.22 to 10.20 (Table 3.1). The average μ value for Lemarchant (9.63) is similar to young upper crust growth curve at 500 Ma (μ = 9.66; Kramers and Tolstikhin, 1997). However, the variance from the average value, and the variation in $^{208}Pb/^{204}Pb$ and $^{207}Pb/^{204}Pb$, requires contributions from both less evolved (lower μ) and, to a lesser extent, more evolved (higher μ), sources (Fig. 3.5).

Outliers in Lemarchant Pb isotope data deviate only from the $^{206}Pb/^{204}Pb$ analyses at 17.393, 17.932 and 16.868 in sample CNF14259, but are within the range of the values for $^{207}Pb/^{204}Pb$ and $^{208}Pb/^{204}Pb$ analyses (Table 3.1). These values were determined from galena in the type 2A assemblage, either within the same grain or in the same mineral assemblage as those grains that have 'normal' $^{206}Pb/^{204}Pb$ ratios. The grains from sample CNF14259 are extensively pitted (i.e., Fig. 3.4c) and have extremely large $^{206}Pb/^{204}Pb$

error relative to other samples (Table 3.1), so these outliers are most likely due to excessive contamination of the highly pitted material by exotic Pb during lapidary preparation.

3.6.3 – Results: Sulfur isotopes

Results for *in situ* S isotope analyses for pyrite, galena and chalcopyrite are presented in Table 3.2. The overall range of $\delta^{34}S$ values in the Lemarchant sulfides is between -6.4 and +15.1‰ (average +5.0±3.3‰ (1σ), n=119).

The $\delta^{34}S$ values of type 1 fine-grained, colloform to recrystallized pyrite range from +0.3 to +4.9‰ (average +3.6±1.7‰, n=8), and are slightly lower than the average values for the entire deposit (Table 3.2; Fig. 3.6). The type 2A galena $\delta^{34}S$ values range from -1.6 to +4.8‰ (average +1.4±2.2‰, n=12), with one outlier at +11.8‰, which is clearly associated with a pitted grain. Chalcopyrite ranges from +5.2 to +6.2‰ (average +5.8±0.5‰, n=6). Type 2B rounded, recrystallized pyrite, and chalcopyrite $\delta^{34}S$ values range from +2.9 to +10.6‰ (average +5.9±1.7‰, n=28) and +3.0 to +5.0‰ (average +4.1±0.7‰, n=12), respectively. S isotope values for type 2B galena are varied, and range from -1.7 to +13.0‰ (average +4.4±4.0‰, n=12).

Type 3 galena has a very wide range of values, from -6.4 to +15.1‰ (average +4.5±6.6‰, n=12); the highest values (+13.2 and +15.1‰) occur in discrete grains and are not caused by pitted surfaces (i.e., Fig. 3.4f). Euhedral pyrite in the type 3 assemblage has $\delta^{34}S$ values ranging from +5.4 to +8.3‰ (average +6.9±0.8‰, n=12).

The type 4 mineral assemblage displays the highest mean $\delta^{34}S$ values in the Lemarchant deposit (Fig. 3.6), largely because of the wide range of $\delta^{34}S$ for galena (+2.2 and +12.0‰; average +7.2±4.2‰, n=5). Chalcopyrite $\delta^{34}S$ values are much less variable and range from +5.8 to +6.5‰ (average +6.2±0.3‰, n=6).

The variability in $\delta^{34}S$ values notably decreases from galena to pyrite to chalcopyrite (Fig. 3.7). Galena exhibits the most variability in $\delta^{34}S$ values, both within and between individual grains (Table 3.2; Fig. 3.7). However, this variability in $\delta^{34}S$ does not appear to correlate with galena texture or contamination from adjacent minerals. Later stage precipitation of galena, relative to pyrite and chalcopyrite, from individual batches of hydrothermal fluid (Vaughn and Craig, 1978; Barton and Skinner, 1979), and progressive fractionation of the S isotope reservoir in each batch of hydrothermal fluid may have contributed to the observed increased variability in $\delta^{34}S$ of the Lemarchant galena.

3.7 – Discussion

3.7.1 – Source(s) of metals

The Lemarchant Pb isotope data from form an elongate cluster (Fig. 3.5) that mimics and overlaps the trend of previously obtained whole rock Pb isotope data from other deposits in the Tally Pond group. The Lemarchant data also overlap whole rock data from other peri-Gondwanan deposits in the Appalachians (Fig. 3.8; Swinden and Thorpe, 1984; Pollock and Wilton, 2001; Pollock, 2004). Furthermore, the restricted cluster of Lemarchant Pb isotope data overlaps the 500 Ma node on the young upper crust growth

curve, and there is no detectable variation in Pb isotopes as a function of paragenesis (Fig. 3.5). These values suggest a homogenization of Pb isotopic signatures and a relatively consistent source of Pb throughout the evolution of the deposit.

The clustering of Pb isotopic data proximal to the young upper crust curve (Fig. 3.5; Kramers and Tolstikhin, 1997) is consistent with the regional geology and tectonics of the Tally Pond group. The volcanic rocks of the Tally Pond group are underlain by ~564 Ma Neoproterozoic volcanic and intrusive rocks that include a bimodal volcanic assemblage (Sandy Brook group) with continental arc signatures and $\varepsilon Nd_t<0$ (Rogers et al., 2006; McNicoll et al., 2010). The Tally Pond volcanic rocks, including the host rocks to mineralization in the Tally Pond group, were erupted through the Neoproterozoic basement rock, and contain zircon inheritance and εNd_t values consistent with some crustal inheritance (Rogers et al., 2006; McNicoll et al., 2010). Thus, the Pb signature of the Lemarchant deposit is consistent with lead originating predominantly from the relatively young, Neoproterozoic basement immediately underlying the Tally Pond group.

Although there is clearly a predominant upper crustal component contributing to the Pb isotopic array of the Lemarchant deposit, many samples have Stacey and Kramers (1976) model ages that are significantly younger than the documented age of the mineralization (~513-509 Ma; Table 3.1; Dunning et al., 1991; McNicoll et al., 2010), and have lower μ values than the ~500 Ma value for young upper crust ($\mu = 9.66$; Kramers and Tolstikhin, 1997). These lower μ values require a more juvenile component to have contributed to the Pb isotope array. The regional framework can also accommodate this. Abundant mafic rocks in the underlying Neoproterozoic Sandy Brook

group, and basalts to basaltic andesites in the lowermost unit of the Tally Pond group (Lake Ambrose formation; Evans and Kean, 2002; Rogers et al., 2006) have arc tholeiitic to calc-alkalic affinities and $\varepsilon Nd_t > 0$. Even felsic rocks within the Tally Pond group have $\varepsilon Nd_t > 0$, implying some contribution of a juvenile component during their genesis (Rogers et al., 2006; McNicoll et al., 2010). Although there are no published Pb isotopic data for the mafic lithologies of the Sandy Brook group or the Tally Pond group, it is reasonable to assume that these lithologies have juvenile Pb isotopic signatures, with μ values lower than young upper crust, based on their published εNd_t. Any Pb leached from these sources would reasonably account for the more juvenile component apparent in the Lemarchant Pb isotope array.

On a regional scale, lead isotope data at Lemarchant correlate well with those for the Dunnage Zone. The Lemarchant deposit and other massive sulfide occurrences in the Exploits subzone, are enriched in radiogenic Pb isotopes relative to mineralized occurrences in the Notre Dame subzone (Fig. 3.8; Swinden and Thorpe, 1984; Pollock and Wilton, 2001; Pollock, 2004; Goodfellow, 2007). This pattern is consistent with the derivation of Pb from different source regions, on opposing sides of the Iapetus Ocean (Rogers and van Staal, 2002; Zagorevski et al., 2007; van Staal and Barr, 2012). The higher $^{207}Pb/^{204}Pb$ signatures of Exploits subzone deposits (i.e., Tally Pond and Tulks volcanic groups, and Wild Bight Group; Fig. 3.8) has been attributed to the proximity of these deposits to the sedimentary rocks of the early Paleozoic Ganderian passive margin (i.e., Gander Group and Spruce Brook Formation; Swinden and Thorpe, 1984; Pollock,

2004; van Staal and Barr, 2012) or, more generally, the Gondwanan realm (Pollock and Wilton, 2001) from which older, more radiogenic Pb was likely sourced.

3.7.2 – Source(s) of sulfur

The possible sources of reduced sulfur (H_2S) in VMS deposits primarily are: 1) reduced seawater sulfate (SO_4^{2-}); 2) sulfide leached from igneous basement rock; and 3) the disproportionation of exsolved magmatic SO_2 (Jensen, 1967; Ohmoto and Rye, 1979; Janecky and Shanks, 1988; Huston, 1999; Shanks, 2001; Seal, 2006). Seawater SO_4^{2-} may be reduced to H_2S either organically (bacterial sulfate reduction – BSR) or inorganically (thermochemical sulfate reduction – TSR) (Huston, 1999; Shanks, 2001; Seal, 2006). Reduction of seawater sulfate through bacterial activity can result in a very wide range of $\delta^{34}S$ values in closed or partially closed systems (Shanks, 2001; Seal, 2006). However, in relatively open systems, such as that inferred for the barite-rich Lemarchant deposit, the source of SO_4^{2-} is continually replenished and preferential reduction of the isotopically light ($^{32}SO_4^{2-}$) sulfate results in the formation of massive sulfides with consistently extremely negative sulfide $\delta^{34}S$ values (i.e., $\leq$ -30‰; Ohmoto and Rye, 1979; Goodfellow and Peter, 1996; Seal, 2006). Although the initial stages of deposition at Lemarchant were relatively low temperature (permissive of bacterial activity; Ohmoto and Rye, 1979; Goodfellow and Peter, 2006), the lightest S isotope values are no less than 0‰ for pyrite and chalcopyrite, and no less than -7‰ for galena. Furthermore, textural evidence of extensive bacterial activity, such as framboidal pyrite, is absent in the Lemarchant sulfides and, along with these generally heavier $\delta^{34}S$ values, suggests that BSR did not contribute significantly the sulfur budget of the sulfides in the deposit.

Thermochemical sulfate reduction of seawater sulfur generally occurs at temperatures >200°C, upon interaction of the hot fluid with reduced iron (or a similar reductant) in the host or basement rocks (Ohmoto and Rye, 1979; Shanks, 2001; Seal, 2006). Reduced sulfur produced by TSR of seawater can display a wide positive range of values, which are dependent on the original $\delta^{34}S$ value of the seawater sulfate (Sakai and Dickson, 1978; Ohmoto and Rye, 1979; Seal, 2006). The $\delta^{34}S$ values of sulfides formed from H_2S derived from TSR are possible to predict, based on estimates of original seawater $\delta^{34}S$, temperature, and the amount of original seawater sulfate reservoir already reduced (after Ohmoto and Rye, 1979; Ohmoto and Goldhaber, 1997):

$$1000ln\alpha_{(H_2S-SO_4)} = A * \frac{10^6}{T^2} + B * \frac{10^3}{T} + C = \delta^{34}S_{H_2S} - \delta^{34}S_{SO_4}$$

[Equation 1],

where $\alpha_{H2S\text{-}SO4}$ is the fractionation factor (difference between sulfide and sulfate ratios during TSR); T is the temperature in Kelvin, A, B, and C are constants (A = -5.26, and B and C are = 0 in this particular equation; Ohmoto and Goldhaber, 1997); $\delta^{34}S_{SO4}$ is the sulfur isotope composition of seawater sulfate; and $\delta^{34}S_{H2S}$ is the sulfur isotope composition of H_2S generated by TSR. Sulfide mineral $\delta^{34}S$ values were calculated at the likeliest lower and upper temperatures of Lemarchant mineralization, based on the presence of Zn-Pb-rich vs. Cu-rich mineral assemblages (200°C and 300°C, respectively), which are within the range of possible temperatures for thermochemical sulfate reduction (Ohmoto and Rye, 1979; Seyfried and Bischoff, 1981; Shanks, 2001; Seal, 2006). The $\delta^{34}S$ of H_2S generated by TSR is calculated using Equation 2:

$$\delta^{34}S_{H_2S} = \delta^{34}S_{SO_4(parent,t)} + 1000(\alpha_{(H_2S-SO_4)} - 1)$$

[Equation 2],

and relates the sulfur isotope compositions of H_2S derived from seawater sulfate to the Rayleigh distillation equation (Eqn. 3), since VMS hydrothermal systems may be considered open systems (Shanks et al., 1995):

$$\delta^{34}S_{SO_4(parent,t)} = \left(\delta^{34}S_{SO_4(parent,t=0)} + 1000\right) * f^{(\alpha_{(H_2S-SO_4)}-1)} - 1000$$

[Equation 3],

describes $\delta^{34}S_{SO4\ (parent,\ t)}$ as the $\delta^{34}S$ value of SO_4^{2-} at some time relative to the parent composition of seawater sulfate ($\delta^{34}S_{SO4\ (parent,\ t=0)}$), and as a function of the amount of seawater sulfate reduced to H_2S (*f*). Given the abundance of barite at Lemarchant it is assumed that the system was open to the seawater sulfate reservoir during TSR and that there was continuous recharge of sulfate during TSR (i.e., $f = 1$). It was also assumed that seawater sulfate had a $\delta^{34}S_{Cambrian}$ ~35‰ (Claypool et al., 1980; Shanks, 2001; Canfield, 2004; Kampschulte and Strauss, 2004; Paytan and Grey, 2012), and that the minerals crystallized between 300-200°C.

Considering only TSR, the $\delta^{34}S$ predicted for phases crystallizing between 300-200°C ranges from 13-20‰ for pyrite, 14-20‰ for galena and 14-19‰ for chalcopyrite (see Appendix F.3). These values are much higher than the majority of samples examined from Lemarchant, and suggest that TSR alone cannot explain the sulfur isotope data. Mixing of TSR-derived H_2S in the hydrothermal fluid with additional source(s) of

reduced sulfur with lower $\delta^{34}S$ values are required to produce the lower $\delta^{34}S$ values observed in the Lemarchant sulfides.

Igneous basement rock and magmatic fluids have similar sulfur isotope signatures (Huston, 1999; Shanks, 2001; Franklin et al., 2005; Seal, 2006). In particular, primitive igneous materials such as mid-ocean ridge basalts (MORB) and ocean island basalts (OIB) have $\delta^{34}S$ values close to the average isotopic value of magmatic fluids (i.e., ~0‰; Ohmoto and Rye, 1979; Sakai et al., 1984; Seal, 2006); continental and island arc basalts are shown to have similarly low isotopic values (Ueda and Sakai, 1984). Tholeiitic basalts with island arc-affinities are present in both the host rock sequence to Lemarchant (i.e., Lake Ambrose formation; Copeland et al., 2008; McNicoll et al., 2010) and in the basement rock underlying Lemarchant (i.e., the Sandy Brook group; Rogers et al., 2006; McNicoll et al., 2010). Furthermore, the intrusive igneous rocks below the deposit (Lemarchant microgranite) and the Neoproterozoic basement rock (Cripplebback Intrusive Suite) likely have magmatic $\delta^{34}S$ values of ~0±3‰ (e.g., Ohmoto and Goldhaber, 1997; Seal, 2006). Although an igneous sulfur source may explain some $\delta^{34}S$ values near 0‰ in the Lemarchant dataset, it cannot explain some of the more negative $\delta^{34}S$ <<0‰ present in sulfides deposited during the earlier stages of mineralization (Figs. 3.6 and 3.7).

The slightly negative $\delta^{34}S$ values, and potentially some of the near 0‰ $\delta^{34}S$ values, may be due to contributions of light sulfur from magmatic fluids (Ohmoto and Rye, 1979; Franklin et al., 2005; Seal, 2006). At temperatures above 300°C the dominant sulfur species in magmatic fluids is SO_2, but with cooling, magmatic SO_2 disproportionates to

form H_2S and H_2SO_4 (Ohmoto, 1972; Ohmoto and Lasaga, 1982; Herzig et al., 1998; Seal, 2006). This reaction is accompanied by a large isotopic fractionation that produces sulfides with negative $\delta^{34}S$ relative to associated sulfates (Rye, 1993; Huston et al., 2011). Furthermore, the early mineral assemblages at Lemarchant contain epithermal suite minerals (i.e., bornite, tetrahedrite, colusite, covellite, electrum) and base metal sulfides that are both enriched in epithermal trace elements (i.e., Au, As, Bi, Co, Cr, In, Mo, Ni, Sb, Se, Te), which are indicative of a magmatic fluid contribution to the deposit (Hedenquist and Lowenstern, 1994; Sillitoe et al., 1996; Hannington et al., 1999). It has also been suggested that the deposition of these early stage epithermal minerals with bladed barite at Lemarchant was a result of fluid boiling (see Chapter 2; Gill et al., 2013; Gill and Piercey, 2014), which would also have caused disproportionation of magmatic SO_2 in the hydrothermal fluid and resulted in light $\delta^{34}S$ signatures in associated sulfides (Ohmoto, 1972; Rye, 1993; Hannington et al., 1999; Huston, 2000; Seal, 2006; Hannington and Monecke, 2009; Huston et al., 2011). The lighter isotopic values in the Lemarchant dataset are therefore consistent with magmatic input, as observed in other ancient precious metal bearing VMS and modern SMS deposits (e.g., Fig. 3.9; Lau Basin; Herzig et al., 1998; Eskay Creek; Sherlock et al., 1999; Mt. Morgan; Ulrich et al., 2002).

3.7.3 – Sulfur isotope geothermometry

Stable isotope geothermometry can provide some insight into the physicochemical conditions of deposit formation if sulfide pairs were deposited simultaneously and in equilibrium (e.g., Kajiwara and Krouse, 1971; Barton and Skinner, 1979; Ohmoto and Rye, 1979). Pyrite-galena, pyrite-chalcopyrite, and chalcopyrite-galena pairs were

selected based on their close proximity (ideally, in contact) and presence in the same stage of mineralization. These parameters provided a limited number of potentially useable pairs, the majority of which yielded calculated temperatures that are much too high for the deposition temperatures indicated by the mineralogy and bulk chemistry of the type mineral assemblages (see Chapter 2; calculations in Appendix F.4), and for VMS deposits in general (i.e., >400°C; Lydon, 1988; Hannington and Scott, 1989; Huston and Large, 1989; Ohmoto, 1996). Oxidized and sulfur-rich fluid conditions that are characteristic of the initial and intermediate stages of mineralization (see Chapter 2), suggest that relatively small fluctuations in oxygen fugacity and/or pH may have also contributed to the wide range of $\delta^{34}S$ values present in type 1, 2A and 2B sulfides (Figs. 3.6 and 3.7; Ohmoto, 1972; Ohmoto and Rye, 1979), and that all sulfides deposited in a given volume were not likely in isotopic equilibrium. The type 3 and 4 assemblages were formed under less oxidized, Cu-rich and sulfate poor conditions; these depositional environments generally produce less drastic variations in $\delta^{34}S$ with fluctuations in fO_2 and/or pH (Ohmoto, 1972; Ohmoto and Rye, 1979; Ohmoto et al., 1983). However, the wide range in $\delta^{34}S$ of type 3 and 4 sulfides suggests that isotopic equilibrium was not attained between these sulfides either. Isotopic disequilibrium is expected at Lemarchant, given: (i) the complex paragenetic and fluid history of the deposit; and (ii) that most VMS deposits are dynamic and isotopically open systems, with complex histories of zone refinement and rapid changes in fluid temperatures and compositions (e.g., Ohmoto, 1972; Ohmoto, 1996; Seal, 2006).

3.8 – Conclusion

Radiogenic and stable isotope data from the precious metal bearing, polymetallic Lemarchant VMS deposit provide insight into the sources of metals and sulfur in the deposit. Lead isotope ratios cluster proximal to the young upper crust growth curve at ~500 Ma, suggesting that the majority of Pb in the deposit was derived from young upper crust. This is consistent with regional tectonic models for the Tally Pond group, and with derivation of Pb mostly from older Neoproterozoic volcanic arc basement rocks in the region. However, the Lemarchant samples trend to lower μ values that require input from more juvenile sources (i.e., basaltic material), which were either derived from more juvenile Neoproterozoic rocks, or the underlying mafic rocks of the Tally Pond group.

Sulfur isotope ratios in Lemarchant sulfides vary throughout the deposit, and throughout its genetic history, and imply derivation of H_2S from three main sources: (1) thermochemically reduced seawater sulfate ($\delta^{34}S > 0$); (2) igneous sulfide leached from basement rock ($\delta^{34}S \sim 0$); and (3) light H_2S derived from disproportionation of magmatic SO_2 ($\delta^{34}S < 0$). In the initial stages of mineralization (stages 1-2), and in particular stage 2, sulfides have lighter $\delta^{34}S$ values that are consistent with a contribution of magmatic sulfur. This conclusion is consistent with the epithermal mineral assemblages, trace element enrichments, and with mineral textures that indicate fluid boiling at the seafloor. The third and final stages of mineralization (stages 3-4) are devoid of these characteristics, and likely contain sulfur derived from the more typical sources of sulfur for VMS deposits, including TSR and leaching of igneous basement rocks.

3.9 – Acknowledgements

The GSC Targeted Geoscience Initiative 4 Program and the Research Affiliate Program of NRCan provide the majority of funding for this project. Grants to Dr. Stephen J. Piercey, including an NSERC Discovery Grant and the NSERC-Altius Industrial Research Chair in Mineral Deposits supported by NSERC, Altius Resources Inc., and the Research and Development Corporation of Newfoundland and Labrador provide additional funding for this project. Access to the Lemarchant drill core was provided by the Canadian Zinc Corporation and the Paragon Minerals Corporation (a 100% owned subsidiary of Canadian Zinc Corporation). Many thanks to Glenn Piercey, Dr. Graham D. Layne, Stefanie Lode and Stefanie Brueckner for their technological help with the SIMS, and their guidance with the treatment and interpretation of Lemarchant Pb and S isotope data. Thanks to editors Dr. Piercey, Jonathan Cloutier and Dr. Layne for their constructive and insightful comments, and to Jan Peter and Aphrodite Indares for their reviews.

3.9 – References

Barton Jr, P., and Skinner, B., 1979. Sulfide mineral stabilities: *in* Barnes, H.L., ed., Geochemistry of hydrothermal ore deposits, 2nd Edition: New York, Wiley, p. 278-403.

Canfield, D.E., 2004. The evolution of the Earth surface sulfur reservoir: American Journal of Science, v. 304, p. 839-861.

Chiaradia, M., Tripodi, D., Fontboté, L., and Reza, B., 2008. Geologic setting, mineralogy, and geochemistry of the early Tertiary Au-rich volcanic-hosted massive sulfide deposit of La Plata, Western Cordillera, Ecuador: Economic Geology, v. 103, p. 161-183.

Claypool, G.E., Holser, W.T., Kaplan, I.R., Sakai, H., and Zak, I., 1980. The age curves of sulfur and oxygen isotopes in marine sulfate and their mutual interpretation: Chemical Geology, v. 28, p. 199-260.

Copeland, D.A., McCleneghan, S.M., and Piercey, S.J., 2008. Ninth year assessment report on diamond drilling, lithogeochemistry, pulse EM surveying and linecutting on license 8183M, South Tally Pond Property, Rogerson Lake area, Newfoundland and Labrador NTS 12A/10 and 12A/07. Newfoundland and Labrador Geological Survey, Assessment Report, 91 p. [for Paragon Minerals and Altius Minerals].

Cumming, G.L., and Krstic, D., 1987. Detailed lead isotope study of Buchans and related ores: *in* Kirkham, R.V., ed., Buchans Geology, Newfoundland: Geological Survey of Canada, v. 86-24, p. 227-234.

de Ronde, C.E.J., 1995. Fluid chemistry and isotopic characteristics of seafloor hydrothermal systems and associated VMS deposits: potential for magmatic contributions: *in* Magmas, fluids and ore deposits, Mineralogical Association of Canada Short Course Series, v. 23, p. 479-509.

de Ronde, C.E.J., Hannington, M.D., Stoffers, P., Wright, I.C., Ditchburn, R.G., Reyes, A.G., Baker, E.T., Massoth, G.J., Lupton, J.E., Walker, S.L., Greene, R.R., Soong, C.W.R., Ishibashi, J., Lebon, G.T., Bray, C.J., and Resing, J.A., 2005. Evolution of a submarine magmatic-hydrothermal system: Brothers Volcano, Southern Kermadec Arc, New Zealand: Economic Geology, v. 100, p. 1097-1133.

Doe, B., and Stacey, J., 1974. The application of lead isotopes to the problems of ore genesis and ore prospect evaluation: a review: Economic Geology, v. 69, p. 757-776.

Dunning, G.R., Swinden, H.S., Kean, B.F., Evans, D.T.W., and Jenner, G.A., 1991. A Cambrian island arc in Iapetus; geochronology and geochemistry of the Lake Ambrose volcanic belt, Newfoundland Appalachians: Geological Magazine, v. 128, p. 1-17.

Evans, D., and Kean, B., 2002. The Victoria Lake Supergroup, central Newfoundland – its definition, setting and volcanogenic massive sulfide mineralization: Newfoundland Department of Mines and Energy, Geological Survey, Open File NFLD/2790, 68 p.

Fouquet, Y., and Marcoux, E., 1995. Lead isotope systematics in Pacific hydrothermal sulfide deposits: Journal of Geophysical Research, v. 100, p. 6025-6040.

Franklin, J., Gibson, H., Jonasson, I., and Galley, A., 2005. Volcanogenic massive sulfides: Economic Geology100th Anniversary Volume, p. 523-560.

Fraser, D., Giroux, G.H., Copeland, D.A., and Devine, C.A., 2012. Technical report and resource minerals estimate on the Lemarchant deposit, South Tally Pond VMS

project, Central Newfoundland, Canada – NI 43-101 Technical Report prepared for Paragon Minerals Corporation, 132 p.

Galley, A., Hannington, M., and Jonasson, I., 2007. Volcanogenic massive sulfide deposits: *in* Goodfellow, W.D., ed., Mineral deposits of Canada: A synthesis of major deposit-types, district metallogeny, the evolution of geological provinces, and exploration methods: Geological Association of Canada, Mineral Deposits Division, Special Publication, v. 5, p. 141-161.

Gibson, H.L., Allen, R.L., Riverin, G., and Lane, T.E., 2007. The VMS model; advances and application to exploration: Abstracts, Decennial International Conference on Mineral Exploration, v. 5, p. 713-730.

Gill, S.B., Piercey, S.J., and Devine, C.A., 2013. Preliminary mineralogy of barite-associated sulfide mineralization in the Ordovician Zn-Pb-Cu-Ag-Au Lemarchant volcanogenic massive sulfide deposit, Newfoundland and Labrador: Geological Survey of Canada, Current Research Report 2013-17, 15 p.

Gill, S.B. and Piercey, S.J., 2014. Styles of mineralization and sulfide mineral zonation in the Cambrian Zn-Pb-Cu-Ag-Au Lemarchant volcanogenic massive sulfide (VMS) deposit, Newfoundland and Labrador – preliminary observations; Geological Survey of Canada, Current Research Report 2014-05, 17 p.

Goodfellow, W.D., and Peter, J.M., 1996. Sulfur isotope composition of the Brunswick No. 12 massive sulfide deposit, Bathurst Mining Camp, New Brunswick: implications for ambient environment, sulfur source, and ore genesis: Canadian Journal of Earth Sciences, v. 33, p. 231-251.

Goodfellow, W.D., 2007. Metallogeny of the Bathurst Mining Camp, northern New Brunswick: *in* Goodfellow, W.D., ed., Mineral Deposits of Canada: A synthesis of major deposit-types, district metallogeny, the evolution of geological provinces, and exploration methods: Geological Association of Canada, Mineral Deposits Division, Special Publication No. 5, p. 449-469.

Halbach, P., Nakamura, K.-i., Wahsner, M., Lange, J., Sakai, H., Kaeselitz, L., Hansen, R.D., Yamano, M., Post, J., Prause, B., Seifert, R., Michaelis, W., Teichmann, F., Kinoshita, M., Maerten, A., Ishibashi, J., Czerwinski, S., and Blum, N., 1989. Probable modern analogue of Kuroko-type massive sulfide deposits in the Okinawa Trough back-arc basin: Nature, v. 338, p. 496-499.

Hannington, M., and Scott, S.D., 1989. Sulfidation equilibria as guides to gold mineralization in volcanogenic massive sulfides; evidence from sulfide mineralogy and the composition of sphalerite: Economic Geology, v. 84, p. 1978-1995.

Hannington, M., and Monecke, T., 2009. Modern submarine hydrothermal systems - A global perspective on distribution, size and tectonic settings: *in* Cousens, B., and Piercey, S.J., eds., Submarine Volcanism and mineralization: modern through

ancient: Geological Association of Canada, Mineral Deposits Division, Short Course Notes, v. 19, p. 91-146.

Hannington, M.D., Jonasson, I.R., Herzig, P.M., and Petersen, S., 1995. Physical and chemical processes of seafloor mineralization at mid-ocean ridges; *in* Humphris, S.E., Zierenberg, R.A., Mullineaux, L.S., Thomson, R.E., eds., Seafloor hydrothermal systems: Physical, chemical, biological, and geological interactions: Geophysical Monograph, v. 91, p. 115-157.

Hannington, M.D., Poulsen, K.H., Thompson, J.F.H., and Sillitoe, R.H., 1999. Volcanogenic gold in the massive sulfide environment: Reviews in Economic Geology, v. 8, p. 325-356.

Hedenquist, J.W., and Lowenstern, J.B., 1994. The role of magmas in the formation of hydrothermal ore deposits: Nature, v. 370, p. 519-527.

Herzig, P.M., Hannington, M.D., Fouquet, Y., von Stackelberg, U., and Petersen, S., 1993. Gold-rich polymetallic sulfides from the Lau back arc and implications for the geochemistry of gold in sea-floor hydrothermal systems of the Southwest Pacific: Economic Geology, v. 88, p. 2182-2209.

Herzig, P., Hannington, M., and Arribas Jr, A., 1998. Sulfur isotopic composition of hydrothermal precipitates from the Lau back-arc: implications for magmatic contributions to seafloor hydrothermal systems: Mineralium Deposita, v. 33, p. 226-237.

Huston, D.L., and Large, R.R., 1989. A chemical model for the concentration of gold in volcanogenic massive sulfide deposits: Ore Geology Reviews, v. 4, p. 171-200.

Huston, D.L., 1999. Stable isotopes and their significance for understanding the genesis of volcanic-hosted massive sulfide deposits: a review: Reviews in Economic Geology, v. 8, p. 157-179.

Huston, D.L., 2000. Gold in volcanic-hosted massive sulfide deposits; distribution, genesis, and exploration: Reviews in Economic Geology, v. 13, p. 401-426.

Huston, D.L., Relvas, J.M.R.S., Gemmell, J.B., Drieberg, S., 2011. The role of granites in volcanic-hosted massive sulfide ore-forming systems: An assessment of magmatic–hydrothermal contributions: Mineralium Deposita, v. 46, p. 473-507.

Janecky, D.R., and Shanks, W.C., 1988. Computational modeling of chemical and sulfur isotopic reaction processes in sea-floor hydrothermal systems; chimneys, massive sulfide, and subjacent alteration zones: The Canadian Mineralogist, v. 26, p. 805-825.

Jensen, M.L., 1967. Sulfur isotopes and mineral genesis: *in* Barnes, H.L., ed., Geochemistry of hydrothermal ore deposits: New York, Rinehart and Winston, p. 143-165.

Kajiwara, Y., and Krouse, H., 1971. Sulfur isotope partitioning in metallic sulfide systems: Canadian Journal of Earth Sciences, v. 8, p. 1397-1408.

Kampschulte, A., and Strauss, H., 2004. The sulfur isotopic evolution of Phanerozoic seawater based on the analysis of structurally substituted sulfate in carbonates: Chemical Geology, v. 204, p. 255-286.

Kramers, J.D., and Tolstikhin, I.N., 1997. Two terrestrial lead isotope paradoxes, forward transport modeling, core formation and the history of the continental crust: Chemical Geology, v. 139, p. 75-110.

Lode, S., Piercey, S.J.P., Copeland, D.A., Devine, C.A., and Sparrow, B., 2012. Setting and styles of hydrothermal mudstones near the Lemarchant volcanogenic massive sulfide (VMS) deposit, Central Mobile Belt, Newfoundland: *in* Abstracts, Geological Association of Canada-Mineralogical Association of Canada, Joint Annual Meeting, v. 35, p. 79.

Lode, S., Piercey, S. J., Devine, C. A., Layne, G. D., Piercey, G., and Hewa, L., 2014. Lithogeochemistry and sulfur isotopic composition of hydrothermal mudstones associated with the Lemarchant volcanogenic massive sulfide (VMS) deposit, Tally Pond Belt, Central Newfoundland: *in* Abstracts, Geological Association of Canada, Newfoundland Spring Technical Meeting, v. 40, p. 20.

Lydon, J.W., 1988. Volcanogenic massive sulfide deposits, Part 2: Genetic models: Geoscience Canada, v. 15, p. 155-181.

Marini, L., Moretti, R., and Accornero, M., 2011. Sulfur isotopes in magmatic-hydrothermal systems, melts, and magmas: Reviews in Mineralogy and Geochemistry, v. 73, p. 423-492.

McGill, R., Tukey, J.W., and Larsen, W.A., 1978. Variations of box plots: The American Statistician, v. 32, p. 12-16.

McNicoll, V., Squires, G., Kerr, A., and Moore, P., 2010. The Duck Pond and Boundary Cu-Zn deposits, Newfoundland; new insights into the ages of host rocks and the timing of VHMS mineralization: Canadian Journal of Earth Sciences, v. 47, p. 1481-1506.

Mortensen, J.K., Dusel-Bacon, C., Hunt, J., and Gabites, J., 2006. Lead isotopic constraints on the metallogeny of middle and late Paleozoic syngenetic base metal occurrences in the Yukon-Tanana and Slide Mountain/Seventymile terranes and adjacent portions of the North American miogeocline: *in* Colpron, M. and Nelson, J.L., eds., Paleozoic evolution and metallogeny of pericratonic terranes at the ancient Pacific margin of North America, Canadian and Alaskan Cordillera: Geological Association of Canada, Special Paper, v. 45, p. 261-279.

Ohmoto, H., 1972. Systematics of sulfur and carbon isotopes in hydrothermal ore deposits: Economic Geology, v. 67, p. 551-578.

Ohmoto, H., 1996. Formation of volcanogenic massive sulfide deposits; the Kuroko perspective: Ore Geology Reviews, v. 10, p. 135-177.

Ohmoto, H., and Rye, R., 1979. Isotopes of sulfur and carbon: *in* Barnes, H.L., ed., Geochemistry of hydrothermal ore deposits, 2nd Edition: New York, Wiley, p. 509-567.

Ohmoto, H., and Lasaga, A.C., 1982. Kinetics of reactions between aqueous sulfates and sulfides in hydrothermal systems: Geochimica et Cosmochimica Acta, v. 46, p. 1727-1745.

Ohmoto, H., and Goldhaber, M.B., 1997. Sulfur and carbon isotopes: *in* Barnes, H.L., ed., Geochemistry of hydrothermal ore deposits, 3rd Edition: New York, Wiley, p. 517-611.

Ohmoto, H., Mizukami, M., Drummond, S., Eldridge, C., Pisutha-Arnond, V., and Lenagh, T., 1983. Chemical processes of Kuroko formation: Economic Geology Monograph, v. 5, p. 570-604.

Paytan, A., Gray, E.T., 2012. Sulfur isotope stratigraphy: *in* Gradstein, F.M., Ogg, J.G., Schmitz, M., Ogg, G., eds., The Geologic Timescale 2012: Elsevier, Amsterdam, p. 167-180.

Piercey, S.J. and Hinchey, J., 2012. Volcanogenic massive sulfide (VMS) deposits of the Central Mineral Belt, Newfoundland: Geological Association of Canada–Mineralogical Association of Canada Joint Annual Meeting, Field Trip Guidebook B, Newfoundland and Labrador Department of Natural Resources, Geological Survey, Open File NFLD/3173, 56 p.

Piercey, S.J., Squires, G.C., and Brace, T.D., 2014. Lithostratigraphic, hydrothermal, and tectonic setting of the Boundary volcanogenic massive sulfide deposit, Newfoundland Appalachians, Canada: Formation by subseafloor replacement in a Cambrian rifted arc: Economic Geology, v. 109, p. 661-687.

Pollock, J., and Wilton, D., 2001. Metallogenic studies of the Tally Pond Belt, Victoria Lake Group: trace element geochemistry and lead isotope data from the Exploits Subzone, Newfoundland: Newfoundland and Labrador Department of Natural Resources, Geological Survey, Current Research Report 01-1, p. 247–266.

Pollock, J., 2004, Geology and paleotectonic history of the Tally Pond Group, Dunnage zone, Newfoundland Appalachians: An integrated geochemical, geochronological, metallogenic and isotopic study of a Cambrian island arc along the Peri-Gondwanan margin of Iapetus: Unpublished M.Sc. thesis, St. John's, Newfoundland, Memorial University, 420 p.

Rogers, N., and van Staal, C., 2002. Toward a Victoria Lake Supergroup: A provisional stratigraphic revision of the Red Indian to Victoria Lakes area, central Newfoundland: Newfoundland Department of Mines and Energy, Geological Survey, Current Research Report 02-1, p. 185-195.

Rogers, N., van Staal, C.R., McNicoll, V., Pollock, J., Zagorevski, A., and Whalen, J., 2006. Neoproterozoic and Cambrian arc magmatism along the eastern margin of the Victoria Lake Supergroup: A remnant of Ganderian basement in central Newfoundland?: Precambrian Research, v. 147, p. 320-341.

Roth, T., Thompson, J.F.H., and Barrett, T.J., 1999. The precious metal-rich Eskay Creek Deposit, northwestern British Columbia: Reviews in Economic Geology, v. 8, p. 357-373.

Rye, R.O., 1993. The evolution of magmatic fluids in the epithermal environment; the stable isotope perspective: Economic Geology, v. 88, p. 733-752.

Sakai, H., and Dickson, F., 1978. Experimental determination of the rate and equilibrium fractionation factors of sulfur isotope exchange between sulfate and sulfide in slightly acid solutions at 300 C and 1000 bars: Earth and Planetary Science Letters, v. 39, p. 151-161.

Sakai, H., Des Marais, D., Ueda, A., and Moore, J., 1984. Concentrations and isotope ratios of carbon, nitrogen and sulfur in ocean-floor basalts: Geochimica et Cosmochimica Acta, v. 48, p. 2433-2441.

Sato, K., Delevaux, M.H., and Doe, B.R., 1981. Lead isotope measurements on ores, igneous and sedimentary rocks from the Kuroko mineralization area: Geochemical Journal, v. 15, p. 135-140.

Seal, R.R., 2006. Sulfur isotope geochemistry of sulfide minerals: Reviews in Mineralogy and Geochemistry, v. 61, p. 633-677.

Seyfried, W.E., Bischoff, J.L., 1981. Experimental seawater-basalt interaction at 300°C, 500 bars, chemical exchange, secondary mineral formation and implications for the transport of heavy metals: Geochimica et Cosmochimica Acta, v. 45, p. 135-149.

Shanks, W., 2001. Stable isotopes in seafloor hydrothermal systems: vent fluids, hydrothermal deposits, hydrothermal alteration, and microbial processes: Reviews in Mineralogy and Geochemistry, v. 43, p. 469-525.

Shanks, W., Böhlke, J.K., Seal, R.R., 1995. Stable isotopes in mid-ocean ridge hydrothermal systems: interactions between fluids, minerals, and organisms: *in* Humphris, S.E., Zierenberg, R.A., Mullineaux, L.S., Thomson, R.E., eds., Seafloor Hydrothermal Systems: physical, chemical, biological, and geological interactions: Geophysical Monograph, v. 91, p. 194-221.

Sillitoe, R.H., Hannington, M.D., and Thompson, J.F.H., 1996. High sulfidation deposits in the volcanogenic massive sulfide environment: Economic Geology, v. 91, p. 204-212.

Sherlock, R.L., Roth, T., Spooner, E.T.C., and Bray, C.J., 1999. Origin of the Eskay Creek precious metal-rich volcanogenic massive sulfide deposit; fluid inclusion and stable isotope evidence: Economic Geology, v. 94, p. 803-824.

Squires, G., and Moore, P., 2004. Volcanogenic massive sulfide environments of the Tally Pool Volcanics and adjacent area; geological, lithogeochemical and geochronological results: Newfoundland Department of Mines and Energy, Geological Survey, Current Research Report 04-1, p. 63-91.

Stacey, J.S., and Kramers, J., 1975. Approximation of terrestrial lead isotope evolution by a two-stage model: Earth and Planetary Science Letters, v. 26, p. 207-221.

Swinden, H.S., and Thorpe, R., 1984. Variations in style of volcanism and massive sulfide deposition in Early to Middle Ordovician island-arc sequences of the Newfoundland Central Mobile Belt: Economic Geology, v. 79, p. 1596-1619.

Swinden, H., Kean, B., and Dunning, G., 1988. Geological and paleotectonic settings of volcanogenic massive sulfide mineralization in Central Newfoundland: The Volcanogenic Sulfide Districts of Newfoundland, Geological Association of Canada, Mineral Deposits Division, p. 2-27.

Thorpe, R.I., 2008. Release of lead isotope data in 4 databases; Canadian, western Superior, foreign, and whole rock and feldspar: Geological Survey of Canada, Open File Report 5664, p. 42.

Tosdal, R., Wooden, J., and Bouse, R., 1999. Pb isotopes, ore deposits, and metallogenic terranes: Application of radiogenic isotopes to ore deposit research and exploration. Reviews in Economic Geology, v. 12, p. 1-28.

Ueda, A., and Sakai, H., 1984. Sulfur isotope study of Quaternary volcanic rocks from the Japanese Islands Arc: Geochimica et Cosmochimica Acta, v. 48, p. 1837-1848.

Ulrich, T., Golding, S.D., Kamber, B.S., Khin, Z., and Taube, A., 2002. Different mineralization styles in a volcanic-hosted ore deposit: the fluid and isotopic signatures of the Mt Morgan Au–Cu deposit, Australia: Ore Geology Reviews, v. 22, p. 61-90.

van Staal, C., and Barr, S., 2012. Lithospheric architecture and tectonic evolution of the Canadian Appalachians and associated Atlantic margin, Chapter 2: *in* Percival, J.A., Cook, F.A., and Clowes, R.M., eds., Tectonic Styles in Canada Revisited: the LITHOPROBE perspective, Geological Association of Canada, Special Paper, v. 49, p. 41-95.

Vaughan, D.J., and Craig, J.R., 1978. Mineral chemistry of metal sulfides: Cambridge, Cambridge University Press, 512 p.

Wilkin, R.T., and Barnes, H.L., 1997. Formation processes of framboidal pyrite: Geochimica et Cosmochimica Acta, v. 61, p. 323-339.

Williams, H., Colman-Sadd, S.P., and Swinden, H.S., 1988. Tectonic-stratigraphic subdivisions of Central Newfoundland: Geological Survey of Canada, Current Research Part B, Paper 88-01, p. 91-98.

Winter, L.S., and Wilton, D.H.C., 2000. New lithogeochemical and Pb isotope data from Buchans area, central Newfoundland: Atlantic Geology, v. 36, p. 176.

Zagorevski, A., Van Staal, C.R., McNicoll, V., and Rogers, N., 2007. Upper Cambrian to upper Ordovician peri-Gondwanan island arc activity in the Victoria Lake Supergroup, Central Newfoundland: tectonic development of the northern Ganderian margin: American Journal of Science, v. 307, p. 339-370.

Zartman, R., and Doe, B., 1981. Plumbotectonics—the model: Tectonophysics, v. 75, p. 135-162.

Table 3.1. Lead-isotope ratios, standard deviation (1σ), calculated model lead ages and μ-values (after Stacey and Kramers, 1975) of analyzed galena samples at Lemarchant.

Drill hole	Depth (m)	Sample	$^{206/204}$Pb	$^{206/204}$Pb (StDev.)	$^{207/204}$Pb	$^{207/204}$Pb (StDev)	$^{208/204}$Pb	$^{208/204}$Pb (StDev)	Model Age (Ma)	μ
Type 2A: Bornite-galena-chalcopyrite stringers in massive barite-sphalerite-pyrite-galena										
LM07-14	185.3	CNF14259 Pb1	17.393	0.149	15.632	0.424	38.003	1.110	972	10.19
LM07-14	185.3	CNF14259 Pb2	17.932	0.267	15.639	0.466	38.016	1.154	595	9.99
LM07-14	185.3	CNF14259 Pb3	18.176	0.039	15.642	0.067	38.002	0.153	429	9.94
LM07-14	185.3	CNF14259 Pb4	16.868	0.307	15.624	0.672	37.842	1.410	1337	10.49
LM07-14	185.3	CNF14259 Pb5	18.092	0.066	15.557	0.102	37.638	0.283	319	9.58
LM07-14	185.3	CNF14259 Pb6	18.211	0.074	15.677	0.110	38.078	0.266	467	10.08
LM11-63	194.1	CNF29957 Pb1	18.098	0.077	15.586	0.094	37.733	0.243	378	9.72
LM11-63	194.1	CNF29957 Pb2	18.181	0.040	15.669	0.055	38.091	0.164	472	10.05
LM11-63	194.1	CNF29957 Pb3	18.138	0.068	15.599	0.076	37.830	0.190	373	9.76
LM11-63	194.1	CNF29957 Pb4	18.137	0.053	15.605	0.088	37.872	0.178	388	9.79
LM11-63	194.1	CNF29957 Pb5	18.134	0.078	15.572	0.098	37.740	0.292	318	9.63
LM11-63	194.1	CNF29957 Pb6	18.129	0.072	15.581	0.094	37.708	0.258	340	9.68
Type 2B: galena-tetrahedrite-barite-pyrite-sphalerite-gold in massive barite-sphalerite-pyrite-galena										
LM11-65	155.2	CNF14291 Pb1	18.092	0.081	15.579	0.122	37.939	0.376	368	9.69
LM11-65	155.2	CNF14291 Pb2	18.100	0.056	15.489	0.080	37.349	0.220	163	9.27
LM11-65	155.2	CNF14291 Pb3	18.043	0.054	15.476	0.066	37.487	0.169	179	9.22
LM11-65	155.2	CNF14291 Pb4	18.061	0.100	15.570	0.117	37.879	0.337	374	9.65
LM11-65	155.2	CNF14291 Pb5	18.103	0.042	15.690	0.094	38.325	0.371	578	10.20
LM11-65	155.2	CNF14291 Pb6	18.076	0.054	15.624	0.098	38.136	0.388	462	9.88
LM11-59	194.7	CNF29962 Pb1	18.069	0.062	15.516	0.090	37.625	0.318	246	9.39
LM11-59	194.7	CNF29962 Pb2	18.116	0.035	15.530	0.050	37.629	0.141	239	9.44
LM11-59	194.7	CNF29962 Pb3	18.081	0.071	15.496	0.079	37.586	0.224	194	9.30
LM11-59	194.7	CNF29962 Pb4	18.108	0.073	15.524	0.089	37.628	0.206	233	9.42
LM11-59	194.7	CNF29962 Pb5	18.062	0.083	15.492	0.123	37.584	0.321	203	9.30
LM11-59	194.7	CNF29962 Pb6	18.143	0.041	15.578	0.060	37.799	0.167	323	9.66
LM08-19	88.5	CNF29986 Pb1	18.140	0.047	15.595	0.068	37.876	0.169	362	9.74
LM08-19	88.5	CNF29986 Pb2	18.171	0.077	15.535	0.113	37.650	0.260	209	9.46
LM08-19	88.5	CNF29986 Pb3	18.120	0.057	15.569	0.078	37.836	0.233	322	9.62
LM08-19	88.5	CNF29986 Pb4	18.127	0.048	15.568	0.066	37.780	0.184	315	9.62
LM08-19	88.5	CNF29986 Pb5	18.127	0.087	15.554	0.114	37.697	0.323	283	9.55
LM08-19	88.5	CNF29986 Pb6	18.063	0.090	15.515	0.112	37.698	0.277	248	9.39
Type 3: Massive sphalerite-pyrite-chalcopyrite-galena										
LM11-59	179.0	CNF29959 Pb1	18.102	0.063	15.552	0.080	37.726	0.200	300	9.55
LM11-59	179.0	CNF29959 Pb2	18.154	0.056	15.630	0.083	38.002	0.202	414	9.88
LM11-59	179.0	CNF29959 Pb3	18.180	0.080	15.629	0.090	37.932	0.240	405	9.89
LM11-59	179.0	CNF29959 Pb4	18.177	0.063	15.625	0.080	37.898	0.183	398	9.87

LM11-59	179.0	CNF29959 Pb5	18.164	0.066	15.604	0.095	37.994	0.289	363	9.78
LM11-59	179.0	CNF29959 Pb6	18.155	0.062	15.635	0.085	38.027	0.285	429	9.91
LM11-59	186.1	CNF29960 Pb1	18.077	0.096	15.486	0.125	37.585	0.328	174	9.26
LM11-59	186.1	CNF29960 Pb2	18.128	0.090	15.578	0.111	37.831	0.283	336	9.66
LM11-59	186.1	CNF29960 Pb3	18.109	0.052	15.528	0.086	37.665	0.198	241	9.44
LM11-59	186.1	CNF29960 Pb4	18.097	0.055	15.522	0.087	37.624	0.212	237	9.41
LM11-59	186.1	CNF29960 Pb5	18.046	0.155	15.496	0.185	37.583	0.527	215	9.30

Table 3.2. Sulfur-isotope values (per mil VCDT) of pyrite, chalcopyrite and galena from each type mineral assemblage at Lemarchant. Standard error of the mean (SEM) included to 1σ.

Drill hole	Depth (m)	Sample	Mineral	$\delta^{34}S$	SEM (1σ)
Type 1: Massive barite-semi-massive sphalerite-pyrite-galena					
LM11-59	186.1	CNF29960 py1	Pyrite	0.3	0.3
LM11-59	186.1	CNF29960 py2	Pyrite	1.7	0.2
LM11-59	186.1	CNF29960 py3	Pyrite	4.9	0.2
LM11-59	186.1	CNF29960 py4	Pyrite	4.4	0.2
LM11-59	186.1	CNF29960 py5	Pyrite	4.9	0.3
LM11-59	186.1	CNF29960 py6	Pyrite	4.2	0.2
LM11-59	186.1	CNF29960 py7	Pyrite	4.1	0.2
LM11-59	186.1	CNF29960 py8	Pyrite	4.6	0.2
Type 2A: Bornite-galena-chalcopyrite stringers					
LM11-63	194.1	CNF29957 gn1	Galena	4.7	0.3
LM11-63	194.1	CNF29957 gn2	Galena	-0.2	0.3
LM11-63	194.1	CNF29957 gn3	Galena	4.1	0.3
LM11-63	194.1	CNF29957 gn4	Galena	3.7	0.3
LM11-63	194.1	CNF29957 gn5	Galena	2.3	0.3
LM11-63	194.1	CNF29957 gn6	Galena	2.5	0.3
LM07-14	185.3	CNF14259 gn1	Galena	-1.6	0.6
LM07-14	185.3	CNF14259 gn2	Galena	-1.5	0.3
LM07-14	185.3	CNF14259 gn3	Galena	11.8	0.3
LM07-14	185.3	CNF14259 gn4	Galena	0.4	0.2
LM07-14	185.3	CNF14259 gn5	Galena	1.1	0.3
LM07-14	185.3	CNF14259 gn6	Galena	-0.2	0.3
LM11-63	194.1	CNF29957 ccp1	Chalcopyrite	5.8	0.3
LM11-63	194.1	CNF29957 ccp2	Chalcopyrite	6.5	0.5
LM11-63	194.1	CNF29957 ccp3	Chalcopyrite	5.4	0.8
LM11-63	194.1	CNF29957 ccp4	Chalcopyrite	6.0	0.6
LM11-63	194.1	CNF29957 ccp5	Chalcopyrite	5.1	0.8
LM11-63	194.1	CNF29957 ccp6	Chalcopyrite	6.2	0.6
Type 2B: Galena-tetrahedrite-barite-pyrite-sphalerite-gold					
LM11-63	194.1	CNF29957 py1	Pyrite	4.2	0.3
LM11-63	194.1	CNF29957 py2	Pyrite	3.8	0.2
LM11-63	194.1	CNF29957 py3	Pyrite	3.9	0.2
LM11-63	194.1	CNF29957 py4	Pyrite	4.1	0.3
LM11-63	194.1	CNF29957 py5	Pyrite	2.9	0.2
LM11-63	194.1	CNF29957 py6	Pyrite	4.0	0.2
LM08-19	88.5	CNF29986 py1	Pyrite	5.5	0.3
LM08-19	88.5	CNF29986 py2	Pyrite	6.5	0.2

LM08-19	88.5	CNF29986 py3	Pyrite	5.6	0.3
LM08-19	88.5	CNF29986 py4	Pyrite	6.5	0.3
LM08-19	88.5	CNF29986 py5	Pyrite	5.4	0.3
LM08-19	88.5	CNF29986 py6	Pyrite	7.4	0.2
LM11-59	194.7	CNF29962 py1	Pyrite	6.4	0.3
LM11-59	194.7	CNF29962 py2	Pyrite	6.6	0.2
LM11-59	194.7	CNF29962 py3	Pyrite	6.4	0.3
LM11-59	194.7	CNF29962 py4	Pyrite	6.1	0.3
LM11-59	194.7	CNF29962 py5	Pyrite	6.8	0.3
LM11-59	194.7	CNF29962 py6	Pyrite	6.8	0.3
LM07-14	185.3	CNF14259 py1	Pyrite	6.1	0.3
LM07-14	185.3	CNF14259 py2	Pyrite	6.3	0.2
LM07-14	185.3	CNF14259 py3	Pyrite	4.8	0.3
LM07-14	185.3	CNF14259 py4	Pyrite	5.8	0.2
LM07-14	185.3	CNF14259 py5	Pyrite	5.1	0.6
LM07-14	185.3	CNF14259 py6	Pyrite	4.8	0.3
LM11-59	179.0	CNF29959 py1	Pyrite	10.6	0.3
LM11-59	179.0	CNF29959 py2	Pyrite	9.5	0.2
LM11-59	179.0	CNF29959 py3	Pyrite	6.2	0.5
LM11-59	179.0	CNF29959 py4	Pyrite	7.6	0.2
LM11-65	155.2	CNF14291 gn1	Galena	6.8	0.3
LM11-65	155.2	CNF14291 gn2	Galena	4.9	0.3
LM11-65	155.2	CNF14291 gn3	Galena	7.9	0.3
LM11-65	155.2	CNF14291 gn4	Galena	5.5	0.2
LM11-65	155.2	CNF14291 gn5	Galena	12.6	0.3
LM11-65	155.2	CNF14291 gn6	Galena	13.0	0.2
LM08-19	88.5	CNF29986 gn1	Galena	-1.7	0.4
LM08-19	88.5	CNF29986 gn2	Galena	0.0	0.4
LM08-19	88.5	CNF29986 gn3	Galena	1.6	0.3
LM08-19	88.5	CNF29986 gn4	Galena	7.4	0.2
LM08-19	88.5	CNF29986 gn5	Galena	2.5	0.3
LM08-19	88.5	CNF29986 gn6	Galena	1.5	0.2
LM11-59	194.7	CNF29962 gn1	Galena	5.3	0.2
LM11-59	194.7	CNF29962 gn2	Galena	3.0	0.3
LM11-59	194.7	CNF29962 gn3	Galena	2.5	0.2
LM11-59	194.7	CNF29962 gn4	Galena	1.6	0.3
LM11-59	194.7	CNF29962 gn5	Galena	0.3	0.4
LM11-59	194.7	CNF29962 gn6	Galena	5.2	0.4
LM11-59	194.7	CNF29962 ccp1	Chalcopyrite	4.3	0.4
LM11-59	194.7	CNF29962 ccp2	Chalcopyrite	3.8	0.3
LM11-59	194.7	CNF29962 ccp3	Chalcopyrite	3.5	0.4

LM11-59	194.7	CNF29962 ccp4	Chalcopyrite	2.9	0.4
LM11-59	194.7	CNF29962 ccp5	Chalcopyrite	3.3	0.4
LM11-59	194.7	CNF29962 ccp6	Chalcopyrite	3.9	0.3
LM08-19	88.5	CNF29986 Ccp1	Chalcopyrite	4.8	0.5
LM08-19	88.5	CNF29986 Ccp2	Chalcopyrite	4.6	0.3
LM08-19	88.5	CNF29986 Ccp3	Chalcopyrite	4.5	0.5
LM08-19	88.5	CNF29986 Ccp4	Chalcopyrite	3.9	0.4
LM08-19	88.5	CNF29986 Ccp5	Chalcopyrite	5.1	0.4
LM08-19	88.5	CNF29986 Ccp6	Chalcopyrite	5.0	0.4
Type 3: Massive sphalerite-pyrite-chalcopyrite-galena					
LM11-65	155.2	CNF14291 py1	Pyrite	8.3	0.2
LM11-65	155.2	CNF14291 py2	Pyrite	7.4	0.2
LM11-65	155.2	CNF14291 py3	Pyrite	7.6	0.3
LM11-65	155.2	CNF14291 py4	Pyrite	7.0	0.2
LM11-65	155.2	CNF14291 py5	Pyrite	6.9	0.2
LM11-65	155.2	CNF14291 py6	Pyrite	7.5	0.3
LM11-59	216.5	CNF29972 py1	Pyrite	6.8	0.4
LM11-59	216.5	CNF29972 py2	Pyrite	6.7	0.2
LM11-59	216.5	CNF29972 py3	Pyrite	6.2	0.3
LM11-59	216.5	CNF29972 py4	Pyrite	6.7	0.2
LM11-59	216.5	CNF29972 py5	Pyrite	6.2	0.4
LM11-59	216.5	CNF29972 py6	Pyrite	5.4	0.2
LM11-59	186.1	CNF29960 gn1	Galena	4.2	0.3
LM11-59	186.1	CNF29960 gn2	Galena	3.0	0.3
LM11-59	186.1	CNF29960 gn3	Galena	-6.0	0.2
LM11-59	186.1	CNF29960 gn4	Galena	2.5	0.3
LM11-59	186.1	CNF29960 gn5	Galena	0.4	0.2
LM11-59	186.1	CNF29960 gn6	Galena	-6.4	0.3
LM11-59	179.0	CNF29959 gn1	Galena	8.8	0.4
LM11-59	179.0	CNF29959 gn2	Galena	7.6	0.4
LM11-59	179.0	CNF29959 gn3	Galena	6.6	0.3
LM11-59	179.0	CNF29959 gn4	Galena	13.2	0.3
LM11-59	179.0	CNF29959 gn5	Galena	5.5	0.3
LM11-59	179.0	CNF29959 gn6	Galena	15.1	0.4
Type 4: Chalcopyrite-pyrite±sphalerite-galena stringers					
LM11-59	216.5	CNF29972 gn1	Galena	5.3	0.3
LM11-59	216.5	CNF29972 gn2	Galena	5.4	0.6
LM11-59	216.5	CNF29972 gn3	Galena	2.2	0.3
LM11-59	216.5	CNF29972 gn4	Galena	11.0	0.3
LM11-59	216.5	CNF29972 gn5	Galena	11.9	0.4
LM11-59	216.5	CNF29972 ccp1	Chalcopyrite	5.8	0.5

LM11-59	216.5	CNF29972 ccp2	Chalcopyrite	6.2	0.3
LM11-59	216.5	CNF29972 ccp3	Chalcopyrite	6.4	0.3
LM11-59	216.5	CNF29972 ccp4	Chalcopyrite	6.5	0.3
LM11-59	216.5	CNF29972 ccp5	Chalcopyrite	6.5	0.3
LM11-59	216.5	CNF29972 ccp6	Chalcopyrite	6.1	0.3

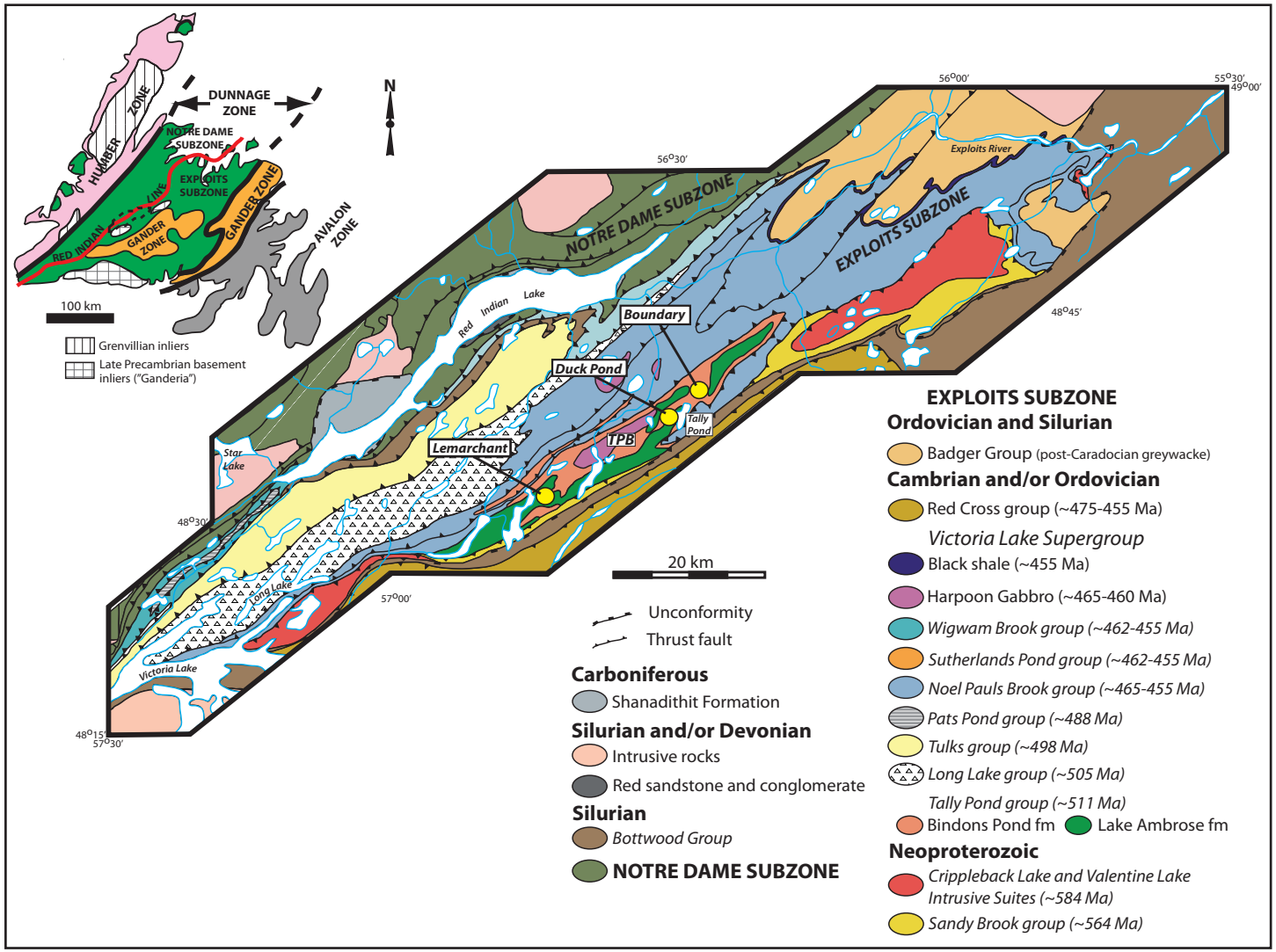

Figure 3.1. Geological map of the Victoria Lake Supergroup in the Exploits subzone, Newfoundland. Locations of the Lemarchant, Duck Pond and Boundary VMS deposits within the Tally Pond belt (TPB) are indicated. Inset map of tectonostratigraphic sequences comprising Newfoundland (modified after Rogers et al., 2006; McNicoll et al., 2010; Piercey and Hinchey, 2012).

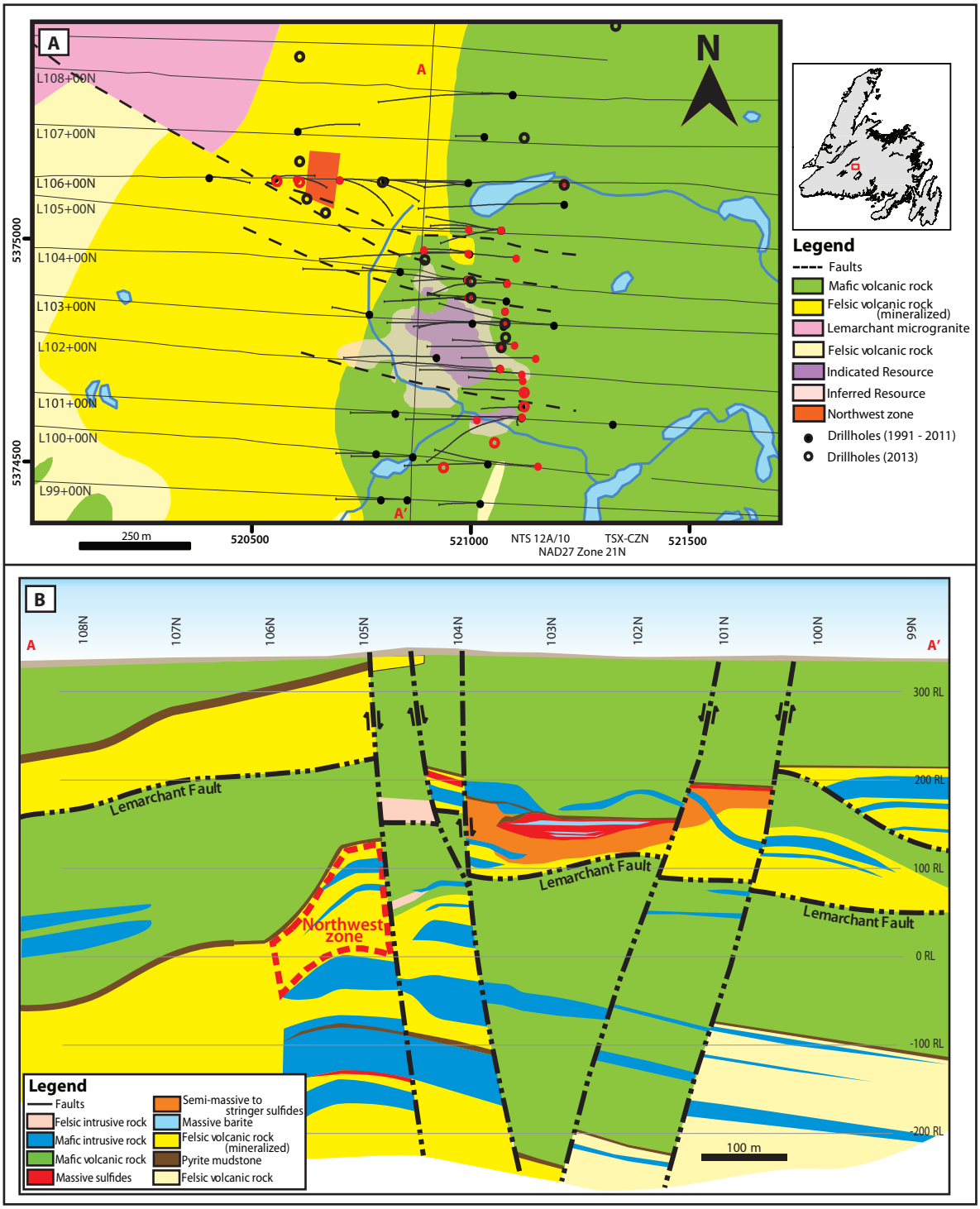

Figure 3.2. Geology of the Lemarchant deposit. A) Schematic geological map with superimposed northing grid; inferred and indicated resources, Northwest Zone and drill hole locations (red holes have been logged) projected to surface; long section A-A' indicated. B) Long section along A-A' through main mineralized zone; depths at given relative survey levels. Plan view and cross section modified from Fraser et al. (2012).

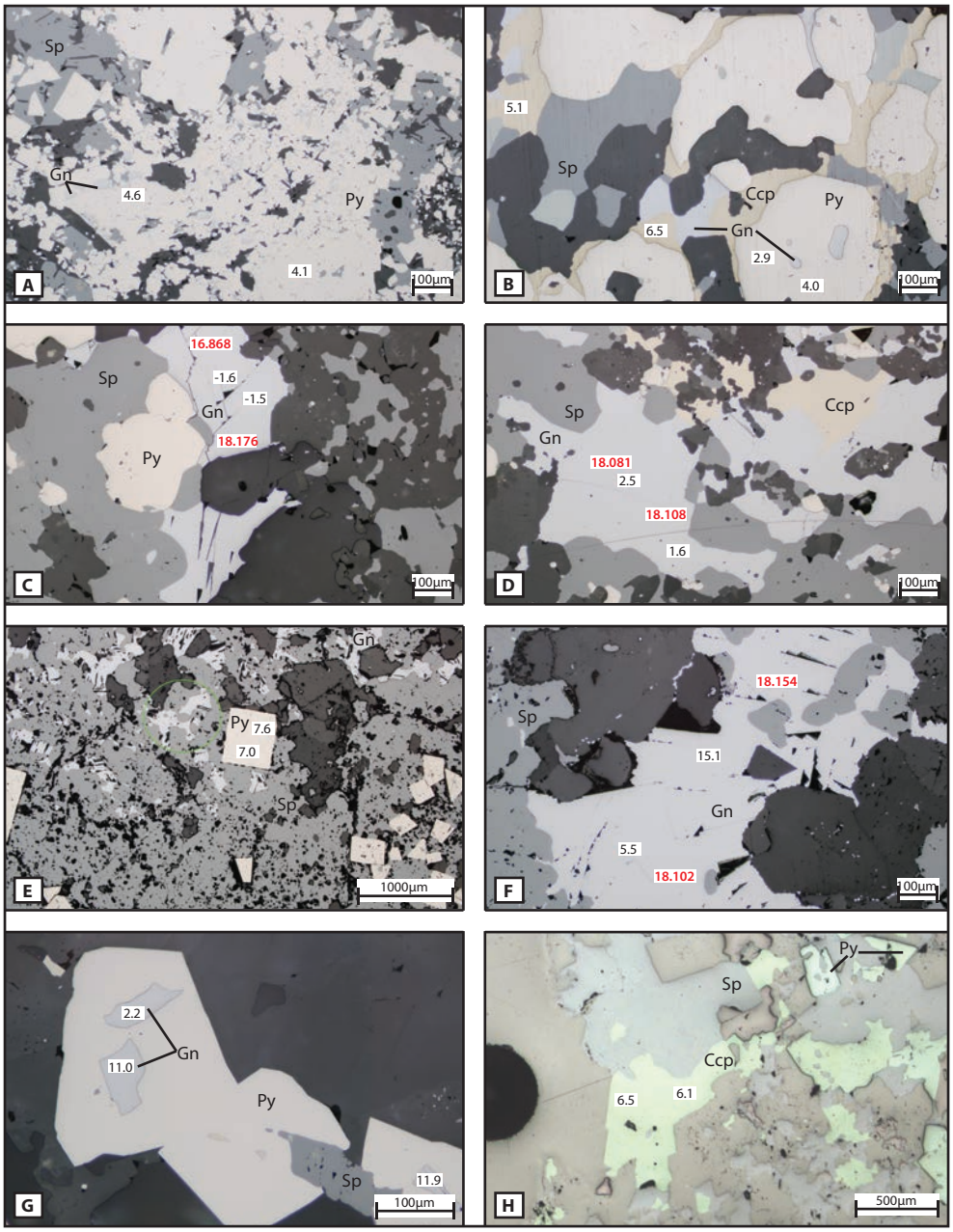

Figure 3.3. Photomicrograph compilation of representative mineral textures in pyrite, galena and chalcopyrite in the type mineral assemblages at Lemarchant. Sulfur-isotope values (per mil; black) and Pb-isotope ratios ($^{206}Pb/^{204}Pb$; red) are shown at spot analyses locations. A) Variably recrystallized colloform pyrite representing stage 1 deposition (Sample CNF29960 in drill hole LM11-59 at 216m depth). B) Rounded atoll pyrite and interstitial type 2A chalcopyrite from stage 2 deposition (CNF29957 in LM11-63 at 210.8m). C) Fractured, pitted type 2A galena from stage 2 deposition (CNF14259 in LM07-14 at 204.4m). D) Amorphous type 2B galena from stage 2 deposition (CNF29962 in LM11-59 at 225.9m). E) Euhedral pyrite representing stage 3 deposition (CNF14291 in LM11-65 at 159.3m). F) Pitted type 3 galena from stage 3 deposition (CNF29959 in LM11-59 at 207.7m). G) Type 4 galena inclusions from stage 3 deposition in recrystallized atoll pyrite (CNF29972 in LM11-59 at 251.2m). H) Type 4 chalcopyrite stringers from stage 3 mineralization (CNF29972 in LM11-59 at 251.2m). Abbreviations as follows: Sp = sphalerite; Py = pyrite; Ccp = chalcopyrite; Gn = galena.

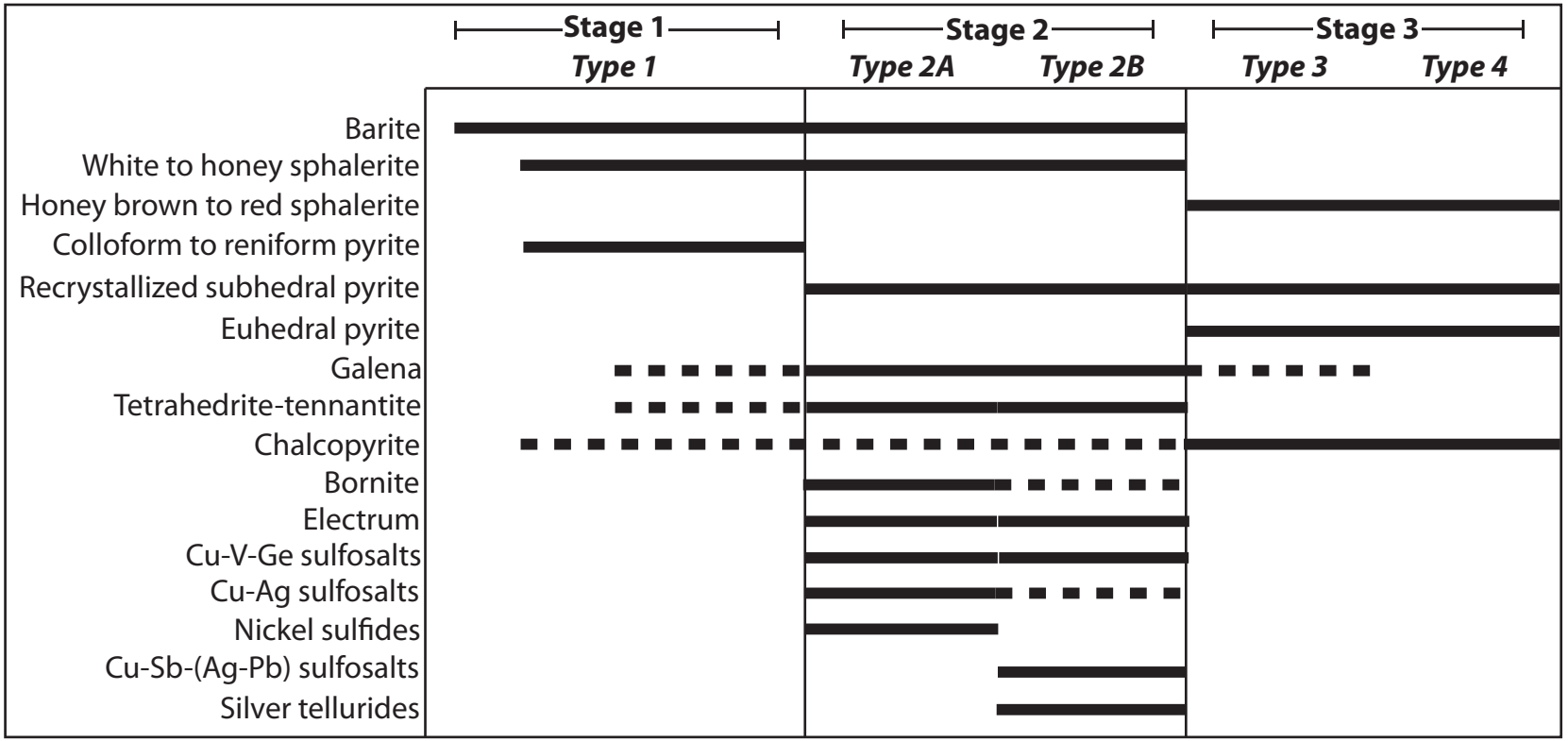

Figure 3.4. Simplified paragenetic flow chart highlighting the three main stages of mineral deposition at the Lemarchant deposit and each of the 5 type mineral assemblages.

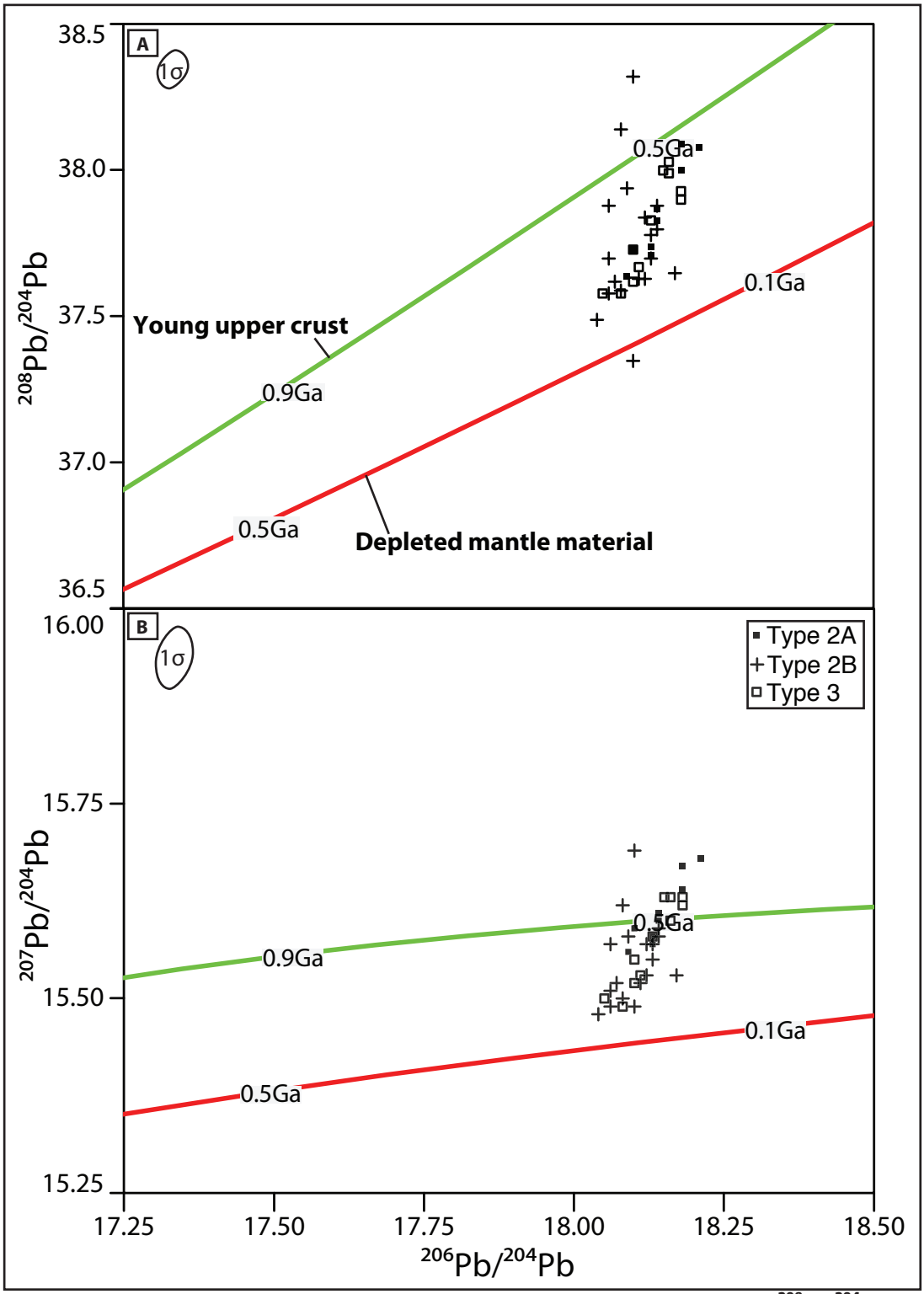

Figure 3.5. Plots of Pb-isotope variation in galena in the Lemarchant deposit. A) $^{208}Pb/^{204}Pb$ vs. $^{206}Pb/^{204}Pb$ (thorogenic lead). B) $^{207}Pb/^{204}Pb$ vs. $^{206}Pb/^{204}Pb$ (uranogenic lead). Growth curves for young upper crust (green line) and depleted mantle material (red line) after Kramers and Tolstikhin (1997). Outliers not included in diagram or error ellipse (1σ).

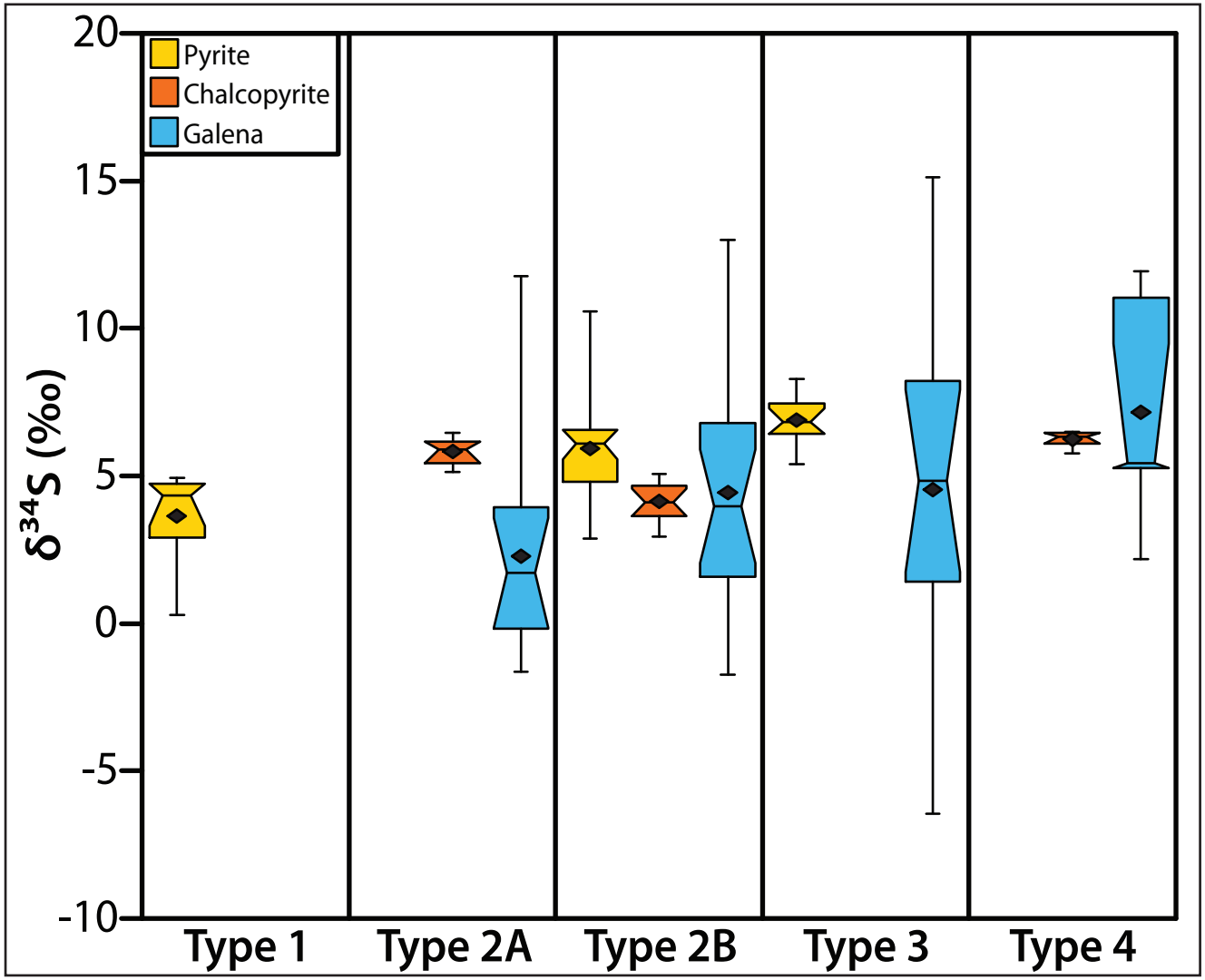

Figure 3.6. Notched box and whisker plot of $\delta^{34}S$ variation in pyrite, chalcopyrite and galena from each type mineral assemblage; data are significantly different (95% confidence level) if notches about medians do not overlap (after McGill et al., 1978). Means for each type sulfide are indicated on notched box and whisker as black diamonds.

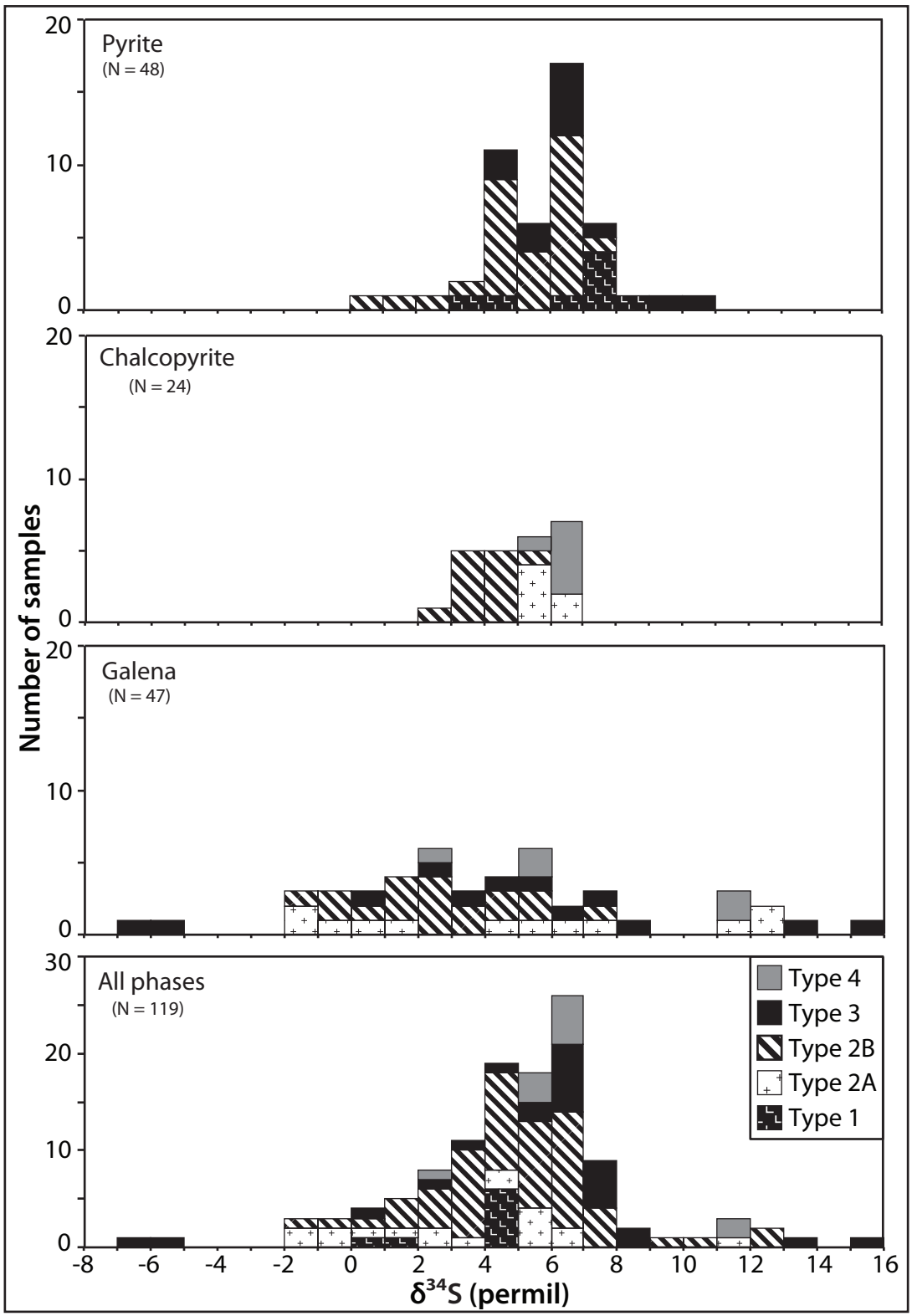

Figure 3.7. Frequency distribution of $\delta^{34}S$ values in analyzed sulfides (pyrite, galena and chalcopyrite) from each of the 5 mineral assemblage types at the Lemarchant deposit.

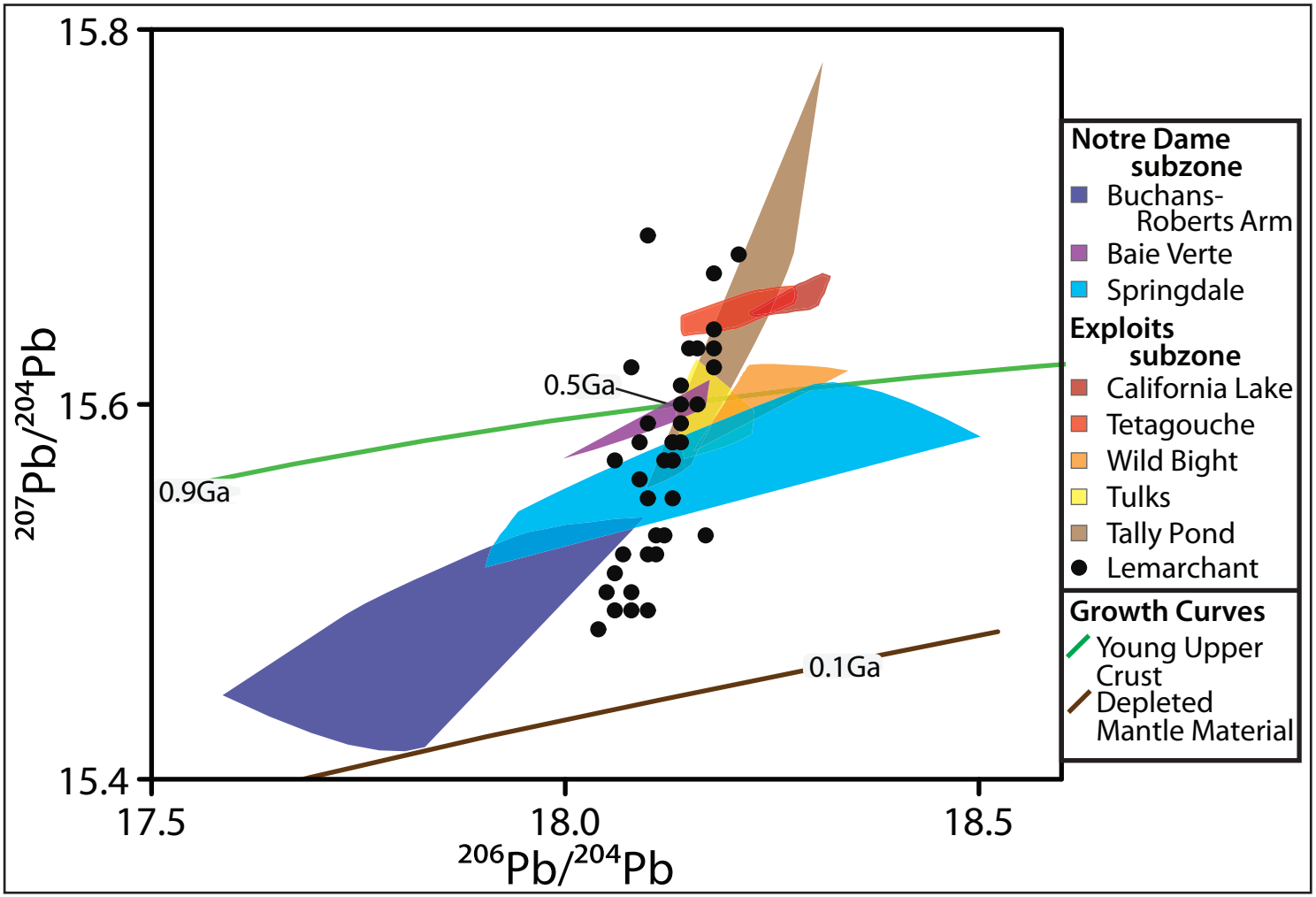

Figure 3.8. Uranogenic lead isotope data for Appalachian VMS deposits, including the Lemarchant deposit (outliers excluded for all datasets). Data for the Springdale, Baie Verte and Buchans-Roberts Arm volcanic belts (Notre Dame subzone), and Tally Pond and Tulks volcanic belts, Wild Bight, California Lake and Tetagouche Groups (Exploits subzone) from Swinden and Thorpe (1984), Cumming and Krstic (1987), Winter and Wilton (2000), Pollock and Wilton (2001), Thorpe (2008), and Wilton (unpublished data). Growth curves for the young upper crust (green line) and depleted mantle material (brown line) (Kramers and Tolstikhin, 1997) also shown for comparison.

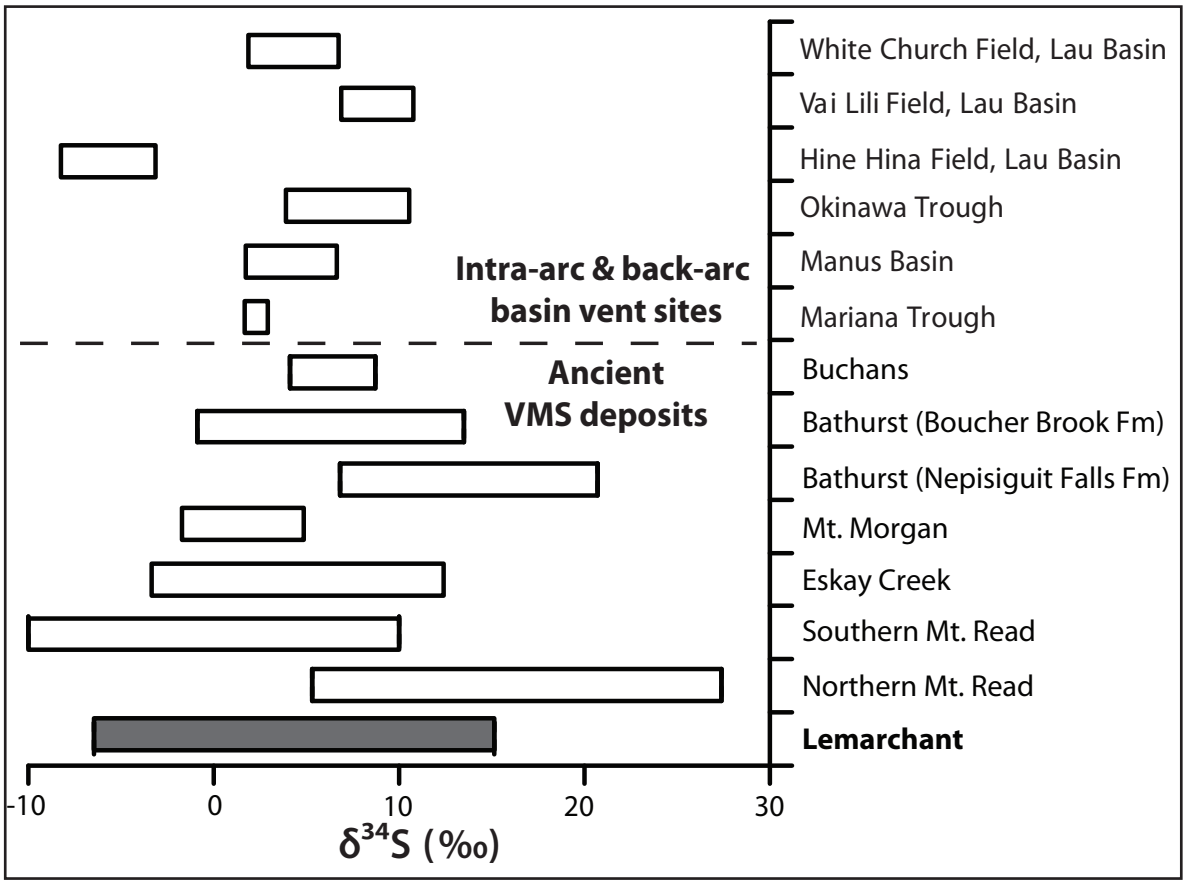

Figure 3.9. Range of $\delta^{34}S$ values from Lemarchant, compared with $\delta^{34}S$ values from modern black smoker deposits (Lau Basin, Okinawa Trough, Manus Basin and Mariana Trough), and from ancient VMS deposits in the Appalachians (Buchans, Bathurst) and globally (Eskay Creek, Mt. Morgan, Mt. Read volcanics) (data from Herzig et al., 1998; Huston, 1999 (does not include $\delta^{34}S$ values from galena); Sherlock et al., 1999; Ulrich et al., 2002).

Chapter 4: Summary

The bimodal felsic Zn-Pb-Cu-Ag-Au Lemarchant VMS deposit is hosted in the Cambrian Tally Pond group in Newfoundland, Canada, and is a classic example of a precious metal bearing massive sulfide deposit. The conclusions of this study on the mineralogy, mineral assemblages, metals zonation, and stable and radiogenic isotopes of the Lemarchant deposit have implications for the mechanism(s) of enrichment of precious metal bearing VMS deposits in the Appalachians and globally. The major conclusions from this study are as follows:

1) The Lemarchant VMS deposit is composed of both intermediate to high (?) sulfidation epithermal-style mineralization and polymetallic, Kuroko-style VMS mineralization, which define three stages of paragenesis: (i) stage 1 – VMS/exhalative mineralization containing massive barite, low-Fe sphalerite, and fine-grained pyrite was deposited from mixing and cooling of low temperature, oxidized, near-neutral hydrothermal fluids at or near the seafloor; (ii) stage 2 – intermediate sulfidation epithermal-style mineralization containing epithermal suite minerals and epithermal suite element enrichments in sulfides and sulfosalts replaced and infilled preliminary mineralization, and was deposited from low temperature, oxidized, acidic to near neutral, low-Fe hydrothermal fluids; and (iii) stage 3 – Cu-rich polymetallic Kuroko-style VMS mineralization with chalcopyrite, euhedral pyrite, and lesser Fe-rich sphalerite replaced and partially

zone refined existing mineralization and was deposited from higher temperature (>300°C), more reduced, neutral hydrothermal fluids.

2) Early stages of mineralization (stages 1 and 2) occurred at relatively shallow depths below sea level (<1500m), allowing boiling of the hydrothermal fluid, and precipitation of associated gold (electrum)-bladed barite-euhedral albite phases. An increase in temperature of the hydrothermal fluid during stage 3 paragenesis, would have required increased confining pressures to suppress boiling, consistent with formation at depths greater than 1500 mbsl, and indicates an increase in water depth between the second and third stages of paragenesis.
3) A direct magmatic contribution to the hydrothermal fluid is suggested by the presence of epithermal suite minerals (i.e., bornite, tetrahedrite, colusite, enargite, covellite) and epithermal suite trace element enrichments (i.e., Au, As, Bi, Co, Cr, In, Mo, Ni, Sb, Se, Te) of sulfides and sulfosalts deposited during stage 2 paragenesis. The deposition of significant gold (electrum) and silver by boiling and cooling/mixing with seawater, respectively, is consistent with a hydrothermal fluid containing precious metals derived from a magmatic fluid.
4) Radiogenic lead isotope data and calculated μ values of the Lemarchant galena are very similar to those for the young upper crust growth curve at ~500 Ma, and suggest that the majority of Pb and base metals at Lemarchant were derived from Neoproterozoic volcanic rocks underlying the mineralization. However, Pb isotope ratios that range to less radiogenic values than the young upper crust indicate that a more juvenile source material, such as juvenile Neoproterozoic

basement rock and/or the tholeiitic basalts of the Tally Pond group, also contributed some Pb/metals to mineralization.

5) Sulfur isotope ratios of Lemarchant sulfides are consistent with contributions of sulfur to the hydrothermal fluid from the following sources: (i) thermochemical reduction of seawater sulfate; (ii) leached sulfur from igneous basement rock; and (iii) sulfur-dioxide (SO_2) from magmatic fluids. A magmatic contribution to the hydrothermal fluid is consistent with the earlier stages of mineralization, particularly during the deposition of epithermal suite sulfides and sulfosalts enriched with the epithermal trace element suite.

4.1 – Directions for Future Research

Some avenues of continued research would benefit the current understanding of Lemarchant sulfide mineralogy, base and precious metal zonation, and paragenesis that has been achieved through this study. Potential areas for future research that would particularly add to the understanding of VMS mineralization and precious metal enrichment in the Newfoundland Appalachians include: 1) the source(s) of sulfur in Lemarchant sulfides, through sulfur isotope analyses of syngenetic barite; 2) detailed physiochemistry of mineralizing hydrothermal fluids, through fluid inclusion analyses; 3) alteration distribution, geochemistry, and genesis in the Lemarchant deposit, in order to further investigate potential intermediate- to high-sulfidation epithermal-type processes that occurred during deposition; 4) the source(s) of lead in the Tally Pond group and Victoria Lake Supergroup, through lead isotope analyses of regional lithologies; and 5) a structural model of the Lemarchant deposit, to understand the relevance and relative

timing of various fault zones associated with mineralization.

References

Amcoff, Ö., 1984. Distribution of silver in massive sulfide ores: Mineralium Deposita, v. 19, p. 63-69.

Ballantyne, J.M., and Moore, J.N., 1988. Arsenic geochemistry in geothermal systems: Geochimica et Cosmochimica Acta, v. 52, p. 475-483.

Barrie, C., and Hannington, M., 1999. Classification of volcanic-associated massive sulfide deposits based on host-rock composition: Reviews in Economic Geology, v. 8, p. 325-356.

Barton Jr, P., and Skinner, B., 1979. Sulfide mineral stabilities: *in* Barnes, H.L., ed., Geochemistry of Hydrothermal Ore Deposits, 2nd Edition, p. 278-403.

Bischoff, J.L., and Rosenbauer, R.J., 1983. A note on the chemistry of seawater in the range 350°–500°C: Geochimica et Cosmochimica Acta, v. 47, p. 139-144.

Bischoff, J.L., and Rosenbauer, R.J., 1984. The critical point and two-phase boundary of seawater, 200–500°C: Earth and Planetary Science Letters, v. 68, p. 172-180.

Blanchard, M., Alfredsson, M., Brodholt, J., Wright, K., and Catlow, C.R.A., 2007. Arsenic incorporation into FeS_2 pyrite and its influence on dissolution: A DFT study: Geochimica et Cosmochimica Acta, v. 71, p. 624-630.

Brueckner, S.M., Piercey, S.J., Sylvester, P.J., Maloney, S., and Pilgrim, L., 2014. Evidence for syngenetic precious metal enrichment in an Appalachian volcanogenic massive sulfide system: the 1806 Zone, Ming Mine, Newfoundland, Canada: Economic Geology, v. 109, p. 1611-1642.

Butterfield, D.A., Massoth, G.J., McDuff, R.E., Lupton, J.E., and Lilley, M.D., 1990. Geochemistry of hydrothermal fluids from Axial Seamount hydrothermal emissions study vent field, Juan de Fuca Ridge: Subseafloor boiling and subsequent fluid‐rock interaction: Journal of Geophysical Research: Solid Earth, v. 95, p. 12895-12921.

Canfield, D.E., 2004. The evolution of the Earth surface sulfur reservoir: American Journal of Science, v. 304, p. 839-861.

Cathles, L.M., Guber, A., Lenagh, T.C., and Dudas, F., 1983. Kuroko-type massive sulfide deposits of Japan: Products of an aborted island arc rift: Economic Geology Monograph, v. 5, p. 96-114.

Cathles, L.M., Erendi, A., and Barrie, T., 1997. How long can a hydrothermal system be sustained by a single intrusive event?: Economic Geology, v. 92, p. 766-771.

Chiaradia, M., Tripodi, D., Fontboté, L., and Reza, B., 2008. Geologic Setting, Mineralogy, and Geochemistry of the Early Tertiary Au-Rich Volcanic-Hosted Massive Sulfide Deposit of La Plata, Western Cordillera, Ecuador: Economic Geology, v. 103, p. 161-183.

Claypool, G.E., Holser, W.T., Kaplan, I.R., Sakai, H., and Zak, I., 1980. The age curves of sulfur and oxygen isotopes in marine sulfate and their mutual interpretation: Chemical Geology, v. 28, p. 199-260.

Cooke, D.R., and Simmons, S.F., 2000. Characteristics and genesis of epithermal gold deposits: Reviews in Economic Geology, v. 13, p. 221-244.

Copeland, D.A., Toole, R.M.S., and Piercey, S.J., 2008a. Assessment report on diamond drilling and soil sampling, License 8183M (10th Year) and 9569M (5th Year) South Tally Pond property, Rogerson Lake area, Newfoundland and Labrador, NTS 12A/10 and 12A/07. Newfoundland and Labrador Geological Survey, Assessment Report, 956 p. [for Paragon Minerals and Altius Minerals].

Copeland, D.A., McCleneghan, S.M., and Piercey, S.J., 2008b. Ninth year assessment report on diamond drilling, lithogeochemistry, pulse EM surveying and linecutting on license 8183M, South Tally Pond Property, Rogerson Lake area, Newfoundland and Labrador NTS 12A/10 and 12A/07. Newfoundland and Labrador Geological Survey, Assessment Report, 91 p. [for Paragon Minerals and Altius Minerals].

Cumming, G.L., and Krstic, D., 1987. Detailed lead isotope study of Buchans and related ores: *in* Kirkham, R.V., ed., Buchans Geology, Newfoundland: Geological Survey of Canada, v. 86-24, p. 227-234.

Czamanske, G.K., 1974. The FeS content of sphalerite along the chalcopyrite-pyrite-bornite sulfur fugacity buffer: Economic Geology, v. 69, p. 1328-1334.

de Ronde, C.E.J., 1995. Fluid chemistry and isotopic characteristics of seafloor hydrothermal systems and associated VMS deposits: potential for magmatic contributions: *in* Magmas, fluids and ore deposits, Mineralogical Association of Canada Short Course Series, v. 23, p. 479-509.

de Ronde, C.E.J., Baker, E.T., Massoth, G.J., Lupton, J.E., Wright, I.C., Feely, R.A., and Greene, R.R., 2001. Intra-oceanic subduction-related hydrothermal venting, Kermadec volcanic arc, New Zealand: Earth and Planetary Science Letters, v. 193, p. 359-369.

de Ronde, C.E.J., Hannington, M.D., Stoffers, P., Wright, I.C., Ditchburn, R.G., Reyes, A.G., Baker, E.T., Massoth, G.J., Lupton, J.E., Walker, S.L., Greene, R.R., Soong, C.W.R., Ishibashi, J., Lebon, G.T., Bray, C.J., and Resing, J.A., 2005. Evolution of a submarine magmatic-hydrothermal system: Brothers Volcano, Southern Kermadec Arc, New Zealand: Economic Geology, v. 100, p. 1097-1133.

Doe, B., and Stacey, J., 1974. The application of lead isotopes to the problems of ore genesis and ore prospect evaluation: a review: Economic Geology, v. 69, p. 757-776.

Drummond, S., and Ohmoto, H., 1985. Chemical evolution and mineral deposition in boiling hydrothermal systems: Economic Geology, v. 80, p. 126-147.

Dubé, B., Gosselin, P., Mercier-Langevin, P., Hannington, M., and Galley, A., 2007a. Gold-rich volcanogenic massive sulfide deposits: *in* Goodfellow, W.D., ed., Mineral deposits of Canada: A synthesis of major deposit-types, district metallogeny, the evolution of geological provinces, and exploration methods: Geological Association of Canada, Mineral Deposits Division, Special Publication, v. 5, p. 75-94.

Dubé, B., Mercier-Langevin, P., Hannington, M., Lafrance, B., Gosselin, G., and Gosselin, P., 2007b. The LaRonde Penna world-class Au-rich volcanogenic massive sulfide deposit, Abitibi, Québec: mineralogy and geochemistry of alteration and implications for genesis and exploration: Economic Geology, v. 102, p. 633-666.

Dunning, G.R., Swinden, H.S., Kean, B.F., Evans, D.T.W., and Jenner, G.A., 1991. A Cambrian island arc in Iapetus; geochronology and geochemistry of the Lake Ambrose volcanic belt, Newfoundland Appalachians: Geological Magazine, v. 128, p. 1-17.

Eggins, S., Rudnick, R., and McDonough, W., 1998. The composition of peridotites and their minerals: a laser-ablation ICP–MS study: Earth and Planetary Science Letters, v. 154, p. 53-71.

Eldridge, C.S., Barton, P.B., Jr., and Ohmoto, H., 1983. Mineral textures and their bearing on formation of the Kuroko orebodies: Economic Geology Monograph, v. 5, p. 241-281.

Evans, D., and Kean, B., 2002. The Victoria Lake Supergroup, central Newfoundland – its definition, setting and volcanogenic massive sulfide mineralization: Newfoundland Department of Mines and Energy, Geological Survey, Open File NFLD/2790, 68 p.

Fleischer, M., 1955. Minor elements in some sulfide minerals: Economic Geology, v. 50, p. 1024.

Fouquet, Y., and Marcoux, E., 1995. Lead isotope systematics in Pacific hydrothermal sulfide deposits: Journal of Geophysical Research, v. 100, p. 6025-6040.

Franklin, J., Lydon, J., and Sangster, D., 1981. Volcanic-associated massive sulfide deposits: Economic Geology, v. 75, p. 485-627.

Franklin, J., Gibson, H., Jonasson, I., and Galley, A., 2005. Volcanogenic massive sulfides: Economic Geology100th Anniversary Volume, p. 523-560.

Fraser, D., Giroux, G.H., Copeland, D.A., and Devine, C.A., 2012. Technical Report and Resource Minerals Estimate on the Lemarchant Deposit, South Tally Pond VMS Project, Central Newfoundland, Canada – NI 43-101 Technical Report prepared for Paragon Minerals Corporation, 132 p.

Galley, A., Hannington, M., and Jonasson, I., 2007. Volcanogenic massive sulfide deposits: *in* Goodfellow, W.D., ed., Mineral deposits of Canada: A synthesis of major deposit-types, district metallogeny, the evolution of geological provinces, and exploration methods: Geological Association of Canada, Mineral Deposits Division, Special Publication, v. 5, p. 141-161.

Gemmell, J.B., and Large, R.R., 1992. Stringer system and alteration zones underlying the Hellyer volcanogenic massive sulfide deposit, Tasmania, Australia: Economic Geology, v. 87, p. 620-649.

Gibson, H., Morton, R., and Hudak, G., 1999. Submarine volcanic processes, deposits, and environments favorable for the location of volcanic-associated massive sulfide deposits: Reviews in Economic Geology, v. 8, p. 13-51.

Gibson, H.L., Allen, R.L., Riverin, G., and Lane, T.E., 2007. The VMS model; advances and application to exploration: Abstracts, Decennial International Conference on Mineral Exploration, v. 5, p. 713-730.

Gill, S.B., Piercey, S.J., and Devine, C.A., 2013. Preliminary mineralogy of barite-associated sulfide mineralization in the Ordovician Zn-Pb-Cu-Ag-Au Lemarchant volcanogenic massive sulfide deposit, Newfoundland and Labrador: Geological Survey of Canada, Current Research Report 2013-17, 15 p.

Gill, S.B. and Piercey, S.J., 2014. Styles of mineralization and sulfide mineral zonation in the Cambrian Zn-Pb-Cu-Ag-Au Lemarchant volcanogenic massive sulfide (VMS) deposit, Newfoundland and Labrador – preliminary observations; Geological Survey of Canada, Current Research Report 2014-05, 17 p.

Glasby, G., and Notsu, K., 2003. Submarine hydrothermal mineralization in the Okinawa Trough, SW of Japan: an overview: Ore Geology Reviews, v. 23, p. 299-339.

Goldfarb, R.J., Baker, T., Dubé, B., Groves, D.I., Hart, C.J., and Gosselin, P., 2005. Distribution, character, and genesis of gold deposits in metamorphic terranes: Economic Geology 100th Anniversary Volume, p. 407-450.

Goodfellow, W.D., and Peter, J.M., 1996. Sulfur isotope composition of the Brunswick No. 12 massive sulfide deposit, Bathurst Mining Camp, New Brunswick: implications for ambient environment, sulfur source, and ore genesis: Canadian Journal of Earth Sciences, v. 33, p. 231-251.

Goodfellow, W.D., 2007. Metallogeny of the Bathurst Mining Camp, northern New Brunswick: *in* Goodfellow, W.D., ed., Mineral Deposits of Canada: A synthesis of

major deposit-types, district metallogeny, the evolution of geological provinces, and exploration methods: Geological Association of Canada, Mineral Deposits Division, Special Publication No. 5, p. 449-469.

Hackbarth, C.J., and Petersen, U., 1984. A fractional crystallization model for the deposition of argentian tetrahedrite: Economic Geology, v. 79, p. 448-460.

Halbach, P., Nakamura, K.-i., Wahsner, M., Lange, J., Sakai, H., Kaeselitz, L., Hansen, R.D., Yamano, M., Post, J., Prause, B., Seifert, R., Michaelis, W., Teichmann, F., Kinoshita, M., Maerten, A., Ishibashi, J., Czerwinski, S., and Blum, N., 1989. Probable modern analogue of Kuroko-type massive sulfide deposits in the Okinawa Trough back-arc basin: Nature, v. 338, p. 496-499.

Hannington, M.D., and Scott, S.D., 1989. Sulfidation equilibria as guides to gold mineralization in volcanogenic massive sulfides; evidence from sulfide mineralogy and the composition of sphalerite: Economic Geology, v. 84, p. 1978-1995.

Hannington, M.D., Jonasson, I.R., Herzig, P.M., and Petersen, S., 1995. Physical and chemical processes of seafloor mineralization at mid-ocean ridges; *in* Humphris, S.E., Zierenberg, R.A., Mullineaux, L.S., Thomson, R.E., eds., Seafloor hydrothermal systems: Physical, chemical, biological, and geological interactions: Geophysical Monograph, v. 91, p. 115-157.

Hannington, M.D., Poulsen, K.H., Thompson, J.F.H., and Sillitoe, R.H., 1999. Volcanogenic gold in the massive sulfide environment: Reviews in Economic Geology, v. 8, p. 325-356.

Hannington, M.D., de Ronde, C.D., and Petersen, S., 2005. Sea-floor tectonics and submarine hydrothermal systems: Economic Geology 100th Anniversary Volume, p. 111–141.

Hannington, M., and Monecke, T., 2009. Modern submarine hydrothermal systems - A global perspective on distribution, size and tectonic settings: *in* Cousens, B., and Piercey, S.J., eds., Submarine Volcanism and mineralization: modern through ancient: Geological Association of Canada, Mineral Deposits Division, Short Course Notes, v. 19, p. 91-146.

Hedenquist, J.W., and Lowenstern, J.B., 1994. The role of magmas in the formation of hydrothermal ore deposits: Nature, v. 370, p. 519-527.

Herzig, P.M., Hannington, M.D., Fouquet, Y., von Stackelberg, U., and Petersen, S., 1993. Gold-rich polymetallic sulfides from the Lau back arc and implications for the geochemistry of gold in sea-floor hydrothermal systems of the Southwest Pacific: Economic Geology, v. 88, p. 2182-2209.

Herzig, P., Hannington, M., and Arribas Jr, A., 1998. Sulfur isotopic composition of hydrothermal precipitates from the Lau back-arc: implications for magmatic

contributions to seafloor hydrothermal systems: Mineralium Deposita, v. 33, p. 226-237.

Hinchey, J., 2007. Volcanogenic massive sulphides of the southern Tulks Volcanic Belt, central Newfoundland: Preliminary findings and overview of styles and environments of mineralization: Newfoundland and Labrador Department of Natural Resources, Geological Survey, Current Research Report 07-1, p. 117-143.

Huston, D.L., and Large, R.R., 1989. A chemical model for the concentration of gold in volcanogenic massive sulfide deposits: Ore Geology Reviews, v. 4, p. 171-200.

Huston, D.L., Jablonski, W., and Sie, S., 1996. The distribution and mineral hosts of silver in eastern Australian volcanogenic massive sulfide deposits: The Canadian Mineralogist, v. 34, p. 529-546.

Huston, D.L., 1999. Stable isotopes and their significance for understanding the genesis of volcanic-hosted massive sulfide deposits: a review: Reviews in Economic Geology, v. 8, p. 157-179.

Huston, D.L., 2000. Gold in volcanic-hosted massive sulfide deposits; distribution, genesis, and exploration: Reviews in Economic Geology, v. 13, p. 401-426.

Huston, D.L., and Kamprad, J., 2001. Zonation of alteration facies at western Tharsis: implications for the genesis of Cu-Au deposits, Mount Lyell field, western Tasmania: Economic Geology, v. 96, p. 1123-1132.

Huston, D.L., Relvas, J.M.R.S., Gemmell, J.B., Drieberg, S., 2011. The role of granites in volcanic-hosted massive sulfide ore-forming systems: An assessment of magmatic–hydrothermal contributions: Mineralium Deposita, v. 46, p. 473-507.

James, R.H., Allen, D.E., and Seyfried Jr, W.E., 2003. An experimental study of alteration of oceanic crust and terrigenous sediments at moderate temperatures (51 to 350°C): insights as to chemical processes in near-shore ridge-flank hydrothermal systems: Geochimica et Cosmochimica Acta, v. 67, p. 681-691.

Janecky, D.R., and Shanks, W.C., 1988. Computational modeling of chemical and sulfur isotopic reaction processes in sea-floor hydrothermal systems; chimneys, massive sulfide, and subjacent alteration zones: The Canadian Mineralogist, v. 26, p. 805-825.

Jensen, M.L., 1967. Sulfur isotopes and mineral genesis: *in* Barnes, H.L., ed., Geochemistry of hydrothermal ore deposits, p. 143-165.

Kajiwara, Y., and Krouse, H., 1971. Sulfur isotope partitioning in metallic sulfide systems: Canadian Journal of Earth Sciences, v. 8, p. 1397-1408.

Kampschulte, A., and Strauss, H., 2004. The sulfur isotopic evolution of Phanerozoic seawater based on the analysis of structurally substituted sulfate in carbonates: Chemical Geology, v. 204, p. 255-286.

Kase, K., Yamamoto, M., and Mitsuno, C., 1994. Germanium-bearing colusite from the Yanahara mine, Japan, and its significance to ore genesis: Journal of the Society of Resource Geology, v. 44, p. 33-38.

Kramers, J.D., and Tolstikhin, I.N., 1997. Two terrestrial lead isotope paradoxes, forward transport modeling, core formation and the history of the continental crust: Chemical Geology, v. 139, p. 75-110.

Large, R.R., 1977. Chemical evolution and zonation of massive sulfide deposits in volcanic terrains: Economic Geology, v. 72, p. 549-572.

Large, R.R., 1992. Australian volcanic-hosted massive sulfide deposits; features, styles, and genetic models: Economic Geology, v. 87, p. 471-510.

Lode, S., Piercey, S.J.P., Copeland, D.A., Devine, C.A., and Sparrow, B., 2012. Setting and styles of hydrothermal mudstones near the Lemarchant volcanogenic massive sulfide (VMS) deposit, Central Mobile Belt, Newfoundland: *in* Abstracts, Geological Association of Canada-Mineralogical Association of Canada, Joint Annual Meeting, v. 35, p. 79.

Lode, S., Piercey, S. J., Devine, C. A., Layne, G. D., Piercey, G., and Hewa, L., 2014. Lithogeochemistry and sulfur isotopic composition of hydrothermal mudstones associated with the Lemarchant volcanogenic massive sulfide (VMS) deposit, Tally Pond Belt, Central Newfoundland: *in* Abstracts, Geological Association of Canada, Newfoundland Spring Technical Meeting, v. 40, p. 20.

Longerich, H.P., Jackson, S.E., and Gunther, D., 1996. Inter-laboratory note – Laser ablation inductively coupled plasma mass spectrometric transient signal data acquisition and analyte concentration calculation: Journal of Analytical Atomic Spectrometry, v. 11, p. 899-904.

Lusk, J., and Calder, B.O.E., 2004. The composition of sphalerite and associated sulfides in reactions of the Cu–Fe–Zn–S, Fe–Zn–S and Cu–Fe–S systems at 1 bar and temperatures between 250 and 535°C: Chemical Geology, v. 203, p. 319-345.

Lydon, J.W., 1984. Volcanogenic massive sulfide deposits, Part 1: A descriptive model: Geoscience Canada, v. 11, p. 145-181.

Lydon, J.W., 1988. Volcanogenic massive sulfide deposits, Part 2: Genetic models: Geoscience Canada, v. 15, p. 155-181.

Lydon, J.W., 1996. Characteristics of volcanogenic massive sulfide deposits; interpretations in terms of hydrothermal convection systems and magmatic hydrothermal systems: Boletin Geologico y Minero, v. 107, p. 215-264.

Marini, L., Moretti, R., and Accornero, M., 2011. Sulfur isotopes in magmatic-hydrothermal systems, melts, and magmas: Reviews in Mineralogy and Geochemistry, v. 73, p. 423-492.

McClenaghan, S.H., Lentz, D.R., Martin, J., and Diegor, W.G., 2009. Gold in the Brunswick No. 12 volcanogenic massive sulfide deposit, Bathurst Mining Camp, Canada: Evidence from bulk ore analysis and laser ablation ICP-MS data on sulfide phases: Mineralium Deposita, v. 44, p. 523-557.

McGill, R., Tukey, J.W., and Larsen, W.A., 1978. Variations of box plots: The American Statistician, v. 32, p. 12-16.

McNicoll, V., Squires, G., Kerr, A., and Moore, P., 2010. The Duck Pond and Boundary Cu-Zn deposits, Newfoundland; new insights into the ages of host rocks and the timing of VHMS mineralization: Canadian Journal of Earth Sciences, v. 47, p. 1481-1506.

Mercier-Langevin, P., Dubé, B., Hannington, M.D., Davis, D.W., Lafrance, B., and Gosselin, G., 2007. The LaRonde Penna Au-rich volcanogenic massive sulfide deposit, Abitibi Greenstone belt, Quebec: Part I. Geology and geochronology: Economic Geology, v. 102, p. 585-609.

Mercier-Langevin, P., Hannington, M., Dubé, B., and Bécu, V., 2011. The gold content of volcanogenic massive sulfide deposits: Mineralium Deposita, v. 46, p. 509-539.

Mortensen, J.K., Dusel-Bacon, C., Hunt, J., and Gabites, J., 2006. Lead isotopic constraints on the metallogeny of middle and late Paleozoic syngenetic base metal occurrences in the Yukon-Tanana and Slide Mountain/Seventymile terranes and adjacent portions of the North American miogeocline: *in* Colpron, M. and Nelson, J.L., eds., Paleozoic evolution and metallogeny of pericratonic terranes at the ancient Pacific margin of North America, Canadian and Alaskan Cordillera: Geological Association of Canada, Special Paper, v. 45, p. 261-279.

Ohmoto, H., 1972. Systematics of sulfur and carbon isotopes in hydrothermal ore deposits: Economic Geology, v. 67, p. 551-578.

Ohmoto, H., and Rye, R., 1979. Isotopes of sulfur and carbon: *in* Barnes, H.L., ed., Geochemistry of Hydrothermal Ore Deposits, 2nd Edition, p. 509-567.

Ohmoto, H., and Lasaga, A.C., 1982. Kinetics of reactions between aqueous sulfates and sulfides in hydrothermal systems: Geochimica et Cosmochimica Acta, v. 46, p. 1727-1745.

Ohmoto, H., Mizukami, M., Drummond, S., Eldridge, C., Pisutha-Arnond, V., and Lenagh, T., 1983. Chemical processes of Kuroko formation: Economic Geology Monograph, v. 5, p. 570-604.

Ohmoto, H., 1996. Formation of volcanogenic massive sulfide deposits; the Kuroko perspective: Ore Geology Reviews, v. 10, p. 135-177.

Ohmoto, H., and Goldhaber, M.B., 1997. Sulfur and carbon isotopes: *in* Barnes, H.L., ed., Geochemistry of hydrothermal ore deposits, 3rd Edition, p. 517-611.

Paytan, A., Gray, E.T., 2012. Sulfur isotope stratigraphy: *in* Gradstein, F.M., Ogg, J.G., Schmitz, M., Ogg, G., eds., The Geologic Timescale 2012: Elsevier, Amsterdam, p. 167-180.

Petersen, E.U., Petersen, U., and Hackbarth, C., 1990. Ore zoning and tetrahedrite compositional variation at Orcopampa, Peru: Economic Geology, v. 85, p. 1491-1503.

Piercey, S., 2007. Volcanogenic massive sulfide (VMS) deposits of the Newfoundland Appalachians: an overview of their setting, classification, grade-tonnage data, and unresolved questions: Newfoundland and Labrador Department of Natural Resources, Geological Survey, Current Research Report 07-1, p. 169-178.

Piercey, S.J., Chaloux, E.C., Péloquin, A.S., Hamilton, M.A., and Creaser, R.A., 2008. Synvolcanic and younger plutonic rocks from the Blake River Group: implications for regional metallogenesis: Economic Geology, v. 103, p. 1243-1268.

Piercey, S.J., 2011. The setting, style, and role of magmatism in the formation of volcanogenic massive sulfide deposits: Mineralium Deposita, v. 46, p. 449-471.

Piercey, S.J. and Hinchey, J., 2012. Volcanogenic massive sulfide (VMS) deposits of the Central Mineral Belt, Newfoundland: Geological Association of Canada–Mineralogical Association of Canada Joint Annual Meeting, Field Trip Guidebook B, Newfoundland and Labrador Department of Natural Resources, Geological Survey, Open File NFLD/3173, 56 p.

Piercey, S.J., Squires, G.C., and Brace, T.D., 2014. Lithostratigraphic, hydrothermal, and tectonic setting of the Boundary volcanogenic massive sulfide deposit, Newfoundland Appalachians, Canada: Formation by subseafloor replacement in a Cambrian rifted arc: Economic Geology, v. 109, p. 661-687.

Pisutha-Arnond, V., and Ohmoto, H., 1983. Thermal history, and chemical and isotopic compositions of the ore-forming fluids responsible for the Kuroko massive sulfide deposits in the Hokuroku District of Japan: Economic Geology Monograph, v. 5, p. 523-558.

Pollock, J., and Wilton, D., 2001. Metallogenic studies of the Tally Pond Belt, Victoria Lake Group: trace element geochemistry and lead isotope data from the Exploits Subzone, Newfoundland: Newfoundland and Labrador Department of Natural Resources, Geological Survey, Current Research Report 01-1, p. 247–266.

Pollock, J., 2004, Geology and paleotectonic history of the Tally Pond Group, Dunnage zone, Newfoundland Appalachians: An integrated geochemical, geochronological, metallogenic and isotopic study of a Cambrian island arc along the Peri-Gondwanan margin of Iapetus: Unpublished M.Sc. thesis, St. John's, Newfoundland, Memorial University, 420 p.

Poulsen, K.H., and Hannington, M.D., 1995. Volcanic-associated massive sulfide gold: *in* Eckstrand, O.R., Sinclair, W.D., and Thorpe, R.I., eds., Geology of Canadian mineral deposit types, Geology of Canada No. 8, Decade of North American Geology (DNAG): Geological Society of America, Part 1, p. 183-196.

Reich, M., and Becker, U., 2006. First-principles calculations of the thermodynamic mixing properties of arsenic incorporation into pyrite and marcasite: Chemical Geology, v. 225, p. 278-290.

Riverin, G., and Hodgson, C.J., 1980. Wall-rock alteration at the Millenbach Cu-Zn mine, Noranda, Quebec: Economic Geology, v. 75, p. 424-444.

Rogers, N., and van Staal, C., 2002. Toward a Victoria Lake Supergroup: A provisional stratigraphic revision of the Red Indian to Victoria Lakes area, central Newfoundland: Newfoundland Department of Mines and Energy, Geological Survey, Current Research Report 02-1, p. 185-195.

Rogers, N., van Staal, C.R., McNicoll, V., Pollock, J., Zagorevski, A., and Whalen, J., 2006. Neoproterozoic and Cambrian arc magmatism along the eastern margin of the Victoria Lake Supergroup: A remnant of Ganderian basement in central Newfoundland?: Precambrian Research, v. 147, p. 320-341.

Roth, T., Thompson, J.F.H., and Barrett, T.J., 1999. The precious metal-rich Eskay Creek Deposit, northwestern British Columbia: Reviews in Economic Geology, v. 8, p. 357-373.

Rye, R.O., 1993. The evolution of magmatic fluids in the epithermal environment; the stable isotope perspective: Economic Geology, v. 88, p. 733-752.

Sangster, D.F., 1980. Quantitative characteristics of volcanogenic massive sulfide deposits; 1. Metal content and size distribution of massive sulfide deposits in volcanic centres: CIM Bulletin, v. 73, p. 74-81.

Sakai, H., and Dickson, F., 1978. Experimental determination of the rate and equilibrium fractionation factors of sulfur isotope exchange between sulfate and sulfide in slightly acid solutions at 300 C and 1000 bars: Earth and Planetary Science Letters, v. 39, p. 151-161.

Sakai, H., Des Marais, D., Ueda, A., and Moore, J., 1984. Concentrations and isotope ratios of carbon, nitrogen and sulfur in ocean-floor basalts: Geochimica et Cosmochimica Acta, v. 48, p. 2433-2441.

Sato, K., Delevaux, M.H., and Doe, B.R., 1981. Lead isotope measurements on ores, igneous and sedimentary rocks from the Kuroko mineralization area: Geochemical Journal, v. 15, p. 135-140.

Scotney, P.M., Roberts, S., Herrington, R.J., Boyce, A.J., and Burgess, R., 2005. The development of volcanic hosted massive sulfide and barite-gold orebodies on Wetar Island, Indonesia: Mineralium Deposita, v. 40, p. 76-99.

Scott, S., and Barnes, H., 1971. Sphalerite geothermometry and geobarometry: Economic Geology, v. 66, p. 653-669.

Seal, R.R., 2006. Sulfur isotope geochemistry of sulfide minerals: Reviews in Mineralogy and Geochemistry, v. 61, p. 633-677.

Seward, T.M., 1973. Thio-complexes of gold and the transport of gold in hydrothermal ore solutions: Geochimica et Cosmochimica Acta, v. 37, p. 379-399.

Seward, T.M., 1976. The stability of chloride complexes of silver in hydrothermal solutions up to 350°C: Geochimica et Cosmochimica Acta, v. 40, p. 1329-1341.

Seyfried, W.E., Bischoff, J.L., 1981. Experimental seawater-basalt interaction at 300°C, 500 bars, chemical exchange, secondary mineral formation and implications for the transport of heavy metals: Geochimica et Cosmochimica Acta, v. 45, p. 135-149.

Seyfried, W., and Ding, K., 1995. Phase equilibria in subseafloor hydrothermal systems: A review of the role of redox, temperature, pH and dissolved Cl on the chemistry of hot spring fluids at mid‐ocean ridges: *in* Seafloor hydrothermal systems: Physical, chemical, biological, and geological interactions: Geophysical Monograph, v. 91, p. 248-272.

Shanks, W., Böhlke, J.K., Seal, R.R., 1995. Stable isotopes in mid-ocean ridge hydrothermal systems: interactions between fluids, minerals, and organisms: *in* Humphris, S.E., Zierenberg, R.A., Mullineaux, L.S., Thomson, R.E., eds., Seafloor Hydrothermal Systems: physical, chemical, biological, and geological interactions: Geophysical Monograph, v. 91, p. 194-221.

Shanks, W., 2001. Stable isotopes in seafloor hydrothermal systems: vent fluids, hydrothermal deposits, hydrothermal alteration, and microbial processes: Reviews in Mineralogy and Geochemistry, v. 43, p. 469-525.

Sherlock, R.L., Roth, T., Spooner, E.T.C., and Bray, C.J., 1999. Origin of the Eskay Creek precious metal-rich volcanogenic massive sulfide deposit; fluid inclusion and stable isotope evidence: Economic Geology, v. 94, p. 803-824.

Sillitoe, R.H., Hannington, M.D., and Thompson, J.F.H., 1996. High sulfidation deposits in the volcanogenic massive sulfide environment: Economic Geology, v. 91, p. 204-212.

Spry, P.G., Merlino, S., Wang, S., Zhang, X., and Buseck, P.R., 1994. New occurrences and refined crystal chemistry of colusite, with comparisons to arsenosulvanite: American Mineralogist, v. 79, p. 750-762.

Squires, G.C.S., Brace, T.D., and Hussey, A.M., 2001. Newfoundland's polymetallic Duck Pond Deposit: earliest Iapetan VMS mineralization, formed within a sub-seafloor, carbonate-rich alteration system: *in* Evans, D.T.W., and Kerr, A., eds., Geology and mineral deposits of the Northern Dunnage Zone, Newfoundland Appalachians: Geological Association of Canada-Mineralogical Association of Canada, Field Trip Guide A2, pp. 167–187.

Squires, G., and Moore, P., 2004. Volcanogenic massive sulfide environments of the Tally Pond Volcanics and adjacent area: Geological, lithogeochemical and geochronological results: Newfoundland and Labrador Department of Natural Resources, Geological Survey, Current Research Report 04-1, p. 63-91.

Stacey, J.S., and Kramers, J., 1975. Approximation of terrestrial lead isotope evolution by a two-stage model: Earth and Planetary Science Letters, v. 26, p. 207-221.

Stanton, R.L., 1991. Understanding volcanic massive sulfides; past, present, and future: Economic Geology Monograph, v. 8, p. 82-95.

Stefánsson, A., and Seward, T., 2004. Gold (I) complexing in aqueous sulphide solutions to 500 C at 500 bar: Geochimica et Cosmochimica Acta, v. 68, p. 4121-4143.

Swinden, H.S., 1991. Paleotectonic settings of volcanogenic massive sulfide deposits in the Dunnage Zone, Newfoundland Appalachians, Canadian Institute of Mining and Metallurgy Bulletin, Volume 84, p. 59-89.

Swinden, H.S., and Thorpe, R., 1984. Variations in style of volcanism and massive sulfide deposition in Early to Middle Ordovician island-arc sequences of the Newfoundland Central Mobile Belt: Economic Geology, v. 79, p. 1596-1619.

Swinden, H., Kean, B., and Dunning, G., 1988. Geological and paleotectonic settings of volcanogenic massive sulfide mineralization in Central Newfoundland: The Volcanogenic Sulfide Districts of Newfoundland, Geological Association of Canada, Mineral Deposits Division, p. 2-27.

Taylor, B.E., 2007. Epithermal gold deposits: *in* Goodfellow, W.D., ed., Mineral deposits of Canada: a synthesis of major deposit-types, district metallogeny, the evolution of geological provinces, and exploration methods: Geological Association of Canada, Mineral Deposits Division, Special Publication, v. 5, p. 113-139.

Thorpe, R.I., 2008. Release of lead isotope data in 4 databases; Canadian, western Superior, foreign, and whole rock and feldspar: Geological Survey of Canada, Open File Report 5664, p. 42.

Thurlow, J., 1996. Geology of a newly discovered cluster of blind massive sulphide deposits, Pilley's Island, central Newfoundland: Newfoundland Department of Natural Resources, Geological Survey, Current Research Report 96-1, p.181-189.

Tosdal, R., Wooden, J., and Bouse, R., 1999. Pb isotopes, ore deposits, and metallogenic terranes: Application of radiogenic isotopes to ore deposit research and exploration. Reviews in Economic Geology, v. 12, p. 1-28.

Ueda, A., and Sakai, H., 1984. Sulfur isotope study of Quaternary volcanic rocks from the Japanese Islands Arc: Geochimica et Cosmochimica Acta, v. 48, p. 1837-1848.

Ulrich, T., Golding, S.D., Kamber, B.S., Khin, Z., and Taube, A., 2002. Different mineralization styles in a volcanic-hosted ore deposit: the fluid and isotopic signatures of the Mt Morgan Au–Cu deposit, Australia: Ore Geology Reviews, v. 22, p. 61-90.

van Staal, C.R., Dewey, J.F., Niocaill, C.M., and McKerrow, W.S., 1998. The Cambrian-Silurian tectonic evolution of the northern Appalachians and British Caledonides: History of a complex, west and southwest Pacific-type segment of Iapetus: Geological Society, London, Special Publications, v. 143, p. 197-242.

van Staal, C.R., Whalen, J.B., McNicoll, V.J., Pehrsson, S., Lissenberg, C.J., Zagorevski, A., van Breemen, O., and Jenner, G.A., 2007. The Notre Dame arc and the Taconic orogeny in Newfoundland: Geological Society of America Memoirs, v. 200, p. 511-552.

van Staal, C., and Barr, S., 2012. Lithospheric architecture and tectonic evolution of the Canadian Appalachians and associated Atlantic margin, Chapter 2: *in* Percival, J.A., Cook, F.A., and Clowes, R.M., eds., Tectonic Styles in Canada Revisited: the LITHOPROBE perspective, Geological Association of Canada, Special Paper, v. 49, p. 41-95.

Vaughan, D.J., and Craig, J.R., 1978. Mineral chemistry of metal sulfides: Cambridge, Cambridge University Press, 512 p.

Wagner, T., and Monecke, T., 2005. Germanium-bearing colusite from the Waterloo volcanic-rock-hosted massive sulfide deposit, Australia: Crystal chemistry and formation of colusite group minerals: The Canadian Mineralogist, v. 43, p. 655-669.

White, N.C., and Hedenquist, J.W., 1995. Epithermal gold deposits: styles, characteristics and exploration: SEG newsletter, v. 23, p. 9-13.

Wilkin, R.T., and Barnes, H.L., 1997. Formation processes of framboidal pyrite: Geochimica et Cosmochimica Acta, v. 61, p. 323-339.

Williams, H., 1979. Appalachian orogen in Canada: Canadian Journal of Earth Sciences, v. 16, p. 792-807.

Williams, H., Colman-Sadd, S.P., and Swinden, H.S., 1988. Tectonic-stratigraphic subdivisions of Central Newfoundland: Geological Survey of Canada, Current Research Part B, Paper 88-01, p. 91-98.

Williams-Jones, A.E., Bowell, R.J., and Migdisov, A.A., 2009. Gold in solution: Elements, v. 5, p. 281-287.

Winter, L.S., and Wilton, D.H.C., 2000. New lithogeochemical and Pb isotope data from Buchans area, central Newfoundland: Atlantic Geology, v. 36, p. 176.

Wright, K., 2009. The incorporation of cadmium, manganese and ferrous iron in sphalerite: Insights from computer simulations: The Canadian Mineralogist, v. 47, p. 615-623.

Yamada, R., Nishitani, Y., Tanimura, S., and Konishi, N., 1988. Recent development and geologic characteristics of the Nurukawa Kuroko deposit: Mining Geology, v. 38, p. 309-322.

Zagorevski, A., Van Staal, C.R., McNicoll, V., and Rogers, N., 2007. Upper Cambrian to upper Ordovician peri-Gondwanan island arc activity in the Victoria Lake Supergroup, Central Newfoundland: tectonic development of the northern Ganderian margin: American Journal of Science, v. 307, p. 339-370.

Zartman, R., and Doe, B., 1981. Plumbotectonics—the model: Tectonophysics, v. 75, p. 135-162.

Appendix A: Graphic Logs

A.1 – Graphic Logs

Preliminary fieldwork at Lemarchant consisted of detailed logging and sampling of the mineralized horizons in drill core. Drill core logs focused on the host rock facies, mineralogy, mineral zoning, mineral assemblages, hand sample textures andcross-cutting relationships of the Lemarchant sulfide mineralogy. Fieldwork was conducted during July-August 2012 and June-August 2013 at the Lemarchant core shack in Buchans Junction, Newfoundland. A total of 44 diamond drill cores were logged and 154 samples (half-cores) were taken, 143 of which were made into thin sections for petrographic analysis.

Below are the Legend and Abbreviation Key (Appendix A.2) for the 44 drill core logs (Appendix A.3). Diamond drill cores are labeled according to the following formula: LM(XX)-(YY), where LM represents 'the Lemarchant deposit', XX contains the last two numbers for the year the core was drilled, and YY represents the number of hole that was drilled in the sequence of total holes drilled (i.e., LM13-74 was drilled at Lemarchant in 2013 and is the 74th hole to be drilled in the entire deposit). Drill core logs have not been corrected for true depth.

A.2 –Abbreviation Key and Legend for Graphic Logs

Table A.2.1 – Abbreviation Key for Graphic Logs

Alteration Types	
hem	Hematite
ep	Epidote
qtz	Quartz
ser	Sericite
chl	Chlorite
carb	Carbonate
sulf	Sulfide mineralization
Host Rock Facies	
mud	Mudstone
tuff	Tuff
lap	Lapilli-stone
brec	Breccia
flow	Volcanic flow
intru	Intrusion
brt	Massive barite
Other (in descriptions)*	
med-g, fine-g, coarse-g	Medium-grained, fine-grained, coarse-grained
dk	Dark
amyg	Amygdules
irreg	Irregular

mono	Monolithic
poly	Polylithic
incl	Includes
alt	Alteration
ang, subang	Angular, subangular
selvs	Selvages
diss	Disseminated
xcut	Cross-cut
honey-b	Honey-brown
lap-tuff	Lapilli-tuff
mag	Magnetic
v.	Very
aphyr, phyr	Aphyric, phyric
puzz-fit	Puzzle-fit
strings	Stringers
kspar	Potassium-feldspar
SS	Stringer sulfides
SMS	Semi-massive sulfides
MS	Massive sulfides

*Some logs include ‘chloritoids’ and ‘leopard spotting’ as descriptive terms; later analyses (i.e. petrography) reveal that these are in fact albite rhombs and ankerite alteration, respectively, and have been included as descriptive terms in later drill core logs

Table A.2.2 – Legend for Graphic Logs

A.3 - Compilation of Graphic Logs

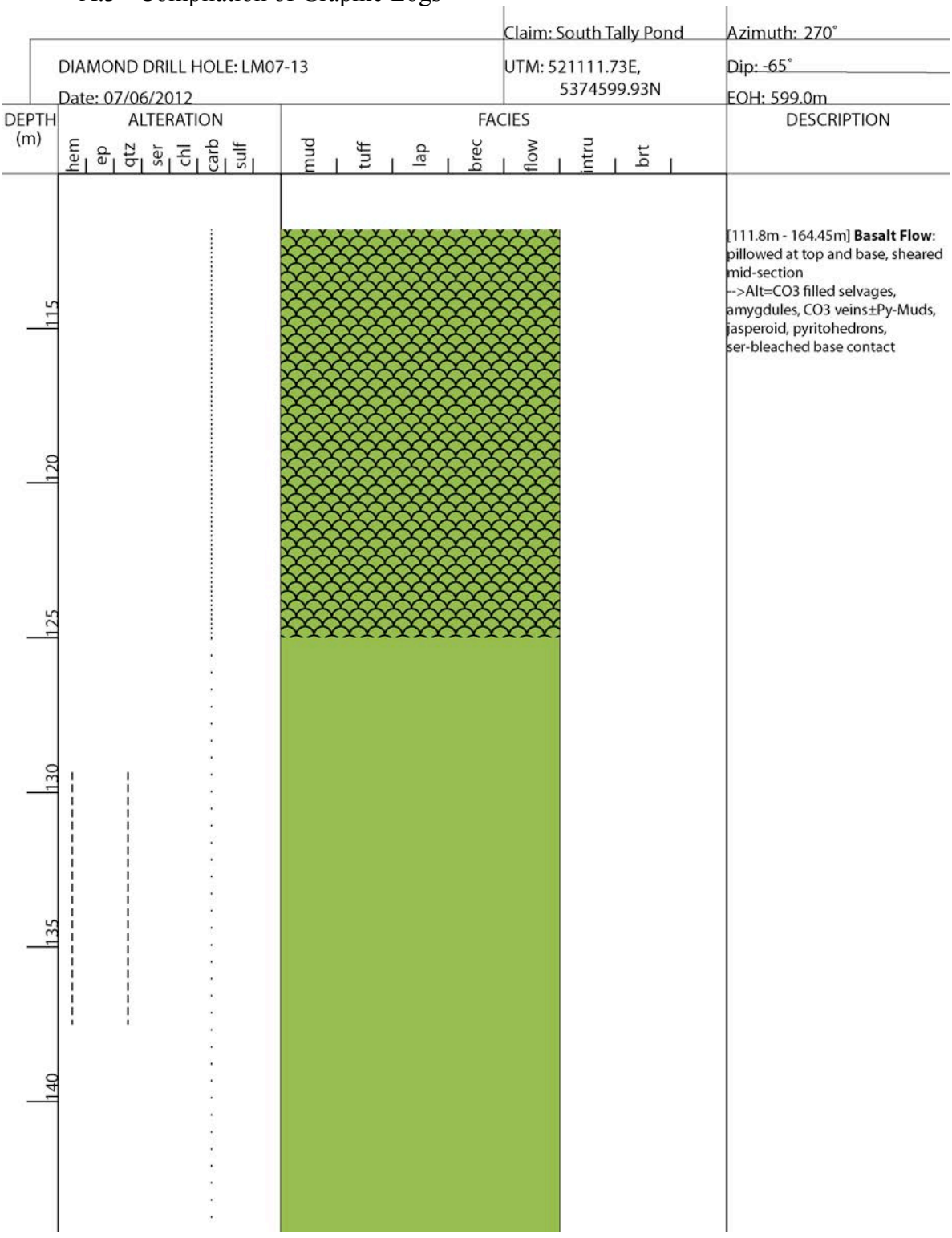

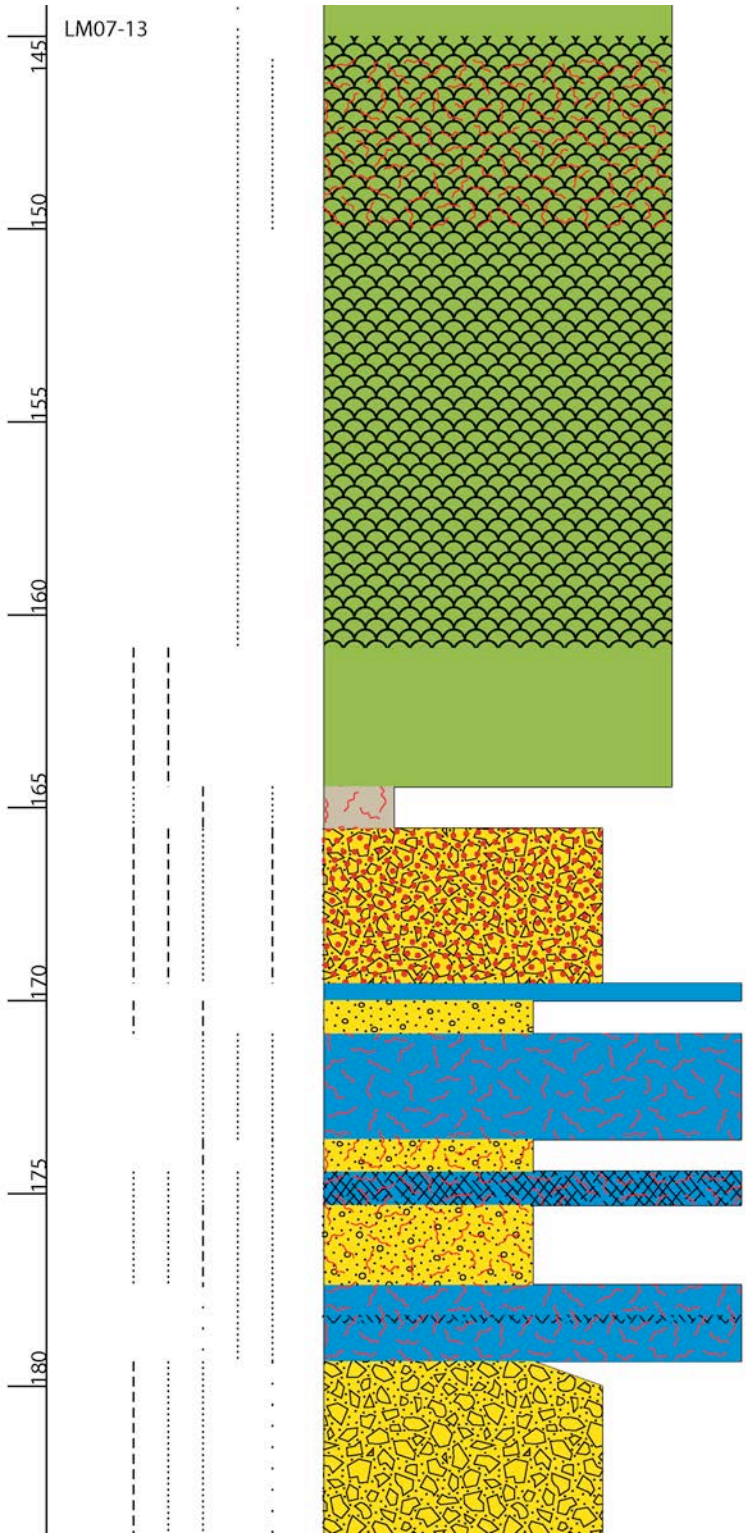

[164.45m - 165.54m] **Chl-Muds**: silicified, Ccp+Py±Brn stringers
[165.54m - 169.55m] **Rhyolite Lapilli Breccia**: diffuse block borders
-->Alt=chl-matrix, semi-massive Sp>Py>Gn±Brn,Ccp

@169.55m **Basalt Dyke**, bleached
[170m - 170.86m] **Rhyolite Lapilli-Tuff**, chl-silicified
[179.86m - 173.6m] **Basalt Dyke** w/ extreme crosscutting chl-CO3±Py veins

[173.6m - 174.43m] **Rhyolite Lapilli-Tuff** (as above),Sp-stringers
[174.43m - 175.3m] **Basalt Dyke**, fault zone w/ Py+Sp+Ccp stringers
[175.3m - 177.37m] **Rhyolite Lapilli-Tuff**, (as above), orange Sp+Ccp stringers

[177.37m - 179.35m] **Basalt Dyke**: sheared w/ fault zone in centre
-->Alt=CO3+Py filled veins, amygdules
[179.35m - 183.86m] **Rhyolite Lapilli Breccia**: graded contact, sheared, distinct block borders
-->Alt=qtz-ser, disseminated orange Sp

[183.86m - 184.74m] **Chl-Muds** w/

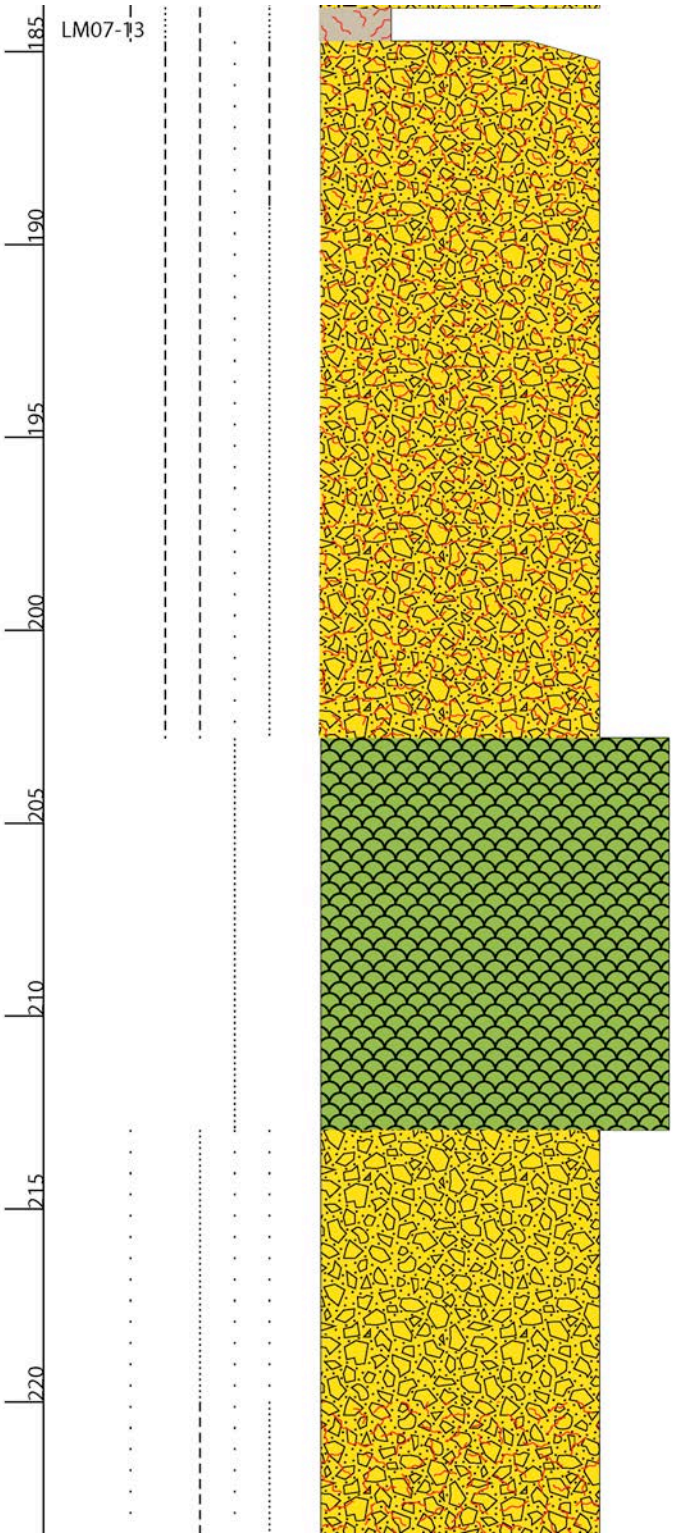

qtz+honey Sp+Ccp+Py±As
[184.74m - 202.8m] **Rhyolite Lapilli Breccia**: graded contact -->Alt=chl-matrix, semi-massive honey Sp+Py±Gn to Py+Ccp stringers, CO3 veins crosscut

[202.8m - 212.95m] **Basalt Flow**: pillowed, sheared -->Alt=CO3 filled amygdules, selvages

[212.95m - 233.0m] **Rhyolite Lapilli Breccia**: distinct block borders -->Alt=chl-matrix, qtz-CO3± epidote veins, Py-stringers at mid-section

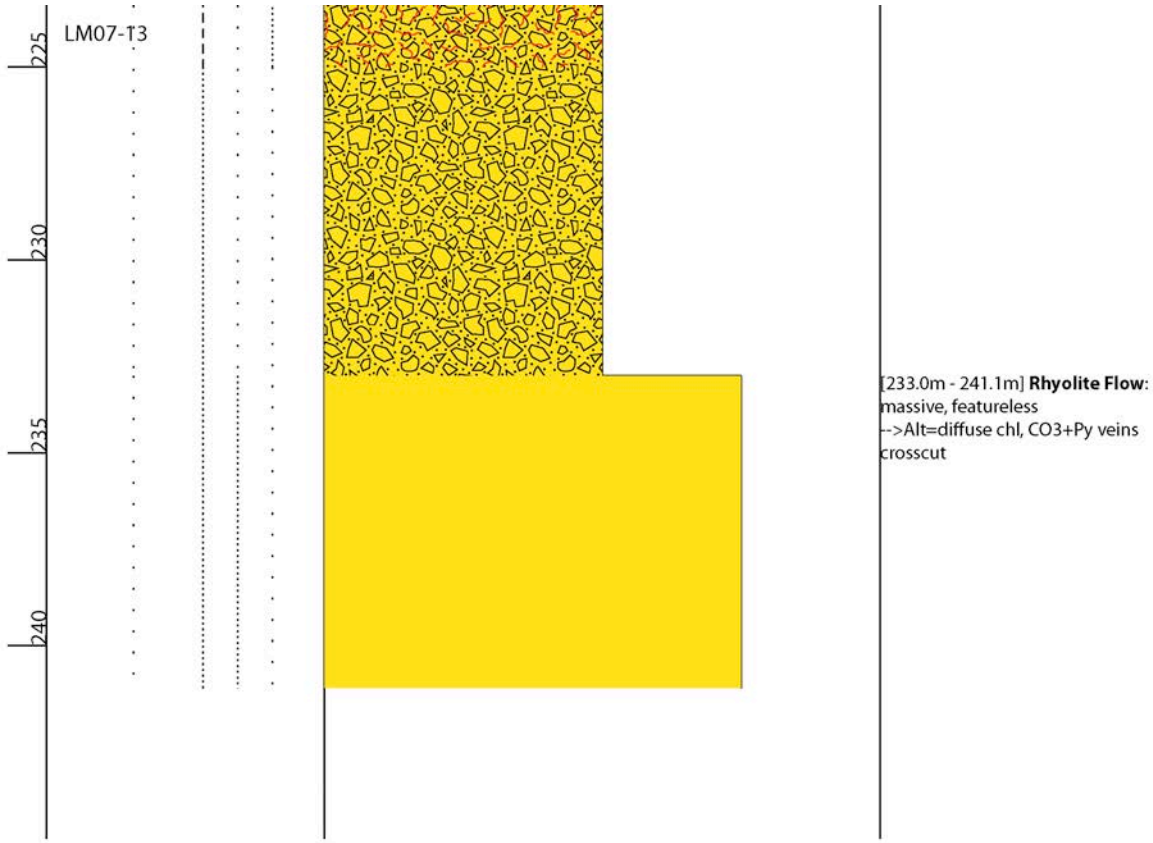
LM07-T3
225
230
235
240
[233.0m - 241.1m] **Rhyolite Flow**:
massive, featureless
-->Alt=diffuse chl, CO3+Py veins
crosscut

DIAMOND DRILL HOLE: LM07-14

Date: 07/21/2012

Claim: South Tally Pond

UTM: 521114.681E, 5374697.204N

Azimuth: 270°

Dip: -65°

EOH: 601.1m

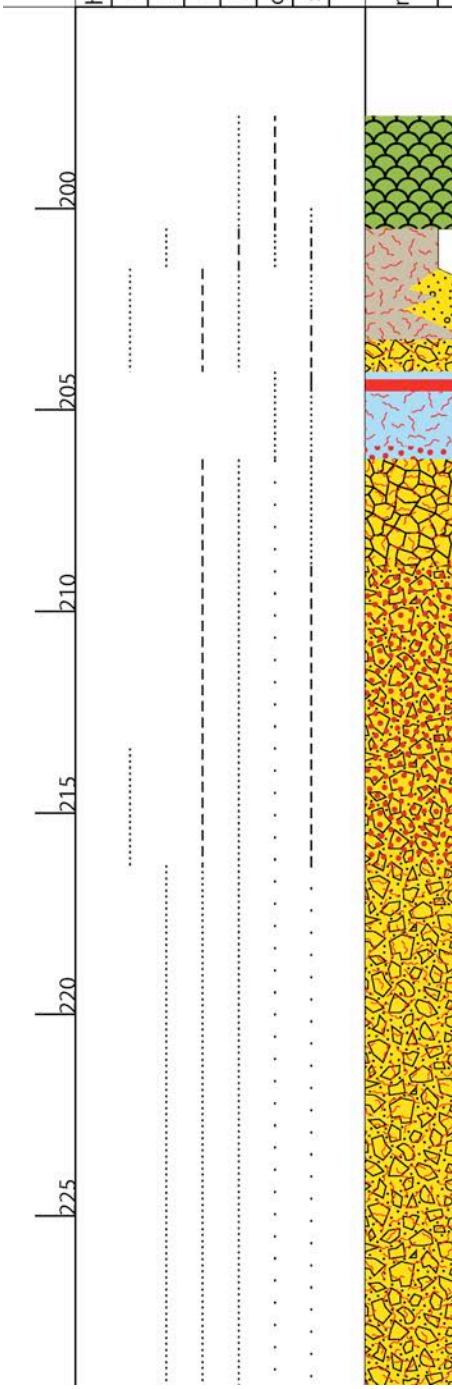

[197.7m - 200.5m]
Basaltic Flow: pillowed, sheared
-->Alt=chl-CO3 filled amygdules+ selvages, ±Py toward base, rhombic FeCO3

[200.5m - 204.05m]
Py-Mud grades to **Tuff Breccia**: transistional sheared **Lapilli-Tuff**
-->Alt=qtz-CO3 veins, ±Py then ±Po+Py then ±honey Sp+Py

[203.05m - 206.23m]
Massive Barite: crystalline
-->Alt=CO3, massive Py+Ccp to honey Sp then Brn+Ccp stringers then semi-massive honey Sp+Py

[206.23m - 208.88m]
Puzzle-Fit Rhyolite Breccia:
-->Alt=qtz-CO3 filled cracks, Ccp+Brn or honey Sp stringers

[208.88m - 216.3m]
Tuff Breccia: spherules >213m, sheared at base
-->Alt=semi-massive interstitial white Sp+Gn>Py, chl-FeCO3 veins w/ sheared base

[216.3m - 232.2m]
Tuff Breccia: diffuse block boundaries, lapilli-tuff matrix
-->Alt=qtz-CO3 veins crosscut, white Sp+Py>Gn stringers, VG @ 222.86m

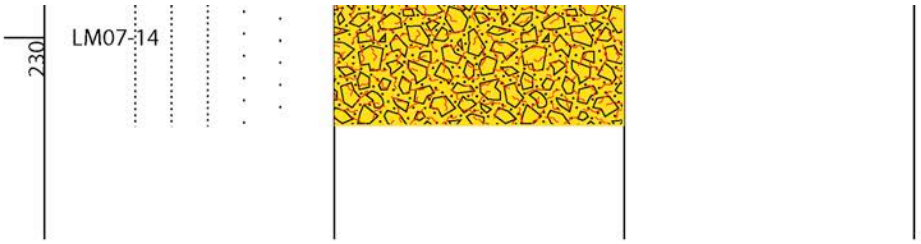
LM07-14
230

DIAMOND DRILL HOLE: LM07-15

Date: 07/04/2012

Claim: South Tally Pond

UTM: 521072.261E, 5374803.855N

Azimuth: 270°

Dip: -65°

EOH: 510.0m

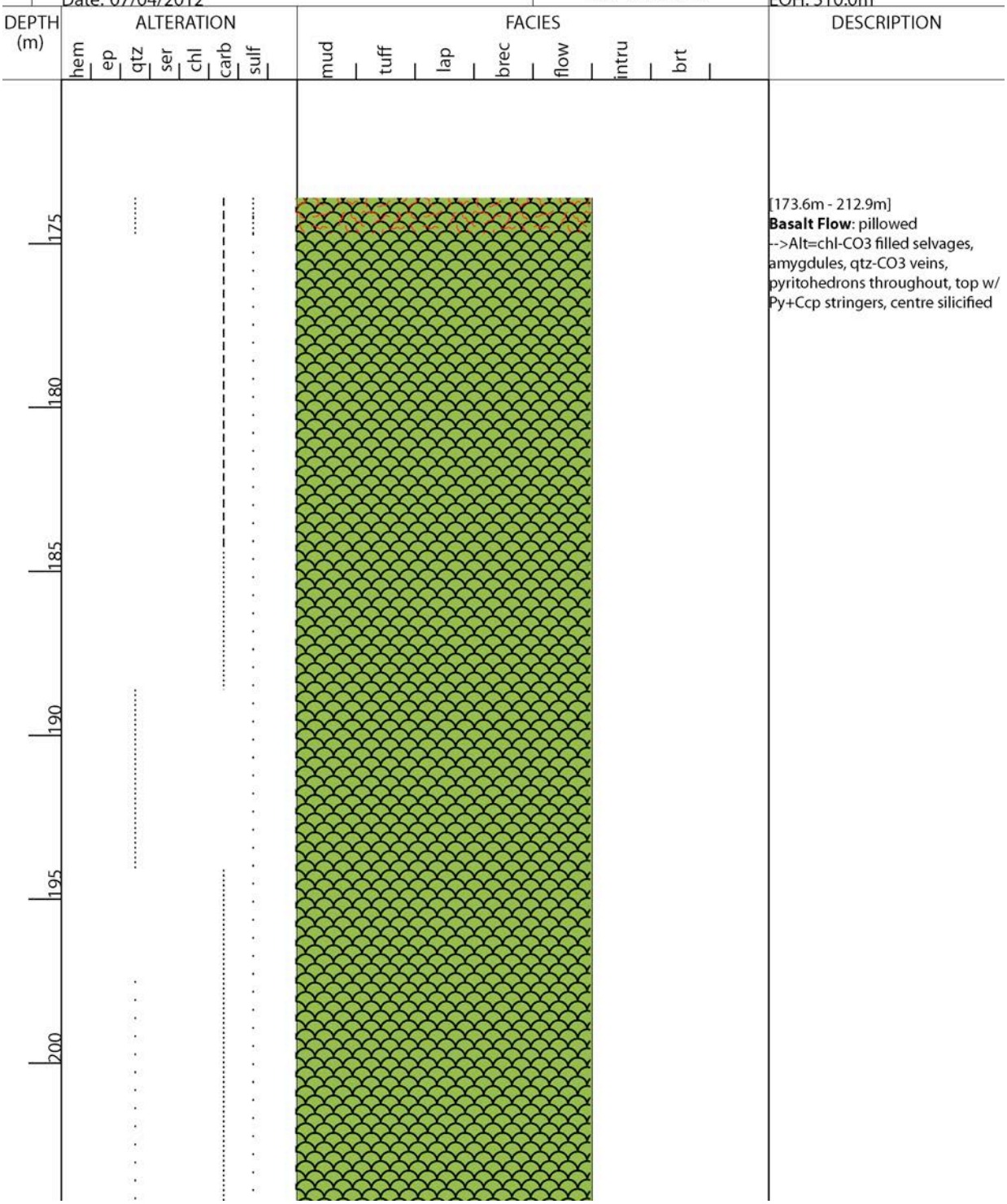

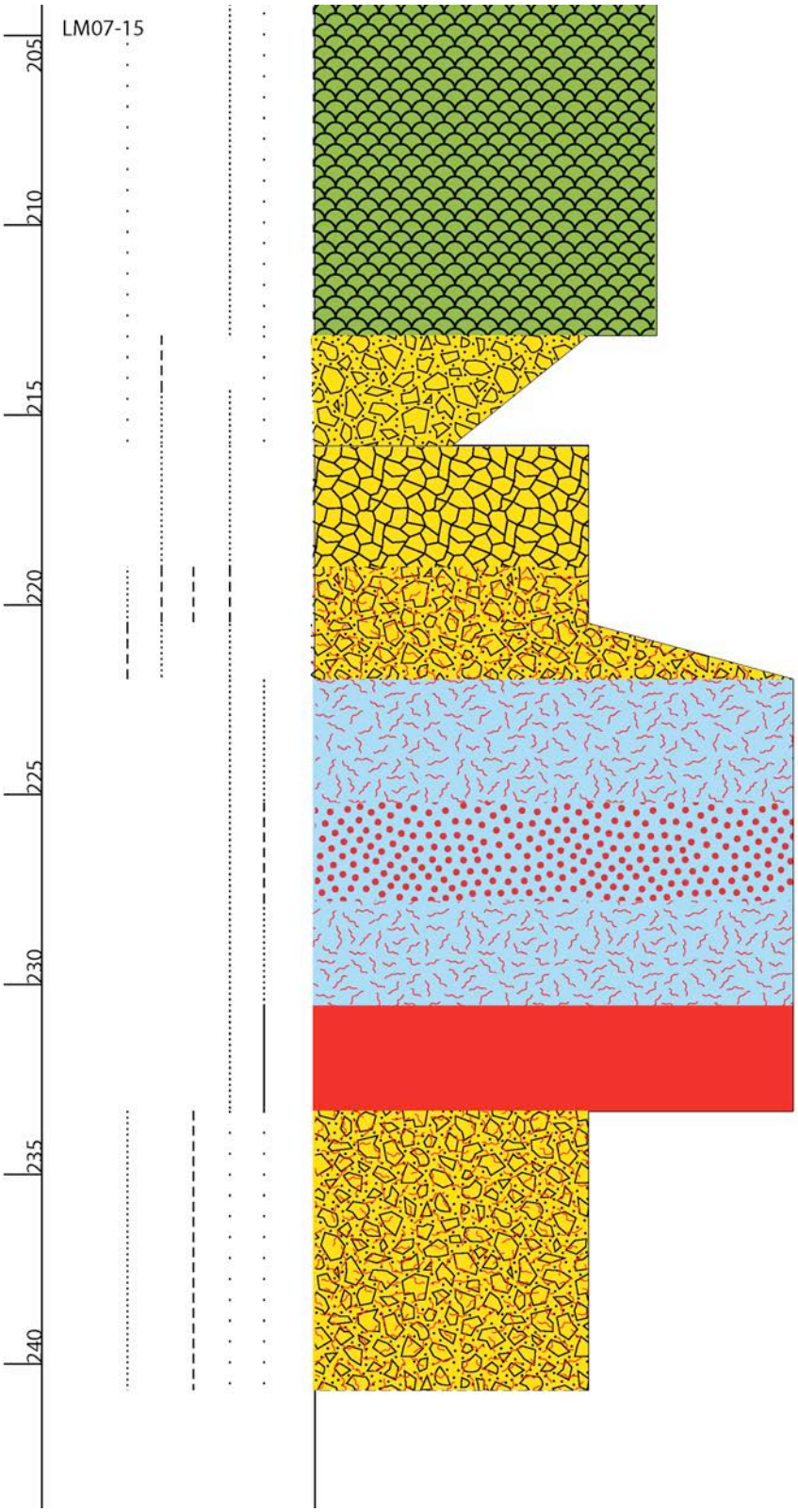

[212.9m - 215.8m] **Rhyolitic Lapilli-Tuff Breccia** grades into sheared **Tuff**
-->Alt=ser to chl downhole, disseiminated Py

[215.8m - 219.0m]
Puzzle-Fit Rhyolite Breccia: block borders indistinct

[219.0m - 221.97m]
Rhyolite Tuff Breccia: grades into massive barite
-->Alt=qtz-chl matrix, honey Sp+Py±Ccp to Py±Brn stringers

[221.97m - 225.2m]
SS Massive Barite: few rotated rhyolite clasts
-->Alt=CO3 overprint, Py+Brn stringers

[225.2m - 227.82m]
SMS Massive Barite: (as above)
-->Alt=Py>Gn,Brn

[227.82m - 230.56m]
SS Massive Barite: (as above)
-->Alt= >Sp+Py+Ccp stringers

[230.56m - 233.33m]
Massive Sulfides: orange to honey Sp+Py+Gn±Brn,Ccp

[233.33m - 240.68m]
Rhyolitic Lapilli-Tuff Breccia: distinct block borders
-->Alt=qtz-chl matrix, qtz-CO3 veins, occasional Sp+Py

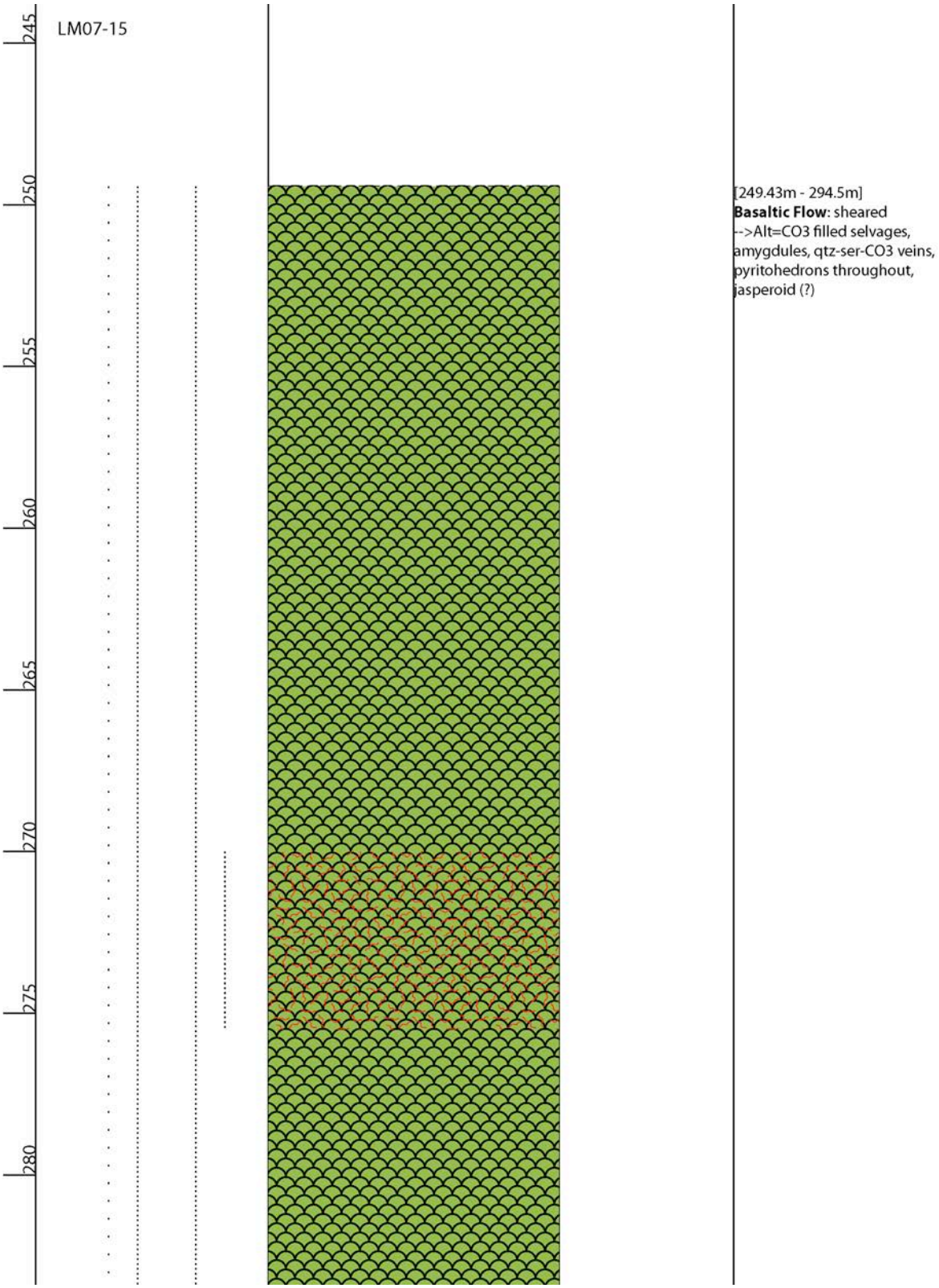
LM07-15
245
250
255
260
265
270
275
280
[249.43m - 294.5m]
Basaltic Flow: sheared
-->Alt=CO3 filled selvages,
amygdules, qtz-ser-CO3 veins,
pyritohedrons throughout,
jasperoid (?)

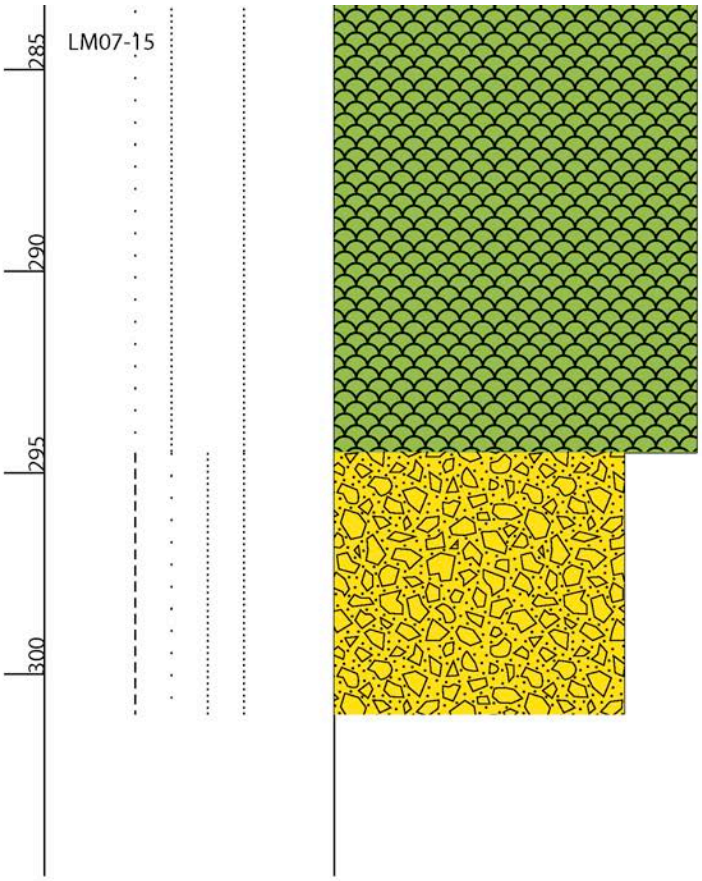

[294.5m - 301.0m]
Polylithic Breccia: lapilli-tuff matrix w/ rhyolite and basaltic fragments
-->Alt=silicified, chl-CO3 veins crosscut

DIAMOND DRILL HOLE: LM07-16

Date: 07/22/2012

Claim: South Tally Pond

UTM: 521080.229E, 5374900.176N

Azimuth: 270°

Dip: -65°

EOH: 480.0m

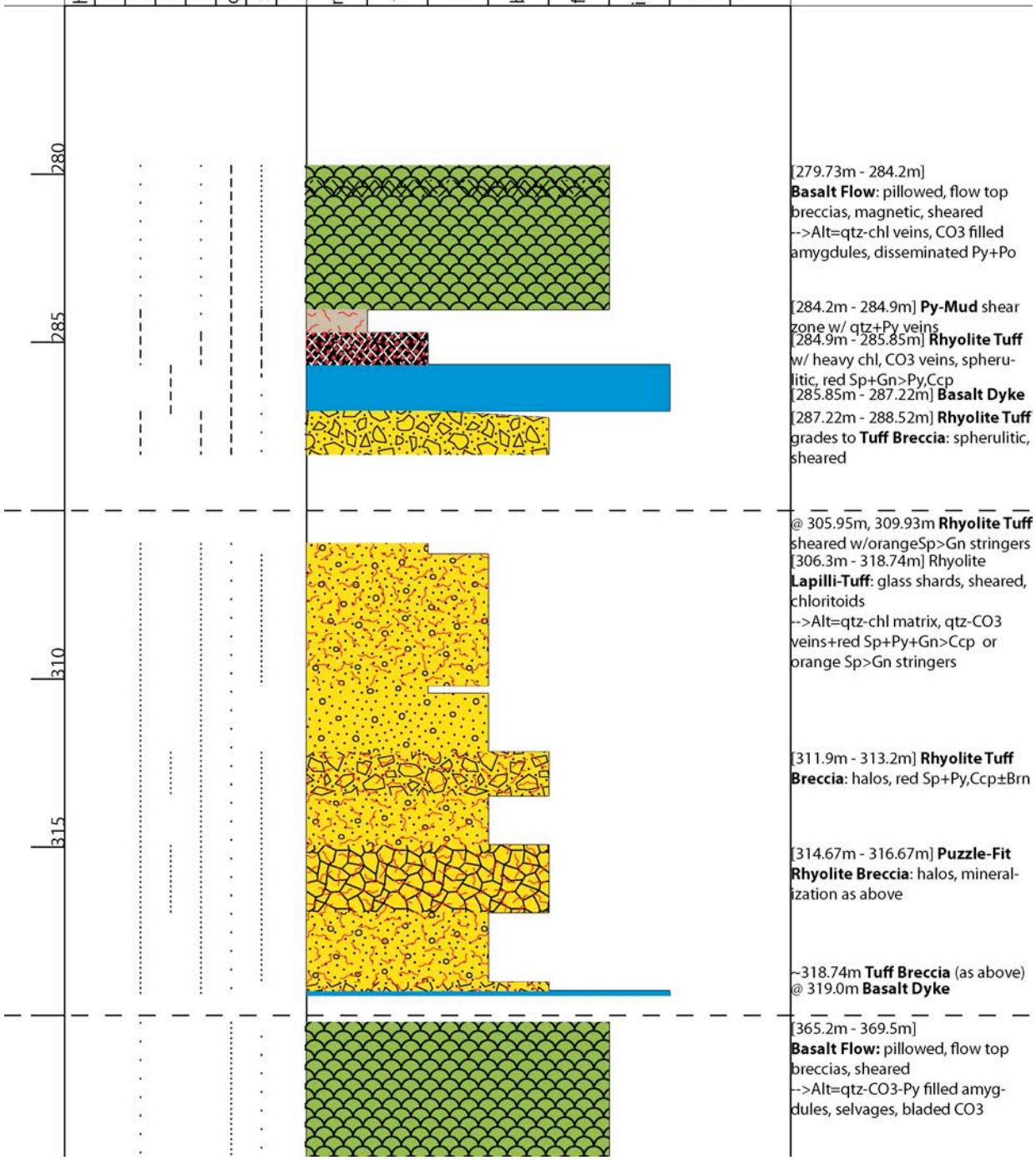

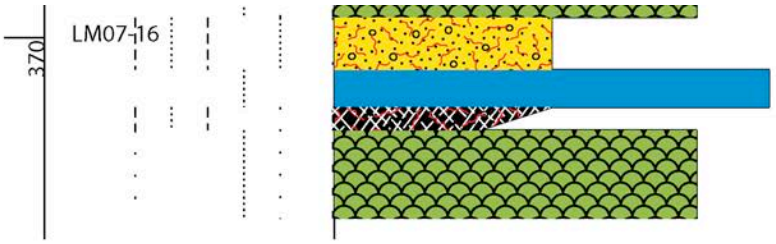

[369.5m - 370.8m]**Rhyolite Lapilli -Tuff** sheared, orangeSp,Gn±Py

[370.8m - 371.73m] **Basalt Dyke**

[371.73m - 372.3m] **Lapilli-Tuff** grades to Chl-**Tuff**, spherulitic

[372.3m - 374.5m]

Basalt Flow: pillowed, flow top breccia, peperitic contact

DIAMOND DRILL HOLE: LM07-17

Date: 06-23-2013

Claim: South Tally Pond

UTM: 520989.959E, 5374908.512N

Azimuth: 270°

Dip: -65°

EOH: 576.4m

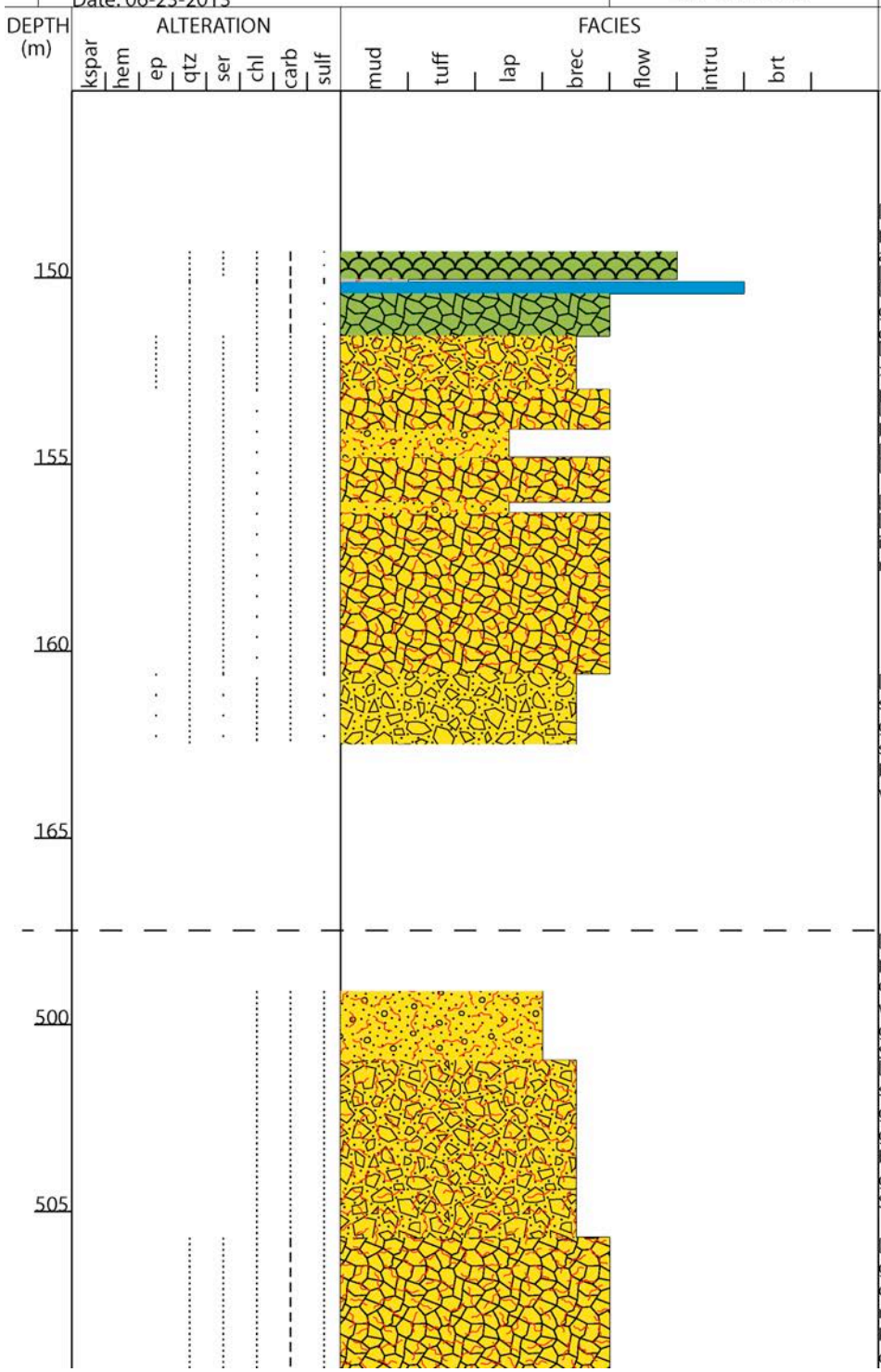

[149.3m] mafic pillow flow: med-g, pyx-bearing, dk green; deformed amygs; ankerite alteration

[150.04m] Py-mud

[150.42m] mafic breccia: green-grey, rounded, amyg, coarse Py; dk green matrix

[151.56m] felsic lapilli-tuff breccia: >1cm, irreg, bleached, qtz-phyric, polylithic, dk grey matrix w/ Py-Gn

[153m] felsic breccia: monolithic, bleached, qtz-p; Py-Gn-red Sp-Ccp

[154.05m] felsic lapilli-tuff: mono

[154.82m] felsic breccia (as above)

[156m] felsic lapilli-tuff (as above)

[156.3m] felsic breccia (as above): incl. concentric alteration; grey matrix; carb-qtz veins crosscut

[160.6m] felsic lapilli-tuff breccia: subround-subangular, 2mm-1cm, grey-beige-green, phyric+non; sheared; rare 4cm oblong Py blebs; green-grey matrix; carb-qtz veinlets & qtz veins crosscut

[499.1m] felsic lapilli-tuff: polylithic, green-grey-white, qtz-phyric, <0.5cm TO heterolithic w/ brown mafic blebs >1cm; dk grey matrix w/ Ccp-Py-Gn-honey Sp-Brt; minor blocks

[500.95m] felsic lapilli-tuff breccia; subround-subangular, white-green, qtz-phyric, 0.3-1cm lapilli; green-grey, qtz-phyric blocks; rare bleached mafic blebs; med-g dk grey tuff; qtz veins w/ honey Sp-Py-Gn-Ccp-Bn-Brt

[505.7m] felsic breccia; puzzle-fit, green-grey, ~10cm, subang, qtz-phyric, monolithic; dk grey matrix; qtz-carb veins w/ Py-white-honey Sp-Gn-brt-coarse chl

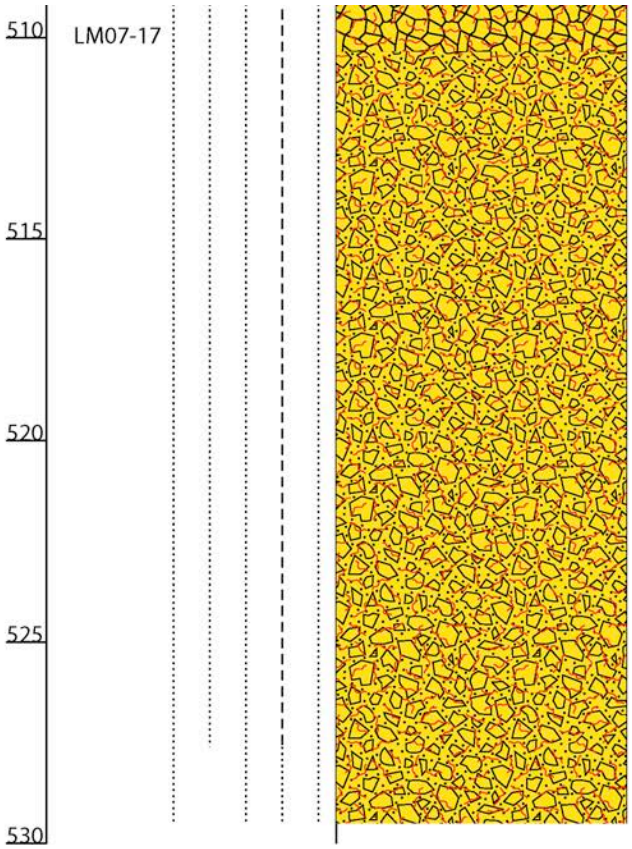

[510.35m] felsic lapilli-tuff breccia: bleached, ~10cm, subang-irreg, beige-green, qtz-phyric, concentric alt; round-subang, white-brown-green, qtz-phyric, lapilli; dk grey ash matrix; cal-coarse chl veins w/ Brt-Py-white Sp-Gn-Ccp

[527.6m] felsic lapilli-tuff breccia (as above); decreased mineralization w/ increased chl-alt

DIAMOND DRILL HOLE: LM07-17

Date: 07/05/2012

Claim: South Tally Pond

UTM: 520989.959E, 5374908.512N

Azimuth: 270°

Dip: -65°

EOH: 576.4m

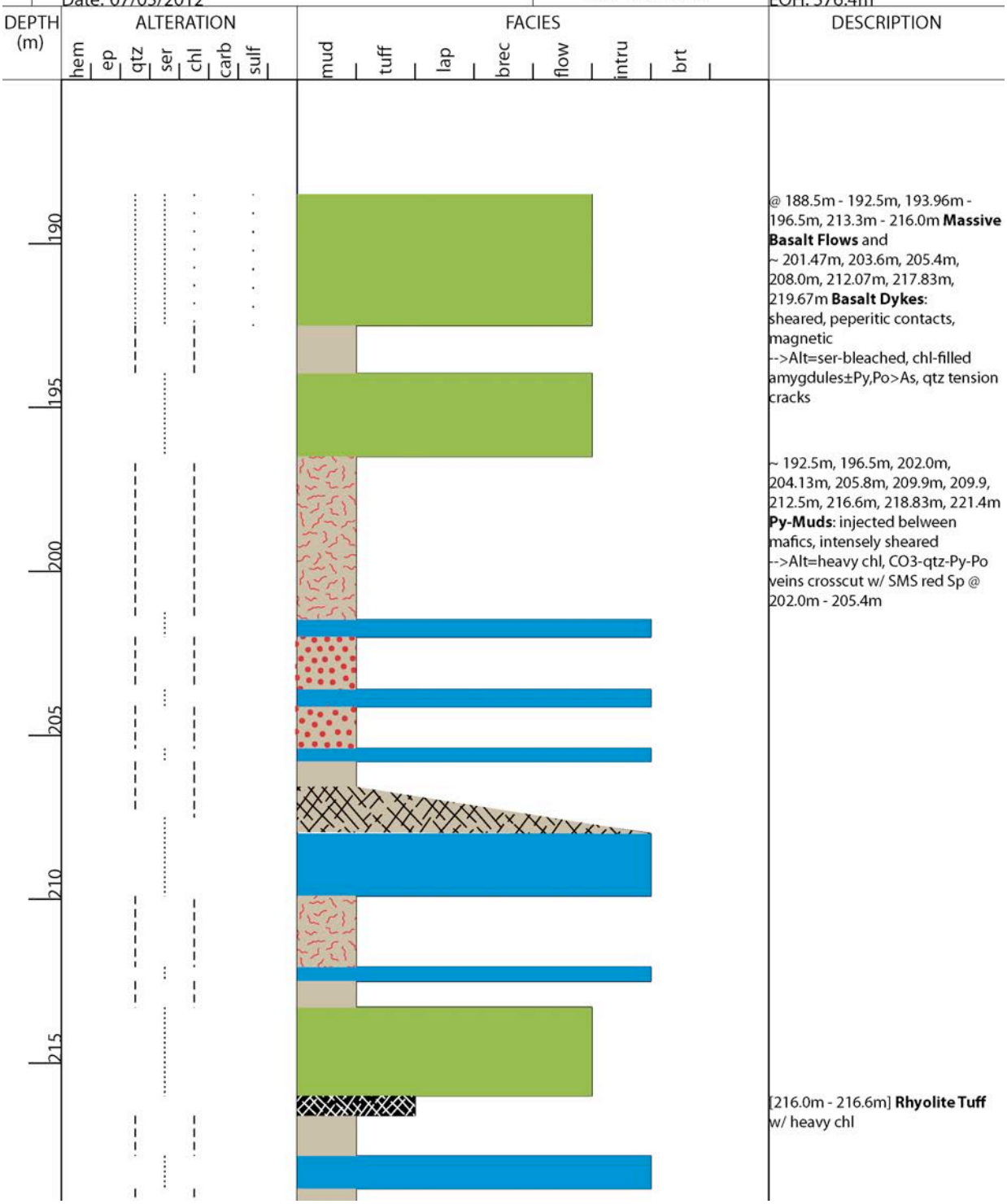

@ 188.5m - 192.5m, 193.96m - 196.5m, 213.3m - 216.0m **Massive Basalt Flows** and ~ 201.47m, 203.6m, 205.4m, 208.0m, 212.07m, 217.83m, 219.67m **Basalt Dykes**: sheared, peperitic contacts, magnetic
-->Alt=ser-bleached, chl-filled amygdules±Py,Po>As, qtz tension cracks

~ 192.5m, 196.5m, 202.0m, 204.13m, 205.8m, 209.9m, 209.9, 212.5m, 216.6m, 218.83m, 221.4m **Py-Muds**: injected belween mafics, intensely sheared
-->Alt=heavy chl, CO3-qtz-Py-Po veins crosscut w/ SMS red Sp @ 202.0m - 205.4m

[216.0m - 216.6m] **Rhyolite Tuff** w/ heavy chl

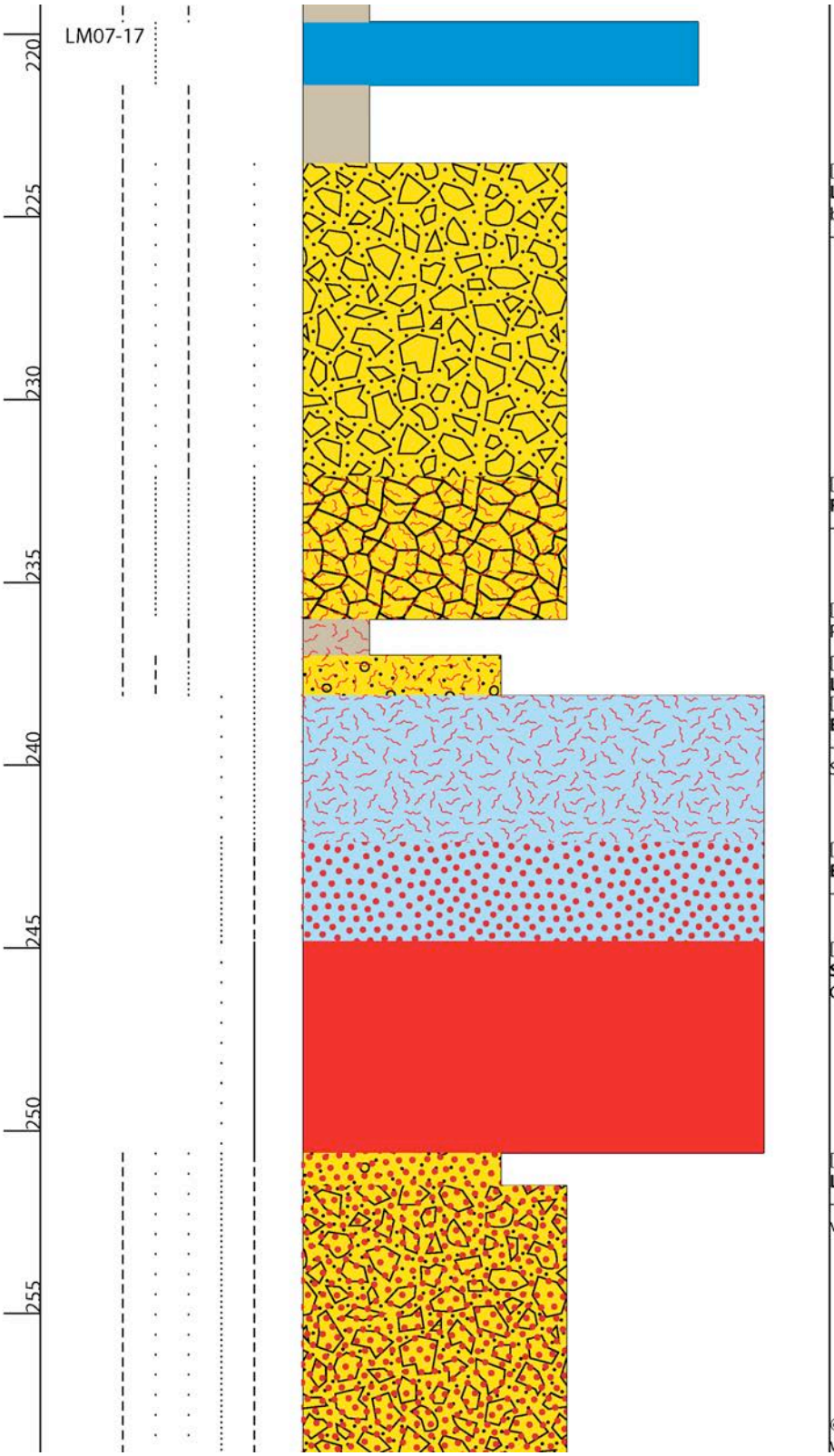

[223.4m - 232.11m] **Rhyolite Lapilli-Tuff Breccia**: diffuse block borders, cracked, spherulitic -->Alt=chl-qtz-Py filled cracks

[232.11m - 236.0m] **Puzzle-Fit Rhyolite Breccia**: massive, diffuse -->Alt=Py+honeySp±Ccp stringers

[236.0m - 237.0m] **Py-Mud** w/ Py>Ccp±honey Sp stringers

[237.0m - 238.1m] **Rhyolite Lapilli-Tuff** w/ Py+Gn> white Sp

[238.1m - 242.1m] **SS Massive Barite:** exhalative texture -->Alt=CO3 overprint, Py+honey Sp±Ccp,Brn stringers

[242.1m - 244.82m] **SMS Massive Barite:** chloritoids present -->Alt=honeySp+Gn+Py+Brn±Ccp

[244.82m - 250.6m] **Massive Sulfides:** honey Sp+Py±Gn w/ Gn+Brn+Ccp dominant @centre

[251.5m - 259.36m] **Rhyolite Lapilli-Tuff to Tuff Breccia:** -->Alt=variable, kspar, qtz-ser veins ±Sp,Ccp

@259.36m heavy chl shear zone w/ Sp+Py stringers, grades into

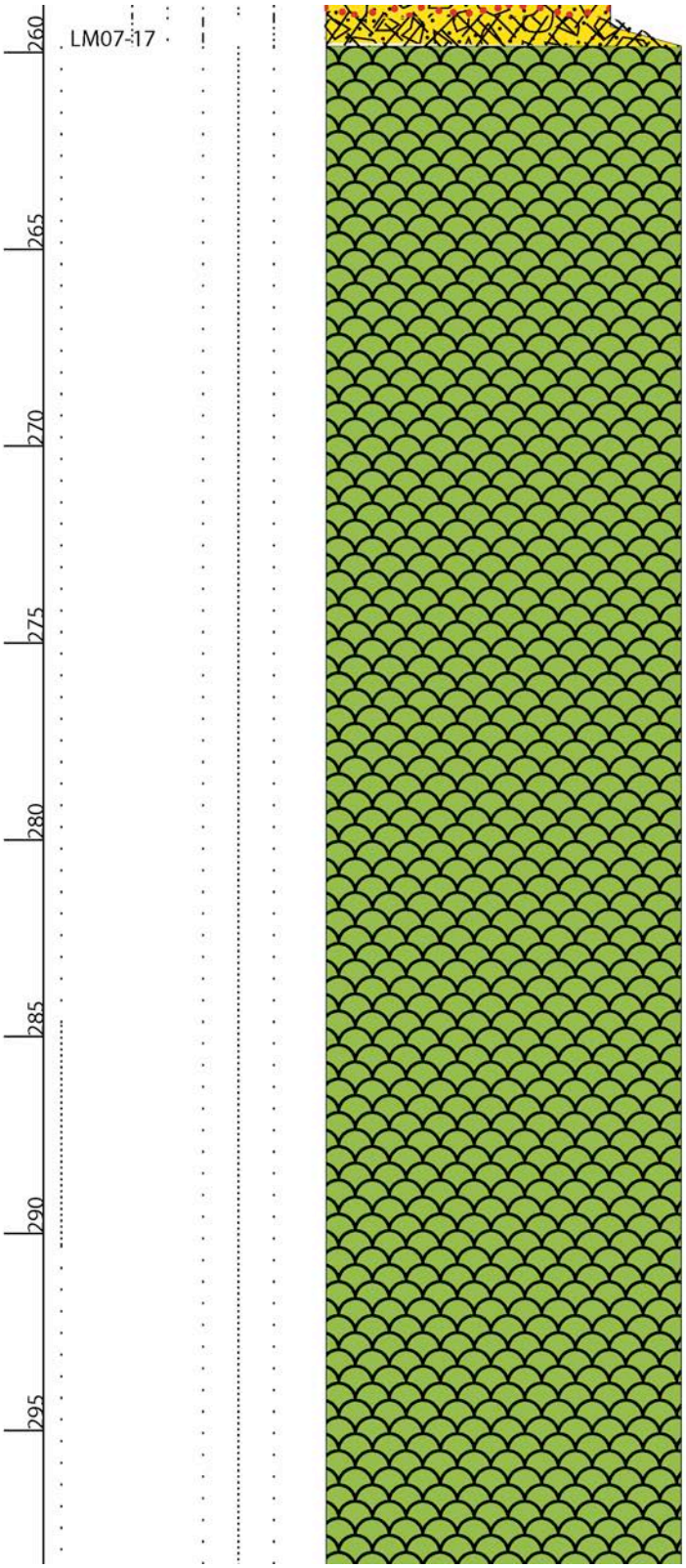

mafic flow

[259.85m - 305.0m]
Basalt Flow: pillowed, few flow top breccias, localized shear zones -->Alt=chl-CO3±jasperoid amygdules, selvages, CO3 veins±Py

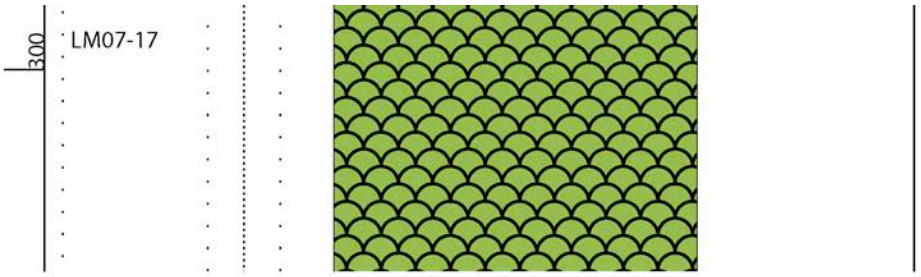
300
LM07-17

Claim: South Tally Pond

Azimuth: 270°

DIAMOND DRILL HOLE: LM08 - 19

UTM: 520991.902E, 5374957.945N

Dip: -65°

Date: 07/16/2012

EOH: 431 m

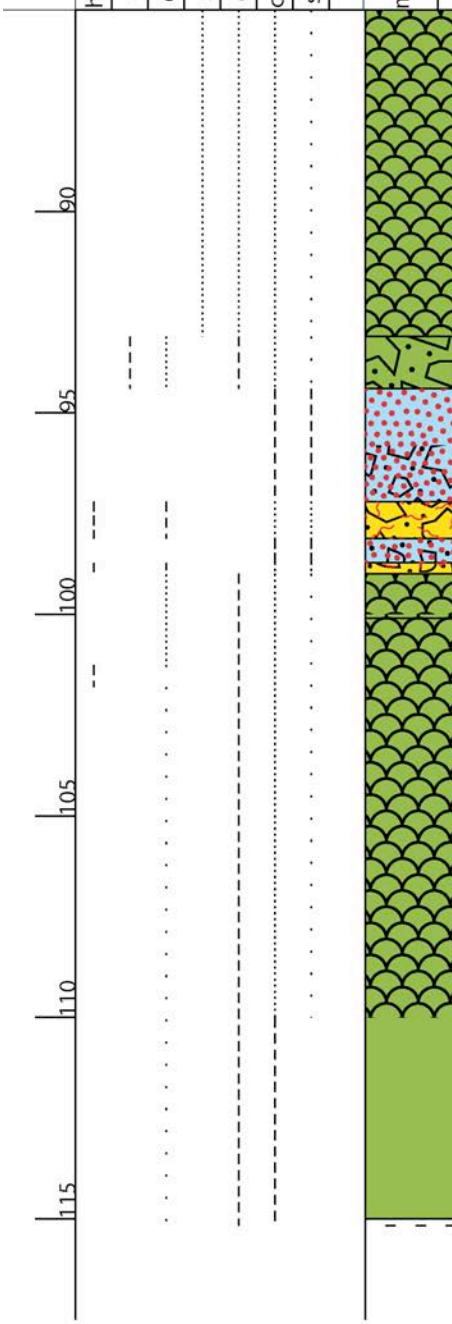

DESCRIPTION

[85.1m - 93.0m]

Basaltic flow: hyaloclastic pillowed flow, amygdular at flow tops and bases, tension cracked
--> Alt = selvages, amygdules filled with chl+CO3, FeCO3 veins crosscut, scattered pyritohedrons

[93.0m - 94.3m]
basalt is brecciated, puzzle-fit
--> Alt = includes rhombic FeCO3

[94.3m - 97.1m, (98.0 - .68m)]

Massive Barite: semi-massive Py+Gn±Ccp,Trt
--> Alt = CO3 overprints barite

[97.1m - 98.95m]

Jasper Breccia: altered rhyolite
--> Alt = jasperoid, FeCO3 veins, Py+Ccp stringers

[98.95m - 115.2m]

Basaltic Flow: hyaloclastic pillow flow, amygdular at flow contacts, tension cracks, massive flow toward base
--> Alt = selvages, amygdules filled with chl+CO3, quatz-FeCO3 veins crosscut ± jasperoid, pyritohedrons decrease toward base

[100.06 - .13m, 110.10 - .45m]

Pyritic Muds: infill of brecciated flow tops

DIAMOND DRILL HOLE: LM08-22

Date: 07/24/2012

Claim: South Tally Pond

UTM: 520992.886E, 5375012.591N

Azimuth: 270°

Dip: -45°

EOH: 221.0m

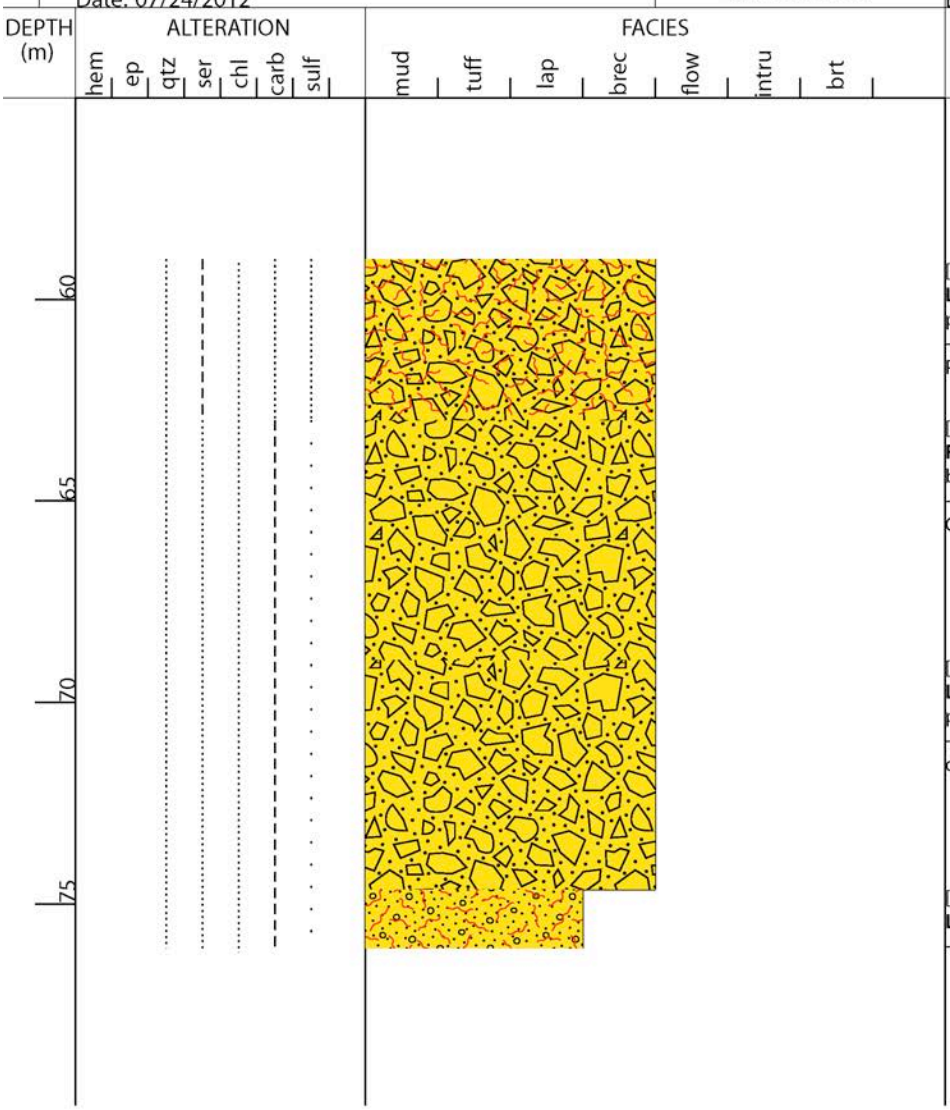

DESCRIPTION

[59.0m - 63.0m]
Lapilli-Tuff Rhyolite Breccia: polylithic, halos, distinct borders -->Alt=chl-qtz matrix, CO3 veins, Py±Gn>white Sp stringers

[63.0m - 68.9m]
Rhyolite Tuff Breccia: diffuse borders, sheared
-->Alt=chl matrix, bladed FeCO3, CO3 veins, disseminated Py

[68.9m - 74.64m]
Lapilli-Tuff Rhyolite Breccia: polylithic, sheared
-->Alt=bladed FeCO3, CO3 veins, disseminated Py

[74.64m - 76.1m] **Rhyolitic Lapilli-Tuff**: sheared
-->Alt=bladed FeCO3

DIAMOND DRILL HOLE: LM08-23

Date: 06-22-2013

Claim: South Tally Pond

UTM: 521066.364E, 5375010.736N

Azimuth: 270°

Dip: -45°

EOH: 245m

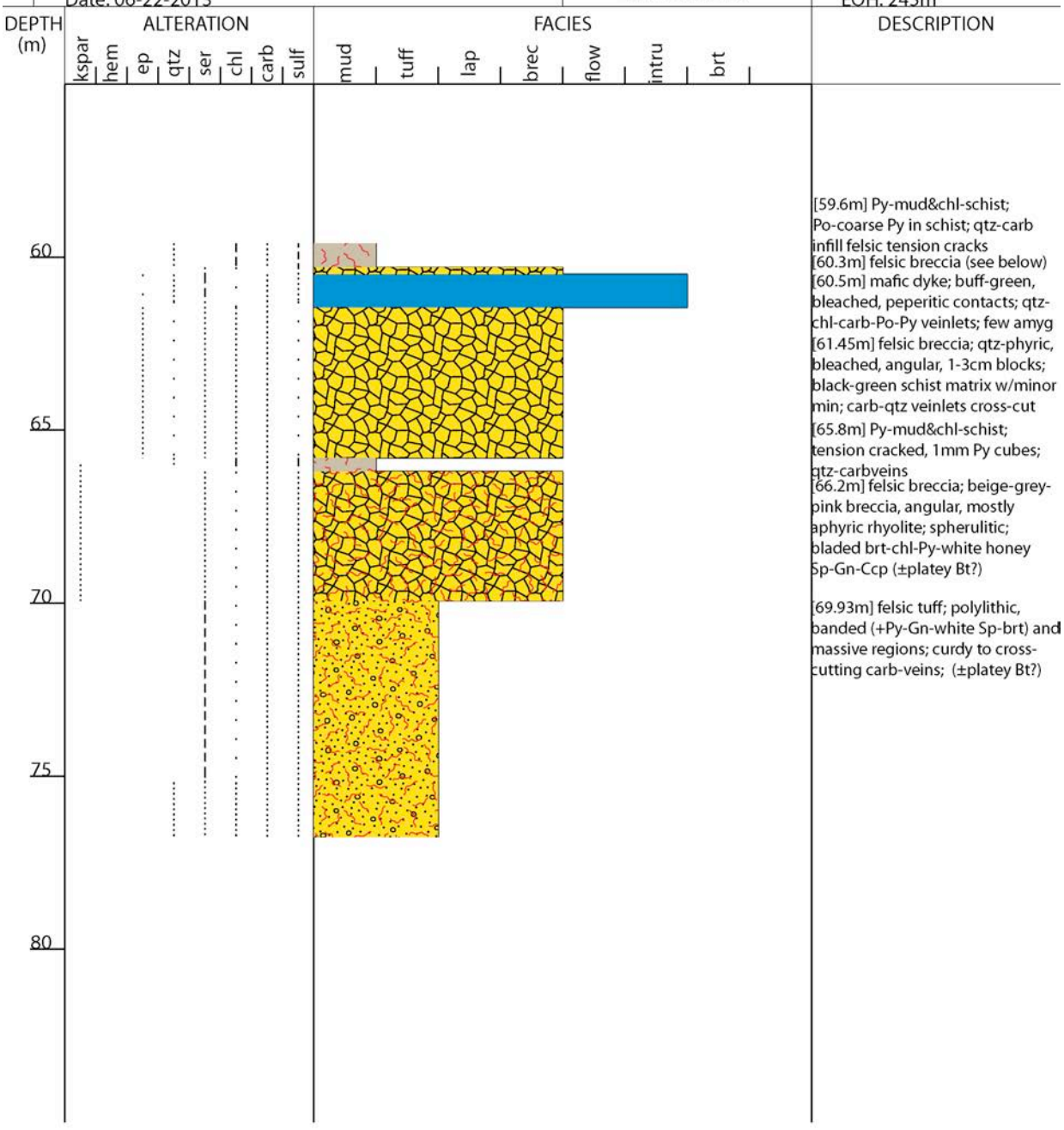

DESCRIPTION

[59.6m] Py-mud&chl-schist; Po-coarse Py in schist; qtz-carb infill felsic tension cracks

[60.3m] felsic breccia (see below)

[60.5m] mafic dyke; buff-green, bleached, peperitic contacts; qtz-chl-carb-Po-Py veinlets; few amyg

[61.45m] felsic breccia; qtz-phyric, bleached, angular, 1-3cm blocks; black-green schist matrix w/minor min; carb-qtz veinlets cross-cut

[65.8m] Py-mud&chl-schist; tension cracked, 1mm Py cubes; qtz-carbveins

[66.2m] felsic breccia; beige-grey-pink breccia, angular, mostly aphyric rhyolite; spherulitic; bladed brt-chl-Py-white honey Sp-Gn-Ccp (±platey Bt?)

[69.93m] felsic tuff; polylithic, banded (+Py-Gn-white Sp-brt) and massive regions; curdy to cross-cutting carb-veins; (±platey Bt?)

DIAMOND DRILL HOLE: LM08-24

Date: 07/12/2012

Claim: South Tally Pond

UTM: 521067.705E, 5375010.664N

Azimuth: 250°

Dip: -70°

EOH: 489.8m

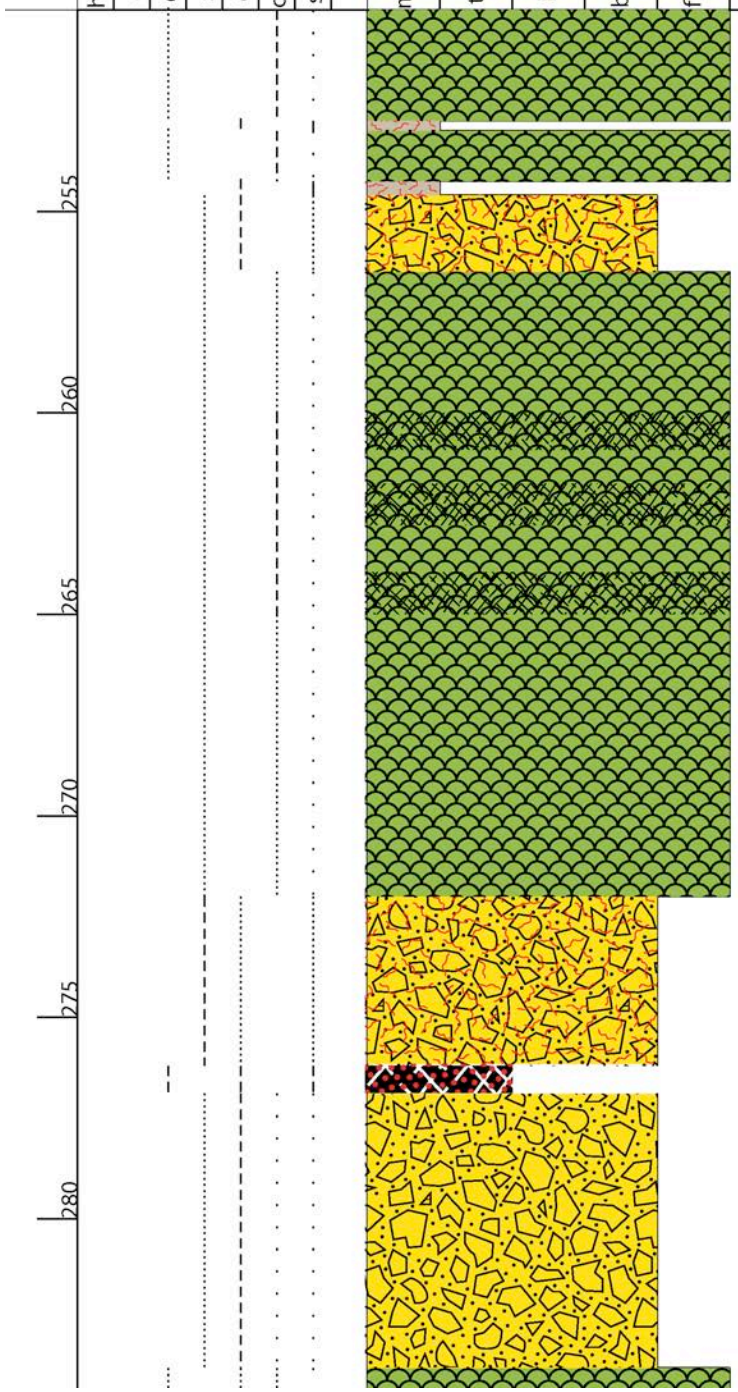

[250.0m - 254.25m] **Basalt Flow**: amygdular at pillow tops
-->Alt=chl-CO3 filled amygdules, selvages, leopard spotting, Py

@ 252.75m, 254.25m **Py-Muds**

[254.6m - 256.5m] **Rhyolite Tuff Breccia**: sheared, distinct borders
-->Alt=chl tension cracks, Py+Po stringers

[256.5m - 272.0m] **Basalt Flow:** pillowed, sheared w/ cataclastite zones, hyaloclastic at base, peperitic top contact
-->Alt=CO3-ser filled amygdules, selvages, disseminated Py, CO3 veins

[272.0m - 283.7m] **Rhyolite Tuff Breccia**: sheared, distinct block borders become ghostly > 276.88m, glass-rich
-->Alt=chl-ser to chl matrix, CO3 veins, minor Py+Gn+Ccp±Trt,As

@ 276.2m chl-qtz fault zone

[283.7m - 289.4m] **Basalt Flow**:

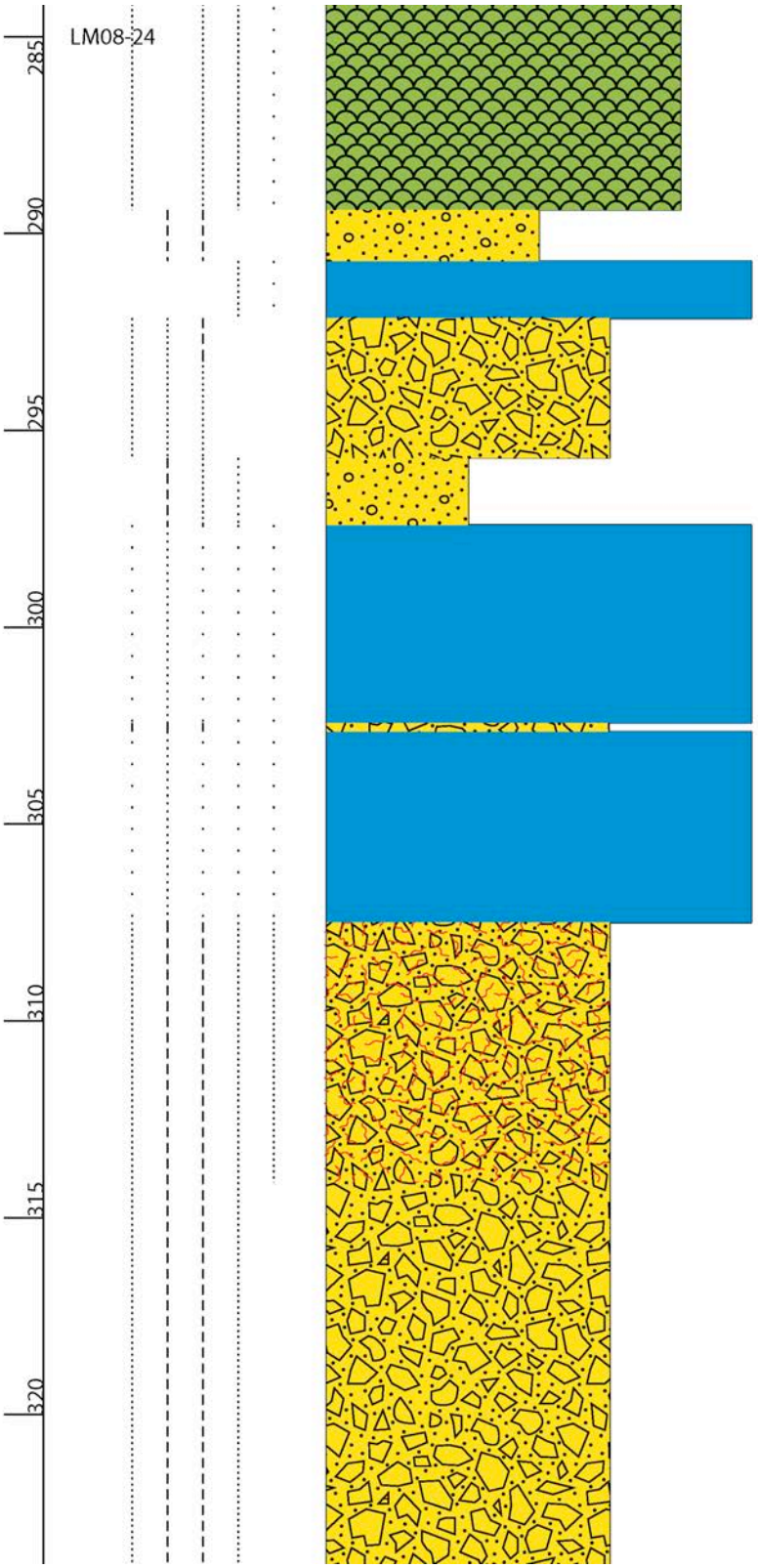

pillowed, sheared
-->Alt=qtz-CO3 selvages, chl amygdules, leopard spotting, pyritohedrons

[289.4m - 290.7m] **Rhyolite Lapilli-Tuff** w/ chl+Py-matrix

[290.7m - 292.15m] **Basalt Dyke** w/ pyritohedrons, qtz-CO3 veins

[292.15m - 295.7m] **Rhyolite Lapilli Breccia:** glass-rich, spherulitic, distinct borders
-->Alt=chl-matrix, qtz-ser, disseminated Py

[295.7m - 297.4m] **Rhyolite Tuff**
-->Alt=qtz-chl, bleached peperitic base, CO3 veins

[297.4m - 307.5m] **Basalt Dyke**
-->Alt=sericitized, chl±Py amygdules, qtz-CO3 veins, pyritohedrons

@ 302.43m entrained **Rhyolite Tuff Breccia**

[307.5m - 358.18m] **Polylithic Felsic Tuff Breccia**: distinct rhyolite (±flow bands), diffuse basalt blocks, glass-rich
-->Alt=ser-chl, CO3 veins, Py+Ccp±Gn,Sp stringers at contacts

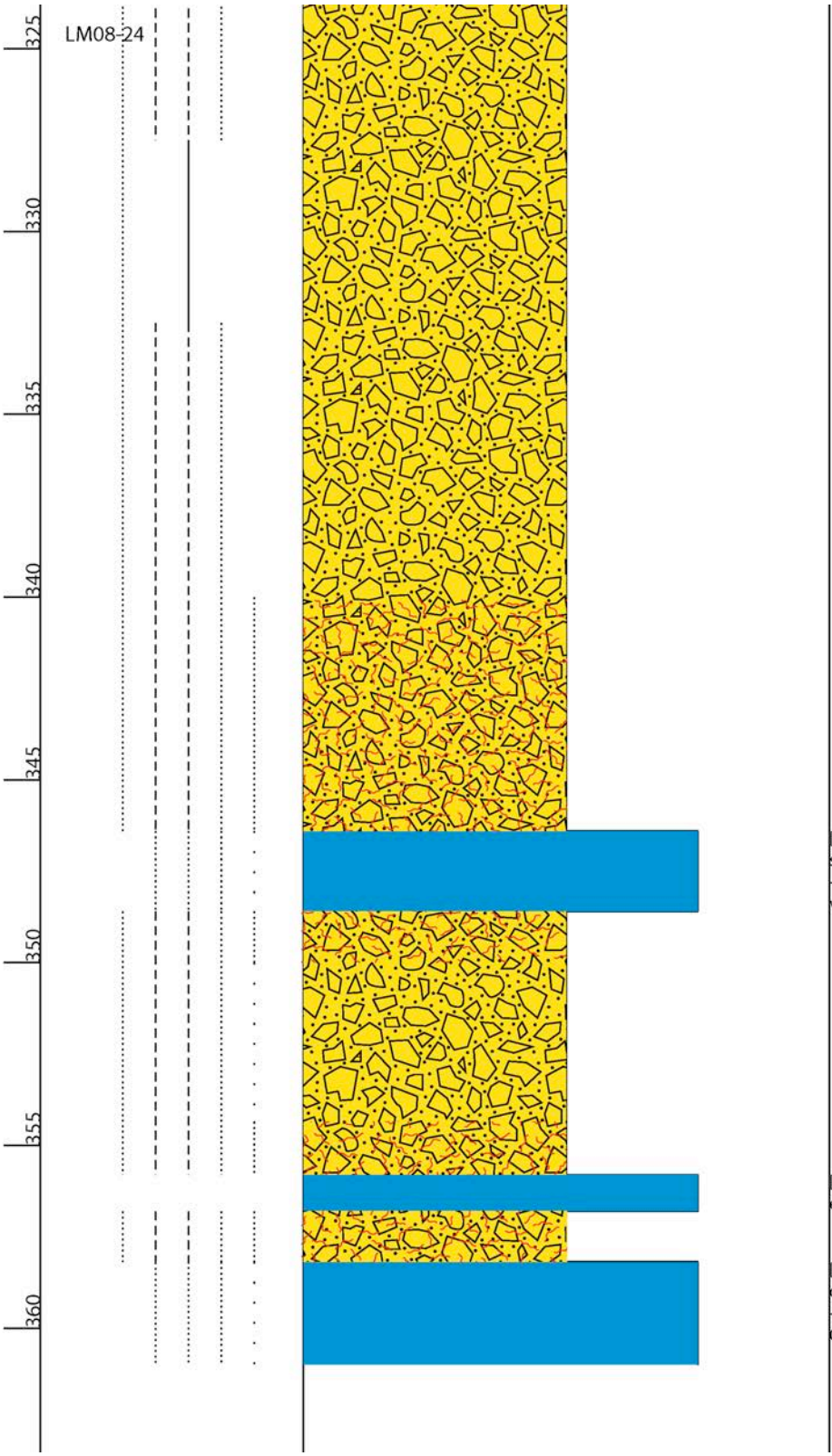
LM08-24
325
330
335
340
345
350
355
360
[346.4m - 348.6m] **Basalt Dyke**: sheared
-->Alt=chl-ser amygdules, CO3+Py veins, pyritic contacts
[255.8m - 356.8m] **Basalt Dyke** w/ entrained rhyolite blocks, >ser
[358.18m - 361.0m] **Basalt Dyke**: coarser grained
-->Alt=>chl, CO3 filled amygdules, CO3-qtz±Py veins

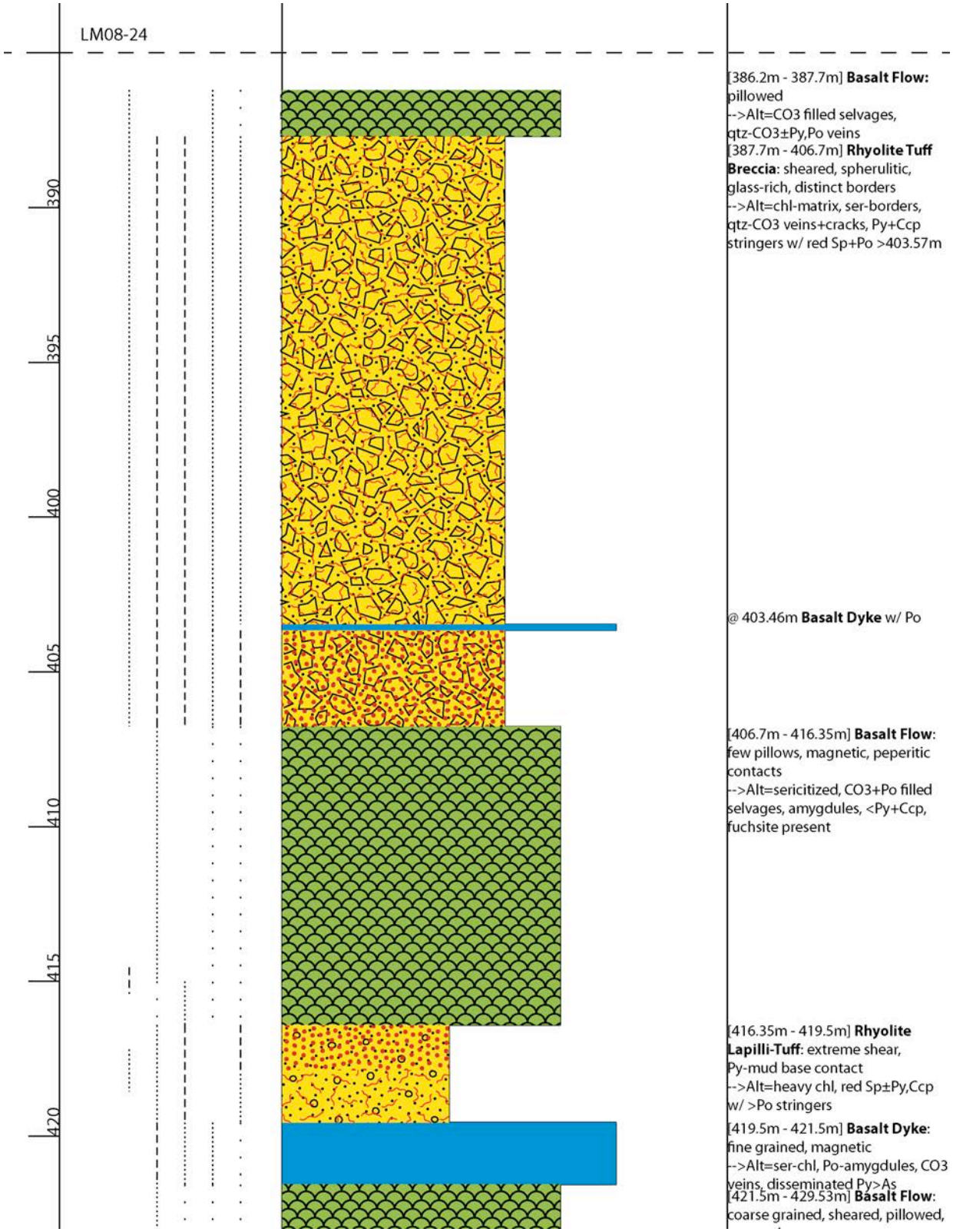

[386.2m - 387.7m] **Basalt Flow:** pillowed
-->Alt=CO3 filled selvages, qtz-CO3±Py,Po veins
[387.7m - 406.7m] **Rhyolite Tuff Breccia**: sheared, spherulitic, glass-rich, distinct borders
-->Alt=chl-matrix, ser-borders, qtz-CO3 veins+cracks, Py+Ccp stringers w/ red Sp+Po >403.57m

@ 403.46m **Basalt Dyke** w/ Po

[406.7m - 416.35m] **Basalt Flow**: few pillows, magnetic, peperitic contacts
-->Alt=sericitized, CO3+Po filled selvages, amygdules, <Py+Ccp, fuchsite present

[416.35m - 419.5m] **Rhyolite Lapilli-Tuff**: extreme shear, Py-mud base contact
-->Alt=heavy chl, red Sp±Py,Ccp w/ >Po stringers

[419.5m - 421.5m] **Basalt Dyke**: fine grained, magnetic
-->Alt=ser-chl, Po-amygdules, CO3 veins, disseminated Py>As

[421.5m - 429.53m] **Basalt Flow**: coarse grained, sheared, pillowed,

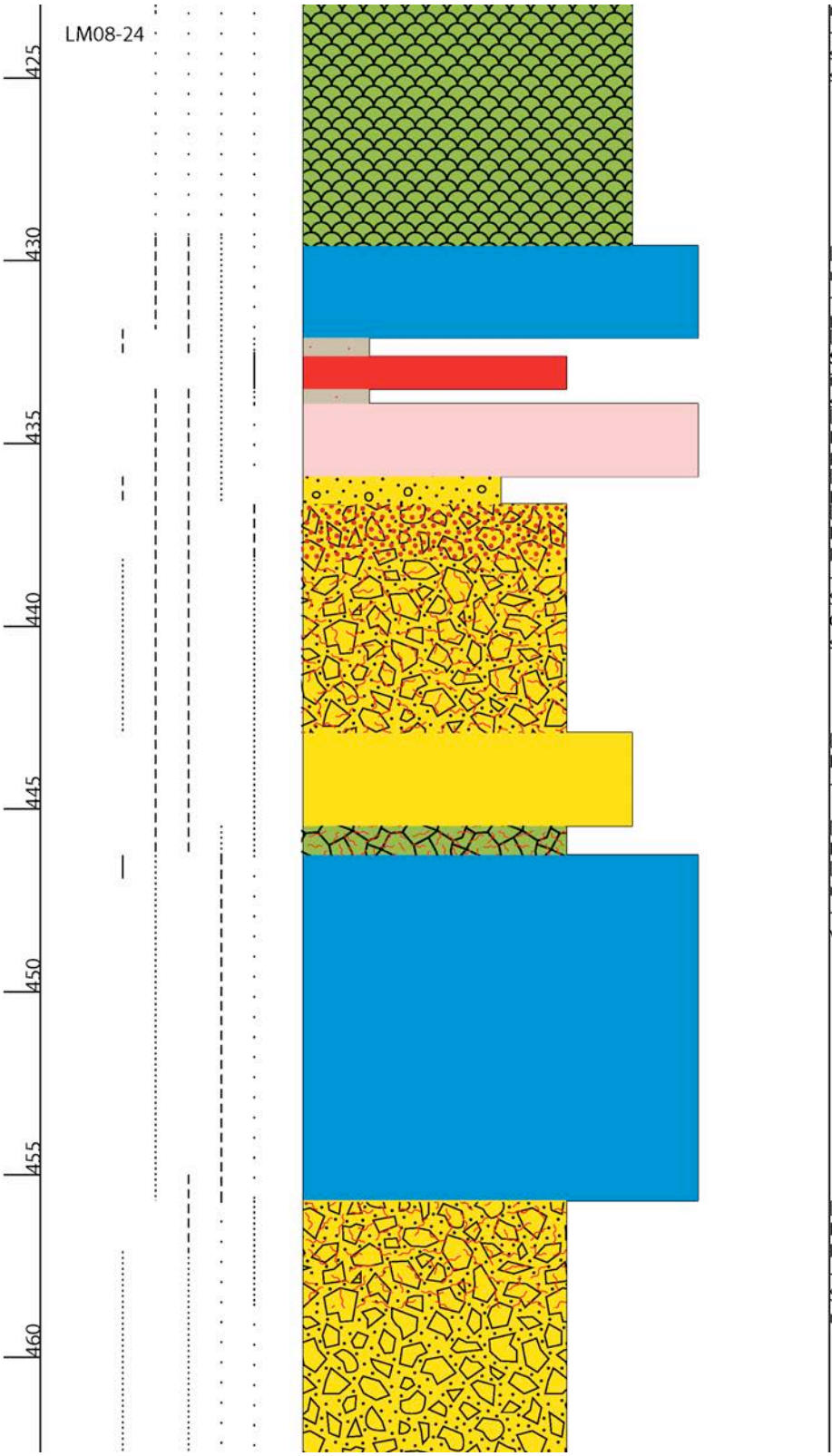

magnetic
-->Alt=chl-ser, CO3+Po±Py selvages, amygdules, leopard spotting

[429.53m - 432.05m] **Basalt Dyke**: magnetic
-->Alt=ser-chl, chl-Po+CO3 veins pyritohedrons

[432.56m - 433.55m] **Massive Sulfides**: red Sp+Gn+Py±Ccp,Po in rhyolite breccia w/ CO3 veins, sheared Py-Po-Mud at contacts

[433.95m - 435.94m] **Rhyolite Dyke** w/ CO3 veins, disseminated Py

[435.94m - 436.7m] **Rhyolite Lapilli-Tuff** w/ glass, CO3 veins

[436.7m - 442.95m] **Rhyolite Tuff Breccia**: glass-rich, distinct borders
-->Alt=ser-chl, SMS orange Sp+Ccp>Gn,Py±Brn then Ccp,Gn,As±Brn and Py+Sp stringers >438.2m

[442.95m - 445.5m] **Rhyolite Flow**: massive, banded
-->Alt=chl-ser, disseminated Py

[445.5m - 446.3m] **Brecciated Basalt Flow** w/ Sp,Py,Po stringers

[446.3m - 455.75m] **Basalt Dyke**: magnetic at contacts, sheared
-->Alt=leopard spotting, CO3-ser veins, Po-amygdules at contacts

[455.75m - 475.8m] **Rhyolite Lapilli Breccia**: glass-rich, diffuse block borders, spherulitic
-->Alt=chl-matrix, CO3 veins, red Sp+Py stringers <457.0m, disseminated Po overall

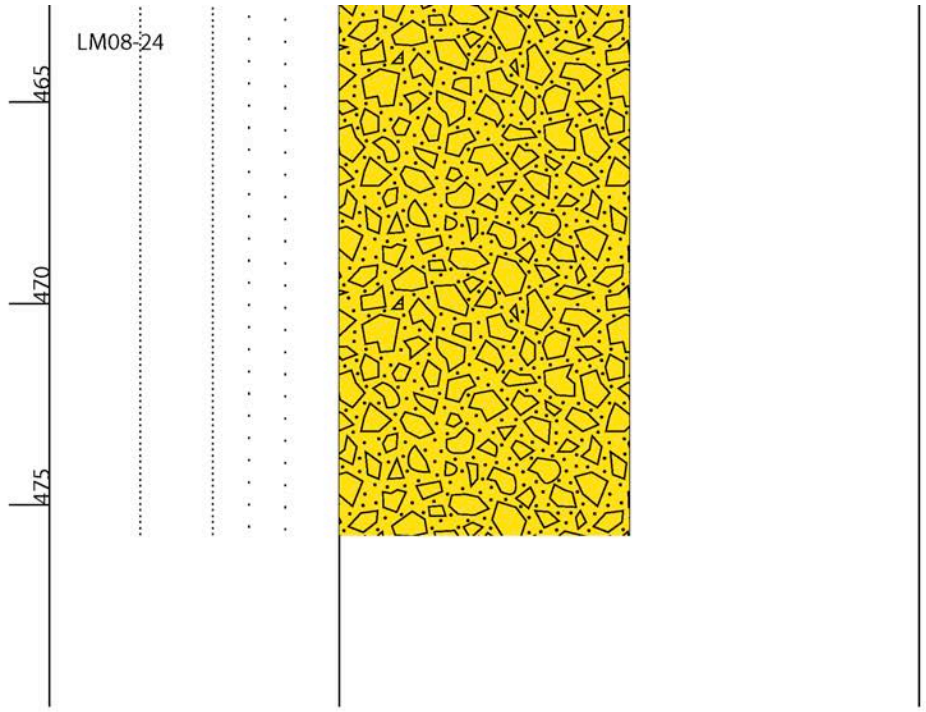
LM08-24
465
470
475

DIAMOND DRILL HOLE: LM08-28

Date: 07/25/2012

Claim: South Tally Pond

UTM: 520698.947E, 5375123.515N

Azimuth: 90°

Dip: -65°

EOH: 515.1m

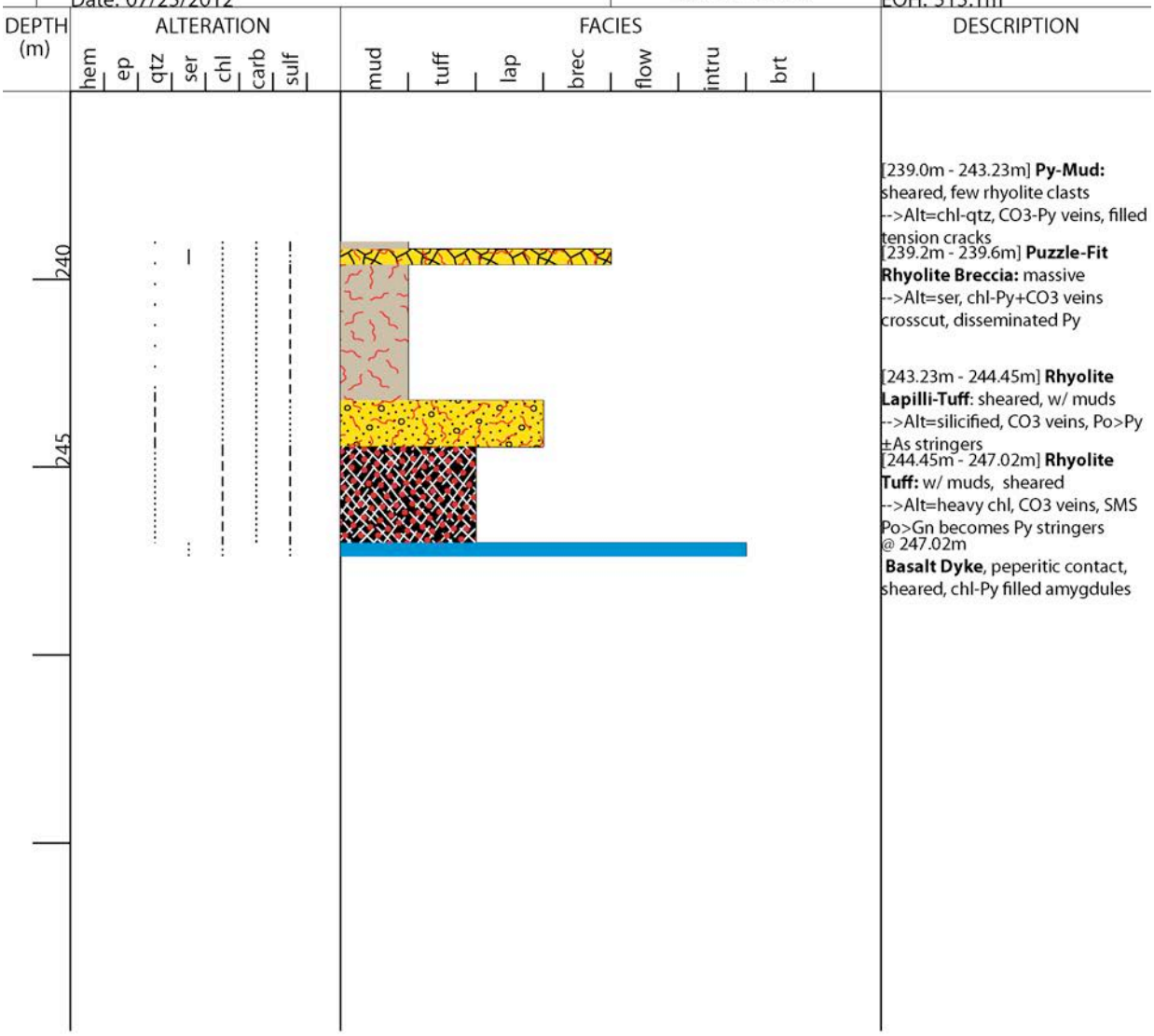

DESCRIPTION

[239.0m - 243.23m] **Py-Mud:** sheared, few rhyolite clasts
-->Alt=chl-qtz, CO3-Py veins, filled tension cracks

[239.2m - 239.6m] **Puzzle-Fit Rhyolite Breccia:** massive
-->Alt=ser, chl-Py+CO3 veins crosscut, disseminated Py

[243.23m - 244.45m] **Rhyolite Lapilli-Tuff**: sheared, w/ muds
-->Alt=silicified, CO3 veins, Po>Py ±As stringers

[244.45m - 247.02m] **Rhyolite Tuff:** w/ muds, sheared
-->Alt=heavy chl, CO3 veins, SMS Po>Gn becomes Py stringers

@ 247.02m
Basalt Dyke, peperitic contact, sheared, chl-Py filled amygdules

Claim: South Tally Pond

Azimuth: 90°

DIAMOND DRILL HOLE: LM08-29

UTM: 520698.52E, 5375123.424N

Dip: -73°

Date: 06-18-2013

EOH: 629m

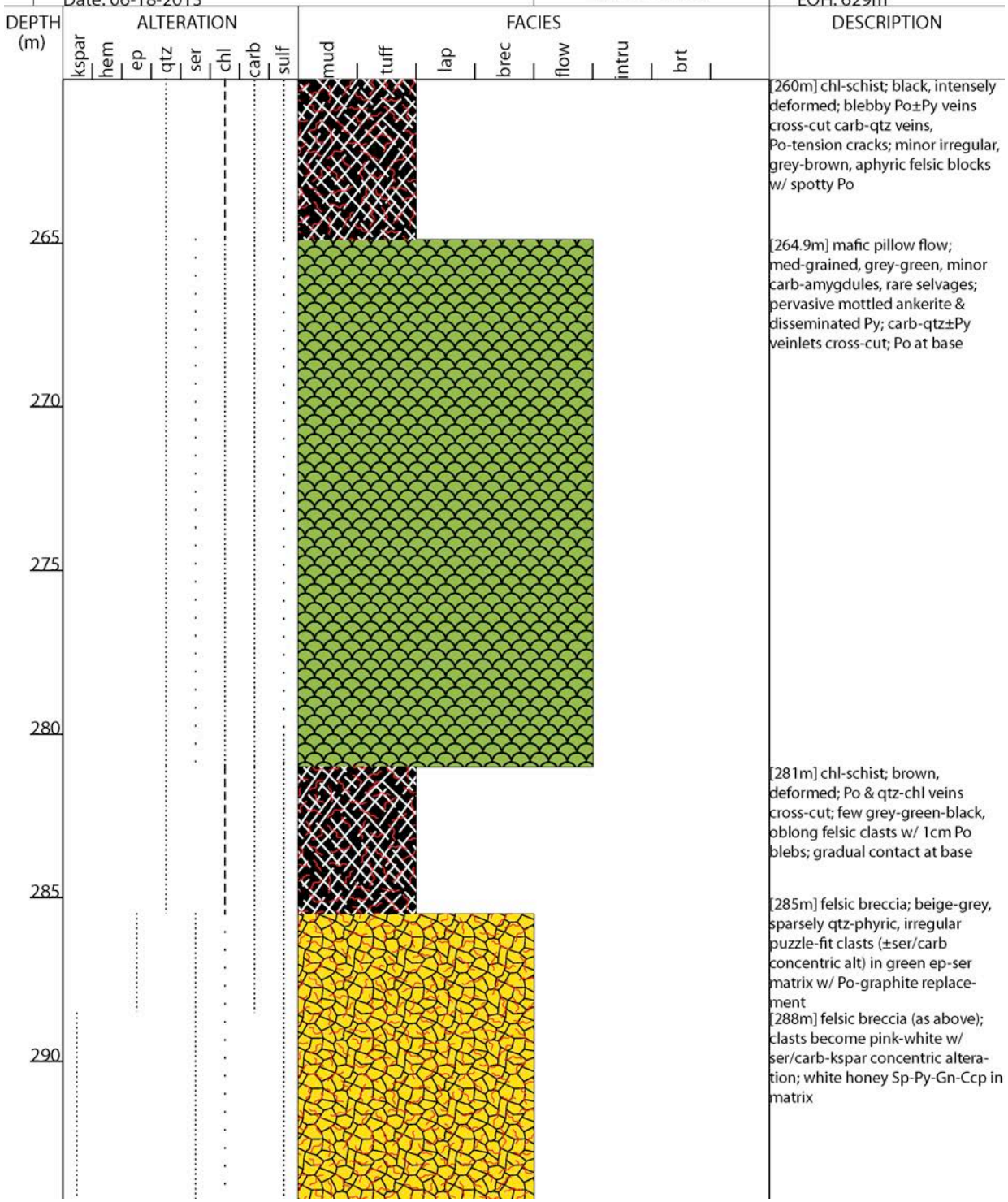

DESCRIPTION

[260m] chl-schist; black, intensely deformed; blebby Po±Py veins cross-cut carb-qtz veins, Po-tension cracks; minor irregular, grey-brown, aphyric felsic blocks w/ spotty Po

[264.9m] mafic pillow flow; med-grained, grey-green, minor carb-amygdules, rare selvages; pervasive mottled ankerite & disseminated Py; carb-qtz±Py veinlets cross-cut; Po at base

[281m] chl-schist; brown, deformed; Po & qtz-chl veins cross-cut; few grey-green-black, oblong felsic clasts w/ 1cm Po blebs; gradual contact at base

[285m] felsic breccia; beige-grey, sparsely qtz-phyric, irregular puzzle-fit clasts (±ser/carb concentric alt) in green ep-ser matrix w/ Po-graphite replacement

[288m] felsic breccia (as above); clasts become pink-white w/ ser/carb-kspar concentric alteration; white honey Sp-Py-Gn-Ccp in matrix

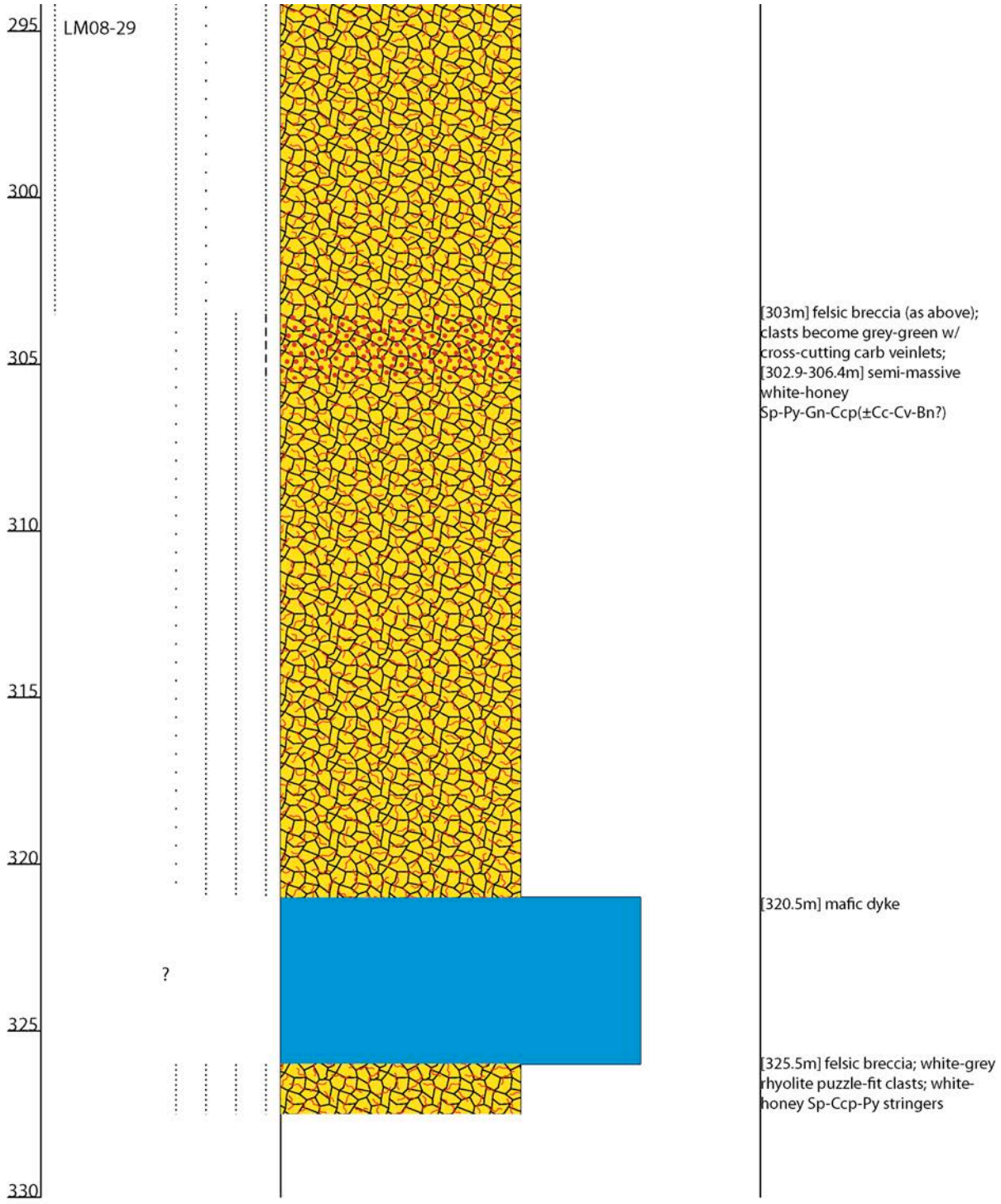
LM08-29
295
300
305
310
315
320
325
330
?
[303m] felsic breccia (as above); clasts become grey-green w/ cross-cutting carb veinlets; [302.9-306.4m] semi-massive white-honey Sp-Py-Gn-Ccp(±Cc-Cv-Bn?)
[320.5m] mafic dyke
[325.5m] felsic breccia; white-grey rhyolite puzzle-fit clasts; white-honey Sp-Ccp-Py stringers

DIAMOND DRILL HOLE: LM08-32

Date: 06-24-2013

Claim: South Tally Pond

UTM: 521063.845E, 5374699.945N

Azimuth: 270°

Dip: -56.5°

EOH: 518m

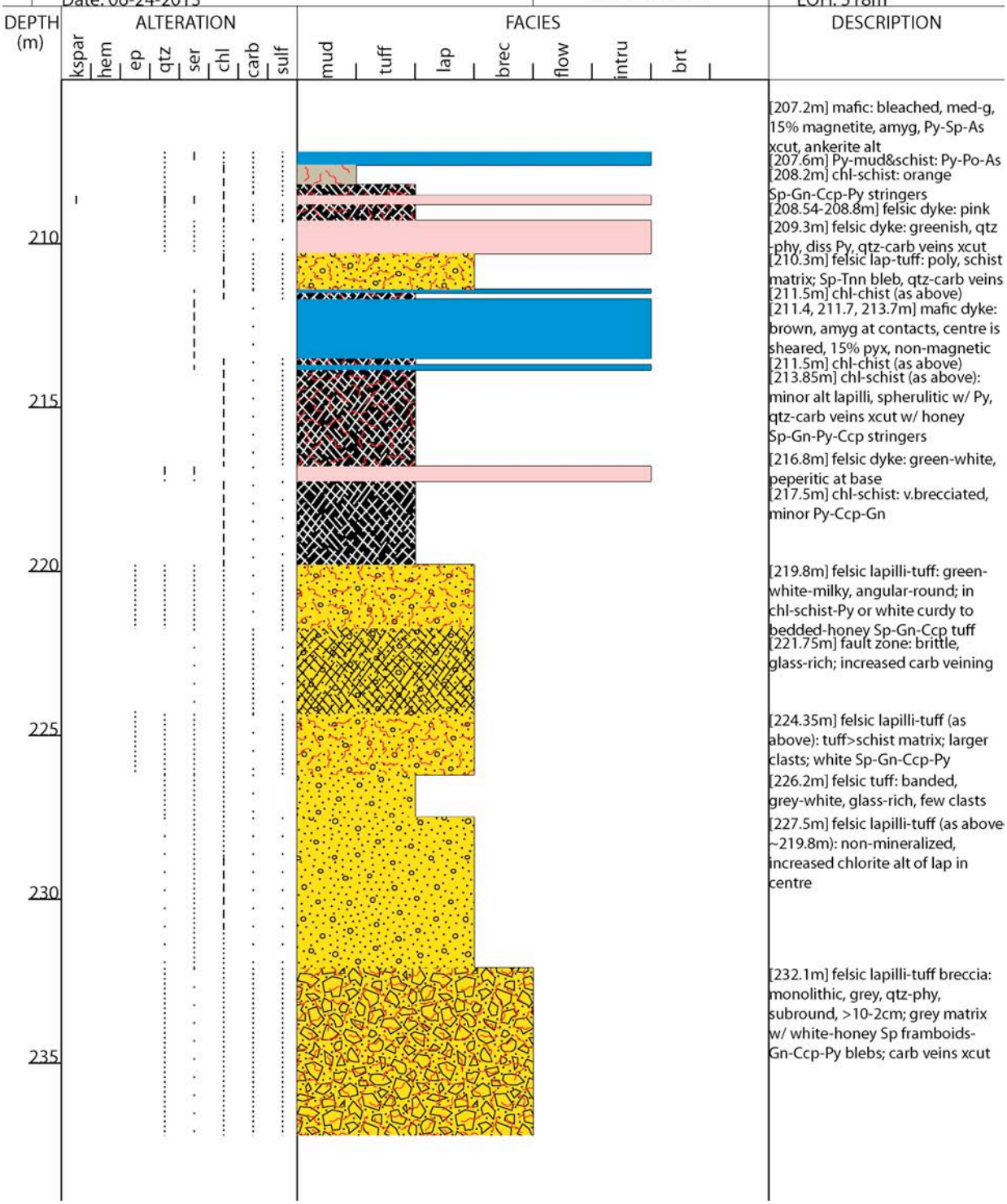

DESCRIPTION

[207.2m] mafic: bleached, med-g, 15% magnetite, amyg, Py-Sp-As xcut, ankerite alt

[207.6m] Py-mud&schist: Py-Po-As

[208.2m] chl-schist: orange Sp-Gn-Ccp-Py stringers

[208.54-208.8m] felsic dyke: pink

[209.3m] felsic dyke: greenish, qtz -phy, diss Py, qtz-carb veins xcut

[210.3m] felsic lap-tuff: poly, schist matrix; Sp-Tnn bleb, qtz-carb veins

[211.5m] chl-chist (as above)

[211.4, 211.7, 213.7m] mafic dyke: brown, amyg at contacts, centre is sheared, 15% pyx, non-magnetic

[211.5m] chl-chist (as above)

[213.85m] chl-schist (as above): minor alt lapilli, spherulitic w/ Py, qtz-carb veins xcut w/ honey Sp-Gn-Py-Ccp stringers

[216.8m] felsic dyke: green-white, peperitic at base

[217.5m] chl-schist: v.brecciated, minor Py-Ccp-Gn

[219.8m] felsic lapilli-tuff: green-white-milky, angular-round; in chl-schist-Py or white curdy to bedded-honey Sp-Gn-Ccp tuff

[221.75m] fault zone: brittle, glass-rich; increased carb veining

[224.35m] felsic lapilli-tuff (as above): tuff>schist matrix; larger clasts; white Sp-Gn-Ccp-Py

[226.2m] felsic tuff: banded, grey-white, glass-rich, few clasts

[227.5m] felsic lapilli-tuff (as above ~219.8m): non-mineralized, increased chlorite alt of lap in centre

[232.1m] felsic lapilli-tuff breccia: monolithic, grey, qtz-phy, subround, >10-2cm; grey matrix w/ white-honey Sp framboids-Gn-Ccp-Py blebs; carb veins xcut

DIAMOND DRILL HOLE: LM08-33

Date: 07/25/2012

Claim: South Tally Pond

UTM: 521071.611E, 5374804.028N

Azimuth: 270°

Dip: -50°

EOH: 341.0m

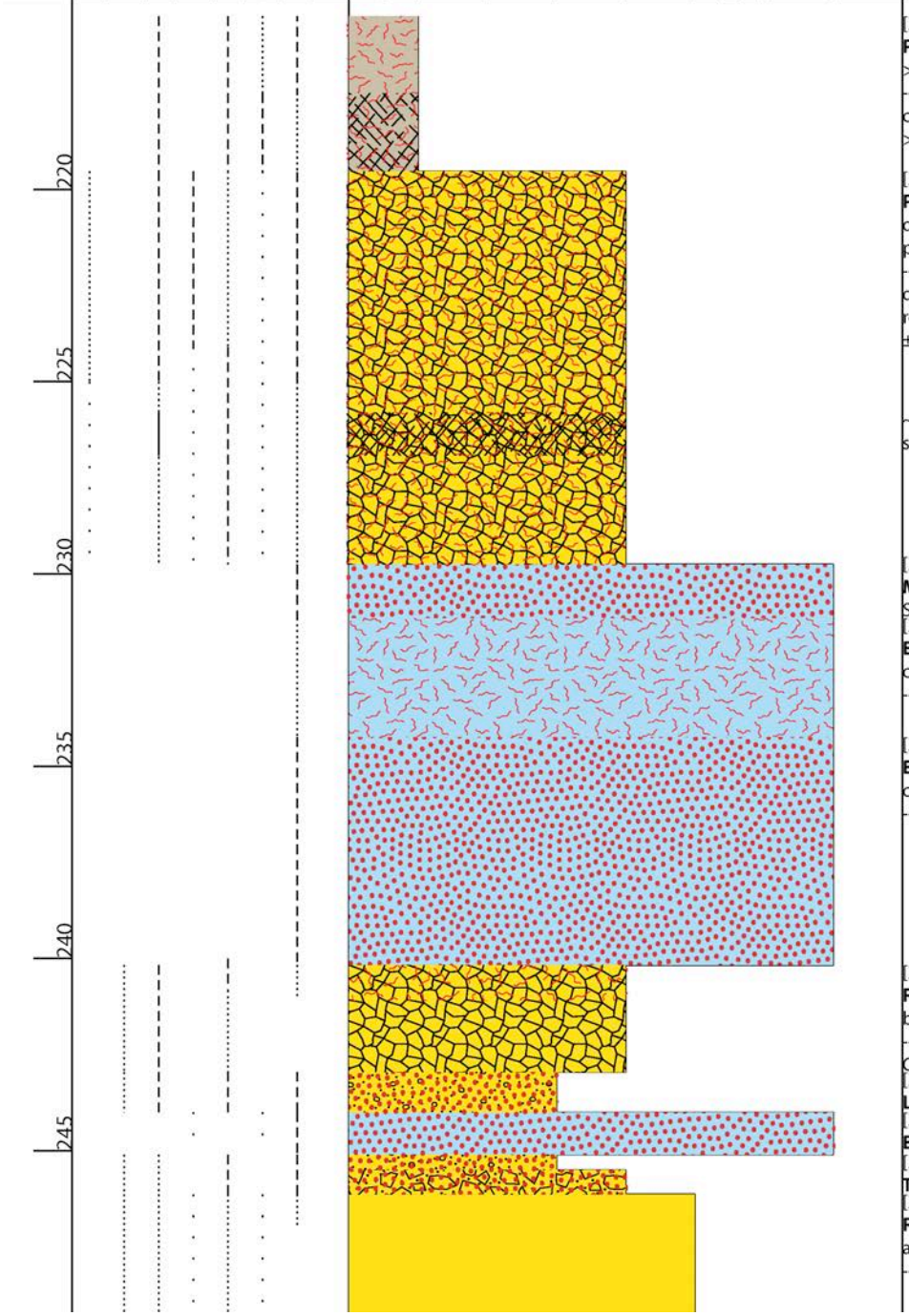

DESCRIPTION

[215.5m - 219.53m]
Py-Mud: sheared, tension cracks >217.3m, some entrained lapilli -->Alt=chl matrix, CO3 filled cracks, qtz veins Po>Py stringers >Ccp toward base

[219.53m - 229.75m]
Puzzle-Fit Rhyolite Breccia: distinct block borders, spherules present >223.6m -->Alt=ser to chl downhole, qtz-CO3 veins, minor jasperoid, red to orange Sp>Py+Ccp+Gn ±Ccp downhole

~226.0m
shear zone, brecciated, silicified

[229.75m - 231.16m] **SMS Massive Barite**: honey Sp+Gn±Py,Ccp,Brn
[231.16m - 234.24m] **SS Massive Barite**: white bladed in grey crystalline -->Alt=Py>Gn±Ccp,Brn stringers

[234.24m - 240.7m] **SMS Massive Barite**: variable 30% - 60%, chloritoids present -->Alt=>Ccp,Brn stringers

[240.7m - 242.95m] **Puzzle-Fit Rhyolite Breccia:** diffuse, rounded block borders, spherulitic -->Alt=qtz-chl veins, white Sp>Py, Ccp stringers until ~240.97m
[242.95m - 244.0m] **Rhyolite Lapilli-Tuff**:SMShoneySp+Py+Ccp
[244.0m - 245.1m] **SMS Massive Barite:** honey Sp+Gn+Py±Ccp
[245.1m - 246.13m] **Lapilli-Tuff** to **Tuff-Breccia**: (see above)
[246.13m - 250.9m] **Massive Rhyolite Flow**: aphyric, brecciated, spherulitic -->Alt=qtz-CO3 veins crosscut

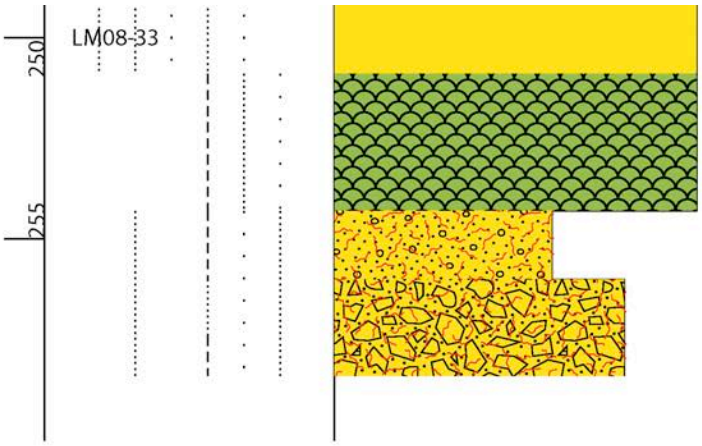

[250.9m - 254.3m] **Basaltic Flow**: pillowed, hyaloclastic flow tops
-->Alt=heavy chl, CO3-filled selvages, amygdules, disseminated Py

[254.3m - 256.0m] **Rhyolite Lapilli-Tuff:** sheared
-->Alt=qtz-chl, Py±Ccp stringers

[256.0m - 258.4m] **Rhyolite Tuff Breccia:** distinct to diffuse block borders downhole
-->Alt=chl matrix, CO3+Py veins

DIAMOND DRILL HOLE: LM08-37

Date: 07/17/2012

Claim: South Tally Pond

UTM: 520599.349E, 5375124.037N

Azimuth: 80°

Dip: -80°

EOH: 434.0m

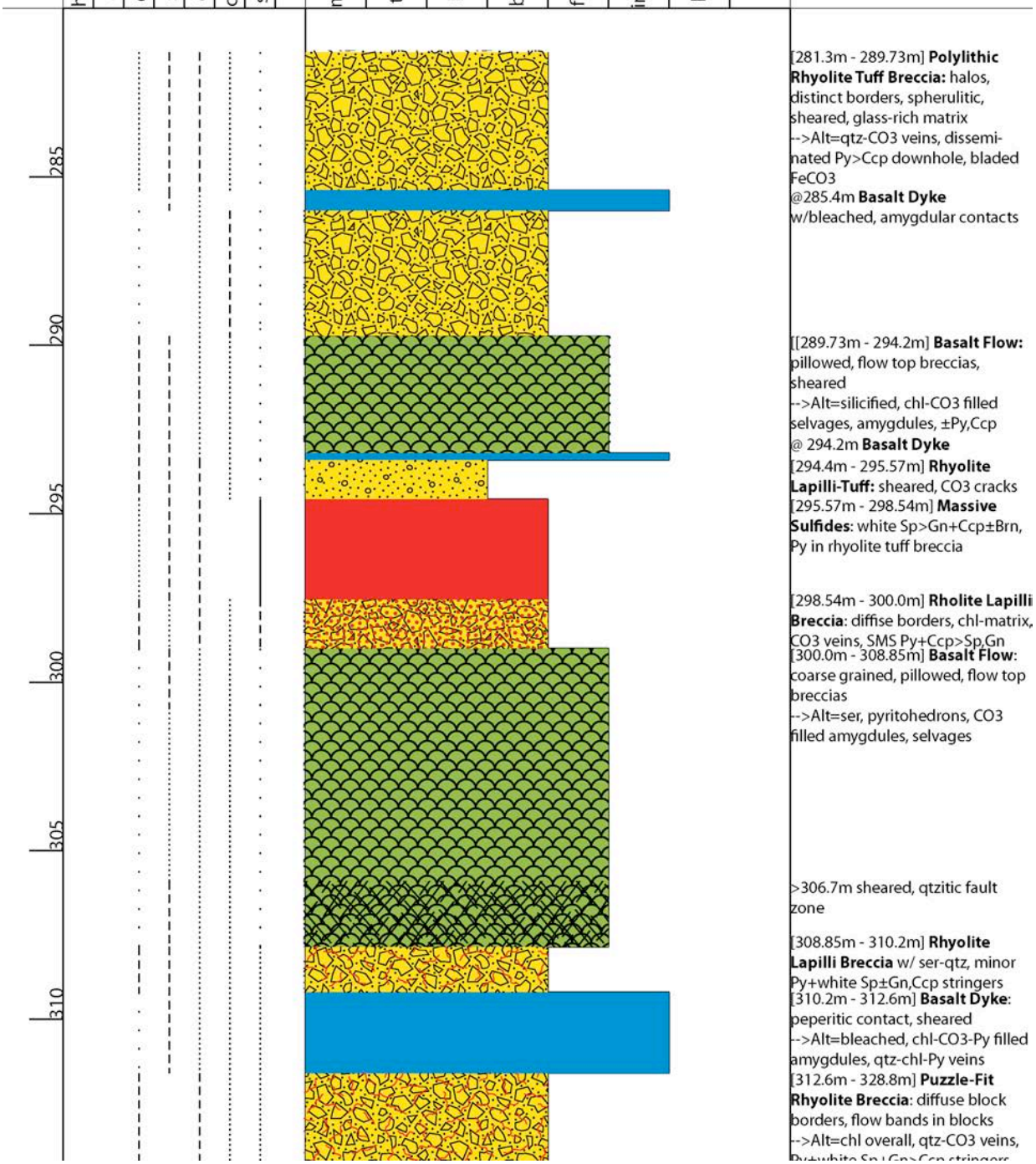

[281.3m - 289.73m] **Polylithic Rhyolite Tuff Breccia:** halos, distinct borders, spherulitic, sheared, glass-rich matrix
-->Alt=qtz-CO3 veins, disseminated Py>Ccp downhole, bladed FeCO3
@285.4m **Basalt Dyke** w/bleached, amygdular contacts

[[289.73m - 294.2m] **Basalt Flow:** pillowed, flow top breccias, sheared
-->Alt=silicified, chl-CO3 filled selvages, amygdules, ±Py,Ccp
@ 294.2m **Basalt Dyke**
[294.4m - 295.57m] **Rhyolite Lapilli-Tuff:** sheared, CO3 cracks
[295.57m - 298.54m] **Massive Sulfides**: white Sp>Gn+Ccp±Brn, Py in rhyolite tuff breccia

[298.54m - 300.0m] **Rholite Lapilli Breccia**: diffise borders, chl-matrix, CO3 veins, SMS Py+Ccp>Sp,Gn
[300.0m - 308.85m] **Basalt Flow**: coarse grained, pillowed, flow top breccias
-->Alt=ser, pyritohedrons, CO3 filled amygdules, selvages

>306.7m sheared, qtzitic fault zone

[308.85m - 310.2m] **Rhyolite Lapilli Breccia** w/ ser-qtz, minor Py+white Sp±Gn,Ccp stringers
[310.2m - 312.6m] **Basalt Dyke**: peperitic contact, sheared
-->Alt=bleached, chl-CO3-Py filled amygdules, qtz-chl-Py veins
[312.6m - 328.8m] **Puzzle-Fit Rhyolite Breccia**: diffuse block borders, flow bands in blocks
-->Alt=chl overall, qtz-CO3 veins, Py+white Sp±Gn>Ccp stringers

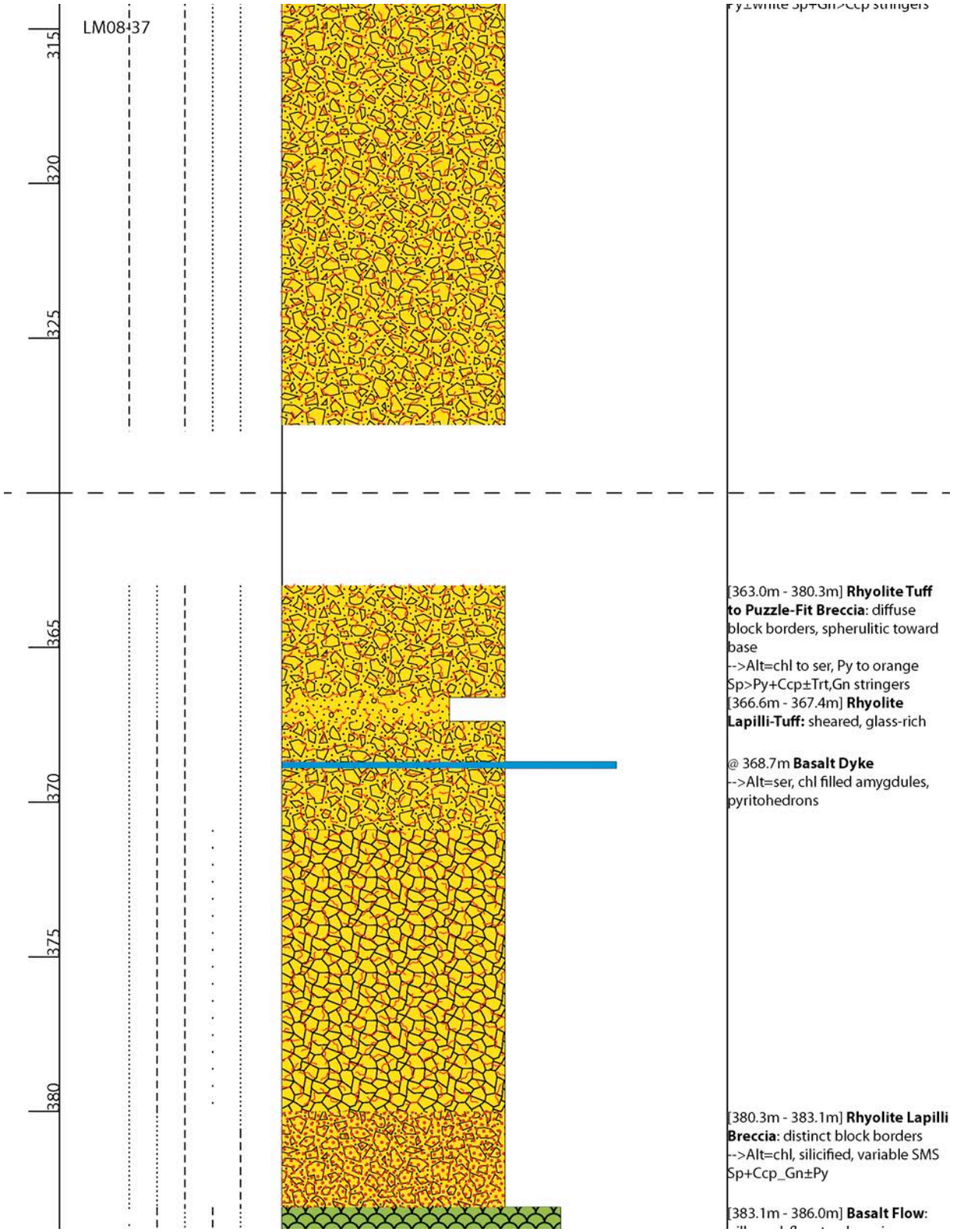
LM08-37
315
320
325
365
370
375
380
Py±white Sp+Gn>Ccp stringers
[363.0m - 380.3m] **Rhyolite Tuff to Puzzle-Fit Breccia**: diffuse block borders, spherulitic toward base
-->Alt=chl to ser, Py to orange Sp>Py+Ccp±Trt,Gn stringers
[366.6m - 367.4m] **Rhyolite Lapilli-Tuff:** sheared, glass-rich
@ 368.7m **Basalt Dyke**
-->Alt=ser, chl filled amygdules, pyritohedrons
[380.3m - 383.1m] **Rhyolite Lapilli Breccia**: distinct block borders
-->Alt=chl, silicified, variable SMS Sp+Ccp_Gn±Py
[383.1m - 386.0m] **Basalt Flow**:

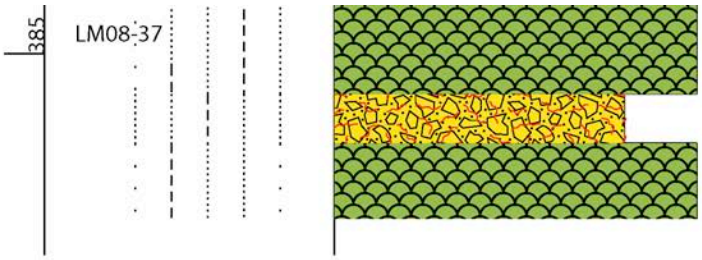

pillowed, flow top breccias, peperitic contacts -->Alt=ser, chl-CO3 filled amygdules, selvages, pyritohedrons [386.0m - 387.22m] **Rhyolite Lapilli Breccia**: sheared, CO3+red Sp+Py>Ccp,Brn±Gn stringers [387.22m - 389.1m] **Basalt Flow**: (as above) w/ minor Py

Claim: South Tally Pond

Azimuth: 270°

DIAMOND DRILL HOLE: LM08-39

UTM: 521150.722E, 5374481.035N

Dip: -45°

Date: 07/27/2012

EOH: 358m

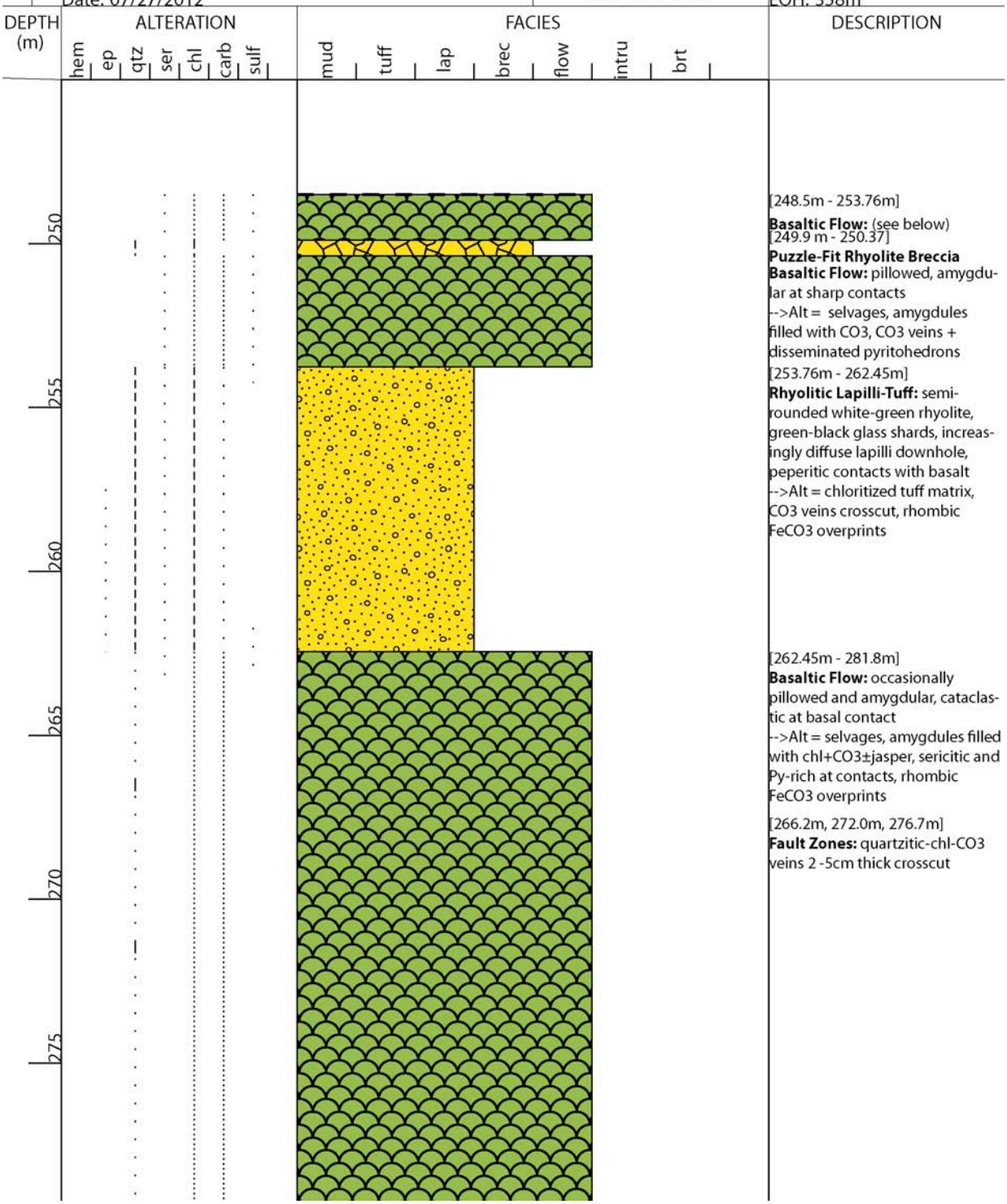

[248.5m - 253.76m]

Basaltic Flow: (see below)

[249.9 m - 250.37]

Puzzle-Fit Rhyolite Breccia

Basaltic Flow: pillowed, amygdular at sharp contacts

-->Alt = selvages, amygdules filled with CO_3, CO_3 veins + disseminated pyritohedrons

[253.76m - 262.45m]

Rhyolitic Lapilli-Tuff: semi-rounded white-green rhyolite, green-black glass shards, increasingly diffuse lapilli downhole, peperitic contacts with basalt

-->Alt = chloritized tuff matrix, CO_3 veins crosscut, rhombic $FeCO_3$ overprints

[262.45m - 281.8m]

Basaltic Flow: occasionally pillowed and amygdular, cataclastic at basal contact

-->Alt = selvages, amygdules filled with chl+CO_3±jasper, sericitic and Py-rich at contacts, rhombic $FeCO_3$ overprints

[266.2m, 272.0m, 276.7m]

Fault Zones: quartzitic-chl-CO_3 veins 2 -5cm thick crosscut

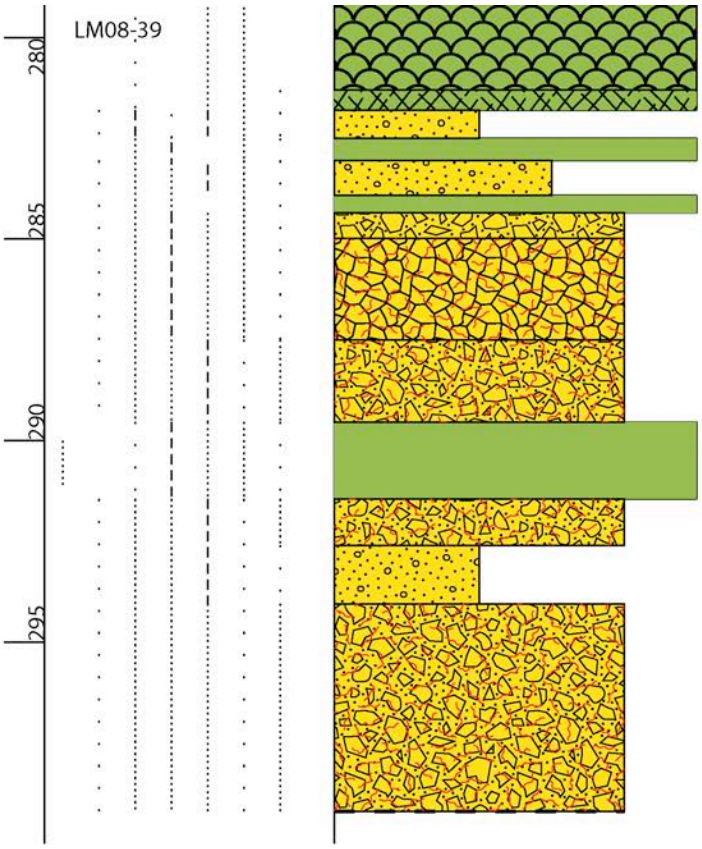

[281.8m - 282.5m] **Rhyolite Tuff**
[282.5m - 283.05m] **Basalt Dyke**

[283.05m - 283.92] **Lapilli-Tuff**

[283.92m - 284.35m] **Basalt Dyke**
[284.35m - 289.54m]
Lapilli-Tuff Breccia: semi-rounded rhyolite clasts in lapilli-tuff with midsection of puzzle-fit breccia
-->Alt = quartz-CO3 veins cross-cut, bladed FeCO3 overprint toward base, Py>Ccp.Gn±Brn,Trt stringers interstitial
[289.54m - 291.45m]
Basalt Dyke: vesicular contacts
-->Alt = qtz-CO3 veins, Py-hedron
[291.45m - 292.6m]
Lapilli-Tuff Breccia: (see above)
[292.6m - 294.15]
Rhyolite Tuff: FeCO3 veins, diss Py

[294.15m - 299.3m]
Tuff Breccia: semi-rounded rhyolite blocks, Fe-chl tuff±lapilli matrix
-->Alt = CO3 veins, rhombic FeCO3 overprints, minor Py±Ccp±Gn stringers
[292.6m, 298.85m]
Fault Zones: quartzitic-CO3 veins

DIAMOND DRILL HOLE: LM10-43

Date: 07/19/2012

Claim: South Tally Pond

UTM: 521098.653E, 5374752.731N

Azimuth: 270°

Dip: -65°

EOH: 318.8m

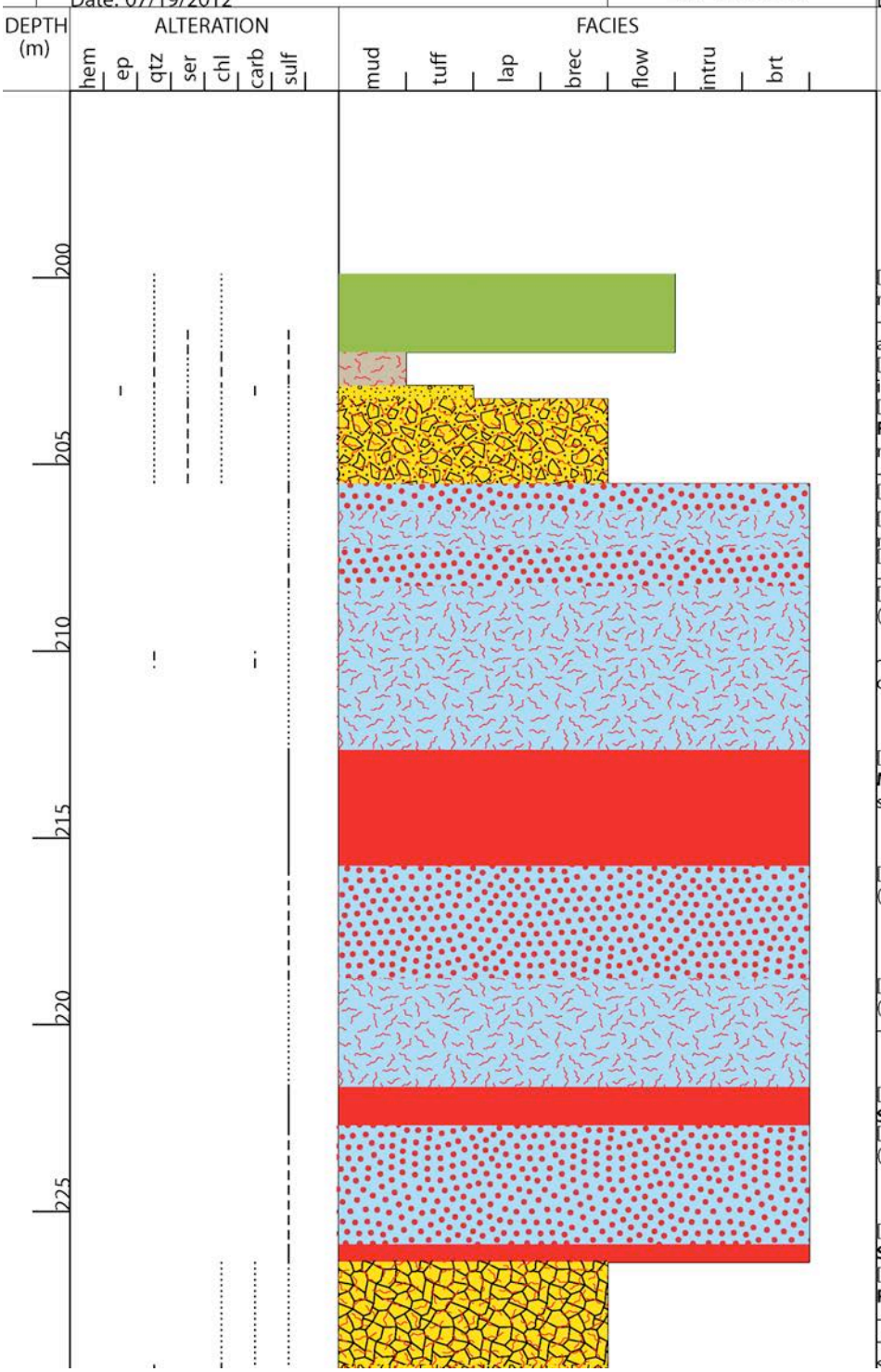

DESCRIPTION

[199.9m - 202m] **Basaltic Flow**: magnetic at base, sheared
-->Alt=qtz-chl±Po amygdules, albitic leopard spotting, ±fuchsite
[202m - 203.25m] **Py-Muds** grade into epidote-rich **Rhyolite Tuff**
[203.25m - 205.52m] **Rhyolite Tuff Breccia:** sheared matrix
-->Alt=kspar, Py+Sp+Gn stringers
[205.52m - 206.25m] **SMS Barite**
[206.25m - 207.25m] **SS Barite:** massive crystalline ± lathes
[207.25m - 208.25m] **SMS Barite:**
-->Alt=Gn+Py+Ccp±Brn,honey Sp
[208.25m - 212.65m] **SS Barite:** (see sbove)

~210.45m: rhyolitic intrusion also cut by stringers

[212.65m - 215.75m] **Massive Sulfides:** >Ccp+Brn, Sp still minor, chloritoids present

[215.75m - 218.75m] **SMS Barite:** (see above)

[218.75m - 221.66m] **SS Barite:** (see above)
-->Alt=visible gold present

[221.66m - 222.7m] **Massive Sulfides:** (see above)
[222.7m - 225.87m] **SMS Barite:** (see above)

[225.87m - 226.35m] **Massive Sulfides:** >honey Sp abundance
[226.35m - 229.85m] **Puzzle-Fit Rhyolite Breccia** to **Tuff Breccia:**
-->Alt=heavy chl-block borders, -matrix, honey Sp+Py+Ccp stringers

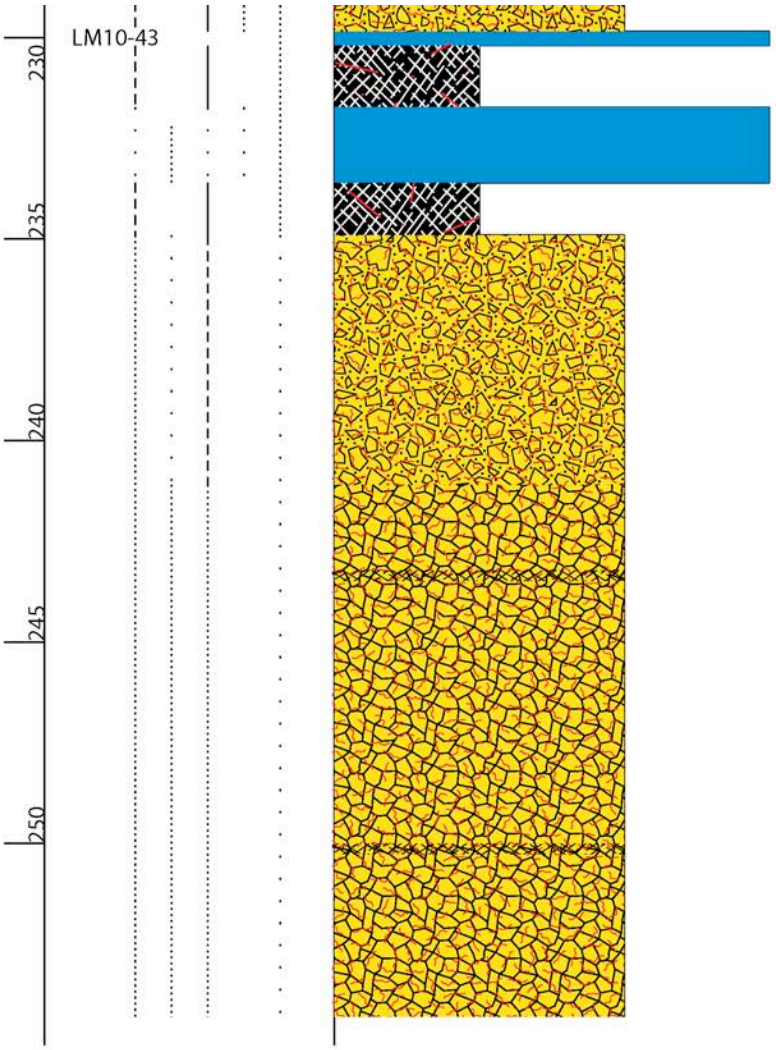

[229.85m - 230.2m] **Basalt Dyke**
[230.2m - 231.73m] **Rhyolite Tuff**
-->Alt=heavy chl, honey
Sp+Py+Ccp stringers, qtz veins
[231.73m - 233.6m] **Basalt Dyke:**
grades brown to green
-->Alt=qtz-CO3 veins, chl-FeCO3 filled amygdules
[233.6m - 234.9m] **Rhyolite Tuff**:
(see above)
[234.9m - 241.1m]
Rhyolite Tuff Breccia: diffuse block borders, sheared matrix
-->Alt=heavy chl-matrix, orange Sp,Py±Ccp,Trt stringers occasional

[241.1m - 254.3m]
Puzzle-Fit Rhyolite Breccia:
distinct block outlines, cataclastite ~ 235.5m, 250.3m
-->Alt= >sericitic, qtz veins crosscut, occasional stringers (above)

DIAMOND DRILL HOLE: LM10-46

Date: 06-27-2013

Claim: South Tally Pond

UTM: 521116.929E, 5374600.137N

Azimuth: 270°

Dip: -55°

EOH: 265.8m

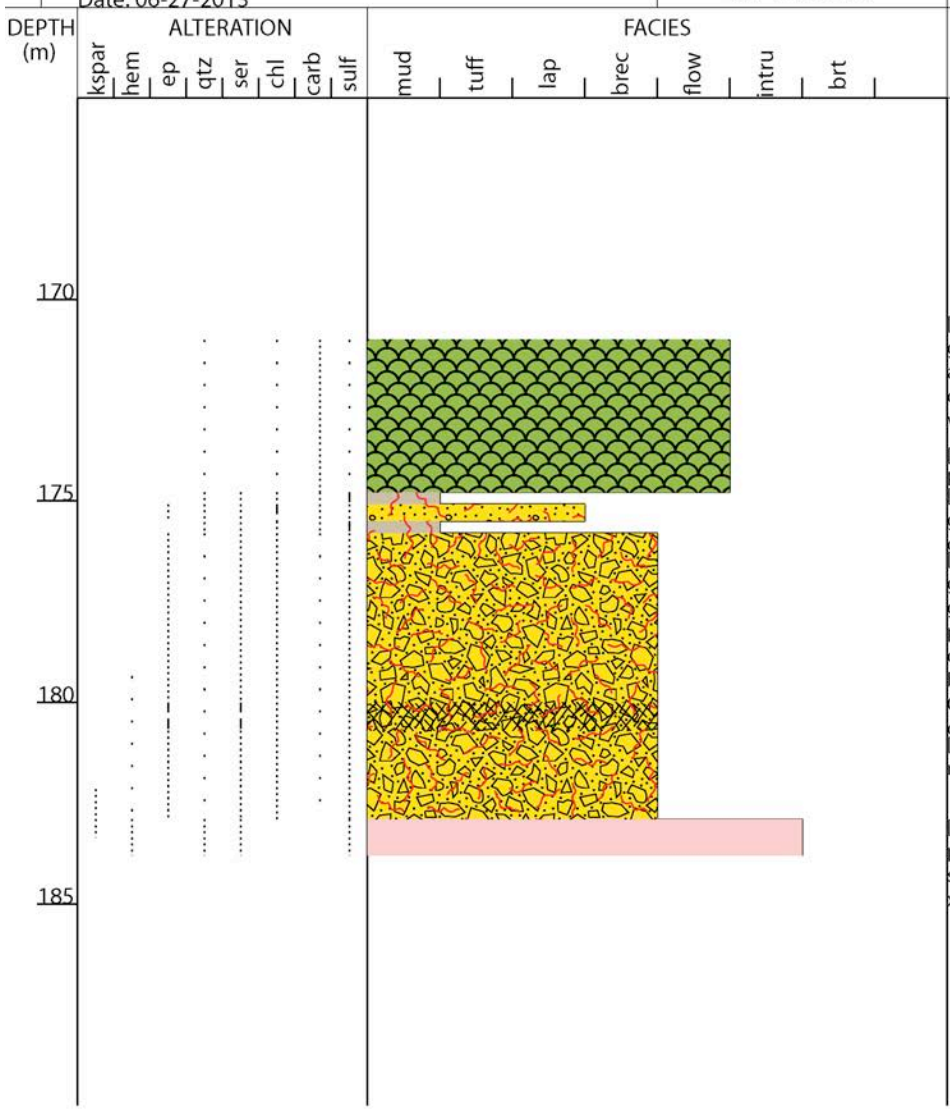

[171m] mafic pillow flow: dk grey-green, pyx, disseminated Py, ankerite alt @selvs, minor amyg, coarse Py @base, extensive carb veining

[174.78m] Py-mud&lap-tuff:coarse Py-qtz-carb veins ass w/ poly

[175.08-175.5m] felsic lap-tuff: dk grey matrix; green-white, irreg, qtz-phy; Py-orange Sp; spherulitic

[175.8m] felsic lap-tuff breccia: green-grey matrix; poly grey-green-milky lap; green-milky to pink, qtz-phy, grey to white concentric alt, <15cm, round blocks; orange Sp-Py-Gn to brt-Ccp-bearing to white-honey Sp; qtz-hematite veining at base

[180-180.7m] fault zone: clay-rich, mineralized

[182.9m] felsic dyke (massive?): peperitic top, pink-red, aphyric, spherulitic; minor sulf veinlets xcut

DIAMOND DRILL HOLE: LM10-48

Date: 07-26-2013

Claim: South Tally Pond

UTM: 521069.508E, 5375010.024N

Azimuth: 270°

Dip: -76°

EOH: 541.3m

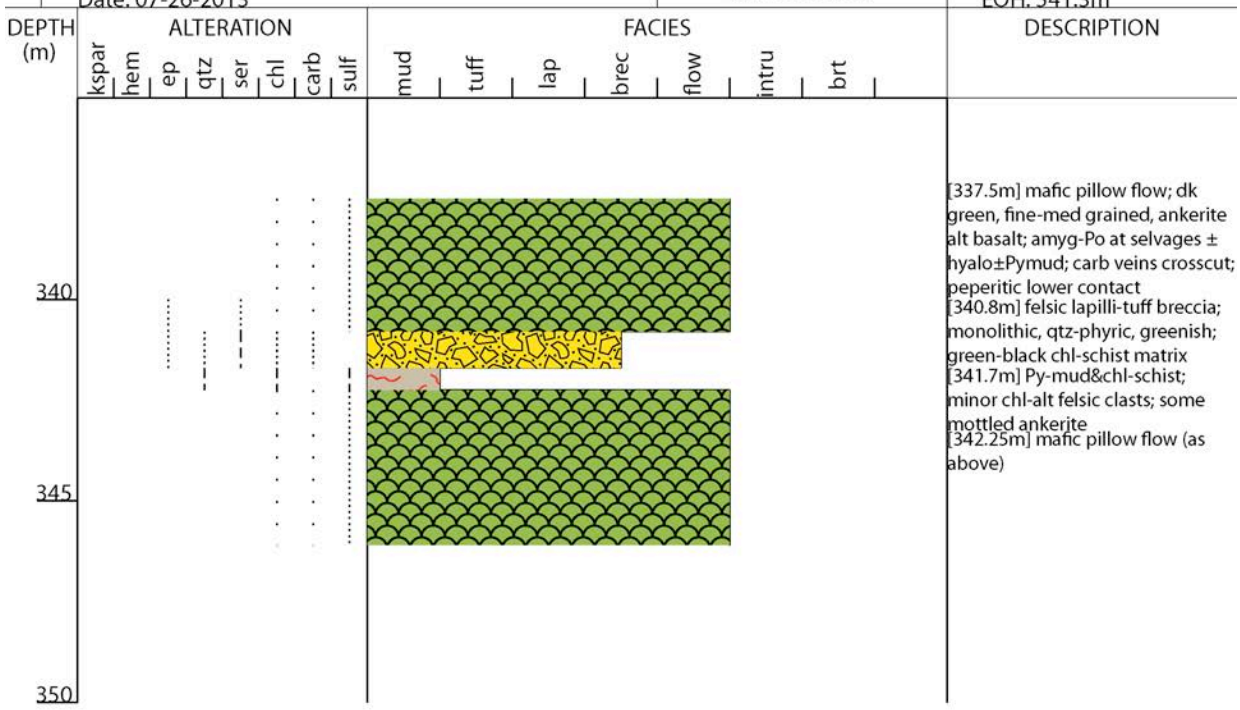

DESCRIPTION

[337.5m] mafic pillow flow; dk green, fine-med grained, ankerite alt basalt; amyg-Po at selvages ± hyalo±Pymud; carb veins crosscut; peperitic lower contact

[340.8m] felsic lapilli-tuff breccia; monolithic, qtz-phyric, greenish; green-black chl-schist matrix

[341.7m] Py-mud&chl-schist; minor chl-alt felsic clasts; some mottled ankerite

[342.25m] mafic pillow flow (as above)

Claim: South Tally Pond | Azimuth: 270°

DIAMOND DRILL HOLE: LM11-52 | UTM: 521062.781E, 5374749.616N | Dip: -62°

Date: 06-21-2013 | EOH: 318.8m

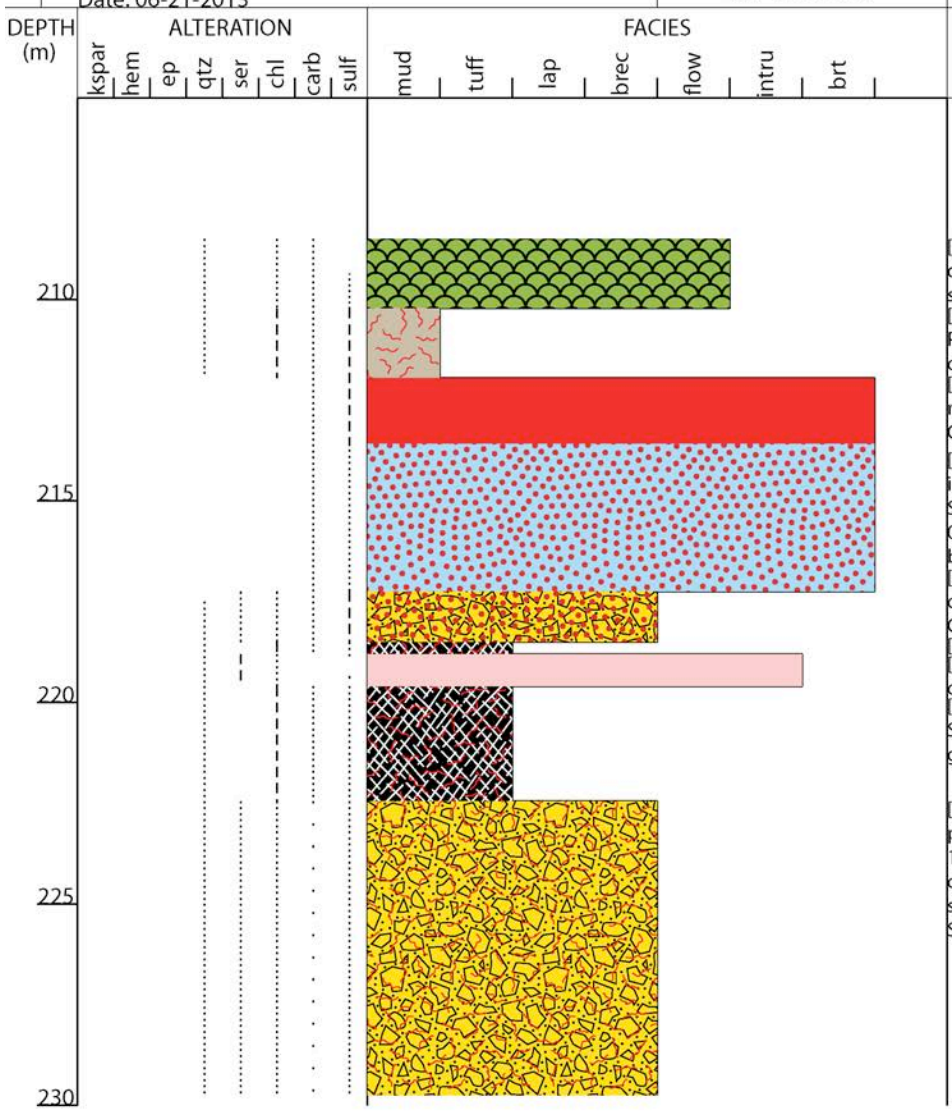

DESCRIPTION

[208.5m] mafic pillow flow: fine-g, dk green, ankerite alt, black amyg, selvages; sheared w/ Po at base

[210.22m] Py-mud&chl-schist: Po-top, coarse-Py w/ schist, ccp & qtz veins xcut at base

[211.95m] MB w/ MS/SMS: grades red-orange-honey-white Sp-Gn-Ccp-Py-Tnn

[~213m] MB w/ SMS: massive & intermittent bladed brt; Gn-white Sp xcut by Tnn-Bn veinlets ± 0.5-2mm free Au; Py veinlets at base

[217.25m] felsic breccia; grey, qtz-phy, spherulitic; white Sp-Py-Ccp-Gn to honey/black Sp, no Gn

[218.5m] chl-schist (see below)

[218.8m] felsic dyke: bleached, qtz-phy, spherulitic, sheared top

[219.6m] chl-schist: streaky orange Sp-Py-Ccp; carb-qtz veins xcut; graded bottom contact

[222.45m] felsic lapilli-tuff breccia: poly, grey-green-white, irreg, 1-5cm, slightly qtz-phy, some concentric alt; banded tuff; sk-grey matrix w/ honey-b Sp-Py-Ccp; qtz-carb veinlets xcut

Claim: South Tally Pond

Azimuth: 270°

DIAMOND DRILL HOLE: LM11-53

UTM: 521115.694E, 5374648.018N

Dip: -65°

Date: 07/24/2012

EOH: 297.8m

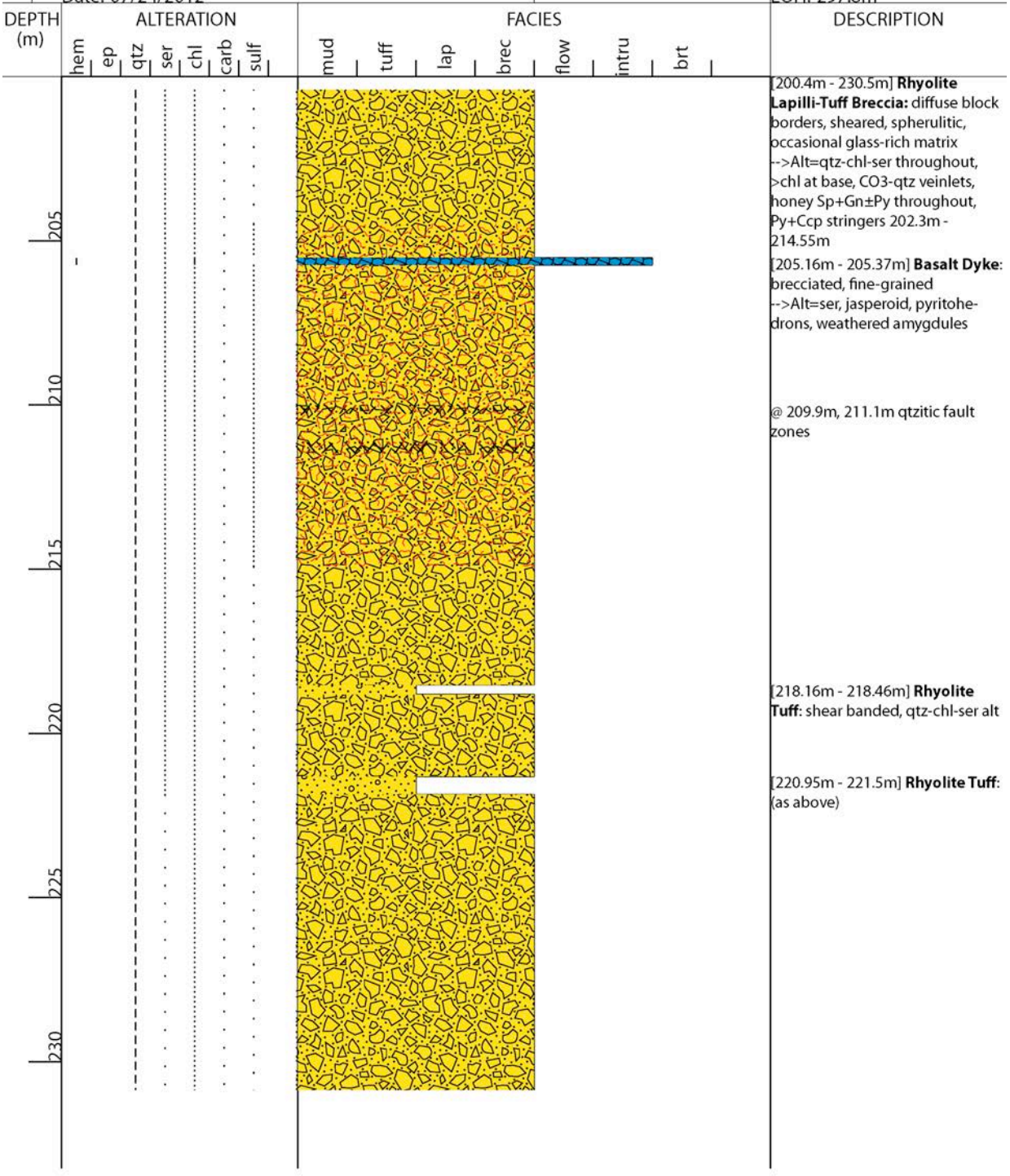

DESCRIPTION

[200.4m - 230.5m] **Rhyolite Lapilli-Tuff Breccia:** diffuse block borders, sheared, spherulitic, occasional glass-rich matrix -->Alt=qtz-chl-ser throughout, >chl at base, CO3-qtz veinlets, honey Sp+Gn±Py throughout, Py+Ccp stringers 202.3m - 214.55m

[205.16m - 205.37m] **Basalt Dyke**: brecciated, fine-grained -->Alt=ser, jasperoid, pyritohedrons, weathered amygdules

@ 209.9m, 211.1m qtzitic fault zones

[218.16m - 218.46m] **Rhyolite Tuff**: shear banded, qtz-chl-ser alt

[220.95m - 221.5m] **Rhyolite Tuff**: (as above)

DIAMOND DRILL HOLE: LM11-54

Date: 07/17/2012

Claim: South Tally Pond

UTM: 521117.291E, 5374670.484N

Azimuth: 270°

Dip: -65°

EOH: 279.5m

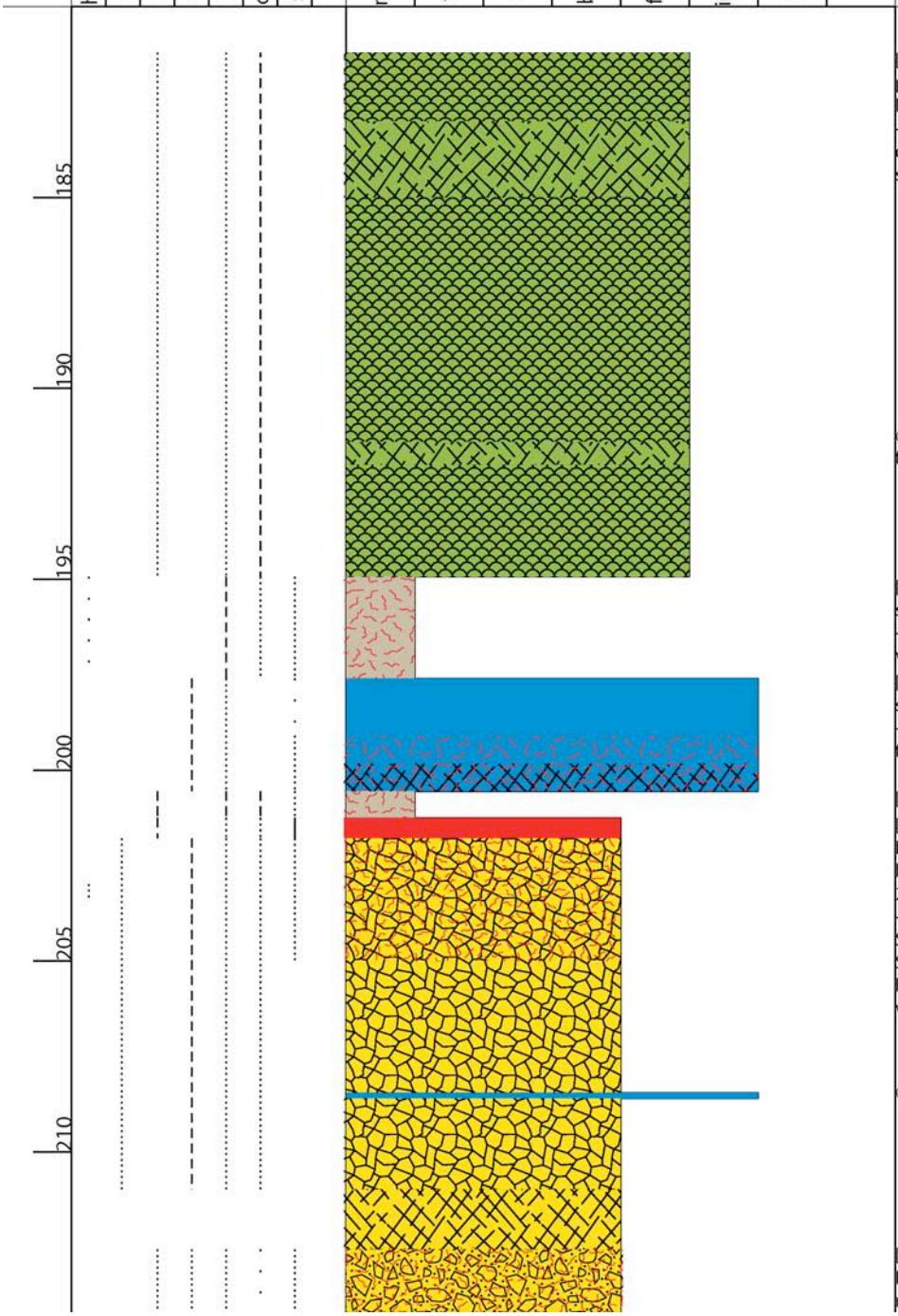

[181.2m - 183.0m] **Basalt Flow**: pillowed, occasional flow top breccia, sheared, magnetic base
-->Alt=qtz-chl-CO3 filled amygdules, selvages, leopard spotting, ser+Po at base

@183.0m-185.0m, 191.4m-192.0m fault zone cataclastite

[194.93m - 197.7m] **Py-Muds**: sheared, entrained basalt dyke
-->Alt=graphitic, heavy chl, CO3 veins, minor jasperoid

[197.7m - 200.65m] **Basalt Dyke**: sheared base
-->Alt=ser, kspar+Py at base, chl filled amygdules

[200.65m - 201.35m] **Py-Muds**

[201.35m - 212.75m] **Puzzle-Fit Rhyolite Breccia**: distinct block borders, cataclastite @ 211.18m-212.75m
-->Alt=massive honey Sp+Gn>Py±Brn to Gn+Py±white Sp stringers, ser-kspar to ser-qtz, bladed FeCO3 at base, chl-CO3 veins

@ 208.65m **Basalt Dyke**

[212.75m - 227.0m] **Rhyolite Tuff Breccia**: occasional banded matrix, polylithic felsic lapilli

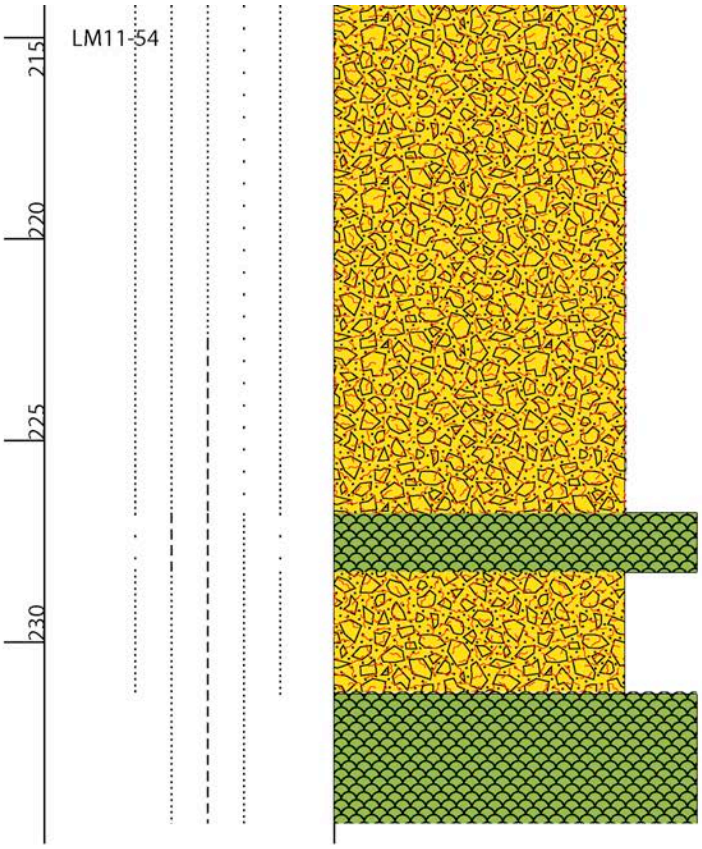

-->Alt=chl-matrix, qtz-CO3 veins, honey Sp+Py±Ccp stringers

[227.0m - 228.46m]**Basalt Flow** w/ qtz-CO3veins,amygdules,selvages

[228.46m - 231.5m] **Rhyolite Tuff Breccia**: (as above) indisinct block borders, sheared, fewer stringers

[231.5m - 234.7m] **Basalt Flow**: peperitic upper contact, pillowed, sheared
-->Alt=chl-ser, CO3 amygdules, selvages

DIAMOND DRILL HOLE: LM11-56

Date: 06-23-2013

Claim: South Tally Pond

UTM: 520990.297E, 5374908.469N

Azimuth: 270°

Dip: -77°

EOH: 358.4m

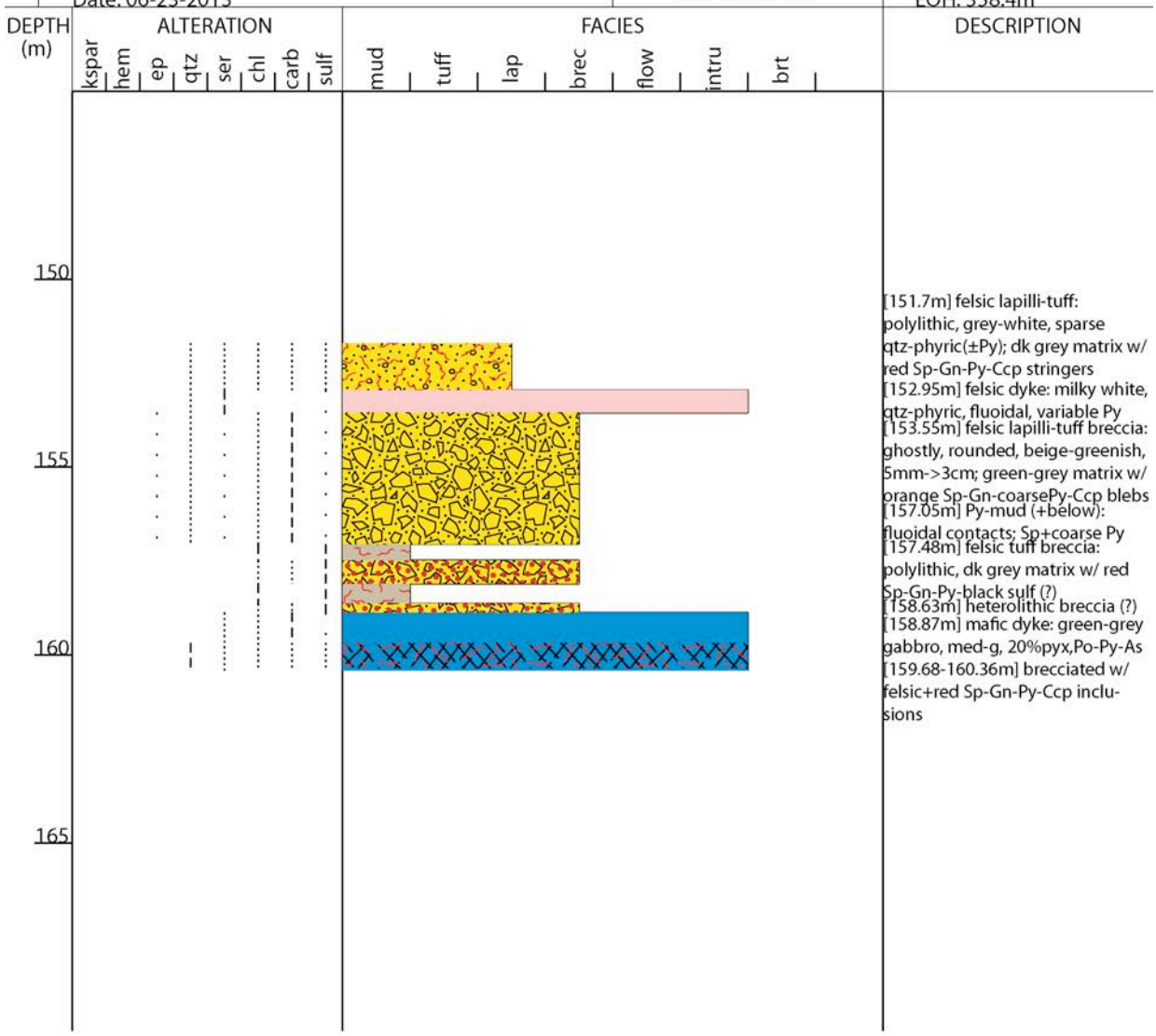

DESCRIPTION

[151.7m] felsic lapilli-tuff: polylithic, grey-white, sparse qtz-phyric(±Py); dk grey matrix w/ red Sp-Gn-Py-Ccp stringers

[152.95m] felsic dyke: milky white, qtz-phyric, fluoidal, variable Py

[153.55m] felsic lapilli-tuff breccia: ghostly, rounded, beige-greenish, 5mm->3cm; green-grey matrix w/ orange Sp-Gn-coarsePy-Ccp blebs

[157.05m] Py-mud (+below): fluoidal contacts; Sp+coarse Py

[157.48m] felsic tuff breccia: polylithic, dk grey matrix w/ red Sp-Gn-Py-black sulf (?)

[158.63m] heterolithic breccia (?)

[158.87m] mafic dyke: green-grey gabbro, med-g, 20%pyx,Po-Py-As

[159.68-160.36m] brecciated w/ felsic+red Sp-Gn-Py-Ccp inclusions

DIAMOND DRILL HOLE: LM11-57

Date: 07-23-2013

Claim: South Tally Pond

UTM: 520989.644E, 5374908.55N

Azimuth: 270°

Dip: -58.5°

EOH: 575.2m

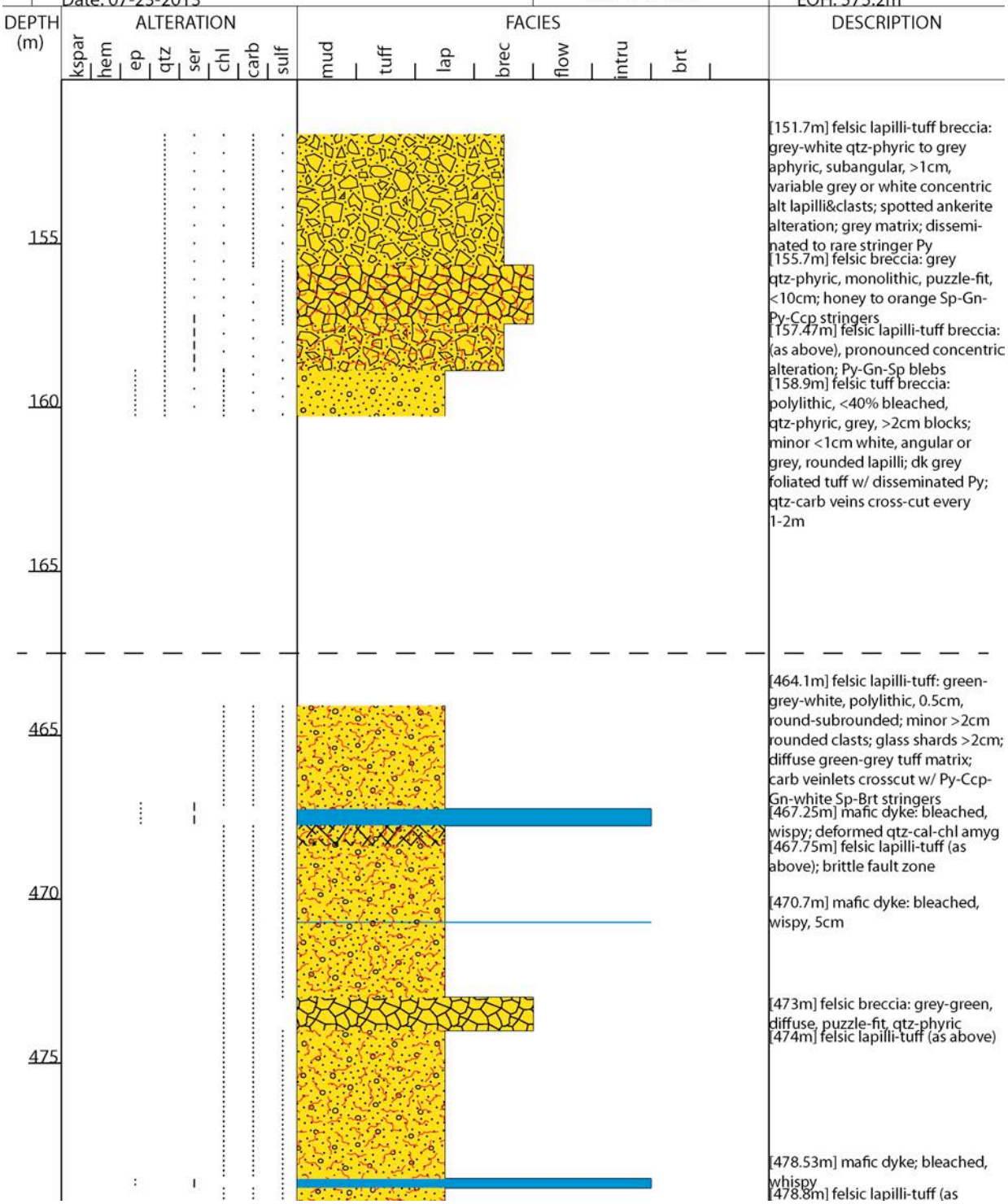

[151.7m] felsic lapilli-tuff breccia: grey-white qtz-phyric to grey aphyric, subangular, >1cm, variable grey or white concentric alt lapilli&clasts; spotted ankerite alteration; grey matrix; disseminated to rare stringer Py

[155.7m] felsic breccia: grey qtz-phyric, monolithic, puzzle-fit, <10cm; honey to orange Sp-Gn-Py-Ccp stringers

[157.47m] felsic lapilli-tuff breccia: (as above), pronounced concentric alteration; Py-Gn-Sp blebs

[158.9m] felsic tuff breccia: polylithic, <40% bleached, qtz-phyric, grey, >2cm blocks; minor <1cm white, angular or grey, rounded lapilli; dk grey foliated tuff w/ disseminated Py; qtz-carb veins cross-cut every 1-2m

[464.1m] felsic lapilli-tuff: green-grey-white, polylithic, 0.5cm, round-subrounded; minor >2cm rounded clasts; glass shards >2cm; diffuse green-grey tuff matrix; carb veinlets crosscut w/ Py-Ccp-Gn-white Sp-Brt stringers

[467.25m] mafic dyke: bleached, wispy; deformed qtz-cal-chl amyg

[467.75m] felsic lapilli-tuff (as above); brittle fault zone

[470.7m] mafic dyke: bleached, wispy, 5cm

[473m] felsic breccia: grey-green, diffuse, puzzle-fit, qtz-phyric

[474m] felsic lapilli-tuff (as above)

[478.53m] mafic dyke; bleached, whispy

[478.8m] felsic lapilli-tuff (as

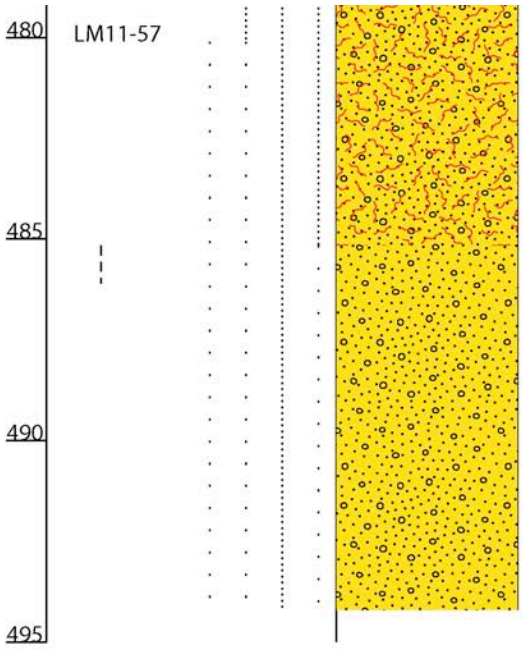

above)

[480.1m] felsic lapilli-tuff: whitish, monolithic (?), qtz-phyric, rounded, deformed, ~1cm; dk grey matrix; carb-qtz veinlets crosscut; blockier toward base; honey-brown Sp-Brt-Ccp stringers

[485.16m] felsic lapilli-tuff (as above); minor sulphides

Claim: South Tally Pond | Azimuth: 270°

DIAMOND DRILL HOLE: LM11-59 | UTM: 521077.866E, 5374828.815N | Dip: -59.5°

Date: 07/07/2012 | EOH: 288.6m

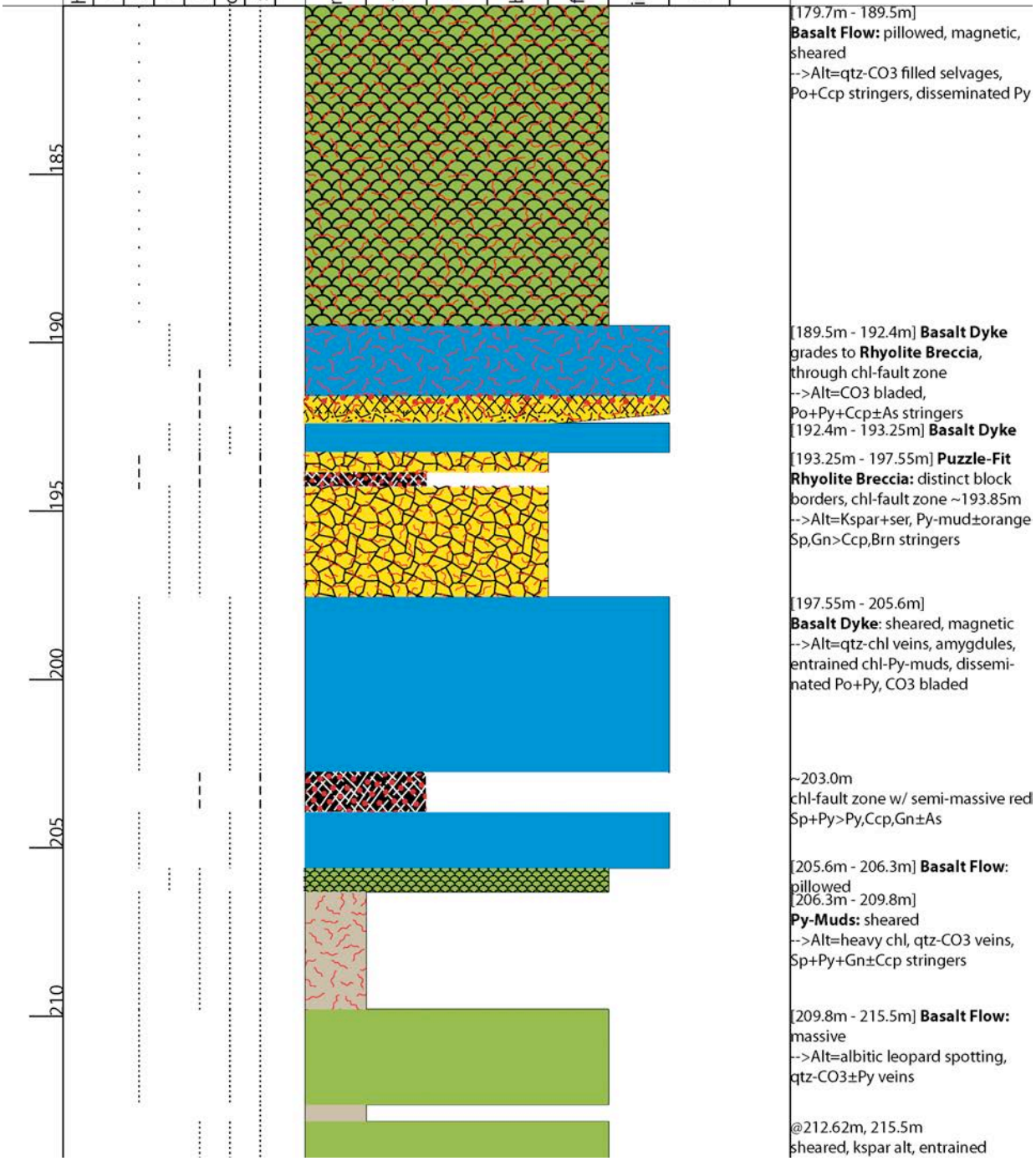

[179.7m - 189.5m]
Basalt Flow: pillowed, magnetic, sheared
-->Alt=qtz-CO3 filled selvages, Po+Ccp stringers, disseminated Py

[189.5m - 192.4m] **Basalt Dyke** grades to **Rhyolite Breccia**, through chl-fault zone
-->Alt=CO3 bladed, Po+Py+Ccp±As stringers

[192.4m - 193.25m] **Basalt Dyke**

[193.25m - 197.55m] **Puzzle-Fit Rhyolite Breccia:** distinct block borders, chl-fault zone ~193.85m
-->Alt=Kspar+ser, Py-mud±orange Sp,Gn>Ccp,Brn stringers

[197.55m - 205.6m]
Basalt Dyke: sheared, magnetic
-->Alt=qtz-chl veins, amygdules, entrained chl-Py-muds, disseminated Po+Py, CO3 bladed

~203.0m
chl-fault zone w/ semi-massive red Sp+Py>Py,Ccp,Gn±As

[205.6m - 206.3m] **Basalt Flow**: pillowed

[206.3m - 209.8m]
Py-Muds: sheared
-->Alt=heavy chl, qtz-CO3 veins, Sp+Py+Gn±Ccp stringers

[209.8m - 215.5m] **Basalt Flow:** massive
-->Alt=albitic leopard spotting, qtz-CO3±Py veins

@212.62m, 215.5m
sheared, kspar alt, entrained

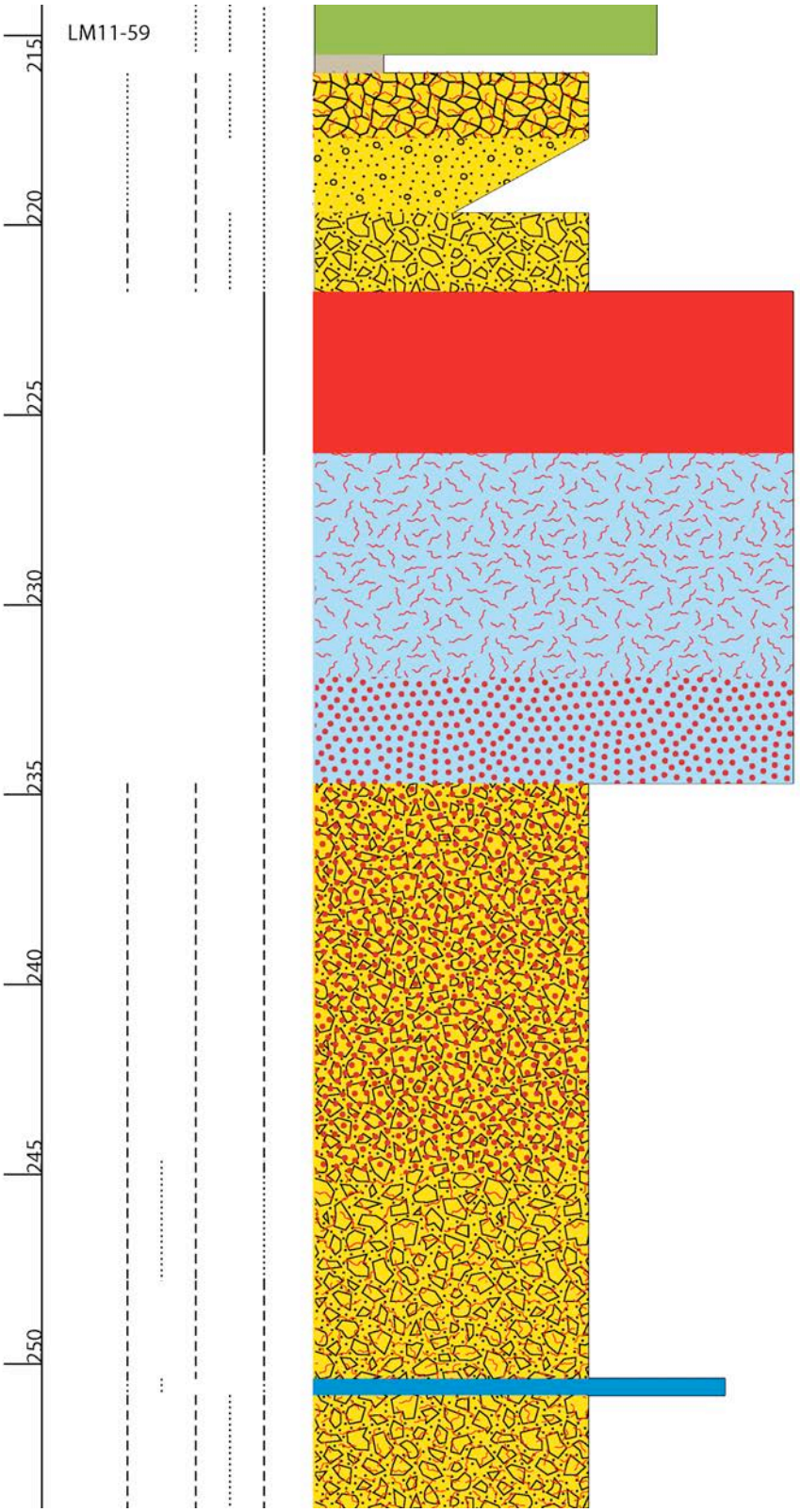

Py-Muds

[216.0m - 221.75m] **Puzzle-Fit Rhyolite Breccia** grades through sheared **Tuff** to **Tuff Breccia**
-->Alt=heavy chl throughout, CO3 veins crosscut, Sp>Py,Ccp stringers at top, silicified toward base

[221.75m - 226.0m] **Massive Sulfides:** honey Sp+Py±Ccp to Gn+honey Sp±Py w/ chloritoids

[226.0m - 231.9m] **SS Massive Barite**: exhalative texture, chloritoids present
-->Alt=honey Sp+Gn,Py,Ccp± Brn,Trt stringers

[231.9m - 234.7m] **SMS Massive Barite:** (as above)
-->Alt=honey Sp+Gn± Py,Ccp,Brn

[234.7m - 265.5m]
Rhyolite Tuff Breccia: distinct blocks become invisible toward base and >shear
-->Alt=chl-matrix, qtz veins crosscut, SMS honey Sp+Py±Ccp,Gn to stringers downhole

@ 250.5m, 256.42m - 258.05m, 258.95m - 260.86m, 266.0m, 270.0m
Basalt Dykes: sheared
-->Alt=CO3 filled amygdules, qtz-CO3 veins, Py±Ccp, >ser

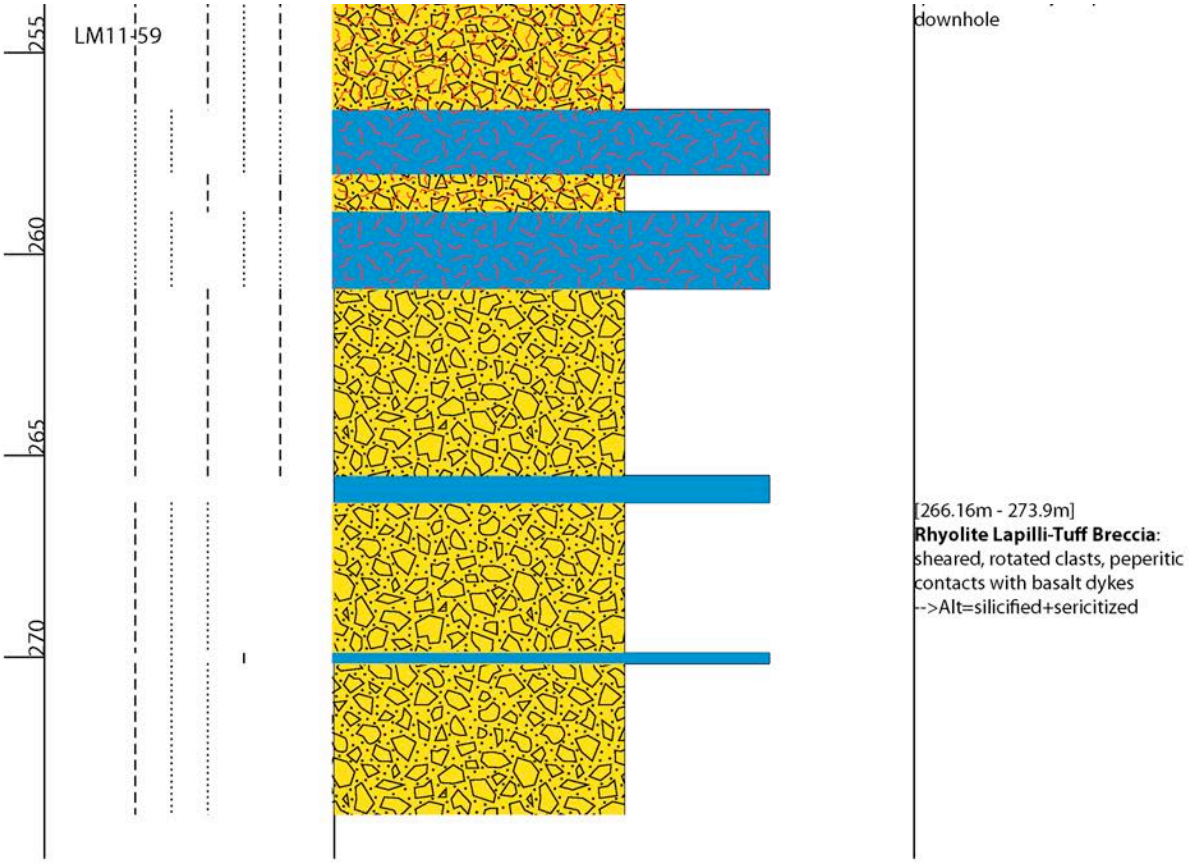
LM11-59
255
260
265
270
downhole
[266.16m - 273.9m]
Rhyolite Lapilli-Tuff Breccia:
sheared, rotated clasts, peperitic
contacts with basalt dykes
-->Alt=silicified+sericitized

Claim: South Tally Pond | Azimuth: 270°

DIAMOND DRILL HOLE: LM11-61 | UTM: 521072.099E, 5374804.292N | Dip: -60°

Date: 06-26-2013 | EOH: 310m

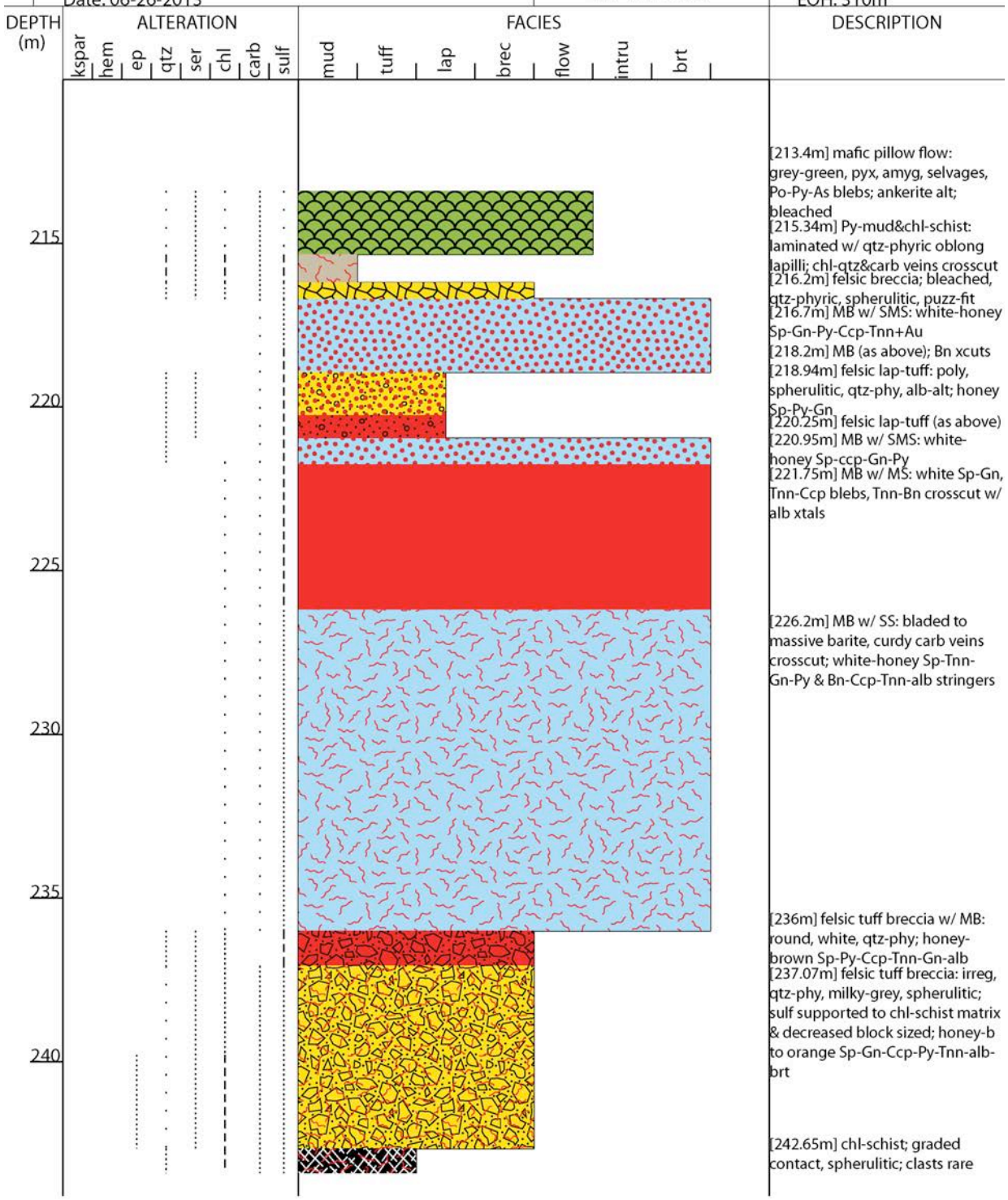

DESCRIPTION

[213.4m] mafic pillow flow: grey-green, pyx, amyg, selvages, Po-Py-As blebs; ankerite alt; bleached

[215.34m] Py-mud&chl-schist: laminated w/ qtz-phyric oblong lapilli; chl-qtz&carb veins crosscut

[216.2m] felsic breccia; bleached, qtz-phyric, spherulitic, puzz-fit

[216.7m] MB w/ SMS: white-honey Sp-Gn-Py-Ccp-Tnn+Au

[218.2m] MB (as above); Bn xcuts

[218.94m] felsic lap-tuff: poly, spherulitic, qtz-phy, alb-alt; honey Sp-Py-Gn

[220.25m] felsic lap-tuff (as above)

[220.95m] MB w/ SMS: white-honey Sp-ccp-Gn-Py

[221.75m] MB w/ MS: white Sp-Gn, Tnn-Ccp blebs, Tnn-Bn crosscut w/ alb xtals

[226.2m] MB w/ SS: bladed to massive barite, curdy carb veins crosscut; white-honey Sp-Tnn-Gn-Py & Bn-Ccp-Tnn-alb stringers

[236m] felsic tuff breccia w/ MB: round, white, qtz-phy; honey-brown Sp-Py-Ccp-Tnn-Gn-alb

[237.07m] felsic tuff breccia: irreg, qtz-phy, milky-grey, spherulitic; sulf supported to chl-schist matrix & decreased block sized; honey-b to orange Sp-Gn-Ccp-Py-Tnn-alb-brt

[242.65m] chl-schist; graded contact, spherulitic; clasts rare

DIAMOND DRILL HOLE: LM11-62

Date: 07/20/2012

Claim: South Tally Pond

UTM: 521071.473E, 5374804.418N

Azimuth: 270°

Dip: -46°

EOH: 291.7m

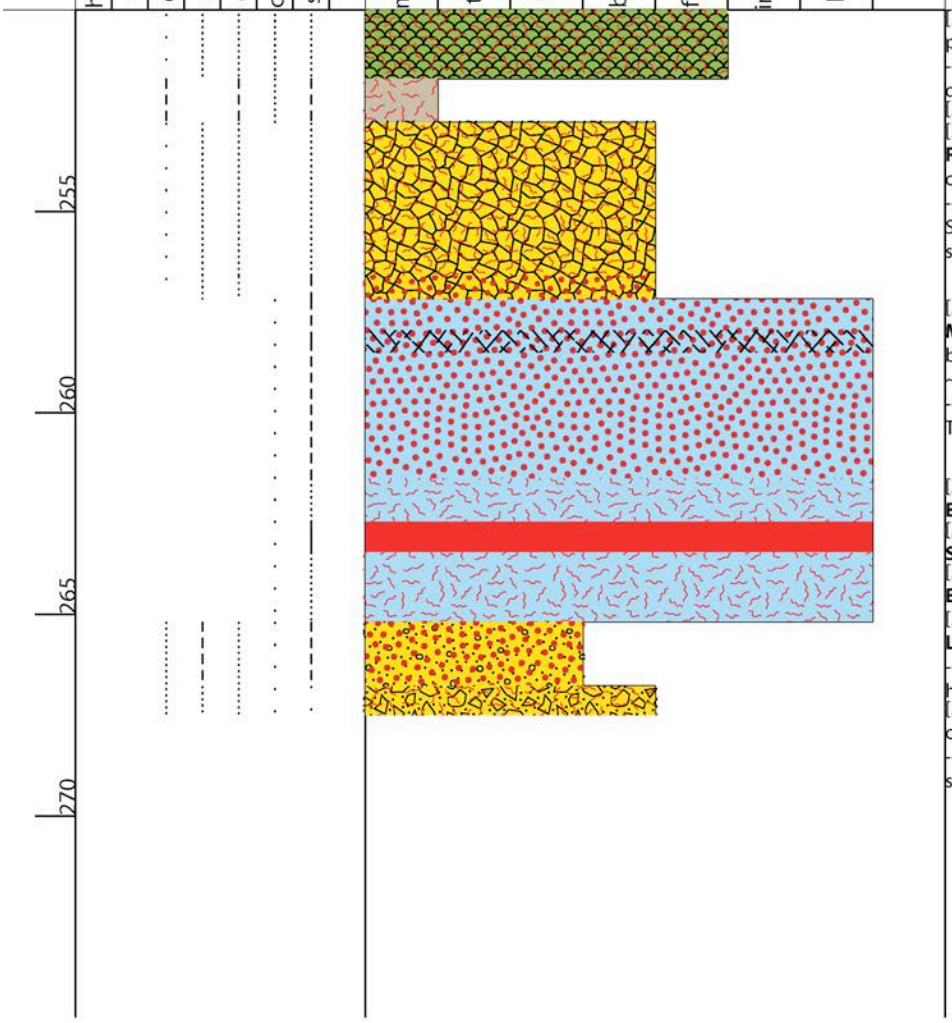

DESCRIPTION

[250.1m - 251.7m] **Basaltic Flow**: pillowed, magnetic
-->Alt=chl-qtz selvages, amygdules, Po±Py stringers

[251.7m - 252.8m] **Py(+Po)-Mud**

[252.8m - 257.18m] **Puzzle-Fit Rhyolite Breccia:** graded upper contact, spherulititc
-->Alt= qtz-chl matrix, Py>orange Sp+Gn±Ccp stringers become semi-massive honey Sp ~256.6m

[257.18m - 265.18m] **SMS Massive Barite:** occasionally bladed, sulfidic muddy shear zone ~258.2m
-->Alt=CO3 overprints, Trt+Gn+Ccp>Py>Brn,honey Sp

[261.2m - 262.7m] **SS Massive Barite:** Py or Ccp,Brn,Trt stringers

[262.7m - 263.45m] **Massive Sulfides:** Gn+Ccp>Py±Brn,Trt

[263.45m - 265.18m] **SS Massive Barite:** (see above)

[265.18m - 266.78m] **Rhyolitic Lapilli-Tuff:** sheared
-->Alt=sericitized, semi-massive honey Sp+Gn+Py>Ccp,Trt

[266.78m - 267.5m] **Tuff Breccia**: curdy block borders
-->Alt=ser-chl, Py+Sp.Gn+Ccp stringers

DIAMOND DRILL HOLE: LM11-63

Date: 07/07/2012

Claim: South Tally Pond

UTM: 521062.349E, 5374749.776N

Azimuth: 270°

Dip: -67°

EOH: 267.9m

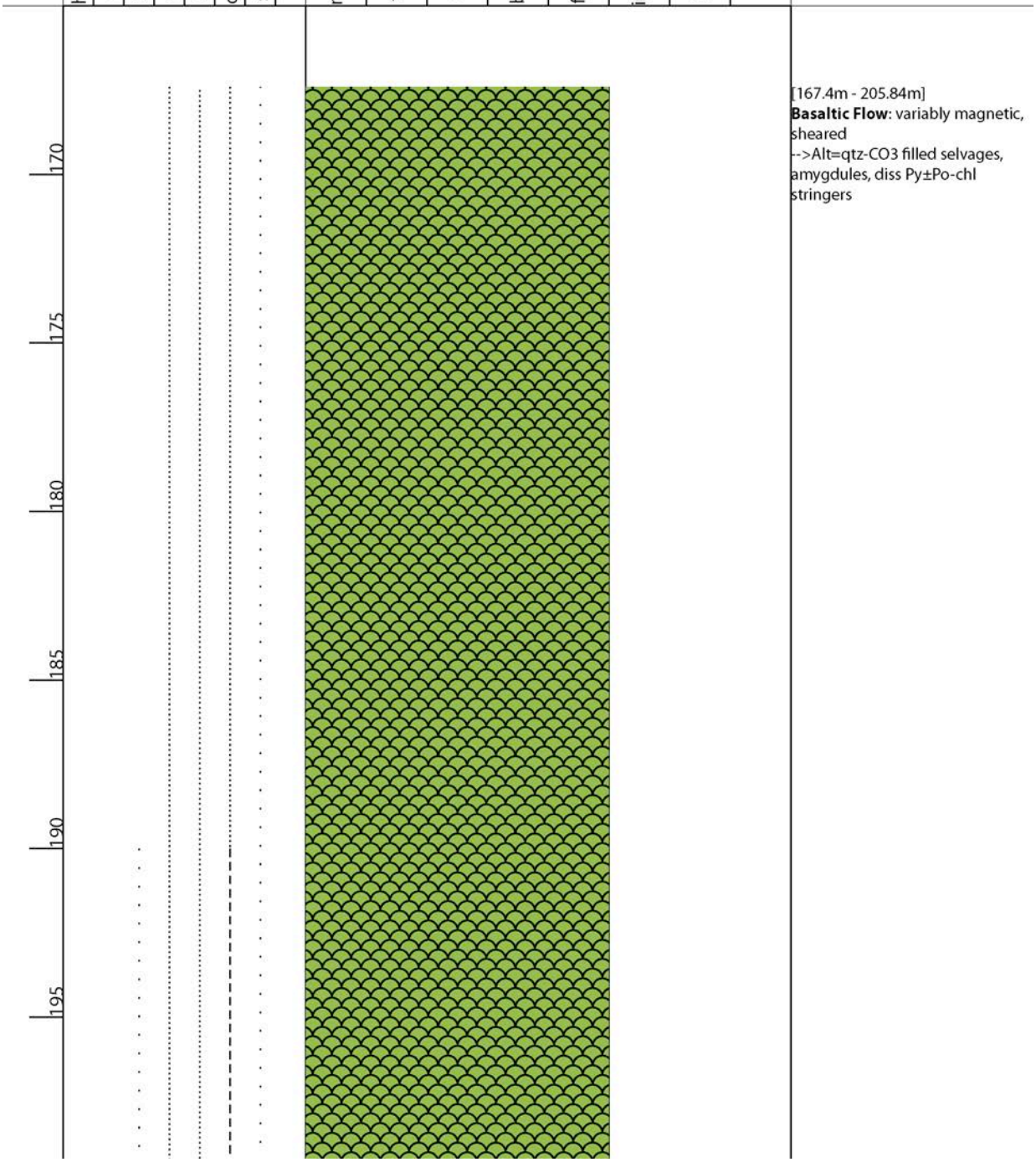

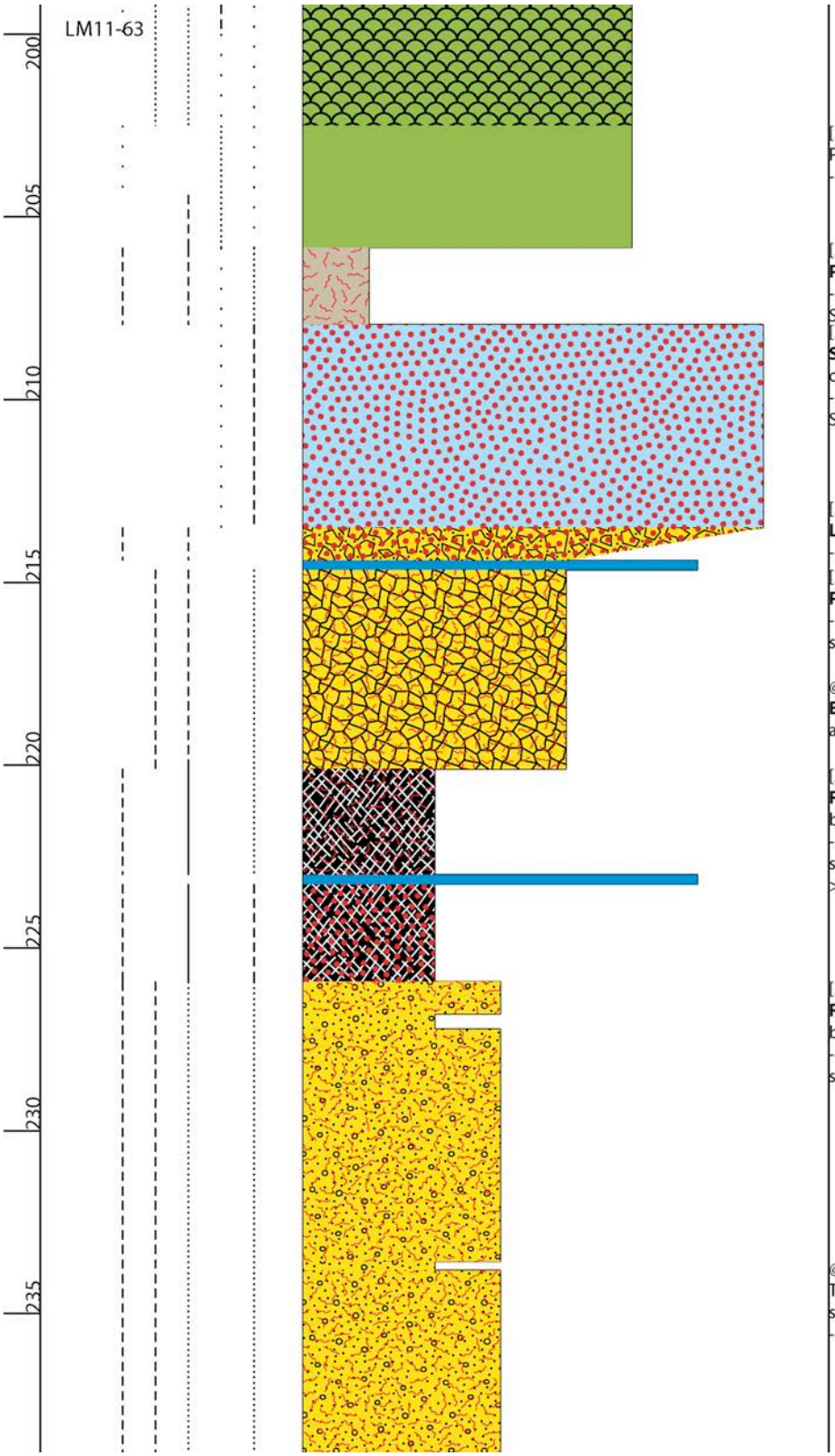

[>202.6m]
Pillow selvages absent
-->Alt=albitic leopard spotting

[205.84m - 207.95m]
Py-Mud: sheared
-->Alt=qtz-CO3 veins,
Sp+Py±Ccp,Trt stringers

[207.95m - 213.5m]
SMS Massive Barite: diffusely crystalline
-->Alt=CO3 overprint,
Sp+Py+Trt±Gn,Ccp,Brn stringers

[213.5m - 214.4m] grades into
Lapilli-Tuff Breccia
-->Alt=chl, Ccp>Py±Brn stringers

[214.63m - 220.0m]
Puzzle-Fit Rhyolite Breccia
-->Alt=qtz-Py veins, Sp+Py+Ccp stringers

@214.4m, 2218.2m, 222.9m
Basalt dykes: thin, w/ Py, chl-CO3 amydules

[220.0m - 225.82m]
Rhyolite Tuff Breccia: indistinct block borders, sheared
-->Alt=heavy chl, Sp+Py.Ccp±Brn stringers become semi-massive >223.15m

[225.82m - 241.6m]
Rhyolitic Lapilli-Tuff: few larger blocks, glass shards present
-->Alt=qtz-ser halos, Py±Ccp,Gn stringers, ±jasperoid

@226.7m, 233.47m, 239.17m
Tuffacious banded rhyolitic sections
-->Alt=disseminated Py only

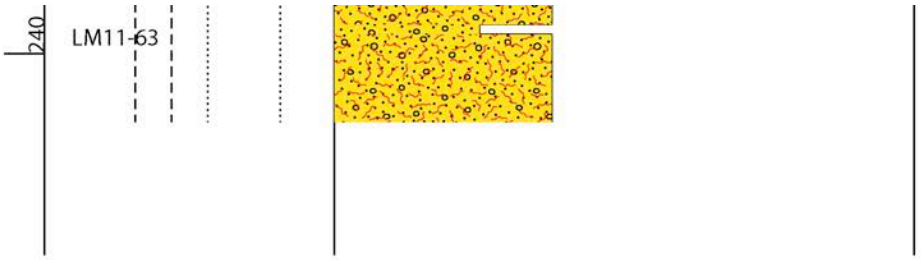
240
LM11-63

Claim: South Tally Pond

Azimuth: 270°

DIAMOND DRILL HOLE: LM11-64

UTM: 521062.015E, 5374749.86N

Dip: -52°

Date: 06-21-2013

EOH: 276.2m

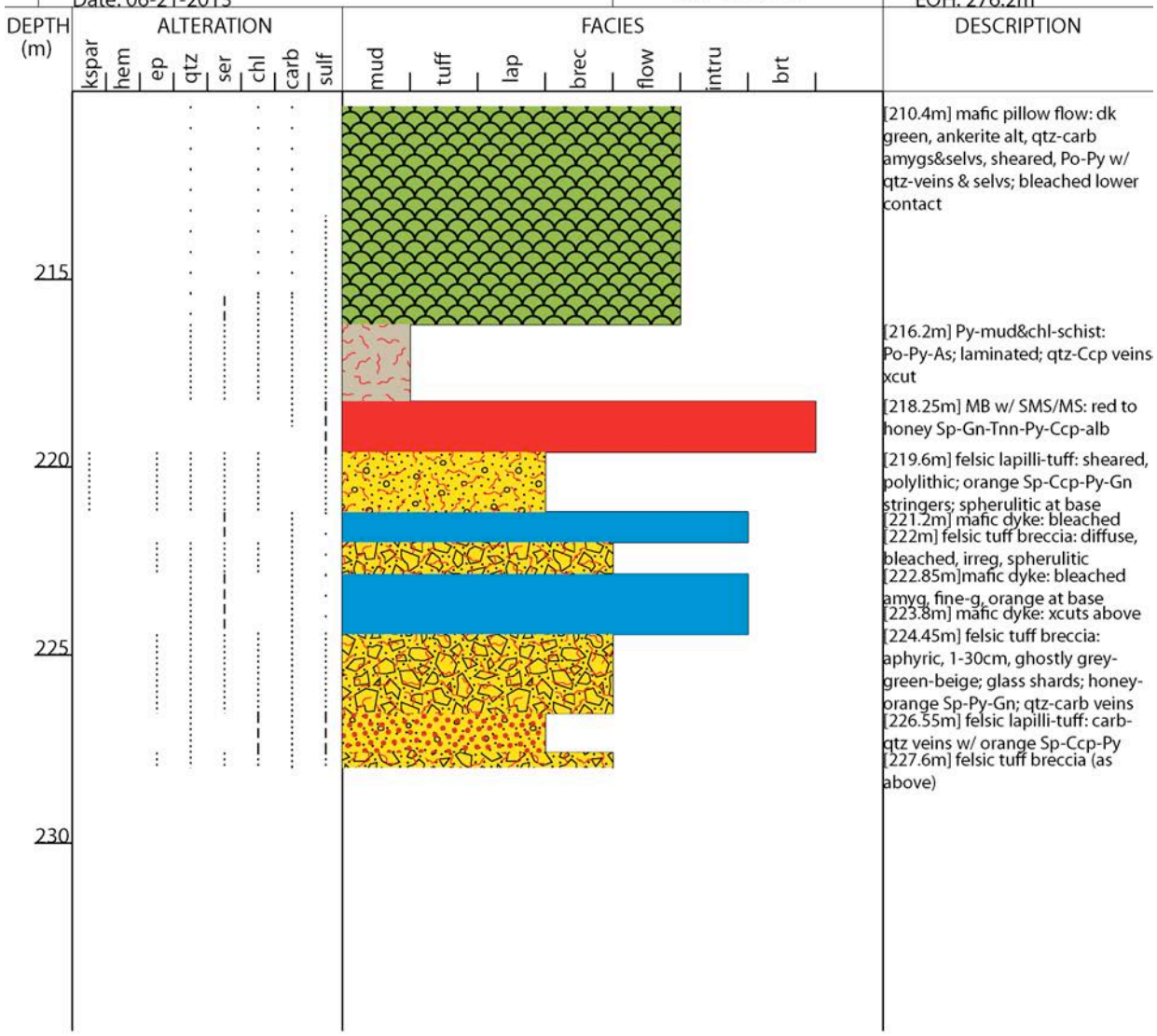

DESCRIPTION

[210.4m] mafic pillow flow: dk green, ankerite alt, qtz-carb amygs&selvs, sheared, Po-Py w/ qtz-veins & selvs; bleached lower contact

[216.2m] Py-mud&chl-schist: Po-Py-As; laminated; qtz-Ccp veins xcut

[218.25m] MB w/ SMS/MS: red to honey Sp-Gn-Tnn-Py-Ccp-alb

[219.6m] felsic lapilli-tuff: sheared, polylithic; orange Sp-Ccp-Py-Gn stringers; spherulitic at base

[221.2m] mafic dyke: bleached

[222m] felsic tuff breccia: diffuse, bleached, irreg, spherulitic

[222.85m]mafic dyke: bleached amyg, fine-g, orange at base

[223.8m] mafic dyke: xcuts above

[224.45m] felsic tuff breccia: aphyric, 1-30cm, ghostly grey-green-beige; glass shards; honey-orange Sp-Py-Gn; qtz-carb veins

[226.55m] felsic lapilli-tuff: carb-qtz veins w/ orange Sp-Ccp-Py

[227.6m] felsic tuff breccia (as above)

DIAMOND DRILL HOLE: LM11-65

Date:07/26/2012

Claim: South Tally Pond

UTM: 521114.134E, 5374599.585N

Azimuth: 270°

Dip: -77°

EOH: 203.3 m

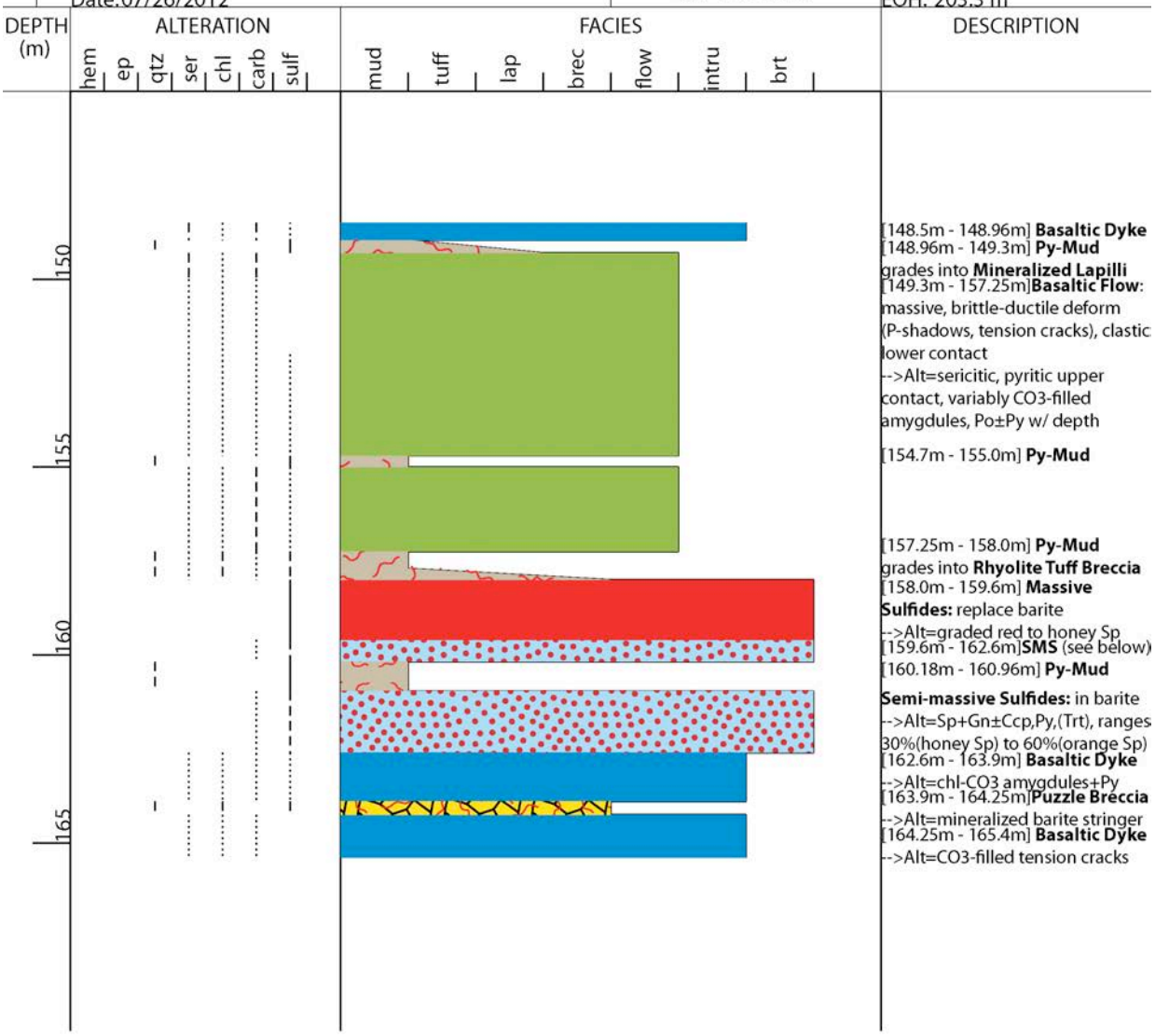

DESCRIPTION

[148.5m - 148.96m] **Basaltic Dyke**
[148.96m - 149.3m] **Py-Mud**
grades into **Mineralized Lapilli**
[149.3m - 157.25m]**Basaltic Flow**:
massive, brittle-ductile deform
(P-shadows, tension cracks), clastic
lower contact
-->Alt=sericitic, pyritic upper
contact, variably CO3-filled
amygdules, Po±Py w/ depth

[154.7m - 155.0m] **Py-Mud**

[157.25m - 158.0m] **Py-Mud**
grades into **Rhyolite Tuff Breccia**
[158.0m - 159.6m] **Massive**
Sulfides: replace barite
-->Alt=graded red to honey Sp
[159.6m - 162.6m]**SMS** (see below)
[160.18m - 160.96m] **Py-Mud**

Semi-massive Sulfides: in barite
-->Alt=Sp+Gn±Ccp,Py,(Trt), ranges
30%(honey Sp) to 60%(orange Sp)
[162.6m - 163.9m] **Basaltic Dyke**
-->Alt=chl-CO3 amygdules+Py
[163.9m - 164.25m]**Puzzle Breccia**
-->Alt=mineralized barite stringer
[164.25m - 165.4m] **Basaltic Dyke**
-->Alt=CO3-filled tension cracks

DIAMOND DRILL HOLE: LM111-67

Claim: South Tally Pond

Azimuth: 270°

Date: 06-24-2013

UTM: 521065.915E, 5374699.232N

Dip: -88°

EOH: 236.8m

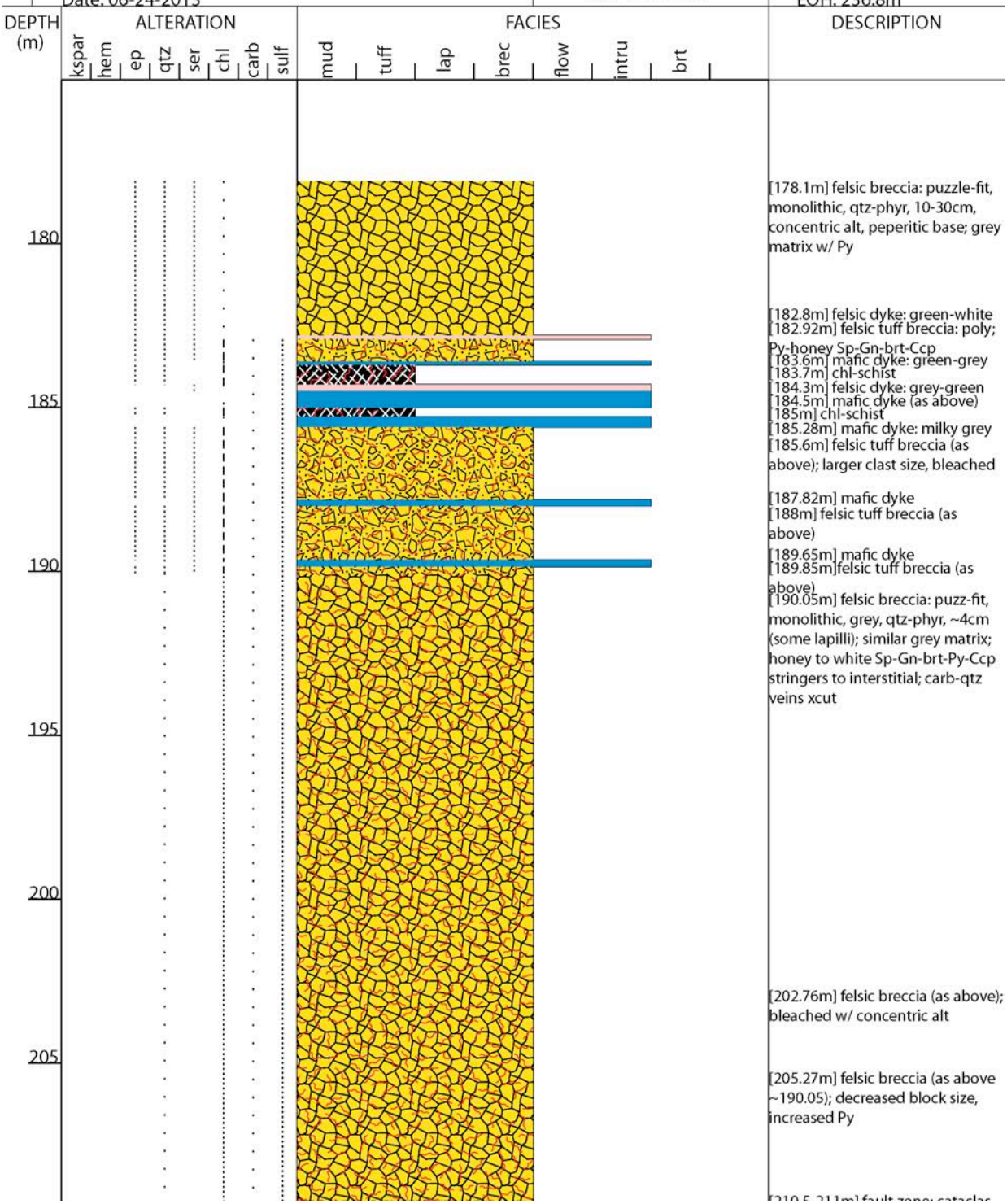

DESCRIPTION

[178.1m] felsic breccia: puzzle-fit, monolithic, qtz-phyr, 10-30cm, concentric alt, peperitic base; grey matrix w/ Py

[182.8m] felsic dyke: green-white
[182.92m] felsic tuff breccia: poly; Py-honey Sp-Gn-brt-Ccp
[183.6m] mafic dyke: green-grey
[183.7m] chl-schist
[184.3m] felsic dyke: grey-green
[184.5m] mafic dyke (as above)
[185m] chl-schist
[185.28m] mafic dyke: milky grey
[185.6m] felsic tuff breccia (as above); larger clast size, bleached

[187.82m] mafic dyke
[188m] felsic tuff breccia (as above)

[189.65m] mafic dyke
[189.85m]felsic tuff breccia (as above)
[190.05m] felsic breccia: puzz-fit, monolithic, grey, qtz-phyr, ~4cm (some lapilli); similar grey matrix; honey to white Sp-Gn-brt-Py-Ccp stringers to interstitial; carb-qtz veins xcut

[202.76m] felsic breccia (as above); bleached w/ concentric alt

[205.27m] felsic breccia (as above ~190.05); decreased block size, increased Py

[210.5-211m] fault zone: cataclas

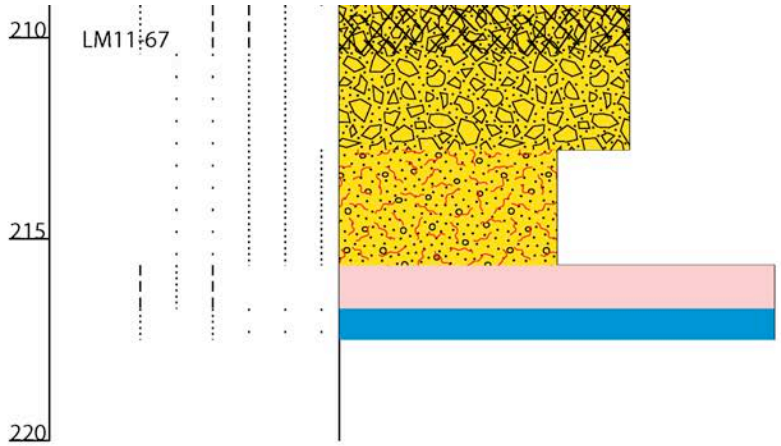

[210.5-211m] fault zone: cataclasite in clay-rich volcanics

[212.78m] felsic lapilli-tuff: grey, monolithic, round, qtz-phy; curdy, white-green-grey tuff, sheared; Py±honey-b Sp-Gn-Ccp-Bn

[215.65m] felsic dyke: green-white, aphyric, deformed

[216.73m] mafic dyke: greenish, amyg, brecciated w/ entrained felsics; sheared, ankerite alt upper contact,

DIAMOND DRILL HOLE: LM11-68

Date: 07/09/2012

Claim: South Tally Pond

UTM: 521065.518E, 5374699.274N

Azimuth: 270°

Dip: -70°

EOH: 252.1m

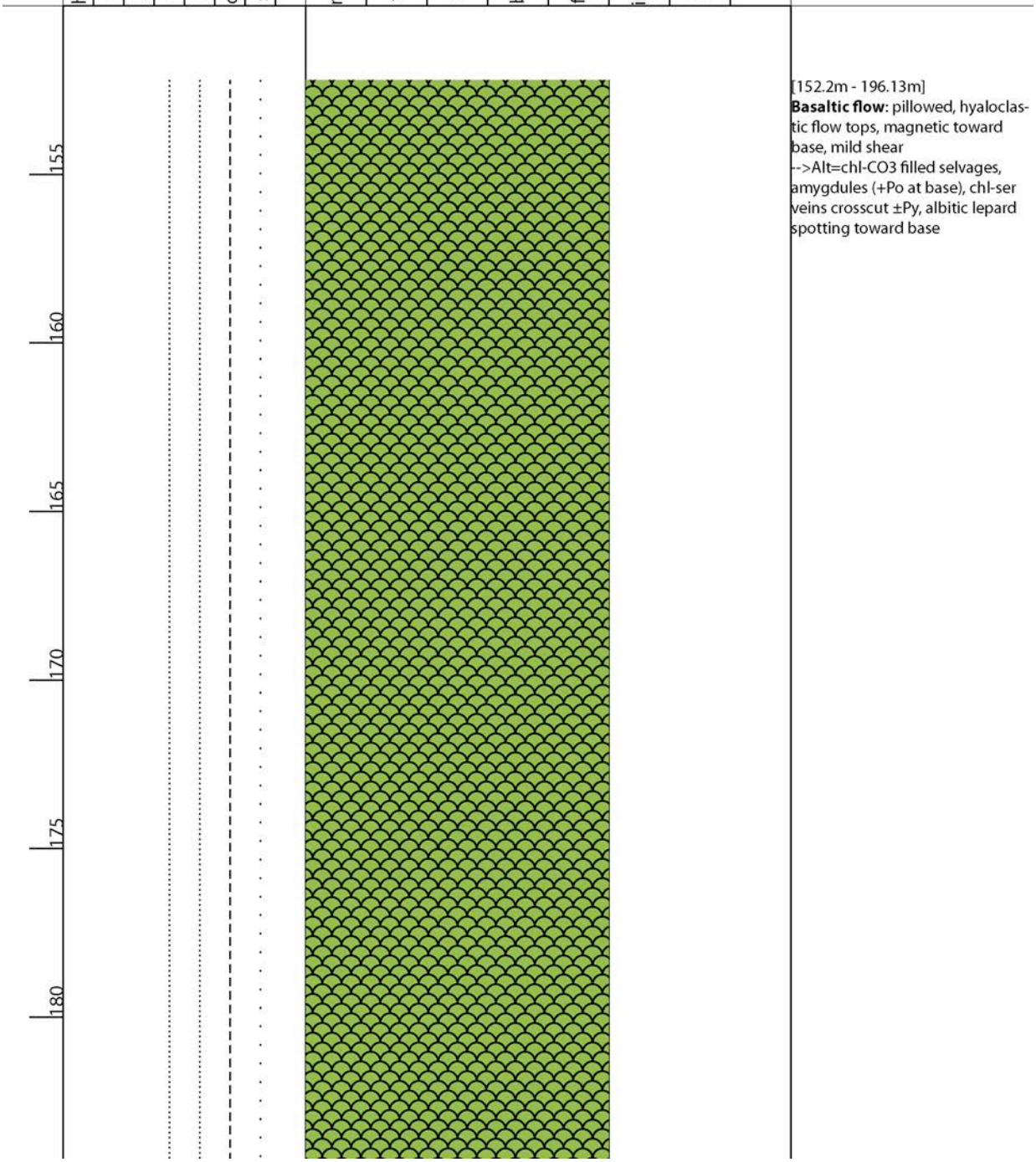

DESCRIPTION

[152.2m - 196.13m]
Basaltic flow: pillowed, hyaloclastic flow tops, magnetic toward base, mild shear
-->Alt=chl-CO3 filled selvages, amygdules (+Po at base), chl-ser veins crosscut ±Py, albitic lepard spotting toward base

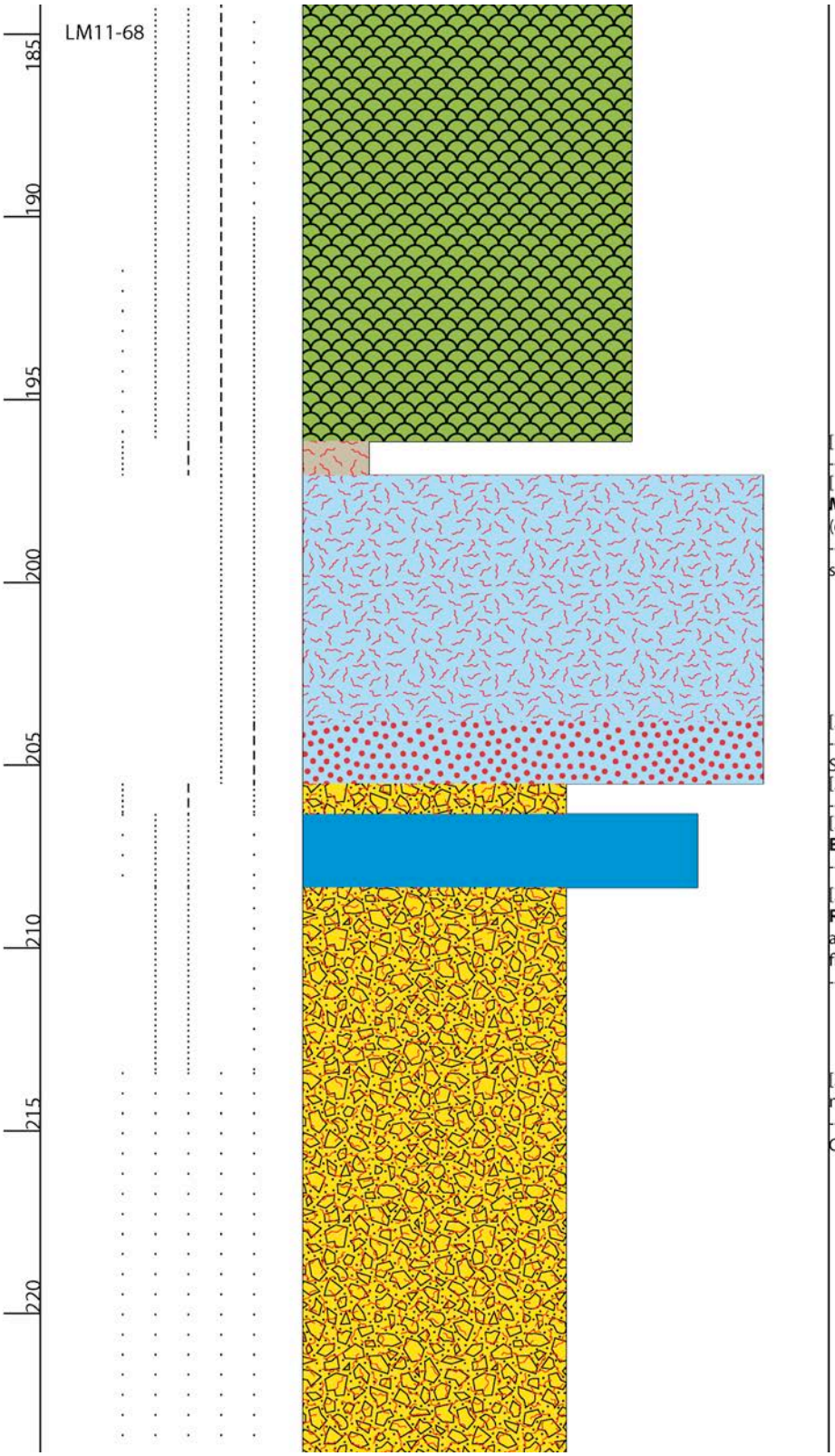

[196.13m - 197.07m] **Py-Muds**
-->Alt=CO3 veins+red Sp stringers
[197.07m - 203.8m]
Massive Barite: crystalline lathes (can be concentric)
-->Alt=Gn+Brn+Py±Ccp,Trt stringers, CO3 overprint

[203.8m - 205.1m] **Massive Barite**
-->Alt=semi-massive honey Sp+Py>Gn±Ccp,Brn,Trt
[205.1m - 205.93m] **Tuff Breccia**
-->Alt=heavy Fe-chl, qtz+Sp veins
[205.93m - 207.94m]
Basalt Dyke: sheared
-->Alt=chl-Py filled amygdules

[207.94m - 213.0m]
Rhyolite Tuff Breccia: (from above), diffuse bordered clasts w/ flow banding, chl-tuff matrix
-->Alt= diss Py+white Sp stringers

[213.0m - 242.9m]
matrix becomes lapilli-tuff
-->Alt=Ccp blebs toward base, CO3 veins crosscut

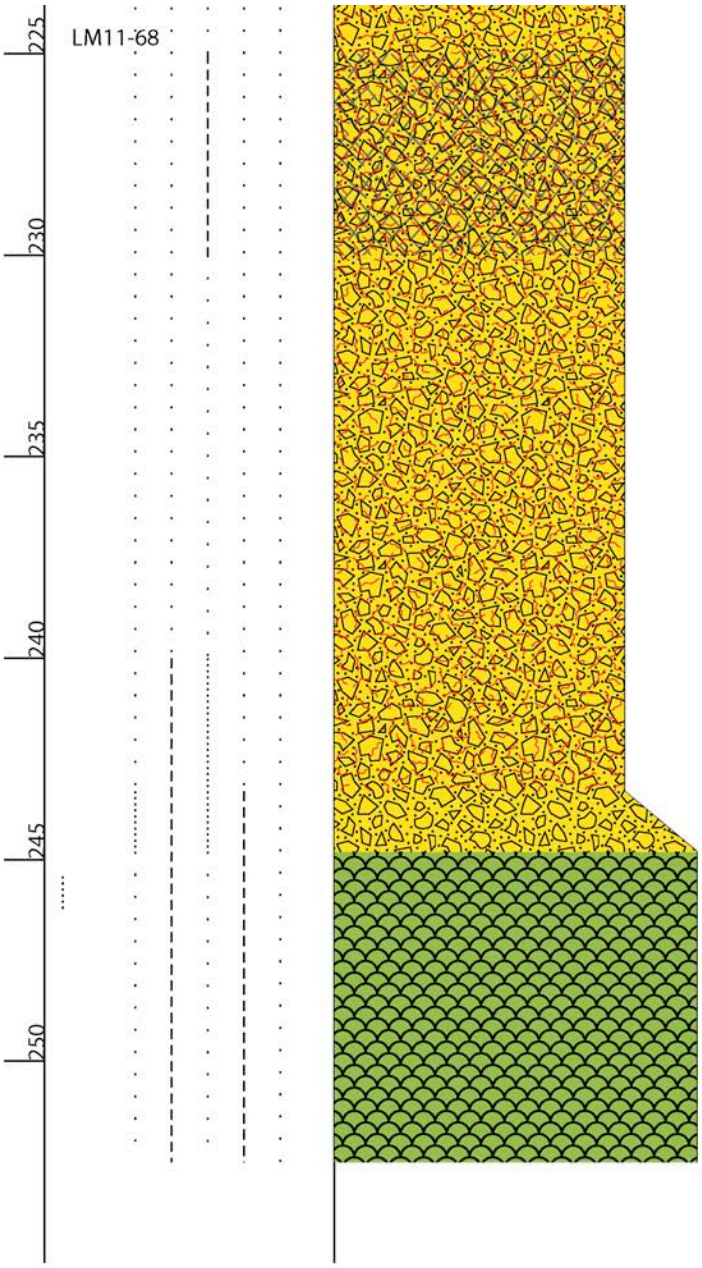

[224.0m - 229.3m]
Cataclastic Rhyolite: fault zone

[242.9m - 244.4m]
Polylithic Breccia: Rhyolite tuff intermingled w/ brecciated basaltic flow
[244.4m - 252.1m]
Basaltic flow: pillowed, hyaloclastite flow tops, sheared, non-vesicular
-->Alt=qtz-CO3 veins±Po,Py, minor jasperoid

DIAMOND DRILL HOLE: LM11-69

Date: 07/18/2012

Claim: South Tally Pond

UTM: 520993.337E, 5374860.131N

Azimuth: 270°

Dip: -74°

EOH: 279.2m

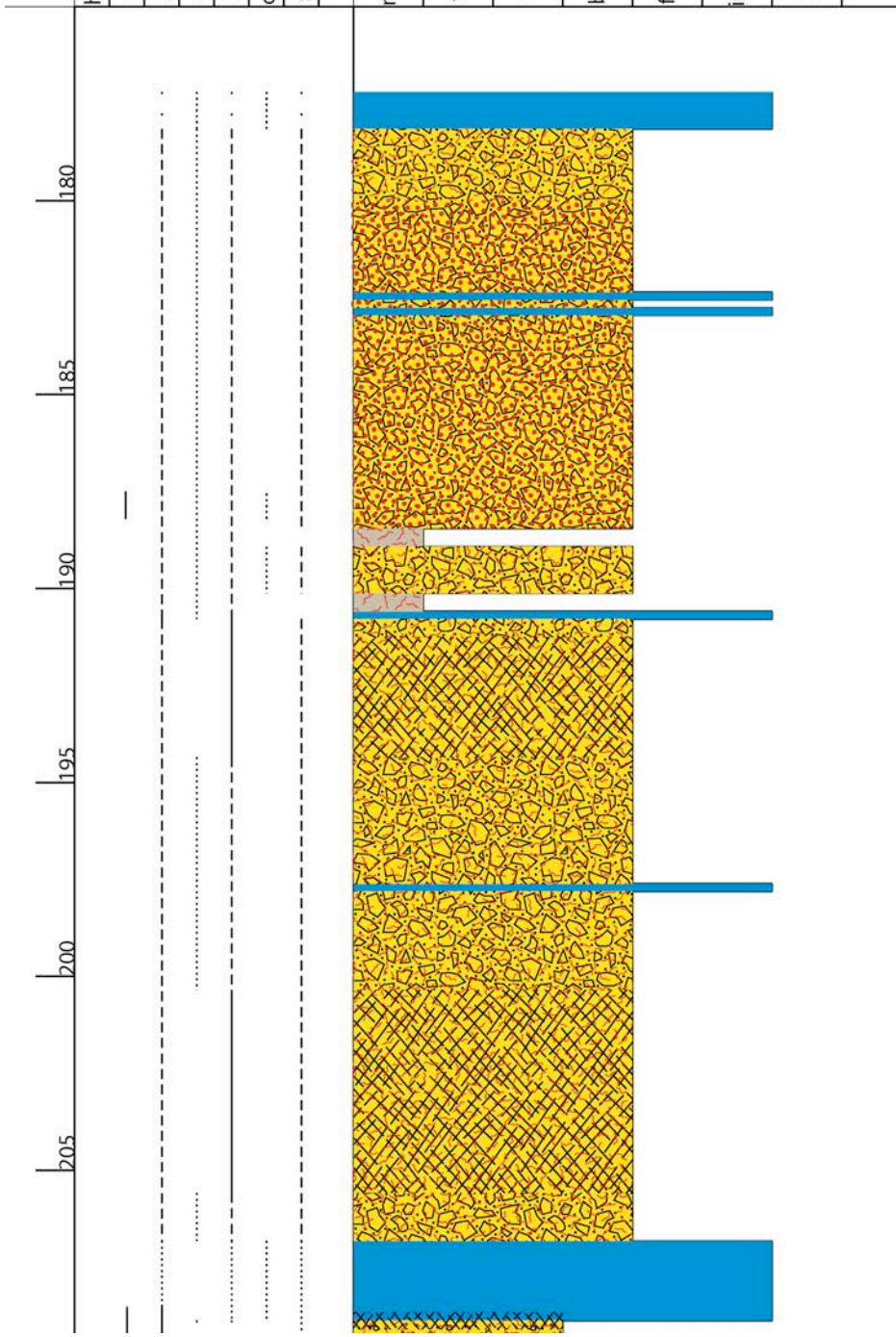

DESCRIPTION

[177.2m - 178.15m] **Basalt Dyke**: magnetic, albite leopard spotting

[178.15m - 206.8m] **Rhyolite Tuff Breccia:** distinct block borders, sheared lapilli-tuff matrix -->Alt=chl-qtz tension cracks, SMS to srtinger Sp+Py+Ccp>Gn, some kspar

@182.36m, 182.76m, 190.57m, 197.59m **Basalt Dykes** w/ wispy contacts, variable ser-qtz to chl-qtz filled amydules

@ 188.43m - 188.9m, 190.1m - 190.57m **Py-Mud** shear zones w/ qtz veins, chl-rhyolite clasts, Py±Ccp,Gn,Brn >As stringers

@ 191.4m - 193.91m, 201.75m - 204.3m **Chl-Tuff Breccia** shear zones w/ qtz veins, spherulitic, Py±Sp,Ccp,Gn or Sp+Py>Gn±Ccp stringers throughout

[206.8m - 209.75m] **Basalt Dyke:** sheared base, amygdular contacts -->Alt=chl-CO3 filled amygdules, qtz-CO3±Py veins

[209.75m - 213.8m] **Rhyolite**

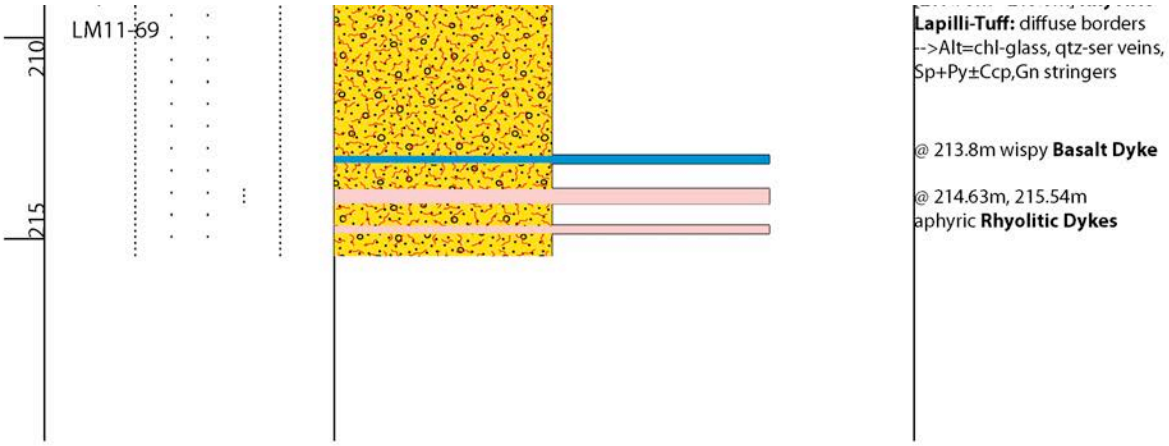
LM11-69
210
215
Lapilli-Tuff: diffuse borders
-->Alt=chl-glass, qtz-ser veins,
Sp+Py±Ccp,Gn stringers
@ 213.8m wispy **Basalt Dyke**
@ 214.63m, 215.54m
aphyric **Rhyolitic Dykes**

DIAMOND DRILL HOLE: LM11-70

Date: 07/25/2012

Claim: South Tally Pond

UTM: 520889.287E, 5374968.186N

Azimuth: 90°

Dip: -65°

EOH: 138.7m

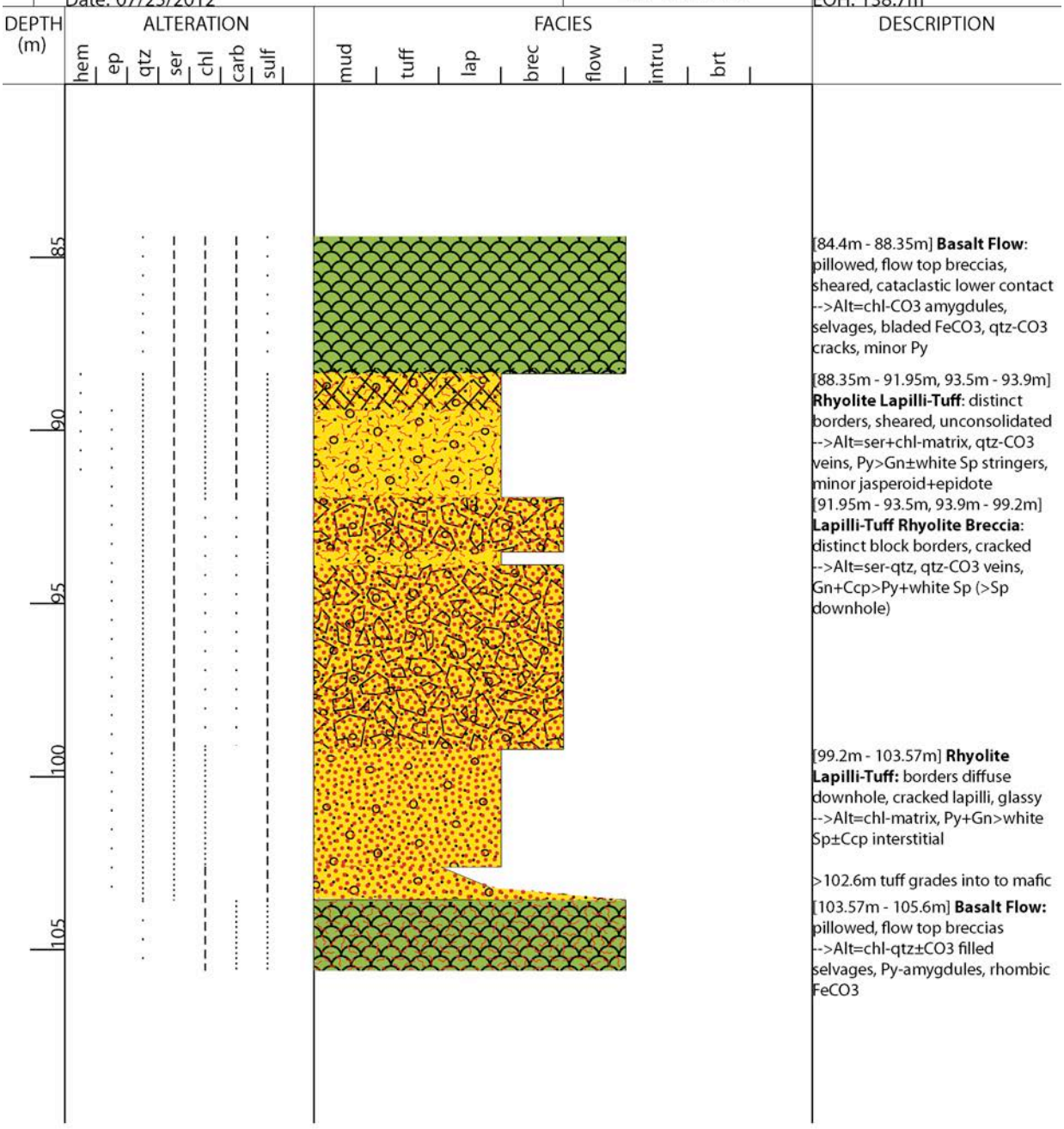

DESCRIPTION

[84.4m - 88.35m] **Basalt Flow**: pillowed, flow top breccias, sheared, cataclastic lower contact -->Alt=chl-CO3 amygdules, selvages, bladed FeCO3, qtz-CO3 cracks, minor Py

[88.35m - 91.95m, 93.5m - 93.9m] **Rhyolite Lapilli-Tuff**: distinct borders, sheared, unconsolidated -->Alt=ser+chl-matrix, qtz-CO3 veins, Py>Gn±white Sp stringers, minor jasperoid+epidote

[91.95m - 93.5m, 93.9m - 99.2m] **Lapilli-Tuff Rhyolite Breccia**: distinct block borders, cracked -->Alt=ser-qtz, qtz-CO3 veins, Gn+Ccp>Py+white Sp (>Sp downhole)

[99.2m - 103.57m] **Rhyolite Lapilli-Tuff:** borders diffuse downhole, cracked lapilli, glassy -->Alt=chl-matrix, Py+Gn>white Sp±Ccp interstitial

>102.6m tuff grades into to mafic

[103.57m - 105.6m] **Basalt Flow:** pillowed, flow top breccias -->Alt=chl-qtz±CO3 filled selvages, Py-amygdules, rhombic FeCO3

DIAMOND DRILL HOLE: LM11-72

Date: 07/16/2012

Claim: South Tally Pond

UTM: 521114.59E, 5374625.355N

Azimuth: 270°

Dip: -64°

EOH: 227.6m

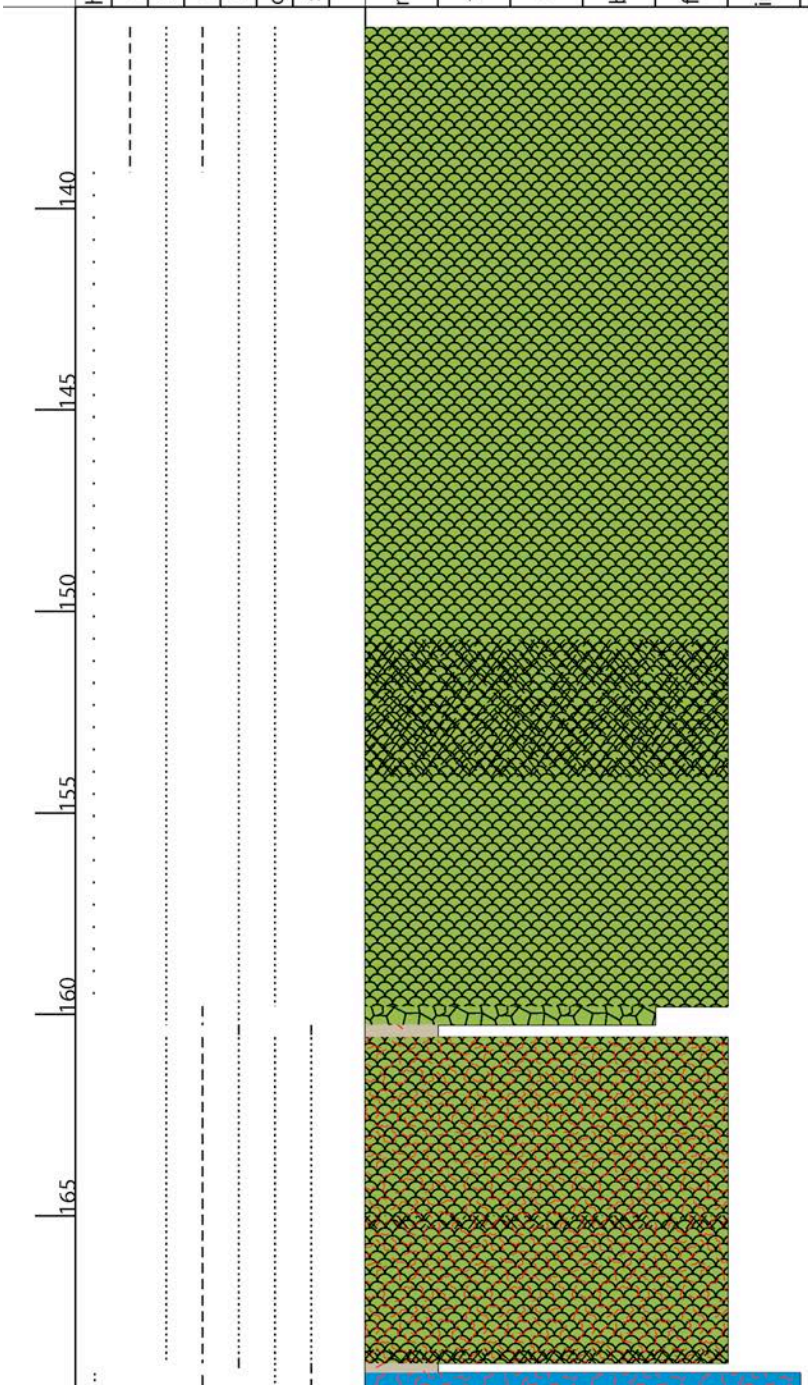

[135.5m - 159.8m] **Basalt Flow**: pillowed, flow top breccia, sheared
-->Alt=qtz-chl-CO3 filled amygdules, selvages (±jasperoid), epidote-ser at top

@ 151.0m - 154.5m
Fault zone cataclastite

[159.8m - 160.26m] **Basalt Breccia** kspar-ser alt, chl-qtz matrix
[160.26m - 160.57m] **Py-Muds**
[160.57m - 168.65m] **Basalt Flow:** pillowed, cataclastite @165.36m, 168.5m
-->Alt=ser base, bladed FeCO3,qtz-chl-CO3 filled amygdules, selvages, Py+Po+As stringers

[168.65m - 168.9m] **Py-Po-Muds**
[168.9m - 169.25m] **Basalt Dyke**

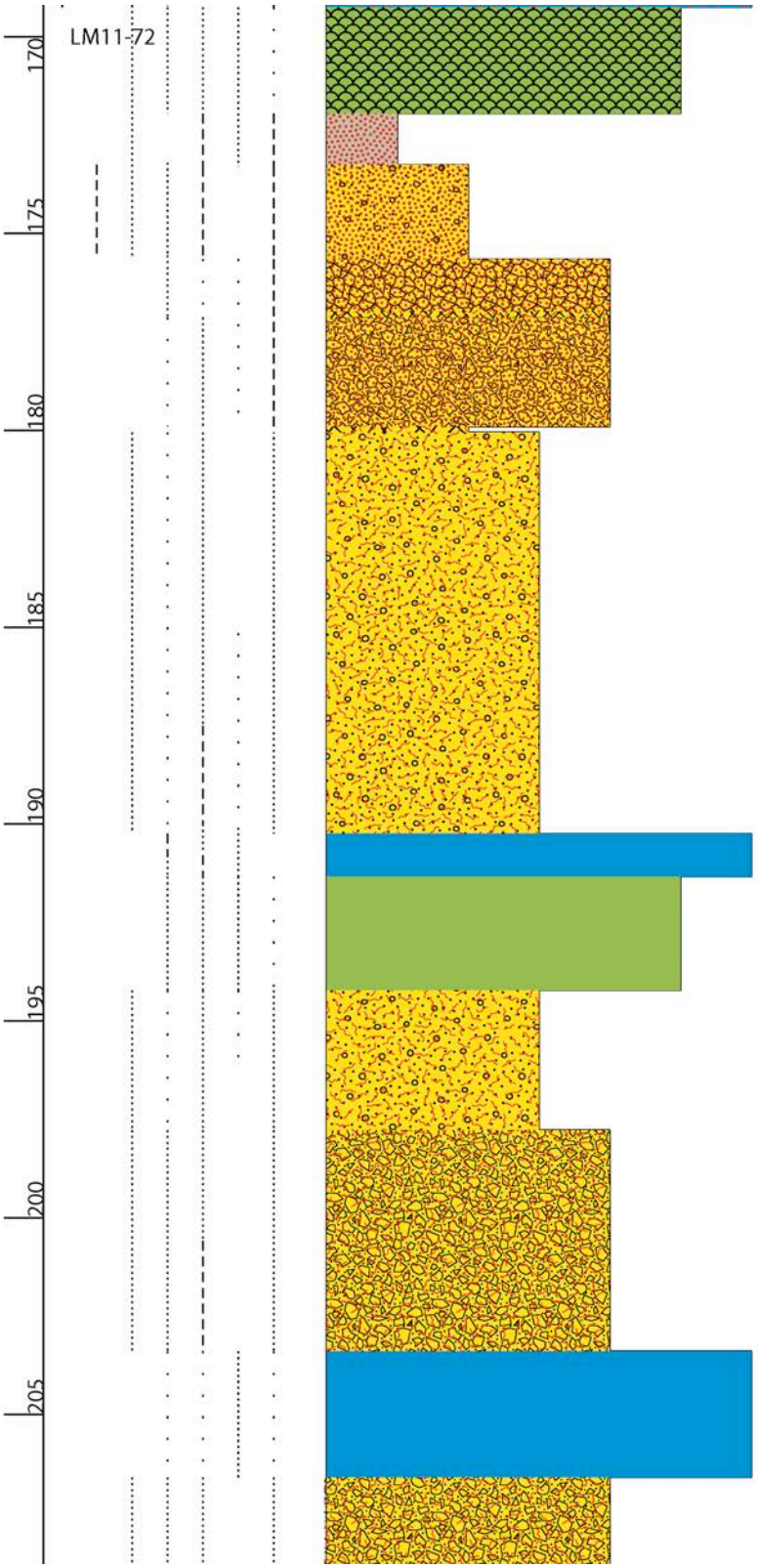

[169.25m - 172.0m] **Basalt Flow**: pillowed, flow top breccia, magnetic, sheared
-->Alt=qtz-CO3-Po filled amygdules, selvages, leopard spotting
[172.0m - 173.3m] **Py-Po-Muds**, chl-alt, graphitic base
[173.3m - 175.7m] **RhyoliteTuff Breccia**: sheared
-->Alt=heavy chl-ep, SMS honey Sp+Py>Gn±CCp,Trt
[175.7m - 179.8m] **Rhyolite Breccia**: grades from puzzle-fit to chl-tuff matrix, cataclastite @ 177.03m, sheared overall
-->Alt=ser, kspar at base, CO3 veins, SMS Py+honey Sp

[179.8m - 178.95m] **Chl-Tuff**
[179.95m - 190.14m] **Rhyolite Lapilli-Tuff**: diffuse borders, occasional blocks
-->Alt=ser-qtz to chl-qtz at base, CO3 veins, honey Sp+Py±Ccp stringers

[190.14m - 191.23m] **Basalt Dyke**: sheared ser-upper, chl-lower contacts
[191.23m - 194.12m] **Basalt Flow**: massive, fine-grained
-->Alt=ser, chl-CO3 veins, amygdules, pyritohedrons

[194.12m - 197.67m] **Ryolite Lapilli-Tuff**: (as above) sheared, glass-rich

[197.67m - 203.05m] **Rhyolite Tuff Breccia**: distinct block borders, polylithic lower contact
-->Alt=chl-qtz-ser, Py+honey Sp±Ccp stringers

[203.05m - 206.25m] **Basalt Dyke**: peperitic contacts
-->Alt=chl-ser, variably CO3 filled amygdules, bladed FeCO3, Py veins

[206.25m - 227.6m] **Polylithic Tuff Breccia**: all felsic, glass-rich, sheared
-->Alt=variable ep,ser,chl clasts,

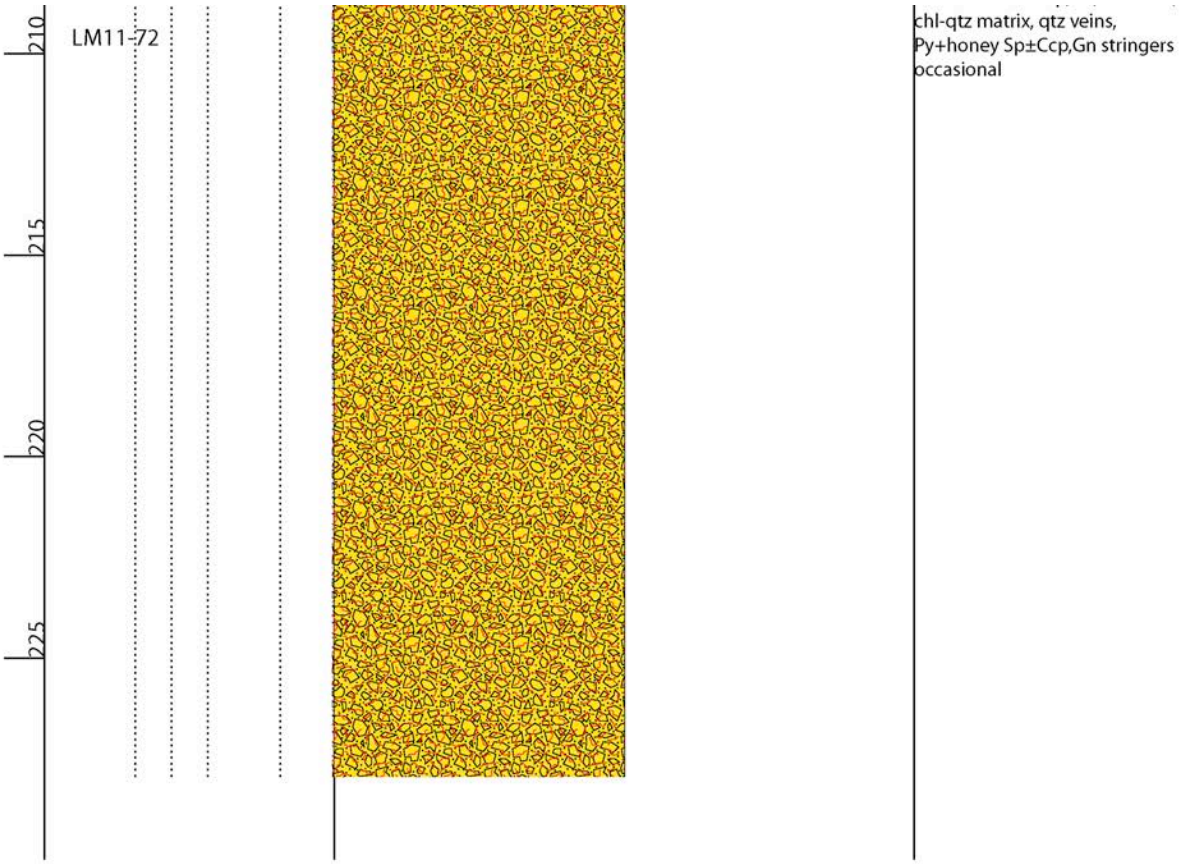
LM11-72
210
215
220
225
chl-qtz matrix, qtz veins,
Py+honey Sp±Ccp,Gn stringers
occasional

Claim: South Tally Pond | Azimuth: 90°

DIAMOND DRILL HOLE: LM13-73 | UTM: 520599.3E, 5375124N | Dip: -72°

Date: 06-18-2013 | EOH: 422m

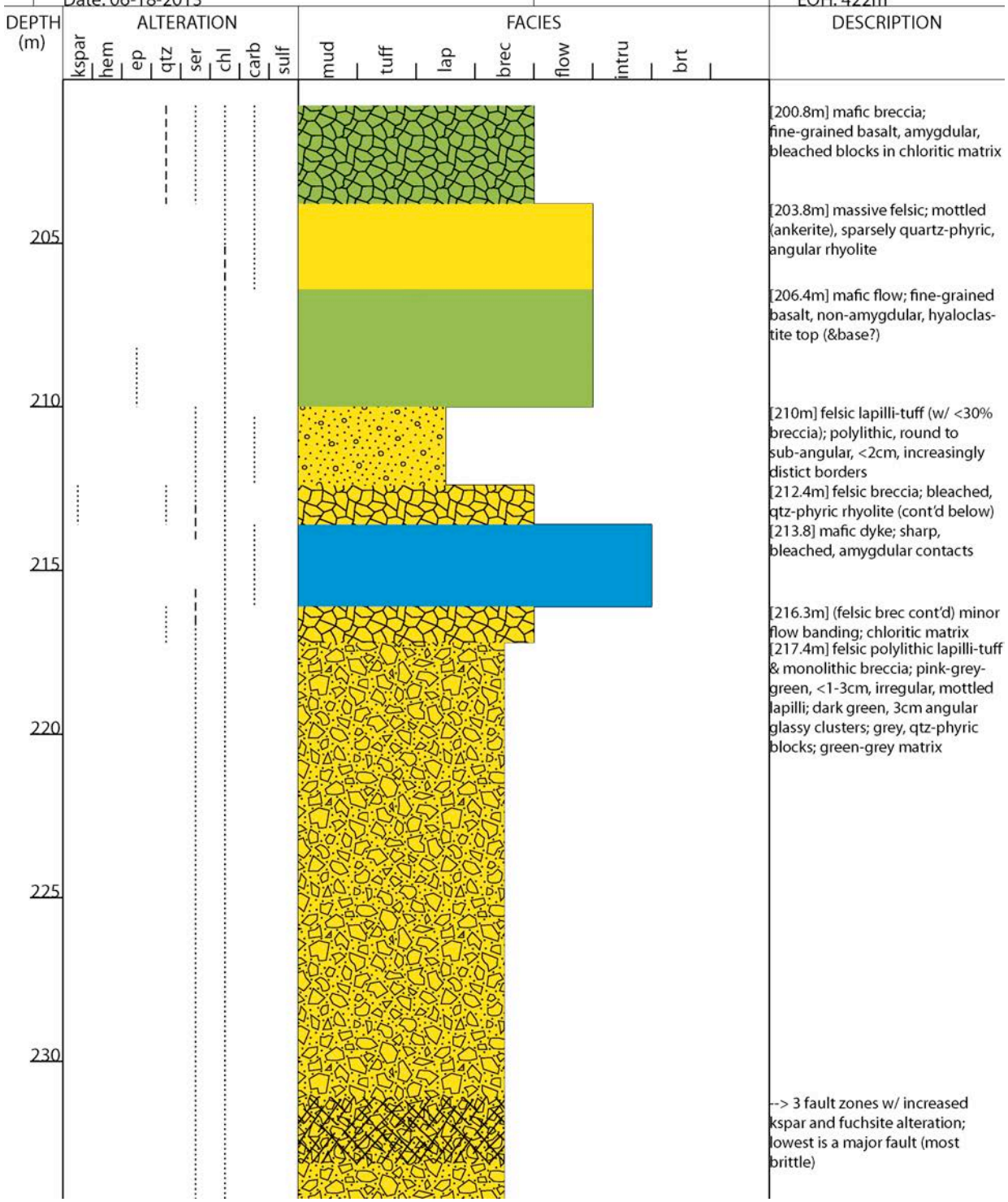

DESCRIPTION

[200.8m] mafic breccia; fine-grained basalt, amygdular, bleached blocks in chloritic matrix

[203.8m] massive felsic; mottled (ankerite), sparsely quartz-phyric, angular rhyolite

[206.4m] mafic flow; fine-grained basalt, non-amygdular, hyaloclastite top (&base?)

[210m] felsic lapilli-tuff (w/ <30% breccia); polylithic, round to sub-angular, <2cm, increasingly distict borders

[212.4m] felsic breccia; bleached, qtz-phyric rhyolite (cont'd below)

[213.8] mafic dyke; sharp, bleached, amygdular contacts

[216.3m] (felsic brec cont'd) minor flow banding; chloritic matrix

[217.4m] felsic polylithic lapilli-tuff & monolithic breccia; pink-grey-green, <1-3cm, irregular, mottled lapilli; dark green, 3cm angular glassy clusters; grey, qtz-phyric blocks; green-grey matrix

--> 3 fault zones w/ increased kspar and fuchsite alteration; lowest is a major fault (most brittle)

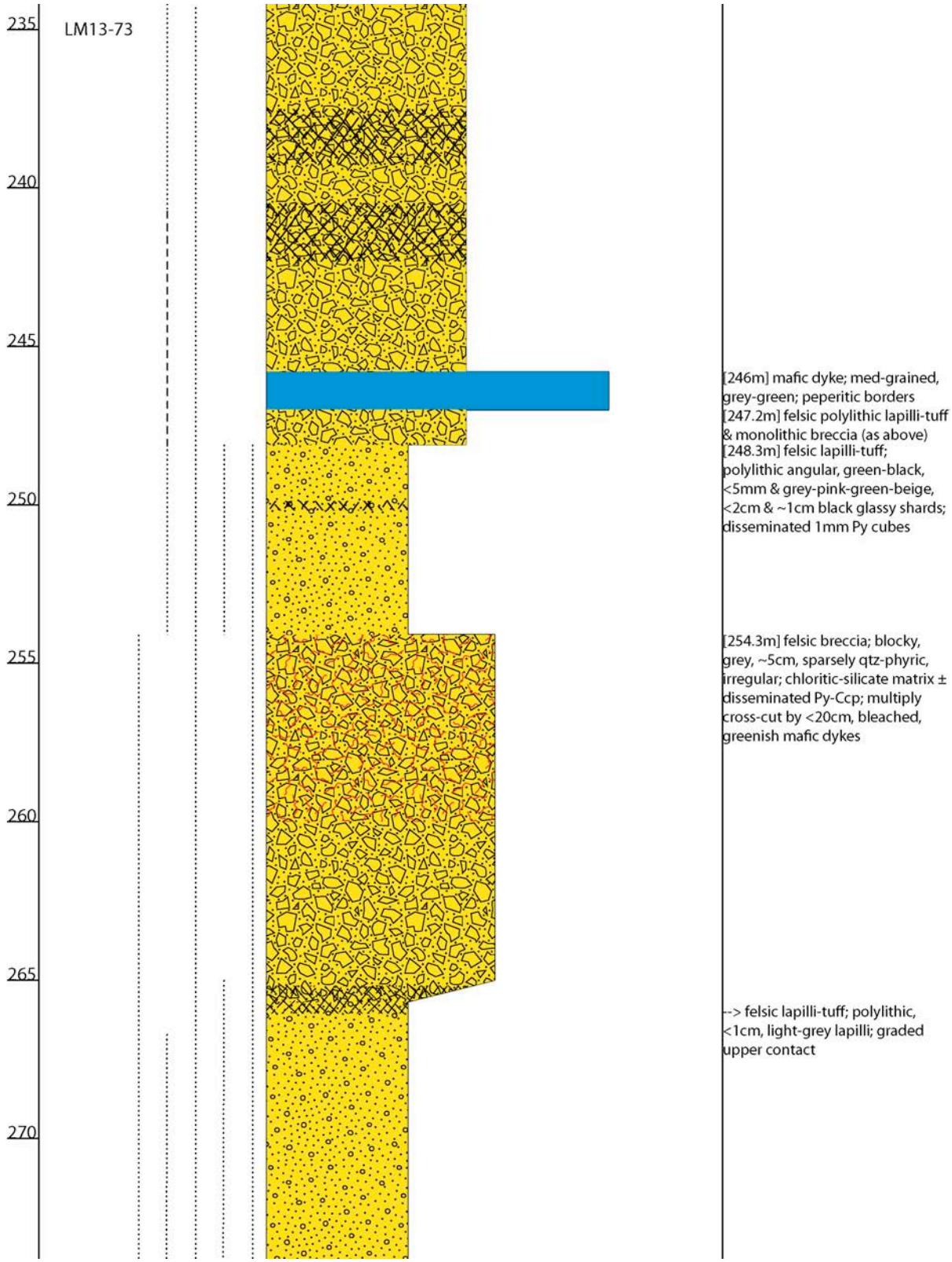
LM13-73
235
240
245
250
255
260
265
270
[246m] mafic dyke; med-grained, grey-green; peperitic borders
[247.2m] felsic polylithic lapilli-tuff & monolithic breccia (as above)
[248.3m] felsic lapilli-tuff; polylithic angular, green-black, <5mm & grey-pink-green-beige, <2cm & ~1cm black glassy shards; disseminated 1mm Py cubes
[254.3m] felsic breccia; blocky, grey, ~5cm, sparsely qtz-phyric, irregular; chloritic-silicate matrix ± disseminated Py-Ccp; multiply cross-cut by <20cm, bleached, greenish mafic dykes
--> felsic lapilli-tuff; polylithic, <1cm, light-grey lapilli; graded upper contact

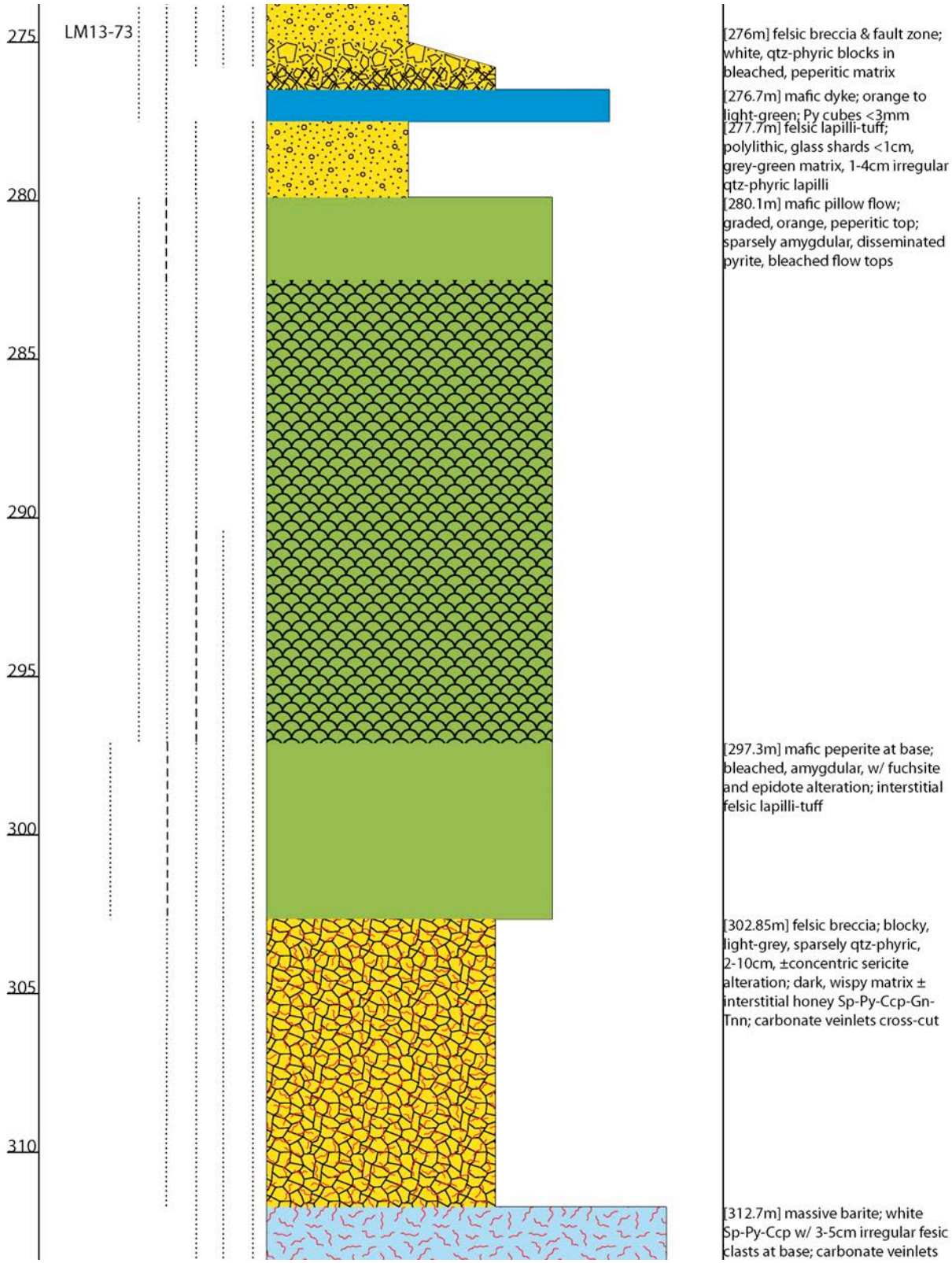
LM13-73
275
280
285
290
295
300
305
310
[276m] felsic breccia & fault zone; white, qtz-phyric blocks in bleached, peperitic matrix
[276.7m] mafic dyke; orange to light-green; Py cubes <3mm
[277.7m] felsic lapilli-tuff; polylithic, glass shards <1cm, grey-green matrix, 1-4cm irregular qtz-phyric lapilli
[280.1m] mafic pillow flow; graded, orange, peperitic top; sparsely amygdular, disseminated pyrite, bleached flow tops
[297.3m] mafic peperite at base; bleached, amygdular, w/ fuchsite and epidote alteration; interstitial felsic lapilli-tuff
[302.85m] felsic breccia; blocky, light-grey, sparsely qtz-phyric, 2-10cm, ±concentric sericite alteration; dark, wispy matrix ± interstitial honey Sp-Py-Ccp-Gn-Tnn; carbonate veinlets cross-cut
[312.7m] massive barite; white Sp-Py-Ccp w/ 3-5cm irregular fesic clasts at base; carbonate veinlets

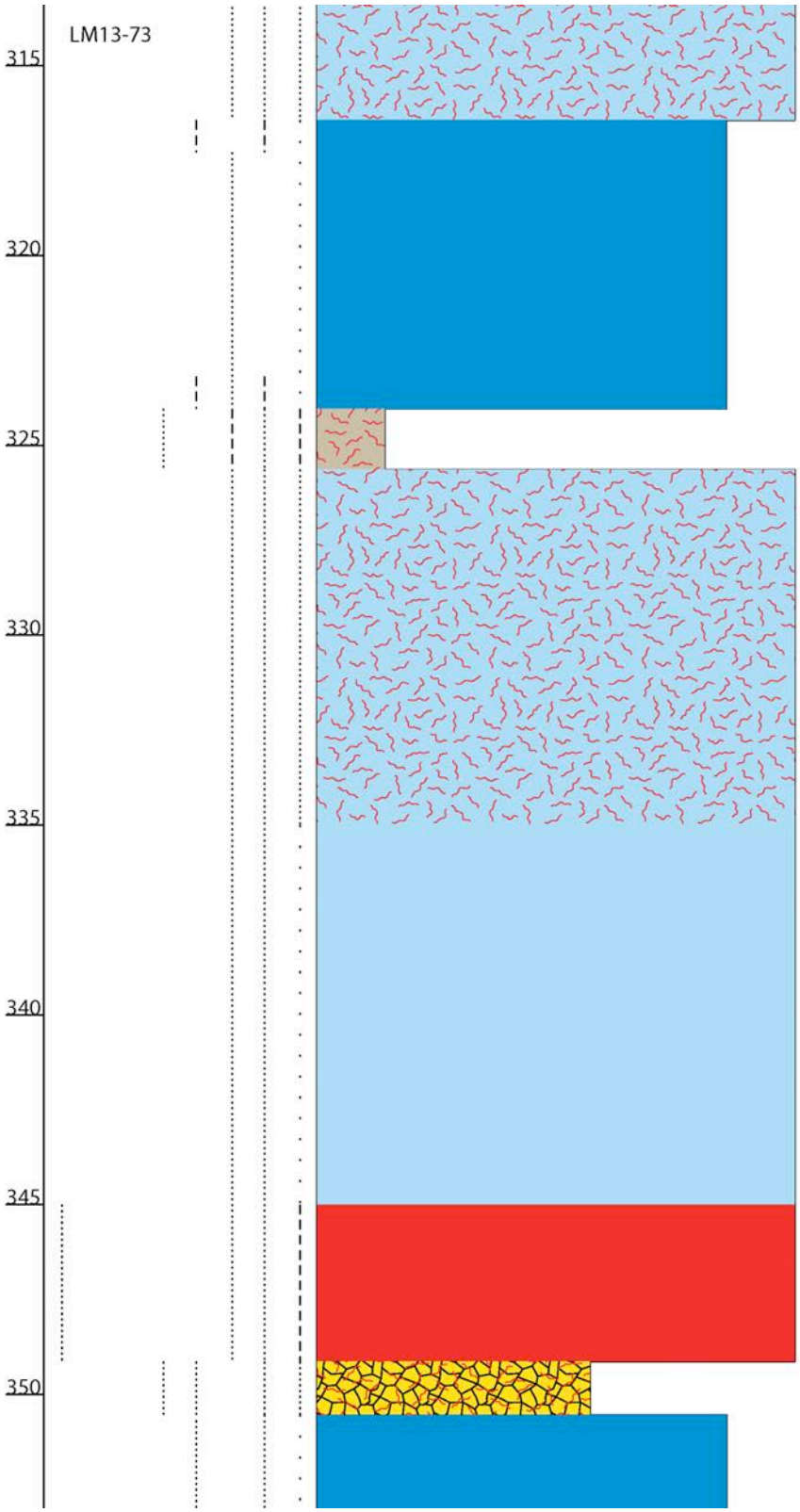
LM13-73
315
320
325
330
335
340
345
350
cross-cut
[317.4m] mafic dyke; bleached, pink rop and base; fine-grained, sparsely amygdular, minor fuchsite, scattered 3mm Py cubes
[325m] Py-mud & chl-schist; finely banded, deformed at base, scattered Ccp
[326.6m] massive barite; Py-white Sp-Ccp-Bn-Tnn-Gn stringers cross-cut; bladed barite clustered and sparse
--> sulphides grade from semi-massive to massive honey to orange Sp-Py-Ccp; albite rhombs throughout
[350.1m] felsic breccia; white, 3-7cm blocks; vuggy qtz+honey Sp-cubic Py-Gn-Ccp
[352m] mafic dyke; bleached, Py cubes scattered, mostly peperitic, intersitial felsic clasts and lapilli

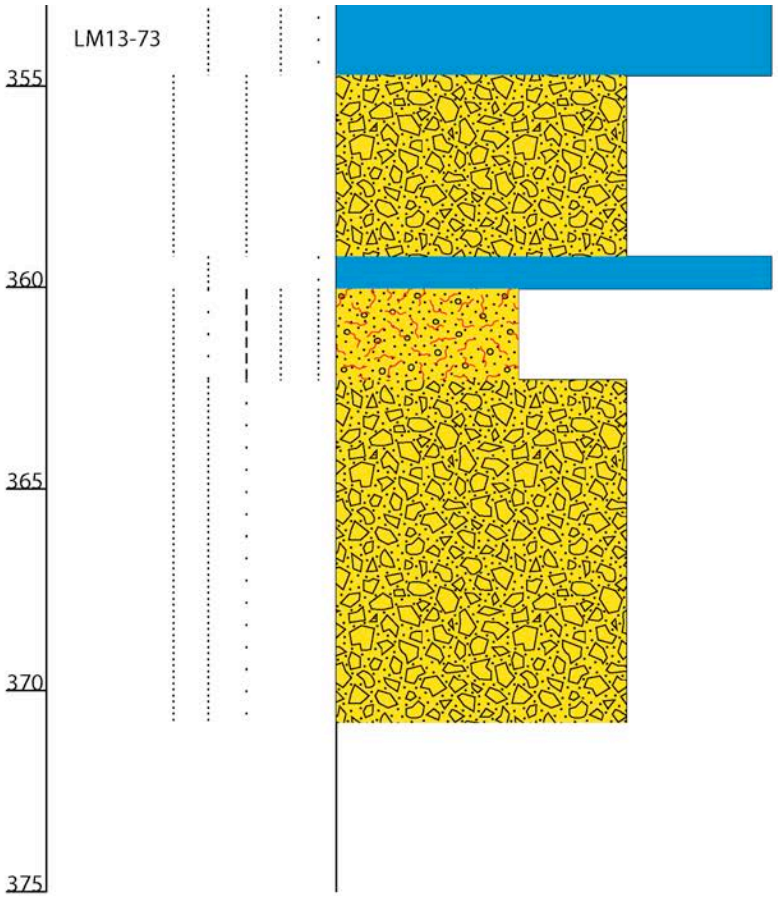

[356.2m] felsic lapilli-tuff & breccia; graded contact with above dyke; monolithic grey-green irregular blocks in black-green matrix

[360.7m] mafic dyke; brown, fine-grained w/ fuchsite, 1cm Py cubes scattered

[361.5m] felsic lapilli-tuff; grey-green irregular lapilli in black matrix; qtz-ser-honey Sp cross-cut

[363.8m] felsic breccia; ghostly, grey-green, 1-3cm, irregular rhyolite in whitish matrix; cross-cutting qtz veins

Claim: South Tally Pond | Azimuth: 90°

DIAMOND DRILL HOLE: LM13-74 | UTM: 520599.3E, 5375124N | Dip: -66°

Date: 06-19-2013 | EOH: 368m

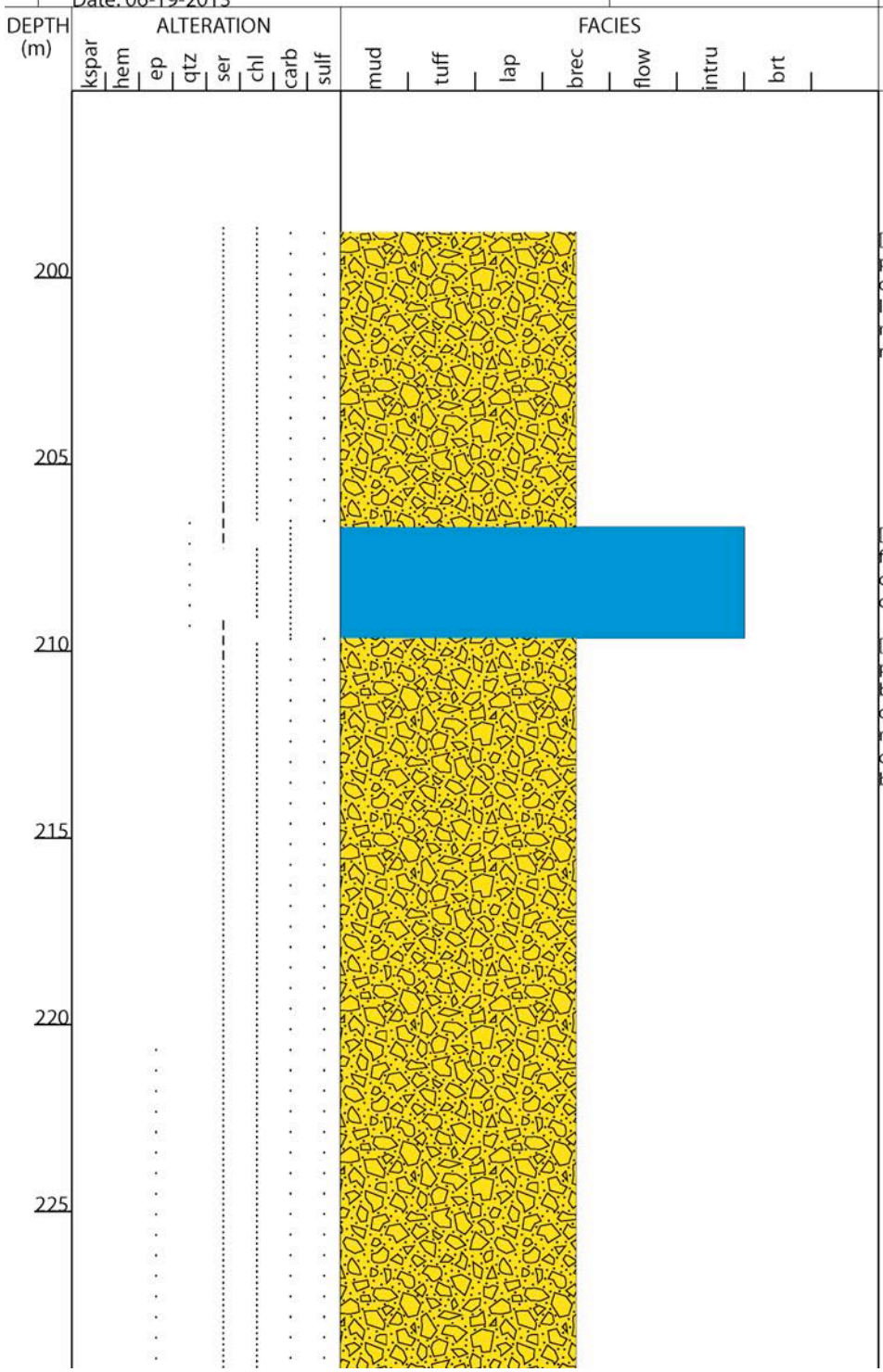

DESCRIPTION

[198.8m] felsic lapilli-tuff breccia; polylithic, pink-grey-green-beige, qtz-aphyric, sub-angular, 1cm lapilli or 2-7cm clasts; green-black matrix, bleached contact, disseminated Py; qtz-chl veins crosscut

[206.72m] mafic dyke; fine-grained, green, bleached contacts; chl-carb amydular; contains "fluoidal" clasts?

[209.68m] felsic lapilli-tuff breccia; polylithic, fragmental; 0.2-5cm, beige-grey-green-yellow, sparsely qtz-phyric, sub-angular to rounded; black glassy shards in clusters; sheared, fluoidal, ep-alt at base; disseminated Py

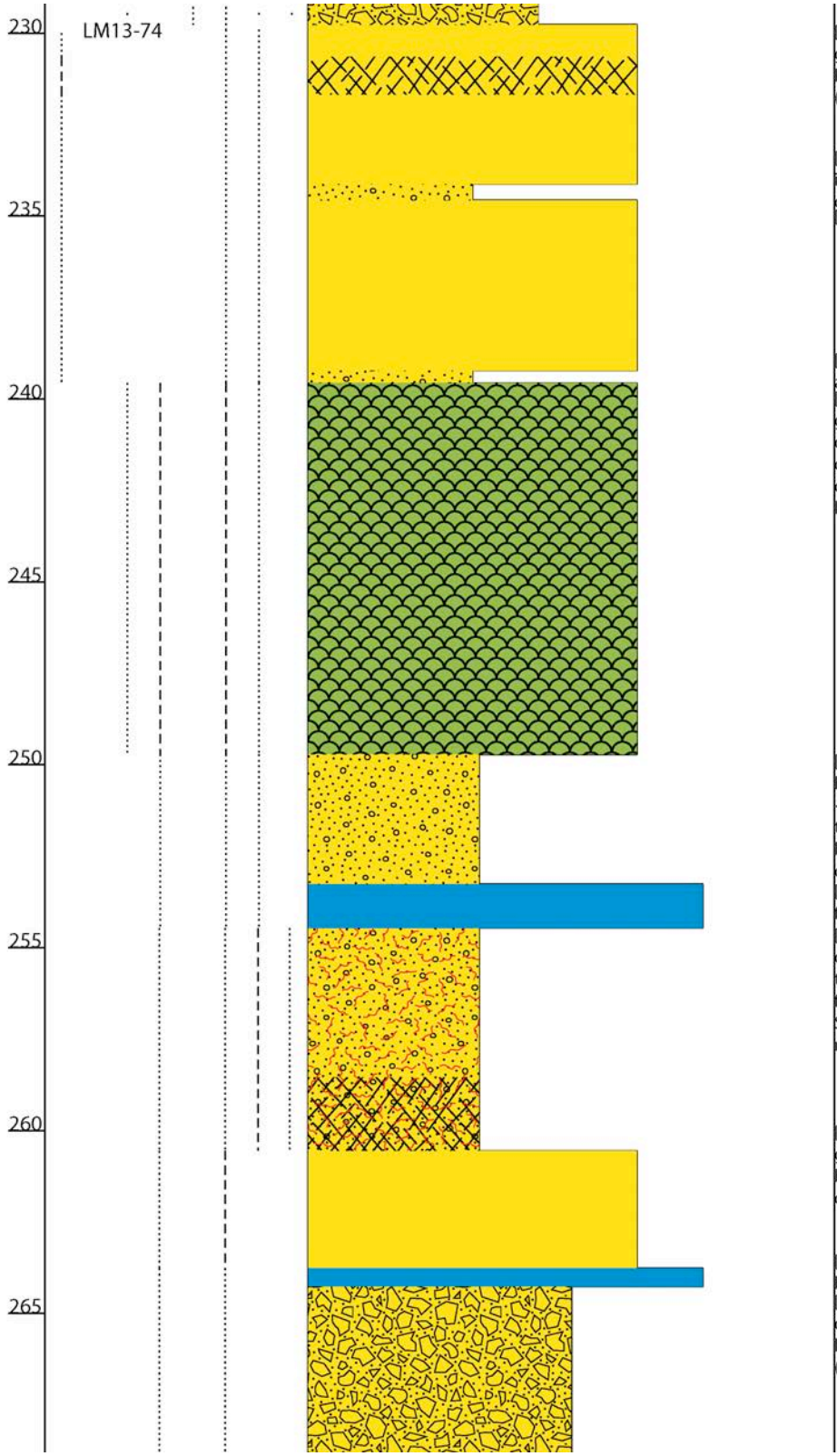
LM13-74
230
235
240
245
250
255
260
265
[229.8m] massive felsic; white-green, chl-alt qtz-phyric rhyolite; kspar alt w/ fault zone; mottled (ankerite)
[234.16m] felsic lapilli-tuff; intermittent; angular to rounded, green-black-beige lapilli
[234.6m] massive felsic (as above)
[239.26m] felsic lapilli-tuff (as above)
[239.6] mafic pillow flow; light-grey, med to fine grained, amygdular (<1mm, sheared) at pillow contacts (also sheared&tension cracked, pyritic, w/ entrained lapilli); carb-qtz veins cross-cut
[249.75m] felsic lapilli-tuff; heterolithic; grey-green, irregular, <1cm lapilli in similar-coloured tuff matrix; fluoidal, <5cm blebs, bleached, amygdular mafics; carb-qtz veins cross-cut
[253.3m] mafic dyke; dark green, fine-grained, fluoidal
[254.5m] felsic lapilli-tuff; extreme ductile deformation of above unit; tension cracks w/ carb-qtz-fuchsite infill; white-honey Sp-Py-Ccp cross-cut felsics and matrix
[260.59m] massive felsic; dark green, mostly aphyric rhyolite; black-green insitu (?) breccia contacts; carb veins cross-cut
[263.8m] mafic dyke; brown, bleached, Py-cubic, amygdular
[264.3m] felsic breccia; grey-white, diffuse, minor qtz-phyric, monolithic rhyolite; brittle fault zone (rubble)

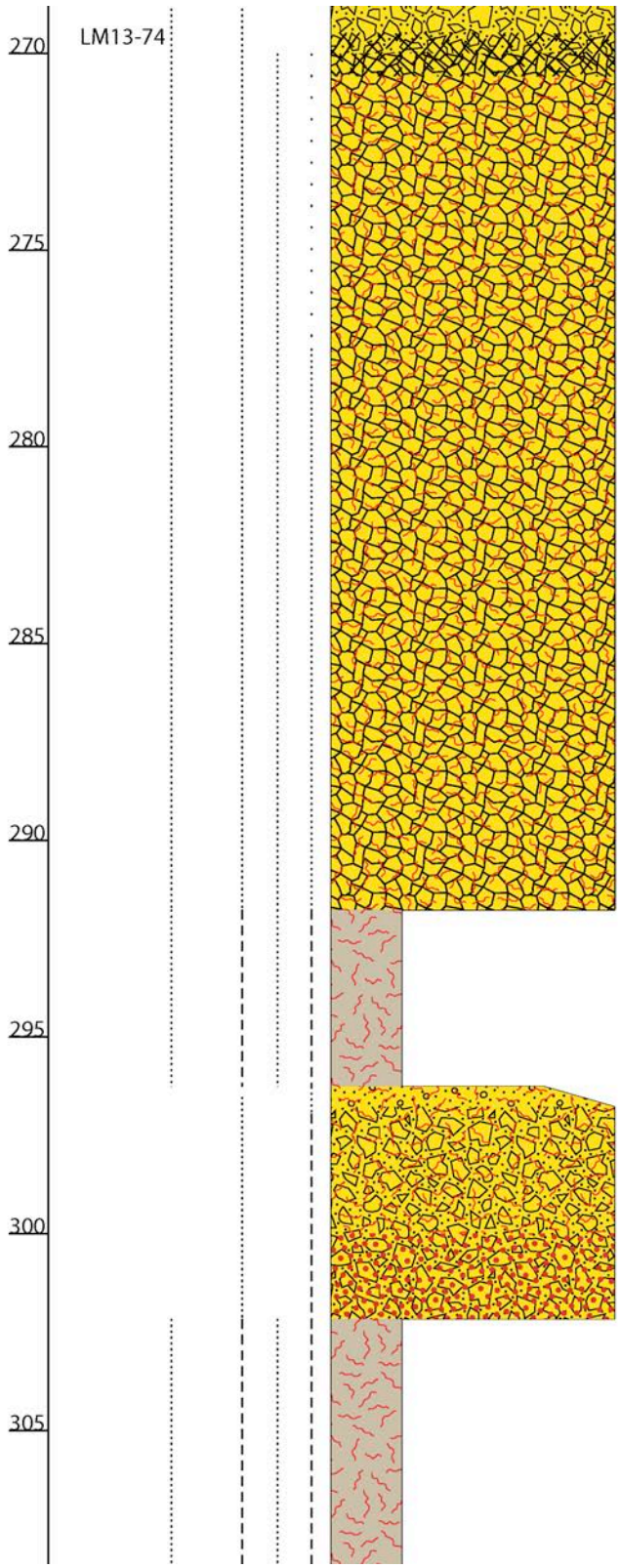

--> intersitial black-green, chloritic matrix; honey Sp-Py-Ccp to orange Sp-Py-Ccp-Gn to red Sp-Py-Ccp-Gn associated w/ carb veins and cross-cutting muds

--> increased deformation; muds-sulfss-carb veins cross-cut; rare flow banding in clasts (2-10cm, size decreases toward base)

[291.8m] Py-mud &chl-schist; laminated top, sheared base; Po-blebs and carb to Po tension crack infill

[296.3m] felsic lapilli-tuff breccia; graded top; monolithic, grey-green, qtz-phyric <2cm lapilli and >10cm clasts; black matrix; red Sp stringers to semi-massive red Sp-Py-Ccp-Gn-Tnn

[302.2m] Py mud (as above); repeats laminated-sheared pattern 2x

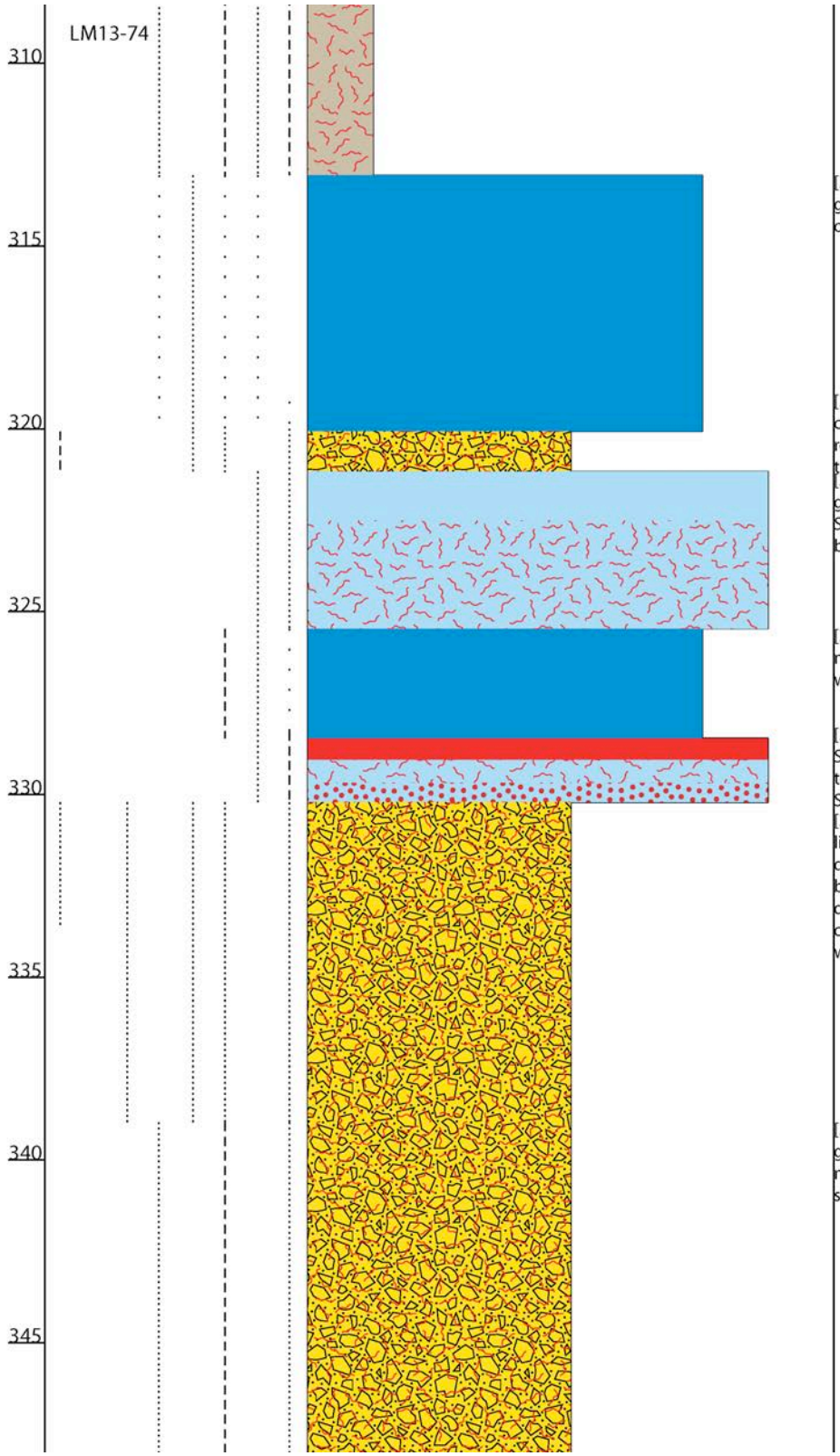
LM13-74
310
315
320
325
330
335
340
345
[313.1m] mafic dyke; brown-green; bleached base, w/Py cubes or fine-grained clusters & fuchsite
[320.1m] felsic breccia; grey, pink concentric alk, qtz-phyric, rounded&oblong, 3-7cm; intersitial chl-Py
[321.2m] massive barite; mottled grey-white at top; Py to honey Sp-Py-Ccp-Gn stringers crosscut at base
[325.5m] mafic dyke; black-green, non-amygdular; carb veins w/cubic Py
[328.5m] barite; massive red Sp-Gn-Py-Ccp to Ccp-Py stringers to semi-massive honey-white Sp-Gn-Py-Ccp w/ albite rhombs
[330.25m] felsic breccia; monolithic, beige-white-pink, 5-10cm, qtz-phyric rhyolite (becomes brown-pink + ep-alt w/ increased deformation); qtz-chl veins cross-cut; interstitial dk chl-Py-white honey Sp-Ccp
[339m] felsic breccia; ghostly, grey green clasts in dark grey-green matrix; blebby honey Sp-Py stringers cross-cut

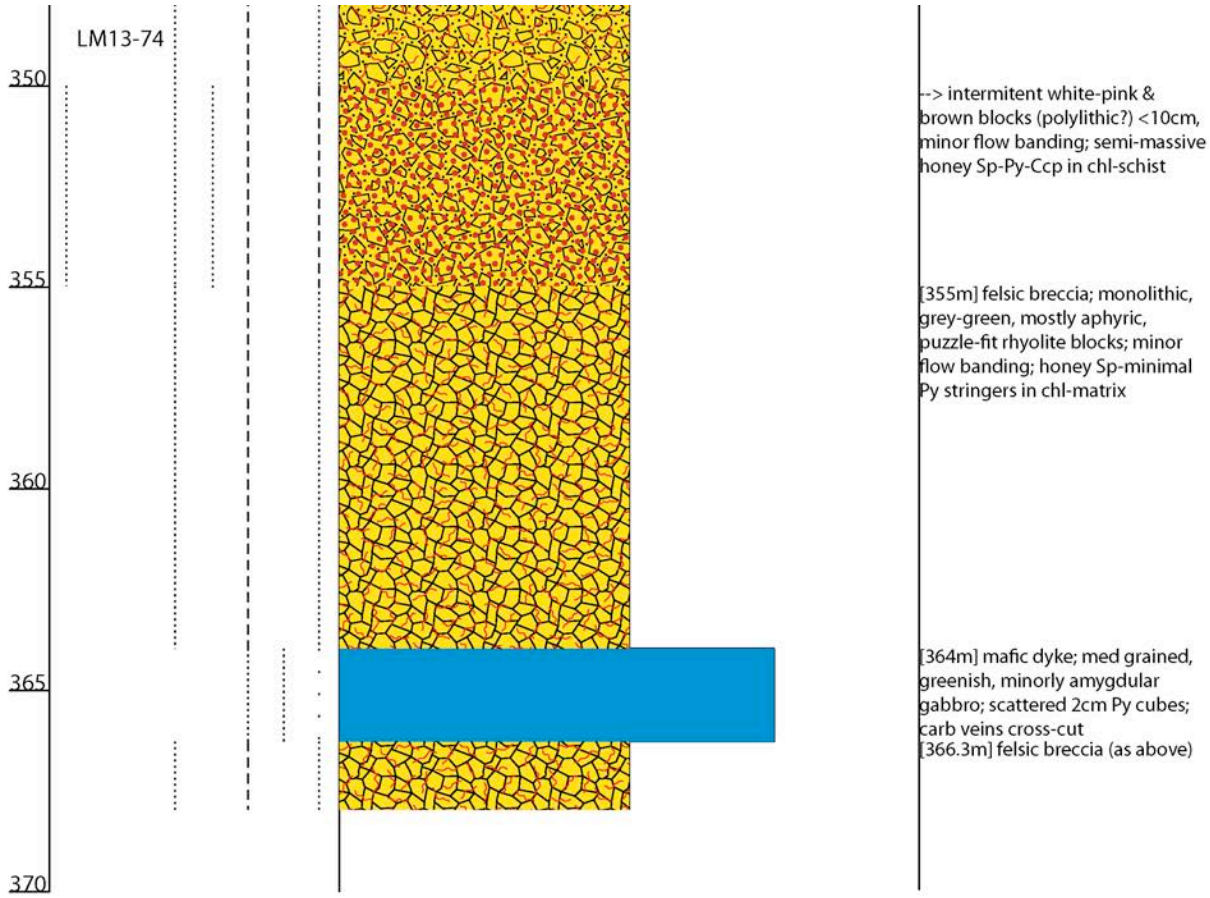
LM13-74
350
355
360
365
370
--> intermitent white-pink & brown blocks (polylithic?) <10cm, minor flow banding; semi-massive honey Sp-Py-Ccp in chl-schist
[355m] felsic breccia; monolithic, grey-green, mostly aphyric, puzzle-fit rhyolite blocks; minor flow banding; honey Sp-minimal Py stringers in chl-matrix
[364m] mafic dyke; med grained, greenish, minorly amygdular gabbro; scattered 2cm Py cubes; carb veins cross-cut
[366.3m] felsic breccia (as above)

DIAMOND DRILL HOLE: LM13-77

Date: 07-25-2013

Claim: South Tally Pond

UTM: 521049E, 5374537N

Azimuth: 90°

Dip: -90°

EOH: 209m

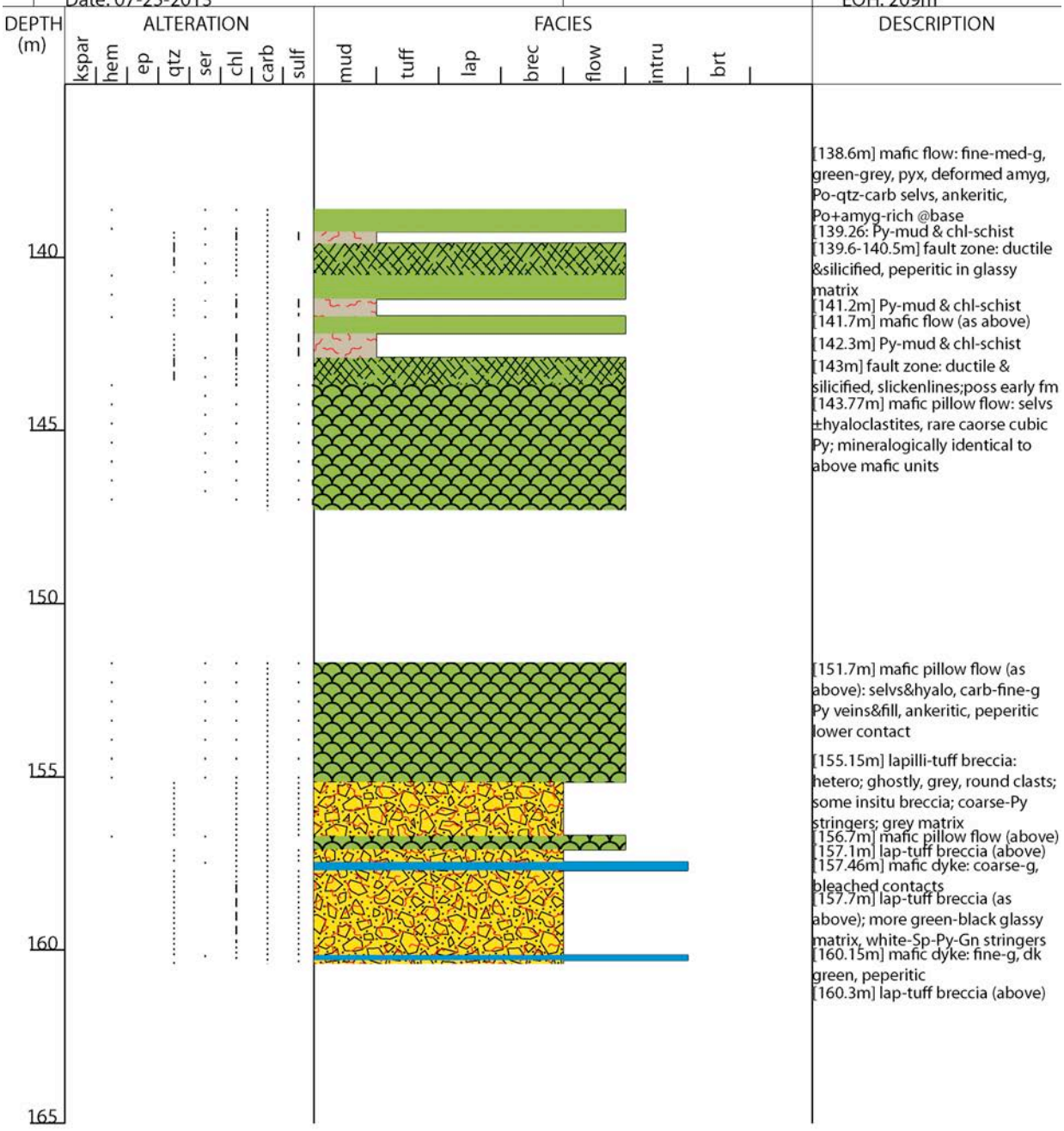

[138.6m] mafic flow: fine-med-g, green-grey, pyx, deformed amyg, Po-qtz-carb selvs, ankeritic, Po+amyg-rich @base

[139.26: Py-mud & chl-schist

[139.6-140.5m] fault zone: ductile &silicified, peperitic in glassy matrix

[141.2m] Py-mud & chl-schist

[141.7m] mafic flow (as above)

[142.3m] Py-mud & chl-schist

[143m] fault zone: ductile & silicified, slickenlines;poss early fm

[143.77m] mafic pillow flow: selvs ±hyaloclastites, rare caorse cubic Py; mineralogically identical to above mafic units

[151.7m] mafic pillow flow (as above): selvs&hyalo, carb-fine-g Py veins&fill, ankeritic, peperitic lower contact

[155.15m] lapilli-tuff breccia: hetero; ghostly, grey, round clasts; some insitu breccia; coarse-Py stringers; grey matrix

[156.7m] mafic pillow flow (above)

[157.1m] lap-tuff breccia (above)

[157.46m] mafic dyke: coarse-g, bleached contacts

[157.7m] lap-tuff breccia (as above); more green-black glassy matrix, white-Sp-Py-Gn stringers

[160.15m] mafic dyke: fine-g, dk green, peperitic

[160.3m] lap-tuff breccia (above)

DIAMOND DRILL HOLE: LM13-78

Claim: South Tally Pond

Azimuth: 270°

Date: 07-24-2013

UTM: 520956E, 5374477N

Dip: -55°

EOH: 187m

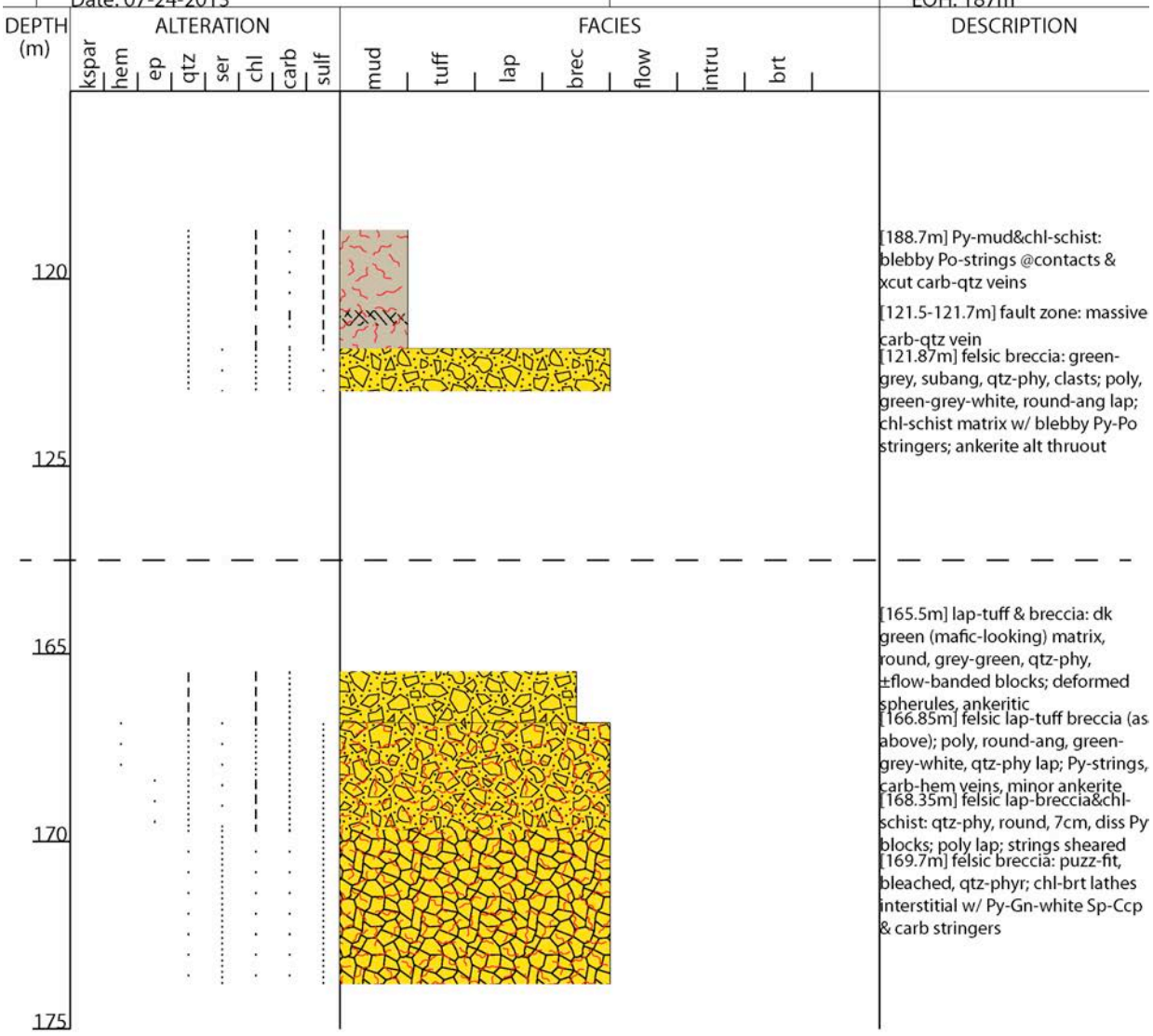

Claim: South Tally Pond | Azimuth: 270°

DIAMOND DRILL HOLE: LM13-79 | UTM: 521114.6E, 5374625N | Dip: -53°

Date: 06-25-2013 | EOH: 229m

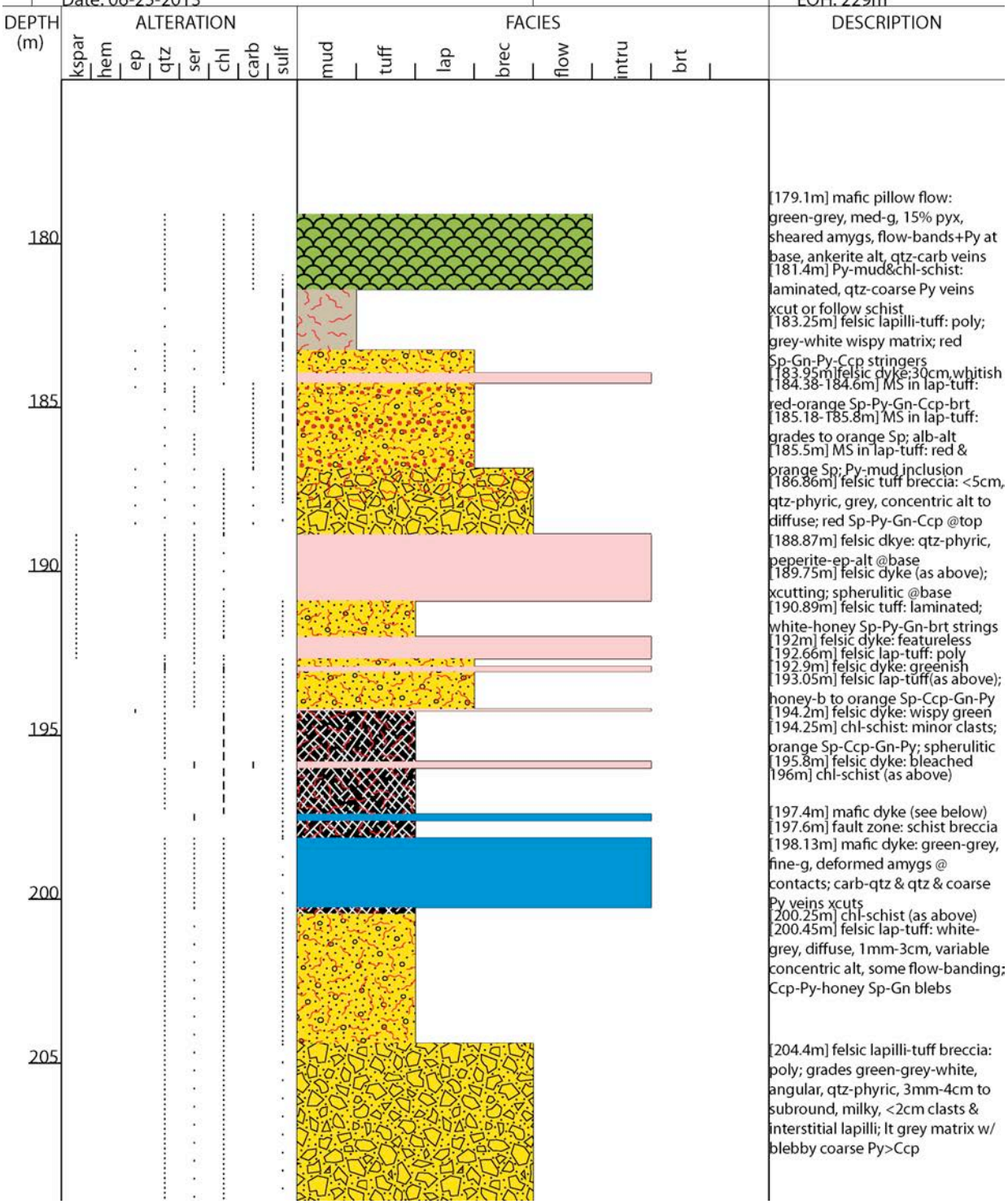

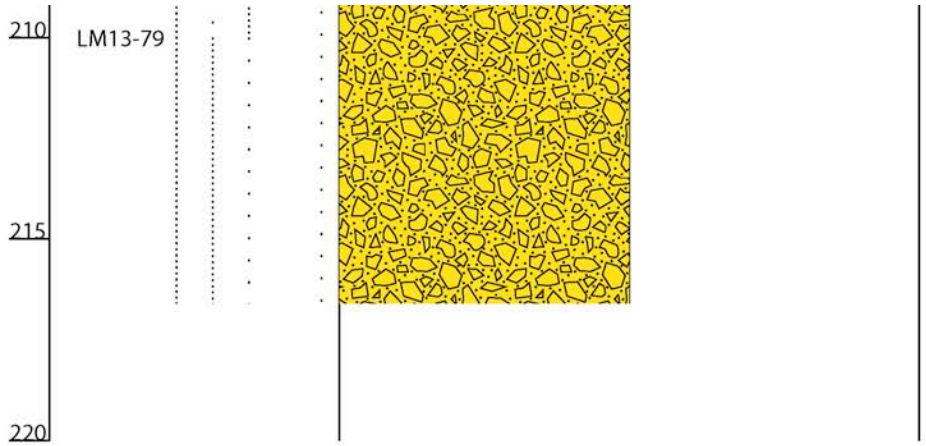
210
LM13-79
215
220

DIAMOND DRILL HOLE: LM13-80

Claim: South Tally Pond

Azimuth: 275°

UTM: 521115E, 5374648N

Dip: -55°

Date: 07-24-2013

EOH: 272m

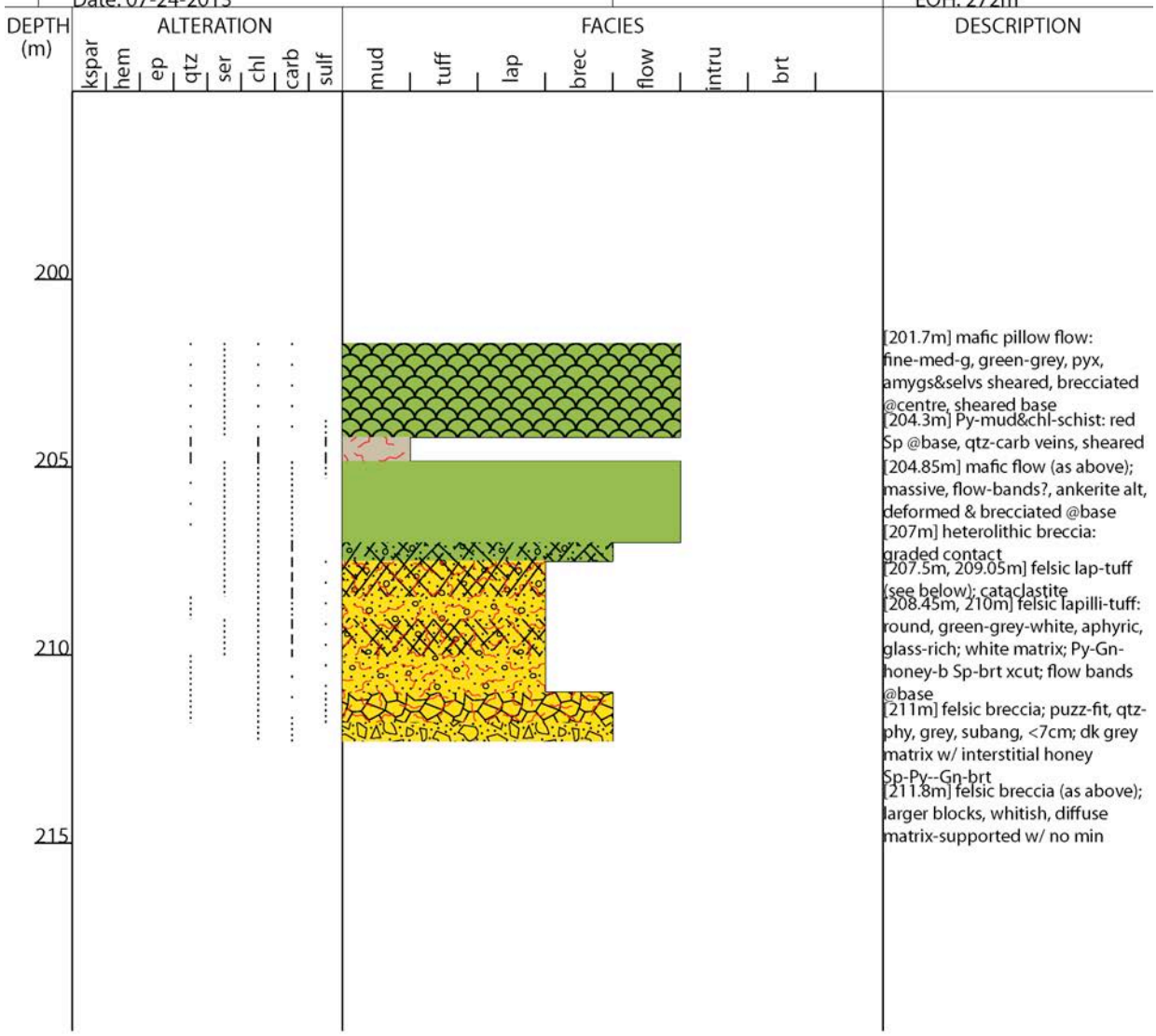

DIAMOND DRILL HOLE: LM92-07

Date: 07-25-2013

Claim: South Tally Pond

UTM: 521009.654E, 5374597.359N

Azimuth: 270°

Dip: -50°

EOH: 249.94m

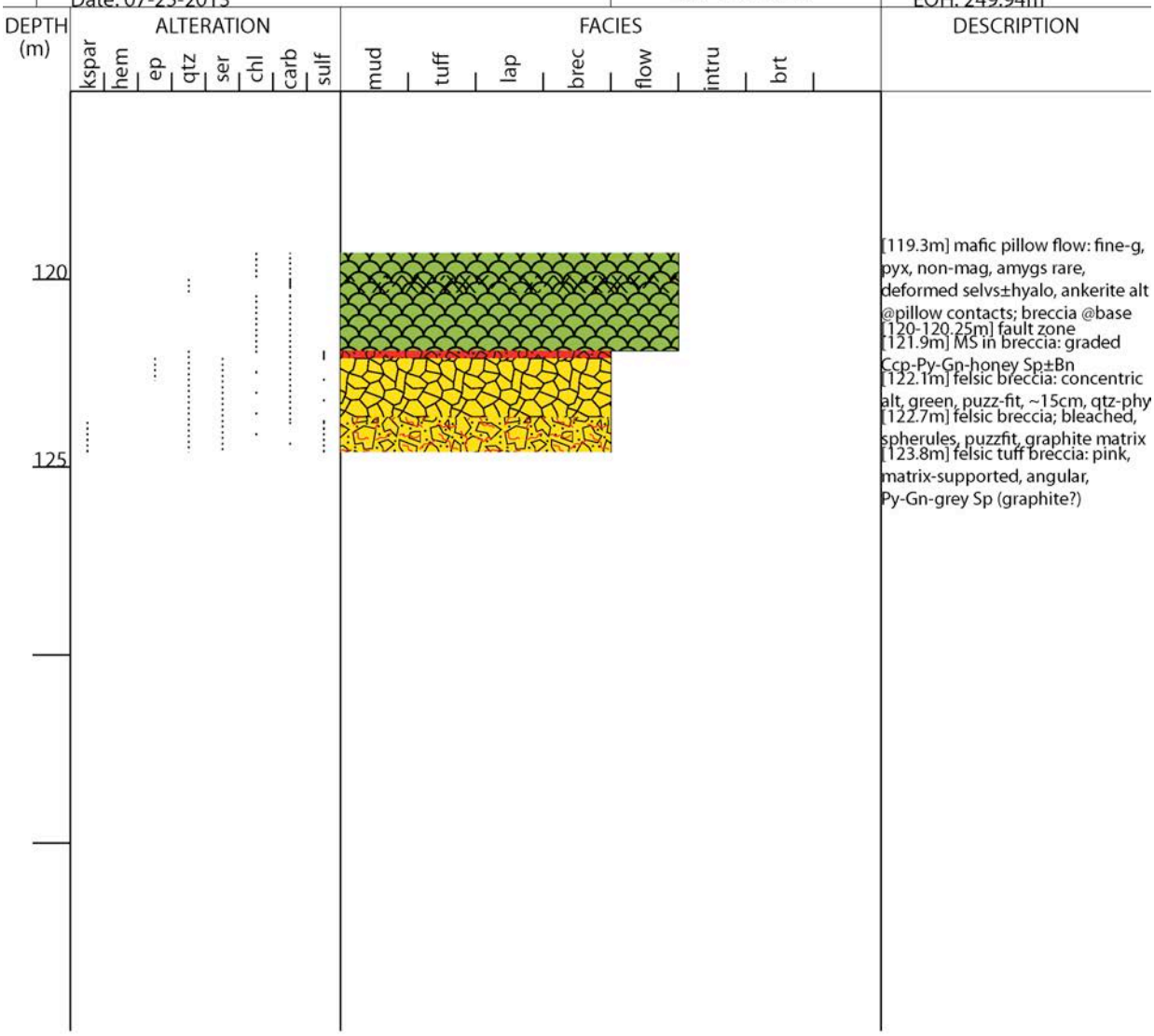

Claim: South Tally Pond | Azimuth: 270°

DIAMOND DRILL HOLE: LM92-08 | UTM: 521002.049E, 5374808.893N | Dip: -45°

Date: 06-26-2013 | EOH: 262.1m

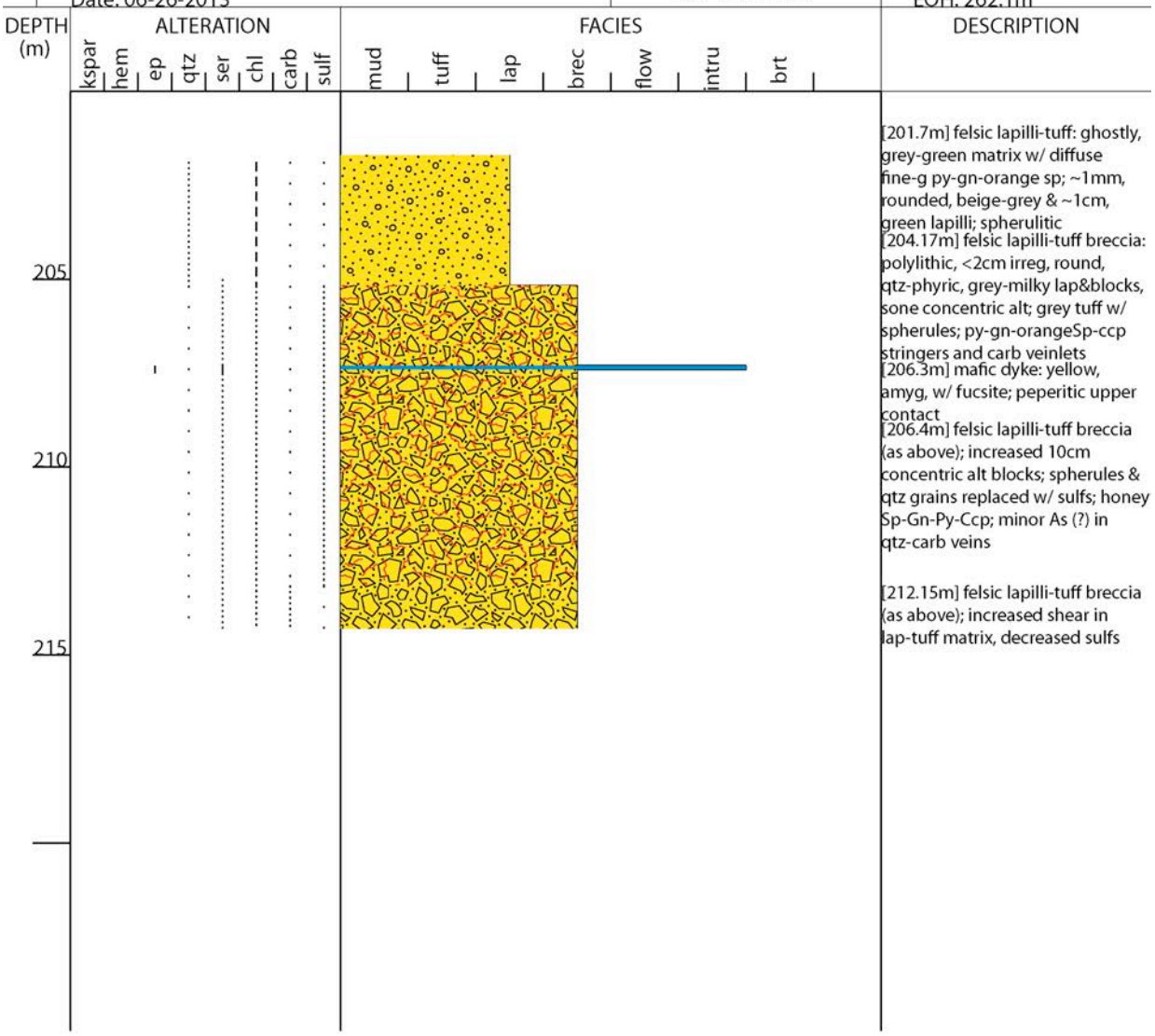

DESCRIPTION

[201.7m] felsic lapilli-tuff: ghostly, grey-green matrix w/ diffuse fine-g py-gn-orange sp; ~1mm, rounded, beige-grey & ~1cm, green lapilli; spherulitic

[204.17m] felsic lapilli-tuff breccia: polylithic, <2cm irreg, round, qtz-phyric, grey-milky lap&blocks, sone concentric alt; grey tuff w/ spherules; py-gn-orangeSp-ccp stringers and carb veinlets

[206.3m] mafic dyke: yellow, amyg, w/ fucsite; peperitic upper contact

[206.4m] felsic lapilli-tuff breccia (as above); increased 10cm concentric alt blocks; spherules & qtz grains replaced w/ sulfs; honey Sp-Gn-Py-Ccp; minor As (?) in qtz-carb veins

[212.15m] felsic lapilli-tuff breccia (as above); increased shear in lap-tuff matrix, decreased sulfs

Claim: South Tally Pond

Azimuth: 270°

DIAMOND DRILL HOLE: LM93-10

UTM: 521114.795E, 5374599.342N

Dip: -90°

Date: 07-25-2013

EOH: 309.8m

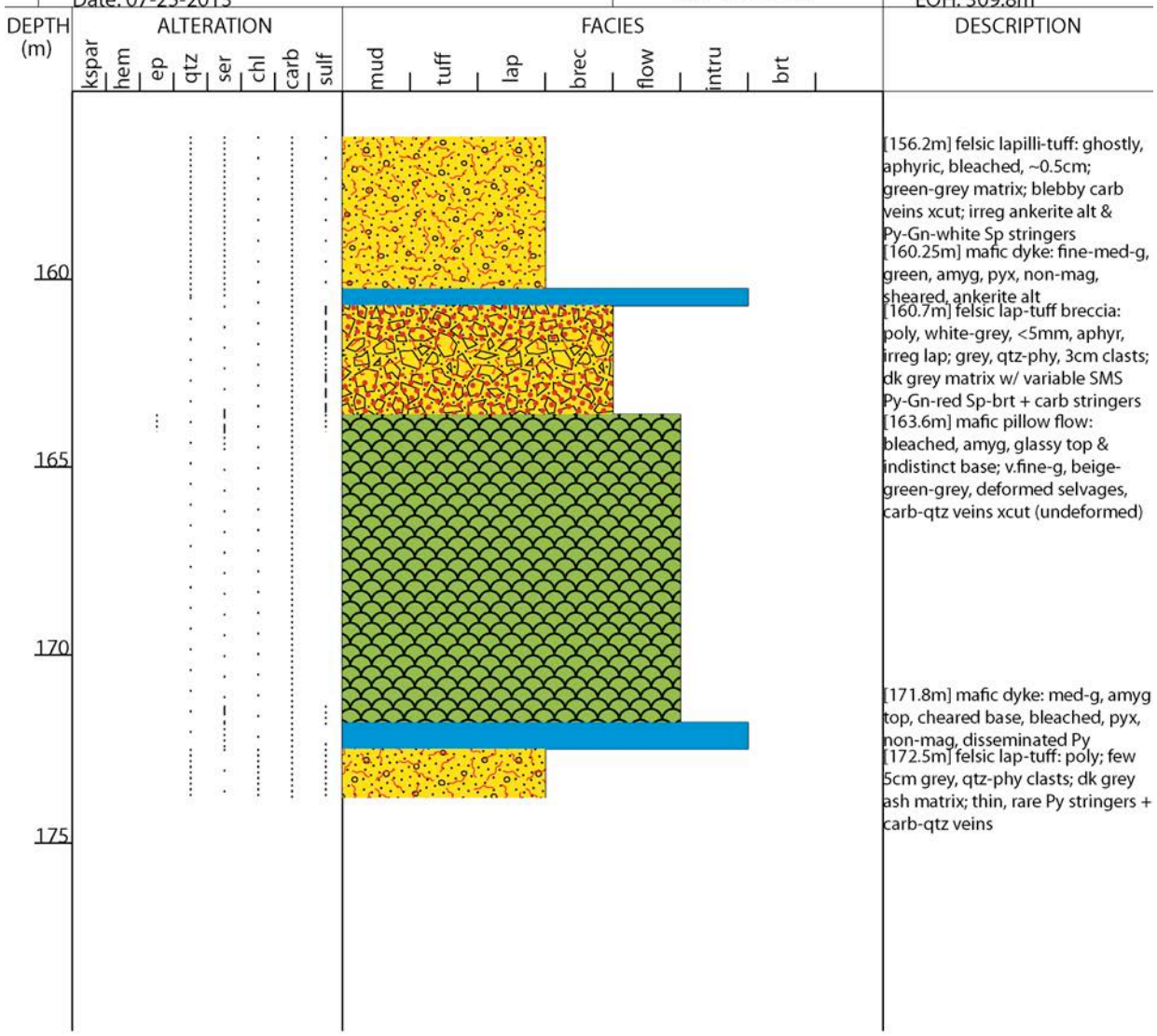

DESCRIPTION

[156.2m] felsic lapilli-tuff: ghostly, aphyric, bleached, ~0.5cm; green-grey matrix; blebby carb veins xcut; irreg ankerite alt & Py-Gn-white Sp stringers

[160.25m] mafic dyke: fine-med-g, green, amyg, pyx, non-mag, sheared, ankerite alt

[160.7m] felsic lap-tuff breccia: poly, white-grey, <5mm, aphyr, irreg lap; grey, qtz-phy, 3cm clasts; dk grey matrix w/ variable SMS Py-Gn-red Sp-brt + carb stringers

[163.6m] mafic pillow flow: bleached, amyg, glassy top & indistinct base; v.fine-g, beige-green-grey, deformed selvages, carb-qtz veins xcut (undeformed)

[171.8m] mafic dyke: med-g, amyg top, cheared base, bleached, pyx, non-mag, disseminated Py

[172.5m] felsic lap-tuff: poly; few 5cm grey, qtz-phy clasts; dk grey ash matrix; thin, rare Py stringers + carb-qtz veins

Claim: South Tally Pond | Azimuth: 270°

DIAMOND DRILL HOLE: LM93-11 | UTM: 521209E, 5375116.366N | Dip: -54°

Date: 07/23/2012 | EOH: 597.0m

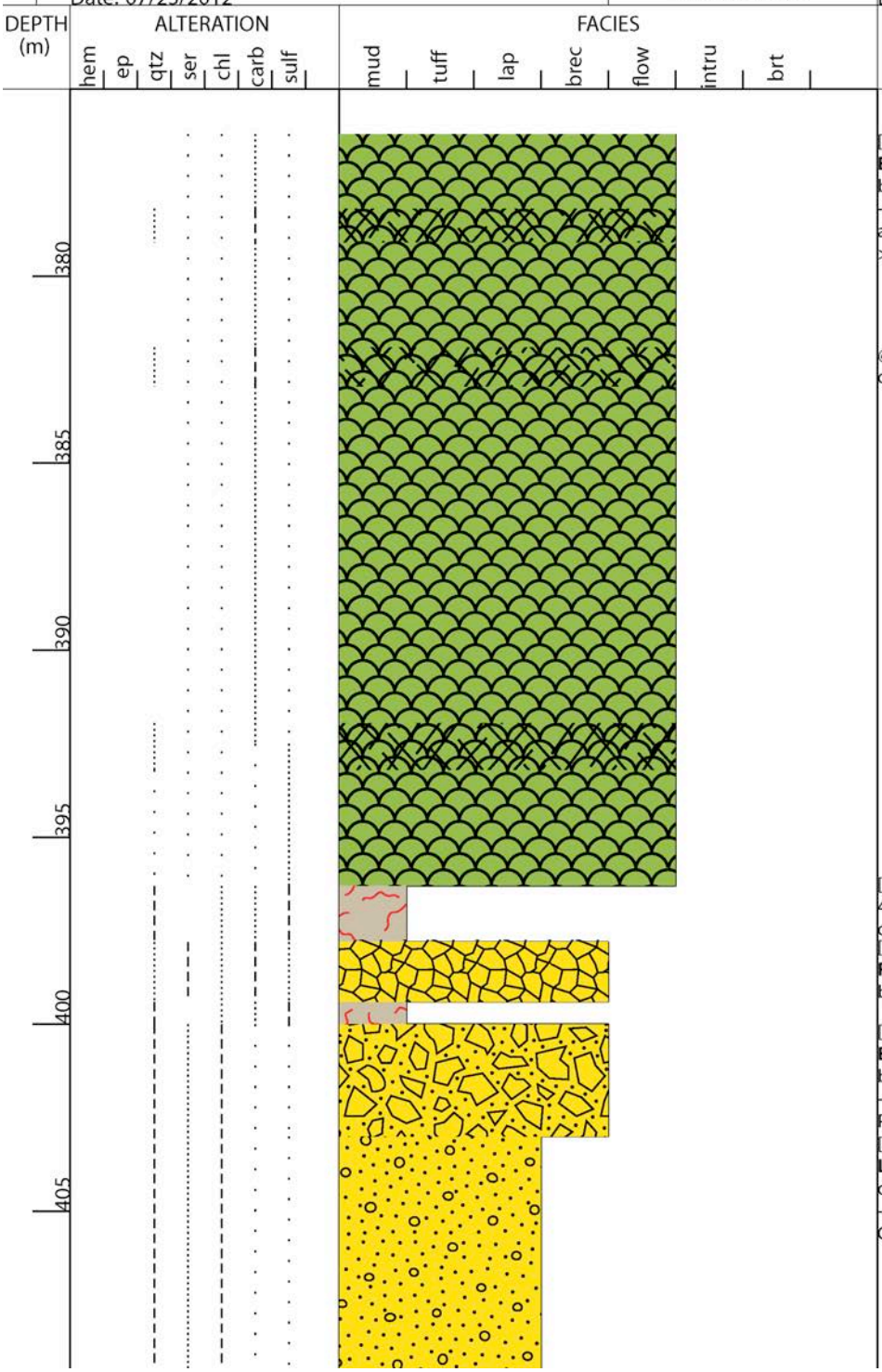

DESCRIPTION

[376.2m - 396.2m] **Basalt Flow**: pillowed, flow top breccias, sheared
-->Alt =chl-Py-CO3 filled selvages, amygdules, bladed FeCO3
>383.0m

@ 378.8m, 382.4m, 391.74m qtz-CO3 veined shear zones

[396.3m - 397.8m, 399.4m - 400.0m] **Py-Muds**: sheared, qtz-chl-CO3 veined

[397.8m - 399.4m] **Puzzle-Fit Rhyolite Breccia**: diffuse block borders, chl-matrix, CO3 veins

[400.0m - 403.0m] **Rhyolite Tuff Breccia:** sheared, chaotic block borders
-->Alt=chl-matrix, disseminated Py, qtz-CO3 veins

[403.0m - 412.47m] **Rhyolite Lapilli-Tuff**: sheared, glass-rich, diffuse borders
-->Alt=qtz-ser+chl, CO3-Py±orange Sp veins

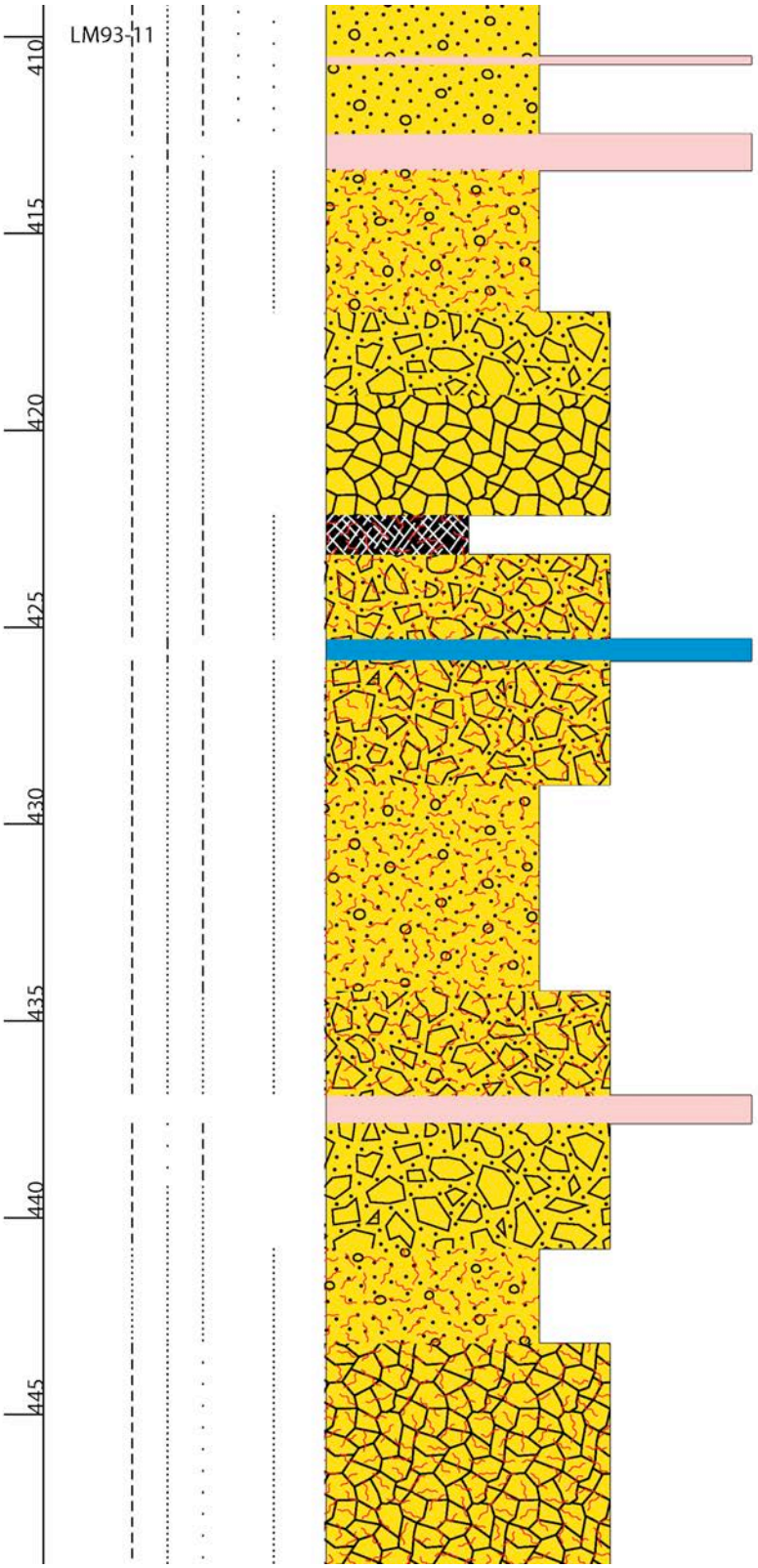

@ 410.5m, 412.47m - 413.4m **Rhyolite Dyke**: aphyric, translucent
-->Alt=spotty ser overprint

[413.4m - 417.0m] **Rholite Lapilli-Tuff**: variably deformed
-->Alt=silicified, chl-tuff, orange Sp+Py>Gn±Ccp,Brn stringers

[417.0m - 422.15m]
Rhyolite Tuff Breccia grades into **Puzzle-Fit Breccia**: halos, distinct borders, sheared
-->Alt=chl, silicified

[422.15m - 423.16m] **Rhyolite Tuff:** heavy chl, orange Sp+Ccp >Py±Trt,Brn stringers

[423.16m - 429.0m] **Rhyolite Tuff Breccia**: diffuse borders
-->Alt=chl-matrix, orange Sp+Ccp >Py±Trt,Brn stringers

@ 425.3m - 425.85m **Basalt Dyke:** sericitic, pyritic, w/ Ccp at contacts

[429.0m - 434.25m] **Rhyolite Lapilli-Tuff**: sheared
-->Alt=chl-qtz, disseminated Py, occasional orange Sp,Py,Gn stringers

[434.25m - 440.78m] **Lapilli-Tuff Rhyolite Breccia**: distinct block borders, glass-rich matrix
-->Alt=silicified, disseminated Py

@ 436.9m **Rhyolite Dyke** w/ sharp upper, flowy lower contact ±Py, orange Sp,Ccp

[440.78m - 443.2m] **Rhyolite Lapilli-Tuff**: glass-rich, shear banded
-->Alt=ser-chl, Py±Ccp stringers

[443.2m - 460.2m]
Puzzle-Fit Rhyolite Breccia: halos, distinct borders, undeformed
-->Alt=chl-ser, qtz-chl veins crosscut, Py,Ccp±orange Sp,Gn,Trt stringers

Appendix B: Current Research 2013

Preliminary mineralogy of barite-associated sulphide mineralization in the Ordovician Zn-Pb-Cu-Ag-Au Lemarchant volcanogenic massive sulphide (VMS) deposit, Newfoundland

Authors: Shannon B. Gill, Stephen J. Piercey, and Christine A. Devine

Address (primary author): s.gill@mun.ca, Memorial University of Newfoundland, St. John's, Newfoundland

Abstract

The bimodal felsic Zn-Pb-Cu-Ag-Au Lemarchant volcanogenic massive sulphide (VMS) deposit is located in Central Newfoundland. Characteristic of the deposit is a mineralized barite lens that contains abundant sulphosalts and anomalous precious metals. While much of the barite is massive, bladed aggregates of barite are locally present. The mineralized barite lens consists of three mineral assemblages (or facies) that grade from the outer barite-rich mineralization toward the sulphide-rich base as follows: 1) facies A honey sphalerite + pyrite + chalcopyrite + bornite > enargite ± Au; 2) facies B white sphalerite + galena + pyrite + tetrahedrite > tennantite + stromeyerite + Ag-tetrahedrite; and 3) facies C honey-brown (and minor red) sphalerite + chalcopyrite + pyrite ± galena. Iron-contents of sphalerite grades from higher values in the outer barite lens and proximal rhyolite, to lower values in the central barite lens. Minor visible free gold is present in barite-rich facies A mineralization.

The interpreted primary mineralization sequence of these three facies begins with deposition of sphalerite and fine-grained pyrite, and penecontemporaneous crystallization

of tennantite-tetrahedrite, galena and enargite, followed by sulphide replacement by bornite and chalcopyrite, late-stage stromeyerite mineralization and recrystallization of euhedral pyrite.

The Lemarchant deposit is similar to other barite-rich, Kuroko-style VMS deposits, and is especially notable for its sulphosalt-rich mineral assemblage and precious metal-bearing minerals. Further detailed mineral chemistry, sulphur and lead isotope analyses and thermodynamic calculations will be undertaken to understand the siting of precious metals and the processes that resulted in precious metal enrichment at Lemarchant.

INTRODUCTION

The Central Mobile Belt of Newfoundland is host to numerous past and present producing VMS deposits, and has been the focus of massive sulphide exploration and development for over a century. The Lemarchant deposit, a recent discovery, is hosted within the Tally Pond volcanic belt of the Victoria Lake Supergroup (Evans and Kean, 2002; Rogers et al., 2006). This belt is also host to the currently producing Cu-Zn-rich Duck Pond deposit, and the soon to be developed Boundary deposit (Squires et al., 2001; Piercey and Hinchey, 2012). The barite-rich Zn-Pb-Cu-Au-Ag-bearing Lemarchant deposit is part of the South Tally Pond property that was initially discovered by Noranda who drilled the deposit in 1983 and from 1990-1993 (Squires and Moore, 2004). From 2007-2011, Paragon Minerals Corporation discovered the bulk of the deposit and obtained a National Instrument 43-101 resource on the deposit (Fraser et al., 2012). Canadian Zinc Corporation acquired Paragon Minerals Corporation in September 2012 and now holds a 100%-interest in the property. The Lemarchant deposit has an indicated

mineral resource of 1.24 Mt at 0.58% Cu, 5.38% Zn, 1.19% Pb, 1.01 g/t Au and 59.17 g/t Ag, and an inferred resource of 1.34 Mt at 0.41% Cu, 3.70% Zn, 0.86% Pb, 1.00 g/t Au and 50.41 g/t Ag (Fraser et al., 2012).

Despite these exploration efforts, little research has been undertaken to document the style of mineralization or to understand the high-grade base and precious metal enrichment at the Lemarchant deposit. In particular, there has been no definition of ore facies, description of 3D ore facies zonation, or siting of precious metals in the ore body. Initial results of field observations and preliminary petrographic and scanning electron microscopy are presented in this report, describing the mineralization associated with barite within the Lemarchant deposit. These preliminary results are procured as part of a Masters project at the Memorial University of Newfoundland and represent a contribution to the precious metal-rich VMS subproject of the Targeted Geoscience Initiative 4 program. The results provide a framework for further detailed work on the Lemarchant deposit, and a means of comparing Lemarchant to other Au-Ag-bearing VMS deposits in Canada and globally.

REGIONAL GEOLOGICAL SETTING

The Lemarchant deposit is hosted in Early Paleozoic accreted island arc and rifted arc complexes that comprise the eastern North American Appalachian Orogen (van Staal et al., 1998). The deposit is located south-southeast of the Red Indian Line, which defines a Silurian-age suture between peri-Laurentian and peri-Gondwanan rocks (Rogers et al., 2006; van Staal et al., 2007). The Red Indian Line also divides the Dunnage Zone, one of four tectonostratigraphic terranes that compose Newfoundland, into two subzones respectively called the Notre Dame and the Exploits subzones (Evans and Kean, 2002;

van Staal et al., 2007). The Lemarchant deposit is in the Exploits subzone (Fig. 1), which is the eastern, peri-Gondwanan section of the Dunnage Zone, and is specifically hosted in the Victoria Lake Supergroup, a stratigraphic sequence younging upward and consisting of Cambrian to Ordovician-age primitive arc, rifted arc, back-arc to mature arc volcanic sequences (Rogers et al., 2006; Zagorevski et al., 2010; Piercey and Hinchey, 2012). Easternmost and oldest of these volcanic belts is the Tally Pond group, an arc to arc-rift sequence that hosts the Lemarchant deposit, as well as the Duck Pond and Boundary VMS deposits (Evans and Kean, 2002; Rogers et al., 2006; Piercey and Hinchey, 2012).

The Tally Pond group is divided into two main formations (Rogers et al., 2006): the older and mafic dominated Lake Ambrose formation (~Lake Ambrose basalts of Dunning et al., 1991 and Evans and Kean, 2002), and the felsic-dominated Bindons Pond formation (~Boundary Brook formation of Dunning et al., 1991 and Evans and Kean, 2002). These formations have U-Pb ages ranging from ~514-509 Ma (Dunning et al., 1991; McNicoll et al., 2010), and the VMS deposits are hosted predominantly in felsic rocks of the Bindons Pond formation (Figs. 1-2; Squires et al., 2001; Piercey and Hinchey, 2012). The Tally Pond group is intruded by the Lemarchant microgranite, which outcrops approximately 500m northwest of the Lemarchant deposit (Fig. 2), and is interpreted to be a synvolcanic intrusion (Squires and Moore, 2004; Piercey and Hinchey, 2012). The Tally Pond group is cross-cut by the middle Ordovician Harpoon Hill gabbro dikes and sills (Squires and Moore, 2004; Piercey and Hinchey, 2012).

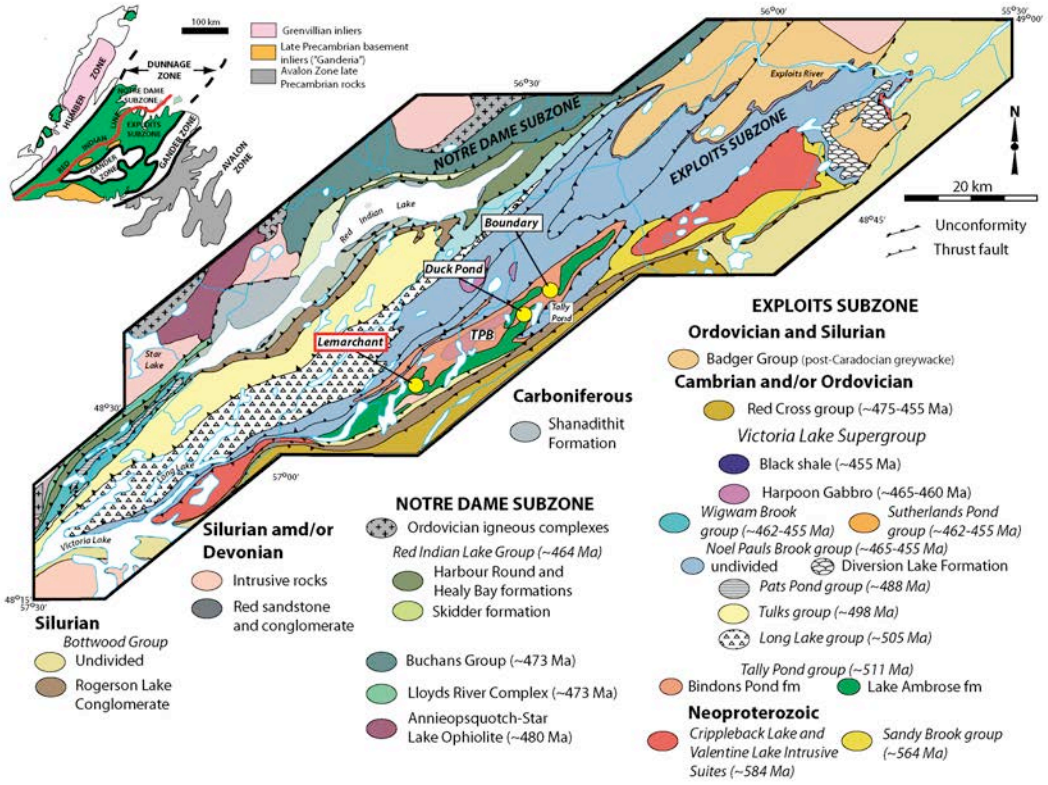

Figure 1. Geological map of volcanic belts that comprise the Exploits subzone, part of the Dunnage Zone of the Newfoundland Central Mobile Belt. The Red Indian Line suture is represented by the fault zone dividing the western edge of the Exploits subzone from the Notre Dame subzone. The Lemarchant deposit is outlined in red and shown in association with Duck Pond and Boundary deposits to the northeast. These deposits are part of the TPB (Tally Pond Belt) volcanic sequence, which lies on the eastern edge of the Exploits subzone. Modified from Piercey and Hinchey (2012).

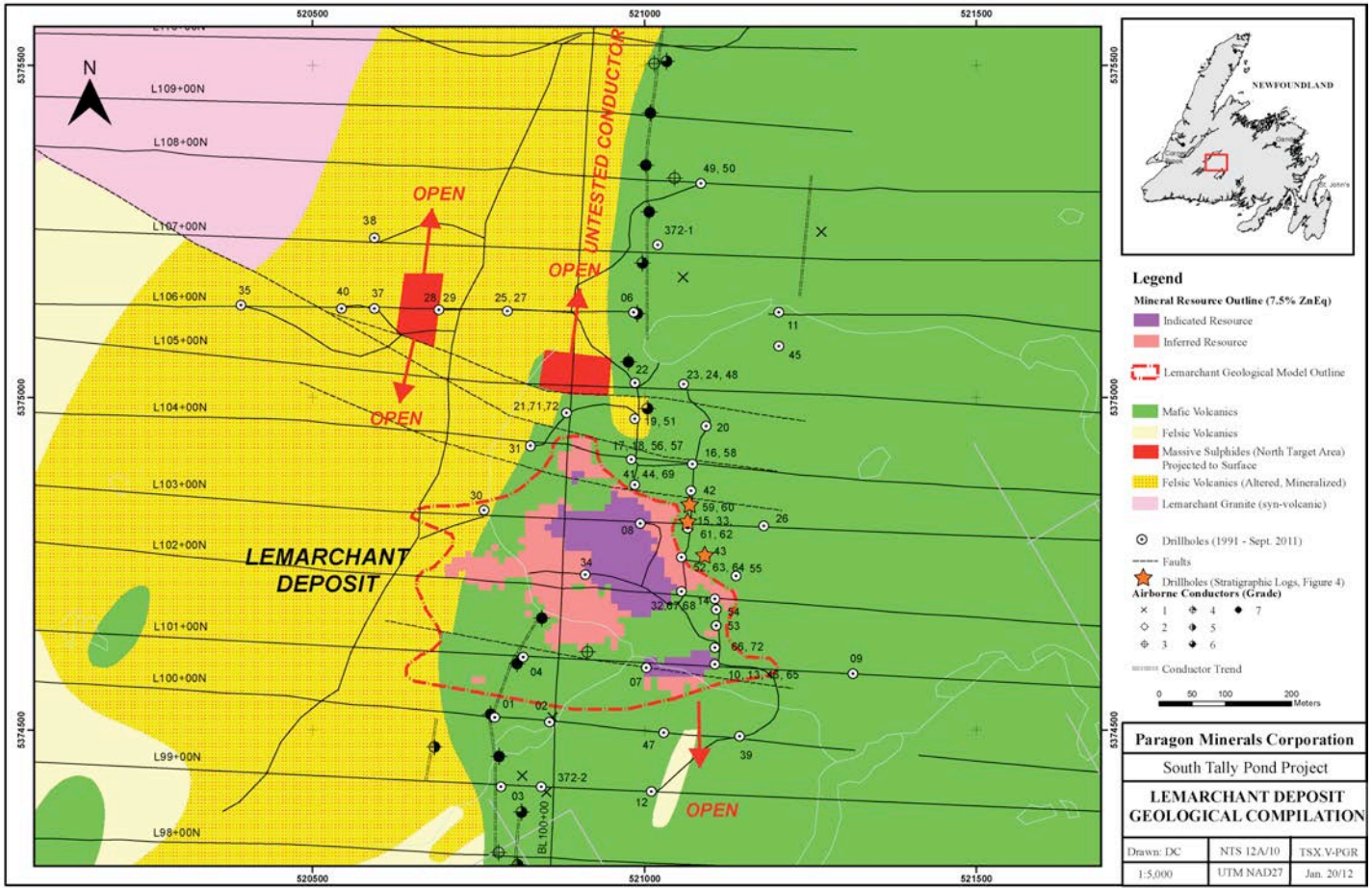

Figure 2. Map of Lemarchant geology and drill hole locations. The bimodal character of the deposit is indicated by co-dominant felsic and mafic geology, with the Lemarchant microgranite intrusion to the northwest. The pink- and purple-coloured Mineral Resource Outline represents the barite-rich mineralized zone projected to surface. A north-striking fault bisects the deposit and is crosscut by the east-west trending group of faults. Orange stars highlight drillholes represented by stratigraphic logs in Fig. 4. Modified from Fraser et al. (2012).

East-northeast-striking folds and thrust faults intersect the Tally Pond volcanic belt, and the entire belt is overprinted by Silurian-Devonian-age greenschist metamorphism (Dunning et al., 1991; Evans and Kean, 2002; Rogers et al., 2006).

DEPOSIT GEOLOGY

The generally tabular Lemarchant deposit strikes north-northwest and is hosted in an upright anticline that is offset by the north-striking, west-dipping, Lemarchant thrust fault and 4 to 5 minor east-west trending normal faults (Figs. 2-3; Fraser et al., 2012). The deposit consists of a thrust-imbricated succession of bimodal volcanic rocks, associated mineralization and hydrothermal sedimentary rocks (Fig. 3). Mineralization is situated at the contact between hanging wall mafic volcanic flows and footwall felsic volcanic rocks (Figs. 3-4). The overlying dark green mafic rocks predominantly consist of pillow lavas and massive flows that have vesicular and variably hyaloclastic flow tops (Fig. 5a). The underlying white to pale pink felsic rocks are composed of rhyolite flows, brecciated flow domes and associated volcaniclastic rocks (i.e., tuff and lapilli tuff after the definition by White and Houghton, 2006; Figs. 5b-c) that are variably spherulitic. These rocks are intruded by brown to greenish mafic dykes that are variably vesicular, fuchsite-bearing and have irregular edges (Fig. 5d); the dykes are strongly deformed and likely synvolcanic in nature (e.g., Gibson et al., 1999). Pyritic-pyrrhotitic, sulphide-rich mudstone is found at the contact between the mineralized barite lens and the hanging wall and grades outward from the deposit; this lithostratigraphic layer is interpreted to represent a dominantly exhalative sedimentary component (Lode et al., 2012).

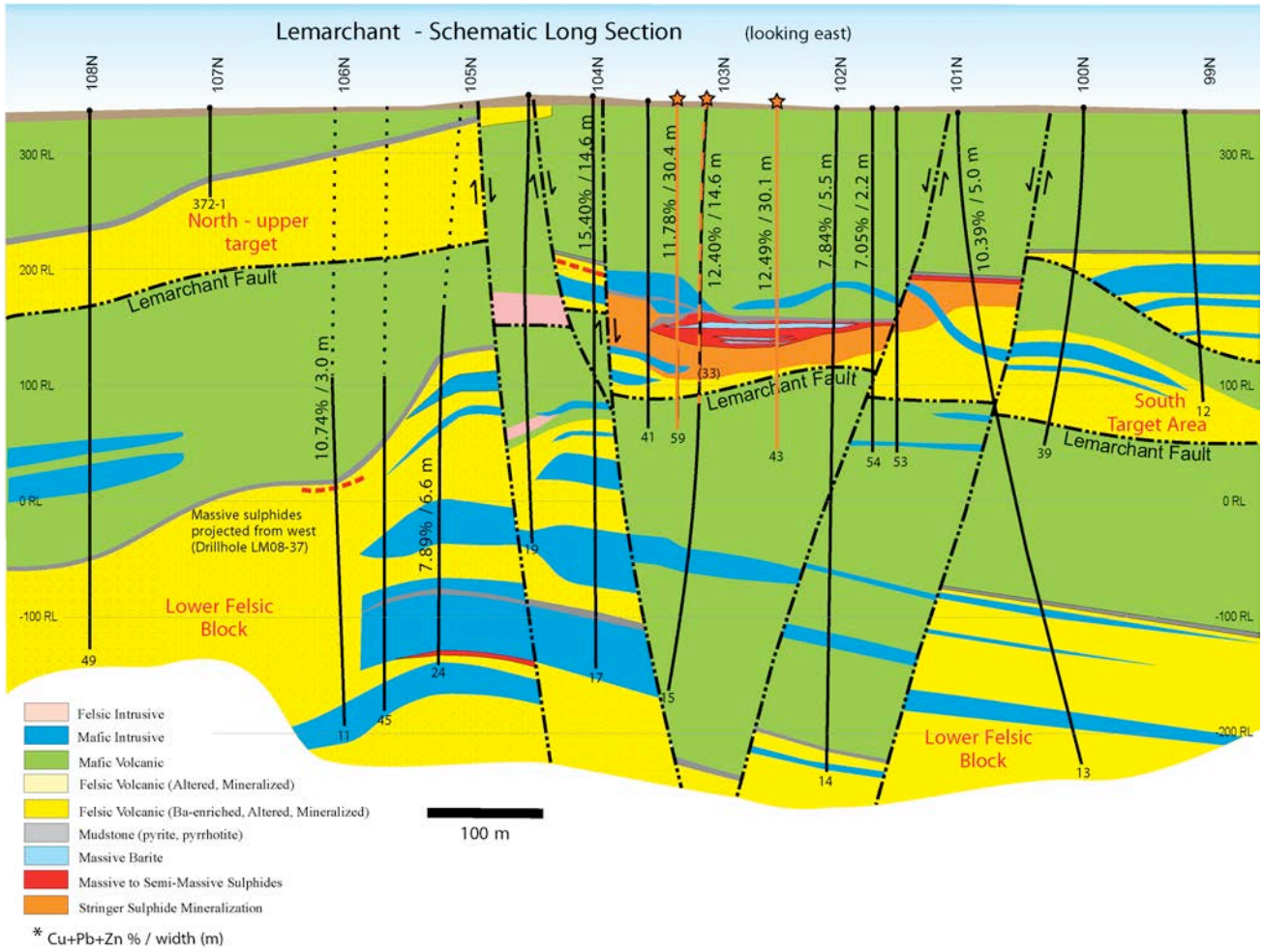

Figure 3. Long-section of Lemarchant deposit geology and drill hole locations along section 101E. The Lemarchant fault divides the repeated sequence of bimodal mafic hanging wall rock and felsic footwall rock. Upright faults parallel each other and further offset the Lemarchant geology. The red and pale-blue lens represents massive barite and sulphide mineralized zones, which are capped by mudstones and lie at the contact between the hanging wall and footwall. Orange stars, lines and dashed lines highlight drillhole locations and traces represented by stratigraphic logs in Fig. 4. Modified from Fraser et al. (2012).

The Lemarchant deposit exhibits variable alteration in the footwall that grades from proximal carbonate-rich chloritic-potassic alteration to distal siliceous-sericitic alteration. The hanging wall is weakly altered, containing only minor quartz-chlorite-epidote alteration with weak silicification proximal to mineralization.

MINERALOGY AND MINERAL ASSEMBLAGES

The mineralized zones at Lemarchant lie at the contact between the mafic hanging wall and the felsic footwall. Mineralization is concentrated in a barite-rich lens that is <20 m thick at its centre and forms the uppermost layer in the deposit (Fig. 3). The deposit is dominated by barite in the upper and distal parts of mineralized zones, which grade downwards into sulphide-rich mineralization with barite gangue (Fig. 4). This semi-massive to massive mineralized zone extends ~300 m from its southern- to northernmost points (Fig.2), and is underlain by the footwall rhyolite-hosted stringer sulphide zone (Figs. 3-4).

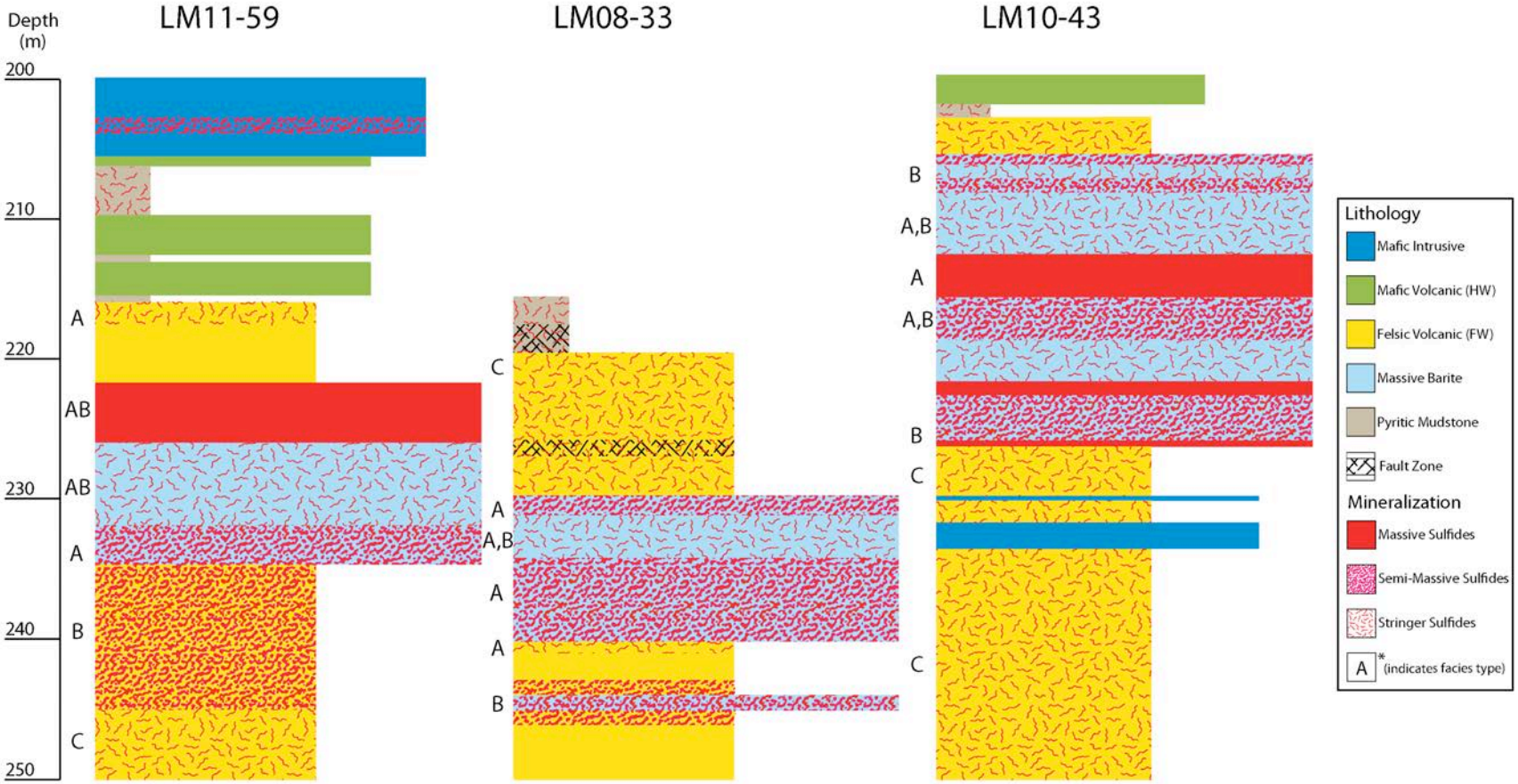

Figure 4. Representative graphic stratigraphic logs (drill holes LM11-59, LM08-33 and LM10-43) of trends in mineralization associated with the barite lens at Lemarchant (depth = 200m – 250m). Sulphide characteristics overprint lithology as massive, semi-massive and stringer mineralization; sulphide mineral assemblages/facies are indicated on the left of each column. Locations and traces of drillholes represented by orange stars, lines and dashed lines in Figs. 2-3.

The Lemarchant deposit consists of three distinct ore mineral assemblages that grade from the outer barite-dominated portion (facies A) of the deposit inward towards massive and semi-massive sulphides (facies C). Facies A consists predominantly of white to honey-coloured sphalerite + pyrite + chalcopyrite + bornite > enargite that are associated with barite and the outer portions of the mineralized zone (Figs. 4 and 5e) and commonly occur as stringers cross-cutting the more central facies B (Figs. 4 and 5f) and facies C sulphides. Though rare, visible gold occurs in facies A stringer sulphides. The facies A assemblage grades inwards towards facies B, which consists of barite + white sphalerite + galena + pyrite + tetrahedrite > tennantite + stromeyerite (Figs. 4 and 5g). Facies C are mostly honey-brown sphalerite + chalcopyrite + pyrite ± galena that form the base of the barite mineralized zone, and are the dominant mineral assemblage in the footwall stringer sulphide zone underlying the barite lens (Figs. 4 and 5h). Red sphalerite is rare but notable in facies C sulphides, and occurs in rhyolite proximal to outer barite mineralization (Fig. 4). The relative abundances of mineral types, including their characteristic textures or features, are summarized according to each of the described facies in Table 1.

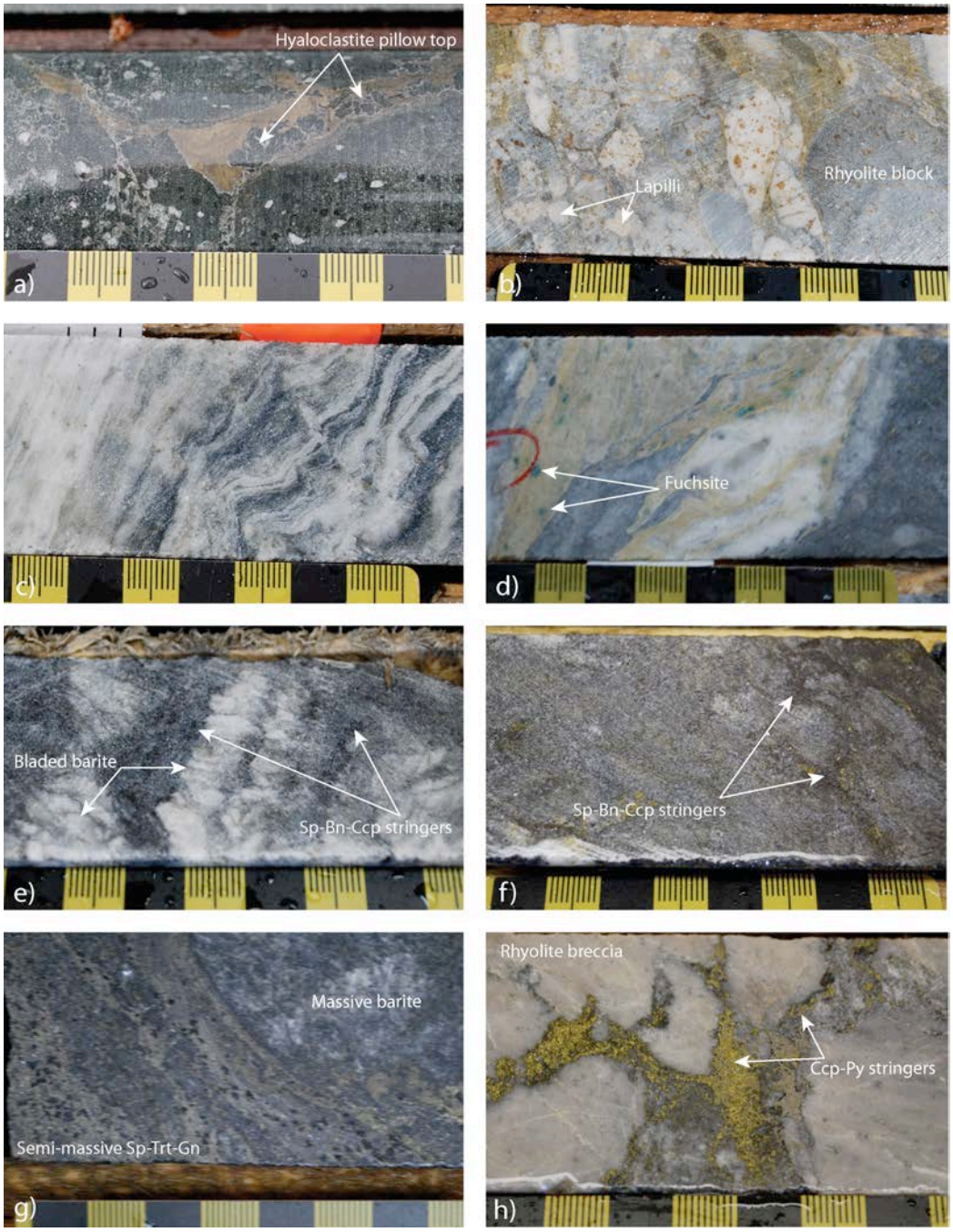

Figure 5. Drill core photograph field mosaic of type lithologies hosting the Lemarchant deposit. Black squares = 1 cm. A) Mafic hanging wall pillow lava with hyaloclastic flow top breccia and deformed, quartz-carbonate-filled amygdules (LM07-13 at 122.80m). B) Felsic footwall rhyolite tuff breccia, exhibiting variable alteration of lapilli and blocks (LM08-22 at 73.90m). C) Felsic footwall flow-banded rhyolite (LM93-11 at 415.6m). D) Wispy (synvolcanic?) mafic dyke crosscutting footwall rhyolite tuff (LM11-70 at 94.85m). E) Massive and bladed barite of the upper mineralized zone with crosscutting Sp-Bn-Ccp stringer sulphide mineralization (LM10-43 at 207.26m). F) Sp-Bn-Ccp stringer and semi-massive sulphide mineralization crosscutting Sp-Gn-Tnn massive sulphides (LM07-14 at 206.14m). G) Semi-massive Sp-Gn-Tnn sulphides crosscut the massive barite matrix (LM11-59 at 225.95m). H) Ccp-Py-Sp stringer sulphide mineralization cross-cutting weakly altered footwall rhyolite block breccia (LM07-14 at 207.4m). Abbreviations as follows: Sp = sphalerite; Bn = bornite; Ccp = chalcopyrite; Gn = galena; Trt = tetrahedrite; Py = pyrite.

Table 1. Modal mineralogy of sulphide facies comprising the Lemarchant VMS deposit, including significant textures and/or features of characteristic sulphide minerals. Percent values estimated from optical microscopy of polished thin sections ("Minor" implies mineral components of less than 5%).

Sulphides	**Textures/Features**	**Modal mineralogy, by facies (% estimated)**		
		Facies A	**Facies B**	**Facies C**
Sphalerite	Red	0	0	10
	Honey-brown	15	0	30
	White	10	25	0
Pyrite	Fine-grained, colloform	5	0	0
	Fine-grained, euhedral	0	0	5
	Coarse-grained, rounded	10	15	10
	Coarse-grained, euhedral	0	0	10
Galena	Angular	10	20	5
	Myrmekitic	0	Minor	0
Tennantite-Tetrahedrite	Tetrahedrite (Sb-rich)	Minor	10	0
	Tennantite (As-rich)	Minor	Minor	0
	Intergrown	0	5	0
Enargite	Amorphous	5	0	0
	Myrmekitic	Minor	0	0
Bornite		5 - 15	0	0
Covellite		Minor	0	0
Chalcopyrite	Amorphous	15	10	30
	Chalcopyrite disease in sphalerite	5	5	Minor
Stromeyerite		0	5	0
Ag-rich Tetrahedrite		0	5	0

Ore Facies A

Facies A sulphides occur predominantly in barite-rich zones at the top of the deposit and inter-finger with facies B (Figs. 6a-d) and C. Barite associated with mineralization is mostly massive in drill core with indistinct mineral boundaries and is variably replaced and cross-cut by sulphides (Figs. 5f-g); occasionally, barite is present as elongate, bladed crystal aggregates (Fig. 5e). White or honey-coloured sphalerite is the dominant sulphide (>30% total sulphides, Table 1) and is generally semi-massive and typically overgrown and cross-cut by bornite, chalcopyrite, enargite and pyrite in thin section. Occasionally sphalerite in thin section forms myrmekitic intergrowths with enargite (Fig. 6e), and atoll-type replacement in rounded pyrite. Semi-quantitative SEM spectral data from massive sphalerite in the barite lens suggest it has low Fe contents (Gill, unpublished data). Pyrite occurs in two distinct crystal habits in thin section: fine grained colloform or euhedral, and coarse-grained subhedral to euhedral; however, in facies A sulphides subhedral and corroded >1mm pyrite is more abundant than fine-grained colloform pyrite. Subhedral pyrite occurs as recrystallized grains in fine-grained pyrite, and often contains galena and sphalerite inclusions in atoll-type structures (Fig. 6f). Bornite is present as medium grained blebs in gangue and rounded pyrite, at the mineral interfaces between sphalerite, pyrite, enargite, chalcopyrite, galena, tennantite-tetrahedrite (Figs. 6a-e), and infilling fractures in gangue. Less commonly, bornite in stringers occurs as massive sheets that comprise up to 15% of the total sulphide assemblage in thin section (Fig. 6g). Covellite is occasionally present at bornite boundaries (Fig. 6c). Enargite is present as rounded to semi-angular blebs and occurs at gangue-sulphide interfaces primarily associated with sphalerite or galena (Figs. 6a-e). Chalcopyrite is variably abundant and commonly occurs as chalcopyrite disease in

sphalerite, atoll-type replacement in pyrite and at mineral boundaries between sphalerite, pyrite, enargite, galena, tennantite-tetrahedrite and bornite (Figs. 6a-e, g). Galena, tennantite and tetrahedrite are not major constituents in facies A. Two occurrences of visible gold are present in facies A. In drill holes LM10-43 and LM07-14 a ~1 mm gold grain is associated with pale honey-coloured (low-Fe?) sphalerite, bornite and chalcopyrite stringer sulphides (Fig. 6h). However, the gold in drill hole LM10-43 is associated with barite-dominated facies A (Fig. 6h), whereas the gold in LM07-14 is associated with facies A stringer sulphides in the footwall rhyolite at the outer edge of the barite lens.

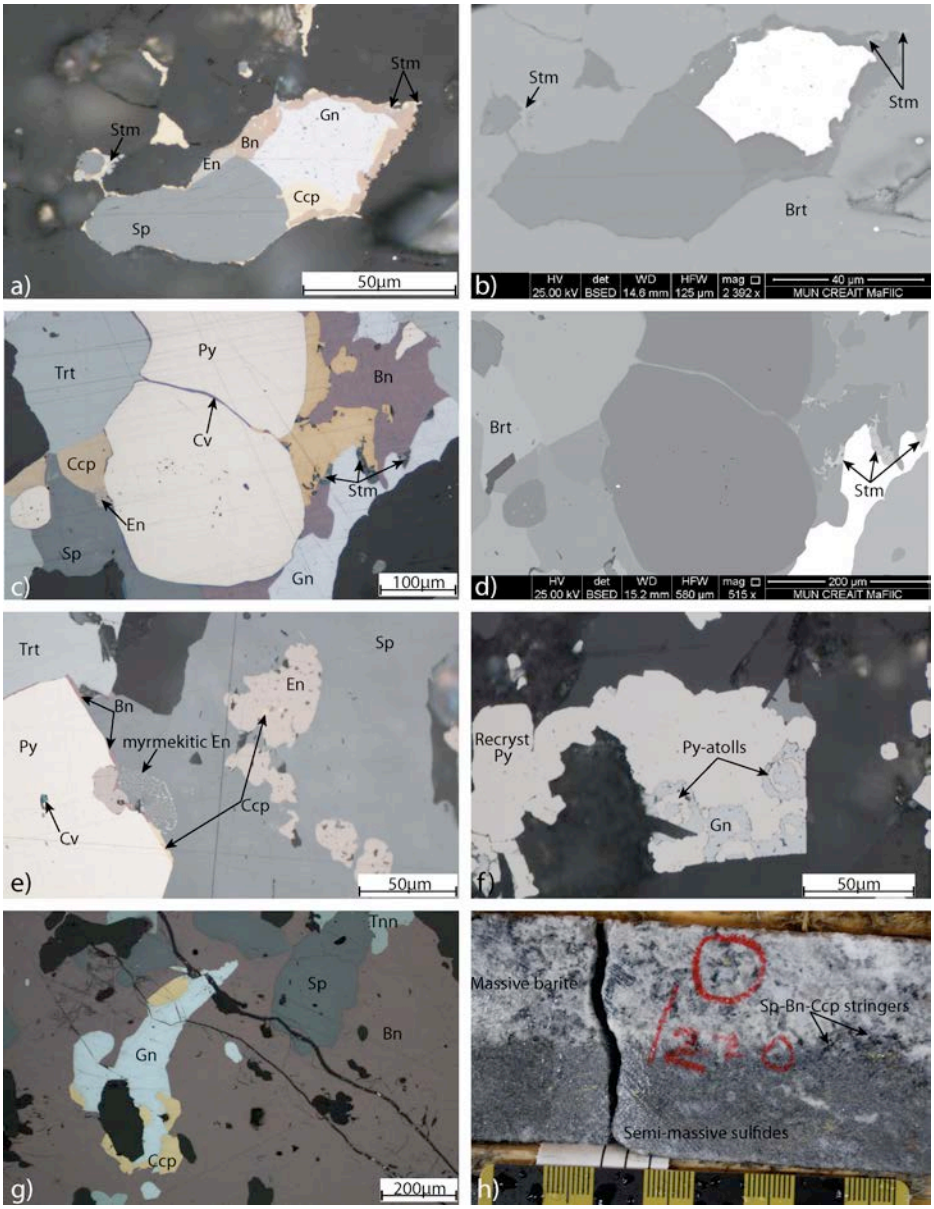

Figure 6. Thin section photomicrographs, backscatter electron (BSE) images and drill core photos of facies A and facies B sulphides at Lemarchant. A) Reflected light photomicrograph of facies A sulphides (Bn, En, Ccp) replacing facies B sulphides (Gn) and Sp at Brt-sulphide mineral boundaries (Sample CNF14259 in drill hole LM07-14 at 204.44m). B) Sample CNF14259 BSE image of Stm present at Brt-sulphide boundaries. C) Reflected light photomicrograph of facies A sulphides (Bn, En, Ccp) overprinting facies B sulphides (Gn, Trt) and Sp in barite; Cv present at barite boundaries is diagenetic (CNF14279 in LM08-33 at 230.75m). D) Sample CNF14279 BSE image of irregular Stm at Ccp-Gn boundaries. E) Reflected light photomicrograph of En myrmekitic intergrowth with Sp; Ccp and Bn present at Py, En boundaries (CNF14279 in LM08-33 at 230.75m). F) Reflected light photomicrograph of euhedral pyrite recrystallization from colloform Py, and relict atoll-structures formed with Gn (CNF29960 in LM11-59 at 216.00m). G) Reflected light photomicrograph of massive sheeted Bn in Sp, Gn and Tnn, with Ccp replacement at Gn-Bn boundaries (CNF29957 in LM11-63 at 210.83m). H) Drill core photo of visible gold (circled in red) in barite and associated facies A stringers (Black square = 1 cm; LM10-43 at 220.05 m). Additional abbreviations: En = enargite; Stm = stromeryite; Brt = barite; Cv = covellite; Tnn = tennantite.

Ore Facies B

Facies B mineralization is massive to semi-massive and lies stratigraphically below facies A mineralization (Fig. 4). These sulphides are dominated by massive white (low Fe?) sphalerite, representing >25% of total sulphides in thin section (Table 1). Angular galena occurs within and forms myrmekitic intergrowths with sphalerite, tetrahedrite and tennantite, and is generally associated with sulphide-gangue boundaries (Figs. 7a-f), whereas blebby galena is present in pyrite atolls. Pyrite is present in facies B sphalerite and barite as rounded, corroded ~1mm grains (Figs. 7a-d) and is variably replaced by chalcopyrite or contains galena inclusions. Tetrahedrite and tennantite are abundant in facies B (~10% total sulphides in thin section, Table 1), and, in some cases, this solid solution occurs as zoned crystals associated with galena, chalcopyrite and barite. Semi-quantitative SEM spectral data indicates tetrahedrite is As- and Ag-bearing (Gill, unpublished data). Angular to massive crystalline tetrahedrite has bright red internal reflections in thin section (Fig. 7b), and is more common in facies B than subangular, opaque tennantite (e.g., facies A tennantite in Fig. 6g; facies B tetrahedrite in Figs. 7a-b, e-f). Stromeyerite occurs as a jagged film along chalcopyrite and galena mineral boundaries (Figs. 6c-d, 7c-d); this phase also occurs in barite with sphalerite, bornite, and tennantite-tetrahedrite (Figs. 6 a-b). Silver-rich tetrahedrite occurs in galena (Figs. 7c-d) or non-silver tetrahedrite (Figs. 7e-f), and is associated with stromeyerite and other Ag-rich sulphides (Figs. 7c-d). Silver tarnish is common to minerals in contact with stromeyerite and Ag-rich tetrahedrite (Figs. 7c, e). Chalcopyrite disease is pervasive in massive sphalerite (Fig. 7e), and commonly occurs in pyrite atolls and replaces massive galena in thin section (Figs. 6a-b, 7a); however, chalcopyrite is not a major constituent of facies B.

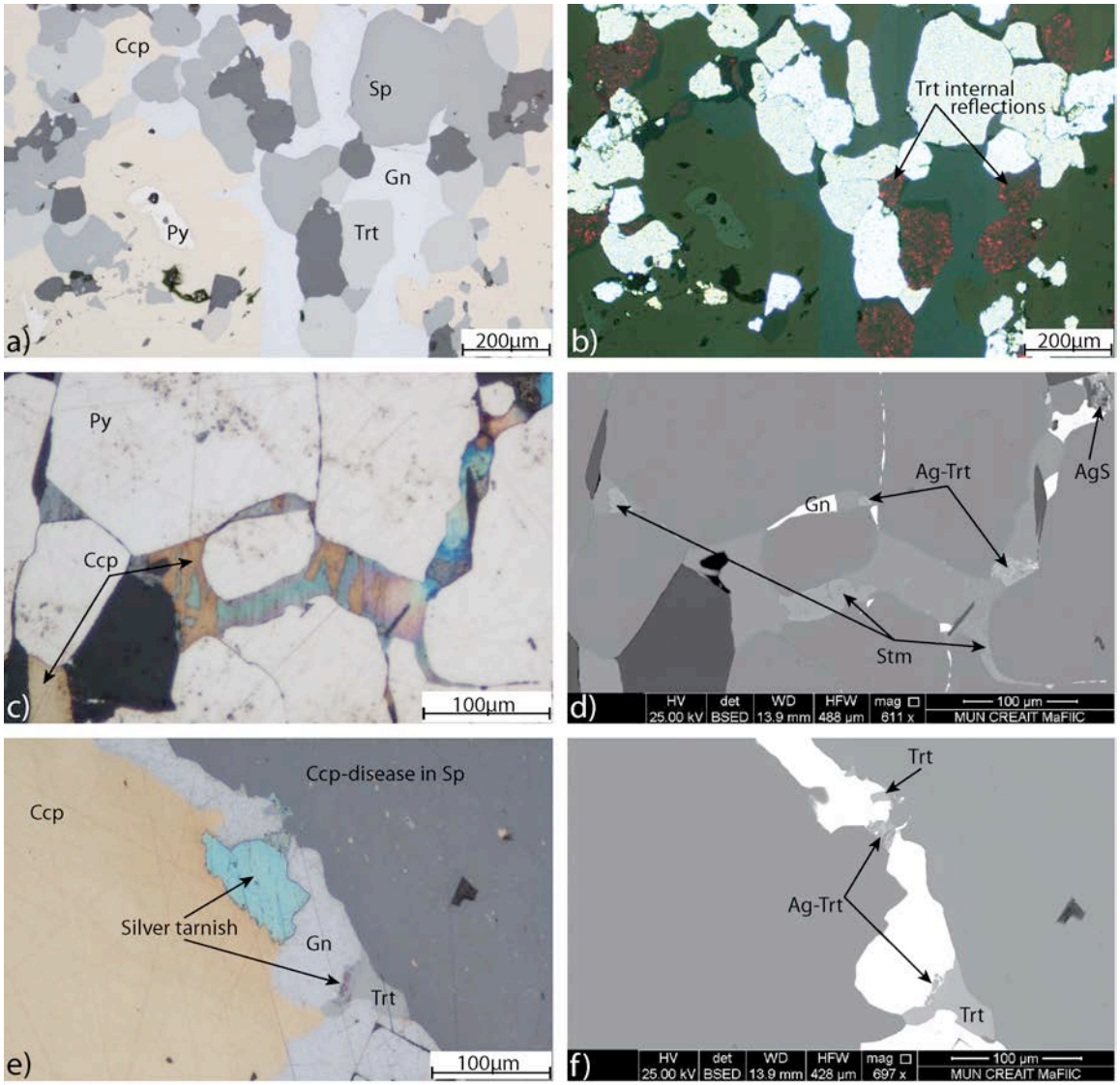

Figure 7. Thin section photomicrographs and BSE images of facies B sulphides at Lemarchant. A) Reflected light photomicrograph of Ccp replacement of angular Trt, sheeted Gn and rounded Py (Sample CNF29957 in drill hole LM11-63 at 210.83m). B) Transmitted light photomicrograph of CNF29957 showing the characteristic bright red internal reflections of Trt in facies B sulphides. C) Reflected light photomicrograph of silver tarnish of interstitial Ccp in subhedral Py (CNF29986 in LM08-19 at 97.63m). D) Sample CNF29986 BSE image of Stm associated with Ccp, and Ag-bearing Trt (Ag-Trt) and other silver sulphides (AgS) associated with Gn; subhedral Py with entrained Gn. E) Reflected light photomicrograph of Sp with Ccp-disease and Ccp replacement of Gn and Trt, with silver tarnish at Ccp-Gn-Trt boundaries (CNF29986 in LM08-19 at 97.63m). F) Sample CNF29986 BSE image of Ag-bearing Trt (Ag-Trt) at Gn-Trt boundaries.

Ore Facies C

Facies C sulphides consist of semi-massive and stringer sulphides and associated with two types of sphalerite: honey-brown sphalerite in facies C is stratigraphically lowest of the barite-rich sulphides and dominant in the footwall-hosted stringer sulphides of the stockwork zone (Figs. 4 and 5h), whereas red sphalerite in facies C is confined to the rhyolite proximal to the outer barite mineralization (Fig. 4). Honey-brown sphalerite is generally the most abundant sulphide in footwall rhyolite immediately below the barite lens (Fig. 8a) and in barite mineralization (Fig. 8b), and is associated with fine-grained pyrite and/or chalcopyrite; however, there is often a gradation into massive sheets of pyrite/chalcopyrite in thin section (Figs. 8a, c). Rarely, semi-massive red sphalerite is present in the drill core in the rhyolite tuff breccia associated with the outer mineralized barite lens (Figs. 4 and 8d); semi-quantitative SEM spectral analysis of red sphalerite in facies C suggests higher Fe-contents than barite-hosted facies A and facies B honey to white-coloured sphalerite (Gill, unpublished data). Sphalerite, pyrite, and galena are often replaced by blebbly chalcopyrite (Figs. 8a-b), which is common to barite-rich and footwall-hosted facies C mineralization. Euhedral and subhedral pyrite can be fine-grained and disseminated or occur as coarse-grained clusters in sphalerite, chalcopyrite and gangue; however, subhedral pyrite is more common and occurs as coarse-grained clusters of corroded, atoll-type pyrite with galena or sphalerite inclusions (Fig. 8d). Pyrite in facies C stringers is increasingly euhedral with increasing depth below the barite lens (e.g., Figs. 4 and 8a). Galena is more abundant in red sphalerite (high Fe?) facies C sulphides in rhyolite associated with outer barite mineralization (Fig. 8d); sometimes, anhedral or interstitial galena is present in the lower barite lens (Figs. 8b-c) and the

footwall rhyolite immediately underlying barite mineralization (Fig. 8a).

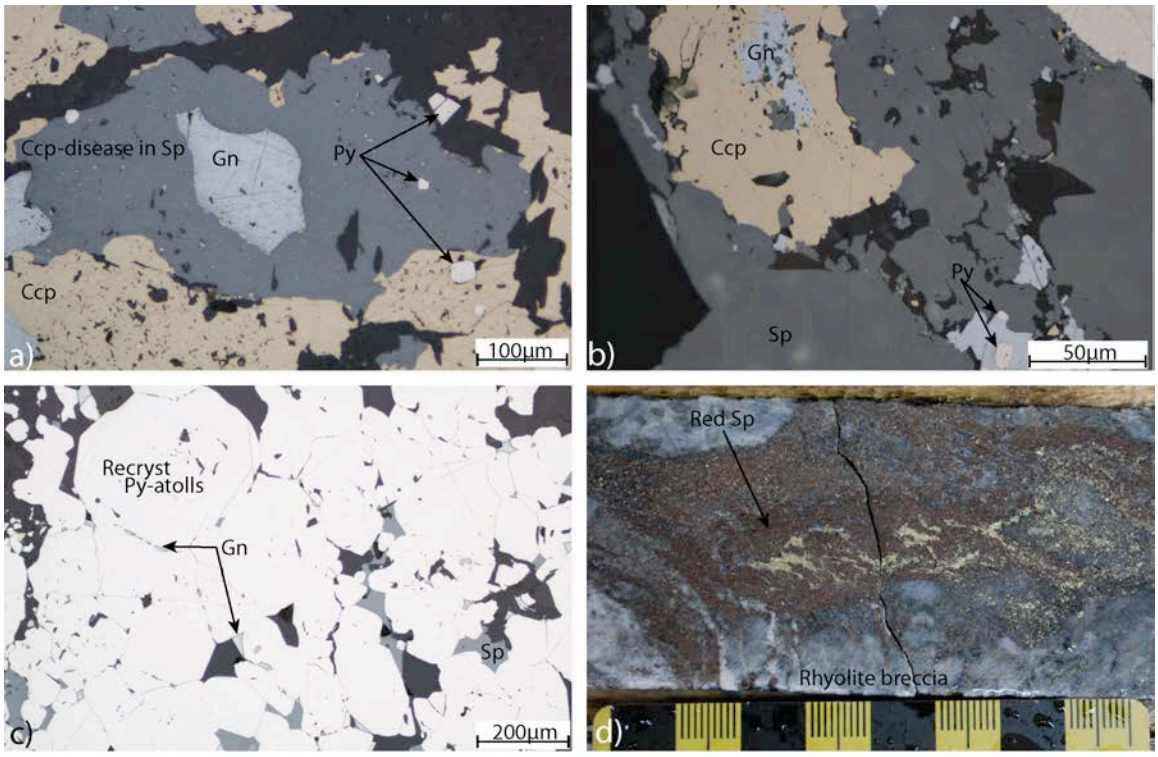

Figure 8. Thin section photomicrographs and drill core photos of facies C sulphides at Lemarchant. A) Reflected light photomicrograph of massive Sp with Ccp disease and Ccp replacement at Sp-gangue and Sp-angular Gn boundaries; euhedral Py overprinting Sp, Ccp and gangue (Sample CNF14288 in drill hole LM11-68 at 235.10m). B) Reflected light photomicrograph of Ccp replacement of Gn in Sp; subhedral to euhedral Py in Gn, Sp and gangue (CNF29965 in LM07-15 at 233.20m). C) Reflected light photomicrograph of recrystallized subhedral Py with entrained Gn in relict atoll-structures (CNF29985 in LM08-19 at 96.25m). D) Drill core photo of red Sp-Ccp-Py stringers crosscutting footwall rhyolite tuff breccia (Black square = 1 cm; LM08-33 at 219.83 m).

SUMMARY

The Lemarchant VMS deposit is hosted in a bimodal-felsic lithostratigraphic sequence and has Au-Ag-bearing, Kuroko-style Zn-Pb-Ba mineralization. Sulphide mineralization can be divided into three general assemblages or facies (i.e., Table 1): A) semi-massive to stringer white-honey sphalerite + pyrite + chalcopyrite + bornite > enargite ± galena + tennantite-tetrahedrite; B) massive and semi-massive white sphalerite + galena + pyrite + tetrahedrite > tennantite + stromeyerite + Ag-rich tetrahedrite + chalcopyrite; and C) semi-massive to stringer honey-brown or red sphalerite + chalcopyrite + pyrite ± galena. Visible gold is only associated with facies A, and no microscopic gold occurrences (i.e., native gold, electrum) have yet been noted; however, the similarities between SEM back-scatter electron characteristics of barite, galena, tetrahedrite, Ag-rich tetrahedrite and gold requires more detailed SEM-mineral liberation analysis (SEM-MLA) to distinguish such fine-grained gold. Iron-contents of sphalerite associated with barite appear to be generally low as deduced from semi-quantitative SEM spectra and colour variations in drill core and thin section. This is consistent with the correlation made by Hannington and Scott (1989) regarding gold enrichment in VMS deposits characterized by Fe-poor sphalerite; however, Fe-concentration does grade from slightly higher values at the outer fringes of barite in the deposit (i.e., facies A), with which free gold is associated, toward lower values at the centre of the barite lens (i.e., facies B; Gill, unpublished data).

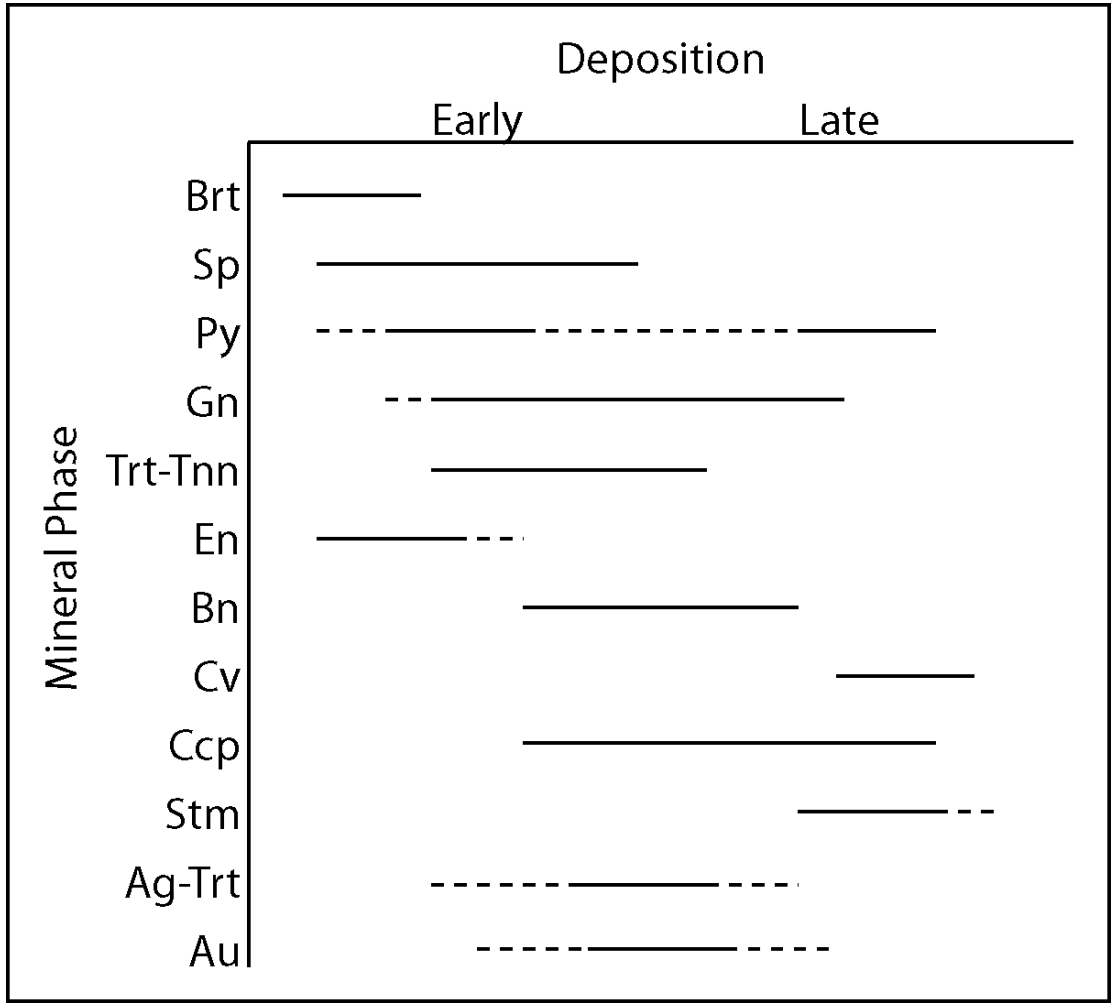

Figure 9. Diagram of interpreted, but preliminary, sulphide mineral paragenesis at Lemarchant. Relative timing of mineral deposition is indicated (solid lines) or inferred (dashed lines) by reported mineral association and textures.

Characteristic textures and mineral associations of sulphides comprising the Lemarchant deposit suggest facies B deposition preceded that of facies A and facies C, and indicate that silver enrichment occurred late in the mineralization sequence. The paragenesis of sulphide mineral phases encompassing all facies can be described as follows (Fig. 9): 1) initial crystallization of fine-grained pyrite and sphalerite was coincident with tennantite-tetrahedrite (± Ag-rich tetrahedrite), galena and enargite deposition; and 2) later replacement of sulphides by chalcopyrite and bornite (accompanied by gold precipitation?) that overlapped with late-stage stromeyerite deposition and mid- to late-stage recrystallization and coarsening to euhedral pyrite. Primary mineralization may be partially obscured by later remobilization of more tractable sulphide phases (e.g., bornite in fractured gangue) during metamorphism and deformation and requires further investigation.

The depositional sequence of mineralization and the composition of sulphides and sulphosalts at Lemarchant (e.g., tennantite-tetrahedrite and enargite followed by bornite and chalcopyrite) suggest that hydrothermal fluid temperatures were initially low to moderate (<250°C), and later rose to slightly elevated temperatures associated with recrystallization of fine grained pyrite to euhedral pyrite (Eldridge et al., 1983; Hannington and Scott, 1989). Furthermore, the mineral assemblages of the Lemarchant deposit that include abundant sulphosalts and high sulphidation mineral assemblages (e.g., enargite-tennantite-tetrahedrite), anomalous Au-Ag phases, and locally bladed barite, are features atypical of normal VMS, but common to Kuroko-type VMS deposits (Shimazaki, 1974) and hybrid VMS-epithermal deposits

(e.g., high sulphidation VMS; Sillitoe et al., 1996; Hannington et al., 1999; de Ronde et al., 2005; Dubé et al., 2007; de Ronde et al., 2011).

Further research will involve additional field and microscopic documentation of sulphide minerals and sulphide mineral facies; detailed SEM-MLA to investigate the location of fine-grained gold in thin section; electron microprobe analyses to study compositional variations of sulphide facies; laser ablation ICP-MS for trace element content of sulphide phases; and secondary ion mass spectrometry (SIMS) for in-situ sulphur and lead isotopes. These data will help refine mineral relationships within the Lemarchant deposit, gold-silver associations, and the physiochemical conditions of deposit formation.

ACKNOWLEDGEMENTS

This project is supported by the GSC TGI-4 Grant Program. This research is also supported by additional grants to Steve Piercey, including an NSERC Discovery Grant and the NSERC-Altius Industrial Research Chair in Mineral Deposits supported by NSERC, Altius Resources Inc., and the Research and Development Corporation of Newfoundland and Labrador. Many thanks to Canadian Zinc Corporation and Paragon Mineral Corporation (a 100% owned subsidiary of Canadian Zinc) for access to the drill core and use of the Buchans Junction core shed; to Stefanie Lode (Ph.D. Candidate, Memorial University of Newfoundland) for the introduction to Lemarchant geology and insightful discussions; to Michael Schaffer for explaining the nuances of SEM analysis; and to Graham Layne for guidance in petrographic interpretation. Reviews by Patrick Mercier-Langevin and Michael Vande Guchte greatly improved this manuscript.

REFERENCES

de Ronde, C., Massoth, G., Butterfield, D., Christenson, B., Ishibashi, J., Ditchburn, R., Hannington, M., Brathwaite, R., Lupton, J., Kamenetsky, V., Graham, I., Zellmer, G., Dziak, R., Embley, R., Dekov, V., Munnik, F., Lahr, J., Evans, L., and Takai, K., 2011, Submarine hydrothermal activity and gold-rich mineralization at Brothers Volcano, Kermadec Arc, New Zealand: Mineralium Deposita, v. 46, p. 541-584.

de Ronde, C. E. J., Hannington, M. D., Stoffers, P., Wright, I. C., Ditchburn, R. G., Reyes, A. G., Baker, E. T., Massoth, G. J., Lupton, J. E., Walker, S. L., Greene, R. R., Soong, C. W. R., Ishibashi, J., Lebon, G. T., Bray, C. J., and Resing, J. A., 2005, Evolution of a Submarine Magmatic-Hydrothermal System: Brothers Volcano, Southern Kermadec Arc, New Zealand: Economic Geology, v. 100, p. 1097-1133.

Dubé, B., Gosselin, P., Mercier-Langevin, P., Hannington, M., and Galley, A., 2007, Gold-rich volcanogenic massive sulphide deposits, *in* Goodfellow, W. D., ed., Mineral Deposits of Canada: A Synthesis of Major Deposit-types, District Metallogeny, the Evolution of Geological Provinces, and Exploration Methods, Special Publication 5, Mineral Deposits Division, Geological Association of Canada, p. 75-94.

Dunning, G. R., Swinden, H. S., Kean, B. F., Evans, D. T. W., and Jenner, G. A., 1991, A Cambrian island arc in Iapetus; geochronology and geochemistry of the Lake Ambrose volcanic belt, Newfoundland Appalachians: Geological Magazine, v. 128, p. 1-17.

Eldridge, C.S., Barton, P.B., Jr., and Ohmoto, H., 1983, Mineral textures and their bearing on formation of the kuroko orebodies: Economic Geology Monograph, v. 5, p. 241-281.

Evans, D.T.W., and Kean, B.F., 2002, The Victoria Lake Supergroup, central Newfoundland - its definition, setting and volcanogenic massive sulphide mineralization, Newfoundland and Labroador Department of Mines and Energy, Geological Survey, Open File NFLD/2790, p. 68.

Fraser, D., Giroux, G.H., Copeland, D.A., and Devine, C.A., 2012, Technical Report and Resource Minerals Estimate on the Lemarchant Deposit, South Tally Pond VMS Project, Central Newfoundland, Canada – NI 43-101 Technical Report prepared for Paragon Minerals Corporation, 132 p., 51 fig.

Gibson, H., Morton, R., and Hudak, G., 1999, Submarine volcanic processes, deposits, and environments favorable for the location of volcanic-associated massive sulfide deposits: Reviews in Economic Geology, v. 8, p. 13-51.

Hannington, M., and Scott, S.D., 1989, Sulfidation equilibria as guides to gold mineralization in volcanogenic massive sulfides; evidence from sulfide mineralogy and the composition of sphalerite: Economic Geology, v. 84, p. 1978-1995.

Hannington, M. D., Poulsen, K. H., Thompson, J. F. H., and Sillitoe, R. H., 1999, Volcanogenic gold in the massive sulfide environment, Reviews in Economic Geology v.8, p. 325-356.

Lode, S., Piercey, S.J.P., Copeland, D.A., Devine, C.A., and Sparrow, B., 2012, Setting and styles of hydrothermal mudstones near the Lemarchant volcanogenic massive sulfide (VMS) deposit, Central Mobile Belt, Newfoundland [abstract]: *In* Abstracts Volume 35, GAC-MAC Joint Annual Meeting, St. John's, Canada, May 27-29, 2012, 166 pages.

McNicoll, V., Squires, G., Kerr, A., and Moore, P., 2010, The Duck Pond and Boundary Cu-Zn deposits, Newfoundland; new insights into the ages of host rocks and the timing of VHMS mineralization: Canadian Journal of Earth Sciences = Revue Canadienne des Sciences de la Terre, v. 47, p. 1481-1506.

Piercey, S. J., and Hinchey, J. G., 2012, Volcanogenic massive sulphide (VMS) deposits of the Central Mobile Belt, Newfoundland, Geological Association of Canada–Mineralogical Association of Canada Joint Annual Meeting, Field Trip Guidebook B4. Open File NFLD/3173, Newfoundland and Labrador Department of Natural Resources, Geological Survey, 56 p.

Rogers, N., van Staal, C. R., McNicoll, V., Pollock, J., Zagorevski, A., and Whalen, J., 2006, Neoproterozoic and Cambrian arc magmatism along the eastern margin of the Victoria Lake Supergroup: A remnant of Ganderian basement in central Newfoundland?: Precambrian Research, v. 147, p. 320-341.

Roth, T., Thompson, J.F.H., and Barrett, T.J., 1999, The precious metal-rich Eskay Creek Deposit, northwestern British Columbia: Reviews in Economic Geology, v. 8, p. 357-373.

Shimazaki, Y., 1974, Ore minerals of the Kuroko-type deposits: Min. Geol. Spec. Issue, No. 6, p. 311-322.

Sillitoe, R. H., Hannington, M. D., and Thompson, J. F. H., 1996, High sulfidation deposits in the volcanogenic massive sulfide environment: Economic Geology, v. 91, p. 204-212.

Squires, G.C.S., Brace, T.D., and Hussey, A.M., 2001, Newfoundland's polymetallic Duck Pond Deposit: earliest Iapetan VMS mineralization, formed within a sub-seafloor, carbonate-rich alteration system, *In* Geology and mineral deposits of the Northern Dunnage Zone, Newfoundland Appalachians, *Edited by* D.T.W. Evans and A. Kerr. Geological Association of Canada – Mineralogical Association of Canada (GAC–MAC) Annual Meeting, St. John's, Nfld., 2001, Field Trip Guide A2, pp. 167–187.

Squires, G., and Moore, P., 2004, Volcanogenic massive sulphide environments of the Tally Pool Volcanics and adjacent area; geological, lithogeochemical and geochronological results: Newfoundland Department of Mines and Energy, Geological Survey: Current research, p. 63.

van Staal, C.R., Dewey, J.F., Niocaill, C.M., and McKerrow, W.S., 1998, The Cambrian-Silurian tectonic evolution of the northern Appalachians and British Caledonides: history of a complex, west and southwest Pacific-type segment of Iapetus: Geological Society, London, Special Publications, v. 143, p. 197-242.

van Staal, C.R., Whalen, J.B., McNicoll, V.J., Pehrsson, S., Lissenberg, C.J., Zagorevski, A., van Breemen, O., and Jenner, G.A., 2007, The Notre Dame arc and the Taconic orogeny in Newfoundland: Geological Society of America Memoirs, v. 200, p. 511-552.

White, J.D.L., and Houghton, B.F., 2006, Primary volcaniclastic rocks: Geology, v. 34, p. 677-680.

Zagorevski, A., Van Staal, C.R., McNicoll, V., and Rogers, N., 2007, Upper Cambrian to Upper Ordovician peri-Gondwanan Island arc activity in the Victoria Lake Supergroup, Central Newfoundland: Tectonic development of the northern Ganderian margin: American Journal of Science, v. 307, p. 339-370.

Appendix C: Current Research 2014

Styles of mineralization and sulphide mineral zonation in the Cambrian Zn-Pb-Cu-Ag-Au Lemarchant volcanogenic massive sulphide deposit, Newfoundland and Labrador – preliminary observations

Authors: Shannon B. Gill*, Stephen J. Piercey

Address (primary author): s.gill@mun.ca, Memorial University of Newfoundland, St. John's, Newfoundland

Abstract

The precious metal-bearing, polymetallic bimodal felsic Lemarchant volcanogenic massive sulphide (VMS) deposit is located in the Tally Pond belt, Dunnage Zone, Newfoundland Appalachians and consists of a stratiform, massive to semi-massive sulphide zone and an underlying stringer sulphide zone. Five principal types of mineral assemblage are present: 1) semi-massive white (low-Fe) sphalerite-granular barite-recrystallized pyrite-galena-minor tetrahedrite; 2A) bornite-galena-stromeyerite±chalcopyrite; 2B) bladed barite-coarse-grained tetrahedrite-galena-electrum-colusite±bournonite-polybasite-miargyrite; 3) massive red (high-Fe) sphalerite-fine- to medium-grained pyrite-chalcopyrite-galena; and 4) chalcopyrite-pyrite±orange sphalerite stringers. The stratiform sulphide zone contains the type 1 assemblage, which is cross-cut by the type 2A and type 2B assemblages. The type 3 assemblage overprints the type 1 assemblage at the top of the stratiform zone. The basal stringer zone is host to the type 4 assemblage. The type 3 and type 4 assemblages represent minor zone refinement of the stratiform and stringer zones, as the hydrothermal fluids from which they were deposited were

relatively hotter (>300°C) than the lower temperature fluid (<250°C) from which the type 1 and type 2 assemblages were deposited.

The Lemarchant deposit shows zone refinement typical of Kuroko-style VMS mineralization. However, the precious metal-enriched low-Fe sphalerite, bornite, electrum and sulphosalt-rich type 2 assemblages suggest processes analogous to high sulphidation epithermal-style VMS mineralization early in the evolution of the deposit. A direct magmatic contribution to the hydrothermal fluid and intermittent boiling during deposition of the type 1 and type 2 assemblages may be partially responsible for precipitation of epithermal-suite minerals and precious metal-enrichment.

INTRODUCTION

The Newfoundland Appalachians are host to numerous volcanogenic massive sulphide (VMS) deposits, including a number of past and are presently producing deposits (e.g. Buchans and Duck Pond; Swinden and Kean, 1988; Piercey and Hinchey, 2012). Although the massive sulphide deposits in this area represent a range of VMS deposit types and have been explored since the 1850s (Martin, 1983; Piercey and Hinchey, 2012), there are few well-studied VMS deposits with significant precious metal enrichment (c.f. Hurley and Crocket, 1985; Santaguida and Hannington, 1993; Santaguida and Hannington, 1996; Brueckner et al., *in press*). The Lemarchant deposit is hosted in the Tally Pond volcanic belt of the Victoria Lake Supergroup (Rogers et al., 2006; McNicoll et al., 2010) and is a type example of precious metal enrichment in Appalachian polymetallic VMS deposits. The Lemarchant deposit occurs in the same volcanic belt as the currently producing Duck Pond and Boundary Cu-Zn deposits, but is distinct in precious metal-content from these deposits as they have normal VMS mineralization without

significant precious metal enrichment (Squires et al., 2001; Piercey and Hinchey, 2012; Piercey et al., 2014).

The Lemarchant deposit was initially discovered in the 1980s with further expansion in the late 2000s, and has since had abundant exploration work undertaken on it; however, the styles of sulphide mineralization at Lemarchant are poorly documented and the cause(s) of precious metal enrichment are not well understood. The objectives of this study are to: 1) produce a more thorough documentation of mineralization styles, siting of precious metals and 3D base- and precious-metal zonation in the Lemarchant deposit; and 2) propose a genetic model of deposition and precious metal enrichment. Refined drill core observations, petrographic and scanning electron microscope results are presented here as part of an MSc project at the Memorial University of Newfoundland and are a contribution to the precious metal-rich VMS subproject of the Geological Survey of Canada Targeted Geoscience Initiative 4 program. The deposit model presented here is the basis for more detailed mineral chemical analysis, which will further constrain the environmental and depositional conditions required for the formation of the Lemarchant deposit and allow comparison to precious metal-enriched VMS deposit analogues in the Appalachians and globally.

EXPLORATION HISTORY

The Lemarchant deposit is part of the South Tally Pond property owned by Canadian Zinc Corporation, and is located approximately 35 km south-southwest of Millertown, in Central Newfoundland. The deposit has an NI 43-101 defined geological resource of 2.58 Mt at 0.49% Cu, 4.51% Zn, 1.01% Pb, 54.62g/t Ag, and 1.00 g/t Au and lies southwest of the currently producing Duck Pond and Boundary Cu-Zn VMS deposits (Fraser et al., 2012). The Lemarchant

deposit was first discovered in 1983 by Noranda and discontinuously drilled until 1993 (Squires and Moore, 2004). In 2001 and 2004, Altius Minerals re-examined the existing data on the property, and tested the geochemical results and airborne surveys to better define the Lemarchant prospect (Fraser et al., 2012). Paragon Minerals drilled the majority of the deposit from 2007 to 2011, through which the National Instrument 43-101 resource was obtained. In 2012, Canadian Zinc Corporation acquired a 100% interest in Paragon Minerals and drilled through the 2013 season, physically expanding the Lemarchant deposit beyond the 2012 resource definition to include the Lower Felsic Block mineralization originally proposed by Fraser et al. (2012).

REGIONAL GEOLOGY

Volcanogenic massive sulphide deposits make a significant contribution to the mineral resources that occur in the Central Mobile Belt of Newfoundland (Swinden and Dunsworth, 1996; Evans and Kean, 2002). This early Paleozoic Appalachian accretionary zone is called the Dunnage Zone, and is divided by the Red Indian Line into the Notre Dame subzone to the west and Exploits subzone to the east (Fig. 1, inset; Evans and Kean, 2002; Rogers et al., 2006; van Staal et al., 2007). The Red Indian Line defines a Silurian suture between island- and rifted-arc volcanic complexes of western, peri-Laurentian and eastern, peri-Gondwanan affinity (Rogers et al., 2006; Zagorevski et al., 2007). The Lemarchant deposit is found in the peri-Gondwanan Exploits subzone, hosted by the Cambrian-Ordovician nascent arc volcanic rocks of the Tally Pond group in the Victoria Lake Supergroup (Swinden and Dunsworth, 1996; McNicoll at al., 2010).

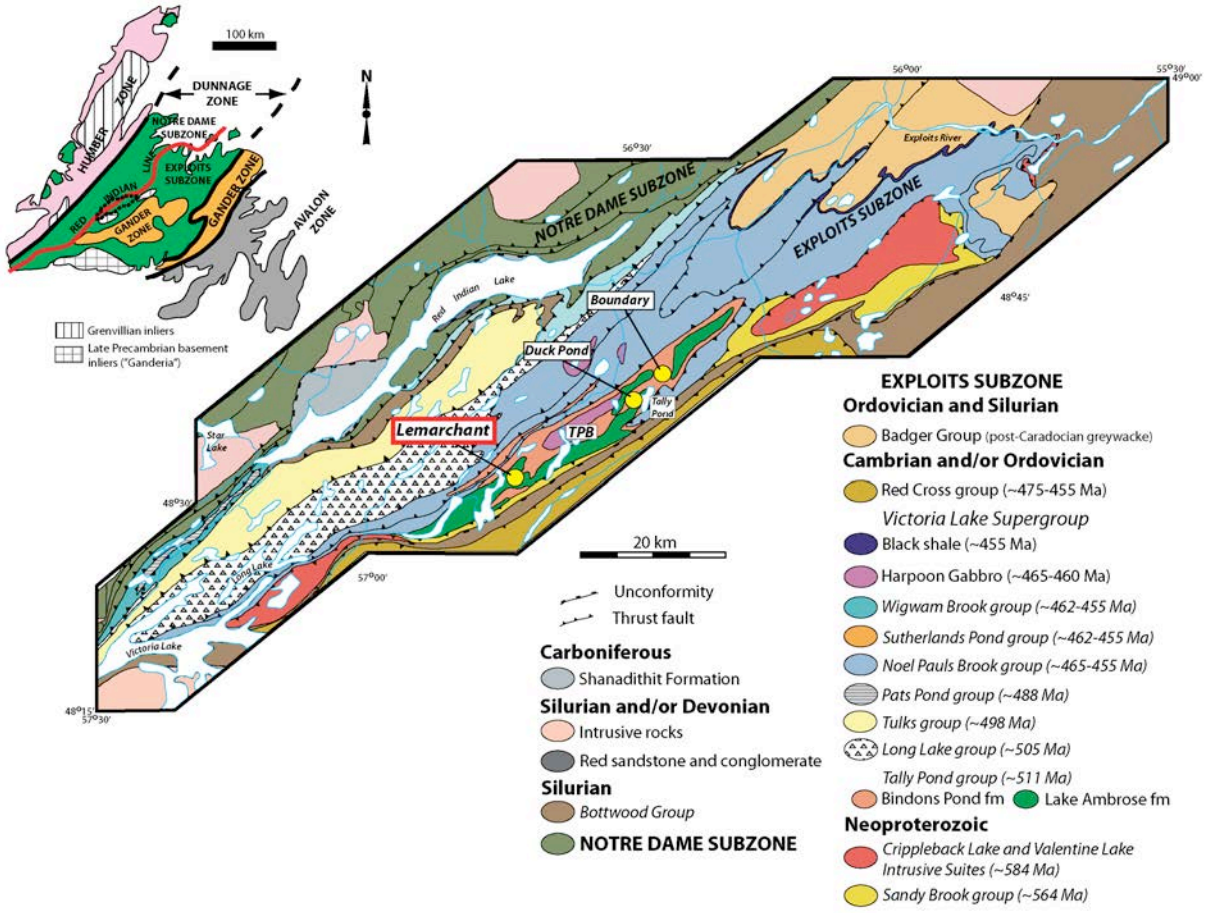

Figure 10. Geological map of volcanic sequences comprising the Exploits subzone, which defines the eastern half of the Dunnage Zone in central Newfoundland. The lowermost assemblage in the Victoria Lake Supergroup of the Exploits subzone is the Tally Pond volcanic belt (TPB). The Tally Pond belt is host to the Lemarchant VMS deposit (in red), as well as the Duck Pond and Boundary VMS deposits to the northeast. Modified from Piercey and Hinchey (2012). Inset after Williams (1979).

The Late Cambrian Tally Pond group is host to the Lemarchant deposit and is the stratigraphically lowest volcanic sequence in the mineral-rich Victoria Lake Supergroup (Fig. 1; Swinden and Dunsworth, 1996; Evans and Kean, 2002). The Victoria Lake Supergroup is composed of nascent- to mature-arc volcanic sequences arranged east to west from Cambrian to Ordovician in age (Rogers et al., 2006; Zagorevski et al., 2007; Piercey and Hinchey, 2012). The Tally Pond group consists of the lower, mafic-dominated Lake Ambrose formation and the upper, felsic-dominated Bindons Pond formation, which range in age from 515 Ma to 509 Ma (Dunning et al., 2001; Rogers et al., 2006; McNicoll et al., 2010). Polymetallic VMS-type mineralization, such as at the Lemarchant deposit and adjacent Duck Pond and Boundary deposits, is abundant in the Bindons Pond formation, whereas Lake Ambrose formation is relatively barren (Squires et al., 2001; Piercey and Hinchey, 2012). The deposits and occurrences in the Bindons Pond formation are hosted in aphyric to quartz-phyric rhyolite and dacite flows and breccias, tuffs and other volcaniclastic sedimentary rocks, with minor pillowed to massive mafic flows (Moore, 2003; McNicoll et al., 2010). Geochemically distinct and younger mafic sills and dykes that crosscut the Tally Pond belt stratigraphy are interpreted to be related to the Ordovician Harpoon Hill gabbro (~465 Ma; Pollock et al., 2004; Squires and Moore, 2004; Piercey and Hinchey, 2012); crosscutting felsic intrusions are also common to the area (McNicoll et al., 2010). Low-grade Silurian-Devonian greenschist metamorphism overprints the host rocks, mineralization and late-stage intrusions of the Lemarchant deposit (Dunning et al., 2001; Evans and Kean, 2002; Fraser et al., 2012).

HOST ROCKS AND ALTERATION

The Lemarchant deposit is hosted in an upright anticlinal structure that is composed of a bimodal volcanic sequence (Fig. 2A; Fraser et al., 2012). The mineralized horizon occurs at a depositional contact between footwall felsic volcanic flows and volcaniclastic rocks, and a hanging wall sequence consisting of a lower pyritic to graphitic mudstone layer immediately overlying sulphide mineralization and an upper layer of mafic volcanic flows (Fig. 2B).

The footwall felsic unit is composed of rhyolite breccias, flows and lapilli-tuffs. The rhyolite is fine-grained and aphyric with local quartz and feldspar phenocrysts, and minor <1mm, black, platy biotite crystals. Massive white-grey rhyolite flows sometimes contain evidence of columnar jointing, which may have concentric banding (Fig. 3A); flow banded rhyolite in the felsic footwall is rare. Rhyolite breccias are generally monolithic, pink- to green-white or grey, and range from angular, clast-supported, in-situ breccias to rounded and sub-angular, tuff and lapilli-tuff. Breccia block size is generally 1-10 cm; some >10m blocks can be flow-banded or spherulitic. Rhyolite lapilli are heterolithic and consist of sub-rounded, 1-10 mm, grey to white, quartz-phyric to aphyric particles. Rhyolite tuff consists of sub-rounded, <2mm, white to grey-green particles. Angular >0.5cm, dark green glass fragments are variably present with lapilli-tuff at rhyolite flow contacts (Fig. 3B).

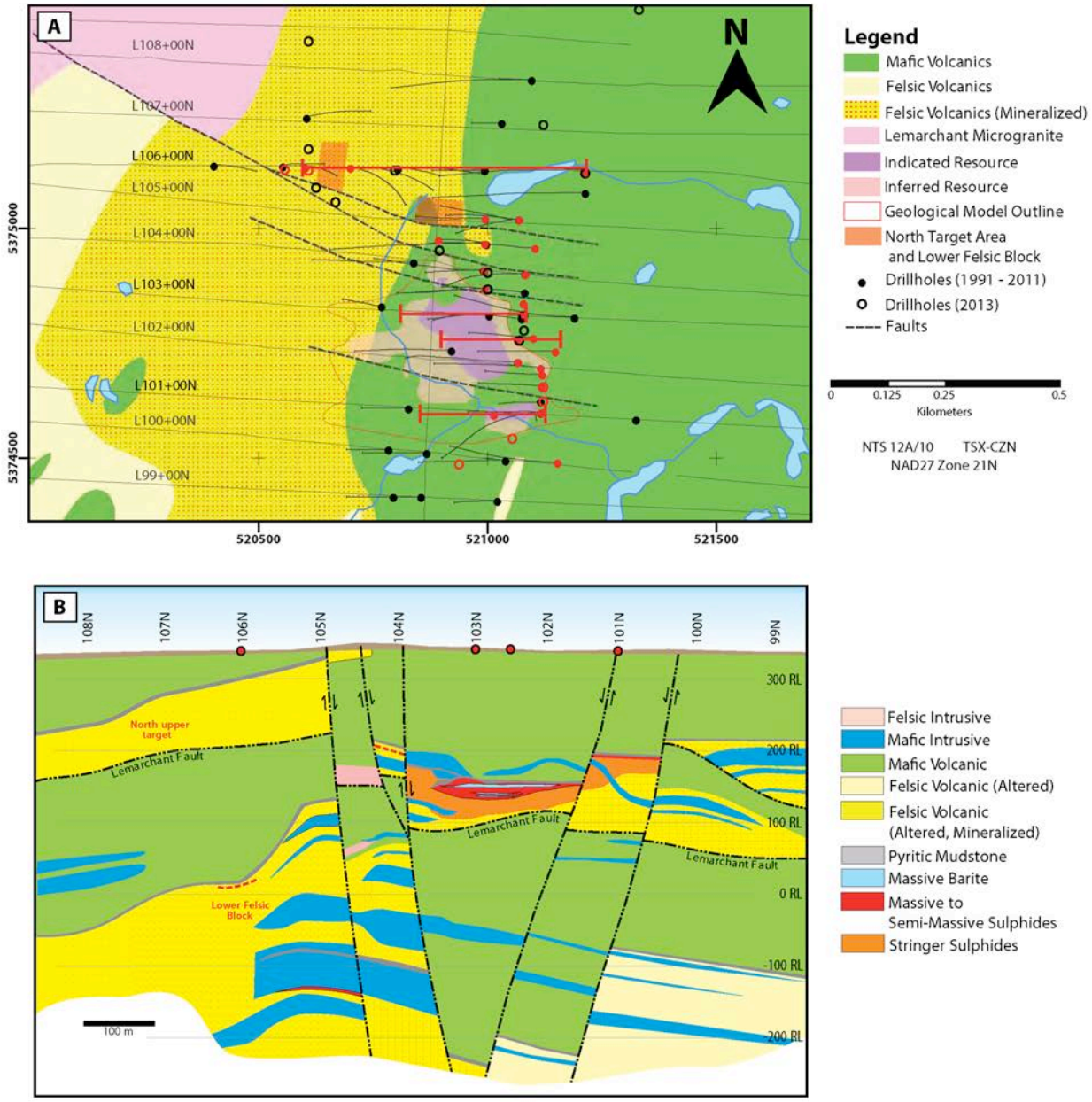

Figure 11. Map and idealized cross-section of the Lemarchant geology. A) Plan view of Lemarchant geology. Red drill holes have been logged for this project. Red cross-sections pictured in Figure 4. B) Idealized N-S cross-section of the Lemarchant deposit looking east. Red markers indicate cross-section locations of Figure 3. Modified from Fraser et al. (2012).

Mineralization consists of medium-grained, granular to locally bladed, white barite with massive to semi-massive sulphides (Fig. 3C-D). The barite and sulphides are interstitial to rhyolite breccia and lapilli-tuff in the footwall, and cross-cut the sulphide-rich mudstone.

The mudstone layer overlying the massive sulphides is thin, and is locally intercalated with the hanging wall mafic volcanic rocks. It is considered to represent a dominatly exhalative sedimentary layer (Lode et al., 2012). Very fine-grained pyrite is disseminated throughout the mudstone, but pyrite also occurs as fine-grained bands and minor coarse-grained euhedra. The pyritic mudstone is variably graphitic and locally contains chalcopyrite stringers, blebby pyrrhotite or euhedral arsenopyrite (<1cm).

The hanging wall mafic rock is composed of massive to pillowed basalt and basaltic andesite. The basalt and basaltic andesite flows are fine-grained, green to grey and variably amygdular. Amygdules and lesser >1mm euhedral pyrite crystals are commonly present at pillow contacts, which sometimes contain hyaloclastic flow-top breccia (Fig. 3E). Pillow selvages and amygdules are filled with chlorite and/or carbonate. Minor pyrrhotite blebs and trace euhedral arsenopyrite occur in the mafic flows proximal to intercalated pyritic mudstone.

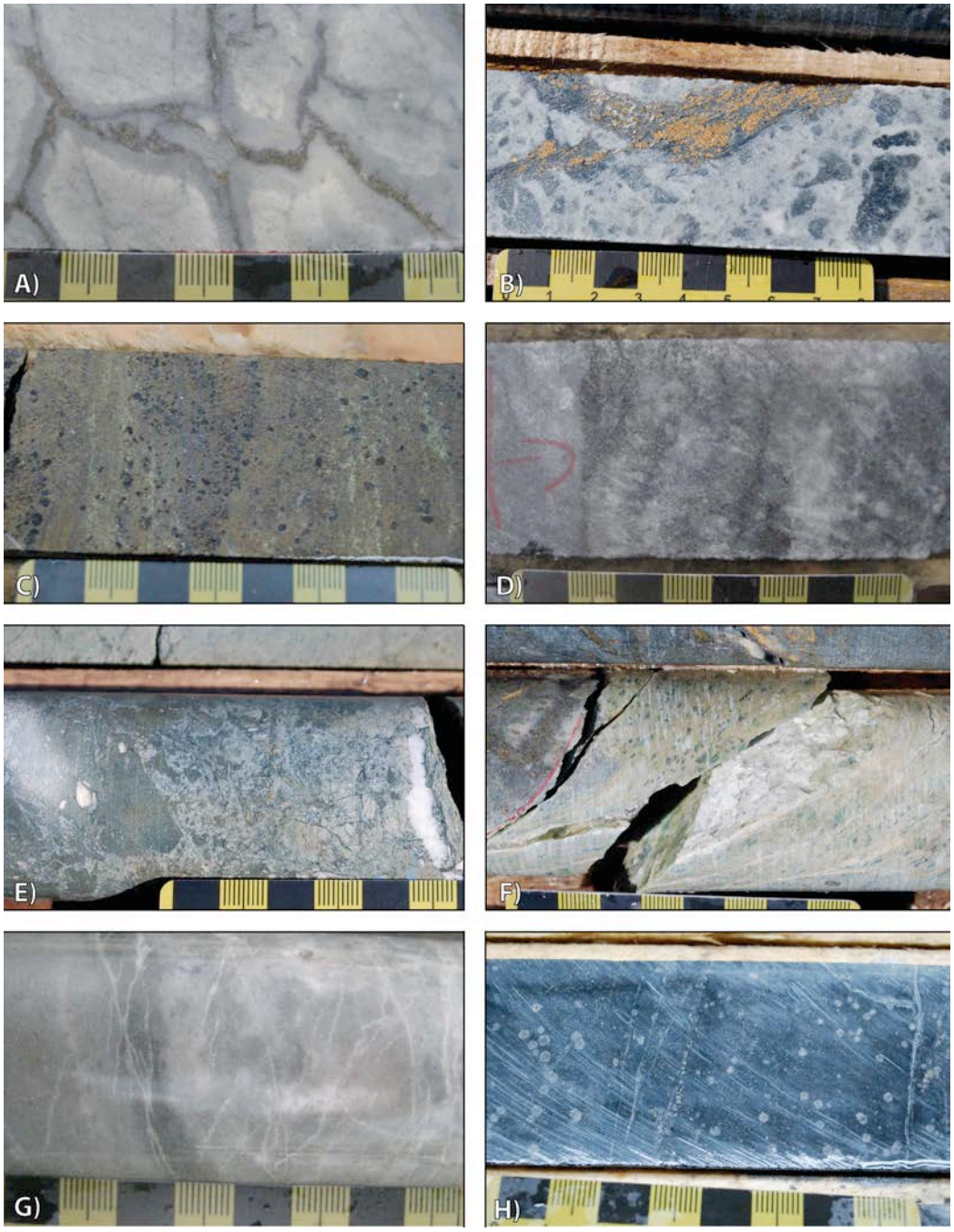

Figure 12. Drill core photograph field mosaic of type lithologies hosting the Lemarchant deposit. Black squares = 1 cm. A) Columnar jointing in massive rhyolite flows with concentric alteration and interstitial sulphide mineralization (Drill hole LM08-29 at 316.3m depth). B) Glass-rich felsic tuff with cross-cutting stringer sulphide mineralization (LM93-11 at 413.8m). C) Albite rhomb alteration replacing massive sulphides (LM11-68 at 205m). D) Massive to bladed mineralized barite (LM13-73 at 330.35m). E) Hyaloclastite flow top breccia in hanging wall basalt. Outermost breccia is partially carbonate altered (LM07-17 at 276.8m). F) Bleached mafic dyke with green mica (fuchsite?) cross-cutting felsic footwall (LM08-39 at 295.4m). G) Amorphous felsic dyke cross-cutting rhyolite breccia (LM08-32 at 208.9m). H) Massive chlorite with spherulitic (carbonate?) alteration (LM11-69 at 203.8m).

Mafic and felsic dykes cross cut the mineralization at Lemarchant. Mafic intrusions are of two main types that include: 1) fine- to medium-grained synvolcanic dykes that are beige-brown and aphanitic, with minor pyroxene phenocrysts, peperitic margins, and carbonate- and/or chlorite-filled amygdules; and 2) medium-grained gabbro to diabase intrusions that cross-cut the synvolcanic dykes and have sharp contacts in surrounding units. The latter mafic intrusions are potentially correlative to the Harpoon Hill gabbro (Pollock et al., 2004; McNicoll et al., 2010). In some cases, the synvolcanic dykes have been deformed and exhibit carbonate bleaching and chlorite/fuchsite clots (Fig. 3F). Felsic intrusions are thin (10-15 cm), white to pink and mostly aphyric (Fig. 3G).

Alteration in the felsic footwall generally consists of quartz-sericite±chlorite; however, chlorite is locally dominant as a <5m dark green massive layer present below barite-rich mineralization in the footwall (Fig. 3H). Barite and massive sulphides have abundant quartz-chlorite-albite±sericite alteration (Fig. 3C). The mafic hanging wall contains some silica-chlorite-epidote, but is not significantly altered. Cross-cutting silica-carbonate veins, spotty ankerite and carbonate bleaching of host rock and synvolcanic dykes occur near faulted, locally deformed zones. The footwall lapilli-tuff and pyritic mudstone layer are the most strained units, and may appear banded.

MINERALIZATION

The Zn-Pb-Cu-Ag-Au Lemarchant deposit is composed of a main massive sulphide lens and a smaller mineralized body that lies to the northwest of the main deposit (Fig.2A). The main Lemarchant deposit consists of a lenticular, stratiform massive to semi-massive zone and underlying stringer sulphide zone. The stratiform sulphide zone occurs at depth ~200m, strikes

north-northwest along its longest axis (~350m) and is generally <20m wide (Fig. 4A). The smaller sulphide mineral body, termed the Lower Felsic Block (LFB) by Fraser et al. (2012), is found ~200m north-northwest of the main sulphide zones, and sits >300m below the surface (Fig. 4B). The Lemarchant deposit is crosscut by the north-striking Lemarchant fault, a west-dipping thrust fault that causes repetition in the host rock stratigraphy and may have displaced part of the main sulphide lens, as evidenced by the LFB (Fig. 2B; Copeland et al., 2008; Fraser et al., 2012). Upright, east-west oriented normal faults crosscut the Lemarchant deposit in four or five locations, resulting in minor offsets within the main sulphide lens, and possibly the LFB. Although the Lemarchant deposit has undergone brittle fault deformation and greenschist facies metamorphism, the primary textures observed in some sulphide phases (e.g. colloform pyrite) suggest exceptional preservation of primary and hydrothermal textures. Local remobilization of the more ductile sulphides (e.g. bornite, chalcopyrite, galena) is minor.

SULPHIDE MINERAL ASSEMBLAGES

The mineralization at Lemarchant is divided into a Zn-Pb-rich stratiform sulphide zone and an underlying Cu-rich stringer sulphide zone, which are characterized by five distinct sulphide mineral assemblages. The stratiform zone is variably composed of massive sulphide and massive barite assemblages. The massive sulphides are dominated by sphalerite, with lesser pyrite and minor galena, and generally overly the barite-rich assemblage containing semi-massive sphalerite, pyrite, marcasite, galena, copper sulphides and sulphosalts. The basal stringer sulphide zone is composed of chalcopyrite- and pyrite-dominated stringers.

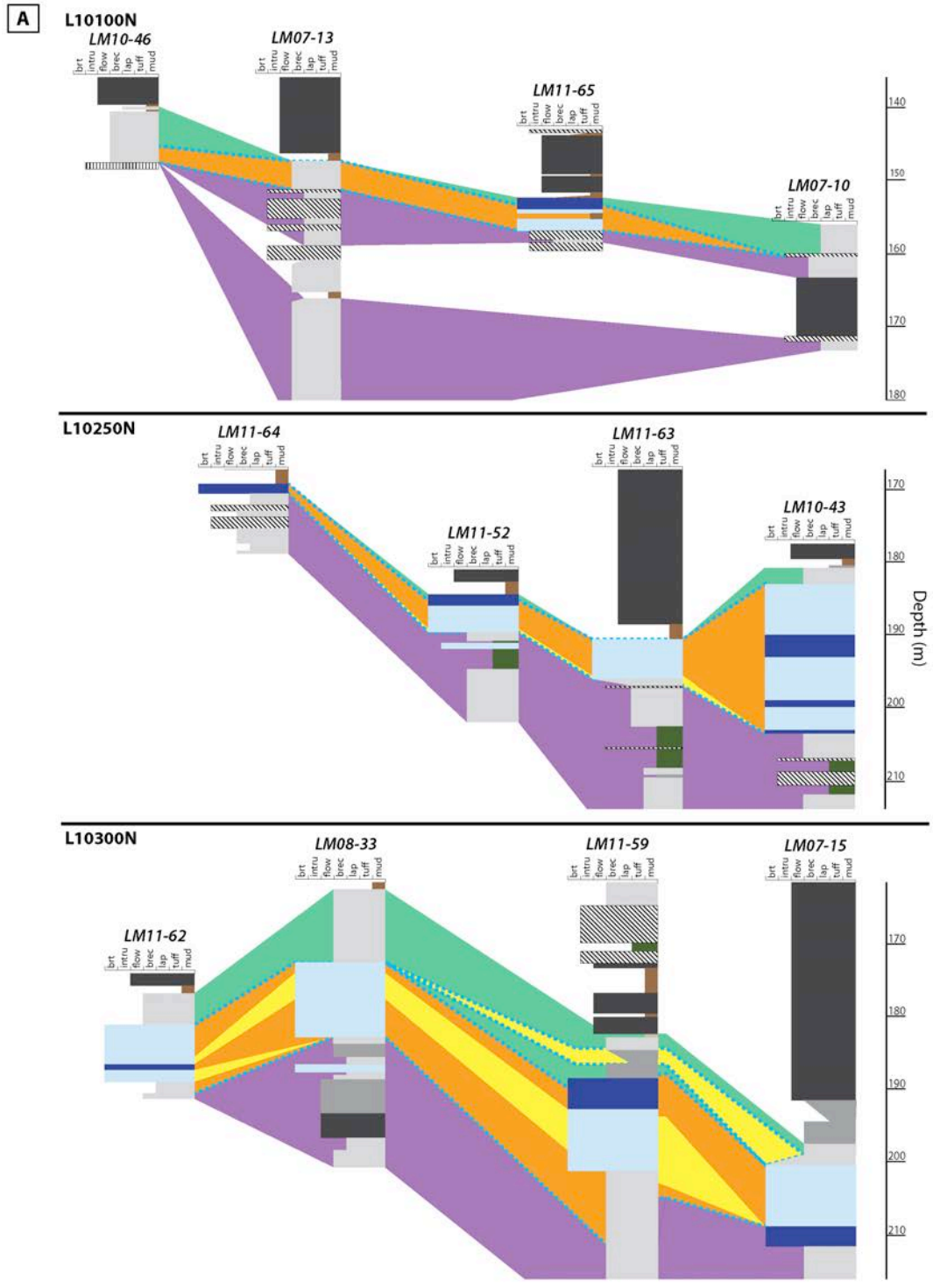
A
L10100N
LM10-46
LM07-13
LM11-65
LM07-10
brt
intru
flow
brec
lap
tuff
mud
140
150
160
170
180
L10250N
LM11-64
LM11-63
LM11-52
LM10-43
170
180
190
200
210
Depth (m)
L10300N
LM08-33
LM11-59
LM07-15
LM11-62
170
180
190
200
210

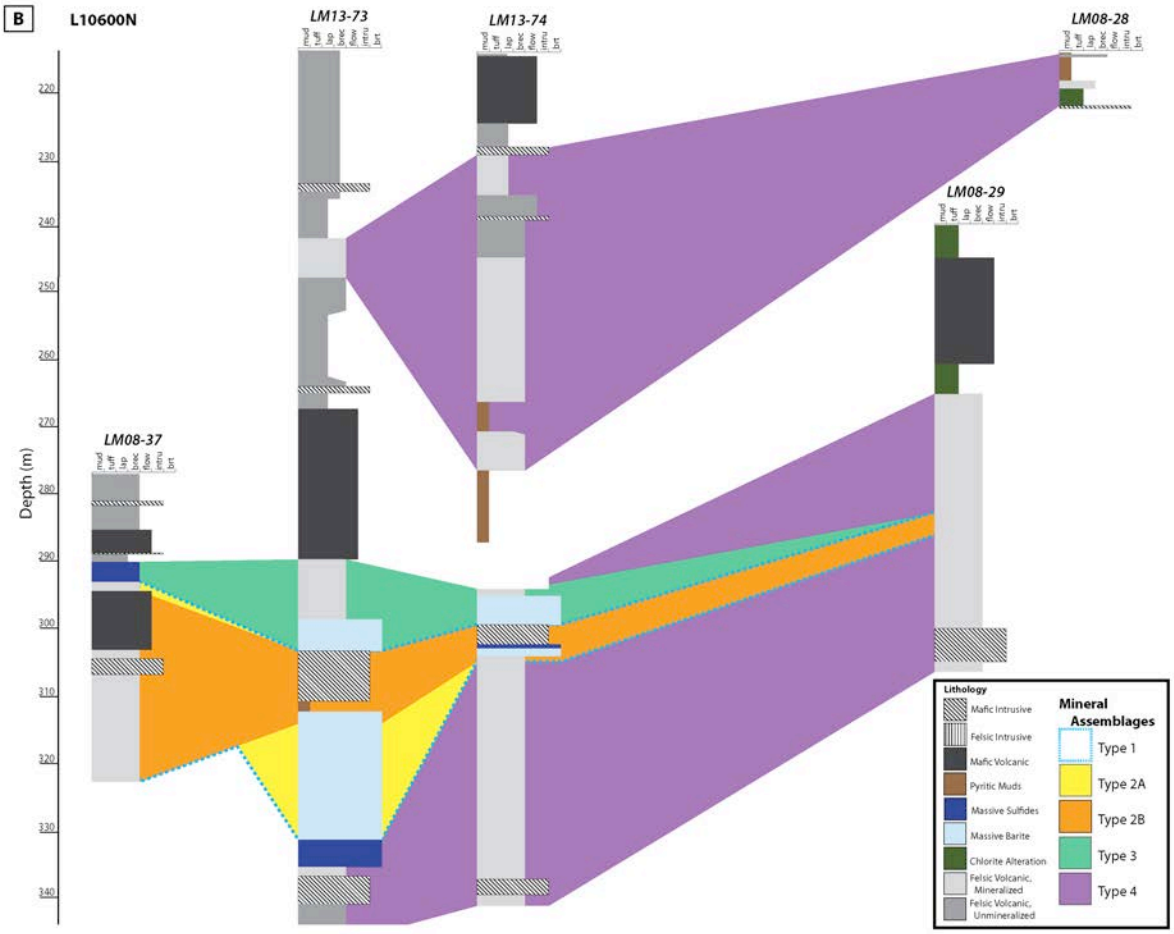

Figure 13. Stratigraphic fence diagrams of representative sections across the Lemarchant deposit. Types of mineralization have been interpolated between drill holes. Locations are shown on Figure 2. A) Sections L10100N, L10250N and L10300N cross-cut the main portion of the Lemarchant deposit. B) Section L10600N cross-cuts the Lower Felsic Block of mineralization.

The stratiform zone contains four sulphide mineral assemblage types (Fig. 4). The type 1 assemblage is composed of granular barite, semi-massive white sphalerite, fine- to medium-grained pyrite, galena, and trace chalcopyrite and tetrahedrite group minerals (Fig. 5A). Two types of copper sulphide and sulphosalt assemblages crosscut the type 1 assemblage: (1) the type 2A assemblage is composed of bornite, galena and chalcopyrite stringers (Fig. 5B); and (2) the type 2B assemblage is composed of locally bladed barite, tetrahedrite group minerals, galena and precious metals (i.e. visible gold; Fig. 5C). Type 2A mineralization occurs only in the central portion of the stratiform zone, whereas type 2B mineralization extends from the centre to the distal edges of the stratiform zone (e.g., L10300N and L10100N, respectively; Fig. 4). The type 3 mineral assemblage overlies the type 1 assemblage and is composed of massive red sphalerite, fine- to medium-grained pyrite, lesser galena and chalcopyrite, and relatively little barite (<15%; Fig. 5D). The basal stringer sulphide zone contains the type 4 assemblage that consists of chalcopyrite, pyrite and lesser orange sphalerite stringers (Fig. 5E).

The type 2A and type 2B mineral assemblages contain minor to trace marcasite, sulphosalts, copper sulphides and precious metal-bearing sulphides. Silver-rich sulphides (e.g. stromeyerite and Ag-bearing bornite; Table 1) and nickel sulphides occur with the type 2A mineral assemblage. Type 2B mineralization contains the tetrahedrite group minerals, which encompass the range of minerals in the tetrahedrite-freibergite-tennantite series and are variably silver-rich, and represent up to 5% of the stratiform zone. The type 2B assemblage also contains marcasite, colusite group minerals, and trace bournonite, polybasite, miargyrite and silver-tellurides.

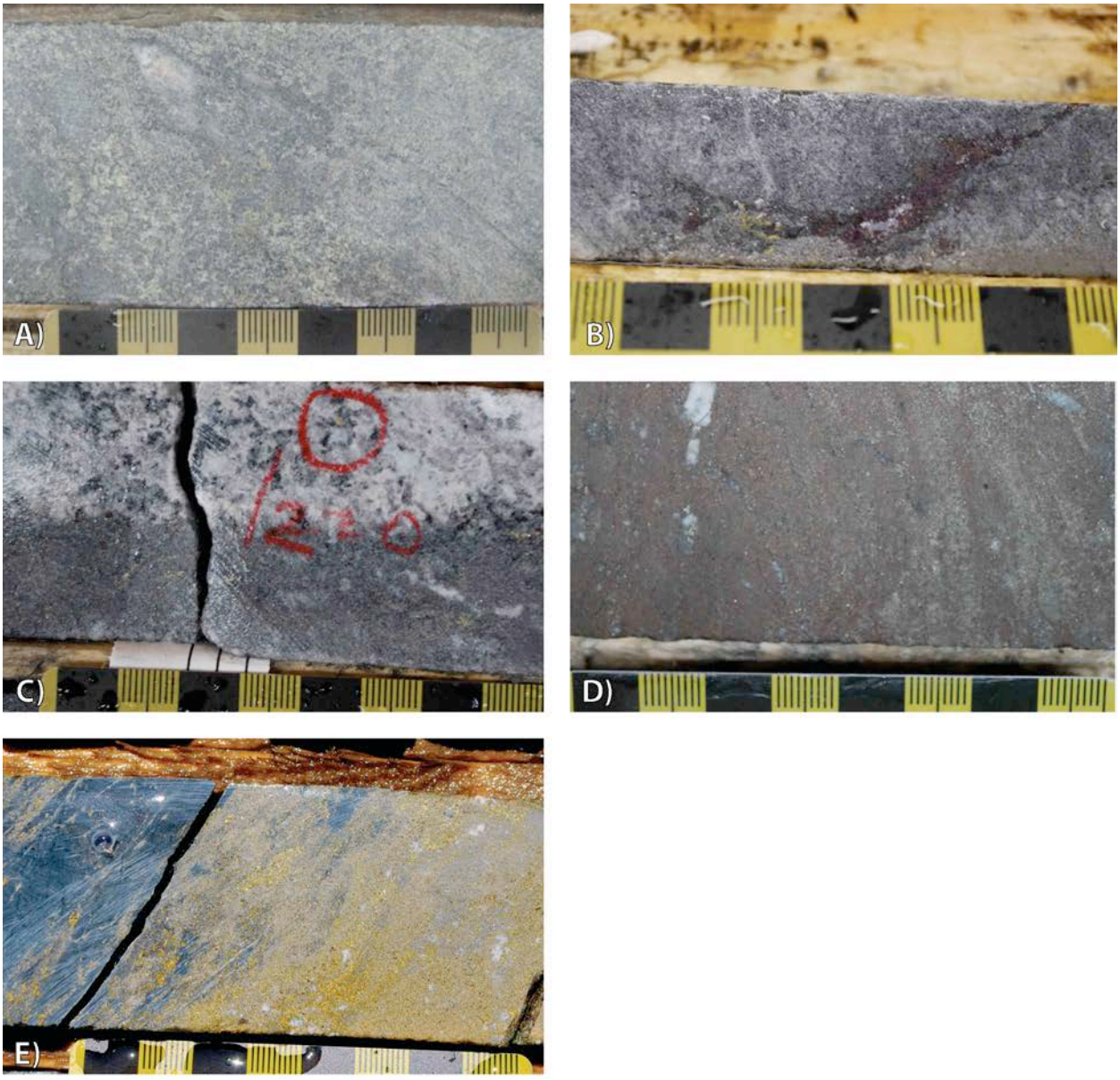

Figure 14. Drill core photograph field mosaic of type mineral assemblages that comprise the Lemarchant deposit. Black squares = 1 cm. A) Type 1 semi-massive white sphalerite, granular barite fine-grained pyrite and galena with minor carbonate-silica alteration (LM11-64 at 218.8m). B) Type 2A bornite-galena-chalcopyrite stringers crosscutting type 1 white sphalerite-barite-pyrite-galena mineralization (LM11-62 at 259.6m). C) Type 2B bladed barite-coarse-grained tetrahedrite-galena stringers with visible gold cross-cutting type 1 white sphalerite-barite-pyrite-galena mineralization (LM10-43 at 220m). D) Type 3 massive red sphalerite with fine- to medium-grained pyrite in minor barite-silica gangue (LM11-69 at 184m). E) Type 4 orange sphalerite-chalcopyrite-pyrite stringers cross-cutting chlorite schist in the felsic footwall (LM 11-63 at 224.7m).

Table 2. Sulphide mineral phases present at the Lemarchant deposit, including mineral formulas. The relative abundance of each phase in each mineral assemblage type is indicated as follows: ( )= absent; (±) = rare; (+) = common; (++) = abundant; (+++) = dominant.

Sulphide phase	Mineral formula	Type 1	Type 2A	Type 2B	Type 3	Type 4
Sphalerite (white to honey)	(Zn,Fe)S	+++		+		
Sphalerite (honey brown to red)	(Zn,Fe)S				+++	+
Pyrite (colloform)	FeS_2	++			+	
Pyrite (recrystallized to atoll)	FeS_2	++		+	++	++
Pyrite (euhedral)	FeS_2			±	+	++
Marcasite	FeS_2			±		±
Galena	PbS	+	++	++	+	±
Chalcopyrite	$CuFeS_2$	±	++	+	+	+++
Tetrahedrite group minerals	$(Cu,Ag]_{10}(Fe,Zn)_2(As,Sb)_4S_{13}$	±		++		
Bornite	Cu_5FeS_4		++			
Stromeyerite	AgCuS		+			
Covellite	CuS		±			
Colusite group minerals	$Cu_{26}V_2(As,Ge,Sb,Sn)_6S_{32}$		±	+		
Electrum	(Au,Ag)			+		
Polybasite	$[(Ag,Cu)_6(Sb,As)_2S_7][Ag_9CuS_4]$			±		
Miargyrite	$AgSbS_2$			±		
Bournonite	$PbCuSbS_3$			±		
Ag-Cu sulphides	------		±	±		
Silver tellurides	------			±		
Nickel sulphides	------		±			

MINERAL DESCRIPTIONS

Sphalerite

Sphalerite is the most abundant sulphide in the Lemarchant deposit and represents more than half of the sulphide minerals. Sphalerite in drill core is massive and blocky or forms local blocky clusters, and ranges from low-iron honey to white sphalerite to high-iron red to honey brown sphalerite (Fig. 6A-B). Honey to white sphalerite occurs in the type 1 assemblage and contains irregular, fine-grained chalcopyrite; the type 1 sphalerite is cross-cut and overgrown by sulphides from the type 2A, 2B and 3 assemblages and late gangue (e.g. galena, tetrahedrite, bornite, chalcopyrite, chlorite, albite, quartz). The type 3 assemblage is composed of red to honey brown sphalerite that is devoid of fine-grained chalcopyrite and in clear in transmitted light (Fig. 6B). Type 3 red to honey brown sphalerite overgrows type 1 sphalerite and galena. Type 1 sphalerite also exists as inclusions in colloform pyrite and recrystallized pyrite atolls (Fig. 6C).

Pyrite and Marcasite

Disseminated fine- to medium-grained pyrite is common in all mineralized drill core from the Lemarchant deposit; massive coarse-grained pyrite is less abundant. In thin section, pyrite forms fine-grained colloform clusters in sphalerite (Fig. 6C), irregular to eudedral medium- to coarse-grained recrystallized atolls (Fig. 6D, E) and euhedral fine-grained disseminations; these textures represent successive stages of pyrite recrystallization and deposition. Pyrite atolls commonly contain galena, sphalerite, and lesser chalcopyrite, tetrahedrite group minerals, bornite and colusite group minerals; recrystallized pyrite may be locally zoned in arsenic (Fig. 6F). The type 1 and type 3 assemblages contain colloform pyrite to variably recrystallized pyrite atolls; however, pyrite euhedra are more common in the type 3

assemblage. Marcasite in the type 4 and type 2B assemblages was distinguished from pyrite by thin section textures (e.g. reniform to dendritic growths and fine-grained lamellae, respectively; Fig. 6D and 6G).

Galena

Galena is abundant in the Lemarchant deposit, but less than sphalerite and pyrite. In drill core, galena forms disseminated, fine- to coarse-grained, metallic silver grains in semi-massive and massive sphalerite. In thin section, individual grains are irregular to angular, and sparsely pitted. Inclusions of galena in type 3 sphalerite and pyrite atolls are sometimes rounded. Galena is primarily associated with type 2A bornite, and type 2B tetrahedrite, electrum, colusite and trace Pb-As-Sb sulphosalts (Fig. 6D-H, 7A-D).

Chalcopyrite

Chalcopyrite is found in every mineral assemblage in the Lemarchant deposit, but is most abundant in the type 4 mineral assemblage. In drill core, chalcopyrite occurs as bronze blebby stringers cross-cutting massive barite and massive sphalerite, and is interstitial to the rhyolite host rock. In thin section, fine-grained chalcopyrite inclusions occur in type 1 white sphalerite, recrystallized pyrite and in type 2B tetrahedrite group minerals (Fig. 6D). Chalcopyrite also infills cracked pyrite, bornite, galena and tetrahedrite group minerals from the type 2A and 2B mineral assemblages (Fig. 7A). Fine-grained, amorphous chalcopyrite is found at sphalerite, galena and tetrahedrite group mineral boundaries (Fig. 7D).

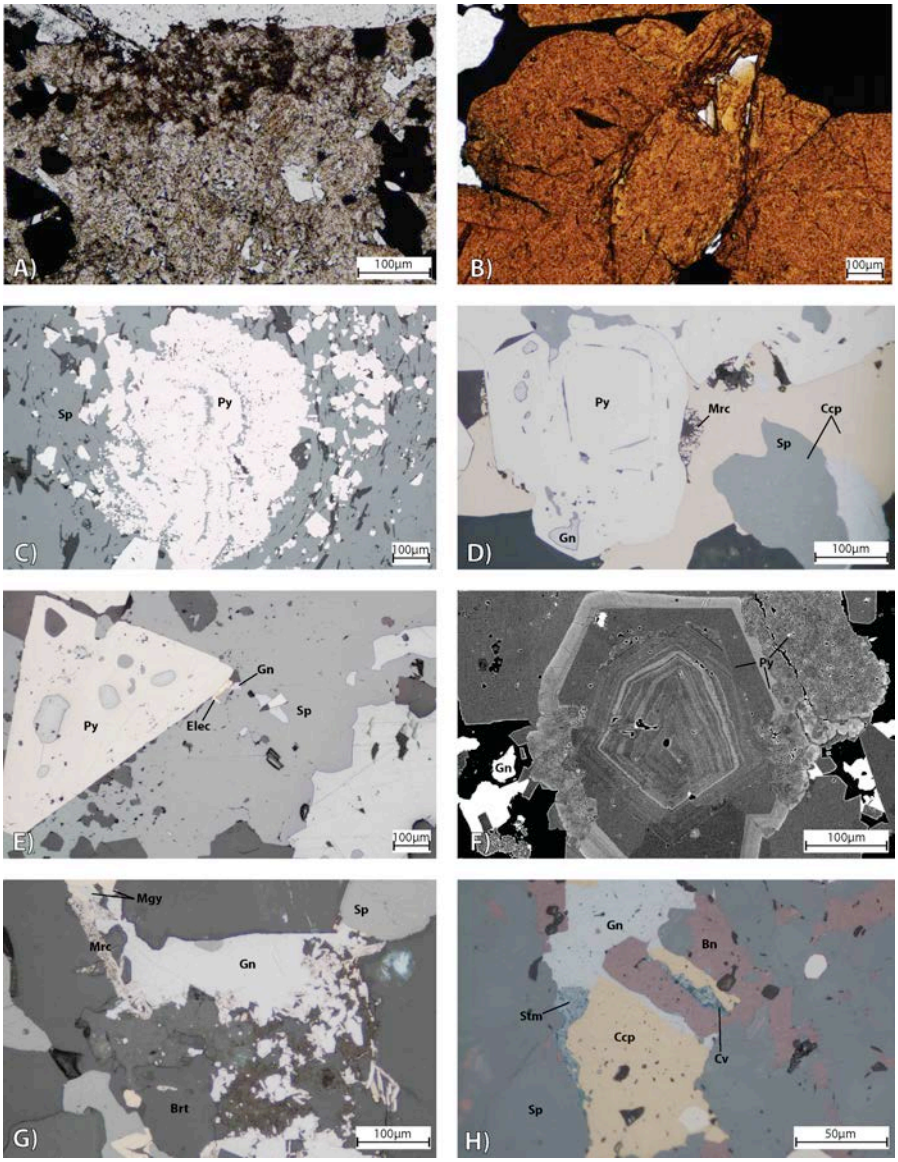

Figure 15. Thin section photomicrographs and back-scatter electron (BSE) images of sulphides and sulphosalts in type mineral assemblages at Lemarchant. A) Transmitted light image of type 1 white sphalerite (Sample CNF29959 in drill hole LM11-59 at 207.7m). B) Transmitted light image of Type 3 massive red sphalerite (CNF29959 from LM11-59 at 207.72m). C) Reflected light image of type 3 colloform and euhedral pyrite in sphalerite (CNF29960 in LM11-59 at 216m). D) Type 4 recrystallized atoll pyrite with entrained galena, in chalcopyrite with dendritic marcasite and diseased sphalerite (CNF14257 in LM11-62 at 266.8m). E) Type 2B galena-electrum at euhedral pyrite atoll boundary in massive sphalerite (CNF14291 in LM11-65 at 159.3m). F) Back-scatter electron image of type 1 recrystallized fine-grained pyrite with zoned growth rings of higher As-content (light grey; CNF25134 in LM11-56 at 158.7m). G) Type 2B assemblage of galena-sphalerite-barite-marcasite-tetrahedrite-miargyrite and type 4 chalcopyrite (CNF25109 in LM13-74 at 328.6m). H) Type 2A bornite-galena-stromeyerite in sphalerite with type 4 chalcopyrite replacement; stromeyerite and chalcopyrite host late blue covellite (CNF29967 in LM07-17 at 247.6m). Abbreviations as follows: Brt = barite; Sp = sphalerite; Py = pyrite; Mrc = marcasite; Gn = galena; Ccp = chalcopyrite; Trt = tetrahedrite; Bn = bornite; Col = colusite; Stm = stromeryite; Cv = covellite; Elec = electrum; Mgy = miargyrite; Bnn = bournonite.

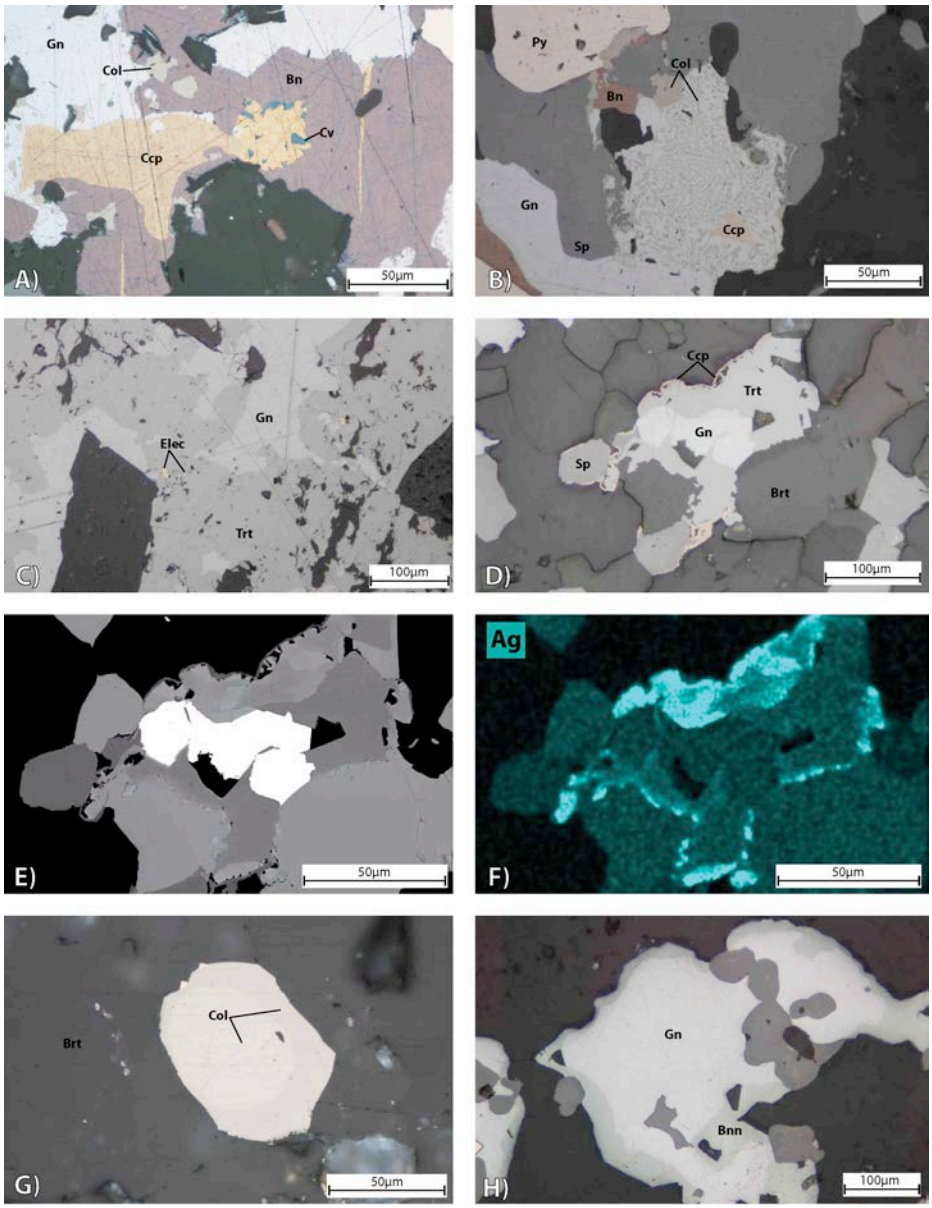

Figure 16. Thin section photomicrographs and back-scatter electron (BSE) images of sulphides and sulfosalts in type mineral assemblages Lemarchant. A) Reflected light image of type 4 chalcopyrite replacing and infilling cracks in type 2 bornite, galena and colusite; chalcopyrite is host to late blue covellite (CNF14279 in LM08-33 at 230.8m). B) Myrmekitic growth of type 2B galena-colusite-sphalerite and replacement of type 2A bornite at the pyrite atoll-sphalerite interface; type 4 chalcopyrite is replacing galena-colusite intergrowth (CNF14279 in LM08-33 at 230.8m). C) Type 2B galena-electrum in tetrahedrite (CNF25121 in LM11-52 at 212.3m). D) Rounded galena in type 2B tetrahedrite, sphalerite and barite; tetrahedrite is rimmed by chalcopyrite (CNF14293 in LM11-65 at 161.8m). E) Backscatter electron image of tetrahedrite zoning in sample CNF14293. F) False colour element map of relative Ag-distribution in type 2B tetrahedrite from sample CNF14293. G) Reflected light image of type 2B zoned colusite in barite (CNF14259 in LM07-14 at 204.4m). H) Type 2B bournonite rimming anhedral galena (CNF14291 in LM11-65 at 159.3m).

Tetrahedrite group minerals

The tetrahedrite-freibergite-tennantite series of sulphosalts occur in drill core as dark grey, metallic, medium-grained crystals with type 2B galena and bladed barite in type 1 semi-massive sphalerite and massive barite. In reflected light, these sulphosalts are amorphous and grey-green (tetrahedrite) to steel grey (tennantite). The tetrahedrite group minerals primarily occur with type 2B galena and type 1 white sphalerite and are closely associated with type 2B colusite, electrum and marcasite (Fig. 7C). Tetrahedrite group minerals are intergrown with type 2A bornite and stromeyerite, and overgrown by chalcopyrite. Some tetrahedrite group minerals are zoned in arsenic, antimony and silver; tennantite mineral boundaries are enriched in Sb and Ag relative to the As-rich core (Fig. 7D-F).

Bornite

Purple bornite occurs in drill core with type 2A galena and chalcopyrite as stringers that cross-cut type 1 white sphalerite and massive barite, but is also present with type 2B tetrahedrite group minerals and bladed barite mineralization. In thin section, bornite forms amorphous grains to wiry strands (Fig. 6H, 7A-B). Bornite occurs as a local dominant phase in thin section, or as inclusions in pyrite atolls and blebs in massive barite. Scanning electron microscopy suggests bornite is enriched in silver relative to other sulphides. Bright blue covellite replaces bornite at stromeyerite and chalcopyrite mineral boundaries (Fig. 6H).

Colusite group minerals

Colusite, germanocolusite and other vanadium-germanium-copper sulphosalts are notable minor components of the type 2B mineral assemblage. These minerals generally occur as amorphous 50μm grains and are only visible in thin section. In reflected light, colusite group minerals are pink- to orange-brown (Fig. 7A); zoning of colusite group minerals can occur in

>50 μm grains (Fig. 7G). Colusite group minerals occur in type 1 white sphalerite and barite with type 2B tetrahedrite group minerals, galena and lesser type 2A bornite, and as inclusions in rounded pyrite atolls. Myrmekitic intergrowths with type 1 sphalerite and type 2B galena are rare but notable (Fig. 7B).

Stromeyerite

Stromeyerite is a minor phase that occurs with other copper-rich sulphide phases in the type 2A mineral assemblage. This mineral is not visible in hand sample, but appears in thin section as thin, rimming, dark grey grains that radiate from sulphide mineral boundaries. Stromeyerite is generally associated with type 2A bornite, chalcopyrite and lesser galena mineral boundaries, and rarely occurs with <10μm nickel sulphides. Irregular blue covellite commonly discolours the grey stromeyerite at mineral boundaries (Fig. 6H, 7A).

Electrum

Currently, the only known source of gold in the Lemarchant deposit is in trace electrum. Visible gold in drill core is situated in type 2B tetrahedrite group minerals and galena stringers or in type 1 massive barite and white sphalerite proximal to type 2B mineralization. In thin section, electrum is found in type 1 white sphalerite or type 2B tetrahedrite group minerals proximal to recrystallized pyrite and type 2B galena and colusite group minerals (Fig. 6E, 7C). Electrum occurs as bright silver-yellow, amorphous grains at sphalerite-pyrite-galena and tetrahedrite-galena mineral boundaries. Some variation in Au:Ag content is suggested by SEM analyses.

Trace minerals

Trace minerals in the Lemarchant deposit are visible only by thin section and SEM analyses. The Cu-Ag-sulphosalts polybasite and miargyrite are associated with type 2B tetrahedrite group minerals and galena (Fig. 6G). Bournonite is dark grey in thin section and rims

type 2B galena (Fig. 7H). Silver-tellurides occur as greenish-grey radiating clusters or tabular crystals and are associated with silver-rich type 2B tetrahedrite in sphalerite and proximal to pyrite. Amorphous nickel sulphides are found with type 2A bornite, galena, stromeyerite and galena.

PARAGENESIS

Sulphide mineral paragenesis at Lemarchant can be broadly divided into three stages of deposition based on cross-cutting relationships (Fig. 8). During stage 1 of the paragenetic sequence, type 1 barite-semi-massive white sphalerite-colloform pyrite-minor galena sulphides were deposited below the early exhalative pyritic mudstone. Stage 2 paragenesis resulted in variable replacement of the central type 1 mineral assemblage by type 2A bornite-galena-stromeyerite-nickel sulphide stringers and the type 2B barite-As-rich tennantite-galena-colusite-electrum-marcasite-silver telluride assemblage. At the end of stage 2 paragenesis, type 2B Sb-Ag-rich tetrahedrite-galena-electrum-Sb-Cu-Ag sulphosalt stringers replaced type 1 barite and white sphalerite at the distal edges of the deposit. Covellite was formed as a result of diagenesis after stage 2 deposition. In the final stage of sulphide mineral deposition, or stage 3 paragenesis, type 3 and type 4 mineral assemblages were deposited with minor zone refinement of the stratiform and stringer zones of the Lemarchant deposit, respectively. The type 3 massive red sphalerite-medium-grained atoll pyrite-galena-chalcopyrite assemblage replaced the upper portion of the type 1 mineral assemblage, and type 1 white sphalerite was partially replaced by fine-grained chalcopyrite. Type 4 chacopyrite-pyrite±sphalerite stringers were deposited in the stringer sulphide zone below the type 1, type 2 and type 3 mineral assemblages.

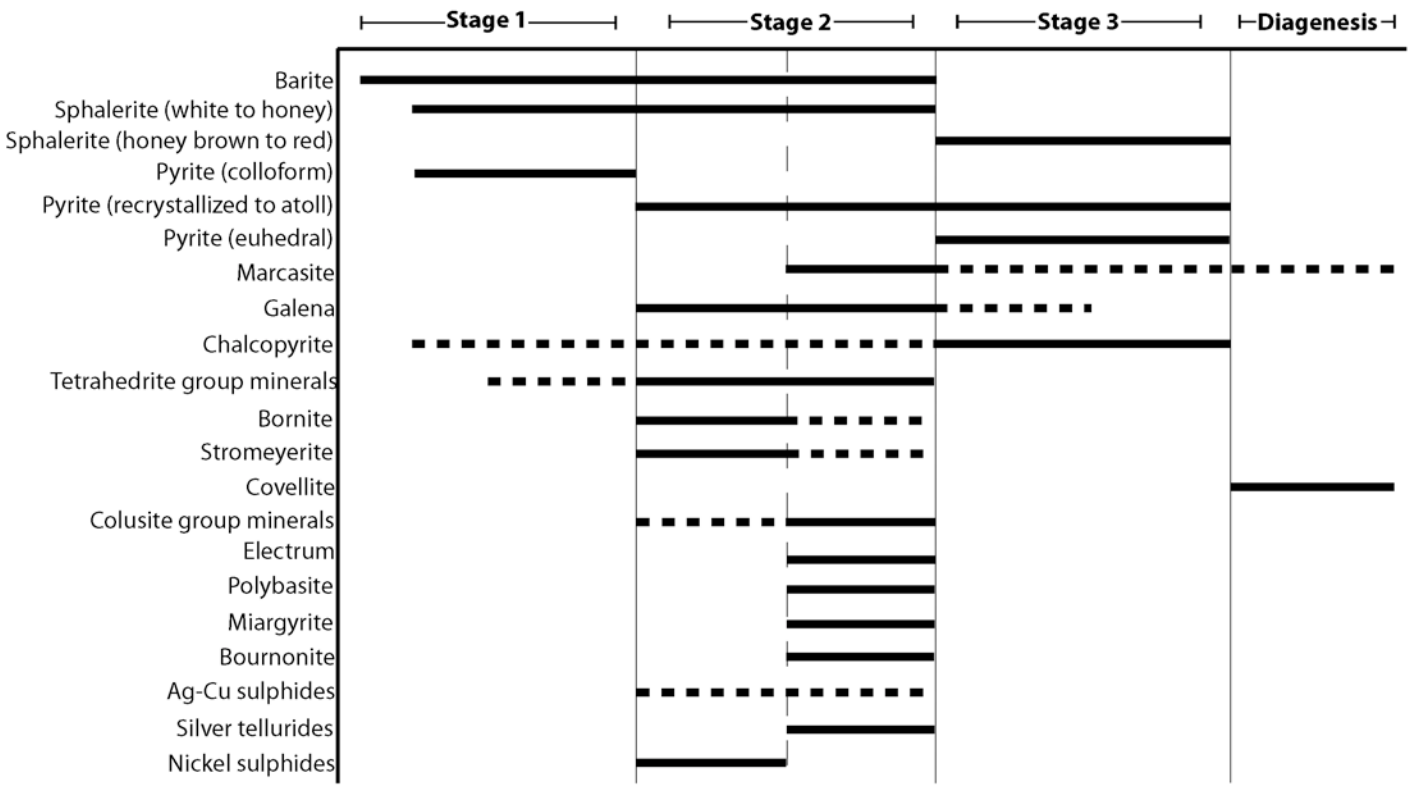

Figure 17. Sulphide mineral paragenesis at Lemarchant. Relative timing of mineral deposition is indicated (solid lines) or inferred (dashed lines) from documented mineral associations and textures.

DISCUSSION AND SUMMARY

The Lemarchant deposit is composed of mineralization styles and mineral assemblages characteristic of polymetallic Kuroko-type VMS deposits and high-sulphidation epithermal gold deposits. The bimodal felsic lithostratigraphic host rock assemblage, sedimentary-exhalative cap rock, abundance of barite and Zn-Pb-rich massive sulphides, and zoning of mineral assemblages are features common to Kuroko-type VMS deposits (Shimazaki, 1974; Eldridge et al., 1983; Ohmoto, 1996). However, the enrichment of precious metals (Ag, Au), sulphosalt- and bornite-rich mineral assemblages and abundance of low-Fe sphalerite are not common to most Kuroko deposits and suggest a possible magmatic contribution to hydrothermal fluids, typical of epithermal gold deposits (Hannington and Scott, 1989; Sillitoe et al., 1996; Dubé et al., 2007).

The spatial arrangement of sulphide mineral assemblages in the Lemarchant deposit has similarities to the idealized Kuroko deposit outlined by Eldridge et al. (1983). In the stratiform zone, type 1 barite-rich semi-massive white sphalerite and type 3 massive red sphalerite assemblages correspond to the barite ore, semi-massive black ore (MSBO) and massive black ore (MBO) in the idealized Kuroko massive sulphides; the type 4 chacopyrite-pyrite±sphalerite assemblage in the underlying stringer zone corresponds to the siliceous black ore (SBO) and siliceous yellow ore (SYO) of the idealized Kuroko stockwork zone (Eldridge et al., 1983). The idealized Kuroko deposit represents a mineralogically zoned sequence that grades from a barite-dominant at the top, to sphalerite > galena, then to chalcopyrite- and pyrite-dominant at the base (Shimazaki, 1974; Eldridge et al., 1983; Ohmoto, 1996). The Lemarchant deposit also shows mineralogical evidence of zonation in the microscopic chalcopyrite in type 1 sphalerite (i.e. chalcopyrite disease; Eldridge et al., 1983), in type 3 red sphalerite overprinting type 1 sulphides

and in type 4 chalcopyrite-dominant stringers below the barite-rich mineralization. However, the Lemarchant deposit differs from the idealized Kuroko deposit zonation as the massive sphalerite (type 3) assemblage is overlying the barite-rich (type 1, type 2A and type 2B) assemblage in the stratiform massive sulphide zone. The absence of a pyrite-dominant assemblage below the type 4 chalcopyrite-rich assemblage in the stringer zone could be attributed either to a relatively short lifetime of the hydrothermal system (Ohmoto, 1996), or to physical displacement of a possible "stockwork" stringer zone due to faulting (i.e. the Lemarchant fault).

The abundance of sulphosalts, precious metals and precious metal-bearing sulphides in the type 2A and type 2B mineral assemblages at Lemarchant are not typical of normal VMS systems. Although bornite, tetrahedrite group minerals and Ag-rich tetrahedrite, stromeyerite, colusite group minerals, electrum, silver tellurides, nickel sulphides, and a number of Sb-Cu-Ag- and Sb-Pb-Ag-sulphosalts have been documented in Kuroko-type VMS deposits (Shimazaki, 1974), they are neither present in abundance nor do they commonly form the complete array observed at Lemarchant. The diverse mineralogy in the type 2A and type 2B assemblages is considered to be primary in the Lemarchant deposit, and indicates that precious metal deposition was synvolcanic (Hannington et al., 1999; Dubé et al., 2007). Further, the type 2A and type 2B assemblages are analogous to a high sulphidation epithermal mineral and trace element suite (i.e. Au, Ag, As, Sb, Te, Ni), and suggest a direct magmatic contribution to the hydrothermal fluid (Sillitoe et al., 1996; Hannington et al., 1999; Roth et al., 1999; Dubé et al., 2007). Currently, an advanced argillic alteration assemblage typical of high sulphidation epithermal systems has not been documented at Lemarchant (Sillitoe et al., 1996; Mercier-Langevin et al., 2011), but is the

focus of ongoing infrared spectroscopic research at the deposit (Jonathan Cloutier, personal communication).

The spatial association of type 2B visible gold (electrum) and type 1 low-Fe, white sphalerite is consistent with the stable transport of gold as a bisulphide complex ($Au(HS)_2^-$) in low temperature (<250°C) hydrothermal fluids (Hannington and Scott, 1989; Huston and Large, 1989), and is also consistent with the lower temperature Zn-Pb-Ba-rich sulphides of the type 1, type 2A and type 2B assemblages. The bladed barite and visible gold in the type 2B assemblage also suggest that localized boiling may have occurred during deposition of the type 2A and 2B assemblages, possibly due to emplacement of the deposit in a shallow water environment (<1500m; Sillitoe et al., 1996; Hannington et al., 1999; Huston et al., 2000; Dubé et al., 2007; Hannington et al., 2009). In contrast, the copper-rich type 4 stringer suphides, type 3 high-Fe sphalerite and recrystallized pyrite of the stratiform zone suggest that the hydrothermal fluids that formed these assemblages were higher temperature (>250°C) than those that deposited type 1, type 2A and type 2B sulphides and sulphosalts (Ohmoto, 1996; Huston and Large, 1989; Huston, 2000).

The combination of Kuroko-style and high-sulphidation epithermal-style VMS mineralization at Lemarchant requires further investigation to determine the source(s) of precious metals, and the conditions of fluid transport and deposition that resulted in precious metal enrichment of the deposit. Variation in mineral chemistry and S- and Pb-isotope characteristics of the Lemarchant sulphides will be investigated with electron microprobe, laser ablation ICP-MS and secondary ion mass spectrometry. These analyses will provide further

insight to the depositional conditions and enrichment mechanisms that caused precious metal enrichment at the Lemarchant deposit and in analogous precious metal-enriched VMS systems in the Appalachians and globally.

ACKNOWLEDGEMENTS

Funding for this project is primarily supported by the GSC Targeted Geoscience Initiative 4 Program and the Research Affiliate Program of NRCan. This research is also supported by additional grants to Dr. Stephen J. Piercey, including an NSERC Discovery Grant and the NSERC-Altius Industrial Research Chair in Mineral Deposits supported by NSERC, Altius Resources Inc., and the Research and Development Corporation of Newfoundland and Labrador. Access to the Lemarchant drill core, core logs, and assay database was provided by the Canadian Zinc Corporation and the Paragon Minerals Corporation (a 100% owned subsidiary of Canadian Zinc Corporation). Many thanks to Stefanie Lode, Graham Layne, Michael Schaeffer, David Grant, and Diane Fost for their technological help and interpretive guidance.

REFERENCES

Brueckner, S.M., Piercey, S.J., Sylvester, P.J., Pilgrim, L., and Maloney, S., *in press*. Evidence for syngenetic precious metal enrichment in an Appalachian volcanogenic massive sulfide (VMS) system: the 1806 Zone, Ming Mine, Newfoundland, Canada: Economic Geology.

Copeland, D.A., Toole, R.M.S., and Piercey, S.J., 2008. Assessment report on diamond drilling and soil sampling, Licence 8183M (10th Year) and 9569M (5th Year) South Tally Pond property, Rogerson Lake area, Newfoundland and Labrador, NTS 12A/10 and 12A/07: Newfoundland and Labrador Geological Survey, Assessment Report, 956 p.

Doyle, M.G., and Allen, R.L., 2003. Subsea-floor replacement in volcanic-hosted massive sulfide deposits: Ore Geology Reviews, v. 23, p. 183-222.

Dubé, B., Gosselin, P., Mercier-Langevin, P., Hannington, M., and Galley, A., 2007. Gold-rich volcanogenic massive sulphide deposits: Mineral Deposits of Canada: A Synthesis of Major Deposit-Types, District Metallogeny, the Evolution of Geological Provinces, and Exploration Methods: Geological Association of Canada, Mineral Deposits Division, Special Publication, v. 5, p. 75-94.

Dunning, G. R., Swinden, H. S., Kean, B. F., Evans, D. T. W., and Jenner, G. A., 1991. A Cambrian island arc in Iapetus; geochronology and geochemistry of the Lake Ambrose volcanic belt, Newfoundland Appalachians; Geological Magazine, v. 128, p. 1-17.

Eldridge, C.S., Barton, P.B., Jr., and Ohmoto, H., 1983. Mineral textures and their bearing on formation of the kuroko orebodies: Economic Geology Monograph, v. 5, p. 241-281.

Evans, D.T.W., and Kean, B.F., 2002. The Victoria Lake Supergroup, central Newfoundland - its definition, setting and volcanogenic massive sulphide mineralization, Newfoundland and Labroador Department of Mines and Energy, Geological Survey; Open File NFLD, v. 2790, p. 68.

Franklin, J., Gibson, H., Jonasson, I., and Galley, A., 2005. Volcanogenic Massive Sulphides: Economic Geology100th Anniversary Volume, p. 523-560.

Fraser, D., Giroux, G.H., Copeland, D.A., and Devine, C.A., 2012. Technical Report and Resource Minerals Estimate on the Lemarchant Deposit, South Tally Pond VMS Project,

Central Newfoundland, Canada – NI 43-101 Technical Report prepared for Paragon Minerals Corporation, 132 p.

Gibson, H., Morton, R., and Hudak, G., 1999. Submarine volcanic processes, deposits, and environments favorable for the location of volcanic-associated massive sulfide deposits: Reviews in Economic Geology, v. 8, p. 13-51.

Hannington, M., and Scott, S.D., 1989, Sulfidation equilibria as guides to gold mineralization in volcanogenic massive sulfides; evidence from sulfide mineralogy and the composition of sphalerite: Economic Geology, v. 84, p. 1978-1995.

Hurley, T.D., and Crocket, J.H., 1985. A gold-sphalerite association in a volcanogenic base-metal-sulfide deposit near Tilt Cove, Newfoundland: The Canadian Mineralogist, v. 23, p. 423-430.

Lode, S., Piercey, S.J.P., Copeland, D.A., Devine, C.A., and Sparrow, B., 2012. Setting and styles of hydrothermal mudstones near the Lemarchant volcanogenic massive sulfide (VMS) deposit, Central Mobile Belt, Newfoundland [abstract]: *in* Abstracts Volume 35, GAC-MAC Joint Annual Meeting, St. John's, Canada, May 27-29, 2012, 166 p.

Martin, W., 1983. Once upon a mine: story of pre-confederation mines on the island of Newfoundland, Canadian Institute of Mining and Metallurgy.

McNicoll, V., Squires, G., Kerr, A., and Moore, P., 2010. The Duck Pond and Boundary Cu-Zn deposits, Newfoundland: new insights into the ages of host rocks and the timing of VHMS mineralization; Canadian Journal of Earth Sciences, v. 47, p. 1481-1506.

Mercier-Langevin, P., Hannington, M., Dubé, B., and Bécu, V., 2011. The gold content of volcanogenic massive sulfide deposits: Mineralium Deposita, v. 46, p. 509-539.

Moore, P., 2003. Stratigraphic implications for mineralization: Preliminary findings of a metallogenic investigation of the Tally Pond volcanics, central Newfoundland; Newfoundland and Labrador Department of Natural Resources, Geological Survey, Report 03-1, p. 241-257.

Ohmoto, H., 1996. Formation of volcanogenic massive sulfide deposits; the Kuroko perspective: Ore Geology Reviews, v. 10, p. 135-177.

Piercey, S. J., and Hinchey, J. G., 2012. Volcanogenic massive sulphide (VMS) deposits of the Central Mobile Belt, Newfoundland, Geological Association of Canada–Mineralogical Association of Canada Joint Annual Meeting, Field Trip Guidebook B4. Open File NFLD/3173, Newfoundland and Labrador Department of Natural Resources, Geological Survey, 56 p.

Piercey, S.J., Squires, G.C., and Brace, T.D., 2014. Lithostratigraphic, Hydrothermal, and Tectonic Setting of the Boundary Volcanogenic Massive Sulfide Deposit, Newfoundland Appalachians, Canada: Formation by Subseafloor Replacement in a Cambrian Rifted Arc: Economic Geology, v. 109, p. 661-687.

Pollock, J., McNicoll, V., van Staal, C.R., and Wilton, D., 2004. Geology of the Tally Pond Group, Newfoundland; new geochronology and geochemical data from the Exploits

Subzone, Dunnage Zone: Abstracts with Programs - Geological Society of America, v. 36, p. 129-129.

Rogers, N., van Staal, C.R., McNicoll, V., Pollock, J., Zagorevski, A., and Whalen, J., 2006. Neoproterozoic and Cambrian arc magmatism along the eastern margin of the Victoria Lake Supergroup: A remnant of Ganderian basement in central Newfoundland; Precambrian Research, v. 147, p. 320-341.

Santaguida, F. and Hannington, M., 1993. Preliminary results on gold mineralization in volcanogenic massive sulphide deposits, central Newfoundland: *In* Current research, *Edited by* C. P. G. Pereira, D. G. Walsh and R. F. Blackwood, Government of Newfoundland and Labrador, Department of Mines and Energy, Geological Survey Branch, Report 93-01, pages 373-381.

Santaguida, F., and Hannington, M., 1996. Characteristics of gold mineralization in volcanogenic massive sulphide deposits of the Notre Dame Bay area, central Newfoundland: Canadian Journal of Earth Sciences, v. 33, p. 316-334.

Shimazaki, Y., 1974. Ore minerals of the Kuroko-type deposits: Min. Geol. Spec. Issue, p. 311-322.

Sillitoe, R.H., Hannington, M.D., and Thompson, J.F.H., 1996. High sulfidation deposits in the volcanogenic massive sulfide environment: Economic Geology and the Bulletin of the Society of Economic Geologists, v. 91, p. 204-212.

Squires, G.C.S., Brace, T.D., and Hussey, A.M., 2001. Newfoundland's polymetallic Duck Pond Deposit: earliest Iapetan VMS mineralization, formed within a sub-seafloor, carbonate-rich alteration system; *in* Geology and mineral deposits of the Northern Dunnage Zone, Newfoundland Appalachians, (ed.) D.T.W. Evans and A. Kerr; Geological Association of Canada – Mineralogical Association of Canada (GAC–MAC) Annual Meeting, St. John's, Nfld., 2001, Field Trip Guide A2, p. 167–187.

Squires, G., and Moore, P., 2004. Volcanogenic massive sulphide environments of the Tally Pool Volcanics and adjacent area; geological, lithogeochemical and geochronological results; Newfoundland Department of Mines and Energy, Geological Survey, Report 04-1, p. 63-91.

Swinden, H., and Kean, B., 1988. The Volcanogenic Sulphide Districts of Newfoundland: A Guidebook and Reference Manual for Volcanogenic Sulphide Deposits in the Early Paleozoic Oceanic Volcanic Terranes of Central Newfoundland: Geological Association of Canada, Mineral Deposits Division, p. 2-27.

Swinden, H.S., and Dunsworth, S.M., 1995. Metallogeny, Chapter 9; *in* Geology of the Appalachian-Caradocian Orogeny in Canada and Greenland, (ed.) H. Williams; Geological Survey of Canada, Geology Canada, No.6, p. 681-814.

van Staal, C.R., Whalen, J.B., McNicoll, V.J., Pehrsson, S., Lissenberg, C.J., Zagorevski, A., van Breemen, O., and Jenner, G.A., 2007. The Notre Dame arc and the Taconic orogeny in Newfoundland; Geological Society of America Memoirs, v. 200, p. 511-552.

Zagorevski, A., Van Staal, C.R., McNicoll, V., and Rogers, N., 2007. Upper Cambrian to Upper Ordovician peri-Gondwanan Island arc activity in the Victoria Lake Supergroup, Central Newfoundland: Tectonic development of the northern Ganderian margin; American Journal of Science, v. 307, p. 339-370.

Appendix D: Electron Microprobe Results

D.1 – Supplementary Electron Microprobe Methods

A total of 22 thin section samples were analyzed for 17 elements (Ag, As, Au, Ba, Bi, Ca, Cd, Cu, Fe, Ge, Hg, Mn, Ni, Pb, S, Sb, Sn, Sr, Te, V, Zn) in 15 phases (excluding unknowns; barite, sphalerite, pyrite, galena, chalcopyrite, tetrahedrite, bornite, colusite, sulvanite, reinerite, electrum, stromeyerite, bournonite, pearceite and miargyrite). LIF, PET and TAP diffracting crystals detected element wavelengths for each mineral phase. Large area and high intensity LIF and PET crystals are indicated with an H and L, respectively. Measured elements using the LIF crystal included: Ba Lα (brt); Fe Kα (brt,); Zn Kα (sp); Cu Kα (py, gn, ccp et al., col); Ni Kα (ccp et al.). Measured elements using the LIFH crystal included: Cu Kα (sp, elec); Mn Kα (sp). Measured elements using the LIFL crystal included: Fe Kα (brt, sp, py, gn, ccp et al., col, elec); Mn Kα (sp); Cu Kα (sp, py, gn, elec); Zn Kα (py, gn, ccp et al., col); Hg Lα (py, gn, ccp et al., elec); Bi Lα (ccp et al.); V Kα (col). Measured elements using the PET crystal included: S Kα (brt, sp, py, gn, ccp et al., col, elec); Ca Kα (brt); Sb Lα (py, gn, ccp et al., col); Pb Mα (pb, gn, elec); Ag Lα (elec); Au Mα (elec). Measured elements using the PETH crystal included: Ag Lα (brt, sp, py, gn, ccp et al., col, elec); Au Mα (brt, py, gn, col, elec); Sr Lα (brt); Pb Mα (brt, ccp et al.); Cd Lα (sp); Sb Lα (py, gn, elec); Te Lα (ccp et al.); Sn Lα (col). Measured elements using the PETL crystal included: Sr Lα (brt); Ca Kα (brt); Pb Mα (brt); Te Lα (brt); Ba Lα (brt); Cd Lα (sp). Measured elements using the TAP crystal included: Ge Lα (brt, sp, col); As Lα (py, gn, ccp et al., col, elec).

The lower limit of detection (LLD) was calculated using the formula below for each spot analyzed by electron microprobe. Abreviations are as follows: ZAF = total matrix correction factor; std = standard; unk = unknown; bkg = background; C = concentration (wt%); I = intensity $((s*nA)^{-1})$; t = count time (s); curr = current (nA) (pers comm B. Joy, 2013).

$$\text{(i) LLD } (3\sigma) = 3*ZAF*(C_std/I_std,net)*\sqrt{2}*\sqrt{(I_unk,bkg/(t_unk,bkg*curr_unk))}$$

$$\text{(ii) } ZAF = C_unk/(I_unk,net/I_std,net)*C_std$$

D.2 – Compiled Electron Microprobe Analyses

Table A.2.1 – Electron Microprobe Analyses for sphalerite

Drill hole	LM13-73	LM13-73	LM13-73	LM13-73	LM13-73	LM13-73	LM13-74	LM13-74	LM13-74	LM08-23	LM08-23
Sample	CNF14299	CNF14299	CNF14299	CNF14299	CNF14299	CNF14299	CNF25109	CNF25109	CNF25109	CNF25127	CNF25127
Depth (m)	327.95	327.95	327.95	327.95	327.95	327.95	328.55	328.55	328.55	66.95	66.95
Probe Analysis	RL4 sp1	RL4 sp2	RL4 sp3	RL10 sp1	RL10 sp2	RL10 sp3	RL1 sp1	RL5 sp1	RL5 sp3	RL3 sp1	RL3 sp2
Date	2013-10-01	2013-10-01	2013-10-01	2013-10-01	2013-10-01	2013-10-01	2013-10-01	2013-10-01	2013-10-01	2013-10-01	2013-10-01
Type Mineralogy	Type 1	Type 1	Type 1	Type 1	Type 1	Type 1	Type 1	Type 1	Type 1	Type 1	Type 1
Zn (wt%)	65.55	65.84	65.53	66.36	66.34	65.90	63.11	63.59	63.38	66.08	66.17
S	32.90	32.92	32.78	32.73	32.68	33.07	33.13	32.86	32.85	33.10	32.70
Cd (ppm)	3160	3190	3120	2970	2980	2890	2890	2920	2860	3920	3810
Fe	1580	1100	2560	BDL	1090	BDL	24080	21670	25820	1140	960
Cu	350	BDL	BDL	BDL	1410	350	BDL	BDL	BDL	BDL	BDL
Mn	330	350	350	310	370	400	BDL	BDL	BDL	BDL	200
Ag	BDL	BDL	BDL	BDL	BDL	BDL	BDL	300	BDL	BDL	BDL
Ge	BDL	BDL	BDL	BDL	BDL	BDL	BDL	BDL	BDL	BDL	BDL
Total	**99.00**	**99.23**	**98.92**	**99.19**	**99.61**	**99.35**	**98.94**	**98.96**	**99.13**	**99.68**	**99.40**
Zn (apfu)	0.98	0.98	0.98	0.99	1.00	0.98	0.93	0.95	0.95	0.98	0.99
S	1.00	1.00	1.00	1.00	1.00	1.00	1.00	1.00	1.00	1.00	1.00
Cd	0.00	0.00	0.00	0.00	0.00	0.00	0.00	0.00	0.00	0.00	0.00
Fe	0.00	0.00	0.00	0.00	0.00	0.00	0.04	0.04	0.05	0.00	0.00
Cu	0.00	0.00	0.00	0.00	0.00	0.00	0.00	0.00	0.00	0.00	0.00
Mn	0.00	0.00	0.00	0.00	0.00	0.00	0.00	0.00	0.00	0.00	0.00
Ag	0.00	0.00	0.00	0.00	0.00	0.00	0.00	0.00	0.00	0.00	0.00
Ge	0.00	0.00	0.00	0.00	0.00	0.00	0.00	0.00	0.00	0.00	0.00
Total	**1.98**	**1.99**	**1.99**	**2.00**	**2.00**	**1.98**	**1.98**	**1.99**	**1.99**	**1.98**	**2.00**

Table A.2.1 cont. – Electron Microprobe Analyses for sphalerite

Drill hole	LM08-23	LM08-23	LM08-23	LM08-24	LM08-24	LM08-24	LM08-24	LM08-24	LM08-24	LM11-56	LM11-56
Sample	CNF25127	CNF25127	CNF25127	CNF29976	CNF29976	CNF29976	CNF29976	CNF29976	CNF29976	CNF25134	CNF25134
Depth (m)	66.95	66.95	66.95	279.8	279.8	279.8	279.8	279.8	279.8	158.7	158.7
Probe Analysis	RL3 sp3	RL6 sp1	RL6 sp2	RL4 sp1	RL4 sp2	RL4 sp3	RL1 sp1	RL1 sp2	RL1 sp3	RL04 sp1	RL04 sp2
Date	2013-10-01	2013-10-01	2013-10-01	2013-10-01	2013-10-01	2013-10-01	2013-10-01	2013-10-01	2013-10-01	2013-10-01	2013-10-01
Type Mineralogy	Type 1	Type 1	Type 1	Type 1	Type 1	Type 1	Type 1	Type 1	Type 1	Type 3	Type 3
Zn (wt%)	66.14	64.90	65.65	66.18	64.96	65.31	65.49	65.96	65.33	58.77	59.59
S	32.49	32.86	32.47	32.92	32.87	32.43	32.78	32.58	32.99	33.06	33.18
Cd (ppm)	3910	3490	3640	2840	2870	2670	2740	2430	2720	2610	2910
Fe	1010	6650	2850	4730	5260	6170	5830	4690	5040	76970	69050
Cu	BDL	4540	200	740	500	190	BDL	BDL	2390	BDL	BDL
Mn	BDL	BDL	BDL	BDL	BDL	BDL	BDL	BDL	BDL	BDL	BDL
Ag	BDL	BDL	BDL	BDL	BDL	BDL	BDL	BDL	160	BDL	BDL
Ge	BDL	BDL	BDL	BDL	BDL	BDL	BDL	BDL	BDL	BDL	BDL
Total	**99.15**	**99.24**	**98.81**	**99.91**	**98.72**	**98.64**	**99.15**	**99.24**	**99.36**	**99.81**	**99.97**
Zn (apfu)	1.00	0.97	0.99	0.99	0.97	0.99	0.98	0.99	0.97	0.87	0.88
S	1.00	1.00	1.00	1.00	1.00	1.00	1.00	1.00	1.00	1.00	1.00
Cd	0.00	0.00	0.00	0.00	0.00	0.00	0.00	0.00	0.00	0.00	0.00
Fe	0.00	0.01	0.01	0.01	0.01	0.01	0.01	0.01	0.01	0.13	0.12
Cu	0.00	0.01	0.00	0.00	0.00	0.00	0.00	0.00	0.00	0.00	0.00
Mn	0.00	0.00	0.00	0.00	0.00	0.00	0.00	0.00	0.00	0.00	0.00
Ag	0.00	0.00	0.00	0.00	0.00	0.00	0.00	0.00	0.00	0.00	0.00
Ge	0.00	0.00	0.00	0.00	0.00	0.00	0.00	0.00	0.00	0.00	0.00
Total	**2.00**	**1.99**	**2.00**	**2.00**	**1.98**	**2.00**	**1.99**	**2.00**	**1.99**	**2.01**	**2.00**

Table A.2.1 cont. – Electron Microprobe Analyses for sphalerite

Drill hole	LM11-56	LM11-56	LM11-56	LM11-56	LM11-52	LM11-52	LM11-52	LM11-52	LM11-52	LM11-52	LM10-46
Sample	CNF25134	CNF25134	CNF25134	CNF25134	CNF25121	CNF25121	CNF25121	CNF25121	CNF25121	CNF25121	CNF25146
Depth (m)	158.7	158.7	158.7	158.7	212.3	212.3	212.3	212.3	212.3	212.3	182.56
Probe Analysis	RL04 sp3	RL02 sp1	RL02 sp2	RL02 sp3	RL2 sp1	RL2 sp2	RL2 sp3	RL4 sp1	RL4 sp2	RL4 sp3	RL5 sp1
Date	2013-10-01	2013-10-01	2013-10-01	2013-10-01	2013-10-01	2013-10-01	2013-10-01	2013-10-01	2013-10-01	2013-10-01	2013-10-01
Type Mineralogy	Type 3	Type 3	Type 3	Type 3	Type 1	Type 1	Type 1	Type 1	Type 1	Type 1	Type 1
Zn (wt%)	60.32	59.56	59.54	58.03	65.25	64.86	64.74	64.74	65.17	64.71	66.28
S	33.03	32.79	32.89	32.91	32.69	32.81	33.09	32.95	32.98	32.98	32.80
Cd (ppm)	3030	2840	3010	2940	2410	2540	2320	2250	2280	2450	3010
Fe	59830	64240	68130	78630	7310	6690	9340	11320	11390	11400	1920
Cu	BDL	BDL	600	2010	350	680	1260	BDL	BDL	BDL	BDL
Mn	BDL	BDL	BDL	BDL	BDL	BDL	260	200	230	250	250
Ag	BDL	BDL	BDL	BDL	BDL	BDL	BDL	BDL	BDL	BDL	BDL
Ge	BDL	BDL	BDL	BDL	BDL	BDL	BDL	BDL	BDL	BDL	BDL
Total	**99.61**	**99.05**	**99.61**	**99.30**	**98.95**	**98.67**	**99.14**	**99.10**	**99.56**	**99.11**	**99.60**
Zn (apfu)	0.90	0.89	0.89	0.86	0.98	0.97	0.96	0.96	0.97	0.96	0.99
S	1.00	1.00	1.00	1.00	1.00	1.00	1.00	1.00	1.00	1.00	1.00
Cd	0.00	0.00	0.00	0.00	0.00	0.00	0.00	0.00	0.00	0.00	0.00
Fe	0.10	0.11	0.12	0.14	0.01	0.01	0.02	0.02	0.02	0.02	0.00
Cu	0.00	0.00	0.00	0.00	0.00	0.00	0.00	0.00	0.00	0.00	0.00
Mn	0.00	0.00	0.00	0.00	0.00	0.00	0.00	0.00	0.00	0.00	0.00
Ag	0.00	0.00	0.00	0.00	0.00	0.00	0.00	0.00	0.00	0.00	0.00
Ge	0.00	0.00	0.00	0.00	0.00	0.00	0.00	0.00	0.00	0.00	0.00
Total	**2.00**	**2.01**	**2.01**	**2.01**	**1.99**	**1.98**	**1.98**	**1.99**	**1.99**	**1.98**	**2.00**

Table A.2.1 cont. – Electron Microprobe Analyses for sphalerite

Drill hole	LM10-46	LM10-46	LM11-61	LM11-61	LM11-61	LM11-61	LM11-61	LM11-61	LM11-61	LM11-61	LM11-61
Sample	CNF25146	CNF25146	CNF25152	CNF25152	CNF25152	CNF25152	CNF25152	CNF25152	CNF25151	CNF25151	CNF25151
Depth (m)	182.56	182.56	237.4	237.4	237.4	237.4	237.4	237.4	222.4	222.4	222.4
Probe Analysis	RL5 sp2	RL5 sp3	RL3 sp1	RL3 sp2	RL3 sp3	RL5 sp1	RL5 sp2	RL5 sp3	RL5 sp1	RL5 sp2	RL5 sp3
Date	2013-10-01	2013-10-01	2013-10-01	2013-10-01	2013-10-01	2013-10-01	2013-10-01	2013-10-01	2013-10-01	2013-10-01	2013-10-01
Type Mineralogy	Type 1	Type 1	Type 1	Type 1	Type 1	Type 1	Type 1	Type 1	Type 1	Type 1	Type 1
Zn (wt%)	65.70	65.46	65.86	65.71	66.04	65.80	65.74	65.86	66.64	66.51	67.00
S	33.11	33.04	33.01	32.76	32.72	32.93	32.83	32.94	32.73	32.96	32.99
Cd (ppm)	2960	2960	2620	2730	2610	2620	2620	2490	3400	3120	3220
Fe	3180	1700	3990	4610	4190	4760	4610	5270	610	BDL	BDL
Cu	230	430	BDL	BDL	1010	BDL	BDL	BDL	1040	530	BDL
Mn	200	270	BDL	BDL	BDL	BDL	BDL	BDL	210	250	300
Ag	BDL	BDL	BDL	BDL	BDL	BDL	BDL	BDL	BDL	BDL	BDL
Ge	BDL	BDL	BDL	BDL	BDL	BDL	BDL	BDL	BDL	BDL	BDL
Total	**99.46**	**99.05**	**99.55**	**99.22**	**99.56**	**99.47**	**99.29**	**99.57**	**99.91**	**99.87**	**100.36**
Zn (apfu)	0.97	0.97	0.98	0.98	0.99	0.98	0.98	0.98	1.00	0.99	1.00
S	1.00	1.00	1.00	1.00	1.00	1.00	1.00	1.00	1.00	1.00	1.00
Cd	0.00	0.00	0.00	0.00	0.00	0.00	0.00	0.00	0.00	0.00	0.00
Fe	0.01	0.00	0.01	0.01	0.01	0.01	0.01	0.01	0.00	0.00	0.00
Cu	0.00	0.00	0.00	0.00	0.00	0.00	0.00	0.00	0.00	0.00	0.00
Mn	0.00	0.00	0.00	0.00	0.00	0.00	0.00	0.00	0.00	0.00	0.00
Ag	0.00	0.00	0.00	0.00	0.00	0.00	0.00	0.00	0.00	0.00	0.00
Ge	0.00	0.00	0.00	0.00	0.00	0.00	0.00	0.00	0.00	0.00	0.00
Total	**1.98**	**1.98**	**1.99**	**1.99**	**2.00**	**1.99**	**1.99**	**1.99**	**2.00**	**1.99**	**2.00**

Table A.2.1 cont. – Electron Microprobe Analyses for sphalerite

Drill hole	LM11-61	LM11-61	LM11-61	LM11-52	LM11-52	LM11-52	LM11-52
Sample	CNF25151	CNF25151	CNF25151	CNF25120	CNF25120	CNF25120	CNF25120
Depth (m)	222.4	222.4	222.4	212	212	212	212
Probe Analysis	RL7 sp1	RL7 sp2	RL7 sp3	RL3 sp1	RL3 sp2	RL8 sp1	RL8 sp3
Date	2013-10-01	2013-10-01	2013-10-01	2013-10-01	2013-10-01	2013-10-01	2013-10-01
Type Mineralogy	Type 1	Type 1	Type 1	Type 3	Type 3	Type 3	Type 3
Zn (wt%)	65.69	66.65	65.99	60.47	60.44	57.41	57.61
S	32.89	32.10	32.62	33.19	32.85	32.81	33.04
Cd (ppm)	3080	3120	3280	3170	2970	4890	4740
Fe	BDL	220	750	50160	49500	79770	81000
Cu	340	BDL	990	BDL	BDL	BDL	1070
Mn	260	200	250	300	310	BDL	BDL
Ag	BDL	BDL	BDL	BDL	BDL	BDL	BDL
Ge	BDL	BDL	BDL	BDL	BDL	230	BDL
Total	**98.96**	**99.11**	**99.15**	**99.00**	**98.56**	**98.72**	**99.33**
Zn (apfu)	0.98	1.02	0.99	0.89	0.90	0.86	0.86
S	1.00	1.00	1.00	1.00	1.00	1.00	1.00
Cd	0.00	0.00	0.00	0.00	0.00	0.00	0.00
Fe	0.00	0.00	0.00	0.09	0.09	0.14	0.14
Cu	0.00	0.00	0.00	0.00	0.00	0.00	0.00
Mn	0.00	0.00	0.00	0.00	0.00	0.00	0.00
Ag	0.00	0.00	0.00	0.00	0.00	0.00	0.00
Ge	0.00	0.00	0.00	0.00	0.00	0.00	0.00
Total	**1.98**	**2.02**	**2.00**	**1.98**	**1.99**	**2.00**	**2.00**

Table A.2.1 cont. – Electron Microprobe Analyses for sphalerite

Drill hole	LM08-33	LM08-33	LM08-33	LM08-33	LM11-63	LM11-63	LM11-63	LM11-63	LM11-63	LM11-63	LM11-63
Sample	CNF14279	CNF14279	CNF14279	CNF14279	CNF29957	CNF29957	CNF29957	CNF29957	CNF29957	CNF29957	CNF29957
Depth (m)	230.75	230.75	230.75	230.75	210.83	210.83	210.83	210.83	210.83	210.83	210.83
Probe Analysis	RL5 sp1	RL5 sp2	RL5 sp3	RL7 sp1	RL3 sp1	RL3 sp2	RL3 sp3	RL3 sp4	RL6 sp1	RL6 sp2	RL6 sp3
Date	2013-04-29	2013-04-29	2013-04-29	2013-04-29	2013-04-29	2013-04-29	2013-04-29	2013-04-29	2013-04-29	2013-04-29	2013-04-29
Type Mineralogy	Type 2B	Type 2B	Type 2B	Type 2B	Type 2B	Type 2B	Type 2B	Type 2B	Type 2B	Type 2B	Type 2B
Zn (wt%)	66.29	66.57	65.96	66.53	65.86	66.17	66.25	66.50	66.12	65.82	66.16
S	32.98	33.03	33.10	32.83	32.74	32.54	32.32	32.63	32.76	32.39	32.72
Cd (ppm)	2200	2330	2360	2540	3410	3400	3610	3590	3900	3820	3900
Fe	BDL	240	1920	770	710	220	1840	1020	BDL	BDL	190
Cu	BDL	BDL	2050	310	450	BDL	1410	910	BDL	BDL	370
Mn	BDL	BDL	BDL	BDL	260	BDL	BDL	BDL	BDL	BDL	BDL
Total	**99.51**	**99.86**	**99.70**	**99.73**	**99.09**	**99.09**	**99.26**	**99.69**	**99.31**	**98.62**	**99.33**
Zn (apfu)	0.99	0.99	0.98	0.99	0.99	1.00	1.01	1.00	0.99	1.00	0.99
S	1.00	1.00	1.00	1.00	1.00	1.00	1.00	1.00	1.00	1.00	1.00
Cd	0.00	0.00	0.00	0.00	0.00	0.00	0.00	0.00	0.00	0.00	0.00
Fe	0.00	0.00	0.00	0.00	0.00	0.00	0.00	0.00	0.00	0.00	0.00
Cu	0.00	0.00	0.00	0.00	0.00	0.00	0.00	0.00	0.00	0.00	0.00
Mn	0.00	0.00	0.00	0.00	0.00	0.00	0.00	0.00	0.00	0.00	0.00
Total	**1.99**	**1.99**	**1.99**	**2.00**	**1.99**	**2.00**	**2.01**	**2.01**	**1.99**	**2.00**	**2.00**

Table A.2.1 cont. – Electron Microprobe Analyses for sphalerite

Drill hole	LM11-63	LM07-14	LM07-14	LM07-14	LM07-14	LM07-14	LM11-65	LM11-65	LM11-65	LM11-65	LM11-65
Sample	CNF29957	CNF14259	CNF14259	CNF14259	CNF14259	CNF14259	CNF14291	CNF14291	CNF14291	CNF14291	CNF14291
Depth (m)	210.83	204.44	204.44	204.44	204.44	204.44	159.3	159.3	159.3	159.3	159.3
Probe Analysis	RL6 sp4	RL6c sp1	RL6c sp2	RL6 sp1	RL6 sp2	RL6 sp3	RL9 sp1	RL9 sp2	RL9 sp3	RL9 sp4	RL7 sp1
Date	2013-04-29	2013-04-29	2013-04-29	2013-04-29	2013-04-29	2013-04-29	2013-04-29	2013-04-29	2013-04-29	2013-04-29	2013-04-29
Type Mineralogy	Type 2B	Type 1	Type 1	Type 1	Type 1	Type 1	Type 1	Type 1	Type 1	Type 1	Type 1
Zn (wt%)	66.21	65.95	66.25	65.34	64.04	64.43	64.55	64.60	64.34	64.74	64.26
S	32.71	32.44	32.55	32.45	32.89	32.81	32.92	32.55	32.34	32.72	32.66
Cd (ppm)	3950	3340	3110	2730	2770	3650	2580	2470	2510	2380	2760
Fe	470	1360	470	2390	10010	6900	18120	18070	17660	18240	18680
Cu	850	1530	620	2000	10730	8190	BDL	BDL	BDL	BDL	BDL
Mn	BDL	BDL	BDL	BDL	BDL	BDL	430	560	460	500	600
Total	**99.46**	**99.02**	**99.22**	**98.51**	**99.28**	**99.12**	**99.58**	**99.22**	**98.75**	**99.55**	**99.11**
Zn (apfu)	0.99	1.00	1.00	0.99	0.95	0.96	0.96	0.97	0.98	0.97	0.97
S	1.00	1.00	1.00	1.00	1.00	1.00	1.00	1.00	1.00	1.00	1.00
Cd	0.00	0.00	0.00	0.00	0.00	0.00	0.00	0.00	0.00	0.00	0.00
Fe	0.00	0.00	0.00	0.00	0.02	0.01	0.03	0.03	0.03	0.03	0.03
Cu	0.00	0.00	0.00	0.00	0.02	0.01	0.00	0.00	0.00	0.00	0.00
Mn	0.00	0.00	0.00	0.00	0.00	0.00	0.00	0.00	0.00	0.00	0.00
Total	**2.00**	**2.00**	**2.00**	**2.00**	**1.99**	**1.99**	**2.00**	**2.01**	**2.01**	**2.01**	**2.00**

Table A.2.1 cont. – Electron Microprobe Analyses for sphalerite

Drill hole	LM11-65	LM11-65	LM11-65	LM11-65	LM11-65	LM11-65	LM11-65	LM11-65	LM11-65	LM11-65	LM11-65
Sample	CNF14291	CNF14291	CNF14290	CNF14290	CNF14290	CNF14293	CNF14293	CNF14293	CNF14293	CNF14293	CNF14293
Depth (m)	159.3	159.3	158.66	158.66	158.66	161.75	161.75	161.75	161.75	161.75	161.75
Probe Analysis	RL7 sp2	RL7 sp3	RL5a sp1	RL5a sp2	RL5a sp3	RL4 sp1	RL4 sp2	RL4 sp3	RL12 sp1	RL12 sp2	RL12 sp3
Date	2013-04-29	2013-04-29	2013-04-29	2013-04-29	2013-04-29	2013-04-29	2013-04-29	2013-04-29	2013-04-29	2013-04-29	2013-04-29
Type Mineralogy	Type 1	Type 1	Type 3	Type 3	Type 3	Type 1	Type 1	Type 1	Type 1	Type 1	Type 1
Zn (wt%)	64.35	64.47	58.53	58.46	58.46	65.58	65.78	66.27	66.26	65.74	66.12
S	32.64	32.98	33.03	33.05	33.25	32.39	33.40	32.84	32.86	32.80	32.75
Cd (ppm)	2570	2420	2280	2080	2190	2080	2080	2110	2030	2040	1950
Fe	18620	18690	76730	77130	76700	5080	5550	5520	6110	6190	6160
Cu	BDL	BDL	BDL	BDL	BDL	2340	BDL	BDL	BDL	BDL	BDL
Mn	670	630	610	460	560	600	550	510	550	390	410
Total	**99.15**	**99.62**	**99.52**	**99.47**	**99.66**	**98.98**	**100.01**	**99.92**	**99.97**	**99.38**	**99.70**
Zn (apfu)	0.97	0.96	0.87	0.87	0.86	0.99	0.97	0.99	0.99	0.98	0.99
S	1.00	1.00	1.00	1.00	1.00	1.00	1.00	1.00	1.00	1.00	1.00
Cd	0.00	0.00	0.00	0.00	0.00	0.00	0.00	0.00	0.00	0.00	0.00
Fe	0.03	0.03	0.13	0.13	0.13	0.01	0.01	0.01	0.01	0.01	0.01
Cu	0.00	0.00	0.00	0.00	0.00	0.00	0.00	0.00	0.00	0.00	0.00
Mn	0.00	0.00	0.00	0.00	0.00	0.00	0.00	0.00	0.00	0.00	0.00
Total	**2.00**	**1.99**	**2.01**	**2.00**	**2.00**	**2.01**	**1.98**	**2.00**	**2.00**	**2.00**	**2.00**

Table A.2.1 cont. – Electron Microprobe Analyses for sphalerite

Drill hole	LM11-65	LM11-65	LM11-65	LM11-59	LM11-59	LM11-59	LM11-59	LM11-59	LM11-59	LM11-59	LM11-59
Sample	CNF14290	CNF14290	CNF14290	CNF29959	CNF29959	CNF29959	CNF29959	CNF29960	CNF29960	CNF29960	CNF29960
Depth (m)	158.66	158.66	158.66	207.72	207.72	207.72	207.72	216	216	216	216
Probe Analysis	RL5b sp1	RL5b sp2	RL5b sp3	RL5 sp2	RL6 sp1	RL6 sp2	RL6 sp3	RL3 sp1	RL3 sp2	RL3 sp3	RL10b sp1
Date	2013-04-29	2013-04-29	2013-04-29	2013-04-29	2013-04-29	2013-04-29	2013-04-29	2013-04-29	2013-04-29	2013-04-29	2013-04-29
Type Mineralogy	Type 3	Type 3	Type 3	Type 3	Type 3	Type 3	Type 3	Type 3	Type 3	Type 3	Type 3
Zn (wt%)	57.04	57.03	56.63	62.31	61.06	61.19	61.28	63.70	63.59	63.57	62.95
S	33.14	33.69	33.34	33.27	33.67	33.14	33.21	33.04	33.10	32.98	32.78
Cd (ppm)	2500	2400	2570	3150	2970	2830	3090	2500	2480	2640	2710
Fe	83470	84110	81980	28460	40620	40630	43250	30640	29460	29950	34670
Cu	1400	1080	1650	BDL	BDL	BDL	BDL	BDL	BDL	BDL	520
Mn	600	540	470	BDL	BDL	BDL	BDL	260	BDL	180	280
Total	**98.98**	**99.53**	**98.63**	**98.765**	**99.08**	**98.629**	**99.091**	**100.07**	**99.876**	**99.815**	**99.545**
Zn (apfu)	0.84	0.83	0.83	0.92	0.89	0.91	0.90	0.95	0.94	0.95	0.94
S	1.00	1.00	1.00	1.00	1.00	1.00	1.00	1.00	1.00	1.00	1.00
Cd	0.00	0.00	0.00	0.00	0.00	0.00	0.00	0.00	0.00	0.00	0.00
Fe	0.14	0.14	0.14	0.05	0.07	0.07	0.07	0.05	0.05	0.05	0.06
Cu	0.00	0.00	0.00	0.00	0.00	0.00	0.00	0.00	0.00	0.00	0.00
Mn	0.00	0.00	0.00	0.00	0.00	0.00	0.00	0.00	0.00	0.00	0.00
Total	**1.99**	**1.98**	**1.98**	**1.97**	**1.96**	**1.98**	**1.98**	**2.00**	**2.00**	**2.00**	**2.01**

Table A.2.1 cont. – Electron Microprobe Analyses for sphalerite

Drill hole	LM11-59	LM07-17	LM07-17	LM07-17	LM07-17	LM07-17	LM07-17	LM07-17	LM11-59	LM11-59	LM11-59
Sample	CNF29960	CNF29967	CNF29967	CNF29967	CNF29967	CNF29967	CNF29967	CNF29967	CNF29972	CNF29972	CNF29972
Depth (m)	216	247.63	247.63	247.63	247.63	247.63	247.63	247.63	251.22	251.22	251.22
Probe Analysis	RL10b sp2	RL3b sp1	RL3b sp2	RL3b sp3	RL3b sp4	RL10 sp1	RL10 sp2	RL10 sp3	RL6 sp1	RL6 sp2	RL6 sp3
Date	2013-04-29	2013-04-29	2013-04-29	2013-04-29	2013-04-29	2013-04-29	2013-04-29	2013-04-29	2013-04-29	2013-04-29	2013-04-29
Type Mineralogy	Type 3	Type 1	Type 1	Type 1	Type 1	Type 1	Type 1	Type 1	Type 4	Type 4	Type 4
Zn (wt%)	63.04	66.65	66.49	66.34	66.24	65.99	65.98	66.33	63.49	63.86	63.55
S	33.06	32.85	32.79	32.84	32.80	32.81	32.75	32.83	32.95	32.90	32.97
Cd (ppm)	3060	3050	3050	2990	3050	2980	3030	2970	2730	2850	3000
Fe	32120	870	1330	2130	1670	5350	4670	5230	29180	27100	27540
Cu	BDL	2710	3940	6100	4290	4430	6620	4210	BDL	BDL	BDL
Mn	260	350	270	260	400	340	340	390	300	230	290
Total	**99.668**	**100.198**	**100.14**	**100.325**	**99.98**	**100.103**	**100.197**	**100.442**	**99.655**	**99.757**	**99.6**
Zn (apfu)	0.94	1.00	0.99	0.99	0.99	0.99	0.99	0.99	0.94	0.95	0.95
S	1.00	1.00	1.00	1.00	1.00	1.00	1.00	1.00	1.00	1.00	1.00
Cd	0.00	0.00	0.00	0.00	0.00	0.00	0.00	0.00	0.00	0.00	0.00
Fe	0.06	0.00	0.00	0.00	0.00	0.01	0.01	0.01	0.05	0.05	0.05
Cu	0.00	0.00	0.01	0.01	0.01	0.01	0.01	0.01	0.00	0.00	0.00
Mn	0.00	0.00	0.00	0.00	0.00	0.00	0.00	0.00	0.00	0.00	0.00
Total	**1.99**	**2.00**	**2.01**	**2.01**	**2.00**	**2.01**	**2.01**	**2.01**	**2.00**	**2.00**	**2.00**

Table A.2.1 cont. – Electron Microprobe Analyses for sphalerite

Drill hole	LM11-59	LM11-59	LM11-59	LM08-19	LM08-19	LM08-19	LM08-19	LM08-19	LM08-19	LM11-59	LM11-59
Sample	CNF29972	CNF29972	CNF29972	CNF29986	CNF29986	CNF29986	CNF29986	CNF29986	CNF29986	CNF29962	CNF29962
Depth (m)	251.22	251.22	251.22	97.63	97.63	97.63	97.63	97.63	97.63	225.95	225.95
Probe Analysis	RL3 sp1	RL3 sp2	RL3 sp3	RL2 sp1	RL2 sp2	RL2 sp3	RL3 sp1	RL3 sp2	RL3 sp3	RL1 sp1	RL1 sp2
Date	2013-04-29	2013-04-29	2013-04-29	2013-04-29	2013-04-29	2013-04-29	2013-04-29	2013-04-29	2013-04-29	2013-04-29	2013-04-29
Type Mineralogy	Type 4	Type 4	Type 4	Type 1	Type 1	Type 1	Type 1	Type 1	Type 1	Type 1	Type 1
Zn (wt%)	62.95	63.46	63.34	66.35	66.74	66.45	66.52	66.53	63.87	65.58	65.60
S	32.48	32.74	32.76	33.25	32.82	32.77	32.74	32.64	32.99	32.59	32.73
Cd (ppm)	2580	2770	2650	2530	2570	2610	2650	2540	2480	3140	3180
Fe	28220	27240	27840	3600	1380	3430	2680	2480	15620	4060	4530
Cu	BDL	BDL	360	1750	BDL	BDL	1830	BDL	15980	BDL	BDL
Mn	BDL	180	220	BDL	BDL	BDL	BDL	BDL	BDL	BDL	BDL
Total	**98.541**	**99.209**	**99.207**	**100.393**	**99.973**	**99.838**	**99.971**	**99.684**	**100.268**	**98.896**	**99.099**
Zn (apfu)	0.95	0.95	0.95	0.98	1.00	0.99	1.00	1.00	0.95	0.99	0.98
S	1.00	1.00	1.00	1.00	1.00	1.00	1.00	1.00	1.00	1.00	1.00
Cd	0.00	0.00	0.00	0.00	0.00	0.00	0.00	0.00	0.00	0.00	0.00
Fe	0.05	0.05	0.05	0.01	0.00	0.01	0.00	0.00	0.03	0.01	0.01
Cu	0.00	0.00	0.00	0.00	0.00	0.00	0.00	0.00	0.02	0.00	0.00
Mn	0.00	0.00	0.00	0.00	0.00	0.00	0.00	0.00	0.00	0.00	0.00
Total	**2.00**	**2.00**	**2.00**	**1.99**	**2.00**	**2.00**	**2.01**	**2.01**	**2.00**	**2.00**	**1.99**

Table A.2.1 cont. – Electron Microprobe Analyses for sphalerite

Drill hole	LM11-59	LM11-59	LM11-59	LM11-59
Sample	CNF29962	CNF29962	CNF29962	CNF29962
Depth (m)	225.95	225.95	225.95	225.95
Probe Analysis	RL1 sp3	RL2 sp1	RL2 sp2	RL2 sp3
Date	2013-04-29	2013-04-29	2013-04-29	2013-04-29
Type Mineralogy	Type 1	Type 1	Type 1	Type 1
Zn (wt%)	65.83	65.39	65.95	65.86
S	32.94	32.78	32.60	32.45
Cd (ppm)	3030	3040	2940	3070
Fe	4440	4330	3970	4220
Cu	BDL	BDL	1580	1690
Mn	BDL	BDL	BDL	BDL
Total	**99.534**	**98.909**	**99.406**	**99.216**
Zn (apfu)	0.98	0.98	0.99	1.00
S	1.00	1.00	1.00	1.00
Cd	0.00	0.00	0.00	0.00
Fe	0.01	0.01	0.01	0.01
Cu	0.00	0.00	0.00	0.00
Mn	0.00	0.00	0.00	0.00
Total	**1.99**	**1.99**	**2.00**	**2.01**

Drill hole	LM11-59	LM11-59
Sample	CNF29959	CNF29959
Depth (m)	207.72	207.72
Probe Analysis	RL4 sp1	RL6b sp1
Date	2013-05-03	2013-05-03
Type Mineralogy	Type 3	Type 3
Zn (wt%)	59.84	59.16
S	33.58	33.96
Fe (ppm)	64090	56080
Cu	BDL	BDL
Pb	1430	1100
Sb	BDL	BDL
As	BDL	BDL
Hg	BDL	BDL
Ag	BDL	BDL
Au	BDL	BDL
Total	**99.956**	**98.756**
Zn (apfu)	0.87	0.85
S	1.00	1.00
Fe	0.11	0.09
Cu	0.00	0.00
Pb	0.00	0.00
Sb	0.00	0.00
As	0.00	0.00
Hg	0.00	0.00
Ag	0.00	0.00
Au	0.00	0.00
Total	**1.98**	**1.95**

Table A.2.2 – Electron Microprobe Analyses for pyrite

Drill hole	LM08-24	LM08-24	LM08-24	LM08-24	LM08-24	LM08-24	LM11-52	LM11-52
Sample	CNF29976	CNF29976	CNF29976	CNF29976	CNF29976	CNF29976	CNF25120	CNF25120
Depth (m)	279.8	279.8	279.8	279.8	279.8	279.8	212	212
Probe Analysis	RL3 py1	RL3 py2	RL3 py3	RL3b py1	RL3b py2	RL3b py3	RL3 py1	RL3 py2
Date	2013-10-01	2013-10-01	2013-10-01	2013-10-01	2013-10-01	2013-10-01	2013-10-01	2013-10-01
Py description	Recrystallized (clustered to subhedral)	Recrystallized (clustered to subhedral)	Recrystallized (clustered to subhedral)	Recrystallized (clustered to subhedral)	Recrystallized (clustered to subhedral)	Recrystallized (clustered to subhedral)	Recrystallized (clustered to subhedral)	Recrystallized (clustered to subhedral)
Py Mineralogy	Type 2	Type 2	Type 2	Type 2	Type 2	Type 2	Type 2	Type 2
Type Mineralogy	Type 1	Type 1	Type 1	Type 1	Type 1	Type 1	Type 3	Type 3
S (wt%)	53.75	53.50	53.84	53.80	53.73	53.83	54.16	53.71
Fe	46.35	45.18	46.02	45.51	45.97	45.68	45.48	44.11
As (ppm)	130	BDL	BDL	BDL	BDL	BDL	390	960
Cu	BDL	BDL	190	BDL	BDL	BDL	240	BDL
Zn	BDL	BDL	BDL	BDL	BDL	880	1050	1110
Pb	BDL	BDL	BDL	BDL	BDL	BDL	BDL	BDL
Sb	BDL	BDL	BDL	BDL	BDL	290	4090	7920
Ag	BDL	BDL	BDL	BDL	BDL	BDL	1530	1880
Hg	BDL	BDL	BDL	BDL	BDL	BDL	BDL	BDL
Total	**100.16**	**98.62**	**99.88**	**99.32**	**99.74**	**99.66**	**100.44**	**99.11**
S (apfu)	2.00	2.00	2.00	2.00	2.00	2.00	2.00	2.00
Fe	0.99	0.97	0.98	0.97	0.98	0.97	0.96	0.94
As	0.00	0.00	0.00	0.00	0.00	0.00	0.00	0.00
Cu	0.00	0.00	0.00	0.00	0.00	0.00	0.00	0.00
Zn	0.00	0.00	0.00	0.00	0.00	0.00	0.00	0.00
Pb	0.00	0.00	0.00	0.00	0.00	0.00	0.00	0.00
Sb	0.00	0.00	0.00	0.00	0.00	0.00	0.00	0.01
Ag	0.00	0.00	0.00	0.00	0.00	0.00	0.00	0.00
Hg	0.00	0.00	0.00	0.00	0.00	0.00	0.00	0.00
Total	**2.99**	**2.97**	**2.98**	**2.97**	**2.98**	**2.98**	**2.97**	**2.96**

Table A.2.2 cont. – Electron Microprobe Analyses for pyrite

Drill hole	LM11-52	LM11-52	LM11-52	LM11-52	LM11-52	LM08-23	LM08-23	LM08-23
Sample	CNF25120	CNF25120	CNF25120	CNF25120	CNF25120	CNF25127	CNF25127	CNF25127
Depth (m)	212	212	212	212	212	66.95	66.95	66.95
Probe Analysis	RL3 py3	RL8 py1	RL8 py2	RL8 py3	RL8 py4	RL6 py1	RL6 py2	RL6 py3
Date	2013-10-01	2013-10-01	2013-10-01	2013-10-01	2013-10-01	2013-10-01	2013-10-01	2013-10-01
Py description	Recrystallized (euhedral)	Recrystallized (clustered to subhedral)	Recrystallized (clustered to subhedral)	Recrystallized (clustered to subhedral)	Recrystallized (clustered to subhedral)	Recrystallized (clustered to subhedral)	Recrystallized (clustered to subhedral)	Recrystallized (clustered to subhedral)
Py Mineralogy	Type 3	Type 2	Type 2	Type 2	Type 2	Type 2	Type 2	Type 2
Type Mineralogy	Type 3	Type 3	Type 3	Type 3	Type 3	Type 1	Type 1	Type 1
S (wt%)	54.20	54.13	53.37	53.42	53.52	53.62	53.87	53.43
Fe	45.85	44.89	43.89	45.04	44.07	46.43	46.37	46.23
As (ppm)	BDL	1700	630	2690	480	2380	BDL	BDL
Cu	BDL	3160	2940	4360	1610	210	BDL	BDL
Zn	1930	750	1050	200	1420	BDL	BDL	BDL
Pb	BDL	BDL	3670	BDL	BDL	BDL	BDL	BDL
Sb	190	6910	18200	5910	11070	160	BDL	110
Ag	BDL	400	1850	580	490	180	BDL	BDL
Hg	BDL	BDL	BDL	BDL	BDL	BDL	BDL	BDL
Total	**100.25**	**100.50**	**100.12**	**99.97**	**99.30**	**100.39**	**100.23**	**99.67**
S (apfu)	2.00	2.00	2.00	2.00	2.00	2.00	2.00	2.00
Fe	0.97	0.95	0.94	0.97	0.95	0.99	0.99	0.99
As	0.00	0.00	0.00	0.00	0.00	0.00	0.00	0.00
Cu	0.00	0.01	0.01	0.01	0.00	0.00	0.00	0.00
Zn	0.00	0.00	0.00	0.00	0.00	0.00	0.00	0.00
Pb	0.00	0.00	0.00	0.00	0.00	0.00	0.00	0.00
Sb	0.00	0.01	0.02	0.01	0.01	0.00	0.00	0.00
Ag	0.00	0.00	0.00	0.00	0.00	0.00	0.00	0.00
Hg	0.00	0.00	0.00	0.00	0.00	0.00	0.00	0.00
Total	**2.98**	**2.97**	**2.98**	**2.99**	**2.96**	**3.00**	**2.99**	**2.99**

Table A.2.2 cont. – Electron Microprobe Analyses for pyrite

Drill hole	LM08-23	LM08-23	LM08-23	LM10-46	LM10-46	LM10-46	LM10-46	LM10-46
Sample	CNF25127	CNF25127	CNF25127	CNF25146	CNF25146	CNF25146	CNF25146	CNF25146
Depth (m)	66.95	66.95	66.95	182.56	182.56	182.56	182.56	182.56
Probe Analysis	RL4 py1	RL4 py2	RL4 py3	RL1 py1	RL1 py2	RL1 py3	RL4b py1	RL4b py2
Date	2013-10-01	2013-10-01	2013-10-01	2013-10-01	2013-10-01	2013-10-01	2013-10-01	2013-10-01
Py description	Recrystallized (clustered to subhedral)	Recrystallized (clustered to subhedral)	Recrystallized (clustered to subhedral)	Recrystallized (euhedral)	Recrystallized (euhedral)	Recrystallized (euhedral)	Recrystallized (euhedral)	Recrystallized (euhedral)
Py Mineralogy	Type 2	Type 2	Type 2	Type 3	Type 3	Type 3	Type 3	Type 3
Type Mineralogy	Type 1	Type 1	Type 1	Type 2B	Type 2B	Type 2B	Type 2B	Type 2B
S (wt%)	52.29	53.81	51.56	53.86	53.97	53.64	53.65	53.76
Fe	45.54	46.23	44.12	45.66	45.58	45.93	45.98	45.83
As (ppm)	23170	BDL	31110	BDL	BDL	BDL	BDL	BDL
Cu	220	170	710	BDL	BDL	BDL	BDL	190
Zn	BDL	BDL	BDL	280	630	580	BDL	BDL
Pb	BDL	BDL	BDL	BDL	BDL	BDL	BDL	BDL
Sb	120	330	4260	BDL	270	200	BDL	310
Ag	660	BDL	5870	BDL	BDL	BDL	BDL	BDL
Hg	BDL	BDL	BDL	BDL	BDL	BDL	BDL	BDL
Total	**100.28**	**100.08**	**99.87**	**99.56**	**99.65**	**99.65**	**99.61**	**99.63**
S (apfu)	2.00	2.00	2.00	2.00	2.00	2.00	2.00	2.00
Fe	1.00	0.99	0.98	0.97	0.97	0.98	0.98	0.98
As	0.04	0.00	0.05	0.00	0.00	0.00	0.00	0.00
Cu	0.00	0.00	0.00	0.00	0.00	0.00	0.00	0.00
Zn	0.00	0.00	0.00	0.00	0.00	0.00	0.00	0.00
Pb	0.00	0.00	0.00	0.00	0.00	0.00	0.00	0.00
Sb	0.00	0.00	0.00	0.00	0.00	0.00	0.00	0.00
Ag	0.00	0.00	0.01	0.00	0.00	0.00	0.00	0.00
Hg	0.00	0.00	0.00	0.00	0.00	0.00	0.00	0.00
Total	**3.04**	**2.99**	**3.05**	**2.97**	**2.97**	**2.98**	**2.98**	**2.98**

Table A.2.2 cont. – Electron Microprobe Analyses for pyrite

Drill hole	LM10-46	LM11-56	LM11-56	LM11-56	LM11-56	LM11-56	LM11-56	LM08-39
Sample	CNF25146	CNF25134	CNF25134	CNF25134	CNF25134	CNF25134	CNF25134	CNF14295
Depth (m)	182.56	158.7	158.7	158.7	158.7	158.7	158.7	286.7
Probe Analysis	RL4b py3	RL8 py1	RL8 py2	RL8 py3	RL4 py1	RL4 py2	RL4 py3	RL3 py1
Date	2013-10-01	2013-10-01	2013-10-01	2013-10-01	2013-10-01	2013-10-01	2013-10-01	2013-10-01
Py description	Recrystallized (euhedral)	Recrystallized (clustered to subhedral)	Recrystallized (clustered to subhedral)	Recrystallized (clustered to subhedral)	Colloform/ reniform	Colloform/ reniform	Colloform/ reniform	Recrystallized (clustered to subhedral)
Py Mineralogy	Type 3	Type 2	Type 2	Type 2	Type 1	Type 1	Type 1	Type 2
Type Mineralogy	Type 2B	Type 3	Type 3	Type 3	Type 3	Type 3	Type 3	Type 4
S (wt%)	53.89	53.67	53.16	53.18	53.70	51.92	52.11	53.45
Fe	45.89	46.15	44.56	45.43	45.83	43.43	43.93	45.50
As (ppm)	BDL	260	11390	3000	4500	35950	31460	BDL
Cu	620	490	BDL	950	BDL	BDL	2970	BDL
Zn	BDL	BDL	BDL	BDL	BDL	BDL	BDL	BDL
Pb	BDL	BDL	BDL	BDL	BDL	BDL	BDL	BDL
Sb	BDL	110	BDL	540	240	BDL	170	BDL
Ag	BDL	BDL	1690	BDL	650	470	BDL	BDL
Hg	BDL	BDL	BDL	BDL	BDL	BDL	BDL	BDL
Total	**99.89**	**99.89**	**99.06**	**99.03**	**100.12**	**98.97**	**99.63**	**98.92**
S (apfu)	2.00	2.00	2.00	2.00	2.00	2.00	2.00	2.00
Fe	0.98	0.99	0.96	0.98	0.98	0.96	0.97	0.98
As	0.00	0.00	0.02	0.00	0.01	0.06	0.05	0.00
Cu	0.00	0.00	0.00	0.00	0.00	0.00	0.01	0.00
Zn	0.00	0.00	0.00	0.00	0.00	0.00	0.00	0.00
Pb	0.00	0.00	0.00	0.00	0.00	0.00	0.00	0.00
Sb	0.00	0.00	0.00	0.00	0.00	0.00	0.00	0.00
Ag	0.00	0.00	0.00	0.00	0.00	0.00	0.00	0.00
Hg	0.00	0.00	0.00	0.00	0.00	0.00	0.00	0.00
Total	**2.98**	**2.99**	**2.98**	**2.99**	**2.99**	**3.02**	**3.03**	**2.98**

Table A.2.2 cont. – Electron Microprobe Analyses for pyrite

Drill hole	LM08-39	LM08-39	LM08-39	LM08-39	LM08-39	LM11-52	LM11-52	LM11-52
Sample	CNF14295	CNF14295	CNF14295	CNF14295	CNF14295	CNF25121	CNF25121	CNF25121
Depth (m)	286.7	286.7	286.7	286.7	286.7	212.3	212.3	212.3
Probe Analysis	RL3 py2	RL3 py3	RL5 py1	RL5 py2	RL5 py3	RL7 py1	RL7 py2	RL7 py3
Date	2013-10-01	2013-10-01	2013-10-01	2013-10-01	2013-10-01	2013-10-01	2013-10-01	2013-10-01
Py description	Recrystallized (clustered to subhedral)	Recrystallized (clustered to subhedral)	Recrystallized (clustered to subhedral)	Recrystallized (clustered to subhedral)	Recrystallized (clustered to subhedral)	Recrystallized (clustered to subhedral)	Recrystallized (clustered to subhedral)	Recrystallized (clustered to subhedral)
Py Mineralogy	Type 2	Type 2	Type 2	Type 2	Type 2	Type 2	Type 2	Type 2
Type Mineralogy	Type 4	Type 4	Type 4	Type 4	Type 4	Type 2B	Type 2B	Type 2B
S (wt%)	53.30	53.49	53.52	53.49	53.78	53.89	53.94	53.83
Fe	45.60	45.64	45.60	46.10	46.38	46.12	45.84	46.10
As (ppm)	BDL	BDL	BDL	BDL	BDL	BDL	BDL	BDL
Cu	BDL	210	BDL	BDL	BDL	300	260	BDL
Zn	BDL	BDL	BDL	BDL	BDL	BDL	BDL	210
Pb	BDL	BDL	BDL	BDL	BDL	BDL	BDL	BDL
Sb	BDL	BDL	80	BDL	BDL	120	240	BDL
Ag	BDL	BDL	BDL	BDL	BDL	BDL	BDL	BDL
Hg	BDL	BDL	BDL	BDL	BDL	BDL	BDL	BDL
Total	**98.91**	**99.15**	**99.15**	**99.56**	**100.20**	**100.05**	**99.84**	**100.00**
S (apfu)	2.00	2.00	2.00	2.00	2.00	2.00	2.00	2.00
Fe	0.98	0.98	0.98	0.99	0.99	0.98	0.98	0.98
As	0.00	0.00	0.00	0.00	0.00	0.00	0.00	0.00
Cu	0.00	0.00	0.00	0.00	0.00	0.00	0.00	0.00
Zn	0.00	0.00	0.00	0.00	0.00	0.00	0.00	0.00
Pb	0.00	0.00	0.00	0.00	0.00	0.00	0.00	0.00
Sb	0.00	0.00	0.00	0.00	0.00	0.00	0.00	0.00
Ag	0.00	0.00	0.00	0.00	0.00	0.00	0.00	0.00
Hg	0.00	0.00	0.00	0.00	0.00	0.00	0.00	0.00
Total	**2.98**	**2.98**	**2.98**	**2.99**	**2.99**	**2.98**	**2.98**	**2.98**

Table A.2.2 cont. – Electron Microprobe Analyses for pyrite

Drill hole	LM11-52	LM11-52	LM11-52	LM11-61	LM11-61	LM11-61	LM11-61	LM11-61
Sample	CNF25121	CNF25121	CNF25121	CNF25151	CNF25151	CNF25151	CNF25151	CNF25151
Depth (m)	212.3	212.3	212.3	222.4	222.4	222.4	222.4	222.4
Probe Analysis	RL4 py1	RL4 py2	RL4 py3	RL1 py1	RL1 py2	RL1 py3	RL8 py1	RL8 py2
Date	2013-10-01	2013-10-01	2013-10-01	2013-10-01	2013-10-01	2013-10-01	2013-10-01	2013-10-01
Py description	Recrystallized (clustered to subhedral)	Recrystallized (clustered to subhedral)	Recrystallized (clustered to subhedral)	Recrystallized (clustered to subhedral)	Recrystallized (clustered to subhedral)	Recrystallized (clustered to subhedral)	Recrystallized (clustered to subhedral)	Recrystallized (clustered to subhedral)
Py Mineralogy	Type 2	Type 2	Type 2	Type 2	Type 2	Type 2	Type 2	Type 2
Type Mineralogy	Type 2B	Type 2B	Type 2B	Type 2A	Type 2A	Type 2A	Type 2A	Type 2A
S (wt%)	53.68	53.83	53.99	54.12	54.26	54.38	53.94	54.10
Fe	46.02	45.85	46.15	46.33	46.20	46.12	46.53	46.52
As (ppm)	BDL	BDL	BDL	BDL	BDL	BDL	BDL	BDL
Cu	BDL	BDL	BDL	160	1100	710	490	310
Zn	510	BDL	1150	BDL	BDL	BDL	BDL	620
Pb	BDL	BDL	BDL	BDL	BDL	BDL	BDL	BDL
Sb	BDL	130	180	BDL	BDL	BDL	BDL	BDL
Ag	BDL	BDL	BDL	BDL	BDL	BDL	BDL	BDL
Hg	BDL	BDL	BDL	BDL	BDL	BDL	BDL	BDL
Total	**99.74**	**99.71**	**100.28**	**100.48**	**100.60**	**100.54**	**100.56**	**100.69**
S (apfu)	2.00	2.00	2.00	2.00	2.00	2.00	2.00	2.00
Fe	0.98	0.98	0.98	0.98	0.98	0.97	0.99	0.99
As	0.00	0.00	0.00	0.00	0.00	0.00	0.00	0.00
Cu	0.00	0.00	0.00	0.00	0.00	0.00	0.00	0.00
Zn	0.00	0.00	0.00	0.00	0.00	0.00	0.00	0.00
Pb	0.00	0.00	0.00	0.00	0.00	0.00	0.00	0.00
Sb	0.00	0.00	0.00	0.00	0.00	0.00	0.00	0.00
Ag	0.00	0.00	0.00	0.00	0.00	0.00	0.00	0.00
Hg	0.00	0.00	0.00	0.00	0.00	0.00	0.00	0.00
Total	**2.99**	**2.98**	**2.98**	**2.98**	**2.98**	**2.98**	**2.99**	**2.99**

Table A.2.2 cont. – Electron Microprobe Analyses for pyrite

Drill hole	LM11-61	LM13-73	LM13-73	LM13-73	LM13-73	LM13-73	LM13-73	LM13-74
Sample	CNF25151	CNF14299	CNF14299	CNF14299	CNF14299	CNF14299	CNF14299	CNF25109
Depth (m)	222.4	327.95	327.95	327.95	327.95	327.95	327.95	328.55
Probe Analysis	RL8 py3	RL1 py1	RL1 py2	RL1 py3	RL11 py1	RL11 py2	RL11 py3	RL3 py1
Date	2013-10-01	2013-10-01	2013-10-01	2013-10-01	2013-10-01	2013-10-01	2013-10-01	2013-10-01
Py description	Recrystallized (clustered to subhedral)	Recrystallized (clustered to subhedral)	Recrystallized (clustered to subhedral)	Recrystallized (clustered to subhedral)	Recrystallized (clustered to subhedral)	Recrystallized (clustered to subhedral)	Recrystallized (clustered to subhedral)	Recrystallized (euhedral)
Py Mineralogy	Type 2	Type 2	Type 2	Type 2	Type 2	Type 2	Type 2	Type 3
Type Mineralogy	Type 2A	Type 2A	Type 2A	Type 2A	Type 2A	Type 2A	Type 2A	Type 2B
S (wt%)	54.07	52.18	53.83	53.60	53.30	52.23	53.09	53.90
Fe	46.46	44.42	46.05	46.36	45.81	44.44	45.62	46.12
As (ppm)	BDL	15690	BDL	BDL	2450	12780	6810	BDL
Cu	1770	2150	1250	310	990	910	890	BDL
Zn	BDL	220	200	BDL	BDL	550	BDL	BDL
Pb	BDL	BDL	BDL	BDL	BDL	BDL	BDL	BDL
Sb	BDL	420	80	BDL	490	250	BDL	BDL
Ag	BDL	11470	BDL	BDL	3280	11590	3310	BDL
Hg	BDL	850	BDL	BDL	BDL	1030	BDL	BDL
Total	**100.66**	**99.69**	**100.03**	**99.98**	**99.90**	**99.37**	**99.89**	**99.98**
S (apfu)	2.00	2.00	2.00	2.00	2.00	2.00	2.00	2.00
Fe	0.99	0.98	0.98	0.99	0.99	0.98	0.99	0.98
As	0.00	0.03	0.00	0.00	0.00	0.02	0.01	0.00
Cu	0.00	0.00	0.00	0.00	0.00	0.00	0.00	0.00
Zn	0.00	0.00	0.00	0.00	0.00	0.00	0.00	0.00
Pb	0.00	0.00	0.00	0.00	0.00	0.00	0.00	0.00
Sb	0.00	0.00	0.00	0.00	0.00	0.00	0.00	0.00
Ag	0.00	0.01	0.00	0.00	0.00	0.01	0.00	0.00
Hg	0.00	0.00	0.00	0.00	0.00	0.00	0.00	0.00
Total	**2.99**	**3.02**	**2.99**	**2.99**	**3.00**	**3.02**	**3.00**	**2.98**

Table A.2.2 cont. – Electron Microprobe Analyses for pyrite

Drill hole	LM13-74	LM13-74	LM13-74	LM13-74	LM13-74
Sample	CNF25109	CNF25109	CNF25109	CNF25109	CNF25109
Depth (m)	328.55	328.55	328.55	328.55	328.55
Probe Analysis	RL3 py2	RL3 py3	RL9 py1	RL9 py2	RL9 py3
Date	2013-10-01	2013-10-01	2013-10-01	2013-10-01	2013-10-01
Py description	Recrystallized (euhedral)	Recrystallized (euhedral)	Recrystallized (euhedral)	Recrystallized (euhedral)	Recrystallized (euhedral)
Py Mineralogy	Type 3	Type 3	Type 3	Type 3	Type 3
Type Mineralogy	Type 2B	Type 2B	Type 2B	Type 2B	Type 2B
S (wt%)	53.95	53.58	53.89	53.83	53.82
Fe	46.03	46.14	46.29	46.51	46.24
As (ppm)	BDL	3770	BDL	BDL	BDL
Cu	BDL	BDL	BDL	BDL	BDL
Zn	BDL	BDL	BDL	BDL	420
Pb	BDL	BDL	BDL	BDL	BDL
Sb	100	BDL	BDL	BDL	BDL
Ag	BDL	BDL	BDL	BDL	BDL
Hg	BDL	BDL	BDL	BDL	BDL
Total	**99.96**	**100.02**	**100.12**	**100.37**	**100.11**
S (apfu)	2.00	2.00	2.00	2.00	2.00
Fe	0.98	0.99	0.99	0.99	0.99
As	0.00	0.01	0.00	0.00	0.00
Cu	0.00	0.00	0.00	0.00	0.00
Zn	0.00	0.00	0.00	0.00	0.00
Pb	0.00	0.00	0.00	0.00	0.00
Sb	0.00	0.00	0.00	0.00	0.00
Ag	0.00	0.00	0.00	0.00	0.00
Hg	0.00	0.00	0.00	0.00	0.00
Total	**2.98**	**3.00**	**2.99**	**2.99**	**2.99**

Table A.2.2 cont. – Electron Microprobe Analyses for pyrite

Drill hole	LM11-65	LM11-65	LM11-65	LM11-65	LM11-65	LM11-65	LM07-14	LM07-14
Sample	CNF14290	CNF14290	CNF14293	CNF14293	CNF14291	CNF14291	CNF14259	CNF14259
Depth (m)	158.66	158.66	161.75	161.75	159.3	159.3	204.44	204.44
Probe Analysis	RL5b py1	RL5a py1	RL3 py1	RL8 py1	RL7 py1	RL9 py1	RL2c py1	RL6d py1
Date	2013-05-03	2013-05-03	2013-05-03	2013-05-03	2013-05-03	2013-05-03	2013-05-03	2013-05-03
Py description	Recrystallized (euhedral)	Recrystallized (euhedral)	Recrystallized (clustered to subhedral)	Recrystallized (clustered to subhedral)	Recrystallized (euhedral)	Recrystallized (euhedral)	Recrystallized (clustered to subhedral)	Recrystallized (clustered to subhedral)
Py Mineralogy	Type 3	Type 3	Type 2	Type 2	Type 3	Type 3	Type 2	Type 2
Type Mineralogy	Type 3	Type 3	Type 2B	Type 2B	Type 2B	Type 2B	Type 2A	Type 2A
S (wt%)	53.74	53.74	53.71	54.00	53.72	53.69	53.43	53.76
Fe	46.15	46.12	46.07	46.29	46.28	46.37	46.19	46.45
As (ppm)	1160	1400	BDL	BDL	BDL	BDL	BDL	BDL
Cu	BDL	BDL	BDL	BDL	BDL	BDL	BDL	BDL
Zn	BDL	BDL	370	BDL	BDL	BDL	500	BDL
Sb	BDL	BDL	BDL	BDL	BDL	BDL	BDL	BDL
Ag	BDL	BDL	BDL	BDL	BDL	BDL	BDL	BDL
Hg	BDL	BDL	BDL	BDL	BDL	BDL	BDL	BDL
Au	BDL	BDL	BDL	BDL	BDL	BDL	BDL	BDL
Total	**99.98**	**99.99**	**99.82**	**100.28**	**100.01**	**100.07**	**99.68**	**100.21**
S (apfu)	2.00	2.00	2.00	2.00	2.00	2.00	2.00	2.00
Fe	0.99	0.99	0.99	0.98	0.99	0.99	0.99	0.99
As	0.00	0.00	0.00	0.00	0.00	0.00	0.00	0.00
Cu	0.00	0.00	0.00	0.00	0.00	0.00	0.00	0.00
Zn	0.00	0.00	0.00	0.00	0.00	0.00	0.00	0.00
Sb	0.00	0.00	0.00	0.00	0.00	0.00	0.00	0.00
Ag	0.00	0.00	0.00	0.00	0.00	0.00	0.00	0.00
Hg	0.00	0.00	0.00	0.00	0.00	0.00	0.00	0.00
Au	0.00	0.00	0.00	0.00	0.00	0.00	0.00	0.00
Total	**2.99**	**2.99**	**2.99**	**2.98**	**2.99**	**2.99**	**2.99**	**2.99**

Table A.2.2 cont. – Electron Microprobe Analyses for pyrite

Drill hole	LM08-33	LM08-33	LM11-63	LM11-63	LM11-59	LM11-59	LM11-59	LM11-59
Sample	CNF14279	CNF14279	CNF29957	CNF29957	CNF29962	CNF29962	CNF29962	CNF29962
Depth (m)	230.75	230.75	210.83	210.83	225.95	225.95	225.95	225.95
Probe Analysis	RL7 py1	RL10 py1	RL3 py1	RL4 py1	RL1 py1	RL1 py2	RL5 py1	RL5 py2
Date	2013-05-03	2013-05-03	2013-05-03	2013-05-03	2013-05-03	2013-05-03	2013-05-03	2013-05-03
Py description	Recrystallized (clustered to subhedral)	Recrystallized (clustered to subhedral)	Recrystallized (clustered to subhedral)	Recrystallized (clustered to subhedral)	Recrystallized (clustered to subhedral)	Recrystallized (clustered to subhedral)	Recrystallized (clustered to subhedral)	Recrystallized (clustered to subhedral)
Py Mineralogy	Type 2	Type 2	Type 2	Type 2	Type 2	Type 2	Type 2	Type 2
Type Mineralogy	Type 2A	Type 2A	Type 2A	Type 2A	Type 2B	Type 2B	Type 2B	Type 2B
S (wt%)	53.76	53.73	53.70	53.50	53.44	53.76	53.67	54.01
Fe	46.35	46.29	46.17	46.14	46.31	46.33	46.43	46.18
As (ppm)	BDL	BDL	BDL	BDL	BDL	BDL	BDL	BDL
Cu	BDL	BDL	990	BDL	BDL	240	BDL	BDL
Zn	BDL	BDL	BDL	170	1460	310	BDL	470
Sb	BDL	BDL	BDL	BDL	BDL	BDL	BDL	BDL
Ag	BDL	BDL	BDL	BDL	BDL	BDL	BDL	BDL
Hg	BDL	BDL	BDL	BDL	BDL	BDL	BDL	BDL
Au	BDL	BDL	BDL	BDL	BDL	BDL	BDL	BDL
Total	**100.11**	**100.03**	**99.94**	**99.67**	**99.90**	**100.14**	**100.10**	**100.22**
S (apfu)	2.00	2.00	2.00	2.00	2.00	2.00	2.00	2.00
Fe	0.99	0.99	0.99	0.99	1.00	0.99	0.99	0.98
As	0.00	0.00	0.00	0.00	0.00	0.00	0.00	0.00
Cu	0.00	0.00	0.00	0.00	0.00	0.00	0.00	0.00
Zn	0.00	0.00	0.00	0.00	0.00	0.00	0.00	0.00
Sb	0.00	0.00	0.00	0.00	0.00	0.00	0.00	0.00
Ag	0.00	0.00	0.00	0.00	0.00	0.00	0.00	0.00
Hg	0.00	0.00	0.00	0.00	0.00	0.00	0.00	0.00
Au	0.00	0.00	0.00	0.00	0.00	0.00	0.00	0.00
Total	**2.99**	**2.99**	**2.99**	**2.99**	**3.00**	**2.99**	**2.99**	**2.98**

Table A.2.2 cont. – Electron Microprobe Analyses for pyrite

Drill hole	LM11-59	LM11-59	LM11-59	LM11-59	LM11-59	LM11-59	LM07-17	LM07-17
Sample	CNF29972	CNF29972	CNF29972	CNF29972	CNF29972	CNF29972	CNF29967	CNF29967
Depth (m)	251.22	251.22	251.22	251.22	251.22	251.22	247.63	247.63
Probe Analysis	RL6 py1	RL6 py2	RL6 py3	RL4 py1	RL4 py2	RL4 py3	RL1 py1	RL1 py2
Date	2013-05-03	2013-05-03	2013-05-03	2013-05-03	2013-05-03	2013-05-03	2013-05-03	2013-05-03
Py description	Recrystallized (euhedral)	Recrystallized (euhedral)	Recrystallized (euhedral)	Recrystallized (euhedral)	Recrystallized (euhedral)	Recrystallized (euhedral)	Recrystallized (clustered to subhedral)	Recrystallized (clustered to subhedral)
Py Mineralogy	Type 3	Type 3	Type 3	Type 3	Type 3	Type 3	Type 2	Type 2
Type Mineralogy	Type 4	Type 4	Type 4	Type 4	Type 4	Type 4	Type 2A	Type 2A
S (wt%)	53.93	53.85	53.60	53.77	53.94	53.80	53.74	54.35
Fe	46.56	46.51	46.47	46.30	46.27	46.44	46.32	46.37
As (ppm)	BDL	BDL	BDL	BDL	BDL	140	BDL	BDL
Cu	BDL	BDL	BDL	BDL	BDL	BDL	2430	2490
Zn	BDL	360	820	1900	7750	340	630	3890
Sb	BDL	BDL	BDL	BDL	BDL	BDL	BDL	BDL
Ag	BDL	BDL	BDL	BDL	BDL	BDL	BDL	130
Hg	BDL	BDL	BDL	BDL	BDL	BDL	BDL	BDL
Au	BDL	BDL	BDL	BDL	BDL	BDL	BDL	BDL
Total	**100.50**	**100.39**	**100.16**	**100.24**	**100.97**	**100.29**	**100.35**	**101.36**
S (apfu)	2.00	2.00	2.00	2.00	2.00	2.00	2.00	2.00
Fe	0.99	0.99	1.00	0.99	0.99	0.99	0.99	0.98
As	0.00	0.00	0.00	0.00	0.00	0.00	0.00	0.00
Cu	0.00	0.00	0.00	0.00	0.00	0.00	0.00	0.00
Zn	0.00	0.00	0.00	0.00	0.01	0.00	0.00	0.01
Sb	0.00	0.00	0.00	0.00	0.00	0.00	0.00	0.00
Ag	0.00	0.00	0.00	0.00	0.00	0.00	0.00	0.00
Hg	0.00	0.00	0.00	0.00	0.00	0.00	0.00	0.00
Au	0.00	0.00	0.00	0.00	0.00	0.00	0.00	0.00
Total	**2.99**	**2.99**	**3.00**	**2.99**	**3.00**	**2.99**	**3.00**	**2.99**

Table A.2.2 cont. – Electron Microprobe Analyses for pyrite

Drill hole	LM07-17	LM07-17	LM08-19	LM08-19	LM08-19	LM08-19	LM11-59	LM11-59
Sample	CNF29967	CNF29967	CNF29986	CNF29986	CNF29986	CNF29986	CNF29959	CNF29959
Depth (m)	247.63	247.63	97.63	97.63	97.63	97.63	207.72	207.72
Probe Analysis	RL10 py1	RL10 py2	RL4 py1	RL4 py2	RL6 py1	RL6 py2	RL6 py1	RL6 py2
Date	2013-05-03	2013-05-03	2013-05-03	2013-05-03	2013-05-03	2013-05-03	2013-05-03	2013-05-03
Py description	Recrystallized (clustered to subhedral)	Recrystallized (clustered to subhedral)	Recrystallized (clustered to subhedral)	Recrystallized (clustered to subhedral)	Recrystallized (clustered to subhedral)	Recrystallized (clustered to subhedral)	Recrystallized (euhedral)	Recrystallized (euhedral)
Py Mineralogy	Type 2	Type 2	Type 2	Type 2	Type 2	Type 2	Type 3	Type 3
Type Mineralogy	Type 2A	Type 2A	Type 2B	Type 2B	Type 2B	Type 2B	Type 3	Type 3
S (wt%)	53.30	53.82	53.65	54.04	53.86	54.16	53.97	54.00
Fe	45.84	46.33	46.66	46.46	46.42	46.56	46.12	46.17
As (ppm)	180	240	BDL	BDL	BDL	BDL	680	200
Cu	10600	2730	BDL	380	990	BDL	BDL	BDL
Zn	5140	3600	BDL	BDL	BDL	BDL	4760	1510
Sb	BDL	BDL	BDL	BDL	BDL	BDL	BDL	BDL
Ag	BDL	BDL	BDL	BDL	BDL	BDL	BDL	BDL
Hg	BDL	BDL	BDL	BDL	BDL	BDL	BDL	BDL
Au	BDL	BDL	BDL	BDL	BDL	BDL	BDL	BDL
Total	**100.73**	**100.78**	**100.28**	**100.54**	**100.40**	**100.74**	**100.59**	**100.34**
S (apfu)	2.00	2.00	2.00	2.00	2.00	2.00	2.00	2.00
Fe	0.99	0.99	1.00	0.99	0.99	0.99	0.98	0.98
As	0.00	0.00	0.00	0.00	0.00	0.00	0.00	0.00
Cu	0.02	0.01	0.00	0.00	0.00	0.00	0.00	0.00
Zn	0.01	0.01	0.00	0.00	0.00	0.00	0.01	0.00
Sb	0.00	0.00	0.00	0.00	0.00	0.00	0.00	0.00
Ag	0.00	0.00	0.00	0.00	0.00	0.00	0.00	0.00
Hg	0.00	0.00	0.00	0.00	0.00	0.00	0.00	0.00
Au	0.00	0.00	0.00	0.00	0.00	0.00	0.00	0.00
Total	**3.02**	**3.00**	**3.00**	**2.99**	**2.99**	**2.99**	**2.99**	**2.99**

Table A.2.2 cont. – Electron Microprobe Analyses for pyrite

Drill hole	LM11-59	LM11-59	LM11-59	LM11-59	LM11-59	LM11-59	LM11-59	LM11-59
Sample	CNF29959	CNF29960	CNF29960	CNF29960	CNF29960	CNF29960	CNF29960	CNF29960
Depth (m)	207.72	216	216	216	216	216	216	216
Probe Analysis	RL6 py3	RL3 py1	RL3 py2	RL3 py3	RL3 py4	RL3 py5	RL8 py1	RL8 py2
Date	2013-05-03	2013-05-03	2013-05-03	2013-05-03	2013-05-03	2013-05-03	2013-05-03	2013-05-03
Py description	Recrystallized (euhedral)	Colloform/ reniform	Colloform/ reniform	Colloform/ reniform	Recrystallized (euhedral)	Recrystallized (euhedral)	Recrystallized (euhedral)	Recrystallized (clustered to subhedral)
Py Mineralogy	Type 3	Type 1	Type 1	Type 1	Type 3	Type 3	Type 3	Type 2
Type Mineralogy	Type 3	Type 3	Type 3	Type 3	Type 3	Type 3	Type 3	Type 3
S (wt%)	53.83	53.16	52.98	53.62	53.29	53.98	53.97	52.91
Fe	46.19	45.92	45.64	46.34	46.23	46.38	46.31	45.54
As (ppm)	BDL	1340	6170	170	3080	570	760	3070
Cu	BDL	BDL	BDL	BDL	BDL	BDL	BDL	BDL
Zn	3610	660	740	830	900	3860	690	480
Sb	BDL	950	4970	BDL	BDL	BDL	BDL	1010
Ag	BDL	BDL	BDL	BDL	BDL	BDL	BDL	BDL
Hg	BDL	BDL	BDL	BDL	BDL	BDL	BDL	BDL
Au	BDL	BDL	BDL	BDL	BDL	BDL	BDL	BDL
Total	**100.34**	**99.39**	**99.85**	**100.05**	**99.92**	**100.80**	**100.41**	**98.93**
S (apfu)	2.00	2.00	2.00	2.00	2.00	2.00	2.00	2.00
Fe	0.99	0.99	0.99	0.99	1.00	0.99	0.99	0.99
As	0.00	0.00	0.01	0.00	0.00	0.00	0.00	0.00
Cu	0.00	0.00	0.00	0.00	0.00	0.00	0.00	0.00
Zn	0.01	0.00	0.00	0.00	0.00	0.01	0.00	0.00
Sb	0.00	0.00	0.00	0.00	0.00	0.00	0.00	0.00
Ag	0.00	0.00	0.00	0.00	0.00	0.00	0.00	0.00
Hg	0.00	0.00	0.00	0.00	0.00	0.00	0.00	0.00
Au	0.00	0.00	0.00	0.00	0.00	0.00	0.00	0.00
Total	**2.99**	**3.00**	**3.01**	**2.99**	**3.00**	**2.99**	**2.99**	**3.00**

Table A.2.2 cont. – Electron Microprobe Analyses for pyrite

Drill hole	LM11-59
Sample	CNF29960
Depth (m)	216
Probe Analysis	RL8 py3
Date	2013-05-03
Py description	Recrystallized (clustered to subhedral)
Py Mineralogy	Type 2
Type Mineralogy	Type 3
S (wt%)	52.85
Fe	45.65
As (ppm)	5040
Cu	BDL
Zn	290
Sb	BDL
Ag	240
Hg	BDL
Au	BDL
Total	**99.08**
S (apfu)	2.00
Fe	0.99
As	0.01
Cu	0.00
Zn	0.00
Sb	0.00
Ag	0.00
Hg	0.00
Au	0.00
Total	**3.00**

Table A.2.3 – Electron Microprobe Analyses for galena

Drill hole	LM08-24	LM08-24	LM08-24	LM08-24	LM08-24	LM08-24	LM11-52	LM11-52	LM11-52	LM11-52	LM11-52
Sample	CNF29976	CNF29976	CNF29976	CNF29976	CNF29976	CNF29976	CNF25120	CNF25120	CNF25120	CNF25120	CNF25120
Depth (m)	279.8	279.8	279.8	279.8	279.8	279.8	212	212	212	212	212
Probe Analysis	RL4 gn1	RL4 gn2	RL4 gn3	RL1 gn1	RL1 gn2	RL1 gn3	RL3 gn1	RL3 gn3	RL8 gn1	RL8 gn2	RL8 gn3
Date	2013-10-02	2013-10-02	2013-10-02	2013-10-02	2013-10-02	2013-10-02	2013-10-02	2013-10-02	2013-10-02	2013-10-02	2013-10-02
Type Mineralogy	Type 1	Type 1	Type 1	Type 1	Type 1	Type 1	Type 3	Type 3	Type 3	Type 3	Type 3
Pb (wt%)	87.42	87.17	86.52	86.91	86.98	86.73	87.29	86.99	86.42	87.32	87.04
S	13.63	13.50	13.47	13.44	13.64	13.35	13.47	13.39	13.47	13.54	13.52
Zn (ppm)	BDL	BDL	BDL	BDL	250	1570	400	400	BDL	BDL	BDL
Fe	BDL	BDL	BDL	BDL	BDL	BDL	1700	530	BDL	250	7380
Cu	BDL	BDL	BDL	BDL	BDL	BDL	BDL	BDL	BDL	BDL	BDL
Ag	BDL	BDL	390	BDL	BDL	BDL	650	650	270	230	230
Sb	BDL	BDL	BDL	BDL	BDL	BDL	720	870	200	410	470
Hg	BDL	BDL	BDL	BDL	BDL	BDL	BDL	BDL	BDL	BDL	BDL
As	BDL	BDL	BDL	BDL	BDL	BDL	BDL	BDL	BDL	BDL	BDL
Total	**101.13**	**100.69**	**100.06**	**100.31**	**100.64**	**100.28**	**101.08**	**100.63**	**99.94**	**100.98**	**101.35**
Pb (apfu)	0.99	1.00	0.99	1.00	0.99	1.01	1.00	1.01	0.99	1.00	1.00
S	1.00	1.00	1.00	1.00	1.00	1.00	1.00	1.00	1.00	1.00	1.00
Zn	0.00	0.00	0.00	0.00	0.00	0.01	0.00	0.00	0.00	0.00	0.00
Fe	0.00	0.00	0.00	0.00	0.00	0.00	0.01	0.00	0.00	0.00	0.03
Cu	0.00	0.00	0.00	0.00	0.00	0.00	0.00	0.00	0.00	0.00	0.00
Ag	0.00	0.00	0.00	0.00	0.00	0.00	0.00	0.00	0.00	0.00	0.00
Sb	0.00	0.00	0.00	0.00	0.00	0.00	0.00	0.00	0.00	0.00	0.00
Hg	0.00	0.00	0.00	0.00	0.00	0.00	0.00	0.00	0.00	0.00	0.00
As	0.00	0.00	0.00	0.00	0.00	0.00	0.00	0.00	0.00	0.00	0.00
Total	**1.99**	**2.00**	**2.00**	**2.00**	**1.99**	**2.01**	**2.01**	**2.01**	**1.99**	**2.00**	**2.03**

Table A.2.3 cont. – Electron Microprobe Analyses for galena

Drill hole	LM08-23	LM08-23	LM08-23	LM08-23	LM08-23	LM08-23	LM10-46	LM10-46	LM10-46	LM10-46	LM10-46
Sample	CNF25127	CNF25127	CNF25127	CNF25127	CNF25127	CNF25127	CNF25146	CNF25146	CNF25146	CNF25146	CNF25146
Depth (m)	66.95	66.95	66.95	66.95	66.95	66.95	182.56	182.56	182.56	182.56	182.56
Probe Analysis	RL3 gn1	RL3 gn2	RL3 gn3	RL6 gn1	RL6 gn2	RL6 gn3	RL1 gn1	RL1 gn2	RL1 gn3	RL4b gn1	RL4b gn2
Date	2013-10-02	2013-10-02	2013-10-02	2013-10-02	2013-10-02	2013-10-02	2013-10-02	2013-10-02	2013-10-02	2013-10-02	2013-10-02
Type Mineralogy	Type 1	Type 1	Type 1	Type 1	Type 1	Type 1	Type 2B	Type 2B	Type 2B	Type 2B	Type 2B
Pb (wt%)	86.09	86.42	86.75	86.30	87.56	87.46	86.95	86.64	87.06	87.41	87.00
S	13.33	13.54	13.37	13.30	13.57	13.56	13.42	13.37	13.42	13.43	13.38
Zn (ppm)	BDL	BDL	BDL	1580	BDL	14760	BDL	BDL	260	BDL	BDL
Fe	BDL	BDL	BDL	BDL	BDL	460	BDL	BDL	BDL	BDL	BDL
Cu	BDL	BDL	BDL	BDL	BDL	BDL	BDL	BDL	BDL	BDL	2210
Ag	BDL	BDL	BDL	170	BDL	190	BDL	BDL	BDL	BDL	BDL
Sb	BDL	BDL	BDL	BDL	BDL	BDL	BDL	BDL	BDL	BDL	BDL
Hg	BDL	BDL	BDL	BDL	BDL	1010	BDL	BDL	BDL	BDL	BDL
As	BDL	BDL	BDL	BDL	BDL	BDL	BDL	BDL	BDL	BDL	BDL
Total	**99.45**	**99.97**	**100.15**	**99.81**	**101.22**	**102.66**	**100.36**	**100.01**	**100.56**	**100.88**	**100.62**
Pb (apfu)	1.00	0.99	1.00	1.00	1.00	1.00	1.00	1.00	1.00	1.01	1.01
S	1.00	1.00	1.00	1.00	1.00	1.00	1.00	1.00	1.00	1.00	1.00
Zn	0.00	0.00	0.00	0.01	0.00	0.05	0.00	0.00	0.00	0.00	0.00
Fe	0.00	0.00	0.00	0.00	0.00	0.00	0.00	0.00	0.00	0.00	0.00
Cu	0.00	0.00	0.00	0.00	0.00	0.00	0.00	0.00	0.00	0.00	0.01
Ag	0.00	0.00	0.00	0.00	0.00	0.00	0.00	0.00	0.00	0.00	0.00
Sb	0.00	0.00	0.00	0.00	0.00	0.00	0.00	0.00	0.00	0.00	0.00
Hg	0.00	0.00	0.00	0.00	0.00	0.00	0.00	0.00	0.00	0.00	0.00
As	0.00	0.00	0.00	0.00	0.00	0.00	0.00	0.00	0.00	0.00	0.00
Total	**2.00**	**1.99**	**2.00**	**2.01**	**2.00**	**2.06**	**2.00**	**2.00**	**2.01**	**2.01**	**2.01**

Table A.2.3 cont. – Electron Microprobe Analyses for galena

Drill hole	LM10-46	LM11-56	LM11-56	LM11-52	LM11-52	LM11-52	LM11-52	LM11-52	LM11-52	LM11-61
Sample	CNF25146	CNF25134	CNF25134	CNF25121	CNF25121	CNF25121	CNF25121	CNF25121	CNF25121	CNF25151
Depth (m)	182.56	158.7	158.7	212.3	212.3	212.3	212.3	212.3	212.3	222.4
Probe Analysis	RL4b gn3	RL4b gn1	RL8b gn2	RL2 gn1	RL2 gn2	RL2 gn3	RL4 gn1	RL4 gn2	RL4 gn3	RL5 gn1
Date	2013-10-02	2013-10-02	2013-10-02	2013-10-02	2013-10-02	2013-10-02	2013-10-02	2013-10-02	2013-10-02	2013-10-02
Type Mineralogy	Type 2B	Type 3	Type 3	Type 2B	Type 2B	Type 2B	Type 2B	Type 2B	Type 2B	Type 2A
Pb (wt%)	86.99	86.73	87.98	86.74	86.83	86.60	86.37	86.24	87.65	86.23
S	13.44	13.51	13.67	13.41	13.40	13.30	13.43	13.43	13.31	13.43
Zn (ppm)	BDL	8090	9620	BDL	BDL	BDL	5250	11120	8120	BDL
Fe	BDL	1280	3420	BDL	BDL	BDL	BDL	BDL	BDL	BDL
Cu	310	BDL	420	BDL	BDL	BDL	BDL	BDL	BDL	BDL
Ag	BDL	BDL	BDL	310	290	420	370	610	540	BDL
Sb	BDL	BDL	BDL	480	420	480	850	660	800	BDL
Hg	BDL	BDL	BDL	BDL	BDL	BDL	BDL	BDL	990	BDL
As	BDL	BDL	BDL	BDL	BDL	BDL	BDL	BDL	BDL	BDL
Total	**100.49**	**101.17**	**102.94**	**100.23**	**100.36**	**99.98**	**100.47**	**100.89**	**102.01**	**99.64**
Pb (apfu)	1.00	0.99	1.00	1.00	1.00	1.01	1.00	0.99	1.02	0.99
S	1.00	1.00	1.00	1.00	1.00	1.00	1.00	1.00	1.00	1.00
Zn	0.00	0.03	0.03	0.00	0.00	0.00	0.02	0.04	0.03	0.00
Fe	0.00	0.01	0.01	0.00	0.00	0.00	0.00	0.00	0.00	0.00
Cu	0.00	0.00	0.00	0.00	0.00	0.00	0.00	0.00	0.00	0.00
Ag	0.00	0.00	0.00	0.00	0.00	0.00	0.00	0.00	0.00	0.00
Sb	0.00	0.00	0.00	0.00	0.00	0.00	0.00	0.00	0.00	0.00
Hg	0.00	0.00	0.00	0.00	0.00	0.00	0.00	0.00	0.00	0.00
As	0.00	0.00	0.00	0.00	0.00	0.00	0.00	0.00	0.00	0.00
Total	**2.00**	**2.03**	**2.05**	**2.00**	**2.00**	**2.01**	**2.02**	**2.04**	**2.05**	**1.99**

Table A.2.3 cont. – Electron Microprobe Analyses for galena

Drill hole	LM11-61	LM11-61	LM11-61	LM11-61	LM11-61	LM13-73	LM13-73	LM13-73	LM11-61	LM11-61	LM11-61
Sample	CNF25151	CNF25151	CNF25151	CNF25151	CNF25151	CNF14299	CNF14299	CNF14299	CNF25152	CNF25152	CNF25152
Depth (m)	222.4	222.4	222.4	222.4	222.4	327.95	327.95	327.95	237.4	237.4	237.4
Probe Analysis	RL5 gn2	RL5 gn3	RL8 gn1	RL8 gn2	RL8 gn3	RL11 gn1	RL11 gn3	RL8 gn2	RL1 gn1	RL1 gn2	RL1 gn3
Date	2013-10-02	2013-10-02	2013-10-02	2013-10-02	2013-10-02	2013-10-02	2013-10-02	2013-10-02	2013-10-02	2013-10-02	2013-10-02
Type Mineralogy	Type 2A	Type 2A	Type 2A	Type 2A	Type 2A	Type 2A	Type 2A	Type 2A	Type 2B	Type 2B	Type 2B
Pb (wt%)	86.91	87.17	87.09	87.18	86.75	87.10	86.90	86.44	86.18	86.84	86.81
S	13.44	13.42	13.33	13.29	13.57	13.46	13.40	13.32	13.24	13.33	13.31
Zn (ppm)	BDL	BDL	BDL	BDL	BDL	BDL	BDL	BDL	320	BDL	BDL
Fe	BDL	BDL	BDL	BDL	BDL	3610	3170	410	BDL	BDL	BDL
Cu	BDL	BDL	BDL	BDL	290	11790	7500	4560	1160	260	230
Ag	BDL	BDL	BDL	BDL	BDL	BDL	BDL	BDL	BDL	BDL	BDL
Sb	BDL	BDL	BDL	BDL	BDL	BDL	BDL	BDL	BDL	BDL	BDL
Hg	BDL	BDL	960	BDL	BDL	BDL	BDL	BDL	BDL	BDL	BDL
As	BDL	BDL	BDL	BDL	BDL	BDL	BDL	BDL	BDL	BDL	BDL
Total	**100.38**	**100.57**	**100.51**	**100.44**	**100.39**	**102.10**	**101.36**	**100.26**	**99.64**	**100.24**	**100.14**
Pb (apfu)	1.00	1.01	1.01	1.02	0.99	1.00	1.00	1.00	1.01	1.01	1.01
S	1.00	1.00	1.00	1.00	1.00	1.00	1.00	1.00	1.00	1.00	1.00
Zn	0.00	0.00	0.00	0.00	0.00	0.00	0.00	0.00	0.00	0.00	0.00
Fe	0.00	0.00	0.00	0.00	0.00	0.02	0.01	0.00	0.00	0.00	0.00
Cu	0.00	0.00	0.00	0.00	0.00	0.04	0.03	0.02	0.00	0.00	0.00
Ag	0.00	0.00	0.00	0.00	0.00	0.00	0.00	0.00	0.00	0.00	0.00
Sb	0.00	0.00	0.00	0.00	0.00	0.00	0.00	0.00	0.00	0.00	0.00
Hg	0.00	0.00	0.00	0.00	0.00	0.00	0.00	0.00	0.00	0.00	0.00
As	0.00	0.00	0.00	0.00	0.00	0.00	0.00	0.00	0.00	0.00	0.00
Total	**2.00**	**2.01**	**2.01**	**2.02**	**1.99**	**2.06**	**2.05**	**2.02**	**2.01**	**2.01**	**2.01**

Table A.2.3 cont. – Electron Microprobe Analyses for galena

Drill hole	LM11-61	LM11-61	LM11-61	LM11-61	LM13-74	LM13-74	LM13-74	LM13-74	LM13-74	LM13-74
Sample	CNF25152	CNF25152	CNF25152	CNF25152	CNF25109	CNF25109	CNF25109	CNF25109	CNF25109	CNF25109
Depth (m)	237.4	237.4	237.4	237.4	328.55	328.55	328.55	328.55	328.55	328.55
Probe Analysis	RL4 gn1	RL4 gn2	RL4 gn3	RL4 gn4	RL3 gn1	RL3 gn2	RL3 gn3	RL9 gn1	RL9 gn2	RL9 gn3
Date	2013-10-02	2013-10-02	2013-10-02	2013-10-02	2013-10-02	2013-10-02	2013-10-02	2013-10-02	2013-10-02	2013-10-02
Type Mineralogy	Type 2B	Type 2B	Type 2B	Type 2B	Type 2B	Type 2B	Type 2B	Type 2B	Type 2B	Type 2B
Pb (wt%)	86.00	85.87	86.23	86.95	86.69	86.28	86.15	85.53	86.85	86.24
S	13.29	13.26	13.34	13.33	13.50	13.44	13.34	13.36	13.49	13.49
Zn (ppm)	BDL	BDL	5950	2890	BDL	BDL	BDL	BDL	BDL	BDL
Fe	BDL	BDL	BDL	BDL	400	BDL	470	BDL	BDL	BDL
Cu	460	BDL	BDL	BDL	BDL	BDL	BDL	BDL	BDL	BDL
Ag	BDL	BDL	BDL	BDL	780	660	580	10240	1210	970
Sb	BDL	BDL	BDL	BDL	1060	840	840	1740	1500	1500
Hg	BDL	BDL	BDL	BDL	BDL	BDL	BDL	BDL	BDL	1230
As	140	BDL	BDL	BDL	BDL	BDL	BDL	BDL	BDL	BDL
Total	**99.36**	**99.12**	**100.15**	**100.67**	**100.41**	**99.91**	**99.72**	**100.18**	**100.64**	**100.10**
Pb (apfu)	1.00	1.00	1.00	1.01	0.99	0.99	1.00	0.99	1.00	0.99
S	1.00	1.00	1.00	1.00	1.00	1.00	1.00	1.00	1.00	1.00
Zn	0.00	0.00	0.02	0.01	0.00	0.00	0.00	0.00	0.00	0.00
Fe	0.00	0.00	0.00	0.00	0.00	0.00	0.00	0.00	0.00	0.00
Cu	0.00	0.00	0.00	0.00	0.00	0.00	0.00	0.00	0.00	0.00
Ag	0.00	0.00	0.00	0.00	0.00	0.00	0.00	0.02	0.00	0.00
Sb	0.00	0.00	0.00	0.00	0.00	0.00	0.00	0.00	0.00	0.00
Hg	0.00	0.00	0.00	0.00	0.00	0.00	0.00	0.00	0.00	0.00
As	0.00	0.00	0.00	0.00	0.00	0.00	0.00	0.00	0.00	0.00
Total	**2.00**	**2.00**	**2.02**	**2.02**	**2.00**	**2.00**	**2.00**	**2.02**	**2.00**	**2.00**

Table A.2.3 cont. – Electron Microprobe Analyses for galena

Drill hole	LM11-65	LM11-65	LM11-65	LM11-65	LM11-65	LM11-65	LM07-14	LM07-14	LM08-33	LM08-33	LM11-63
Sample	CNF14290	CNF14290	CNF14293	CNF14293	CNF14291	CNF14291	CNF14259	CNF14259	CNF14279	CNF14279	CNF29957
Depth (m)	158.66	158.66	161.75	161.75	159.3	159.3	204.44	204.44	230.75	230.75	210.83
Probe Analysis	RL5b gn1	RL5b gn2	RL3 gn3	RL8 gn1	RL7 gn1	RL9 gn1	RL2b gn1	RL6 gn1	RL7 gn1	RL10 gn1	RL3 gn1
Date	2013-05-03	2013-05-03	2013-05-03	2013-05-03	2013-05-03	2013-05-03	2013-05-03	2013-05-03	2013-05-03	2013-05-03	2013-05-03
Type Mineralogy	Type 3	Type 3	Type 2B	Type 2B	Type 2B	Type 2B	Type 2A	Type 2A	Type 2A	Type 2A	Type 2A
Pb (wt%)	86.36	86.32	86.23	86.20	86.29	86.53	86.17	85.88	86.71	86.39	85.58
S	13.36	13.47	13.28	13.39	13.29	13.46	13.33	13.20	13.27	13.35	13.28
Zn (ppm)	430	1530	BDL	BDL	250	190	BDL	BDL	BDL	BDL	310
Fe	260	1170	BDL	1460	BDL	BDL	BDL	BDL	BDL	BDL	250
Cu	400	1780	BDL	BDL	BDL	BDL	BDL	BDL	BDL	BDL	260
Ag	580	230	540	BDL	1060	670	BDL	230	BDL	BDL	BDL
Sb	720	780	490	BDL	1350	980	BDL	BDL	BDL	BDL	BDL
Hg	BDL	BDL	BDL	BDL	BDL	BDL	BDL	BDL	BDL	BDL	BDL
As	BDL	BDL	BDL	BDL	BDL	BDL	BDL	BDL	BDL	BDL	BDL
Au	BDL	BDL	BDL	BDL	BDL	BDL	BDL	BDL	BDL	BDL	BDL
Total	**99.97**	**100.34**	**99.61**	**99.79**	**99.83**	**100.14**	**99.56**	**99.12**	**99.95**	**99.72**	**98.96**
Pb (apfu)	1.00	0.99	1.00	1.00	1.00	1.00	1.00	1.01	1.01	1.00	1.00
S	1.00	1.00	1.00	1.00	1.00	1.00	1.00	1.00	1.00	1.00	1.00
Fe	0.00	0.00	0.00	0.01	0.00	0.00	0.00	0.00	0.00	0.00	0.00
Zn	0.00	0.01	0.00	0.00	0.00	0.00	0.00	0.00	0.00	0.00	0.00
Cu	0.00	0.01	0.00	0.00	0.00	0.00	0.00	0.00	0.00	0.00	0.00
Ag	0.00	0.00	0.00	0.00	0.00	0.00	0.00	0.00	0.00	0.00	0.00
Sb	0.00	0.00	0.00	0.00	0.00	0.00	0.00	0.00	0.00	0.00	0.00
Hg	0.00	0.00	0.00	0.00	0.00	0.00	0.00	0.00	0.00	0.00	0.00
As	0.00	0.00	0.00	0.00	0.00	0.00	0.00	0.00	0.00	0.00	0.00
Au	0.00	0.00	0.00	0.00	0.00	0.00	0.00	0.00	0.00	0.00	0.00
Total	**2.01**	**2.01**	**2.01**	**2.00**	**2.01**	**2.00**	**2.00**	**2.01**	**2.01**	**2.00**	**2.00**

Table A.2.3 cont. – Electron Microprobe Analyses for galena

Drill hole	LM11-63	LM11-59	LM11-59	LM11-59	LM11-59	LM11-59	LM11-59	LM11-59	LM11-59	LM07-17	LM07-17
Sample	CNF29957	CNF29962	CNF29962	CNF29962	CNF29962	CNF29972	CNF29972	CNF29972	CNF29972	CNF29967	CNF29967
Depth (m)	210.83	225.95	225.95	225.95	225.95	251.22	251.22	251.22	251.22	247.63	247.63
Probe Analysis	RL3 gn2	RL1 gn1	RL1 gn2	RL5 gn1	RL5 gn2	RL6 gn1	RL6 gn2	RL4 gn1	RL4 gn2	RL1 gn1	RL1 gn2
Date	2013-05-03	2013-05-03	2013-05-03	2013-05-03	2013-05-03	2013-05-03	2013-05-03	2013-05-03	2013-05-03	2013-05-03	2013-05-03
Type Mineralogy	Type 2A	Type 2B	Type 2B	Type 2B	Type 2B	Type 4	Type 4	Type 4	Type 4	Type 2A	Type 2A
Pb (wt%)	85.57	86.42	85.64	86.27	86.23	85.55	85.75	84.57	85.53	85.87	86.99
S	13.17	13.41	13.28	13.29	13.25	13.12	13.19	13.11	13.24	13.33	13.42
Zn (ppm)	320	230	BDL	BDL	2240	520	880	4110	5000	1420	850
Fe	BDL	BDL	BDL	BDL	BDL	4200	8690	11370	17440	BDL	390
Cu	BDL	380	BDL	BDL	BDL	BDL	BDL	BDL	1170	280	4530
Ag	BDL	BDL	BDL	BDL	BDL	170	920	350	380	BDL	BDL
Sb	BDL	BDL	BDL	BDL	BDL	BDL	900	BDL	BDL	BDL	BDL
Hg	BDL	BDL	BDL	BDL	BDL	940	BDL	BDL	BDL	BDL	BDL
As	BDL	BDL	BDL	BDL	BDL	BDL	BDL	BDL	BDL	BDL	BDL
Au	BDL	BDL	BDL	BDL	BDL	BDL	BDL	BDL	BDL	BDL	BDL
Total	**98.77**	**99.89**	**98.95**	**99.64**	**99.75**	**99.26**	**100.09**	**99.27**	**101.11**	**99.32**	**100.98**
Pb (apfu)	1.01	1.00	1.00	1.01	1.01	1.01	1.01	1.00	1.00	1.00	1.00
S	1.00	1.00	1.00	1.00	1.00	1.00	1.00	1.00	1.00	1.00	1.00
Fe	0.00	0.00	0.00	0.00	0.00	0.02	0.04	0.05	0.08	0.00	0.00
Zn	0.00	0.00	0.00	0.00	0.01	0.00	0.00	0.02	0.02	0.01	0.00
Cu	0.00	0.00	0.00	0.00	0.00	0.00	0.00	0.00	0.00	0.00	0.02
Ag	0.00	0.00	0.00	0.00	0.00	0.00	0.00	0.00	0.00	0.00	0.00
Sb	0.00	0.00	0.00	0.00	0.00	0.00	0.00	0.00	0.00	0.00	0.00
Hg	0.00	0.00	0.00	0.00	0.00	0.00	0.00	0.00	0.00	0.00	0.00
As	0.00	0.00	0.00	0.00	0.00	0.00	0.00	0.00	0.00	0.00	0.00
Au	0.00	0.00	0.00	0.00	0.00	0.00	0.00	0.00	0.00	0.00	0.00
Total	**2.01**	**2.00**	**2.00**	**2.01**	**2.02**	**2.03**	**2.05**	**2.06**	**2.10**	**2.00**	**2.03**

Table A.2.3 cont. – Electron Microprobe Analyses for galena

Drill hole	LM07-17	LM07-17	LM07-17	LM08-19	LM08-19	LM11-59	LM11-59	LM11-59	LM11-59	LM11-59	LM11-59
Sample	CNF29967	CNF29967	CNF29967	CNF29986	CNF29986	CNF29959	CNF29959	CNF29959	CNF29960	CNF29960	CNF29960
Depth (m)	247.63	247.63	247.63	97.63	97.63	207.72	207.72	207.72	216	216	216
Probe Analysis	RL1 gn3	RL3 gn1	RL3 gn2	RL2 gn1	RL2 gn2	RL4 gn1	RL4 gn2	RL6b gn1	RL10b gn1	RL10b gn2	RL10b gn3
Date	2013-05-03	2013-05-03	2013-05-03	2013-05-03	2013-05-03	2013-05-03	2013-05-03	2013-05-03	2013-05-03	2013-05-03	2013-05-03
Type Mineralogy	Type 2A	Type 2A	Type 2A	Type 2B	Type 2B	Type 3	Type 3	Type 3	Type 3	Type 3	Type 3
Pb (wt%)	86.66	86.31	85.59	86.82	87.02	87.27	86.50	87.21	86.62	87.45	87.15
S	13.44	13.40	13.29	13.53	13.49	13.41	13.49	13.42	13.21	13.42	13.48
Zn (ppm)	4490	BDL	BDL	320	BDL	3860	BDL	3230	BDL	BDL	BDL
Fe	440	BDL	BDL	230	BDL	180	BDL	330	630	1020	850
Cu	2680	BDL	680	370	BDL	BDL	BDL	BDL	390	1990	1190
Ag	340	BDL	BDL	270	BDL	470	620	BDL	230	210	340
Sb	BDL	BDL	BDL	BDL	BDL	450	890	BDL	BDL	330	410
Hg	BDL	BDL	BDL	BDL	BDL	BDL	BDL	BDL	BDL	BDL	BDL
As	BDL	BDL	BDL	BDL	BDL	BDL	BDL	BDL	BDL	BDL	BDL
Au	BDL	BDL	BDL	BDL	BDL	BDL	BDL	BDL	BDL	BDL	BDL
Total	**100.84**	**99.68**	**98.95**	**100.48**	**100.53**	**101.18**	**100.14**	**100.98**	**99.96**	**101.25**	**100.91**
Pb (apfu)	1.00	1.00	1.00	0.99	1.00	1.01	0.99	1.01	1.02	1.01	1.00
S	1.00	1.00	1.00	1.00	1.00	1.00	1.00	1.00	1.00	1.00	1.00
Fe	0.00	0.00	0.00	0.00	0.00	0.00	0.00	0.00	0.00	0.00	0.00
Zn	0.02	0.00	0.00	0.00	0.00	0.01	0.00	0.01	0.00	0.00	0.00
Cu	0.01	0.00	0.00	0.00	0.00	0.00	0.00	0.00	0.00	0.01	0.00
Ag	0.00	0.00	0.00	0.00	0.00	0.00	0.00	0.00	0.00	0.00	0.00
Sb	0.00	0.00	0.00	0.00	0.00	0.00	0.00	0.00	0.00	0.00	0.00
Hg	0.00	0.00	0.00	0.00	0.00	0.00	0.00	0.00	0.00	0.00	0.00
As	0.00	0.00	0.00	0.00	0.00	0.00	0.00	0.00	0.00	0.00	0.00
Au	0.00	0.00	0.00	0.00	0.00	0.00	0.00	0.00	0.00	0.00	0.00
Total	**2.03**	**2.00**	**2.00**	**2.00**	**2.00**	**2.02**	**2.00**	**2.02**	**2.02**	**2.02**	**2.01**

Table A.2.4 – Electron Microprobe Analyses for chalcopyrite

Drill hole	LM08-24	LM08-24	LM08-24	LM08-24	LM08-24	LM08-24	LM11-52	LM11-52	LM11-52	LM11-52	LM11-52
Sample	CNF29976	CNF29976	CNF29976	CNF29976	CNF29976	CNF29976	CNF25120	CNF25120	CNF25120	CNF25120	CNF25120
Depth (m)	279.8	279.8	279.8	279.8	279.8	279.8	212	212	212	212	212
Probe Analysis	RL1 Ccp1	RL1 Ccp2	RL1 Ccp3	RL3 Ccp1	RL3 Ccp2	RL3 Ccp3	RL7 Ccp1	RL7 Ccp2	RL7 Ccp3	RL8 Ccp1	RL8 Ccp2
Date	2013-10-04	2013-10-04	2013-10-04	2013-10-04	2013-10-04	2013-10-04	2013-10-04	2013-10-04	2013-10-04	2013-10-04	2013-10-04
Type Mineralogy	Type 1	Type 1	Type 1	Type 1	Type 1	Type 1	Type 3	Type 3	Type 3	Type 3	Type 3
S (wt%)	35.29	34.90	35.25	35.09	35.08	35.11	35.34	35.50	35.21	35.19	35.28
Cu	34.51	34.25	34.44	33.86	34.17	34.27	34.37	34.45	34.38	34.08	34.29
Fe	30.43	30.20	30.16	29.93	30.33	30.38	30.56	30.69	30.63	30.67	30.65
Zn (ppm)	1010	3890	1700	380	BDL	290	610	590	470	490	580
Pb	BDL	BDL	BDL	BDL	BDL	BDL	BDL	BDL	BDL	BDL	BDL
As	BDL	BDL	BDL	BDL	BDL	BDL	BDL	BDL	BDL	BDL	BDL
Sb	BDL	BDL	BDL	BDL	BDL	BDL	BDL	BDL	BDL	BDL	BDL
Ag	BDL	BDL	BDL	BDL	BDL	BDL	BDL	BDL	180	430	280
Hg	BDL	BDL	BDL	BDL	BDL	BDL	BDL	BDL	BDL	BDL	BDL
Bi	BDL	BDL	BDL	BDL	BDL	BDL	BDL	BDL	BDL	BDL	BDL
Te	BDL	BDL	BDL	BDL	BDL	BDL	BDL	BDL	BDL	BDL	BDL
Ni	BDL	BDL	BDL	BDL	BDL	BDL	BDL	BDL	BDL	BDL	BDL
Total	**100.32**	**99.73**	**99.96**	**98.89**	**99.67**	**99.79**	**100.36**	**100.85**	**100.27**	**100.02**	**100.28**
S (apfu)	2.00	2.00	2.00	2.00	2.00	2.00	2.00	2.00	2.00	2.00	2.00
Cu	0.99	0.99	0.99	0.97	0.98	0.99	0.98	0.98	0.99	0.98	0.98
Fe	0.99	0.99	0.98	0.98	0.99	0.99	0.99	0.99	1.00	1.00	1.00
Zn	0.00	0.01	0.00	0.00	0.00	0.00	0.00	0.00	0.00	0.00	0.00
Pb	0.00	0.00	0.00	0.00	0.00	0.00	0.00	0.00	0.00	0.00	0.00
As	0.00	0.00	0.00	0.00	0.00	0.00	0.00	0.00	0.00	0.00	0.00
Sb	0.00	0.00	0.00	0.00	0.00	0.00	0.00	0.00	0.00	0.00	0.00
Ag	0.00	0.00	0.00	0.00	0.00	0.00	0.00	0.00	0.00	0.00	0.00
Hg	0.00	0.00	0.00	0.00	0.00	0.00	0.00	0.00	0.00	0.00	0.00
Bi	0.00	0.00	0.00	0.00	0.00	0.00	0.00	0.00	0.00	0.00	0.00
Te	0.00	0.00	0.00	0.00	0.00	0.00	0.00	0.00	0.00	0.00	0.00
Ni	0.00	0.00	0.00	0.00	0.00	0.00	0.00	0.00	0.00	0.00	0.00
Total	**3.98**	**4.00**	**3.97**	**3.95**	**3.98**	**3.98**	**3.98**	**3.97**	**3.99**	**3.98**	**3.98**

Table A.2.4 cont. – Electron Microprobe Analyses for chalcopyrite

Drill hole	LM11-52	LM08-23	LM08-23	LM11-56	LM11-56	LM11-56	LM08-39	LM08-39	LM08-39	LM08-39	LM08-39
Sample	CNF25120	CNF25127	CNF25127	CNF25134	CNF25134	CNF25134	CNF14295	CNF14295	CNF14295	CNF14295	CNF14295
Depth (m)	212	66.95	66.95	158.7	158.7	158.7	286.7	286.7	286.7	286.7	286.7
Probe Analysis	RL8 Ccp3	RL2 Ccp2	RL2 Ccp3	RL5 Ccp1	RL5 Ccp2	RL5 Ccp3	RL4 Ccp1	RL4 Ccp2	RL4 Ccp3	RL3 Ccp1	RL3 Ccp2
Date	2013-10-04	2013-10-04	2013-10-04	2013-10-05	2013-10-05	2013-10-05	2013-10-05	2013-10-05	2013-10-05	2013-10-05	2013-10-05
Type Mineralogy	Type 3	Type 1	Type 1	Type 3	Type 3	Type 3	Type 4	Type 4	Type 4	Type 4	Type 4
S (wt%)	35.50	35.18	35.08	34.85	34.68	34.93	34.57	35.00	34.55	34.76	34.46
Cu	34.18	33.64	33.67	33.84	33.66	33.63	34.25	34.42	34.23	34.08	34.10
Fe	30.62	29.96	29.84	30.15	30.31	30.50	30.37	30.35	30.28	30.14	30.07
Zn (ppm)	970	330	380	1800	2440	1780	240	BDL	350	290	340
Pb	BDL	BDL	BDL	BDL	BDL	BDL	BDL	BDL	BDL	BDL	BDL
As	BDL	BDL	BDL	BDL	BDL	BDL	BDL	BDL	BDL	BDL	BDL
Sb	BDL	BDL	BDL	BDL	BDL	BDL	BDL	BDL	BDL	BDL	BDL
Ag	560	BDL	BDL	300	380	220	BDL	BDL	BDL	BDL	BDL
Hg	BDL	BDL	BDL	BDL	BDL	BDL	BDL	BDL	BDL	BDL	BDL
Bi	BDL	BDL	BDL	BDL	BDL	BDL	BDL	BDL	BDL	BDL	BDL
Te	BDL	BDL	BDL	BDL	BDL	BDL	BDL	BDL	BDL	BDL	BDL
Ni	BDL	BDL	BDL	BDL	BDL	BDL	BDL	BDL	BDL	BDL	BDL
Total	**100.59**	**98.77**	**98.54**	**98.91**	**98.63**	**99.08**	**99.18**	**99.93**	**99.07**	**99.04**	**98.79**
S (apfu)	2.00	2.00	2.00	2.00	2.00	2.00	2.00	2.00	2.00	2.00	2.00
Cu	0.97	0.96	0.97	0.98	0.98	0.97	1.00	0.99	1.00	0.99	1.00
Fe	0.99	0.98	0.98	0.99	1.00	1.00	1.01	1.00	1.01	1.00	1.00
Zn	0.00	0.00	0.00	0.01	0.01	0.00	0.00	0.00	0.00	0.00	0.00
Pb	0.00	0.00	0.00	0.00	0.00	0.00	0.00	0.00	0.00	0.00	0.00
As	0.00	0.00	0.00	0.00	0.00	0.00	0.00	0.00	0.00	0.00	0.00
Sb	0.00	0.00	0.00	0.00	0.00	0.00	0.00	0.00	0.00	0.00	0.00
Ag	0.00	0.00	0.00	0.00	0.00	0.00	0.00	0.00	0.00	0.00	0.00
Hg	0.00	0.00	0.00	0.00	0.00	0.00	0.00	0.00	0.00	0.00	0.00
Bi	0.00	0.00	0.00	0.00	0.00	0.00	0.00	0.00	0.00	0.00	0.00
Te	0.00	0.00	0.00	0.00	0.00	0.00	0.00	0.00	0.00	0.00	0.00
Ni	0.00	0.00	0.00	0.00	0.00	0.00	0.00	0.00	0.00	0.00	0.00
Total	**3.97**	**3.94**	**3.95**	**3.98**	**3.99**	**3.98**	**4.01**	**3.99**	**4.01**	**3.99**	**4.00**

Table A.2.4 cont.– Electron Microprobe Analyses for chalcopyrite

Drill hole	LM08-39	LM11-61	LM11-61	LM11-61	LM11-61	LM11-61	LM11-61	LM11-61	LM11-61	LM11-61
Sample	CNF14295	CNF25151	CNF25151	CNF25151	CNF25151	CNF25151	CNF25151	CNF25152	CNF25152	CNF25152
Depth (m)	286.7	222.4	222.4	222.4	222.4	222.4	222.4	237.4	237.4	237.4
Probe Analysis	RL3 Ccp3	RL1 Ccp1	RL1 Ccp2	RL1 Ccp3	RL5 Ccp1	RL5 Ccp2	RL5 Ccp3	RL3 Ccp1	RL3 Ccp2	RL6 Ccp3
Date	2013-10-05	2013-10-06	2013-10-06	2013-10-06	2013-10-06	2013-10-06	2013-10-06	2013-10-06	2013-10-06	2013-10-06
Type Mineralogy	Type 4	Type 2A	Type 2A	Type 2A	Type 2A	Type 2A	Type 2A	Type 2B	Type 2B	Type 2B
S (wt%)	34.58	34.97	34.93	34.79	34.43	34.87	34.77	34.51	34.64	34.57
Cu	34.06	34.29	34.45	34.38	34.10	34.19	34.17	33.53	33.43	34.04
Fe	29.98	30.18	30.15	30.24	30.14	29.96	30.28	29.29	29.41	30.01
Zn (ppm)	230	470	BDL	260	380	480	320	12780	12540	330
Pb	BDL	BDL	BDL	BDL	440	BDL	BDL	BDL	BDL	BDL
As	BDL	BDL	BDL	BDL	BDL	BDL	BDL	BDL	BDL	BDL
Sb	BDL	BDL	BDL	BDL	BDL	BDL	BDL	BDL	BDL	BDL
Ag	BDL	480	480	600	BDL	BDL	BDL	BDL	BDL	BDL
Hg	BDL	BDL	BDL	BDL	BDL	BDL	BDL	BDL	BDL	BDL
Bi	BDL	BDL	BDL	BDL	BDL	BDL	BDL	BDL	BDL	BDL
Te	BDL	BDL	BDL	BDL	BDL	BDL	BDL	BDL	BDL	BDL
Ni	BDL	BDL	BDL	BDL	BDL	BDL	BDL	BDL	BDL	BDL
Total	**98.57**	**99.53**	**99.56**	**99.42**	**98.85**	**99.10**	**99.22**	**98.55**	**98.73**	**98.66**
S (apfu)	2.00	2.00	2.00	2.00	2.00	2.00	2.00	2.00	2.00	2.00
Cu	0.99	0.99	1.00	1.00	1.00	0.99	0.99	0.98	0.97	0.99
Fe	1.00	0.99	0.99	1.00	1.01	0.99	1.00	0.97	0.98	1.00
Zn	0.00	0.00	0.00	0.00	0.00	0.00	0.00	0.04	0.04	0.00
Pb	0.00	0.00	0.00	0.00	0.00	0.00	0.00	0.00	0.00	0.00
As	0.00	0.00	0.00	0.00	0.00	0.00	0.00	0.00	0.00	0.00
Sb	0.00	0.00	0.00	0.00	0.00	0.00	0.00	0.00	0.00	0.00
Ag	0.00	0.00	0.00	0.00	0.00	0.00	0.00	0.00	0.00	0.00
Hg	0.00	0.00	0.00	0.00	0.00	0.00	0.00	0.00	0.00	0.00
Bi	0.00	0.00	0.00	0.00	0.00	0.00	0.00	0.00	0.00	0.00
Te	0.00	0.00	0.00	0.00	0.00	0.00	0.00	0.00	0.00	0.00
Ni	0.00	0.00	0.00	0.00	0.00	0.00	0.00	0.00	0.00	0.00
Total	**3.99**	**3.98**	**3.99**	**4.00**	**4.01**	**3.98**	**3.99**	**3.99**	**3.98**	**3.99**

Table A.2.4 cont. – Electron Microprobe Analyses for chalcopyrite

Drill hole	LM13-74	LM13-74
Sample	CNF25109	CNF25109
Depth (m)	328.55	328.55
Probe Analysis	RL5 Ccp1	RL5 Ccp2
Date	2013-10-06	2013-10-06
Type Mineralogy	Type 2B	Type 2B
S (wt%)	34.57	34.65
Cu	33.97	33.85
Fe	30.01	30.15
Zn (ppm)	900	520
Pb	BDL	BDL
As	BDL	BDL
Sb	BDL	BDL
Ag	BDL	BDL
Hg	BDL	BDL
Bi	BDL	BDL
Te	BDL	BDL
Ni	BDL	BDL
Total	**98.67**	**98.81**
S (apfu)	2.00	2.00
Cu	0.99	0.99
Fe	1.00	1.00
Zn	0.00	0.00
Pb	0.00	0.00
As	0.00	0.00
Sb	0.00	0.00
Ag	0.00	0.00
Hg	0.00	0.00
Bi	0.00	0.00
Te	0.00	0.00
Ni	0.00	0.00
Total	**3.99**	**3.99**

Table A.2.4 cont. – Electron Microprobe Analyses for chalcopyrite

Drill hole	LM11-59	LM11-59	LM11-59	LM11-59	LM07-17	LM07-17	LM07-17	LM07-17	LM07-17	LM07-17	LM11-59
Sample	CNF29960	CNF29960	CNF29960	CNF29960	CNF29967	CNF29967	CNF29967	CNF29967	CNF29967	CNF29967	CNF29972
Depth (m)	216	216	216	216	247.63	247.63	247.63	247.63	247.63	247.63	251.22
Probe Analysis	RL10b ccp1	RL10b ccp2	RL10b ccp3	RL10b ccp4	RL3b ccp1	RL3b ccp2	RL3b ccp3	RL1 ccp1	RL1 ccp2	RL1 ccp3	RL3 ccp1
Date	2013-04-30	2013-04-30	2013-04-30	2013-04-30	2013-04-30	2013-04-30	2013-04-30	2013-04-30	2013-04-30	2013-04-30	2013-04-30
Type Mineralogy	Type 3	Type 3	Type 3	Type 3	Type 2A	Type 2A	Type 2A	Type 2A	Type 2A	Type 2A	Type 4
S (wt%)	35.14	34.86	35.09	35.22	34.88	34.79	34.84	34.81	34.77	34.91	34.96
Cu	34.53	34.85	34.72	34.87	34.57	34.70	34.62	34.59	34.70	34.57	34.57
Fe	30.40	30.39	30.46	30.35	30.38	30.33	30.22	30.15	30.19	30.23	30.14
Zn (ppm)	420	430	1040	650	BDL	1000	BDL	2060	2550	3110	740
Pb	1320	1380	1100	1560	1200	1300	1540	1080	1400	1380	1310
As	BDL	BDL	BDL	BDL	BDL	BDL	BDL	BDL	BDL	BDL	BDL
Sb	BDL	BDL	BDL	BDL	BDL	BDL	BDL	BDL	BDL	BDL	BDL
Ag	BDL	BDL	BDL	BDL	770	790	1500	1150	830	890	BDL
Hg	BDL	BDL	BDL	BDL	BDL	BDL	BDL	BDL	BDL	BDL	BDL
Bi	BDL	BDL	BDL	BDL	1560	BDL	BDL	BDL	BDL	BDL	BDL
Te	BDL	BDL	BDL	BDL	BDL	BDL	BDL	BDL	BDL	BDL	BDL
Total	**100.25**	**100.39**	**100.63**	**100.77**	**100.21**	**100.24**	**100.08**	**100.04**	**100.16**	**100.18**	**99.88**
S (apfu)	2.00	2.00	2.00	2.00	2.00	2.00	2.00	2.00	2.00	2.00	2.00
Cu	0.99	1.01	1.00	1.00	1.00	1.01	1.00	1.00	1.01	1.00	1.00
Fe	0.99	1.00	1.00	0.99	1.00	1.00	1.00	1.00	1.00	0.99	0.99
Zn	0.00	0.00	0.00	0.00	0.00	0.00	0.00	0.01	0.01	0.01	0.00
Pb	0.00	0.00	0.00	0.00	0.00	0.00	0.00	0.00	0.00	0.00	0.00
As	0.00	0.00	0.00	0.00	0.00	0.00	0.00	0.00	0.00	0.00	0.00
Sb	0.00	0.00	0.00	0.00	0.00	0.00	0.00	0.00	0.00	0.00	0.00
Ag	0.00	0.00	0.00	0.00	0.00	0.00	0.00	0.00	0.00	0.00	0.00
Hg	0.00	0.00	0.00	0.00	0.00	0.00	0.00	0.00	0.00	0.00	0.00
Bi	0.00	0.00	0.00	0.00	0.00	0.00	0.00	0.00	0.00	0.00	0.00
Te	0.00	0.00	0.00	0.00	0.00	0.00	0.00	0.00	0.00	0.00	0.00
Total	**3.99**	**4.01**	**4.00**	**3.99**	**4.00**	**4.01**	**4.00**	**4.01**	**4.01**	**4.01**	**3.99**

Table A.2.4 cont. – Electron Microprobe Analyses for chalcopyrite

Drill hole	LM11-59	LM11-59	LM11-59	LM11-59	LM11-59	LM08-19	LM08-19	LM08-19	LM08-19	LM08-19	LM08-19
Sample	CNF29972	CNF29972	CNF29972	CNF29972	CNF29972	CNF29986	CNF29986	CNF29986	CNF29986	CNF29986	CNF29986
Depth (m)	251.22	251.22	251.22	251.22	251.22	97.63	97.63	97.63	97.63	97.63	97.63
Probe Analysis	RL3 ccp2	RL3 ccp3	RL4 ccp1	RL4 ccp2	RL4 ccp3	RL2 ccp1	RL2 ccp2	RL2 ccp3	RL7 ccp1	RL7 ccp2	RL7 ccp3
Date	2013-04-30	2013-04-30	2013-04-30	2013-04-30	2013-04-30	2013-04-30	2013-04-30	2013-04-30	2013-04-30	2013-04-30	2013-04-30
Type Mineralogy	Type 4	Type 4	Type 4	Type 4	Type 4	Type 2B	Type 2B	Type 2B	Type 2B	Type 2B	Type 2B
S (wt%)	35.00	35.11	35.22	35.09	34.94	34.90	35.10	34.93	34.95	35.07	35.16
Cu	34.59	34.84	35.03	34.89	34.54	34.96	34.94	35.01	34.88	34.82	35.03
Fe	30.29	30.13	30.45	30.30	30.26	30.41	30.21	30.39	30.15	30.46	30.49
Zn (ppm)	2690	3310	1400	1480	1840	BDL	BDL	BDL	BDL	420	BDL
Pb	1400	1590	1210	1270	1440	1390	1300	1470	1070	1520	1330
As	BDL	BDL	BDL	BDL	BDL	BDL	BDL	BDL	BDL	BDL	BDL
Sb	BDL	BDL	BDL	BDL	BDL	BDL	BDL	BDL	BDL	BDL	BDL
Ag	BDL	BDL	BDL	BDL	BDL	BDL	BDL	BDL	1120	900	1350
Hg	BDL	BDL	BDL	BDL	BDL	BDL	BDL	BDL	BDL	BDL	BDL
Bi	1570	BDL	BDL	BDL	BDL	BDL	BDL	BDL	BDL	1690	BDL
Te	BDL	BDL	BDL	BDL	BDL	BDL	BDL	BDL	BDL	BDL	BDL
Total	**100.40**	**100.68**	**100.96**	**100.54**	**99.98**	**100.58**	**100.35**	**100.56**	**100.29**	**100.76**	**101.09**
S (apfu)	2.00	2.00	2.00	2.00	2.00	2.00	2.00	2.00	2.00	2.00	2.00
Cu	1.00	1.00	1.00	1.00	1.00	1.01	1.00	1.01	1.01	1.00	1.01
Fe	0.99	0.99	0.99	0.99	0.99	1.00	0.99	1.00	0.99	1.00	1.00
Zn	0.01	0.01	0.00	0.00	0.01	0.00	0.00	0.00	0.00	0.00	0.00
Pb	0.00	0.00	0.00	0.00	0.00	0.00	0.00	0.00	0.00	0.00	0.00
As	0.00	0.00	0.00	0.00	0.00	0.00	0.00	0.00	0.00	0.00	0.00
Sb	0.00	0.00	0.00	0.00	0.00	0.00	0.00	0.00	0.00	0.00	0.00
Ag	0.00	0.00	0.00	0.00	0.00	0.00	0.00	0.00	0.00	0.00	0.00
Hg	0.00	0.00	0.00	0.00	0.00	0.00	0.00	0.00	0.00	0.00	0.00
Bi	0.00	0.00	0.00	0.00	0.00	0.00	0.00	0.00	0.00	0.00	0.00
Te	0.00	0.00	0.00	0.00	0.00	0.00	0.00	0.00	0.00	0.00	0.00
Total	**4.00**	**4.00**	**4.00**	**4.00**	**4.00**	**4.01**	**3.99**	**4.01**	**4.00**	**4.01**	**4.00**

Table A.2.4 cont. – Electron Microprobe Analyses for chalcopyrite

Drill hole	LM11-59	LM11-59	LM11-59	LM11-59	LM11-59	LM11-59	LM11-65	LM11-65	LM11-65	LM11-65	LM11-65
Sample	CNF29962	CNF29962	CNF29962	CNF29962	CNF29962	CNF29962	CNF14290	CNF14290	CNF14290	CNF14290	CNF14290
Depth (m)	225.95	225.95	225.95	225.95	225.95	225.95	158.66	158.66	158.66	158.66	158.66
Probe Analysis	RL1 ccp1	RL1 ccp2	RL1 ccp3	RL2 ccp1	RL2 ccp2	RL2 ccp3	RL5b ccp1	RL5b ccp2	RL5b ccp3	RL9 ccp1	RL9 ccp2
Date	2013-04-30	2013-04-30	2013-04-30	2013-04-30	2013-04-30	2013-04-30	2013-04-30	2013-04-30	2013-04-30	2013-04-30	2013-04-30
Type Mineralogy	Type 2B	Type 2B	Type 2B	Type 2B	Type 2B	Type 2B	Type 3	Type 3	Type 3	Type 3	Type 3
S (wt%)	35.09	34.98	34.87	34.68	34.89	34.83	35.05	35.50	35.18	35.08	35.02
Cu	34.59	34.70	34.56	34.92	34.65	34.67	34.59	34.79	34.48	34.88	34.60
Fe	29.76	29.92	29.61	30.09	30.04	29.87	30.19	30.15	30.04	30.60	30.34
Zn (ppm)	2140	620	1210	1330	5450	1550	710	1890	1190	1820	7040
Pb	1330	1320	1350	1230	1240	1500	1710	1520	1550	1360	1330
As	BDL	BDL	BDL	BDL	BDL	BDL	BDL	BDL	BDL	BDL	BDL
Sb	BDL	BDL	BDL	BDL	BDL	BDL	BDL	BDL	BDL	BDL	BDL
Ag	BDL	BDL	BDL	BDL	BDL	BDL	BDL	250	BDL	BDL	BDL
Hg	BDL	BDL	BDL	BDL	BDL	BDL	BDL	BDL	BDL	BDL	BDL
Bi	BDL	BDL	BDL	BDL	BDL	BDL	BDL	BDL	BDL	BDL	BDL
Te	BDL	BDL	BDL	BDL	BDL	BDL	BDL	BDL	BDL	BDL	BDL
Total	**99.81**	**99.76**	**99.27**	**99.87**	**100.29**	**99.77**	**100.19**	**100.86**	**100.06**	**100.98**	**100.86**
S (apfu)	2.00	2.00	2.00	2.00	2.00	2.00	2.00	2.00	2.00	2.00	2.00
Cu	0.99	1.00	1.00	1.02	1.00	1.00	1.00	0.99	0.99	1.00	1.00
Fe	0.97	0.98	0.98	1.00	0.99	0.99	0.99	0.98	0.98	1.00	1.00
Zn	0.01	0.00	0.00	0.00	0.02	0.00	0.00	0.01	0.00	0.01	0.02
Pb	0.00	0.00	0.00	0.00	0.00	0.00	0.00	0.00	0.00	0.00	0.00
As	0.00	0.00	0.00	0.00	0.00	0.00	0.00	0.00	0.00	0.00	0.00
Sb	0.00	0.00	0.00	0.00	0.00	0.00	0.00	0.00	0.00	0.00	0.00
Ag	0.00	0.00	0.00	0.00	0.00	0.00	0.00	0.00	0.00	0.00	0.00
Hg	0.00	0.00	0.00	0.00	0.00	0.00	0.00	0.00	0.00	0.00	0.00
Bi	0.00	0.00	0.00	0.00	0.00	0.00	0.00	0.00	0.00	0.00	0.00
Te	0.00	0.00	0.00	0.00	0.00	0.00	0.00	0.00	0.00	0.00	0.00
Total	**3.98**	**3.99**	**3.98**	**4.02**	**4.01**	**4.00**	**3.99**	**3.97**	**3.97**	**4.01**	**4.01**

Table A.2.4 cont. – Electron Microprobe Analyses for chalcopyrite

Drill hole	LM11-65	LM11-65	LM11-65	LM11-65	LM11-65	LM11-65	LM11-65	LM11-65	LM11-65	LM11-59	LM11-59
Sample	CNF14290	CNF14293	CNF14293	CNF14293	CNF14291	CNF14291	CNF14291	CNF14291	CNF14291	CNF14259	CNF14259
Depth (m)	158.66	161.75	161.75	161.75	159.3	159.3	159.3	159.3	159.3	207.72	207.72
Probe Analysis	RL9 ccp3	RL9 ccp1	RL9 ccp2	RL9 ccp3	RL9b ccp1	RL9b ccp2	RL9b ccp3	RL8 ccp1	RL8 ccp2	RL2b ccp1	RL2b ccp2
Date	2013-04-30	2013-04-30	2013-04-30	2013-04-30	2013-04-30	2013-04-30	2013-04-30	2013-04-30	2013-04-30	2013-04-30	2013-04-30
Type Mineralogy	Type 3	Type 2B	Type 2B	Type 2B	Type 2B	Type 2B	Type 2B	Type 2B	Type 2B	Type 2A	Type 2A
S (wt%)	34.86	35.53	34.89	35.20	34.94	34.97	35.08	35.13	35.02	34.65	34.78
Cu	34.93	34.98	34.48	34.60	35.05	35.06	35.17	34.82	34.74	34.72	34.73
Fe	30.30	29.87	29.83	29.75	30.41	30.35	30.45	29.84	29.96	29.36	29.31
Zn (ppm)	6750	640	460	BDL	900	470	580	2820	1300	BDL	900
Pb	1320	1390	1440	1240	1280	1510	1570	1450	1460	1740	1530
As	BDL	BDL	BDL	BDL	BDL	BDL	BDL	BDL	BDL	BDL	BDL
Sb	BDL	BDL	BDL	BDL	BDL	BDL	BDL	BDL	BDL	BDL	BDL
Ag	BDL	BDL	BDL	920	380	410	410	BDL	BDL	BDL	BDL
Hg	BDL	BDL	BDL	BDL	BDL	BDL	BDL	BDL	1070	BDL	BDL
Bi	BDL	BDL	1480	BDL	BDL	BDL	BDL	BDL	1800	BDL	BDL
Te	BDL	BDL	BDL	BDL	BDL	BDL	BDL	BDL	BDL	BDL	BDL
Total	**100.90**	**100.65**	**99.14**	**99.63**	**100.68**	**100.63**	**101.04**	**100.22**	**100.28**	**98.95**	**99.03**
S (apfu)	2.00	2.00	2.00	2.00	2.00	2.00	2.00	2.00	2.00	2.00	2.00
Cu	1.01	0.99	1.00	0.99	1.01	1.01	1.01	1.00	1.00	1.01	1.01
Fe	1.00	0.97	0.98	0.97	1.00	1.00	1.00	0.98	0.98	0.97	0.97
Zn	0.02	0.00	0.00	0.00	0.00	0.00	0.00	0.01	0.00	0.00	0.00
Pb	0.00	0.00	0.00	0.00	0.00	0.00	0.00	0.00	0.00	0.00	0.00
As	0.00	0.00	0.00	0.00	0.00	0.00	0.00	0.00	0.00	0.00	0.00
Sb	0.00	0.00	0.00	0.00	0.00	0.00	0.00	0.00	0.00	0.00	0.00
Ag	0.00	0.00	0.00	0.00	0.00	0.00	0.00	0.00	0.00	0.00	0.00
Hg	0.00	0.00	0.00	0.00	0.00	0.00	0.00	0.00	0.00	0.00	0.00
Bi	0.00	0.00	0.00	0.00	0.00	0.00	0.00	0.00	0.00	0.00	0.00
Te	0.00	0.00	0.00	0.00	0.00	0.00	0.00	0.00	0.00	0.00	0.00
Total	**4.03**	**3.96**	**3.98**	**3.97**	**4.02**	**4.01**	**4.01**	**3.99**	**3.99**	**3.99**	**3.98**

Table A.2.4 cont. – Electron Microprobe Analyses for chalcopyrite

Drill hole	LM11-59	LM11-59	LM11-59	LM08-33	LM08-33	LM11-63	LM11-63	LM11-63	LM11-63	LM11-63
Sample	CNF14259	CNF14259	CNF14259	CNF14279	CNF14279	CNF29957	CNF29957	CNF29957	CNF29957	CNF29957
Depth (m)	207.72	207.72	207.72	230.75	230.75	210.83	210.83	210.83	210.83	210.83
Probe Analysis	RL6c ccp1	RL6c ccp2	RL6c ccp3	RL7 ccp1	RL7 ccp2	RL3 ccp1	RL3 ccp2	RL3 ccp3	RL6 ccp1	RL6 ccp2
Date	2013-04-30	2013-04-30	2013-04-30	2013-04-30	2013-04-30	2013-04-30	2013-04-30	2013-04-30	2013-04-30	2013-04-30
Type Mineralogy	Type 2A	Type 2A	Type 2A	Type 2A	Type 2A	Type 2A	Type 2A	Type 2A	Type 2A	Type 2A
S (wt%)	34.84	34.74	34.91	35.19	35.04	34.92	34.79	34.99	34.91	34.85
Cu	34.72	34.54	35.40	35.13	35.13	34.95	35.12	34.88	34.99	35.10
Fe	29.34	29.20	28.91	30.10	30.18	30.26	30.36	30.19	30.05	30.20
Zn (ppm)	3860	BDL	1450	BDL	BDL	BDL	510	510	BDL	BDL
Pb	1450	1490	1340	1490	1680	1880	1720	1320	1330	1610
As	BDL	BDL	BDL	BDL	BDL	BDL	BDL	BDL	BDL	BDL
Sb	BDL	BDL	BDL	BDL	BDL	BDL	BDL	BDL	BDL	BDL
Ag	BDL	BDL	BDL	BDL	580	BDL	BDL	BDL	BDL	BDL
Hg	BDL	BDL	BDL	BDL	BDL	BDL	BDL	BDL	BDL	BDL
Bi	BDL	BDL	BDL	BDL	BDL	BDL	BDL	BDL	BDL	BDL
Te	BDL	BDL	BDL	BDL	BDL	BDL	BDL	BDL	BDL	BDL
Total	**99.47**	**98.67**	**99.21**	**100.66**	**100.59**	**100.44**	**100.57**	**100.39**	**100.18**	**100.39**
S (apfu)	2.00	2.00	2.00	2.00	2.00	2.00	2.00	2.00	2.00	2.00
Cu	1.01	1.00	1.02	1.01	1.01	1.01	1.02	1.01	1.01	1.02
Fe	0.97	0.97	0.95	0.98	0.99	1.00	1.00	0.99	0.99	1.00
Zn	0.01	0.00	0.00	0.00	0.00	0.00	0.00	0.00	0.00	0.00
Pb	0.00	0.00	0.00	0.00	0.00	0.00	0.00	0.00	0.00	0.00
As	0.00	0.00	0.00	0.00	0.00	0.00	0.00	0.00	0.00	0.00
Sb	0.00	0.00	0.00	0.00	0.00	0.00	0.00	0.00	0.00	0.00
Ag	0.00	0.00	0.00	0.00	0.00	0.00	0.00	0.00	0.00	0.00
Hg	0.00	0.00	0.00	0.00	0.00	0.00	0.00	0.00	0.00	0.00
Bi	0.00	0.00	0.00	0.00	0.00	0.00	0.00	0.00	0.00	0.00
Te	0.00	0.00	0.00	0.00	0.00	0.00	0.00	0.00	0.00	0.00
Total	**3.99**	**3.97**	**3.98**	**3.99**	**4.00**	**4.01**	**4.02**	**4.00**	**4.00**	**4.01**

Table A.2.5 – Electron Microprobe Analyses for tetrahedrite

Drill hole	LM08-24	LM08-24	LM10-46	LM10-46	LM10-46	LM10-46	LM10-46	LM10-46	LM11-52	LM11-52	LM11-52
Sample	CNF29976	CNF29976	CNF25146	CNF25146	CNF25146	CNF25146	CNF25146	CNF25146	CNF25121	CNF25121	CNF25121
Depth (m)	279.8	279.8	182.56	182.56	182.56	182.56	182.56	182.56	212.3	212.3	212.3
Probe Analysis	RL2 Tnn1	RL2 Tnn2	RL3 Tnn1	RL3 Tnn2	RL3 Tnn3	RL5 Tnn1	RL5 Tnn2	RL5 Tnn3	RL2 Tnn1	RL2 Tnn2	RL2 Tnn3
Date	2013-10-04	2013-10-04	2013-10-05	2013-10-05	2013-10-05	2013-10-05	2013-10-05	2013-10-05	2013-10-06	2013-10-06	2013-10-06
Type Mineralogy	Type 1	Type 1	Type 2B	Type 2B	Type 2B	Type 2B	Type 2B	Type 2B	Type 2B	Type 2B	Type 2B
Cu (wt%)	24.51	24.42	41.68	41.13	41.51	41.22	41.76	41.72	40.48	40.83	40.75
S	23.63	23.81	28.31	27.95	28.07	27.74	27.66	27.95	27.16	27.37	27.42
Sb	26.35	26.15	3.78	4.31	3.89	5.58	5.65	5.48	10.27	10.23	10.29
As	0.75	0.88	17.33	17.08	17.32	16.33	16.38	16.41	13.01	13.02	12.96
Zn	6.51	6.43	5.66	5.36	5.80	5.68	5.58	6.23	4.88	4.86	4.87
Fe	1.07	1.12	2.56	2.66	2.43	3.39	2.76	2.36	3.02	3.05	2.99
Ag	17.89	17.96	0.42	0.50	0.44	0.33	0.39	0.46	0.73	0.80	0.86
Te (ppm)	BDL	BDL	BDL	BDL	BDL	BDL	BDL	BDL	BDL	BDL	BDL
Pb	1140	1310	BDL	BDL	BDL	BDL	BDL	BDL	BDL	BDL	BDL
Hg	BDL	BDL	BDL	BDL	BDL	BDL	BDL	BDL	BDL	BDL	BDL
Bi	BDL	BDL	BDL	BDL	BDL	BDL	BDL	BDL	BDL	BDL	BDL
Ni	BDL	BDL	BDL	BDL	BDL	BDL	BDL	BDL	BDL	BDL	BDL
Total	**100.86**	**100.96**	**99.69**	**98.99**	**99.46**	**100.29**	**100.19**	**100.63**	**99.52**	**100.20**	**100.20**
Cu (apfu)	6.80	6.73	9.66	9.65	9.70	9.75	9.90	9.79	9.78	9.79	9.75
S	13.00	13.00	13.00	13.00	13.00	13.00	13.00	13.00	13.00	13.00	13.00
Sb	3.82	3.76	0.46	0.53	0.47	0.69	0.70	0.67	1.29	1.28	1.28
As	0.18	0.21	3.41	3.40	3.43	3.28	3.30	3.27	2.66	2.65	2.63
Zn	1.76	1.72	1.27	1.22	1.32	1.31	1.29	1.42	1.14	1.13	1.13
Fe	0.34	0.35	0.68	0.71	0.65	0.91	0.75	0.63	0.83	0.83	0.82
Pb	0.01	0.01	0.00	0.00	0.00	0.00	0.00	0.00	0.00	0.00	0.00
Ag	2.93	2.92	0.06	0.07	0.06	0.05	0.05	0.06	0.10	0.11	0.12
Te	0.00	0.00	0.00	0.00	0.00	0.00	0.00	0.00	0.00	0.00	0.00
Hg	0.00	0.00	0.00	0.00	0.00	0.00	0.00	0.00	0.00	0.00	0.00
Bi	0.00	0.00	0.00	0.00	0.00	0.00	0.00	0.00	0.00	0.00	0.00
Ni	0.00	0.00	0.00	0.00	0.00	0.00	0.00	0.00	0.00	0.00	0.00
Total	**28.83**	**28.70**	**28.53**	**28.58**	**28.63**	**28.98**	**28.98**	**28.85**	**28.82**	**28.79**	**28.73**

Table A.2.5 cont. – Electron Microprobe Analyses for tetrahedrite

Drill hole	LM11-52	LM11-52	LM11-52	LM11-61	LM11-61	LM11-61	LM11-61	LM11-61	LM11-61	LM11-61	LM13-73
Sample	CNF25121	CNF25121	CNF25121	CNF25151	CNF25151	CNF25151	CNF25151	CNF25151	CNF25151	CNF25151	CNF14299
Depth (m)	212.3	212.3	212.3	222.4	222.4	222.4	222.4	222.4	222.4	222.4	327.95
Probe Analysis	RL6 Tnn1	RL6 Tnn2	RL6 Tnn3	RL3 Tnn1	RL3 Tnn2	RL3 Tnn3	RL8 Tnn1	RL8 Tnn2	RL8 Tnn3	RL8 Tnn4	RL4 Tnn1
Date	2013-10-06	2013-10-06	2013-10-06	2013-10-06	2013-10-06	2013-10-06	2013-10-06	2013-10-06	2013-10-06	2013-10-06	2013-10-06
Type Mineralogy	Type 2B	Type 2B	Type 2B	Type 2A/2B	Type 2A/2B	Type 2A/2B	Type 2A/2B	Type 2A/2B	Type 2A/2B	Type 2A/2B	Type 2A/2B
Cu (wt%)	40.65	39.95	40.41	42.48	42.41	42.37	42.13	42.32	41.98	42.17	41.21
S	27.38	27.58	27.36	27.43	27.01	26.73	27.36	27.59	26.58	26.54	27.21
Sb	10.62	10.43	10.56	8.56	10.66	10.97	8.17	7.90	13.35	12.87	9.20
As	12.79	12.82	12.61	13.27	11.01	10.96	14.02	14.02	9.04	9.23	13.53
Zn	3.72	3.69	3.92	7.68	7.02	7.08	7.88	7.91	6.72	6.65	7.91
Fe	4.18	4.25	3.99	0.07	0.12	0.15	0.18	0.18	0.16	0.27	0.13
Ag	1.17	1.23	1.13	0.07	0.07	0.09	0.06	0.06	0.18	0.11	0.07
Te (ppm)	BDL	BDL	BDL	12190	22310	21800	5450	5810	25970	26680	3170
Pb	BDL	BDL	BDL	BDL	BDL	BDL	BDL	BDL	BDL	BDL	BDL
Hg	BDL	BDL	BDL	BDL	BDL	BDL	BDL	BDL	BDL	BDL	BDL
Bi	BDL	BDL	BDL	BDL	BDL	1400	BDL	BDL	BDL	BDL	BDL
Ni	BDL	BDL	BDL	BDL	BDL	BDL	BDL	BDL	BDL	BDL	BDL
Total	**100.52**	**99.90**	**100.05**	**100.82**	**100.61**	**100.65**	**100.39**	**100.45**	**100.79**	**100.48**	**99.68**
Cu (apfu)	9.74	9.50	9.69	10.16	10.30	10.40	10.10	10.06	10.36	10.42	9.94
S	13.00	13.00	13.00	13.00	13.00	13.00	13.00	13.00	13.00	13.00	13.00
Sb	1.33	1.29	1.32	1.07	1.35	1.40	1.02	0.98	1.72	1.66	1.16
As	2.60	2.59	2.56	2.69	2.27	2.28	2.85	2.83	1.89	1.94	2.77
Zn	0.87	0.85	0.91	1.79	1.66	1.69	1.84	1.83	1.61	1.60	1.85
Fe	1.14	1.15	1.09	0.02	0.03	0.04	0.05	0.05	0.04	0.08	0.04
Pb	0.00	0.00	0.00	0.00	0.00	0.00	0.00	0.00	0.00	0.00	0.00
Ag	0.17	0.17	0.16	0.01	0.01	0.01	0.01	0.01	0.03	0.02	0.01
Te	0.00	0.00	0.00	0.15	0.27	0.27	0.07	0.07	0.32	0.33	0.04
Hg	0.00	0.00	0.00	0.00	0.00	0.00	0.00	0.00	0.00	0.00	0.00
Bi	0.00	0.00	0.00	0.00	0.00	0.01	0.00	0.00	0.00	0.00	0.00
Ni	0.00	0.00	0.00	0.00	0.00	0.00	0.00	0.00	0.00	0.00	0.00
Total	**28.84**	**28.56**	**28.73**	**28.88**	**28.89**	**29.11**	**28.93**	**28.83**	**28.97**	**29.04**	**28.80**

Table A.2.5 cont. – Electron Microprobe Analyses for tetrahedrite

Drill hole	LM13-73	LM13-73	LM13-73	LM13-73	LM11-61	LM11-61	LM11-61	LM11-61	LM11-61	LM11-61	LM13-74
Sample	CNF14299	CNF14299	CNF14299	CNF14299	CNF25152	CNF25152	CNF25152	CNF25152	CNF25152	CNF25152	CNF25109
Depth (m)	327.95	327.95	327.95	327.95	237.4	237.4	237.4	237.4	237.4	237.4	328.55
Probe Analysis	RL4 Tnn2	RL4 Tnn3	RL8 Tnn1	RL8 Tnn2	RL1 Tnn1	RL1 Tnn3	RL1 Tnn4	RL3 Tnn1	RL3 Tnn2	RL3 Tnn3	RL3 Tnn1
Date	2013-10-06	2013-10-06	2013-10-06	2013-10-06	2013-10-06	2013-10-06	2013-10-06	2013-10-06	2013-10-06	2013-10-06	2013-10-06
Type Mineralogy	Type 2A/2B	Type 2A/2B	Type 2A/2B	Type 2A/2B	Type 2B	Type 2B	Type 2B	Type 2B	Type 2B	Type 2B	Type 2B
Cu (wt%)	41.18	40.96	40.83	40.77	42.49	41.58	41.91	42.74	42.81	43.01	26.04
S	27.04	27.08	26.97	26.92	28.18	28.23	28.23	28.32	28.31	28.03	23.47
Sb	9.26	8.81	9.14	9.23	1.18	1.03	1.05	1.24	1.23	1.23	26.87
As	13.32	13.48	13.53	13.36	19.23	19.22	19.33	19.22	19.27	19.35	0.40
Zn	8.04	7.86	7.78	7.80	5.73	6.05	5.59	5.14	5.10	4.69	4.75
Fe	0.14	0.30	0.19	0.30	2.56	2.51	2.50	3.13	3.16	3.51	3.45
Ag	0.07	0.07	0.11	0.10	0.23	0.25	0.23	0.28	0.26	0.28	15.38
Te (ppm)	3050	2930	3110	3060	590	BDL	390	470	500	430	BDL
Pb	BDL	BDL	BDL	BDL	BDL	BDL	BDL	BDL	BDL	BDL	BDL
Hg	BDL	BDL	BDL	BDL	BDL	BDL	BDL	BDL	BDL	BDL	BDL
Bi	BDL	BDL	1730	BDL	BDL	BDL	BDL	BDL	BDL	BDL	BDL
Ni	BDL	BDL	BDL	BDL	BDL	BDL	BDL	BDL	BDL	BDL	BDL
Total	**99.40**	**98.85**	**99.04**	**98.90**	**99.69**	**98.80**	**98.94**	**100.06**	**100.16**	**100.12**	**100.34**
Cu (apfu)	9.99	9.92	9.93	9.94	9.89	9.66	9.74	9.90	9.92	10.07	7.28
S	13.00	13.00	13.00	13.00	13.00	13.00	13.00	13.00	13.00	13.00	13.00
Sb	1.17	1.11	1.16	1.17	0.14	0.13	0.13	0.15	0.15	0.15	3.92
As	2.74	2.77	2.79	2.76	3.80	3.79	3.81	3.78	3.79	3.84	0.09
Zn	1.89	1.85	1.84	1.85	1.30	1.37	1.26	1.16	1.15	1.07	1.29
Fe	0.04	0.08	0.05	0.08	0.68	0.66	0.66	0.83	0.83	0.94	1.10
Pb	0.00	0.00	0.00	0.00	0.00	0.00	0.00	0.00	0.00	0.00	0.00
Ag	0.01	0.01	0.02	0.01	0.03	0.03	0.03	0.04	0.04	0.04	2.53
Te	0.04	0.04	0.04	0.04	0.01	0.00	0.00	0.01	0.01	0.01	0.00
Hg	0.00	0.00	0.00	0.00	0.00	0.00	0.00	0.00	0.00	0.00	0.00
Bi	0.00	0.00	0.01	0.00	0.00	0.00	0.00	0.00	0.00	0.00	0.00
Ni	0.00	0.00	0.00	0.00	0.00	0.00	0.00	0.00	0.00	0.00	0.00
Total	**28.88**	**28.78**	**28.84**	**28.85**	**28.85**	**28.64**	**28.63**	**28.85**	**28.88**	**29.10**	**29.22**

Table A.2.5 cont. – Electron Microprobe Analyses for tetrahedrite

Drill hole	LM13-74	LM13-74	LM13-74
Sample	CNF25109	CNF25109	CNF25109
Depth (m)	328.55	328.55	328.55
Probe Analysis	RL3 Tnn2	RL3 Tnn3	RL7 Tnn1
Date	2013-10-06	2013-10-06	2013-10-06
Type Mineralogy	Type 2B	Type 2B	Type 2B
Cu (wt%)	24.04	24.54	17.44
S	23.13	23.21	21.42
Sb	27.24	26.22	26.30
As	0.16	0.47	0.06
Zn	2.00	1.49	0.69
Fe	4.63	4.87	5.97
Ag	18.43	17.81	27.77
Te (ppm)	BDL	330	380
Pb	BDL	3120	BDL
Hg	BDL	BDL	BDL
Bi	BDL	BDL	BDL
Ni	BDL	BDL	BDL
Total	**99.72**	**98.99**	**99.86**
Cu (apfu)	6.82	6.94	5.34
S	13.00	13.00	13.00
Sb	4.03	3.87	4.20
As	0.04	0.11	0.02
Zn	0.55	0.41	0.21
Fe	1.49	1.57	2.08
Pb	0.00	0.03	0.00
Ag	3.08	2.97	5.01
Te	0.00	0.00	0.01
Hg	0.00	0.00	0.00
Bi	0.00	0.00	0.00
Ni	0.00	0.00	0.00
Total	**29.01**	**28.89**	**29.86**

Table A.2.5 cont. – Electron Microprobe Analyses for tetrahedrite

Drill hole	LM07-17	LM07-17	LM07-17	LM07-17	LM07-17	LM07-17	LM08-19	LM08-19	LM08-19	LM08-19	LM08-19
Sample	CNF29967	CNF29967	CNF29967	CNF29967	CNF29967	CNF29967	CNF29986	CNF29986	CNF29986	CNF29986	CNF29986
Depth (m)	247.63	247.63	247.63	247.63	247.63	247.63	97.63	97.63	97.63	97.63	97.63
Probe Analysis	RL3b tnn1	RL3b tnn2	RL3b tnn3	RL6 tnn1	RL6 tnn2	RL6 tnn3	RL3 tnn1	RL3 tnn2	RL3 tnn3	RL3 tnn4	RL3 tnn5
Date	2013-04-30	2013-04-30	2013-04-30	2013-04-30	2013-04-30	2013-04-30	2013-04-30	2013-04-30	2013-04-30	2013-04-30	2013-04-30
Type Mineralogy	Type 2A/2B	Type 2A/2B	Type 2A/2B	Type 2A/2B	Type 2A/2B	Type 2A/2B	Type 2B	Type 2B	Type 2B	Type 2B	Type 2B
Cu (wt%)	42.89	42.69	42.79	42.16	41.91	41.18	33.20	32.21	30.78	32.77	31.42
S	26.93	27.15	27.08	26.63	26.84	26.50	24.45	24.45	24.21	24.56	24.28
Sb	7.46	7.33	7.47	10.67	8.07	11.46	21.84	22.43	22.74	20.33	21.81
As	14.70	14.94	14.75	11.70	14.14	11.39	4.27	3.84	3.51	5.21	4.14
Zn	7.94	8.09	7.99	7.33	8.11	8.77	7.07	6.75	7.11	6.97	6.89
Fe	0.25	0.17	0.16	0.53	0.29	0.21	0.60	0.74	0.44	0.68	0.68
Ag	0.46	0.30	0.30	0.10	0.15	0.24	9.26	10.10	11.82	9.64	11.24
Te (ppm)	6260	5620	6450	19340	7640	14710	BDL	BDL	BDL	BDL	BDL
Pb	830	1080	950	820	990	880	800	750	1060	1110	1210
Hg	BDL	BDL	BDL	BDL	BDL	BDL	BDL	BDL	BDL	BDL	BDL
Bi	BDL	BDL	BDL	BDL	BDL	BDL	BDL	BDL	BDL	BDL	BDL
Total	**101.30**	**101.35**	**101.30**	**101.18**	**100.45**	**101.30**	**100.84**	**100.73**	**100.81**	**100.44**	**100.73**
Cu (apfu)	10.45	10.32	10.37	10.38	10.25	10.20	8.91	8.64	8.34	8.75	8.49
S	13.00	13.00	13.00	13.00	13.00	13.00	13.00	13.00	13.00	13.00	13.00
Sb	0.95	0.92	0.94	1.37	1.03	1.48	3.06	3.14	3.22	2.83	3.08
As	3.04	3.06	3.03	2.44	2.93	2.39	0.97	0.87	0.81	1.18	0.95
Zn	1.88	1.90	1.88	1.75	1.93	2.11	1.84	1.76	1.87	1.81	1.81
Fe	0.07	0.05	0.04	0.15	0.08	0.06	0.18	0.23	0.13	0.21	0.21
Pb	0.01	0.01	0.01	0.01	0.01	0.01	0.01	0.01	0.01	0.01	0.01
Ag	0.07	0.04	0.04	0.01	0.02	0.03	1.46	1.60	1.89	1.52	1.79
Te	0.08	0.07	0.08	0.24	0.09	0.18	0.00	0.00	0.00	0.00	0.00
Hg	0.00	0.00	0.00	0.00	0.00	0.00	0.00	0.00	0.00	0.00	0.00
Bi	0.00	0.00	0.00	0.00	0.00	0.00	0.00	0.00	0.00	0.00	0.00
Total	**29.53**	**29.37**	**29.40**	**29.36**	**29.34**	**29.46**	**29.44**	**29.25**	**29.26**	**29.31**	**29.34**

Table A.2.5 cont. – Electron Microprobe Analyses for tetrahedrite

Drill hole	LM08-19	LM08-19	LM08-19	LM08-19	LM11-59	LM11-59	LM11-59	LM11-59	LM11-59	LM11-59	LM11-59
Sample	CNF29986	CNF29986	CNF29986	CNF29986	CNF29962	CNF29962	CNF29962	CNF29962	CNF29962	CNF29962	CNF29962
Depth (m)	97.63	97.63	97.63	97.63	225.95	225.95	225.95	225.95	225.95	225.95	225.95
Probe Analysis	RL3 tnn6	RL3 tnn7	RL2 tnn3	RL7 tnn1	RL1 tnn1	RL1 tnn2	RL1 tnn3	RL2 tnn1	RL2 tnn2	RL2 tnn3	RL2 tnn4
Date	2013-04-30	2013-04-30	2013-04-30	2013-04-30	2013-04-30	2013-04-30	2013-04-30	2013-04-30	2013-04-30	2013-04-30	2013-04-30
Type Mineralogy	Type 2B	Type 2B	Type 2B	Type 2B	Type 2B	Type 2B	Type 2B	Type 2B	Type 2B	Type 2B	Type 2B
Cu (wt%)	32.32	28.23	28.35	25.40	42.47	42.40	42.34	42.71	42.73	42.77	41.83
S	24.45	23.49	23.37	23.44	27.18	27.36	27.22	27.22	27.01	27.03	26.77
Sb	21.07	25.03	24.90	20.06	6.17	6.24	5.91	5.79	5.61	6.00	8.99
As	4.77	1.85	1.72	3.75	15.55	15.75	15.96	15.93	15.97	15.71	13.48
Zn	7.14	7.12	7.08	0.09	4.97	5.12	4.99	5.15	5.20	4.99	5.89
Fe	0.43	0.19	0.26	7.87	2.56	2.54	2.83	2.64	2.60	2.72	1.72
Ag	10.39	14.03	13.97	19.40	0.23	0.21	0.18	0.21	0.19	0.21	0.30
Te (ppm)	BDL	BDL	BDL	1020	BDL	270	280	1480	1090	2100	BDL
Pb	970	1190	1440	1920	1270	1140	1000	1360	880	1250	750
Hg	BDL	BDL	BDL	BDL	BDL	BDL	BDL	BDL	BDL	BDL	BDL
Bi	BDL	BDL	BDL	BDL	BDL	BDL	BDL	BDL	BDL	BDL	BDL
Total	**100.71**	**100.19**	**99.83**	**100.43**	**99.24**	**99.74**	**99.59**	**99.92**	**99.46**	**99.73**	**99.07**
Cu (apfu)	8.67	7.88	7.96	7.11	10.25	10.16	10.20	10.29	10.38	10.38	10.25
S	13.00	13.00	13.00	13.00	13.00	13.00	13.00	13.00	13.00	13.00	13.00
Sb	2.95	3.65	3.65	2.93	0.78	0.78	0.74	0.73	0.71	0.76	1.15
As	1.09	0.44	0.41	0.89	3.18	3.20	3.26	3.26	3.29	3.23	2.80
Zn	1.86	1.93	1.93	0.02	1.17	1.19	1.17	1.21	1.23	1.18	1.40
Fe	0.13	0.06	0.08	2.51	0.70	0.69	0.78	0.72	0.72	0.75	0.48
Pb	0.01	0.01	0.01	0.02	0.01	0.01	0.01	0.01	0.01	0.01	0.01
Ag	1.64	2.31	2.31	3.20	0.03	0.03	0.02	0.03	0.03	0.03	0.04
Te	0.00	0.00	0.00	0.01	0.00	0.00	0.00	0.02	0.01	0.03	0.00
Hg	0.00	0.00	0.00	0.00	0.00	0.00	0.00	0.00	0.00	0.00	0.00
Bi	0.00	0.00	0.00	0.00	0.00	0.00	0.00	0.00	0.00	0.00	0.00
Total	**29.35**	**29.28**	**29.35**	**29.69**	**29.12**	**29.08**	**29.19**	**29.26**	**29.37**	**29.37**	**29.14**

Table A.2.5 cont. – Electron Microprobe Analyses for tetrahedrite

Drill hole	LM11-65	LM11-65	LM11-65	LM11-65	LM11-65	LM11-65	LM11-65	LM11-65	LM11-65	LM11-65	LM11-65
Sample	CNF14293	CNF14293	CNF14293	CNF14293	CNF14293	CNF14293	CNF14293	CNF14293	CNF14293	CNF14293	CNF14293
Depth (m)	161.75	161.75	161.75	161.75	161.75	161.75	161.75	161.75	161.75	161.75	161.75
Probe Analysis	RL4 tnn1	RL4 tnn2	RL4 tnn3	RL4 tnn4	RL4 tnn5	RL4 tnn6	RL4 tnn7	RL4 tnn8	RL4 tnn9	RL4 tnn10	RL6 tnn2
Date	2013-04-30	2013-04-30	2013-04-30	2013-04-30	2013-04-30	2013-04-30	2013-04-30	2013-04-30	2013-04-30	2013-04-30	2013-04-30
Type Mineralogy	Type 2B	Type 2B	Type 2B	Type 2B	Type 2B	Type 2B	Type 2B	Type 2B	Type 2B	Type 2B	Type 2B
Cu (wt%)	32.64	34.94	38.48	39.47	42.49	42.38	39.22	31.95	25.51	42.43	39.45
S	24.36	24.28	25.36	25.72	27.04	27.06	25.97	24.30	22.97	26.94	26.43
Sb	24.22	25.10	19.14	16.85	5.49	5.61	11.16	19.89	25.31	5.82	15.84
As	2.97	2.45	6.97	8.38	16.36	16.30	12.32	5.51	1.36	16.09	9.08
Zn	3.41	3.75	4.32	4.54	4.51	4.52	4.06	4.66	3.46	4.65	4.23
Fe	3.87	3.64	3.55	3.45	3.67	3.71	3.86	2.93	3.93	3.40	3.57
Ag	8.89	5.74	2.62	2.02	0.65	0.64	3.14	10.61	18.02	0.66	2.58
Te (ppm)	BDL	BDL	BDL	BDL	BDL	BDL	BDL	BDL	BDL	BDL	BDL
Pb	1010	780	780	1030	1090	790	690	830	600	670	930
Hg	BDL	BDL	BDL	BDL	BDL	BDL	BDL	BDL	BDL	BDL	BDL
Bi	BDL	BDL	BDL	BDL	BDL	BDL	BDL	BDL	BDL	BDL	BDL
Total	**100.42**	**100.07**	**100.61**	**100.54**	**100.28**	**100.27**	**99.91**	**100.09**	**100.75**	**100.07**	**101.31**
Cu (apfu)	8.79	9.44	9.95	10.07	10.31	10.27	9.91	8.63	7.28	10.33	9.79
S	13.00	13.00	13.00	13.00	13.00	13.00	13.00	13.00	13.00	13.00	13.00
Sb	3.40	3.54	2.58	2.24	0.70	0.71	1.47	2.80	3.77	0.74	2.05
As	0.68	0.56	1.53	1.81	3.37	3.35	2.64	1.26	0.33	3.32	1.91
Zn	0.89	0.98	1.09	1.13	1.06	1.06	1.00	1.22	0.96	1.10	1.02
Fe	1.19	1.12	1.05	1.00	1.01	1.02	1.11	0.90	1.28	0.94	1.01
Pb	0.01	0.01	0.01	0.01	0.01	0.01	0.01	0.01	0.01	0.01	0.01
Ag	1.41	0.91	0.40	0.30	0.09	0.09	0.47	1.69	3.03	0.09	0.38
Te	0.00	0.00	0.00	0.00	0.00	0.00	0.00	0.00	0.00	0.00	0.00
Hg	0.00	0.00	0.00	0.00	0.00	0.00	0.00	0.00	0.00	0.00	0.00
Bi	0.00	0.00	0.00	0.00	0.00	0.00	0.00	0.00	0.00	0.00	0.00
Total	**29.37**	**29.57**	**29.60**	**29.56**	**29.55**	**29.52**	**29.60**	**29.51**	**29.66**	**29.54**	**29.17**

Table A.2.5 cont. – Electron Microprobe Analyses for tetrahedrite

Drill hole	LM11-65	LM11-65	LM11-65	LM11-65	LM11-65	LM07-14	LM07-14	LM11-65	LM11-65	LM11-65	LM11-65
Sample	CNF14293	CNF14293	CNF14293	CNF14293	CNF14293	CNF14259	CNF14259	CNF14291	CNF14291	CNF14291	CNF14291
Depth (m)	161.75	161.75	161.75	161.75	161.75	204.44	204.44	159.3	159.3	159.3	159.3
Probe Analysis	RL6 tnn3	RL6 tnn4	RL6 tnn5	RL6 tnn6	RL6 tnn7	RL2b tnn1	RL2b tnn2	RL9b tnn3	RL9b tnn4	RL8 tnn1	RL8 tnn2
Date	2013-04-30	2013-04-30	2013-04-30	2013-04-30	2013-04-30	2013-04-30	2013-04-30	2013-04-30	2013-04-30	2013-04-30	2013-04-30
Type Mineralogy	Type 2B	Type 2B	Type 2B	Type 2B	Type 2B	Type 2A/2B	Type 2A/2B	Type 2B	Type 2B	Type 2B	Type 2B
Cu (wt%)	36.25	42.78	42.09	35.12	28.61	41.91	41.63	18.08	18.10	28.57	29.10
S	25.28	27.34	26.86	24.51	23.58	27.60	27.09	21.61	21.64	23.55	23.92
Sb	21.36	5.50	5.46	21.41	22.92	2.83	5.77	25.80	25.85	24.04	23.08
As	4.87	15.89	16.36	4.54	3.01	18.11	16.01	0.14	0.12	2.50	3.18
Zn	4.22	4.36	4.10	4.33	3.78	4.76	4.97	2.03	1.99	3.67	3.52
Fe	3.22	3.75	3.96	3.25	3.74	3.58	3.23	4.46	4.53	3.43	3.64
Ag	5.86	0.62	0.73	6.17	14.10	0.27	0.36	27.78	27.47	14.17	13.79
Te (ppm)	BDL	BDL	BDL	BDL	BDL	BDL	BDL	360	550	BDL	BDL
Pb	820	800	940	670	570	830	890	800	820	890	1130
Hg	BDL	BDL	BDL	BDL	BDL	BDL	BDL	BDL	BDL	BDL	BDL
Bi	BDL	BDL	BDL	BDL	BDL	BDL	BDL	BDL	BDL	BDL	BDL
Total	**101.13**	**100.36**	**99.66**	**99.33**	**99.89**	**99.11**	**99.12**	**100.08**	**99.93**	**100.07**	**100.51**
Cu (apfu)	9.41	10.26	10.28	9.40	7.96	9.96	10.08	5.49	5.49	7.96	7.98
S	13.00	13.00	13.00	13.00	13.00	13.00	13.00	13.00	13.00	13.00	13.00
Sb	2.89	0.69	0.70	2.99	3.33	0.35	0.73	4.09	4.09	3.50	3.30
As	1.07	3.23	3.39	1.03	0.71	3.65	3.29	0.04	0.03	0.59	0.74
Zn	1.06	1.02	0.97	1.13	1.02	1.10	1.17	0.60	0.59	0.99	0.94
Fe	0.95	1.02	1.10	0.99	1.18	0.97	0.89	1.54	1.56	1.09	1.14
Pb	0.01	0.01	0.01	0.01	0.00	0.01	0.01	0.01	0.01	0.01	0.01
Ag	0.90	0.09	0.10	0.97	2.31	0.04	0.05	4.97	4.91	2.32	2.23
Te	0.00	0.00	0.00	0.00	0.00	0.00	0.00	0.01	0.01	0.00	0.00
Hg	0.00	0.00	0.00	0.00	0.00	0.00	0.00	0.00	0.00	0.00	0.00
Bi	0.00	0.00	0.00	0.00	0.00	0.00	0.00	0.00	0.00	0.00	0.00
Total	**29.29**	**29.32**	**29.55**	**29.52**	**29.52**	**29.07**	**29.22**	**29.73**	**29.68**	**29.46**	**29.34**

Table A.2.5 cont. – Electron Microprobe Analyses for tetrahedrite

Drill hole	LM11-65	LM11-65	LM11-65	LM07-14	LM07-14	LM08-33	LM08-33	LM08-33	LM08-33	LM08-33	LM11-63
Sample	CNF14291	CNF14291	CNF14291	CNF14259	CNF14259	CNF14279	CNF14279	CNF14279	CNF14279	CNF14279	CNF29957
Depth (m)	159.3	159.3	159.3	204.44	204.44	230.75	230.75	230.75	230.75	230.75	210.83
Probe Analysis	RL8 tnn3	RL8 tnn4	RL8 tnn5	RL6b tnn1	RL6b tnn2	RL7 tnn1	RL7 tnn2	RL7 tnn3	RL3 tnn1	RL3 tnn2	RL3 tnn1
Date	2013-04-30	2013-04-30	2013-04-30	2013-04-30	2013-04-30	2013-04-30	2013-04-30	2013-04-30	2013-04-30	2013-04-30	2013-04-30
Type Mineralogy	Type 2B	Type 2B	Type 2B	Type 2A/2B	Type 2A/2B	Type 2A/2B	Type 2A/2B	Type 2A/2B	Type 2A/2B	Type 2A/2B	Type 2A/2B
Cu (wt%)	24.40	24.36	28.41	41.60	40.33	41.19	40.82	41.22	40.04	40.09	42.90
S	23.12	22.95	24.04	26.61	26.28	26.04	26.14	26.19	26.05	25.94	27.18
Sb	26.30	27.06	21.64	9.92	14.82	16.49	16.38	16.58	17.49	17.19	6.01
As	0.66	0.26	3.06	12.98	10.04	8.60	8.54	8.49	8.03	7.95	15.57
Zn	3.95	3.95	2.91	4.84	5.55	8.15	8.28	8.18	8.04	8.05	8.41
Fe	3.15	3.08	6.60	3.10	2.28	0.05	0.09	0.04	BDL	0.03	0.11
Ag	19.14	18.91	14.49	0.32	0.38	0.16	0.16	0.16	0.22	0.22	0.03
Te (ppm)	BDL	BDL	BDL	BDL	BDL	BDL	BDL	BDL	BDL	BDL	BDL
Pb	720	1000	1070	790	860	1040	1170	840	1190	700	960
Hg	BDL	BDL	BDL	BDL	BDL	BDL	BDL	BDL	BDL	BDL	BDL
Bi	BDL	BDL	BDL	BDL	BDL	BDL	BDL	BDL	BDL	BDL	BDL
Total	**100.75**	**100.67**	**101.27**	**99.40**	**99.72**	**100.90**	**100.64**	**100.94**	**100.07**	**99.54**	**100.23**
Cu (apfu)	6.92	6.96	7.75	10.26	10.07	10.38	10.24	10.33	10.09	10.14	10.36
S	13.00	13.00	13.00	13.00	13.00	13.00	13.00	13.00	13.00	13.00	13.00
Sb	3.89	4.04	3.08	1.28	1.93	2.17	2.15	2.17	2.30	2.27	0.76
As	0.16	0.06	0.71	2.71	2.13	1.84	1.82	1.80	1.72	1.70	3.19
Zn	1.09	1.10	0.77	1.16	1.35	2.00	2.02	1.99	1.97	1.98	1.97
Fe	1.02	1.00	2.05	0.87	0.65	0.02	0.03	0.01	0.00	0.01	0.03
Pb	0.01	0.01	0.01	0.01	0.01	0.01	0.01	0.01	0.01	0.01	0.01
Ag	3.20	3.18	2.33	0.05	0.06	0.02	0.02	0.02	0.03	0.03	0.00
Te	0.00	0.00	0.00	0.00	0.00	0.00	0.00	0.00	0.00	0.00	0.00
Hg	0.00	0.00	0.00	0.00	0.00	0.00	0.00	0.00	0.00	0.00	0.00
Bi	0.00	0.00	0.00	0.00	0.00	0.00	0.00	0.00	0.00	0.00	0.00
Total	**29.29**	**29.35**	**29.70**	**29.33**	**29.18**	**29.43**	**29.29**	**29.33**	**29.11**	**29.14**	**29.32**

Table A.2.5 cont. – Electron Microprobe Analyses for tetrahedrite

Drill hole	LM11-63	LM11-63	LM11-63	LM11-63	LM11-63
Sample	CNF29957	CNF29957	CNF29957	CNF29957	CNF29957
Depth (m)	210.83	210.83	210.83	210.83	210.83
Probe Analysis	RL3 tnn2	RL3 tnn3	RL6 tnn1	RL6 tnn2	RL6 tnn3
Date	2013-04-30	2013-04-30	2013-04-30	2013-04-30	2013-04-30
Type Mineralogy	Type 2A/2B	Type 2A/2B	Type 2A/2B	Type 2A/2B	Type 2A/2B
Cu (wt%)	42.93	42.81	42.74	42.79	42.77
S	27.01	27.09	27.08	27.11	26.94
Sb	5.94	5.98	5.77	5.77	5.79
As	15.64	15.55	15.66	15.82	15.92
Zn	8.32	8.31	8.27	8.56	8.38
Fe	0.13	0.14	0.18	0.21	0.07
Ag	0.03	0.04	0.03	0.04	0.03
Te (ppm)	BDL	BDL	BDL	BDL	BDL
Pb	1210	900	940	850	830
Hg	BDL	BDL	BDL	BDL	BDL
Bi	BDL	BDL	BDL	BDL	BDL
Total	**100.05**	**100.04**	**99.84**	**100.40**	**99.98**
Cu (apfu)	10.43	10.37	10.35	10.36	10.41
S	13.00	13.00	13.00	13.00	13.00
Sb	0.75	0.76	0.73	0.73	0.74
As	3.22	3.19	3.22	3.25	3.29
Zn	1.96	1.95	1.95	2.01	1.98
Fe	0.04	0.04	0.05	0.06	0.02
Pb	0.01	0.01	0.01	0.01	0.01
Ag	0.00	0.01	0.00	0.01	0.00
Te	0.00	0.00	0.00	0.00	0.00
Hg	0.00	0.00	0.00	0.00	0.00
Bi	0.00	0.00	0.00	0.00	0.00
Total	**29.42**	**29.33**	**29.31**	**29.41**	**29.45**

Table A.2.6 – Electron Microprobe Analyses for bornite

Drill hole	LM11-61	LM11-61	LM11-61	LM11-61	LM11-61	LM11-61	LM13-73
Sample	CNF25151	CNF25151	CNF25151	CNF25151	CNF25151	CNF25151	CNF14299
Depth (m)	222.4	222.4	222.4	222.4	222.4	222.4	327.95
Probe Analysis	RL1 Bn1	RL1 Bn2	RL1 Bn3	RL5 Bn1	RL5 Bn2	RL5 Bn3	RL4 Bn2
Date	2013-10-06	2013-10-06	2013-10-06	2013-10-06	2013-10-06	2013-10-06	2013-10-06
Type Mineralogy	Type 2A	Type 2A	Type 2A	Type 2A	Type 2A	Type 2A	Type 2A
Cu (wt%)	62.30	62.43	62.33	62.16	61.80	61.55	61.78
S	25.99	25.83	25.74	25.63	25.76	25.97	25.65
Fe	11.52	11.30	11.24	11.32	11.57	11.31	11.30
Zn (ppm)	500	420	710	320	450	900	600
Ag	5870	5640	5540	6450	6880	11130	1840
Pb	BDL	BDL	BDL	BDL	BDL	BDL	BDL
Sb	BDL	BDL	BDL	BDL	BDL	BDL	BDL
As	BDL	BDL	BDL	BDL	BDL	BDL	BDL
Hg	BDL	BDL	BDL	BDL	BDL	BDL	BDL
Te	BDL	BDL	BDL	BDL	BDL	BDL	BDL
Bi	BDL	BDL	BDL	BDL	BDL	BDL	BDL
Ni	BDL	BDL	BDL	BDL	BDL	BDL	BDL
Total	**100.41**	**100.22**	**99.98**	**99.82**	**99.99**	**100.15**	**99.01**
Cu (apfu)	4.84	4.88	4.89	4.89	4.84	4.78	4.86
S	4.00	4.00	4.00	4.00	4.00	4.00	4.00
Fe	1.02	1.00	1.00	1.01	1.03	1.00	1.01
Zn	0.00	0.00	0.01	0.00	0.00	0.01	0.00
Ag	0.03	0.03	0.03	0.03	0.03	0.05	0.01
Pb	0.00	0.00	0.00	0.00	0.00	0.00	0.00
Sb	0.00	0.00	0.00	0.00	0.00	0.00	0.00
As	0.00	0.00	0.00	0.00	0.00	0.00	0.00
Hg	0.00	0.00	0.00	0.00	0.00	0.00	0.00
Te	0.00	0.00	0.00	0.00	0.00	0.00	0.00
Bi	0.00	0.00	0.00	0.00	0.00	0.00	0.00
Ni	0.00	0.00	0.00	0.00	0.00	0.00	0.00
Total	**9.89**	**9.91**	**9.92**	**9.94**	**9.91**	**9.84**	**9.89**

Table A.2.6 cont. – Electron Microprobe Analyses for bornite

Drill hole	LM11-59	LM07-17	LM07-17	LM07-17	LM07-17	LM07-17	LM07-17	LM08-33	LM08-33	LM08-33	LM08-33
Sample	CNF29960	CNF29967	CNF29967	CNF29967	CNF29967	CNF29967	CNF29967	CNF14279	CNF14279	CNF14279	CNF14279
Depth (m)	216	247.63	247.63	247.63	247.63	247.63	247.63	230.75	230.75	230.75	230.75
Probe Analysis	RL10 bn1	RL3b bn1	RL3b bn2	RL3b bn3	RL10 bn1	RL10 bn2	RL10 bn3	RL7 bn1	RL7 bn2	RL7 bn3	RL9 bn1
Date	2013-04-30	2013-04-30	2013-04-30	2013-04-30	2013-04-30	2013-04-30	2013-04-30	2013-04-30	2013-04-30	2013-04-30	2013-04-30
Type Mineralogy	Type 2A	Type 2A	Type 2A	Type 2A	Type 2A	Type 2A	Type 2A	Type 2A	Type 2A	Type 2A	Type 2A
Cu (wt%)	61.54	61.91	62.06	62.27	61.60	61.36	60.85	62.40	62.00	63.06	62.61
S	25.43	25.49	25.23	25.35	25.61	25.88	25.72	25.62	25.26	25.64	25.27
Fe	11.04	11.51	11.49	11.38	11.31	11.00	11.07	11.48	11.35	11.43	11.26
Zn (ppm)	1030	1170	980	490	8860	13100	13220	640	750	770	620
Ag	4240	13780	12620	12440	7890	8330	7410	14720	13850	6630	5460
Pb	1280	1130	720	790	620	990	1070	900	950	890	980
Sb	BDL	BDL	BDL	BDL	BDL	BDL	BDL	BDL	BDL	BDL	BDL
As	BDL	BDL	BDL	BDL	BDL	BDL	BDL	BDL	BDL	BDL	BDL
Hg	BDL	BDL	BDL	BDL	BDL	BDL	BDL	BDL	BDL	BDL	BDL
Te	BDL	BDL	BDL	BDL	BDL	BDL	BDL	BDL	BDL	BDL	BDL
Bi	BDL	BDL	BDL	BDL	BDL	BDL	BDL	BDL	BDL	BDL	BDL
Total	**98.72**	**100.49**	**100.22**	**100.32**	**100.27**	**100.51**	**99.80**	**101.14**	**100.19**	**101.08**	**99.90**
Cu (apfu)	4.88	4.90	4.97	4.96	4.85	4.79	4.78	4.92	4.96	4.96	5.00
S	4.00	4.00	4.00	4.00	4.00	4.00	4.00	4.00	4.00	4.00	4.00
Fe	1.00	1.04	1.05	1.03	1.01	0.98	0.99	1.03	1.03	1.02	1.02
Zn	0.01	0.01	0.01	0.00	0.07	0.10	0.10	0.00	0.01	0.01	0.00
Ag	0.02	0.06	0.06	0.06	0.04	0.04	0.03	0.07	0.07	0.03	0.03
Pb	0.00	0.00	0.00	0.00	0.00	0.00	0.00	0.00	0.00	0.00	0.00
Sb	0.00	0.00	0.00	0.00	0.00	0.00	0.00	0.00	0.00	0.00	0.00
As	0.00	0.00	0.00	0.00	0.00	0.00	0.00	0.00	0.00	0.00	0.00
Hg	0.00	0.00	0.00	0.00	0.00	0.00	0.00	0.00	0.00	0.00	0.00
Te	0.00	0.00	0.00	0.00	0.00	0.00	0.00	0.00	0.00	0.00	0.00
Bi	0.00	0.00	0.00	0.00	0.00	0.00	0.00	0.00	0.00	0.00	0.00
Total	**9.91**	**10.02**	**10.08**	**10.06**	**9.98**	**9.90**	**9.90**	**10.02**	**10.06**	**10.03**	**10.06**

Table A.2.6 cont. – Electron Microprobe Analyses for bornite

Drill hole	LM08-33	LM08-33	LM11-63	LM11-63	LM11-63
Sample	CNF14279	CNF14279	CNF29957	CNF29957	CNF29957
Depth (m)	230.75	230.75	210.83	210.83	210.83
Probe Analysis	RL9 bn2	RL9 bn3	RL6 bn1	RL6 bn2	RL6 bn3
Date	2013-04-30	2013-04-30	2013-04-30	2013-04-30	2013-04-30
Type Mineralogy	Type 2A	Type 2A	Type 2A	Type 2A	Type 2A
Cu (wt%)	62.96	62.49	63.70	63.54	63.60
S	25.33	25.68	25.71	25.63	25.39
Fe	11.26	11.18	11.43	11.29	11.37
Zn (ppm)	BDL	410	520	520	BDL
Ag	4540	4960	2040	1840	1720
Pb	1220	980	1020	700	940
Sb	BDL	BDL	BDL	BDL	BDL
As	BDL	BDL	BDL	BDL	BDL
Hg	BDL	BDL	BDL	BDL	BDL
Te	BDL	BDL	BDL	BDL	BDL
Bi	BDL	BDL	BDL	BDL	BDL
Total	**100.16**	**100.08**	**101.21**	**100.87**	**100.67**
Cu (apfu)	5.02	4.91	5.00	5.00	5.06
S	4.00	4.00	4.00	4.00	4.00
Fe	1.02	1.00	1.02	1.01	1.03
Zn	0.00	0.00	0.00	0.00	0.00
Ag	0.02	0.02	0.01	0.01	0.01
Pb	0.00	0.00	0.00	0.00	0.00
Sb	0.00	0.00	0.00	0.00	0.00
As	0.00	0.00	0.00	0.00	0.00
Hg	0.00	0.00	0.00	0.00	0.00
Te	0.00	0.00	0.00	0.00	0.00
Bi	0.00	0.00	0.00	0.00	0.00
Total	**10.06**	**9.94**	**10.04**	**10.03**	**10.10**

Table A.2.7 – Electron Microprobe Analyses for colusite

Drill hole	LM11-52	LM11-52	LM11-52	LM11-52	LM11-52	LM11-52	LM11-52	LM11-52	LM13-73	LM13-73
Sample	CNF25121	CNF25121	CNF25121	CNF25121	CNF25121	CNF25121	CNF25121	CNF25121	CNF14299	CNF14299
Depth (m)	212.3	212.3	212.3	212.3	212.3	212.3	212.3	212.3	327.95	327.95
Probe Analysis	RL3 col1	RL3 col2	RL3 col3	RL4 col1	RL4 col2	RL4 col3	RL5 col1	RL5 col2	RL6 col1	RL6 col2
Date	2013-10-07	2013-10-07	2013-10-07	2013-10-07	2013-10-07	2013-10-07	2013-10-07	2013-10-07	2013-10-07	2013-10-07
Type Mineralogy	Type 2B	Type 2B	Type 2B	Type 2B	Type 2B	Type 2B	Type 2B	Type 2B	Type 2B	Type 2B
Cu (wt%)	42.88	42.72	42.55	43.08	42.95	43.04	41.80	41.90	50.60	50.39
S	31.97	31.98	31.77	31.99	32.14	32.02	32.35	31.92	32.11	32.25
V	3.18	3.18	3.14	3.21	3.20	3.20	3.12	3.05	3.17	3.23
Ge	11.40	11.56	11.40	11.45	11.48	11.50	11.63	11.47	3.38	3.47
As (ppm)	4440	4060	4250	4560	4470	4260	3790	4470	91700	92180
Fe	28840	29010	29040	29550	30200	29990	34560	38810	7910	5690
Zn	57000	61510	62840	60160	58320	58860	72680	66680	370	330
Sn	2280	2420	2910	1370	1380	1250	1680	3220	770	730
Sb	BDL	BDL	BDL	BDL	BDL	BDL	370	630	7800	7730
Ag	BDL	BDL	BDL	BDL	BDL	BDL	BDL	BDL	BDL	BDL
Total	**98.69**	**99.17**	**98.78**	**99.15**	**99.07**	**99.12**	**100.20**	**99.72**	**100.10**	**100.02**
Cu (apfu)	21.66	21.57	21.63	21.75	21.58	21.70	20.86	21.20	25.45	25.23
S	32.00	32.00	32.00	32.00	32.00	32.00	32.00	32.00	32.00	32.00
V	2.00	2.00	1.99	2.02	2.00	2.01	1.94	1.92	1.99	2.02
Ge	5.04	5.11	5.07	5.06	5.05	5.08	5.08	5.08	1.49	1.52
As	0.19	0.17	0.18	0.20	0.19	0.18	0.16	0.19	3.91	3.91
Fe	1.66	1.67	1.68	1.70	1.73	1.72	1.96	2.23	0.45	0.32
Zn	2.80	3.02	3.10	2.95	2.85	2.88	3.53	3.28	0.02	0.02
Sn	0.06	0.07	0.08	0.04	0.04	0.03	0.04	0.09	0.02	0.02
Sb	0.00	0.00	0.00	0.00	0.00	0.00	0.01	0.02	0.20	0.20
Ag	0.00	0.00	0.00	0.00	0.00	0.00	0.00	0.00	0.00	0.00
Total	**65.41**	**65.61**	**65.74**	**65.71**	**65.44**	**65.61**	**65.59**	**66.01**	**65.53**	**65.25**

Table A.2.7 cont. – Electron Microprobe Analyses for colusite

Drill hole	LM13-73	LM13-73	LM13-73	LM13-73
Sample	CNF14299	CNF14299	CNF14299	CNF14299
Depth (m)	327.95	327.95	327.95	327.95
Probe Analysis	RL6 col3	RL5 col1	RL5 col2	RL5 col3
Date	2013-10-07	2013-10-07	2013-10-07	2013-10-07
Type Mineralogy	Type 2B	Type 2B	Type 2B	Type 2B
Cu (wt%)	50.30	51.20	51.11	50.81
S	31.97	32.30	32.03	31.87
V	3.17	3.28	3.22	3.23
Ge	3.61	3.63	3.71	3.74
As (ppm)	89670	89170	90360	87940
Fe	9950	2870	4510	2980
Zn	490	450	590	270
Sn	490	550	500	430
Sb	7990	8240	8250	7940
Ag	BDL	BDL	BDL	430
Total	**99.92**	**100.53**	**100.49**	**99.65**
Cu (apfu)	25.41	25.60	25.77	25.74
S	32.00	32.00	32.00	32.00
V	2.00	2.04	2.03	2.04
Ge	1.60	1.59	1.64	1.66
As	3.84	3.78	3.86	3.78
Fe	0.57	0.16	0.26	0.17
Zn	0.02	0.02	0.03	0.01
Sn	0.01	0.01	0.01	0.01
Sb	0.21	0.22	0.22	0.21
Ag	0.00	0.00	0.00	0.01
Total	**65.66**	**65.43**	**65.82**	**65.64**

Table A.2.7 cont. – Electron Microprobe Analyses for colusite

Drill hole	LM08-33	LM08-33	LM11-63	LM11-63	LM11-63	LM07-14	LM07-14	LM07-14	LM07-14	LM07-14
Sample	CNF14279	CNF14279	CNF29957	CNF29957	CNF29957	CNF14259	CNF14259	CNF14259	CNF14259	CNF14259
Depth (m)	230.75	230.75	210.83	210.83	210.83	204.44	204.44	204.44	204.44	204.44
Probe Analysis	RL9 col2	RL9 col3	RL6 col1	RL6 col2	RL6 col3	RL6b col1	RL6b col2	RL6b col3	RL6b col4	RL6c col1
Date	2013-05-21	2013-05-21	2013-05-21	2013-05-21	2013-05-21	2013-05-21	2013-05-21	2013-05-21	2013-05-21	2013-05-21
Type Mineralogy	Type 2B	Type 2B	Type 2B	Type 2B	Type 2B	Type 2B	Type 2B	Type 2B	Type 2B	Type 2B
Cu (wt%)	50.21	49.70	50.51	49.82	49.96	44.77	45.49	46.62	45.66	45.59
S	31.62	31.47	31.77	31.58	31.75	31.72	31.73	31.55	31.82	31.71
V	3.17	3.16	3.13	3.21	3.15	3.19	3.18	3.21	3.20	3.20
Ge	3.98	4.13	4.60	4.62	4.65	10.61	9.93	8.49	9.41	10.96
As (ppm)	80700	80400	83200	81200	81200	16900	24200	36800	28200	20700
Fe	767	1162	3577	BDL	BDL	14100	12800	15400	13900	5938
Zn	445	574	7103	5863	8568	47700	41700	31300	39200	54100
Sn	264	BDL	3440	3070	3317	BDL	BDL	290	336	BDL
Sb	19500	17000	4160	4313	4121	6635	8668	12100	8427	4492
Ag	331	1538	443	BDL	BDL	BDL	BDL	BDL	BDL	BDL
Au	BDL	BDL	BDL	BDL	BDL	BDL	BDL	BDL	BDL	BDL
Total	**99.18**	**98.56**	**100.22**	**98.69**	**99.24**	**98.85**	**99.09**	**99.46**	**99.10**	**99.98**
Cu (apfu)	25.64	25.50	25.67	25.48	25.41	22.79	23.15	23.86	23.17	23.22
S	32.00	32.00	32.00	32.00	32.00	32.00	32.00	32.00	32.00	32.00
V	2.02	2.02	1.98	2.05	2.00	2.03	2.02	2.05	2.03	2.03
Ge	1.78	1.85	2.05	2.07	2.07	4.73	4.42	3.80	4.18	4.89
As	3.50	3.50	3.59	3.52	3.50	0.73	1.04	1.60	1.21	0.89
Fe	0.04	0.07	0.21	0.00	0.00	0.82	0.74	0.90	0.80	0.34
Zn	0.02	0.03	0.35	0.29	0.42	2.36	2.06	1.56	1.93	2.68
Sn	0.01	0.00	0.09	0.08	0.09	0.00	0.00	0.01	0.01	0.00
Sb	0.52	0.46	0.11	0.12	0.11	0.18	0.23	0.32	0.22	0.12
Ag	0.01	0.05	0.01	0.00	0.00	0.00	0.00	0.00	0.00	0.00
Au	0.00	0.00	0.00	0.00	0.00	0.00	0.00	0.00	0.00	0.00
Total	**65.54**	**65.48**	**66.07**	**65.60**	**65.61**	**65.63**	**65.67**	**66.10**	**65.56**	**66.17**

Table A.2.8 – Electron Microprobe Analyses for sulvanite

Drill hole	LM08-33	LM08-33	LM08-33	LM08-33
Sample	CNF14279	CNF14279	CNF14279	CNF14279
Depth (m)	230.75	230.75	230.75	230.75
Probe Analysis	RL10 col1	RL10 col2	RL10 col3	RL10 col4
Date	2013-05-21	2013-05-21	2013-05-21	2013-05-21
Type Mineralogy	Type 2B	Type 2B	Type 2B	Type 2B
Cu (wt%)	50.43	50.30	50.40	50.32
S	34.83	34.93	34.83	34.80
V	13.76	13.77	13.78	13.55
Fe (ppm)	13500	13800	14600	6732
Zn	3552	3403	3097	12500
Ag	727	401	644	651
Ge	BDL	BDL	BDL	BDL
As	BDL	BDL	BDL	BDL
Sb	BDL	BDL	BDL	BDL
Sn	BDL	BDL	BDL	BDL
Au	BDL	BDL	BDL	BDL
Total	**100.83**	**100.79**	**100.87**	**100.67**
Cu (apfu)	2.92	2.91	2.92	2.92
S	4.00	4.00	4.00	4.00
V	0.99	0.99	1.00	0.98
Fe	0.09	0.09	0.10	0.04
Zn	0.02	0.02	0.02	0.07
Ag	0.00	0.00	0.00	0.00
Ge	0.00	0.00	0.00	0.00
As	0.00	0.00	0.00	0.00
Sb	0.00	0.00	0.00	0.00
Sn	0.00	0.00	0.00	0.00
Au	0.00	0.00	0.00	0.00
Total	**8.03**	**8.01**	**8.03**	**8.02**

Table A.2.9 – Electron Microprobe Analyses for reinerite

Drill hole	LM07-14
Sample	CNF14259
Depth (m)	204.44
Probe Analysis	RL2b col3
Date	2013-05-21
Type Mineralogy	Type 2B
Cu (wt%)	45.23
S	31.01
Fe	12.73
Ge	8.29
Zn (ppm)	5428
As	1052
V	BDL
Sb	BDL
Sn	BDL
Ag	BDL
Au	BDL
Total	**97.92**
Cu (apfu)	23.55
S	32.00
Fe	7.54
Zn	0.27
Ge	3.78
As	0.05
V	0.00
Sb	0.00
Sn	0.00
Ag	0.00
Au	0.00
Total	**67.20**

Table A.2.10 – Electron Microprobe Analyses for electrum

Drill hole	LM11-52	LM11-52	LM11-52	LM11-52	LM11-52	LM11-52	LM11-52
Sample	CNF25121	CNF25121	CNF25121	CNF25121	CNF25121	CNF25121	CNF25121
Depth (m)	212.3	212.3	212.3	212.3	212.3	212.3	212.3
Probe Analysis	RL1 elec1	RL1 elec2	RL1 elec3	RL1 elec4	RL2 elec1	RL2 elec2	RL2 elec3
Date	2013-10-05	2013-10-05	2013-10-05	2013-10-05	2013-10-05	2013-10-05	2013-10-05
Type Mineralogy	Type 2B	Type 2B	Type 2B	Type 2B	Type 2B	Type 2B	Type 2B
Au (wt%)	82.72	83.64	81.17	83.66	86.18	85.75	86.36
Ag	13.56	12.17	12.75	12.47	11.10	11.01	10.97
S (ppm)	2030	2020	2900	1290	2020	1850	2070
Fe	320	450	370	BDL	280	480	690
Cu	8030	7580	6400	5250	8990	10900	12840
Hg	BDL	BDL	BDL	BDL	1530	BDL	BDL
As	370	320	580	290	510	440	470
Sb	BDL	320	BDL	320	BDL	BDL	380
Pb	BDL	BDL	BDL	BDL	BDL	1190	BDL
Total	**97.492**	**96.921**	**95.089**	**96.969**	**98.70**	**98.36**	**99.14**
Au/(Au+Ag)	**0.77**	**0.79**	**0.78**	**0.79**	**0.81**	**0.81**	**0.81**

Table A.2.10 cont. – Electron Microprobe Analyses for electrum

Drill hole	LM08-19	LM08-19	LM08-19	LM08-19	LM08-19
Sample	CNF29986	CNF29986	CNF29986	CNF29986	CNF29986
Depth (m)	97.63	97.63	97.63	97.63	97.63
Probe Analysis	RL7 elec1	RL7 elec2	RL7 elec3	RL7 elec4	MLA tag 54411 elec1
Date	2013-05-24	2013-05-24	2013-05-24	2013-05-24	2013-05-24
Type Mineralogy	Type 2B	Type 2B	Type 2B	Type 2B	Type 2B
Au (wt%)	58.27	57.76	58.81	57.26	63.77
Ag	39.86	39.83	41.19	40.62	34.50
S (ppm)	1490	1999	1556	1421	19800
Fe	3886	5168	4517	5764	842
Cu	673	353	371	1116	3452
Hg	2699	2210	2523	3142	1732
As	BDL	BDL	BDL	BDL	BDL
Sb	BDL	BDL	BDL	BDL	BDL
Total	**99.00**	**98.56**	**100.90**	**99.04**	**100.85**
Au/(Au+Ag)	**0.44**	**0.44**	**0.44**	**0.44**	**0.50**

Table A.2.10 cont. – Electron Microprobe Analyses for electrum

Drill hole	LM11-65	LM11-65
Sample	CNF14291	CNF14291
Depth (m)	159.3	159.3
Probe Analysis	RL7 elec1	RL7 elec2
Date	2013-05-03	2013-05-03
Type Mineralogy	Type 2B	Type 2B
Au	76.21	78.95
Ag	19.68	20.80
S (ppm)	1210	1040
Fe	960	1350
Zn	13020	11840
Cu	BDL	BDL
Hg	BDL	BDL
As	BDL	BDL
Sb	BDL	BDL
Total	**97.24**	**101.07**
Au/(Au+Ag)	**0.68**	**0.68**

Table A.2.11 – Electron Microprobe Analyses for stromeyerite

Drill hole	LM11-61	LM11-61	LM11-61	LM11-61	LM11-61	LM11-61
Sample	CNF25151	CNF25151	CNF25151	CNF25151	CNF25151	CNF25151
Depth (m)	222.4	222.4	222.4	222.4	222.4	222.4
Probe Analysis	RL1 Ag1	RL5 Ag1	RL5 Ag2	RL8 Ag2	RL8 Ag4	RL1 Ag2
Date	2013-10-06	2013-10-06	2013-10-06	2013-10-06	2013-10-06	2013-10-06
Type Mineralogy	Type 2A	Type 2A	Type 2A	Type 2A	Type 2A	Type 2B
Cu (wt%)	26.05	24.74	26.63	38.00	36.66	31.15
S	14.17	18.53	18.34	17.22	17.06	18.83
Ag	56.72	54.76	52.60	45.38	42.99	49.50
Fe (ppm)	11660	BDL	1300	490	2330	9810
Zn	340	380	790	350	570	380
Pb	3630	5100	7520	8050	8360	5160
As	BDL	BDL	BDL	BDL	370	BDL
Sb	BDL	BDL	BDL	BDL	BDL	BDL
Te	1540	1010	980	1020	810	930
Hg	BDL	BDL	BDL	BDL	BDL	BDL
Bi	BDL	BDL	BDL	BDL	BDL	BDL
Ni	BDL	BDL	BDL	BDL	BDL	BDL
Total	**98.69**	**98.76**	**98.70**	**101.58**	**98.01**	**101.19**
Cu (apfu)	0.93	0.67	0.73	1.11	1.08	0.83
S	1.00	1.00	1.00	1.00	1.00	1.00
Ag	1.19	0.88	0.85	0.78	0.75	0.78
Fe	0.05	0.00	0.00	0.00	0.01	0.03
Zn	0.00	0.00	0.00	0.00	0.00	0.00
Pb	0.00	0.00	0.01	0.01	0.01	0.00
As	0.00	0.00	0.00	0.00	0.00	0.00
Sb	0.00	0.00	0.00	0.00	0.00	0.00
Te	0.00	0.00	0.00	0.00	0.00	0.00
Hg	0.00	0.00	0.00	0.00	0.00	0.00
Bi	0.00	0.00	0.00	0.00	0.00	0.00
Ni	0.00	0.00	0.00	0.00	0.00	0.00
Total	**3.17**	**2.56**	**2.60**	**2.91**	**2.85**	**2.65**

Table A.2.11 cont. – Electron Microprobe Analyses for stromeyerite

Drill hole	LM07-17	LM07-17	LM08-33	LM08-33	LM08-33
Sample	CNF29967	CNF29967	CNF14279	CNF14279	CNF14279
Depth (m)	247.63	247.63	230.75	230.75	230.75
Probe Analysis	RL3b stm1	RL3b stm2	RL7 stm1	RL7 stm2	RL7 stm3
Date	2013-04-30	2013-04-30	2013-04-30	2013-04-30	2013-04-30
Type Mineralogy	Type 2A	Type 2A	Type 2A	Type 2A	Type 2A
Cu (wt%)	27.43	27.39	36.58	33.10	34.86
S	14.48	14.84	16.26	15.31	17.57
Ag	58.55	57.79	44.57	49.67	45.95
Fe (ppm)	1940	5260	2110	580	970
Zn	BDL	BDL	950	1210	530
Pb	630	530	17140	9160	9870
As	BDL	BDL	BDL	BDL	BDL
Sb	BDL	BDL	BDL	BDL	BDL
Te	1100	1050	1140	1280	1300
Hg	BDL	BDL	BDL	BDL	BDL
Bi	BDL	2030	BDL	BDL	1860
Total	**100.94**	**100.88**	**99.61**	**99.33**	**99.80**
Cu (apfu)	0.96	0.93	1.13	1.09	1.00
S	1.00	1.00	1.00	1.00	1.00
Ag	1.20	1.16	0.81	0.96	0.78
Fe	0.01	0.02	0.01	0.00	0.00
Zn	0.00	0.00	0.00	0.00	0.00
Pb	0.00	0.00	0.02	0.01	0.01
As	0.00	0.00	0.00	0.00	0.00
Sb	0.00	0.00	0.00	0.00	0.00
Te	0.00	0.00	0.00	0.00	0.00
Hg	0.00	0.00	0.00	0.00	0.00
Bi	0.00	0.00	0.00	0.00	0.00
Total	**3.17**	**3.11**	**2.98**	**3.07**	**2.80**

Table A.2.12 – Electron Microprobe Analyses for polybasite

Drill hole	LM08-19
Sample	CNF29986
Depth (m)	97.63
Probe Analysis	RL7 stm2
Date	2013-04-30
Type Mineralogy	Type 2B
Cu (wt%)	6.05
Ag	66.05
S	16.40
Fe (ppm)	17370
Zn	BDL
Pb	810
Te	1910
As	25410
Sb	67100
Hg	BDL
Bi	BDL
Total	**99.89**
Cu (apfu)	2.05
Ag	13.17
S	11.00
Fe	0.67
Zn	0.00
Pb	0.01
Te	0.03
As	0.73
Sb	1.19
Hg	0.00
Bi	0.00
Total	**28.84**

Table A.2.13 – Electron Microprobe Analyses for miargyrite

Drill hole	LM13-74	LM13-74
Sample	CNF25109	CNF25109
Depth (m)	328.55	328.55
Probe Analysis	RL7 Tnn2	RL7 Tnn3
Date	2013-10-06	2013-10-06
Type Mineralogy	Type 2B	Type 2B
Sb (wt%)	40.97	41.09
Ag	35.14	35.42
S	21.66	21.45
Cu (ppm)	600	BDL
Fe	1000	1900
Zn	BDL	BDL
Pb	13300	3300
As	700	1000
Te	600	600
Hg	BDL	BDL
Bi	BDL	BDL
Ni	BDL	BDL
Total	**99.44**	**98.64**
Sb (apfu)	1.00	1.01
Ag	0.96	0.98
S	2.00	2.00
Cu	0.00	0.00
Fe	0.01	0.01
Zn	0.00	0.00
Pb	0.02	0.00
As	0.00	0.00
Te	0.00	0.00
Hg	0.00	0.00
Bi	0.00	0.00
Ni	0.00	0.00
Total	**3.99**	**4.01**

Table A.2.14 – Electron Microprobe Analyses for bournonite

Drill hole	LM11-65	LM11-65	LM11-65	LM11-65	LM11-65	LM11-65	LM11-65
Sample	CNF14291	CNF14291	CNF14291	CNF14291	CNF14291	CNF14291	CNF14291
Depth (m)	159.3	159.3	159.3	159.3	159.3	159.3	159.3
Probe Analysis	RL6 bnn1	RL6 bnn2	RL6 bnn3	RL9 bnn1	RL9 bnn2	RL9 bnn3	RL9 bnn4
Date	2013-04-30	2013-04-30	2013-04-30	2013-04-30	2013-04-30	2013-04-30	2013-04-30
Type Mineralogy	Type 2B	Type 2B	Type 2B	Type 2B	Type 2B	Type 2B	Type 2B
Pb (wt%)	42.87	43.11	42.61	42.92	42.57	42.46	42.63
Sb	24.39	24.69	24.55	23.92	24.66	24.09	24.31
S	19.63	19.59	19.66	19.23	19.88	19.52	19.66
Cu	13.49	13.44	13.49	13.51	13.57	13.54	13.42
Zn (ppm)	800	670	BDL	1330	1050	2720	2000
As	2470	720	BDL	2650	2820	2710	3460
Fe	BDL	BDL	BDL	BDL	BDL	BDL	BDL
Ag	BDL	BDL	BDL	BDL	BDL	BDL	BDL
Te	BDL	BDL	BDL	BDL	BDL	BDL	BDL
Hg	BDL	BDL	BDL	BDL	BDL	BDL	BDL
Bi	BDL	BDL	BDL	BDL	BDL	BDL	BDL
Total	**100.77**	**101.12**	**100.45**	**100.16**	**101.13**	**100.28**	**100.50**
Pb (apfu)	1.01	1.02	1.01	1.04	0.99	1.01	1.01
Sb	0.98	1.00	0.99	0.98	0.98	0.98	0.98
S	3.00	3.00	3.00	3.00	3.00	3.00	3.00
Cu	1.04	1.04	1.04	1.06	1.03	1.05	1.03
Zn	0.01	0.01	0.00	0.01	0.01	0.02	0.01
As	0.02	0.00	0.00	0.02	0.02	0.02	0.02
Fe	0.00	0.00	0.00	0.00	0.00	0.00	0.00
Ag	0.00	0.00	0.00	0.00	0.00	0.00	0.00
Te	0.00	0.00	0.00	0.00	0.00	0.00	0.00
Hg	0.00	0.00	0.00	0.00	0.00	0.00	0.00
Bi	0.00	0.00	0.00	0.00	0.00	0.00	0.00
Total	**6.06**	**6.07**	**6.03**	**6.11**	**6.03**	**6.07**	**6.06**

Table A.2.15 – Electron Microprobe Analyses for unknowns

Mineral type	Cu-Ag-S		
Drill hole	LM11-61	LM11-61	LM11-61
Sample	CNF25151	CNF25151	CNF25151
Depth (m)	222.4	222.4	222.4
Probe Analysis	RL5 Ag1	RL5 Ag2	RL5 Ag4
Date	2013-10-06	2013-10-06	2013-10-06
Type Mineralogy	Type 2A	Type 2A	Type 2A
Cu (wt%)	24.74	26.63	55.26
S	18.53	18.34	20.62
Ag	54.76	52.60	23.23
Fe (ppm)	BDL	1300	5650
Zn	380	790	1170
Pb	5100	7520	13540
As	BDL	BDL	BDL
Sb	BDL	BDL	BDL
Te	1010	980	470
Hg	BDL	BDL	BDL
Bi	BDL	BDL	BDL
Ni	BDL	BDL	BDL
Total	**98.76**	**98.70**	**101.29**

Mineral type	Ag-Te
Drill hole	LM13-74
Sample	CNF25109
Depth (m)	328.55
Probe Analysis	RL7 Ag2
Date	2013-10-06
Type Mineralogy	Type 2B
Te (wt%)	34.11
S	4.31
Ag	50.90
Fe	4.36
Pb	4.96
Sb (ppm)	1950
Zn	BDL
Cu	BDL
As	BDL
Hg	BDL
Bi	BDL
Ni	BDL
Total	**98.85**

Mineral type	Ni-S	
Drill hole	LM13-73	LM13-73
Sample	CNF14299	CNF14299
Depth (m)	327.95	327.95
Probe Analysis	RL8 Ni1	RL8 Ni2
Date	2013-10-06	2013-10-06
Type Mineralogy	Type 2A	Type 2A
Ni (wt%)	52.53	53.23
S	40.92	41.41
Cu	2.05	2.07
Fe	1.30	1.10
Te (ppm)	BDL	260
Zn	BDL	BDL
Pb	BDL	BDL
As	BDL	BDL
Sb	BDL	BDL
Ag	BDL	BDL
Hg	BDL	BDL
Bi	BDL	BDL
Total	**96.66**	**97.85**

Table A.2.15 cont. – Electron Microprobe Analyses for unknowns

Mineral type	Unknown		
Drill hole	LM08-24	LM08-24	LM11-61
Sample	CNF29976	CNF29976	CNF25151
Depth (m)	279.8	279.8	222.4
Probe Analysis	RL1 Ag1	RL1 Ag3	RL8 Ag3
Date	2013-10-04	2013-10-04	2013-10-06
Type Mineralogy	Type 2B	Type 2B	Type 2A
Cu (wt%)	12.43	22.00	9.03
S	28.86	23.07	8.14
Ag	8.53	22.19	66.49
Sb	9.97	16.79	0.08
Zn	38.01	1.14	BDL
Fe	1.26	9.21	0.17
As	1.27	1.83	BDL
Te	BDL	3.53	15.41
Pb	BDL	0.52	BDL
Hg	BDL	BDL	BDL
Bi	BDL	BDL	BDL
Ni	BDL	BDL	BDL
Total	**100.48**	**100.29**	**99.26**

Mineral type	Cu-S
Drill hole	LM13-73
Sample	CNF14299
Depth (m)	327.95
Probe Analysis	RL4 col2
Date	2013-10-07
Type Mineralogy	Type 2B
Cu (wt%)	42.21
S	33.20
V	3.21
Ge	BDL
As (ppm)	BDL
Fe	196390
Zn	3580
Sn	BDL
Sb	BDL
Ag	BDL
Total	**98.58**

Table A.2.15 cont. – Electron Microprobe Analyses for unknowns

Mineral type	Cu-Ag-S	
Drill hole	LM08-33	LM08-33
Sample	CNF14279	CNF14279
Depth (m)	230.75	230.75
Probe Analysis	RL9 stm1	RL9 stm2
Date	2013-04-30	2013-04-30
Type Mineralogy	Type 2A	Type 2B
Cu (wt%)	51.81	46.77
S	22.49	32.18
Ag	24.94	20.59
Pb (ppm)	1011	1750
Fe	103	650
Zn	87	10940
Te	32	790
As	BDL	BDL
Sb	BDL	BDL
Hg	BDL	BDL
Bi	BDL	BDL
Total	**100.36**	**100.77**

Mineral type	Cu-V-Ge-S		
Drill hole	LM07-14	LM07-14	LM07-14
Sample	CNF14259	CNF14259	CNF14259
Depth (m)	204.44	204.44	204.44
Probe Analysis	RL6c col4	RL6c col5	RL6c col6
Date	2013-05-21	2013-05-21	2013-05-21
Type Mineralogy	Type 2B	Type 2B	Type 2B
Cu (wt %)	54.04	54.10	53.88
S	31.29	31.12	31.18
V	6.26	6.26	6.28
Ge	8.13	8.27	8.05
As (ppm)	BDL	1005	624
Fe	382	421	363
Zn	761	628	1056
Sn	BDL	BDL	BDL
Sb	BDL	BDL	BDL
Ag	BDL	BDL	BDL
Au	BDL	BDL	BDL
Total	**99.87**	**99.97**	**99.60**

Mineral type	Ag-Au-Hg-(S)
Drill hole	LM07-14
Sample	CNF14259
Depth (m)	204.44
Probe Analysis	MLA tag 33564 elec1
Date	2013-05-24
Type Mineralogy	Type 2B
Ag (wt%)	61.86
Au	21.32
Hg	11.98
S (ppm)	23000
Fe	5846
Cu	465
Sb	4279
As	BDL
Total	**98.95**

Table A.2.16 – Electron Microprobe Analyses for barite

Drill hole	LM10-46	LM10-46	LM10-46	LM10-46	LM10-46	LM11-52	LM11-52	LM11-52
Sample	CNF25146	CNF25146	CNF25146	CNF25146	CNF25146	CNF25121	CNF25121	CNF25121
Depth (m)	182.56	182.56	182.56	182.56	182.56	212.3	212.3	212.3
Probe Analysis	RL3 brt2	RL3 brt3	RL5 brt1	RL5 brt2	RL5 brt3	RL9 brt1	RL9 brt2	RL9 brt3
Date	2013-10-05	2013-10-05	2013-10-05	2013-10-05	2013-10-05	2013-10-07	2013-10-07	2013-10-07
Type Mineralogy	Type 1	Type 1	Type 1	Type 1	Type 1	Type 1	Type 1	Type 1
Barite Morphology	granular/interstitial	granular/interstitial	granular/interstitial	granular/interstitial	granular/interstitial	granular/interstitial	granular/interstitial	granular/interstitial
BaO (oxide wt%)	64.16	64.13	64.98	64.85	65.34	64.66	65.97	65.73
SO3	34.56	34.04	33.85	34.33	34.03	33.76	33.96	34.36
SrO (ppm)	12580	13700	3920	3620	2290	BDL	5060	9120
CaO	1440	1360	BDL	BDL	480	BDL	BDL	BDL
FeO	BDL	BDL	BDL	BDL	670	530	BDL	BDL
PbO	BDL	BDL	BDL	BDL	BDL	BDL	BDL	BDL
GeO2	BDL	BDL	BDL	BDL	BDL	BDL	BDL	BDL
Total	**100.09**	**99.62**	**99.19**	**99.54**	**99.72**	**98.53**	**100.47**	**101.04**
BaO (apfu)	0.97	0.98	1.00	0.99	1.00	1.00	1.01	0.99
SO3	1.00	0.99	1.00	1.00	1.00	1.00	0.99	1.00
SrO	0.03	0.03	0.01	0.01	0.01	0.00	0.01	0.02
CaO	0.01	0.01	0.00	0.00	0.00	0.00	0.00	0.00
FeO	0.00	0.00	0.00	0.00	0.00	0.00	0.00	0.00
PbO	0.00	0.00	0.00	0.00	0.00	0.00	0.00	0.00
GeO2	0.00	0.00	0.00	0.00	0.00	0.00	0.00	0.00
Total	**2.00**	**2.01**	**2.01**	**2.00**	**2.01**	**2.00**	**2.01**	**2.01**

Table A.2.16 cont. – Electron Microprobe Analyses for barite

Drill hole	LM11-52	LM11-52	LM11-52	LM13-73	LM13-73	LM13-73	LM13-73	LM13-73
Sample	CNF25121	CNF25121	CNF25121	CNF14299	CNF14299	CNF14299	CNF14299	CNF14299
Depth (m)	212.3	212.3	212.3	327.95	327.95	327.95	327.95	327.95
Probe Analysis	RL6b brt1	RL6b brt2	RL6b brt3	RL4 brt1	RL4 brt2	RL4 brt3	RL8 brt1	RL8 brt2
Date	2013-10-07	2013-10-07	2013-10-07	2013-10-07	2013-10-07	2013-10-07	2013-10-07	2013-10-07
Type Mineralogy	Type 1	Type 1	Type 1	Type 1	Type 1	Type 1	Type 1	Type 1
Barite Morphology	granular/interstitial	granular/interstitial	granular/interstitial	granular/interstitial	granular/interstitial	granular/interstitial	granular/interstitial	granular/interstitial
BaO (oxide wt%)	65.38	65.84	65.70	66.85	66.48	66.68	66.81	66.90
SO3	34.33	34.14	34.51	33.68	33.35	33.64	34.01	33.52
SrO (ppm)	11370	3890	9320	2420	1850	1920	820	830
CaO	BDL	BDL	BDL	880	380	360	490	670
FeO	BDL	BDL	BDL	540	BDL	BDL	2650	820
PbO	BDL	BDL	BDL	BDL	BDL	BDL	BDL	BDL
GeO2	BDL	BDL	BDL	BDL	BDL	BDL	BDL	BDL
Total	**100.84**	**100.35**	**101.12**	**100.87**	**100.05**	**100.49**	**101.21**	**100.65**
BaO (apfu)	0.99	1.00	0.99	1.02	1.03	1.02	1.02	1.03
SO3	1.00	1.00	1.00	0.99	0.99	0.99	0.99	0.99
SrO	0.03	0.01	0.02	0.01	0.00	0.00	0.00	0.00
CaO	0.00	0.00	0.00	0.00	0.00	0.00	0.00	0.00
FeO	0.00	0.00	0.00	0.00	0.00	0.00	0.01	0.00
PbO	0.00	0.00	0.00	0.00	0.00	0.00	0.00	0.00
GeO2	0.00	0.00	0.00	0.00	0.00	0.00	0.00	0.00
Total	**2.01**	**2.01**	**2.01**	**2.02**	**2.02**	**2.02**	**2.02**	**2.02**

Table A.2.16 cont. – Electron Microprobe Analyses for barite

Drill hole	LM13-73	LM11-61	LM11-61	LM11-61	LM11-61	LM11-61	LM11-61	LM13-74
Sample	CNF14299	CNF25152	CNF25152	CNF25152	CNF25152	CNF25152	CNF25152	CNF25109
Depth (m)	327.95	237.4	237.4	237.4	237.4	237.4	237.4	328.55
Probe Analysis	RL8 brt3	RL1 brt1	RL1 brt2	RL1 brt3	RL3 brt1	RL3 brt2	RL3 brt3	RL3 brt1
Date	2013-10-07	2013-10-07	2013-10-07	2013-10-07	2013-10-07	2013-10-07	2013-10-07	2013-10-07
Type Mineralogy	Type 1	Type 2B	Type 2B	Type 2B	Type 2B	Type 2B	Type 2B	Type 1
Barite Morphology	granular/interstitial	bladed/tabular	bladed/tabular	bladed/tabular	bladed/tabular	bladed/tabular	bladed/tabular	granular/interstitial
BaO (oxide wt%)	66.87	65.93	66.90	65.67	66.48	65.92	66.02	66.84
SO3	33.89	34.07	33.76	33.53	34.18	33.72	34.04	33.77
SrO (ppm)	780	7160	6050	7730	3950	7440	4970	3860
CaO	460	490	340	BDL	BDL	BDL	BDL	BDL
FeO	720	BDL	BDL	BDL	BDL	BDL	BDL	BDL
PbO	BDL	BDL	BDL	BDL	BDL	BDL	BDL	BDL
GeO2	BDL	BDL	BDL	BDL	BDL	BDL	BDL	BDL
Total	**100.94**	**100.78**	**101.31**	**99.94**	**101.02**	**100.41**	**100.58**	**101.05**
BaO (apfu)	1.02	1.00	1.02	1.01	1.01	1.01	1.01	1.02
SO3	0.99	0.99	0.99	0.99	0.99	0.99	0.99	0.99
SrO	0.00	0.02	0.01	0.02	0.01	0.02	0.01	0.01
CaO	0.00	0.00	0.00	0.00	0.00	0.00	0.00	0.00
FeO	0.00	0.00	0.00	0.00	0.00	0.00	0.00	0.00
PbO	0.00	0.00	0.00	0.00	0.00	0.00	0.00	0.00
GeO2	0.00	0.00	0.00	0.00	0.00	0.00	0.00	0.00
Total	**2.02**	**2.01**	**2.02**	**2.02**	**2.01**	**2.02**	**2.01**	**2.02**

Table A.2.16 cont. – Electron Microprobe Analyses for barite

Drill hole	LM13-74	LM13-74	LM13-74	LM13-74	LM13-74
Sample	CNF25109	CNF25109	CNF25109	CNF25109	CNF25109
Depth (m)	328.55	328.55	328.55	328.55	328.55
Probe Analysis	RL3 brt2	RL3 brt3	RL5 brt1	RL5 brt2	RL5 brt3
Date	2013-10-07	2013-10-07	2013-10-07	2013-10-07	2013-10-07
Type Mineralogy	Type 1	Type 1	Type 1	Type 1	Type 1
Barite Morphology	granular/interstitial	granular/interstitial	granular/interstitial	granular/interstitial	granular/interstitial
BaO (oxide wt%)	67.23	66.92	66.67	66.85	66.78
SO3	33.71	33.44	33.79	33.69	33.46
SrO (ppm)	3740	5530	4730	4160	3390
CaO	BDL	BDL	BDL	350	360
FeO	BDL	BDL	BDL	BDL	BDL
PbO	BDL	BDL	BDL	BDL	BDL
GeO2	BDL	BDL	BDL	BDL	BDL
Total	**101.39**	**100.99**	**100.90**	**101.01**	**100.62**
BaO (apfu)	1.03	1.03	1.02	1.02	1.03
SO3	0.99	0.99	0.99	0.99	0.99
SrO	0.01	0.01	0.01	0.01	0.01
CaO	0.00	0.00	0.00	0.00	0.00
FeO	0.00	0.00	0.00	0.00	0.00
PbO	0.00	0.00	0.00	0.00	0.00
GeO2	0.00	0.00	0.00	0.00	0.00
Total	**2.02**	**2.03**	**2.02**	**2.02**	**2.03**

Table A.2.16 cont. – Electron Microprobe Analyses for barite

Drill hole	LM08-33	LM08-33	LM08-33	LM08-33	LM11-63	LM11-63	LM11-63	LM11-63
Sample	CNF14279	CNF14279	CNF14279	CNF14279	CNF29957	CNF29957	CNF29957	CNF29957
Depth (m)	230.75	230.75	230.75	230.75	210.83	210.83	210.83	210.83
Probe Analysis	RL9 brt1	RL9 brt2	RL10 brt1	RL10 bt2	RL3 brt1	RL3 brt2	RL6 brt1	RL6 brt2
Date	2013-05-22	2013-05-22	2013-05-22	2013-05-22	2013-05-22	2013-05-22	2013-05-22	2013-05-22
Type Mineralogy	Type 1	Type 1	Type 1	Type 1	Type 1	Type 1	Type 1	Type 1
Barite Morphology	granular/interstitial	granular/interstitial	granular/interstitial	granular/interstitial	granular/interstitial	granular/interstitial	granular/interstitial	granular/interstitial
BaO (oxide wt%)	65.23	64.99	65.14	65.61	64.03	65.10	65.56	65.33
SO3	34.47	34.56	34.39	34.59	34.47	34.47	34.64	34.66
SrO (ppm)	6451	5302	5495	1374	6776	5878	5740	6063
CaO	601	BDL	BDL	BDL	BDL	BDL	195	BDL
FeO	BDL	BDL	556	BDL	BDL	BDL	BDL	BDL
PbO	BDL	BDL	209	BDL	BDL	BDL	BDL	BDL
TeO2	BDL	BDL	BDL	BDL	BDL	BDL	BDL	BDL
Ag2O	BDL	BDL	BDL	BDL	BDL	BDL	BDL	BDL
Au2O	BDL	BDL	BDL	BDL	BDL	BDL	BDL	BDL
Total	**100.44**	**100.13**	**100.16**	**100.35**	**99.19**	**100.17**	**100.81**	**100.66**
BaO (apfu)	0.99	0.98	0.99	0.99	0.97	0.99	0.99	0.98
SO3	1.00	1.00	1.00	1.00	1.00	1.00	1.00	1.00
SrO	0.01	0.01	0.01	0.00	0.02	0.01	0.01	0.01
CaO	0.00	0.00	0.00	0.00	0.00	0.00	0.00	0.00
FeO	0.00	0.00	0.00	0.00	0.00	0.00	0.00	0.00
PbO	0.00	0.00	0.00	0.00	0.00	0.00	0.00	0.00
TeO2	0.00	0.00	0.00	0.00	0.00	0.00	0.00	0.00
Ag2O	0.00	0.00	0.00	0.00	0.00	0.00	0.00	0.00
Au2O	0.00	0.00	0.00	0.00	0.00	0.00	0.00	0.00
Total	**2.00**	**2.00**	**2.00**	**2.00**	**1.99**	**2.00**	**2.00**	**2.00**

Table A.2.16 cont. – Electron Microprobe Analyses for barite

Drill hole	LM07-14	LM07-14	LM07-14	LM11-65	LM11-65	LM11-59	LM11-59	LM08-19
Sample	CNF14259	CNF14259	CNF14259	CNF14290	CNF14290	CNF29960	CNF29960	CNF29986
Depth (m)	204.44	204.44	204.44	158.66	158.66	216	216	97.63
Probe Analysis	RL2b brt1	RL6b brt1	RL6b brt2	RL5a brt1	RL5a brt3	RL10b brt1	RL10b brt2	RL8 brt1
Date	2013-05-22	2013-05-22	2013-05-22	2013-05-22	2013-05-22	2013-05-22	2013-05-22	2013-05-22
Type Mineralogy	Type 1	Type 1	Type 1	Type 1	Type 1	Type 1	Type 1	Type 1
Barite Morphology	granular/interstitial	granular/interstitial	granular/interstitial	granular/interstitial	granular/interstitial	granular/interstitial	granular/interstitial	granular/interstitial
BaO (oxide wt%)	65.33	65.85	66.78	66.07	64.73	65.02	65.69	65.12
SO3	34.62	34.35	34.40	34.67	35.28	34.35	34.49	34.75
SrO (ppm)	3116	2528	751	4119	6014	3487	3819	11535
CaO	BDL	BDL	BDL	1703	1070	246	BDL	339
FeO	BDL	BDL	BDL	722	900	2205	1984	BDL
PbO	BDL	347	BDL	BDL	BDL	BDL	BDL	171
TeO2	BDL	BDL	BDL	BDL	BDL	BDL	BDL	BDL
Ag2O	BDL	BDL	BDL	BDL	BDL	BDL	BDL	BDL
Au2O	BDL	BDL	BDL	BDL	BDL	BDL	BDL	BDL
Total	**100.27**	**100.49**	**101.29**	**101.39**	**100.81**	**99.96**	**100.79**	**101.09**
BaO (apfu)	0.99	1.00	1.01	0.99	0.96	0.99	0.99	0.98
SO3	1.00	1.00	1.00	1.00	1.00	1.00	1.00	1.00
SrO	0.01	0.01	0.00	0.01	0.01	0.01	0.01	0.03
CaO	0.00	0.00	0.00	0.01	0.00	0.00	0.00	0.00
FeO	0.00	0.00	0.00	0.00	0.01	0.01	0.01	0.00
PbO	0.00	0.00	0.00	0.00	0.00	0.00	0.00	0.00
TeO2	0.00	0.00	0.00	0.00	0.00	0.00	0.00	0.00
Ag2O	0.00	0.00	0.00	0.00	0.00	0.00	0.00	0.00
Au2O	0.00	0.00	0.00	0.00	0.00	0.00	0.00	0.00
Total	**2.00**	**2.00**	**2.01**	**2.01**	**1.99**	**2.01**	**2.01**	**2.00**

Table A.2.16 cont. – Electron Microprobe Analyses for barite

Drill hole	LM08-19	LM08-19	LM11-65	LM11-65	LM11-59	LM11-59	LM11-59	LM11-65
Sample	CNF29986	CNF29986	CNF14291	CNF14291	CNF29962	CNF29962	CNF29962	CNF14293
Depth (m)	97.63	97.63	159.3	159.3	225.95	225.95	225.95	161.75
Probe Analysis	RL8 brt2	RL8 brt3	RL9b brt1	RL9b brt2	RL6 brt1	RL6 brt2	RL6 brt3	RL6 brt1
Date	2013-05-22	2013-05-22	2013-05-22	2013-05-22	2013-05-22	2013-05-22	2013-05-22	2013-05-22
Type Mineralogy	Type 1	Type 1	Type 1	Type 1	Type 1	Type 1	Type 1	Type 1
Barite Morphology	granular/interstitial	granular/interstitial	granular/interstitial	granular/interstitial	granular/interstitial	granular/interstitial	granular/interstitial	granular/interstitial
BaO (oxide wt%)	64.65	64.72	63.56	65.45	65.16	65.98	65.34	66.24
SO3	34.66	34.52	34.80	34.60	34.30	34.32	34.55	34.36
SrO (ppm)	6238	8834	15700	9203	6253	6711	6155	2556
CaO	137	310	BDL	BDL	439	330	441	204
FeO	BDL	BDL	548	524	BDL	BDL	BDL	BDL
PbO	BDL	BDL	170	BDL	BDL	BDL	BDL	161
TeO2	BDL	BDL	BDL	BDL	BDL	BDL	BDL	BDL
Ag2O	BDL	BDL	BDL	BDL	BDL	BDL	BDL	BDL
Au2O	BDL	BDL	BDL	BDL	BDL	BDL	BDL	BDL
Total	**99.97**	**100.19**	**100.01**	**101.04**	**100.14**	**101.01**	**100.57**	**100.90**
BaO (apfu)	0.98	0.98	0.96	0.98	0.99	1.00	0.99	1.00
SO3	1.00	1.00	1.00	1.00	1.00	0.99	1.00	1.00
SrO	0.01	0.02	0.03	0.02	0.01	0.02	0.01	0.01
CaO	0.00	0.00	0.00	0.00	0.00	0.00	0.00	0.00
FeO	0.00	0.00	0.00	0.00	0.00	0.00	0.00	0.00
PbO	0.00	0.00	0.00	0.00	0.00	0.00	0.00	0.00
TeO2	0.00	0.00	0.00	0.00	0.00	0.00	0.00	0.00
Ag2O	0.00	0.00	0.00	0.00	0.00	0.00	0.00	0.00
Au2O	0.00	0.00	0.00	0.00	0.00	0.00	0.00	0.00
Total	**1.99**	**2.00**	**2.00**	**2.01**	**2.00**	**2.01**	**2.00**	**2.01**

Table A.2.16 cont. – Electron Microprobe Analyses for barite

Drill hole	LM11-65	LM11-65	LM11-65
Sample	CNF14293	CNF14293	CNF14293
Depth (m)	161.75	161.75	161.75
Probe Analysis	RL6 brt2	RL12 brt1	RL12 brt2
Date	2013-05-22	2013-05-22	2013-05-22
Type Mineralogy	Type 1	Type 1	Type 1
Barite Morphology	granular/interstitial	granular/interstitial	granular/interstitial
BaO (oxide wt%)	66.40	65.64	65.68
SO3	34.00	34.38	34.02
SrO (ppm)	3538	3343	3638
CaO	BDL	BDL	1196
FeO	BDL	BDL	BDL
PbO	BDL	BDL	379
TeO2	BDL	BDL	BDL
Ag2O	BDL	BDL	BDL
Au2O	BDL	BDL	BDL
Total	**100.78**	**100.39**	**100.23**
BaO (apfu)	1.01	1.00	1.00
SO3	0.99	1.00	0.99
SrO	0.01	0.01	0.01
CaO	0.00	0.00	0.00
FeO	0.00	0.00	0.00
PbO	0.00	0.00	0.00
TeO2	0.00	0.00	0.00
Ag2O	0.00	0.00	0.00
Au2O	0.00	0.00	0.00
Total	**2.01**	**2.00**	**2.01**

D.3 – Methods for Mineral Formula Calculations

The CITZAF V3.5 program for JEOL On-line software written by J. T. Armstrong (California Institute of Technology) generated element mass data in weight percent (wt%) during analysis (pers. comm., B.Joy, 2013). Three procedures were required to calculate mineral formulas from EMPA weight percent data, based on the type of phase analyzed: (1) sulfides and sulfosalts (sphalerite, pyrite, galena, chalchopyrite, tetrahedrite, bornite, colusite, sulvanite, reinerite, stromeyerite, pearceite, miargyrite and bournonite); (2) non-sulfide ore (electrum); and (3) sulfates (barite). Example calculations for each type of phase are included below, using sphalerite, electrum and barite to represent each type of phase calculation.

D.3.1 – Mineral Formula Calculation for sulfides and sulfosalts

The mineral formula for sphalerite, (Zn,Fe)S, indicates that a unit cell for this phase contains 1 S atom and 2 atoms total. The number of sulfur atoms and total atoms per unit cell will change with each different analyzed sulfide or sulfosalt phase.

(1) Element weight percent of each element is known from probe analyses. Analyses below detection limit (BDL) are considered to be zero in the mineral calculation procedure.
(2) Atomic weight percent is the accepted mass value for each element.
(3) Atomic proportion is calculated by dividing (1) by (2) for each element.
(4) Total S in the sphalerite unit cell ((Zn,Fe)S) is equal to 1.
(5) Conversion factor is calculated by dividing (4) by (3, S only).
(6) Unit cell proportion is calculated by multiplying (5) and (3) for each element.
(7) Calculated total atoms is equal to the sum of each element in (6).
(8) Accepted total atoms is the ideal number of atoms (two) in the sphalerite unit cell (Zn,Fe)S. This value is used to check the relative stoichiometry of the analyzed phase.

Table D.3.1 – Example Mineral Formula Calculation for sphalerite

Sample		**Probe Analysis**	**Date**					
CNF14299		**RL4 sp1**	**2013-10-01**					
1	**Element mass (wt%)**	(LLD applied)						
	Ge	Fe	Mn	Cu	S	Zn	Ag	Cd
	BDL	0.16	0.03	0.04	32.90	65.55	BDL	0.32
2	**Atomic mass (wt%)**							
	Ge	Fe	Mn	Cu	S	Zn	Ag	Cd
	72.61	55.84	54.94	63.55	32.07	65.39	107.87	112.41
3	**Atomic proportion**	(Element mass/Atomic mass)						
	Ge	Fe	Mn	Cu	S	Zn	Ag	Cd
	0.00	0.00	0.00	0.00	1.03	1.00	0.00	0.00
4	**Total S in (Zn,Fe)S**							
	1.00							
5	**Conversion factor**	(Total S in (Zn,Fe)S/Atomic Proportion of S)						
	0.97							
6	**Unit cell proportion**	(Conversion factor*Atomic proportion)						
	Ge	Fe	Mn	Cu	S	Zn	Ag	Cd
	0.00	0.00	0.00	0.00	1.00	0.98	0.00	0.00
7	**Calculated total atoms**							
	1.98							
8	**Accepted total atoms in (Zn,Fe)S**							
	2.00							

D.3.2 – Mineral Formula Calculation for non-sulfides

The mineral formula for electrum, (Zn,Fe)S, indicates that a unit cell for this phase contains 1 S atom and 2 atoms total.

(1) Element weight percent of each element is known from probe analyses. Analyses below detection limit (BDL) are considered to be zero in the mineral calculation procedure.
(2) Atomic weight percent is the accepted mass value for each element.
(3) Atomic proportion is calculated by dividing (1) by (2) for each element.
(4) Total of atomic proportions is calculated from the sum of each element in (3).
(5) Atomic proportion normalized to 1.0 is calculated by dividing each element in (3) by (4).
(6) Gold proportion is calculated by dividing Au by the sum of Au and Ag from (5). This calculation assumes an ideal electrum formula (Au,Ag).

Table D.3.2 – Example Mineral Formula Calculation for electrum

Sample		**Probe Analysis**	**Date**						
CNF25121		**RL1 elec1**	**2013-10-05**						
1	**Element mass (wt%)**	(LLD applied)							
	As	Cu	Hg	Fe	S	Pb	Ag	Au	Sb
	0.04	0.80	BDL	0.03	0.20	BDL	13.56	82.72	BDL
2	**Atomic mass (wt%)**								
	As	Cu	Hg	Fe	S	Pb	Ag	Au	Sb
	74.92	63.55	200.59	55.84	32.07	207.20	107.87	196.97	121.76
3	**Atomic proportion**	(Element mass/Atomic mass)							
	As	Cu	Hg	Fe	S	Pb	Ag	Au	Sb
	0.00	0.01	0.00	0.00	0.01	0.00	0.13	0.42	0.00
4	**Total of atomic proportions**								
	0.57								
5	**Atomic proportion normalized to 1.0**	(Atomic proportion/Total of atomic proportions)							
	As	Cu	Hg	Fe	S	Pb	Ag	Au	Sb
	0.00	0.02	0.00	0.00	0.01	0.00	0.22	0.74	0.00
6	**Au proportion**	Au/(Au+Ag)							
	0.77								

D.3.3 – Mineral Formula Calculation for sulfates

The mineral formula for barite, $BaSO_4$, indicates that a unit cell for this phase contains 4 oxygen atoms and 2 total cations. The number of oxygen atoms and total cations per unit cell will change with each different analyzed sulfate phase.

(1) Oxide weight percent of each element is known from probe analyses. Analyses below detection limit (BDL) are considered to be zero in the mineral calculation procedure.
(2) Formula weight percent is the sum of accepted mass values for each element in the oxide unit cell.
(3) Oxide mole percent is calculated by dividing (1) by (2), and multiplying this product by the number of oxygen atoms in each oxide unit cell.
(4) Total oxide mole percent is equal to the sum of each oxide mole percent in (3).
(5) Total oxygen in the barite unit cell ($BaSO_4$) is equal to 4.
(6) Conversion factor is calculated by dividing (5) by (4).
(7) Cation mole percent is calculated by multiplying (3) and (6), and multiplying this product to the total cations per oxide unit cell relative to oxygen atoms. For Ba, Fe, Ca, Sr and Pb the total cations is equal to 1; however, for S and Ge the total cations are equal to ⅓ and ½, respectively.
(8) Calculated total cations is equal to the sum of each cation mole % in (6).
(9) Accepted total cations is the ideal number of cations in the barite unit cell $BaSO_4$. This value is used to check the relative stoichiometry of the analyzed phase.

Table D.3.3 – Example Mineral Formula Calculation for barite

Sample		**Probe analysis**	**Date**				
CNF25146		**RL3 brt1**	**2013-10-05**				
1	**Oxide mass (wt%)**	(LLD applied)					
	BaO	FeO	SO_3	CaO	GeO_2	SrO	PbO
	62.32	BDL	34.49	0.08	BDL	0.85	BDL
2	**Formula mass (wt%)**						
	BaO	FeO	SO_3	CaO	GeO_2	SrO	PbO
	153.33	71.85	80.07	56.08	104.61	103.62	223.20
3	**Oxide mole %**	((Oxide mass/Formula mass)*Total O atoms per formula unit)					
	BaO	FeO	SO_3	CaO	GeO_2	SrO	PbO
	0.41	0.00	1.29	0.00	0.00	0.01	0.00
4	**Total oxide mole %**						
	1.71						
5	**Total O in SO_4**						
	4.00						
6	**Conversion factor**	(Total O in $BaSO_4$/Total oxide mole %)					
	2.34						
7	**Cation mole %**	(Oxide mole %*Conversion factor*Total cations per formula unit)					
	BaO	FeO	SO_3	CaO	GeO_2	SrO	PbO
	0.95	0.00	1.01	0.00	0.00	0.02	0.00
8	**Calculated total cations**						
	1.98						
9	**Accepted total cations in $BaSO_4$**						
	2.00						

Appendix E: Laser Ablation ICP-MS Results

E.1 – Supplementary Laser Ablation ICPMS Methods

Of the 33 total elements detected in this study, 14 elements (Ba, Cu, Fe, Hg, Ir, Nb, Pt, Rb, Sc, Sr, Te, W, Zn, Zr) were not considered due to: (i) lack of standard data; (ii) inconsistencies with preferred values for the calibration curve; (iii) inconsistencies with preferred values for the external standard; (iv) below lower limit of detection in unknowns; or (v) above upper limit of detection in unknowns. Published and preferred data for the standards used (GSC-1G, GSD-1G, GSE-1G and BHVO-2G) were found on the Geological and Environmental Reference Materials database (http://georem.mpch-mainz.gwdg.de/sample_query_pref.asp) and are included in Table E.1.1. A total of 185 analyses were conducted on 6 phases (sphalerite, pyrite, galena, chalcopyrite, tetrahedrite and bornite). Analyses were mostly conducted using the spot technique for laser ablation of in-situ minerals; however, some line analyses were conducted for the sake of comparison. The lower limit of detection (LLD) was calculated for each set of unknown analyses using the gas blank, and applied to corrected laser data (Equation E.1.1). Abbreviations are as follows: x_{blank} = element mass in He-ArF carrier gas; σ_{blank} = standard deviation of element mass in carrier gas.

$$LLD = x_{blank} + 3\,\sigma_{blank}$$

Table E.1.1 – List of Standard Reference Materials

Element mass (ppm)	USGS Standard				
	GSC-1G	**GSD-1G**	**GSE-1G**	**BHVO-2G**	**MASS-1**
Ag	4.1	23	200		67
As	3.2	27	260		65
Au	6	4	7		47.72
Ba	34.8	67	427	131	
Bi	3.4	35	320	0.01	7
Cd	1.9	18	160	0.1	70
Co	5.9	40	380	44	67.45
Cr	10.3	42	400	293	37
Cu	16	42	380	127	129500
Fe	106531.9	103421.5	98755.8	87869.4	156000
Ge	4	32	320	1.6	50
Hg					57
In	4.5	38	370	0.1	50
Ir	2	12	120		63.51
Mn				1316.8	260
Mo	4.6	39	390	3.8	61
Nb	4.5	42	420	18.3	
Ni	21	58	440	116	91.49
Pb	14	50	378	1.7	
Pt	2	6	30	0.46	61.78
Rb	4.92	37.3	356	9.2	
Sb	5.3	43	450	0.3	55
Sc	5.4	52	530	33	
Se	0.2	2	20		53
Sn	5.3	29	280	2.6	55
Sr	32.3	69.4	447	396	
Te					
Ti	8213.4	7434.1	449.6	16726.6	
Tl	0.27	0.9	2		
V	5.4	44	440	308	63
W	4.5	43	430	0.23	
Zn	12.7	54	460	102	210000
Zr	6.8	42	410	170	

E.2 – Compiled Laser Ablation ICP-MS Analyses

Table E.2.1 – Laser Ablation Spot Analyses for the type 1 mineral assemblage

Type Min	Phase	Sample	Spot	Sc (ppm)	Ti (ppm)	V (ppm)	Cr (ppm)	Mn (ppm)	Fe (ppm)	Co (ppm)	60Ni (ppm)	61Ni (ppm)	63Cu (ppm)	65Cu (ppm)	Zn (ppm)
Type 1	sp	29986	RL3	BDL	0	BDL	BDL	BDL	0	BDL	BDL	BDL	3354	3141	280019
Type 1	sp	29986	RL3	BDL	0	BDL	BDL	BDL	0	BDL	BDL	BDL	3232	3041	278603
Type 1	sp	29986	RL2	BDL	0	BDL	BDL	BDL	0	BDL	BDL	BDL	3081	3154	289365
Type 1	sp	29986	RL2	BDL	0	BDL	BDL	BDL	0	BDL	BDL	BDL	1752	1831	277682
Type 1	sp	25152	RL3	BDL	BDL	BDL	BDL	116	BDL	BDL	BDL	BDL	520	713	316407
Type 1	sp	25152	RL3	BDL	BDL	BDL	BDL	114	BDL	BDL	BDL	BDL	107	129	300935
Type 1	sp	25152	RL5	BDL	BDL	BDL	BDL	101	BDL	BDL	BDL	BDL	69	70	302853
Type 1	sp	25152	RL5	BDL	BDL	BDL	BDL	86	BDL	BDL	BDL	BDL	60	68	287419
Type 1	sp	14299	RL4	BDL	BDL	BDL	BDL	451	BDL	8	93	63	399	829	227660
Type 1	sp	14299	RL4	BDL	BDL	BDL	BDL	545	83293	19	168	158	7144	12016	220375
Type 1	sp	14299	RL10	BDL	BDL	6	BDL	309	BDL	BDL	BDL	0	190	190	230246
Type 1	sp	14299	RL10	BDL	BDL	BDL	BDL	408	BDL	BDL	BDL	0	351	360	330989
Type 1	sp	29962	RL1	BDL	BDL	BDL	BDL	BDL	BDL	BDL	BDL	BDL	142	139	367572
Type 1	sp	29962	RL1	BDL	BDL	BDL	BDL	54	BDL	BDL	BDL	BDL	153	167	362174
Type 1	sp	29962	RL2	BDL	BDL	BDL	BDL	38	BDL	BDL	BDL	BDL	284	418	288801
Type 1	sp	29962	RL2	BDL	BDL	BDL	BDL	123	BDL	BDL	BDL	BDL	281	261	337811
Type 1	sp	14291	RL7	BDL	BDL	BDL	BDL	806	0	BDL	14	BDL	75	82	375895
Type 1	sp	14291	RL7	BDL	BDL	BDL	BDL	710	0	BDL	BDL	BDL	84	69	332800
Type 1	sp	14291	RL9	BDL	BDL	BDL	BDL	685	BDL	BDL	BDL	BDL	77	83	320414
Type 1	sp	14291	RL9	BDL	BDL	BDL	BDL	720	BDL	BDL	BDL	BDL	67	83	313605
Type 1	sp	25146	RL1	0	BDL	BDL	0	206	BDL	0	BDL	BDL	26	33	362602
Type 1	sp	25146	RL1	0	BDL	BDL	0	519	BDL	0	BDL	BDL	BDL	BDL	1258
Type 1	sp	25146	RL5	0	BDL	BDL	0	194	BDL	0	BDL	BDL	214	197	378034
Type 1	sp	25146	RL5	0	BDL	BDL	0	220	BDL	0	BDL	BDL	72	86	359186
Type 1	py	29960	RL3	BDL	BDL	15	BDL	BDL	318886	17	1657	1628	480	569	9474
Type 1	py	29960	RL3	BDL	BDL	6	BDL	558	318212	6	188	151	3976	3702	144
Type 1	py	29960	RL3	BDL	BDL	7	BDL	1189	297422	7	452	450	1388	1202	49159
Type 1	py	29960	RL3	BDL	BDL	34	4	282	299154	8	625	643	1862	2105	8326
Type 1	py	25134	RL4	0	174	12	0	762	343277	16	1164	1600	1358	1467	430
Type 1	py	25134	RL4	0	214	116	0	497	318935	40	2283	2961	1860	2078	8318
Type 1	py	25134	RL4	0	256	118	0	299	301378	55	2000	2603	1625	1628	86297
Type 1	py	25134	RL4	0	232	84	0	342	328313	69	2213	2832	1958	1967	1178

Table E.2.1 cont. – Laser Ablation Spot Analyses for the type 1 mineral assemblage

TypeMin	Phase	Sample	Spot	Ge (ppm)	As (ppm)	Se (ppm)	Rb (ppm)	Sr (ppm)	Zr (ppm)	Nb (ppm)	Mo (ppm)	Ag (ppm)	Cd (ppm)	In (ppm)	Sn (ppm)
Type 1	sp	29986	RL3	7	BDL	BDL	BDL	BDL	BDL	BDL	192	63	2557	BDL	6
Type 1	sp	29986	RL3	BDL	BDL	83	BDL	BDL	14	BDL	50	42	2557	BDL	8
Type 1	sp	29986	RL2	BDL	BDL	BDL	BDL	BDL	BDL	0	BDL	16	2570	BDL	5
Type 1	sp	29986	RL2	BDL	BDL	BDL	BDL	BDL	BDL	0	97	14	2570	BDL	6
Type 1	sp	25152	RL3	5	683	BDL	BDL	BDL	BDL	BDL	BDL	7	2653	BDL	11
Type 1	sp	25152	RL3	BDL	BDL	BDL	BDL	BDL	BDL	BDL	87	5	2653	BDL	9
Type 1	sp	25152	RL5	6	BDL	BDL	BDL	BDL	BDL	BDL	BDL	BDL	2577	BDL	7
Type 1	sp	25152	RL5	BDL	BDL	BDL	BDL	BDL	BDL	BDL	65	9	2577	BDL	6
Type 1	sp	14299	RL4	16	173	0	BDL	57	BDL	BDL	BDL	26	3157	BDL	8
Type 1	sp	14299	RL4	14	2174	0	BDL	821	7	BDL	236	172	3157	BDL	10
Type 1	sp	14299	RL10	5	BDL	BDL	BDL	BDL	BDL	BDL	6	4	2306	BDL	12
Type 1	sp	14299	RL10	8	BDL	BDL	BDL	BDL	BDL	BDL	64	32	3450	BDL	24
Type 1	sp	29962	RL1	8	BDL	0	BDL	BDL	BDL	0	55	6	3117	BDL	11
Type 1	sp	29962	RL1	6	BDL	0	BDL	BDL	BDL	0	BDL	BDL	3117	BDL	10
Type 1	sp	29962	RL2	6	BDL	BDL	BDL	BDL	BDL	BDL	52	7	3017	BDL	10
Type 1	sp	29962	RL2	8	124	BDL	BDL	34	BDL	0	BDL	7	3017	BDL	12
Type 1	sp	14291	RL7	12	BDL	0	BDL	BDL	BDL	BDL	129	9	2583	BDL	10
Type 1	sp	14291	RL7	11	BDL	0	BDL	BDL	BDL	0	54	10	2583	BDL	12
Type 1	sp	14291	RL9	8	0	BDL	BDL	BDL	BDL	0	28	8	2485	BDL	19
Type 1	sp	14291	RL9	9	0	BDL	BDL	15	BDL	BDL	354	10	2485	BDL	16
Type 1	sp	25146	RL1	0	BDL	0	BDL	0	0	0	0	3	3187	BDL	5
Type 1	sp	25146	RL1	0	BDL	0	BDL	190	0	0	0	0	5	BDL	0
Type 1	sp	25146	RL5	0	BDL	0	BDL	0	0	0	0	12	2977	BDL	9
Type 1	sp	25146	RL5	3	BDL	0	BDL	0	0	0	102	11	2977	BDL	5
Type 1	py	29960	RL3	5	2660	0	4	9	BDL	BDL	1233	19	26	BDL	4
Type 1	py	29960	RL3	5	744	0	BDL	BDL	BDL	BDL	4	1355	21	BDL	3
Type 1	py	29960	RL3	6	3041	0	BDL	BDL	BDL	BDL	29	322	213	BDL	3
Type 1	py	29960	RL3	5	1990	0	11	BDL	BDL	0	171	576	40	BDL	3
Type 1	py	25134	RL4	6	45600	12040	BDL	0	0	0	1482	1013	0	BDL	0
Type 1	py	25134	RL4	5	32830	17430	9	0	0	0	1421	936	27	BDL	0
Type 1	py	25134	RL4	7	36330	14070	10	39	0	0	2411	637	611	BDL	0
Type 1	py	25134	RL4	7	39580	17740	8	33	0	0	2610	865	4	BDL	0

Table E.2.1 cont. – Laser Ablation Spot Analyses for the type 1 mineral assemblage

Type Min	Phase	Sample	Spot	Sb (ppm)	Ba (ppm)	W (ppm)	W (ppm)	W (ppm)	Ir (ppm)	Ir (ppm)	Pt (ppm)	Pt (ppm)	Au (ppb)	Pb (ppm)	Tl (ppm)
Type 1	sp	29986	RL3	68	80	BDL	BDL	BDL	BDL	BDL	BDL	BDL	BDL	530	BDL
Type 1	sp	29986	RL3	12	19	BDL	BDL	BDL	BDL	BDL	BDL	BDL	BDL	427	BDL
Type 1	sp	29986	RL2	BDL	34	BDL	BDL	BDL	BDL	BDL	BDL	BDL	BDL	490	BDL
Type 1	sp	29986	RL2	BDL	61	BDL	BDL	BDL	BDL	BDL	BDL	BDL	BDL	546	BDL
Type 1	sp	25152	RL3	36	0	BDL	BDL	BDL	0	0	0	0	BDL	466	BDL
Type 1	sp	25152	RL3	16	-1	BDL	BDL	BDL	0	0	0	0	BDL	294	BDL
Type 1	sp	25152	RL5	BDL	-4	BDL	BDL	BDL	0	0	0	0	BDL	260	BDL
Type 1	sp	25152	RL5	BDL	-3	BDL	BDL	BDL	0	0	0	0	BDL	181	BDL
Type 1	sp	14299	RL4	93	89	BDL	BDL	BDL	0	0	0	1	BDL	892	29
Type 1	sp	14299	RL4	892	1817	BDL	BDL	BDL	0	0	0	-3	BDL	680	425
Type 1	sp	14299	RL10	0	373	BDL	BDL	BDL	BDL	BDL	BDL	3	BDL	1433	1
Type 1	sp	14299	RL10	0	8	BDL	BDL	BDL	BDL	-1	BDL	BDL	927	438	3
Type 1	sp	29962	RL1	3	11	BDL	BDL	BDL	BDL	BDL	BDL	BDL	BDL	227	0
Type 1	sp	29962	RL1	BDL	BDL	BDL	BDL	BDL	BDL	BDL	BDL	BDL	BDL	119	BDL
Type 1	sp	29962	RL2	35	-2	BDL	BDL	BDL	BDL	BDL	BDL	BDL	BDL	160	BDL
Type 1	sp	29962	RL2	37	-4	BDL	BDL	BDL	BDL	BDL	BDL	BDL	BDL	139	BDL
Type 1	sp	14291	RL7	9	-4	BDL	BDL	BDL	-2	-1	BDL	BDL	BDL	2400	BDL
Type 1	sp	14291	RL7	20	132	BDL	BDL	BDL	-2	-1	BDL	BDL	BDL	164	BDL
Type 1	sp	14291	RL9	10	3679	BDL	BDL	BDL	-1	-2	0	0	BDL	590	BDL
Type 1	sp	14291	RL9	11	20986	BDL	BDL	BDL	BDL	-2	0	0	BDL	252	0
Type 1	sp	25146	RL1	0	-8	0	0	0	0	0	0	-7	0	316	BDL
Type 1	sp	25146	RL1	0	18	0	0	0	0	0	0	BDL	0	BDL	BDL
Type 1	sp	25146	RL5	3	-5	0	0	0	0	0	0	-10	0	281	BDL
Type 1	sp	25146	RL5	3	0	0	0	0	0	0	0	-10	0	438	BDL
Type 1	py	29960	RL3	23	574	5	BDL	5	BDL	BDL	BDL	BDL	1540	294	1
Type 1	py	29960	RL3	608	14	BDL	BDL	BDL	BDL	BDL	BDL	BDL	6305	5070	1599
Type 1	py	29960	RL3	2391	181	BDL	BDL	BDL	BDL	BDL	BDL	BDL	4744	26980	1584
Type 1	py	29960	RL3	291	3206	BDL	BDL	BDL	BDL	BDL	BDL	BDL	5683	38310	962
Type 1	py	25134	RL4	3319	58	0	0	0	BDL	BDL	-1	-5	15250	50650	902
Type 1	py	25134	RL4	2273	854	0	0	0	BDL	BDL	-1	BDL	14300	88300	813
Type 1	py	25134	RL4	1857	777	0	0	0	-4	-4	-1	-5	13150	42280	2566
Type 1	py	25134	RL4	2165	548	0	0	0	-3	-3	-1	-5	12870	67480	2411

Table E.2.1 cont. – Laser Ablation Spot Analyses for the type 1 mineral assemblage

Type Min	Phase	Sample	Spot	206Pb (ppm)	207Pb (ppm)	208Pb (ppm)	Bi (ppm)
Type 1	sp	29986	RL3	19	22	22	BDL
Type 1	sp	29986	RL3	BDL	11	11	BDL
Type 1	sp	29986	RL2	24	22	25	BDL
Type 1	sp	29986	RL2	14	14	14	BDL
Type 1	sp	25152	RL3	BDL	BDL	BDL	BDL
Type 1	sp	25152	RL3	11	11	11	BDL
Type 1	sp	25152	RL5	BDL	6	BDL	BDL
Type 1	sp	25152	RL5	21	21	21	BDL
Type 1	sp	14299	RL4	24	37	27	BDL
Type 1	sp	14299	RL4	201	221	229	BDL
Type 1	sp	14299	RL10	BDL	BDL	BDL	BDL
Type 1	sp	14299	RL10	27	22	23	BDL
Type 1	sp	29962	RL1	103	126	113	BDL
Type 1	sp	29962	RL1	BDL	7	BDL	BDL
Type 1	sp	29962	RL2	9	9	10	BDL
Type 1	sp	29962	RL2	9	9	9	BDL
Type 1	sp	14291	RL7	1629	2196	1893	BDL
Type 1	sp	14291	RL7	17	20	19	BDL
Type 1	sp	14291	RL9	479	346	416	BDL
Type 1	sp	14291	RL9	52	40	56	BDL
Type 1	sp	25146	RL1	43	49	42	0
Type 1	sp	25146	RL1	28	9	43	0
Type 1	sp	25146	RL5	24	28	29	0
Type 1	sp	25146	RL5	164	184	179	0
Type 1	py	29960	RL3	253	272	270	BDL
Type 1	py	29960	RL3	4195	4470	3371	BDL
Type 1	py	29960	RL3	11910	13370	11120	BDL
Type 1	py	29960	RL3	14940	16140	15840	BDL
Type 1	py	25134	RL4	23550	26720	25930	12
Type 1	py	25134	RL4	42150	46760	46120	22
Type 1	py	25134	RL4	24280	26550	25430	12
Type 1	py	25134	RL4	38330	41790	40550	19

Table E.2.2 – Laser Ablation Spot Analyses for the type 2A mineral assemblage

Type Min	Phase	Sample	Spot	Sc (ppm)	Ti (ppm)	V (ppm)	Cr (ppm)	Mn (ppm)	Fe (ppm)	Co (ppm)	60Ni (ppm)	61Ni (ppm)
Type 2A	gn	29960	RL10b	38	499	BDL	27	BDL	BDL	19	87	1292
Type 2A	gn	29957	RL3	47	675	BDL	35	35	BDL	22	94	1964
Type 2A	gn	29957	RL3	40	651	BDL	31	28	BDL	20	99	1899
Type 2A	gn	14279	RL7	26	428	BDL	20	BDL	BDL	13	57	1410
Type 2A	gn	14279	RL7	31	509	BDL	22	BDL	BDL	15	59	1317
Type 2A	gn	14279	RL10	38	602	BDL	27	BDL	BDL	18	75	1859
Type 2A	gn	14279	RL10	46	681	BDL	32	BDL	BDL	22	102	2032
Type 2A	ccp	25151	RL5	BDL	BDL	BDL	BDL	37	213144	BDL	BDL	BDL
Type 2A	ccp	25151	RL5	BDL	BDL	BDL	BDL	37	187945	BDL	BDL	33
Type 2A	ccp	14299	RL8	BDL	BDL	18	7	69	145517	7	39	106
Type 2A	ccp	29960	RL10b	BDL	BDL	BDL	BDL	BDL	155160	BDL	BDL	BDL
Type 2A	ccp	29960	RL10b	BDL	BDL	BDL	BDL	BDL	157277	BDL	BDL	BDL
Type 2A	ccp	29957	RL3	BDL	BDL	7	4	BDL	162169	BDL	BDL	BDL
Type 2A	ccp	29957	RL3	BDL	BDL	BDL	BDL	BDL	146265	BDL	BDL	49
Type 2A	ccp	29957	RL6	BDL	BDL	BDL	BDL	BDL	353630	4	14	25
Type 2A	ccp	29957	RL6	BDL	BDL	9	BDL	31	336345	BDL	BDL	58
Type 2A	bn	25151	RL1	8	261	14	8	68	239102	10	BDL	BDL
Type 2A	bn	25151	RL1	7	233	14	6	59	224614	9	BDL	BDL
Type 2A	bn	25151	RL5	8	236	11	8	60	254557	10	17	59
Type 2A	bn	25151	RL5	26	370	BDL	19	42	100891	14	54	1050
Type 2A	bn	14299	RL4	8	243	20	9	75	258320	37	520	837
Type 2A	bn	14299	RL8	8	368	BDL	BDL	BDL	292189	BDL	13	93
Type 2A	bn	14299	RL8	7	293	9	BDL	BDL	248605	BDL	12	35
Type 2A	bn	29957	RL6	BDL	BDL	18	8	41	302068	5	10	32
Type 2A	bn	29957	RL6	5	BDL	8	6	172	417026	6	BDL	BDL
Type 2A	bn	14279	RL7	0	380	BDL	7	BDL	286000	7	BDL	242
Type 2A	bn	14279	RL7	0	BDL	BDL	BDL	BDL	149353	BDL	BDL	BDL
Type 2A	bn	29967	RL3b	BDL	BDL	9	BDL	BDL	135768	BDL	BDL	BDL
Type 2A	bn	29967	RL3b	BDL	BDL	56	3	BDL	139620	BDL	BDL	BDL

Table E.2.2 cont. – Laser Ablation Spot Analyses for the type 2A mineral assemblage

Type Min	Phase	Sample	Spot	63Cu (ppm)	65Cu (ppm)	Zn (ppm)	Ge (ppm)	As (ppm)	Se (ppm)	Rb (ppm)	Sr (ppm)	Zr (ppm)	Nb (ppm)
Type 2A	gn	29960	RL10b	202	390	117	29	BDL	0	9	10	8	5
Type 2A	gn	29957	RL3	638	789	17302	42	BDL	9192	9	11	10	6
Type 2A	gn	29957	RL3	1867	3939	690	39	209	8533	9	10	10	6
Type 2A	gn	14279	RL7	656	798	104	26	BDL	0	7	BDL	3	4
Type 2A	gn	14279	RL7	482	249	406	22	BDL	0	7	11	5	4
Type 2A	gn	14279	RL10	57	72	91	37	BDL	0	7	BDL	6	5
Type 2A	gn	14279	RL10	69	112	137	40	BDL	0	10	BDL	5	6
Type 2A	ccp	25151	RL5	166730	164716	40	55	BDL	0	BDL	BDL	BDL	0
Type 2A	ccp	25151	RL5	185920	172022	48	62	BDL	0	BDL	BDL	BDL	0
Type 2A	ccp	14299	RL8	136065	141185	93	11	BDL	0	BDL	2029	BDL	1
Type 2A	ccp	29960	RL10b	183328	198721	579	9	BDL	0	BDL	BDL	BDL	0
Type 2A	ccp	29960	RL10b	206590	203309	601	10	BDL	0	BDL	BDL	BDL	0
Type 2A	ccp	29957	RL3	212587	200267	82	16	BDL	BDL	BDL	11	BDL	1
Type 2A	ccp	29957	RL3	168699	177995	55	8	BDL	BDL	BDL	BDL	BDL	1
Type 2A	ccp	29957	RL6	201954	191442	135	10	BDL	0	BDL	7	BDL	0
Type 2A	ccp	29957	RL6	203662	197943	352	14	BDL	0	BDL	8	3	0
Type 2A	bn	25151	RL1	573741	611315	888	33	BDL	0	8	18	8	1
Type 2A	bn	25151	RL1	580980	563147	72	36	BDL	0	8	15	8	0
Type 2A	bn	25151	RL5	646301	620038	128	54	BDL	0	8	15	9	1
Type 2A	bn	25151	RL5	221310	220791	82	35	BDL	0	BDL	11	10	3
Type 2A	bn	14299	RL4	369497	388302	5201	37	BDL	0	9	80	9	1
Type 2A	bn	14299	RL8	712360	694313	1062	21	BDL	332	BDL	2938	8	1
Type 2A	bn	14299	RL8	662395	623803	815	19	BDL	180	BDL	6971	8	2
Type 2A	bn	29957	RL6	527056	532415	326	23	45	0	BDL	21	3	0
Type 2A	bn	29957	RL6	599036	572724	333	23	BDL	0	5	133	4	1
Type 2A	bn	14279	RL7	898813	816501	863	21	BDL	0	6	BDL	0	2
Type 2A	bn	14279	RL7	418734	429340	76	9	BDL	0	BDL	BDL	0	0
Type 2A	bn	29967	RL3b	387672	385489	38	6	BDL	BDL	BDL	11	BDL	0
Type 2A	bn	29967	RL3b	409159	422651	207	8	BDL	53	6	16	BDL	1

Table E.2.2 cont. – Laser Ablation Spot Analyses for the type 2A mineral assemblage

Type Min	Phase	Sample	Spot	Nb (ppm)	Mo (ppm)	Ag (ppm)	Cd (ppm)	In (ppm)	Sn (ppm)	Sb (ppm)	Ba (ppm)	182W (ppm)	183W (ppm)	184W (ppm)
Type 2A	gn	29960	RL10b	5	21	2270	82	6	44	2568	38	6	9	6
Type 2A	gn	29957	RL3	6	38	59	144	8	36	39	200	BDL	12	8
Type 2A	gn	29957	RL3	6	30	48	63	6	26	40	245	BDL	13	7
Type 2A	gn	14279	RL7	4	11	68	34	BDL	51	93	9	BDL	7	BDL
Type 2A	gn	14279	RL7	4	17	37	45	BDL	50	60	1003	BDL	7	BDL
Type 2A	gn	14279	RL10	5	24	51	50	5	57	15	124	5	10	5
Type 2A	gn	14279	RL10	6	29	72	68	BDL	72	48	15	5	10	5
Type 2A	ccp	25151	RL5	0	7	14	BDL	7	7	2	-6	BDL	BDL	BDL
Type 2A	ccp	25151	RL5	0	271	22	2	7	8	3	-1	BDL	BDL	BDL
Type 2A	ccp	14299	RL8	1	1604	714	3	7	8	14	3145	14	13	15
Type 2A	ccp	29960	RL10b	0	BDL	211	5	BDL	25	BDL	BDL	BDL	BDL	BDL
Type 2A	ccp	29960	RL10b	0	BDL	111	6	BDL	22	BDL	BDL	BDL	BDL	BDL
Type 2A	ccp	29957	RL3	1	162	18	5	14	9	BDL	158	BDL	BDL	BDL
Type 2A	ccp	29957	RL3	1	BDL	28	3	13	5	BDL	0	BDL	BDL	BDL
Type 2A	ccp	29957	RL6	0	6	9	5	14	3	4	-12	BDL	4	BDL
Type 2A	ccp	29957	RL6	0	20	63	6	13	5	0	173	BDL	BDL	BDL
Type 2A	bn	25151	RL1	1	1385	5683	6	13	26	7	BDL	13	13	13
Type 2A	bn	25151	RL1	0	1102	5683	3	11	24	5	197	12	12	12
Type 2A	bn	25151	RL5	1	251	6665	10	12	26	6	BDL	12	12	12
Type 2A	bn	25151	RL5	3	22	2566	46	8	24	70	2	9	11	8
Type 2A	bn	14299	RL4	1	441	7012	35	13	15	24	9792	13	13	13
Type 2A	bn	14299	RL8	1	682	5683	4	BDL	75	0	5676	7	6	5
Type 2A	bn	14299	RL8	2	14	5683	0	4	59	38	6006	BDL	BDL	BDL
Type 2A	bn	29957	RL6	0	61	1867	11	5	11	0	132	5	5	5
Type 2A	bn	29957	RL6	1	170	1867	11	5	14	0	2612	6	7	5
Type 2A	bn	14279	RL7	2	11	6630	17	5	41	BDL	73	BDL	5	BDL
Type 2A	bn	14279	RL7	0	BDL	6630	4	BDL	8	BDL	-3	BDL	BDL	BDL
Type 2A	bn	29967	RL3b	0	82	3230	3	BDL	12	0	65	BDL	BDL	BDL
Type 2A	bn	29967	RL3b	1	76	3429	6	BDL	14	0	623	BDL	BDL	BDL

Table E.2.2 cont. – Laser Ablation Spot Analyses for the type 2A mineral assemblage

Type Min	Phase	Sample	Spot	191Ir (ppm)	193Ir (ppm)	195Pt (ppm)	196Pt (ppm)	Au (ppb)	204Pb (ppm)	Tl (ppm)	206Pb (ppm)	207Pb (ppm)	208Pb (ppm)	Bi (ppm)
Type 2A	gn	29960	RL10b	BDL	BDL	7	9	2074	1604000	12	1420000	1547000	1446000	53
Type 2A	gn	29957	RL3	12	7	5	6	3019	1535000	7	1432000	1572000	1515000	82
Type 2A	gn	29957	RL3	13	5	5	6	3005	1247000	5	1228000	1316000	1317000	77
Type 2A	gn	14279	RL7	4	-1	3	1	2170	1880000	7	1135777	1476907	1382379	40
Type 2A	gn	14279	RL7	5	-2	5	5	2219	1881000	6	1120503	1408820	1283233	45
Type 2A	gn	14279	RL10	15	1	5	10	3135	1858000	8	1067350	1425479	1295980	56
Type 2A	gn	14279	RL10	16	5	8	11	3597	1935000	9	1141887	1505156	1403624	77
Type 2A	ccp	25151	RL5	0	0	0	BDL	BDL	27	0	21	43	59	BDL
Type 2A	ccp	25151	RL5	0	0	0	BDL	BDL	1371	1	711	747	918	BDL
Type 2A	ccp	14299	RL8	0	0	0	-9	BDL	91300	11	43540	50010	46450	7
Type 2A	ccp	29960	RL10b	BDL	BDL	BDL	BDL	BDL	BDL	BDL	BDL	BDL	BDL	BDL
Type 2A	ccp	29960	RL10b	BDL	BDL	BDL	BDL	BDL	BDL	0	BDL	BDL	BDL	BDL
Type 2A	ccp	29957	RL3	BDL	BDL	BDL	BDL	BDL	54	1	34	34	33	BDL
Type 2A	ccp	29957	RL3	BDL	BDL	BDL	BDL	BDL	58	1	30	32	31	BDL
Type 2A	ccp	29957	RL6	-3	BDL	1	1	BDL	BDL	0	6	6	6	BDL
Type 2A	ccp	29957	RL6	-2	BDL	1	BDL	BDL	26	1	10	8	9	5
Type 2A	bn	25151	RL1	0	0	0	BDL	BDL	382	4	122	129	109	10
Type 2A	bn	25151	RL1	0	0	0	BDL	BDL	59	4	54	56	54	9
Type 2A	bn	25151	RL5	0	0	0	BDL	BDL	638	1	478	552	518	9
Type 2A	bn	25151	RL5	0	0	1	6	BDL	716300	9	647400	706500	668300	45
Type 2A	bn	14299	RL4	0	0	0	BDL	2566	735	4	640	645	574	9
Type 2A	bn	14299	RL8	BDL	BDL	4	3	3540	1675	7	1830	1500	1532	BDL
Type 2A	bn	14299	RL8	BDL	BDL	3	2	2685	840	4	1015	854	769	BDL
Type 2A	bn	29957	RL6	-2	-1	2	1	BDL	2722	2	1479	1505	1040	6
Type 2A	bn	29957	RL6	-2	BDL	2	1	BDL	3518	1	2093	2609	2405	7
Type 2A	bn	14279	RL7	0	0	0	BDL	2033	629687	4	385853	502841	460618	16
Type 2A	bn	14279	RL7	BDL	0	0	BDL	BDL	90	2	21	42	28	BDL
Type 2A	bn	29967	RL3b	0	-8	0	BDL	BDL	19	0	17	18	18	BDL
Type 2A	bn	29967	RL3b	0	-8	0	BDL	BDL	BDL	1	10	10	11	BDL

Table E.2.3 – Laser Ablation Spot Analyses for the type 2B mineral assemblage (sphalerite, pyrite)

Type Min	Phase	Sample	Spot	Sc (ppm)	Ti (ppm)	V (ppm)	Cr (ppm)	Mn (ppm)	Fe (ppm)	Co (ppm)	60Ni (ppm)	61Ni (ppm)	63Cu (ppm)	65Cu (ppm)
Type 2B	sp	29957	RL3	BDL	BDL	BDL	BDL	185	BDL	BDL	BDL	BDL	525	632
Type 2B	sp	29957	RL3	BDL	BDL	8	BDL	333	BDL	BDL	BDL	BDL	76808	75549
Type 2B	sp	29957	RL6	BDL	BDL	266	BDL	217	BDL	BDL	BDL	39	11658	14874
Type 2B	sp	29957	RL6	BDL	BDL	BDL	BDL	197	BDL	BDL	BDL	BDL	16213	23570
Type 2B	sp	14279	RL7	0	BDL	BDL	BDL	178	BDL	BDL	BDL	BDL	705	621
Type 2B	sp	14279	RL7	0	BDL	93	BDL	156	BDL	BDL	BDL	BDL	4837	4971
Type 2B	sp	14279	RL5	0	BDL	135	10	195	BDL	BDL	BDL	BDL	256	252
Type 2B	sp	14279	RL5	0	BDL	274	9	178	BDL	BDL	BDL	BDL	5296	5510
Type 2	py	29986	RL4	BDL	257	9	BDL	39	188781	10	102	76	12	12
Type 2	py	29986	RL4	BDL	253	9	BDL	39	177985	11	172	186	13	11
Type 2	py	29986	RL6	BDL	255	BDL	BDL	40	187420	8	67	83	14	14
Type 2	py	29986	RL6	BDL	255	9	5	40	225351	8	44	33	13	13
Type 2	py	25121	RL7	BDL	236	9	BDL	43	221752	8	2225	2341	12876	15967
Type 2	py	25121	RL7	BDL	246	18	BDL	49	229339	8	1555	1495	74	79
Type 2	py	25121	RL4	BDL	235	32	5	45	229630	8	2376	2213	34	29
Type 2	py	25121	RL4	BDL	236	191	BDL	52	264644	8	1480	1454	29	33
Type 2	py	14299	RL1	BDL	BDL	BDL	6	1008	461935	11	666	799	1118	1027
Type 2	py	14299	RL1	BDL	BDL	8	BDL	1390	426930	34	933	1314	6481	12961
Type 2	py	14299	RL11	BDL	BDL	11	17	1277	361502	56	820	943	11822	16348
Type 2	py	14299	RL11	BDL	BDL	8	12	968	417217	54	930	1054	6608	7907
Type 2	py	29976	RL3	BDL	BDL	BDL	3	BDL	405706	6	38	39	2095	2207
Type 2	py	29976	RL3	BDL	26228	6	BDL	BDL	412155	5	10	40	5139	5664
Type 2	py	29957	RL4	BDL	BDL	BDL	BDL	BDL	242151	7	99	174	26733	42086
Type 2	py	29957	RL4	BDL	BDL	BDL	BDL	BDL	266697	5	96	231	72	113
Type 2	py	14279	RL7	0	BDL	BDL	BDL	BDL	387237	BDL	462	569	32	48
Type 2	py	14279	RL7	0	BDL	BDL	BDL	BDL	378919	BDL	1205	1709	49	30
Type 2	py	14279	RL10	0	BDL	312	20	BDL	389819	5	52	88	1735	1647
Type 2	py	14279	RL10	0	163	762	110	BDL	322411	9	131	289	974	785
Type 2	py	14295	RL5	BDL	BDL	BDL	BDL	BDL	598171	16	BDL	BDL	240	261
Type 2	py	14295	RL5	BDL	BDL	BDL	BDL	BDL	575703	19	BDL	51	35	25
Type 2	py	14295	RL3	BDL	BDL	BDL	BDL	BDL	538150	6	BDL	26	10	25
Type 2	py	14295	RL3	BDL	BDL	BDL	BDL	BDL	535048	22	BDL	32	313	479

Table E.2.3 cont. – Laser Ablation Spot Analyses for the type 2B mineral assemblage (sphalerite, pyrite)

Type Min	Phase	Sample	Spot	Zn (ppm)	Ge (ppm)	As (ppm)	Se (ppm)	Rb (ppm)	Sr (ppm)	Zr (ppm)	Nb (ppm)	Mo (ppm)	Ag (ppm)	Cd (ppm)	In (ppm)	Sn (ppm)
Type 2B	sp	29957	RL3	295878	10	BDL	BDL	BDL	BDL	BDL	0	13	7	3503	28	10
Type 2B	sp	29957	RL3	250607	11	57451	131	BDL	80	BDL	0	19	213	3503	25	15
Type 2B	sp	29957	RL6	331428	741	1620	BDL	BDL	BDL	BDL	0	124	62	3893	29	156
Type 2B	sp	29957	RL6	323972	13	BDL	BDL	BDL	BDL	BDL	0	31	79	3893	30	15
Type 2B	sp	14279	RL7	493804	6	BDL	0	BDL	249	0	BDL	BDL	13	2437	BDL	17
Type 2B	sp	14279	RL7	426660	5	BDL	0	BDL	BDL	0	0	4	42	2437	BDL	15
Type 2B	sp	14279	RL5	435016	12	BDL	0	BDL	BDL	0	BDL	82	36	2297	BDL	15
Type 2B	sp	14279	RL5	472138	14	BDL	0	BDL	331	0	0	35	70	2297	BDL	21
Type 2	py	29986	RL4	BDL	7	BDL	BDL	BDL	13	BDL	BDL	BDL	BDL	BDL	BDL	4
Type 2	py	29986	RL4	BDL	8	BDL	BDL	BDL	13	54	0	5	4	BDL	BDL	BDL
Type 2	py	29986	RL6	BDL	5	BDL	BDL	BDL	13	BDL	BDL	5	4	BDL	BDL	BDL
Type 2	py	29986	RL6	BDL	9	BDL	BDL	BDL	13	BDL	BDL	BDL	BDL	BDL	BDL	4
Type 2	py	25121	RL7	3595	7	25740	BDL	BDL	14	BDL	BDL	125	325	33	BDL	4
Type 2	py	25121	RL7	55820	8	181	BDL	BDL	16	6	0	1301	68	230	BDL	5
Type 2	py	25121	RL4	21	16	171	BDL	BDL	42	BDL	BDL	436	4	BDL	BDL	BDL
Type 2	py	25121	RL4	24	10	116	BDL	BDL	73	BDL	BDL	209	BDL	BDL	BDL	BDL
Type 2	py	14299	RL1	97	8	37160	0	BDL	11	BDL	BDL	27	140	4	BDL	BDL
Type 2	py	14299	RL1	89	BDL	32250	0	BDL	137	BDL	BDL	33	120	BDL	BDL	BDL
Type 2	py	14299	RL11	80	6	29140	0	BDL	327	9	BDL	284	290	6	BDL	BDL
Type 2	py	14299	RL11	43	BDL	28050	0	BDL	180	BDL	BDL	52	92	BDL	BDL	BDL
Type 2	py	29976	RL3	BDL	9	173	0	BDL	BDL	BDL	BDL	BDL	16	BDL	BDL	4
Type 2	py	29976	RL3	36	6	169	0	BDL	BDL	142	160	11	22	BDL	BDL	6
Type 2	py	29957	RL4	BDL	5	137	BDL	BDL	BDL	BDL	BDL	18	23	BDL	4	3
Type 2	py	29957	RL4	BDL	5	144	BDL	BDL	BDL	BDL	0	28	6	BDL	BDL	3
Type 2	py	14279	RL7	BDL	BDL	51	0	BDL	BDL	0	BDL	12	3	BDL	BDL	0
Type 2	py	14279	RL7	25	3	BDL	0	BDL	BDL	0	BDL	BDL	BDL	BDL	BDL	0
Type 2	py	14279	RL10	9285	64	BDL	0	6	485	0	BDL	214	111	18	BDL	0
Type 2	py	14279	RL10	BDL	BDL	BDL	0	5	839	0	0	141	97	BDL	BDL	0
Type 2	py	14295	RL5	BDL	BDL	494	51	BDL	BDL	BDL	BDL	BDL	14	BDL	BDL	BDL
Type 2	py	14295	RL5	BDL	4	BDL	223	BDL	BDL	BDL	BDL	BDL	BDL	BDL	BDL	BDL
Type 2	py	14295	RL3	BDL	BDL	68	508	BDL	BDL	BDL	BDL	BDL	BDL	1	BDL	BDL
Type 2	py	14295	RL3	BDL	BDL	53	183	BDL	BDL	BDL	BDL	BDL	26	BDL	BDL	3

Table E.2.3 cont. – Laser Ablation Spot Analyses for the type 2B mineral assemblage (sphalerite, pyrite)

Type Min	Phase	Sample	Spot	Sb (ppm)	Ba (ppm)	182W (ppm)	183W (ppm)	184W (ppm)	191Ir (ppm)	193Ir (ppm)	195Pt (ppm)	196Pt (ppm)
Type 2B	sp	29957	RL3	BDL	-6	BDL	BDL	BDL	BDL	BDL	BDL	BDL
Type 2B	sp	29957	RL3	18126	7827	BDL	BDL	BDL	BDL	BDL	BDL	BDL
Type 2B	sp	29957	RL6	82	145	BDL	BDL	BDL	BDL	BDL	BDL	BDL
Type 2B	sp	29957	RL6	BDL	-3	BDL	BDL	BDL	BDL	BDL	BDL	BDL
Type 2B	sp	14279	RL7	27	26951	BDL	BDL	BDL	-6	-6	0	-3
Type 2B	sp	14279	RL7	24	2404	BDL	BDL	BDL	-4	-5	0	BDL
Type 2B	sp	14279	RL5	BDL	239	BDL	BDL	BDL	-5	-7	0	-1
Type 2B	sp	14279	RL5	9	35926	BDL	BDL	BDL	-6	BDL	0	-2
Type 2	py	29986	RL4	BDL	BDL	BDL	BDL	BDL	0	0	0	0
Type 2	py	29986	RL4	3	-1	BDL	BDL	BDL	0	0	0	0
Type 2	py	29986	RL6	4	7	BDL	BDL	BDL	0	0	0	0
Type 2	py	29986	RL6	BDL	BDL	BDL	BDL	BDL	0	0	0	0
Type 2	py	25121	RL7	5637	-1	10	10	9	0	0	0	0
Type 2	py	25121	RL7	41	4	9	8	8	0	0	0	0
Type 2	py	25121	RL4	10	1620	19	21	21	0	0	0	0
Type 2	py	25121	RL4	5	3694	14	15	13	0	0	0	0
Type 2	py	14299	RL1	2090	178	BDL	BDL	BDL	0	0	0	-11
Type 2	py	14299	RL1	4863	574	BDL	BDL	BDL	0	0	0	-5
Type 2	py	14299	RL11	6804	1445	BDL	7	8	0	0	0	0
Type 2	py	14299	RL11	4007	1031	BDL	BDL	7	0	0	0	-9
Type 2	py	29976	RL3	1	8	BDL	BDL	BDL	BDL	BDL	BDL	BDL
Type 2	py	29976	RL3	15	8	8	8	8	BDL	BDL	BDL	BDL
Type 2	py	29957	RL4	1	3	BDL	BDL	BDL	BDL	BDL	BDL	BDL
Type 2	py	29957	RL4	12	0	BDL	BDL	BDL	BDL	BDL	BDL	BDL
Type 2	py	14279	RL7	BDL	0	BDL	BDL	BDL	BDL	BDL	0	BDL
Type 2	py	14279	RL7	26	0	BDL	BDL	BDL	BDL	BDL	0	BDL
Type 2	py	14279	RL10	21	2458	BDL	BDL	BDL	BDL	0	0	BDL
Type 2	py	14279	RL10	BDL	1449	BDL	BDL	BDL	BDL	0	0	BDL
Type 2	py	14295	RL5	0	0	BDL	BDL	BDL	0	BDL	0	BDL
Type 2	py	14295	RL5	0	0	BDL	BDL	BDL	0	BDL	0	BDL
Type 2	py	14295	RL3	0	0	BDL	BDL	BDL	0	BDL	0	BDL
Type 2	py	14295	RL3	1	0	BDL	BDL	BDL	0	BDL	0	BDL

Table E.2.3 cont. – Laser Ablation Spot Analyses for the type 2B mineral assemblage (sphalerite, pyrite)

Type Min	Phase	Sample	Spot	Au (ppb)	204Pb (ppm)	Tl (ppm)	206Pb (ppm)	207Pb (ppm)	208Pb (ppm)	Bi (ppm)
Type 2B	sp	29957	RL3	BDL	1716	1	1215	1272	1177	BDL
Type 2B	sp	29957	RL3	BDL	244	2	30	37	34	BDL
Type 2B	sp	29957	RL6	BDL	325	1	29	33	34	BDL
Type 2B	sp	29957	RL6	BDL	186	1	13	12	13	BDL
Type 2B	sp	14279	RL7	BDL	596	1	66	66	50	BDL
Type 2B	sp	14279	RL7	BDL	411	2	30	37	36	BDL
Type 2B	sp	14279	RL5	BDL	415	4	22	29	28	BDL
Type 2B	sp	14279	RL5	BDL	457	2	14	18	17	BDL
Type 2	py	29986	RL4	BDL	BDL	BDL	8	7	8	BDL
Type 2	py	29986	RL4	BDL	BDL	BDL	9	8	9	BDL
Type 2	py	29986	RL6	BDL	BDL	BDL	14	15	14	BDL
Type 2	py	29986	RL6	BDL	BDL	BDL	10	8	9	BDL
Type 2	py	25121	RL7	BDL	106	0	39	42	39	BDL
Type 2	py	25121	RL7	758	9983	1	6919	8031	4051	BDL
Type 2	py	25121	RL4	BDL	76	0	90	94	92	BDL
Type 2	py	25121	RL4	BDL	45	0	50	50	51	BDL
Type 2	py	14299	RL1	103800	815	433	496	491	488	BDL
Type 2	py	14299	RL1	51830	1274	1544	246	255	272	BDL
Type 2	py	14299	RL11	132800	3328	1781	1827	2064	1712	BDL
Type 2	py	14299	RL11	72060	878	1280	200	209	206	BDL
Type 2	py	29976	RL3	BDL	30	1	27	28	32	BDL
Type 2	py	29976	RL3	BDL	42	0	30	31	31	BDL
Type 2	py	29957	RL4	BDL	28	1	23	25	25	BDL
Type 2	py	29957	RL4	BDL	21	0	11	13	11	BDL
Type 2	py	14279	RL7	BDL	BDL	BDL	BDL	5	6	BDL
Type 2	py	14279	RL7	BDL	16	BDL	BDL	5	BDL	BDL
Type 2	py	14279	RL10	7001	1101	8	704	934	889	BDL
Type 2	py	14279	RL10	1185	2348	4	1335	1670	1518	BDL
Type 2	py	14295	RL5	1097	BDL	BDL	14	15	13	7
Type 2	py	14295	RL5	BDL	BDL	BDL	BDL	BDL	BDL	BDL
Type 2	py	14295	RL3	BDL	BDL	BDL	BDL	BDL	BDL	BDL
Type 2	py	14295	RL3							

Table E.2.3 cont. – Laser Ablation Spot Analyses for the type 2B mineral assemblage (galena, chalcopyrite)

Type Min	Phase	Sample	Spot	Sc (ppm)	Ti (ppm)	V (ppm)	Cr (ppm)	Mn (ppm)	Fe (ppm)	Co (ppm)	60Ni (ppm)	61Ni (ppm)	63Cu (ppm)	65Cu (ppm)
Type 2B	gn	29986	RL2	12	363	BDL	12	51	BDL	11	29	431	252	596
Type 2B	gn	29986	RL2	10	329	BDL	8	53	BDL	11	30	231	659	465
Type 2B	gn	25121	RL2	8	285	BDL	10	69	BDL	9	34	225	1066	890
Type 2B	gn	25121	RL2	11	286	9	10	48	BDL	10	25	159	273	293
Type 2B	gn	25121	RL4	13	338	70	12	205	BDL	11	26	321	236	235
Type 2B	gn	25151	RL5	29	437	BDL	22	43	BDL	16	59	1275	62	79
Type 2B	gn	25151	RL5	43	574	BDL	32	47	BDL	20	84	1921	61	81
Type 2B	gn	25151	RL8	49	635	BDL	36	50	BDL	24	96	2113	57	87
Type 2B	gn	25151	RL8	60	782	BDL	46	52	BDL	26	113	2563	75	123
Type 2B	gn	29976	RL4	15	177	BDL	13	53	BDL	10	31	438	125	55
Type 2B	gn	29976	RL4	22	282	BDL	17	53	BDL	12	53	821	75	79
Type 2B	gn	29962	RL1	22	379	BDL	18	BDL	BDL	13	43	887	103	204
Type 2B	gn	29962	RL1	19	338	BDL	15	BDL	BDL	10	47	750	372	430
Type 2B	gn	29962	RL5	38	568	BDL	31	29	BDL	17	71	1710	615	636
Type 2B	gn	29962	RL5	49	701	BDL	38	31	BDL	22	113	2138	290	300
Type 2B	gn	14291	RL7	18	316	BDL	17	51	0	9	42	552	144	219
Type 2B	gn	14291	RL7	16	238	BDL	13	48	0	10	42	555	100	95
Type 2B	gn	14291	RL7	10	176	BDL	11	63	0	7	22	318	34	43
Type 2B	gn	14291	RL7	11	174	BDL	10	40	0	7	21	296	26	31
Type 2B	gn	14291	RL7	11	200	BDL	14	42	0	8	26	418	42	59
Type 2B	gn	14291	RL9	25	364	BDL	16	44	0	13	38	843	53764	49490
Type 2B	gn	25109	RL3a	20	385	BDL	17	BDL	BDL	9	47	1001	62	91
Type 2B	gn	25109	RL3a	9	340	BDL	10	32	BDL	7	26	524	148	78
Type 2B	gn	25109	RL9	21	407	BDL	14	BDL	BDL	12	47	872	56	86
Type 2B	gn	25109	RL9	20	255	BDL	11	BDL	BDL	8	50	940	360	55
Type 2B	ccp	29986	RL2	BDL	0	BDL	BDL	85	0	BDL	BDL	BDL	165816	167638
Type 2B	ccp	29986	RL2	BDL	260	BDL	BDL	38	133829	8	9	BDL	145889	150282
Type 2B	ccp	25152	RL6	BDL	247	9	5	40	136066	8	11	BDL	153785	156659
Type 2B	ccp	25152	RL6	6	242	9	BDL	42	132468	8	BDL	BDL	115727	121405
Type 2B	ccp	29976	RL3	BDL	BDL	BDL	BDL	BDL	166614	BDL	BDL	31	207365	198065
Type 2B	ccp	29976	RL3	BDL	BDL	BDL	BDL	BDL	170175	BDL	BDL	BDL	206811	195880
Type 2B	ccp	29976	RL1	BDL	BDL	BDL	BDL	1506	BDL	BDL	BDL	24	956	498
Type 2B	ccp	14291	RL9b	BDL	157	BDL	BDL	BDL	149692	BDL	BDL	BDL	206281	198721

Table E.2.3 cont. – Laser Ablation Spot Analyses for the type 2B mineral assemblage (galena, chalcopyrite)

Type Min	Phase	Sample	Spot	Zn (ppm)	Ge (ppm)	As (ppm)	Se (ppm)	Rb (ppm)	Sr (ppm)	Zr (ppm)	Nb (ppm)	Mo (ppm)	Ag (ppm)	Cd (ppm)	In (ppm)	Sn (ppm)
Type 2B	gn	29986	RL2	367	12	BDL	217	BDL	20	5	2	10	663	38	7	13
Type 2B	gn	29986	RL2	976	8	BDL	BDL	BDL	22	6	1	9	448	24	8	11
Type 2B	gn	25121	RL2	1107	7	765	526	BDL	21	10	0	10	605	15	BDL	9
Type 2B	gn	25121	RL2	403	10	89	471	BDL	16	7	1	11	678	16	BDL	9
Type 2B	gn	25121	RL4	214700	225	BDL	530	BDL	315	7	1	54	1257	2211	BDL	26
Type 2B	gn	25151	RL5	54	27	BDL	0	7	11	10	4	26	132	55	8	23
Type 2B	gn	25151	RL5	73	42	BDL	0	8	13	13	5	136	124	78	9	26
Type 2B	gn	25151	RL8	75	40	47	0	9	13	15	6	69	52	67	10	28
Type 2B	gn	25151	RL8	103	50	BDL	0	11	14	18	7	124	117	91	10	31
Type 2B	gn	29976	RL4	468	13	BDL	0	6	12	4	2	9	6549	32	5	16
Type 2B	gn	29976	RL4	546	20	BDL	0	7	11	5	3	10	882	67	5	19
Type 2B	gn	29962	RL1	4423	18	BDL	0	6	9	4	3	10	938	91	BDL	17
Type 2B	gn	29962	RL1	964	15	BDL	0	5	11	4	2	9	505	49	BDL	14
Type 2B	gn	29962	RL5	881	28	BDL	1668	8	9	9	4	27	3244	203	6	40
Type 2B	gn	29962	RL5	697	34	BDL	1955	9	9	10	6	38	1450	137	7	45
Type 2B	gn	14291	RL7	959	16	66	0	5	13	14	1	476	2734	48	5	15
Type 2B	gn	14291	RL7	936	13	43	0	5	10	6	2	127	2616	56	5	16
Type 2B	gn	14291	RL7	13720	10	BDL	0	4	12	8	1	105	844	90	BDL	5
Type 2B	gn	14291	RL7	613	9	BDL	0	4	11	6	1	87	855	18	BDL	5
Type 2B	gn	14291	RL7	469	11	BDL	0	5	11	8	1	90	822	26	BDL	5
Type 2B	gn	14291	RL9	404	19	1766	0	5	18	10	3	308	1839	30	5	16
Type 2B	gn	25109	RL3a	236	10	BDL	0	BDL	BDL	0	3	8	2554	46	BDL	20
Type 2B	gn	25109	RL3a	371	11	BDL	0	BDL	BDL	0	2	7	1715	32	BDL	18
Type 2B	gn	25109	RL9	523	17	BDL	0	5	BDL	0	4	9	3087	48	BDL	29
Type 2B	gn	25109	RL9	674	11	BDL	121	BDL	BDL	5	3	7	1337	15	BDL	14
Type 2B	ccp	29986	RL2	152	9	BDL	BDL	BDL	19	7	0	BDL	22	3	BDL	5
Type 2B	ccp	29986	RL2	44	7	BDL	BDL	BDL	12	BDL	BDL	5	19	2	BDL	6
Type 2B	ccp	25152	RL6	282	9	BDL	BDL	BDL	13	BDL	0	5	6	BDL	BDL	16
Type 2B	ccp	25152	RL6	404	7	BDL	BDL	BDL	13	BDL	BDL	5	5	BDL	BDL	14
Type 2B	ccp	29976	RL3	202	7	BDL	0	BDL	9	BDL	0	BDL	88	2	5	14
Type 2B	ccp	29976	RL3	81	7	BDL	0	BDL	BDL	BDL	0	BDL	90	BDL	BDL	13
Type 2B	ccp	29976	RL1	96367	5	BDL	0	BDL	143	BDL	0	BDL	910	664	BDL	13
Type 2B	ccp	14291	RL9b	222	40	0	BDL	BDL	BDL	BDL	0	4	660	BDL	BDL	109

Table E.2.3 cont. – Laser Ablation Spot Analyses for the type 2B mineral assemblage (galena, chalcopyrite)

Type Min	Phase	Sample	Spot	Sb (ppm)	Ba (ppm)	182W (ppm)	183W (ppm)	184W (ppm)	191Ir (ppm)	193Ir (ppm)	195Pt (ppm)	196Pt (ppm)
Type 2B	gn	29986	RL2	737	812	8	8	7	0	0	0	0
Type 2B	gn	29986	RL2	545	1118	8	8	7	0	0	0	0
Type 2B	gn	25121	RL2	809	311	BDL	BDL	BDL	0	0	0	0
Type 2B	gn	25121	RL2	957	168	12	10	9	0	0	0	0
Type 2B	gn	25121	RL4	1888	9331	9	9	8	0	0	0	0
Type 2B	gn	25151	RL5	132	4	9	12	10	-3	0	3	10
Type 2B	gn	25151	RL5	117	7	11	14	10	17	-1	20	20
Type 2B	gn	25151	RL8	17	12	11	15	10	46	7	33	26
Type 2B	gn	25151	RL8	56	15	12	17	11	81	20	41	35
Type 2B	gn	29976	RL4	947	52	5	6	5	BDL	BDL	BDL	BDL
Type 2B	gn	29976	RL4	961	42	5	8	5	BDL	BDL	BDL	BDL
Type 2B	gn	29962	RL1	999	13	4	5	4	BDL	BDL	BDL	BDL
Type 2B	gn	29962	RL1	446	31	BDL	5	BDL	BDL	BDL	BDL	BDL
Type 2B	gn	29962	RL5	2239	9	BDL	10	6	9	2	5	5
Type 2B	gn	29962	RL5	1823	9	BDL	12	7	14	5	6	7
Type 2B	gn	14291	RL7	3499	136	7	7	6	2	0	2	3
Type 2B	gn	14291	RL7	3664	50	6	8	5	0	2	2	3
Type 2B	gn	14291	RL7	1282	26	5	6	5	1	0	2	2
Type 2B	gn	14291	RL7	1468	33	5	6	5	0	0	2	2
Type 2B	gn	14291	RL7	1172	21	5	7	5	3	1	2	3
Type 2B	gn	14291	RL9	140400	184	7	8	6	3	3	4	4
Type 2B	gn	25109	RL3a	2933	131	BDL	BDL	BDL	0	-7	0	1
Type 2B	gn	25109	RL3a	2214	607	BDL	BDL	BDL	-6	BDL	-2	BDL
Type 2B	gn	25109	RL9	3735	25	BDL	7	BDL	-1	-6	2	2
Type 2B	gn	25109	RL9	1616	60	BDL	BDL	BDL	-5	-5	0	3
Type 2B	ccp	29986	RL2	BDL	92	BDL	BDL	BDL	BDL	BDL	BDL	BDL
Type 2B	ccp	29986	RL2	4	BDL	BDL	BDL	BDL	0	0	0	0
Type 2B	ccp	25152	RL6	BDL	BDL	BDL	BDL	BDL	0	0	0	0
Type 2B	ccp	25152	RL6	BDL	BDL	BDL	BDL	BDL	0	0	0	0
Type 2B	ccp	29976	RL3	BDL	33	BDL	BDL	BDL	BDL	BDL	BDL	BDL
Type 2B	ccp	29976	RL3	BDL	BDL	BDL	BDL	BDL	BDL	BDL	BDL	BDL
Type 2B	ccp	29976	RL1	159	21	BDL	BDL	BDL	BDL	BDL	BDL	BDL
Type 2B	ccp	14291	RL9b	0	0	BDL	BDL	BDL	BDL	-3	0	BDL

Table E.2.3 cont. – Laser Ablation Spot Analyses for the type 2B mineral assemblage (galena, chalcopyrite)

Type Min	Phase	Sample	Spot	Au (ppb)	204Pb (ppm)	Tl (ppm)	206Pb (ppm)	207Pb (ppm)	208Pb (ppm)	Bi (ppm)
Type 2B	gn	29986	RL2	773	788600	1	725700	785800	744700	18
Type 2B	gn	29986	RL2	937	579100	1	496200	515000	487100	14
Type 2B	gn	25121	RL2	799	272000	12	229400	249500	259600	17
Type 2B	gn	25121	RL2	877	402000	17	380800	419600	383100	21
Type 2B	gn	25121	RL4	1113	572600	21	507400	573500	538100	25
Type 2B	gn	25151	RL5	2190	1316000	13	1208000	1315000	1227000	52
Type 2B	gn	25151	RL5	2730	1406000	16	1263000	1383000	1310000	75
Type 2B	gn	25151	RL8	2922	1264000	9	1142000	1260000	1182000	82
Type 2B	gn	25151	RL8	3383	1343000	13	1206000	1317000	1240000	105
Type 2B	gn	29976	RL4	1282	876800	1	724500	845600	746900	18
Type 2B	gn	29976	RL4	1479	1318000	2	1096000	1219000	1118000	29
Type 2B	gn	29962	RL1	1093	1161000	24	1044000	1106000	1018000	41
Type 2B	gn	29962	RL1	1556	710500	11	644100	667200	645100	28
Type 2B	gn	29962	RL5	5063	1747000	38	1731000	1912000	1815000	68
Type 2B	gn	29962	RL5	8552	1944000	39	1842000	2046000	1965000	90
Type 2B	gn	14291	RL7	1715	969648	8	633400	686200	689800	38
Type 2B	gn	14291	RL7	1527	1097689	8	816100	863200	828000	45
Type 2B	gn	14291	RL7	922	366066	3	260600	284000	274400	19
Type 2B	gn	14291	RL7	763	355894	2	259700	280100	276700	19
Type 2B	gn	14291	RL7	1103	400142	3	289800	317200	306800	22
Type 2B	gn	14291	RL9	3624	1254847	11	918700	956800	910100	55
Type 2B	gn	25109	RL3a	1525	902900	122	542473	603438	543320	29
Type 2B	gn	25109	RL3a	848	578800	92	368960	433945	433835	22
Type 2B	gn	25109	RL9	944	1022000	294	617682	774308	703937	36
Type 2B	gn	25109	RL9	BDL	329100	113	278000	350700	316900	12
Type 2B	ccp	29986	RL2	BDL	53	BDL	38	39	36	BDL
Type 2B	ccp	29986	RL2	BDL	21	BDL	10	9	10	BDL
Type 2B	ccp	25152	RL6	BDL	BDL	BDL	8	8	BDL	BDL
Type 2B	ccp	25152	RL6	BDL	24	0	8	8	8	BDL
Type 2B	ccp	29976	RL3	BDL	49	BDL	28	31	31	BDL
Type 2B	ccp	29976	RL3	BDL	BDL	0	BDL	7	7	BDL
Type 2B	ccp	29976	RL1	BDL	7247	0	4008	3836	3076	BDL
Type 2B	ccp	14291	RL9b	BDL	BDL	0	8	5	7	BDL

Table E.2.3 cont. – Laser Ablation Spot Analyses for the type 2B mineral assemblage (chalcopyrite, tetrahedrite)

Type Min	Phase	Sample	Spot	Sc (ppm)	Ti (ppm)	V (ppm)	Cr (ppm)	Mn (ppm)	Fe (ppm)	Co (ppm)	60Ni (ppm)	61Ni (ppm)	63Cu (ppm)	65Cu (ppm)
Type 2B	ccp	14291	RL9b	BDL	163	5	BDL	BDL	136593	4	BDL	52	167229	176221
Type 2B	ccp	25109	RL2	0	BDL	BDL	BDL	BDL	155277	BDL	BDL	BDL	133176	123053
Type 2B	ccp	25109	RL5	BDL	BDL	BDL	BDL	40	199854	BDL	BDL	BDL	178117	188881
Type 2B	ccp	25109	RL5	BDL	BDL	BDL	BDL	BDL	163264	BDL	BDL	BDL	172575	190585
Type 2B	trt	29986	RL3	BDL	0	BDL	BDL	86	0	BDL	BDL	29	192025	193492
Type 2B	trt	29986	RL3	BDL	0	BDL	BDL	105	0	BDL	BDL	BDL	236045	226821
Type 2B	trt	25152	RL1	BDL	0	BDL	BDL	114	0	BDL	BDL	62	159453	170733
Type 2B	trt	25152	RL1	BDL	0	BDL	BDL	91	0	BDL	BDL	BDL	171975	165083
Type 2B	trt	25152	RL3	BDL	0	BDL	BDL	BDL	0	BDL	BDL	BDL	176078	172242
Type 2B	trt	25152	RL3	BDL	0	BDL	BDL	BDL	0	BDL	BDL	BDL	214494	212856
Type 2B	trt	25121	RL2	BDL	0	BDL	BDL	BDL	0	BDL	BDL	BDL	164996	173492
Type 2B	trt	25121	RL2	BDL	0	BDL	BDL	93	0	BDL	BDL	BDL	210186	210626
Type 2B	trt	25121	RL6	BDL	0	BDL	BDL	243	0	BDL	BDL	BDL	115246	127865
Type 2B	trt	25121	RL6	BDL	0	14	BDL	89	0	BDL	BDL	BDL	78358	79978
Type 2B	trt	25151	RL3	BDL	0	BDL	BDL	474	0	BDL	BDL	BDL	235820	229180
Type 2B	trt	25151	RL3	BDL	0	BDL	BDL	305	0	BDL	BDL	53	433780	433086
Type 2B	trt	25151	RL8	BDL	0	BDL	BDL	282	0	BDL	BDL	BDL	359886	341350
Type 2B	trt	25151	RL8	BDL	0	BDL	7	284	0	BDL	BDL	BDL	354234	356213
Type 2B	trt	14299	RL4	BDL	0	BDL	BDL	180	0	9	16	39	136247	144344
Type 2B	trt	29962	RL1	BDL	BDL	BDL	BDL	465	56787	BDL	BDL	34	254551	272312
Type 2B	trt	29962	RL1	BDL	BDL	BDL	BDL	884	BDL	BDL	11	86	218119	190479
Type 2B	trt	29962	RL2	BDL	BDL	BDL	BDL	128	BDL	BDL	BDL	BDL	295886	283563
Type 2B	trt	29962	RL2	BDL	BDL	BDL	BDL	857	BDL	BDL	BDL	36	326659	280365
Type 2B	trt	29957	RL3	BDL	287	BDL	BDL	470	BDL	5	23	105	325334	338475
Type 2B	trt	29957	RL3	BDL	BDL	BDL	BDL	470	BDL	5	24	71	261804	264352
Type 2B	trt	29957	RL6	BDL	BDL	13	BDL	589	BDL	6	19	65	215062	221334
Type 2B	trt	14279	RL7	0	BDL	BDL	BDL	166	BDL	BDL	BDL	35	336340	335209
Type 2B	trt	14279	RL7	0	BDL	BDL	BDL	176	BDL	BDL	BDL	BDL	371864	329484
Type 2B	trt	29967	RL3b	BDL	BDL	BDL	BDL	467	BDL	BDL	BDL	22	339170	360338

Table E.2.3 cont. – Laser Ablation Spot Analyses for the type 2B mineral assemblage (chalcopyrite, tetrahedrite)

Type Min	Phase	Sample	Spot	Zn (ppm)	Ge (ppm)	As (ppm)	Se (ppm)	Rb (ppm)	Sr (ppm)	Zr (ppm)	Nb (ppm)	Mo (ppm)	Ag (ppm)	Cd (ppm)	In (ppm)	Sn (ppm)
Type 2B	ccp	14291	RL9b	1001	31	0	BDL	BDL	9	BDL	0	255	643	7	5	111
Type 2B	ccp	25109	RL2	503	7	BDL	0	BDL	BDL	0	BDL	BDL	101	5	BDL	17
Type 2B	ccp	25109	RL5	551	3	BDL	56	BDL	BDL	BDL	0	7	12	1	BDL	8
Type 2B	ccp	25109	RL5	353	3	BDL	BDL	BDL	BDL	BDL	0	BDL	13	7	BDL	13
Type 2B	trt	29986	RL3	70067	8	74277	BDL	BDL	26	8	BDL	BDL	91543	3968	BDL	6
Type 2B	trt	29986	RL3	70067	11	82885	99	BDL	27	BDL	0	BDL	85285	4733	BDL	5
Type 2B	trt	25152	RL1	56828	9	135043	214	BDL	23	8	0	BDL	2301	547	BDL	BDL
Type 2B	trt	25152	RL1	56828	7	119905	87	BDL	18	BDL	0	BDL	2323	543	BDL	BDL
Type 2B	trt	25152	RL3	49740	BDL	115270	117	BDL	BDL	BDL	0	22	3012	502	BDL	BDL
Type 2B	trt	25152	RL3	49740	BDL	153851	BDL	BDL	BDL	11	0	BDL	3823	641	BDL	BDL
Type 2B	trt	25121	RL2	48693	10	82594	BDL	BDL	BDL	BDL	BDL	BDL	8969	562	BDL	BDL
Type 2B	trt	25121	RL2	48693	9	101066	82	BDL	19	10	0	23	9093	732	BDL	5
Type 2B	trt	25121	RL6	143761	13	76490	BDL	BDL	21	BDL	0	24	8606	1556	BDL	5
Type 2B	trt	25121	RL6	37747	8	48131	BDL	BDL	18	BDL	BDL	114	5790	375	BDL	BDL
Type 2B	trt	25151	RL3	323066	13	120800	BDL	BDL	33	9	0	3173	3324	6088	BDL	8
Type 2B	trt	25151	RL3	72610	16	170006	192	BDL	21	9	0	7	2043	4130	BDL	6
Type 2B	trt	25151	RL8	72908	11	198877	236	BDL	BDL	BDL	0	BDL	1218	2908	BDL	4
Type 2B	trt	25151	RL8	72908	11	194899	147	BDL	BDL	BDL	0	BDL	1252	3049	BDL	6
Type 2B	trt	14299	RL4	47018	8	99780	151	BDL	19	7	BDL	BDL	682	1348	BDL	BDL
Type 2B	trt	29962	RL1	50277	13	102070	0	BDL	BDL	BDL	0	BDL	3505	736	BDL	12
Type 2B	trt	29962	RL1	50277	10	88247	BDL	BDL	BDL	3	0	6	2903	1578	BDL	13
Type 2B	trt	29962	RL2	53058	11	118077	BDL	BDL	16	BDL	0	52	4706	844	5	20
Type 2B	trt	29962	RL2	53058	12	128542	BDL	BDL	BDL	BDL	1	158	4375	1297	BDL	15
Type 2B	trt	29957	RL3	83473	22	143787	382	BDL	BDL	2	1	90	832	3145	14	17
Type 2B	trt	29957	RL3	83473	17	117009	118	BDL	21	BDL	0	64	617	2715	11	13
Type 2B	trt	29957	RL6	276194	23	91790	256	BDL	BDL	BDL	0	168	575	4966	29	19
Type 2B	trt	14279	RL7	82063	6	82543	0	BDL	BDL	0	1	14	3656	1927	BDL	12
Type 2B	trt	14279	RL7	92728	7	84021	0	BDL	BDL	0	BDL	BDL	3808	2246	BDL	23
Type 2B	trt	29967	RL3b	77328	7	102017	78	BDL	BDL	3	0	64	1167	2055	BDL	10

Table E.2.3 cont. – Laser Ablation Spot Analyses for the type 2B mineral assemblage (chalcopyrite, tetrahedrite)

Type Min	Phase	Sample	Spot	Sb (ppm)	Ba (ppm)	182W (ppm)	183W (ppm)	184W (ppm)	191Ir (ppm)	193Ir (ppm)	195Pt (ppm)	196Pt (ppm)
Type 2B	ccp	14291	RL9b	15	1204	5	5	4	BDL	-3	0	BDL
Type 2B	ccp	25109	RL2	3	52	BDL	BDL	BDL	-7	0	0	BDL
Type 2B	ccp	25109	RL5	0	142	BDL	BDL	BDL	0	-8	0	BDL
Type 2B	ccp	25109	RL5	0	0	BDL	BDL	BDL	0	-8	0	BDL
Type 2B	trt	29986	RL3	193486	270	BDL	BDL	BDL	BDL	BDL	BDL	16
Type 2B	trt	29986	RL3	199776	466	BDL	10	BDL	BDL	BDL	2	59
Type 2B	trt	25152	RL1	12988	20	BDL	BDL	BDL	BDL	BDL	1	BDL
Type 2B	trt	25152	RL1	12583	37	BDL	BDL	BDL	BDL	BDL	1	BDL
Type 2B	trt	25152	RL3	10827	22	BDL	BDL	BDL	BDL	BDL	BDL	BDL
Type 2B	trt	25152	RL3	12378	35	BDL	BDL	BDL	BDL	BDL	BDL	BDL
Type 2B	trt	25121	RL2	57530	11	BDL	BDL	BDL	BDL	BDL	BDL	BDL
Type 2B	trt	25121	RL2	78051	26	10	14	13	BDL	BDL	1	BDL
Type 2B	trt	25121	RL6	45570	183	BDL	BDL	BDL	BDL	BDL	1	BDL
Type 2B	trt	25121	RL6	28563	1234	BDL	BDL	BDL	BDL	BDL	BDL	BDL
Type 2B	trt	25151	RL3	80930	2477	BDL	BDL	BDL	BDL	BDL	1	BDL
Type 2B	trt	25151	RL3	140969	14	8	9	BDL	BDL	BDL	2	BDL
Type 2B	trt	25151	RL8	100592	8	BDL	BDL	BDL	BDL	BDL	1	BDL
Type 2B	trt	25151	RL8	98628	6	BDL	BDL	BDL	BDL	BDL	1	BDL
Type 2B	trt	14299	RL4	39870	89	BDL	BDL	BDL	BDL	BDL	BDL	BDL
Type 2B	trt	29962	RL1	51590	-4	BDL	BDL	BDL	BDL	BDL	BDL	BDL
Type 2B	trt	29962	RL1	50918	-1	BDL	BDL	BDL	BDL	BDL	BDL	BDL
Type 2B	trt	29962	RL2	61065	0	BDL	BDL	BDL	BDL	BDL	BDL	BDL
Type 2B	trt	29962	RL2	62012	7	BDL	BDL	BDL	BDL	BDL	BDL	BDL
Type 2B	trt	29957	RL3	74675	38	BDL	5	4	BDL	BDL	BDL	2
Type 2B	trt	29957	RL3	61808	2345	BDL	5	BDL	BDL	BDL	BDL	BDL
Type 2B	trt	29957	RL6	47400	50	BDL	6	BDL	BDL	BDL	BDL	BDL
Type 2B	trt	14279	RL7	218597	1	BDL	BDL	BDL	-5	-7	0	BDL
Type 2B	trt	14279	RL7	219957	4	BDL	BDL	BDL	-6	-7	0	BDL
Type 2B	trt	29967	RL3b	76610	2	BDL	BDL	BDL	-8	-7	0	BDL

Table E.2.3 cont. – Laser Ablation Spot Analyses for the type 2B mineral assemblage (chalcopyrite, tetrahedrite)

Type Min	Phase	Sample	Spot	Au (ppb)	204Pb (ppm)	Tl (ppm)	206Pb (ppm)	207Pb (ppm)	208Pb (ppm)	Bi (ppm)
Type 2B	ccp	14291	RL9b	BDL	78	0	65	51	64	BDL
Type 2B	ccp	25109	RL2	BDL	3010	1	1590	2122	1899	BDL
Type 2B	ccp	25109	RL5	BDL	361	0	345	344	378	BDL
Type 2B	ccp	25109	RL5	BDL	51	0	83	93	85	BDL
Type 2B	trt	29986	RL3	BDL	2675	0	263	342	329	BDL
Type 2B	trt	29986	RL3	BDL	6408	0	1380	2362	2399	BDL
Type 2B	trt	25152	RL1	BDL	209	BDL	29	31	36	BDL
Type 2B	trt	25152	RL1	BDL	153	BDL	18	18	18	BDL
Type 2B	trt	25152	RL3	BDL	119	BDL	18	18	18	BDL
Type 2B	trt	25152	RL3	BDL	67	BDL	22	20	20	BDL
Type 2B	trt	25121	RL2	BDL	497	BDL	232	282	238	BDL
Type 2B	trt	25121	RL2	BDL	371	BDL	108	136	117	BDL
Type 2B	trt	25121	RL6	BDL	389	0	118	134	133	BDL
Type 2B	trt	25121	RL6	BDL	136	0	22	25	23	BDL
Type 2B	trt	25151	RL3	1666	237	11	118	120	115	BDL
Type 2B	trt	25151	RL3	1512	179	3	28	33	31	BDL
Type 2B	trt	25151	RL8	BDL	150	1	27	30	28	BDL
Type 2B	trt	25151	RL8	BDL	131	1	24	26	24	BDL
Type 2B	trt	14299	RL4	BDL	374	1	28	30	28	BDL
Type 2B	trt	29962	RL1	BDL	1127	1	623	657	2380	BDL
Type 2B	trt	29962	RL1	BDL	75765	1	49006	58242	54758	5
Type 2B	trt	29962	RL2	BDL	224	0	104	127	115	5
Type 2B	trt	29962	RL2	BDL	254	1	37	36	36	BDL
Type 2B	trt	29957	RL3	BDL	3411	1	2541	3750	2385	5
Type 2B	trt	29957	RL3	BDL	631	1	115	117	304	BDL
Type 2B	trt	29957	RL6	BDL	464	3	43	43	44	5
Type 2B	trt	14279	RL7	BDL	709	2	25	38	33	BDL
Type 2B	trt	14279	RL7	BDL	778	3	26	138	31	BDL
Type 2B	trt	29967	RL3b	BDL	129	1	30	32	28	BDL

Table E.2.4 – Laser Ablation Spot Analyses for the type 3 mineral assemblage

Type Min	Phase	Sample	Spot	Sc (ppm)	Ti (ppm)	V (ppm)	Cr (ppm)	Mn (ppm)	Fe (ppm)	Co (ppm)	60Ni (ppm)	61Ni (ppm)	63Cu (ppm)	65Cu (ppm)
Type 3	sp	25120	RL3	BDL	BDL	25	BDL	406	69662	BDL	BDL	BDL	244	250
Type 3	sp	25120	RL3	BDL	BDL	126	17	418	69529	BDL	BDL	BDL	66	67
Type 3	sp	25127	RL3	0	BDL	BDL	0	186	BDL	0	BDL	BDL	14	9
Type 3	sp	25127	RL3	0	BDL	BDL	0	104	BDL	0	BDL	BDL	34	33
Type 3	py	14291	RL7	BDL	BDL	20	BDL	34	873476	BDL	3342	3329	40	39
Type 3	py	14291	RL7	BDL	BDL	BDL	BDL	BDL	1197972	5	2961	2492	BDL	BDL
Type 3	py	14291	RL9	BDL	156	8	BDL	BDL	252303	BDL	3957	3429	13	14
Type 3	py	14291	RL9	5	166	BDL	BDL	BDL	244424	5	1419	1258	BDL	12
Type 3	ccp	25120	RL7	BDL	BDL	BDL	BDL	BDL	252064	BDL	BDL	31	216793	212405
Type 3	ccp	25120	RL7	BDL	BDL	15	6	BDL	180061	BDL	BDL	BDL	219394	205246

Table E.2.4 cont. – Laser Ablation Spot Analyses for the type 3 mineral assemblage

Type Min	Phase	Sample	Spot	Zn (ppm)	Ge (ppm)	As (ppm)	Se (ppm)	Rb (ppm)	Sr (ppm)	Zr (ppm)	Nb (ppm)	Mo (ppm)	Ag (ppm)	Cd (ppm)	In (ppm)	Sn (ppm)
Type 3	sp	25120	RL3	417458	5	BDL	BDL	BDL	17	BDL	BDL	313	89	3047	BDL	21
Type 3	sp	25120	RL3	422145	5	BDL	BDL	BDL	BDL	11	0	137	62	3047	BDL	25
Type 3	sp	25127	RL3	386576	5	BDL	0	BDL	0	0	0	0	0	3880	6	8
Type 3	sp	25127	RL3	367708	4	BDL	0	BDL	0	0	0	0	59	3880	6	20
Type 3	py	14291	RL7	BDL	5	426	0	BDL	7	BDL	BDL	2714	77	15	BDL	BDL
Type 3	py	14291	RL7	BDL	5	320	0	BDL	7	BDL	BDL	BDL	BDL	BDL	BDL	BDL
Type 3	py	14291	RL9	56	4	353	BDL	BDL	BDL	BDL	BDL	130	BDL	BDL	BDL	BDL
Type 3	py	14291	RL9	BDL	3	110	BDL	BDL	BDL	1743	0	BDL	BDL	BDL	BDL	3
Type 3	ccp	25120	RL7	1018	6	BDL	BDL	BDL	BDL	BDL	0	BDL	245	10	BDL	62
Type 3	ccp	25120	RL7	714	BDL	BDL	BDL	BDL	BDL	45	0	120	224	8	BDL	55

Table E.2.4 cont. – Laser Ablation Spot Analyses for the type 3 mineral assemblage

Type Min	Phase	Sample	Spot	Sb (ppm)	Ba (ppm)	182W (ppm)	183W (ppm)	184W (ppm)	191Ir (ppm)	193Ir (ppm)	195Pt (ppm)	196Pt (ppm)	Au (ppb)
Type 3	sp	25120	RL3	97	288	6	6	5	-8	-6	0	BDL	BDL
Type 3	sp	25120	RL3	71	208	BDL	BDL	BDL	-8	-6	0	BDL	BDL
Type 3	sp	25127	RL3	0	-11	0	0	0	0	0	0	-7	0
Type 3	sp	25127	RL3	5	-11	0	0	0	0	0	0	1	0
Type 3	py	14291	RL7	144	-7	8	7	8	BDL	-1	BDL	BDL	BDL
Type 3	py	14291	RL7	0	0	BDL	BDL	BDL	BDL	BDL	BDL	BDL	BDL
Type 3	py	14291	RL9	3	37	BDL	BDL	BDL	BDL	BDL	0	BDL	BDL
Type 3	py	14291	RL9	0	438	BDL	BDL	BDL	BDL	BDL	BDL	BDL	BDL
Type 3	ccp	25120	RL7	2	0	BDL	BDL	BDL	0	BDL	0	BDL	BDL
Type 3	ccp	25120	RL7	24	32	BDL	BDL	BDL	0	-8	0	BDL	BDL

Table E.2.4 cont. – Laser Ablation Spot Analyses for the type 3 mineral assemblage

Type Min	Phase	Sample	Spot	204Pb (ppm)	Tl (ppm)	206Pb (ppm)	207Pb (ppm)	208Pb (ppm)	Bi (ppm)
Type 3	sp	25120	RL3	1015	0	723	775	787	BDL
Type 3	sp	25120	RL3	551	0	466	557	518	BDL
Type 3	sp	25127	RL3	857	BDL	0	0	0	0
Type 3	sp	25127	RL3	2015	1	949	1126	1071	0
Type 3	py	14291	RL7	52475	0	17030	18140	17310	6
Type 3	py	14291	RL7	BDL	BDL	4	5	5	BDL
Type 3	py	14291	RL9	130	BDL	86	69	88	BDL
Type 3	py	14291	RL9	BDL	BDL	26	4	6	BDL
Type 3	ccp	25120	RL7	15	0	6	5	6	BDL
Type 3	ccp	25120	RL7	1038	1	881	837	952	BDL

Table E.2.5 – Laser Ablation Spot Analyses for the type 4 mineral assemblage

Type Min	Phase	Sample	Spot	Sc (ppm)	Ti (ppm)	V (ppm)	Cr (ppm)	Mn (ppm)	Fe (ppm)	Co (ppm)	60Ni (ppm)	61Ni (ppm)	63Cu (ppm)	65Cu (ppm)
Type 4	ccp	14295	RL4	BDL	BDL	BDL	BDL	BDL	245110	BDL	BDL	BDL	186259	207746
Type 4	ccp	14295	RL4	BDL	BDL	BDL	BDL	BDL	238798	BDL	BDL	BDL	197455	209564

Table E.2.5 cont. – Laser Ablation Spot Analyses for the type 4 mineral assemblage

Type Min	Phase	Sample	Spot	Zn (ppm)	Ge (ppm)	As (ppm)	Se (ppm)	Rb (ppm)	Sr (ppm)	Zr (ppm)	Nb (ppm)	Mo (ppm)	Ag (ppm)	Cd (ppm)	In (ppm)	Sn (ppm)
Type 4	ccp	14295	RL4	64	4	BDL	107	BDL	BDL	BDL	0	BDL	162	3	18	22
Type 4	ccp	14295	RL4	59	4	BDL	84	BDL	BDL	BDL	0	BDL	178	4	16	19

Table E.2.5 cont. – Laser Ablation Spot Analyses for the type 4 mineral assemblage

Type Min	Phase	Sample	Spot	Sb (ppm)	Ba (ppm)	182W (ppm)	183W (ppm)	184W (ppm)	191Ir (ppm)	193Ir (ppm)	195Pt (ppm)	196Pt (ppm)
Type 4	ccp	14295	RL4	0	0	BDL	BDL	BDL	0	BDL	0	BDL
Type 4	ccp	14295	RL4	0	0	BDL	BDL	BDL	0	-8	0	BDL

Table E.2.5 cont. – Laser Ablation Spot Analyses for the type 4 mineral assemblage

Type Min	Phase	Sample	Spot	Au (ppb)	204Pb (ppm)	Tl (ppm)	206Pb (ppm)	207Pb (ppm)	208Pb (ppm)	Bi (ppm)
Type 4	ccp	14295	RL4	BDL	BDL	0	BDL	BDL	BDL	BDL
Type 4	ccp	14295	RL4	BDL	BDL	0	BDL	BDL	BDL	BDL

E.3 – Methods for Laser Ablation Correction Calculations

The ThermoFisher Scientific PlasmaLab software generated element mass data in parts per million (ppm) during analysis from detected counts per second (cps). Calibration curves were also generated automatically from analysis of GSC-1G, GSD-1G and GSE-1G standards prior to and after analysis of 20 unknowns; GSD-1G was also analyzed after the analysis of 10 unknowns to monitor instrumental drift. The external standard (BHVO-2G) was also analyzed before and after each set of unknown analyses. Steps required to correct these raw element data were threefold: (1) a calibration curve check; (2) an element ionization potential correction; and (3) a laser yield correction. Corrected laser ablation data is semi-quantitative. Justification and instruction for each correction are included below; Table B.3.3.1 shows example correction calculations for a single sphalerite analysis.

E.3.1 – Calibration Curve Correction

This initial correction is to check the accuracy of instrument detection. The curve intercept was set at the gas blank interference value for all elements. The R-value of the calibration curve for each element determined the accuracy of the standard data. Elements with very low R-values (<0.95) or that did not generate calibration curves (i.e. no preferred standard values; Table E.1.1) were not considered.

E.3.2 – Element Ionization Correction

Variation in element ionization potentials due to laser ablation causes error in data and must be corrected using adjusted external standard values. The element ionization correction was not applied when preferred element masses in BHVO-2G (Online) were below the detected element mass in the gas blank.

(1) Element mass value for BHVO-2G prior to analysis of unknowns.
(2) Element mass values (ppm) for unknown phase generated from ThermoFisher Scientific PlasmaLab software.
(3) Element mass value for BHVO-2G post analysis of unknowns.
(4) Preferred element mass value for BHVO-2G (Online).
(5) Average BHVO-2G value is calculated from the initial (2) and final (3) element mass values in BHVO-2G for each set of 20 unknown analyses.
(6) Correction factor is calculated from the subtraction of [(4) divided by (5)] from 1.
(7) Adjusted element mass values are calculated by subtracting [(1) multiplied (6)] from (1).

Table E.3.2.1 – Example Element Ionization Correction for sphalerite (sample CNF14299, spot RL4)

	Ti (ppm)	V (ppm)	Mn (ppm)	Cr (ppm)	Co (ppm)	Ni (ppm)	Ge (ppm)	As (ppm)	Se (ppm)	Mo (ppm)	Ag (ppm)	Cd (ppm)	In (ppm)	Sn (ppm)	Sb (ppm)	Au (ppm)	Tl (ppm)	Bi (ppm)
GSC-1G	9356	8	189	10	8	25	6	0	0	5	4	0	7	6	9	256	0	5
GSD-1G	6153	41	204	42	38	51	29	31	0	38	23	19	36	28	39	4830	1	33
GSE-1G	570	437	588	396	376	429	316	260	0	386	196	156	365	277	442	3957	2	315
(1) BHVO-2G	17300	346	1385	333	52	144	6	1	0	9	3	0	7	6	1	-984	0	5
(2) CNF14299 RL4	131	8	646	6	13	90	23	249	0	8	37	4549	7	13	134	1323	42	5
(3) BHVO-2G	15480	307	1233	309	50	292	9	-43	0	14	6	7	7	7	4	1774	1	5
GSC-1G	9073	7	187	10	8	27	5	-7	0	6	5	0	7	7	10	2227	0	5
GSD-1G	6478	42	208	42	38	52	31	38	0	38	22	20	35	28	38	2667	1	33
GSE-1G	545	440	591	400	380	441	320	259	0	390	200	160	370	280	450	7606	2	320
(4) Preferred BHVO-2G	15100	308	1317	293	44	116	2	1		4	1	0	0	6	0	1230	0	0
(5) Average BHVO-2G	16390	327	1309	321	51	218	8	-21	0	11	4	3	7	7	2	395	0	5
(6) Correction factor	0	0	0	0	0									0				
GSC-1G	8620	8	191	9	7	25	6	0		5	4	0	7	5	9	256	0	5
GSD-1G	5669	39	205	38	32	51	29	31		38	23	19	36	25	39	4830	1	33
GSE-1G	525	412	591	362	323	429	316	260		386	196	156	365	242	442	3957	2	315
BHVO-2G	15938	327	1393	304	45	144	6	1		9	3	0	7	5	1	-984	0	5
(7) CNF14299 RL4	120	7	650	5	11	90	23	249		8	37	4549	7	11	134	1323	42	5
BHVO-2G	14262	289	1240	282	43	292	9	-43		14	6	7	7	6	4	1774	1	5
GSC-1G	8359	7	188	9	6	27	5	-7		6	5	0	7	6	10	2227	0	5
GSD-1G	5968	40	209	39	33	52	31	38		38	22	20	35	24	38	2667	1	33
GSE-1G	502	415	595	365	326	441	320	259		390	200	160	370	244	450	7606	2	320

E.3.3 – Laser Yield Correction

The amount of material ablated by the laser varies with the relative absorption of laser energy between different coloured mineral phases. This error was corrected using an internal standard known from electron microprobe analysis (EMPA). The laser yield correction was not applied to phases with no viable internal standard (i.e. pyrite, galena and chalcopyrite in this study).

(1) Element mass values (ppm) for unknown phase (sphalerite) generated by laser ablation ICPMS using ThermoFisher Scientific PlasmaLab software and corrected for element ionization potential (B.3.3.1, step 7).
(2) Element mass value (Cd, ppm) for unknown phase (sphalerite) known from (EMPA).
(3) Average element mass value (Cd, ppm) of all probe analyses (2) for a particular grain.
(4) Element mass value (Cd, ppm) for unknown phase (sphalerite) generated by laser ablation ICPMS using ThermoFisher Scientific PlasmaLab software and corrected for element ionization potential (B.3.3.1, step 7).
(5) Correction factor calculated by dividing (3) by (4).
(6) Adjusted element mass values are calculated by multiplying (5) by all elements in (1).

Table E.3.3.1 – Example Laser Yield Correction for sphalerite (sample CNF14299, spot RL4)

		Ti (ppm)	V (ppm)	Mn (ppm)	Cr (ppm)	Co (ppm)	Ni (ppm)	Ge (ppm)	As (ppm)	Se (ppm)	Mo (ppm)	Ag (ppm)	Cd (ppm)	In (ppm)	Sn (ppm)	Sb (ppm)	Au (ppm)	Tl (ppm)	Bi (ppm)
(1) Element mass		120	7	5	650	11	90	23	249		8	37	4549	7	11	134	1323	42	5
(2) EMPA analysis	Cd (ppm)																		
RL4 sp1	3160																		
RL4 sp2	3190																		
RL4 sp3	3120																		
(3) Average of EMPA analyses	3157																		
(4) LAICPMS analysis	4549																		
(5) Correction factor	0.694																		
(6) Adjusted element mass		84	5	4	451	8	63	16	173	0	6	26	3157	5	8	93	918	29	3

Appendix F: Secondary Ion Mass Spectrometry Results

F.1 – Analytical Methods for Pb-Isotopes in SIMS

Description of Pb-isotope procedures after G. D. Layne (unpublished).

Sample Preparation

Small slabs of sulfide-bearing rock were embedded in two-component epoxy in 25 mm diameter aluminum retaining rings and prepared as flat polished mounts. After lapidary preparation, all samples were sputter coated with 300 Å of Au, to mitigate charging under primary ion bombardment.

Instrumentation

All analyses were performed using the Cameca IMS 4f Secondary Ion Mass Spectrometer at the MAF-IIC Microanalysis Facility of Memorial University. This instrument has been updated with additional source lensing in the primary column, enhancing the ability to deliver more finely focused beams of O^-, which improves the spatial resolution for Pb isotope analyses. It has also been equipped with modernized ion detection systems that augment precision and reproducibility for stable isotope determinations in general.

Analytical Parameters

Pb isotope determinations were performed by bombarding the sample with a primary ion microbeam of 14-16 nA of O^-, accelerated through a nominal 10 keV potential, and focused into an ~20 μm diameter spot. To exclude exotic material in the polished surface from analysis, each spot was first pre-sputtered for 120 s with a 25 μm square raster applied to the beam. A smaller square raster (10μm) was applied to the beam during analysis, to improve the homogeneity of primary ion delivery, while maintaining lateral resolution at better than 20-25 μm. The sample was pre-sputtered in this mode for an additional 75 s before data collection began.

Positively charged sputtered secondary ions (Pb^+) were accelerated into the mass spectrometer of the instrument through a nominal potential of -4.5 keV. The instrument was operated with a medium Contrast Aperture (150 μm), and Entrance and Exit Slits paired to give flat topped peaks at a minimum mass resolving power (MRP) of 300 (10% peak height definition). A sample offset voltage of -60eV and Energy Window of 60eV width were deployed to effectively eliminate minor isobaric interferences through energy filtering. Maximum count rates ($^{208}Pb^+$) were generally less than 250,000 cps. Since absolute transmission is not an issue for these determinations, the simple 150 μm Transfer Lens mode was used, along with a large Field Aperture (1800 μm), giving an approximately 125 μm field of view in the mass spectrometer, and enabling easy monitoring of spot and sample centring.

Signals for $^{204}Pb^+$, $^{206}Pb^+$, $^{207}Pb^+$ and $^{208}Pb^+$, and a background position at 203.67 Da, were obtained by cyclical magnetic peak switching. Standard counting times and peak sequence

used were; 1.0 s at the background position, 8.0 s on $^{204}Pb^{+}$ and 4.0 s on each of $^{206}Pb^{+}$, $^{207}Pb^{+}$, and $^{208}Pb^{+}$. Waiting times of 0.4 s (0.5 s for background position) were inserted before each peak counting position to allow for magnet settling. A typical analysis consisted of accumulating 15 of these peak cycles, which takes a total of 9.0 minutes (including pre-sputtering times).

All peak signals were collected with an ETP 133H multiple-dynode electron multiplier (em) and processed through ECL-based pulse-counting electronics with a system dead time of 12 ns. Background measurements at the nominal mass 203.67 Da were taken during each magnetic switching cycle – and were routinely less than 0.05–0.10 counts per second.

Any change in overall peak intensities with time - which is typically monotonic in homogeneous lead-rich sulfide mineral phases (and thus quantitatively minor in its effect on measured Pb ratios) - was compensated for using a standard double interpolation ratio algorithm (an approach adopted from TIMS analysis), with each $^{204,207,208}Pb^{+}$ peak ratioed to the time-corrected interpolation of the two immediately adjacent $^{206}Pb^{+}$ peaks.

Beyond the excellent spatial resolution, a further advantage of SIMS stems from the gradual nature of material removal by sputtering, with each counting interval producing depth-resolved data on the sample. Inclusions of other sulfide phases, in particular, have the potential to produce excursions in the measured Pb isotope ratios. However, the depth-resolved characteristic of SIMS allows the detection of even small inclusions, or other heterogeneities within the sample, simply by monitoring sharp excursions in signal intensity ($I^{204, 206, 207, 208}Pb^{+}$) with time. These signal time intervals can then easily be eliminated from the measured data during processing.

Calibration of Instrumental Fractionation

The production and detection of sputtered secondary ions produces a mass dependent bias between the actual $^{204}Pb/^{206}Pb/^{207}Pb/^{208}Pb$ of the sample and that measured by the mass spectrometer – termed Instrumental Mass Fractionation (IMF). IMF in SIMS can generally be considered as a combination of mass discrimination effects at the site of sample sputtering with those in the ion detector(s) themselves. Other effects, related to the ion optics of the mass spectrometer, are reduced to comparatively insignificant levels in a properly and consistently aligned instrument.

The magnitude of IMF is modest for heavy elements like Pb – typically 0.05 – 0.15%/Da, depending largely on the age and condition of the em detector. Variation of IMF between galena and other lead-rich sulfides and sulfosalts is relatively insignificant. Pb isotope measurements measured in samples of these minerals were corrected for IMF by comparison to replicate in run measurements of reference materials F19 (galena: $^{204}Pb/^{206}Pb$ 16.960; $^{207}Pb/^{206}Pb$ 15.535; $^{208}Pb/^{206}Pb$ 36.538) and JMBH (galena: $^{204}Pb/^{206}Pb$ 16.069; $^{207}Pb/^{206}Pb$ 15.451; $^{208}Pb/^{206}Pb$ 35.795).

Accuracy and Reproducibility

15 cycle analyses accumulated in 9 min routinely yield internal precisions (standard error of the mean) on $^{204}Pb/^{206}Pb$, $^{207}Pb/^{206}Pb$ and $^{208}Pb/^{206}Pb$ determinations of better than ±0.05-0.10% (1σ), while producing sputter craters only a few μm deep. Overall reproducibility, based on replicate analyses of the secondary standard JMBH, is typically better than ±0.10-0.15% for these same ratios.

F.2 – Analytical Methods for S-Isotopes in SIMS

Description of S-isotope procedures after G. D. Layne (unpublished).

Sample Preparation

Small slabs of sulfide-bearing drill core were embedded in epoxy in 1 inch diameter aluminum retaining rings and prepared as simple flat polished mounts. After lapidary preparation, all samples were sputter coated with 300 Å of Au, to mitigate charging under primary ion bombardment.

Instrumentation

All analyses were performed using the Cameca IMS 4f Secondary Ion Mass Spectrometer at the MAF-IIC Microanalysis Facility of Memorial University. This instrument has been updated with additional source lensing in the primary column, enhancing the ability to deliver finely focused beams of Cs^+ for analyses that require both high precision and high spatial resolution. It has also been equipped with modernized ion detection systems that augment performance for stable isotope determinations.

Analytical Parameters

$\delta^{34}S$ determinations were performed by bombarding the sample with a primary ion microbeam of 850 -1200 pA of Cs^+ (beam current was optimized between 0.6 – 0.8 nA for pyrite and chalcopyrite, and 0.9 -1.0 nA for galena), accelerated through a 10 keV potential, and focused into a 5–15 μm diameter spot. To exclude exotic material in the polished surface from analysis, each spot was first pre-sputtered for 120 s with a 25 μm square raster applied to the beam then pre-sputtered again using a 10 μm raster for 200 s. Depending on the minimum diameter of the critically focused primary beam during each session, a smaller square raster (5μm to 15μm) was applied to the beam during analysis, to improve the homogeneity of primary ion delivery, while maintaining lateral resolution at better than 20μm.

Negatively charged sputtered secondary ions were accelerated into the mass spectrometer of the instrument through a potential of 4.5 keV.

The instrument was operated with a medium Contrast Aperture (150 μm), and Entrance and Exit Slits paired to give flat topped peaks at a mass resolving power (MRP) of 2975 (10% peak height definition) - sufficient to discriminate $^{33}SH^-$ (and $^{32}SH_2^-$) from $^{34}S^-$. In addition, a sample offset voltage of -60eV and Energy Window of 40eV width were deployed to purposely reduce transmission, enabling a higher primary beam current (and concomitantly faster sputter

rate). This permitted faster pre-sputtering of the sample and better exclusion of exotic surface material, while maintaining count rates on $^{32}S^-$ around 1,000,000 cps.

Since absolute transmission is not an issue for these determinations, the simple 150 μm Transfer Lens mode was used, along with a large Field Aperture (1800 μm), giving an approximately 125μm field of view in the mass spectrometer, and enabling easy monitoring of spot and sample centering.

Signals for $^{32}S^-$, $^{34}S^-$ and a background position at 31.67 Da were obtained by cyclical magnetic peak switching. Standard counting times and peak sequence used were; 0.5 s at the background position, 2.0 s on $^{32}S^-$, and 6.0 s on $^{34}S^-$. Waiting times of 0.25 s were inserted before each peak counting position to allow for magnet settling. A typical analysis consisted of accumulating 80 of these peak cycles, which takes less than 15 min (including pre-sputtering time).

All peak signals were collected with an ETP 133H multiple-dynode electron multiplier (em) and processed through ECL-based pulse-counting electronics with an overall dead time of 11 ns. Background measurements at the nominal mass 31.67 Da were taken during each magnetic switching cycle – and were routinely less than 0.05–0.1 counts per second. Count rates on $^{32}S^-$ were maintained between 1,000,000 and less than 1,500,000 counts per second by adjusting the primary beam current appropriately for each sulfide phase of interest.

Any change in overall peak intensities with time - which was typically monotonic (and quantitatively minor in its effect on measured $^{34}S/^{32}S$) in a homogeneous sulfide mineral phase - was compensated for using a standard double interpolation ratio algorithm (an approach adopted from TIMS analysis), with each $^{34}S^-$ peak ratioed to the time-corrected interpolation of adjacent $^{32}S^-$ peaks.

Beyond the excellent spatial resolution, a further advantage of SIMS stems from the gradual nature of material removal by sputtering, with each counting interval producing depth-resolved data on the sample. Inclusions of other sulfide phases, in particular, have the potential to produce excursions in the measured $\delta^{34}S$. However, the depth-resolved characteristic of SIMS allows the detection of inclusions, or other heterogeneities within a mineral, simply by monitoring sharp excursions in $I^{32}S^-$ with time. These signal time intervals can then easily be eliminated from the measured data.

Calibration of Instrumental Fractionation

The production and detection of sputtered secondary ions produces a bias between the actual $^{34}S/^{32}S$ of the sample and that measured by the mass spectrometer – termed Instrumental Mass Fractionation (IMF). IMF in SIMS can generally be considered as a combination of mass discrimination effects at the site of sample sputtering with those in the ion detectors themselves. Other effects, related to the ion optics of the mass spectrometer, are reduced to comparatively insignificant levels in a properly and consistently aligned instrument.

The magnitude of IMF varies substantially between sulfide minerals. For this reason, the $^{34}S/^{32}S$ measured in samples of pyrite, galena and chalcopyrite from Lemarchant were corrected for IMF by comparison to replicate in run measurements of reference materials UL9B (pyrite; $\delta^{34}S$: 15.8‰), HT10 (galena; $\delta^{34}S$: 14.2‰) and Norilsk (chalcopyrite; $\delta^{34}S$: 8.3‰).

Accuracy and Reproducibility

Analyses accumulated in 12 min routinely yield internal precisions on individual $\delta^{34}S$ determinations of better than ±0.3‰ (1σ), while producing sputter craters only a few µm deep. These precisions closely approach the optimum possible precision as calculated from Poisson counting statistics. Overall reproducibility, based on replicate standard analyses, is typically better than ±0.35-0.45‰ (1σ).

F.3 – Methods for TSR-derived $\delta^{34}S$ Calculations

Ideal $\delta^{34}S$ values in sulfides with sulfur derived exclusively from thermochemical sulfate reduction (TSR) can be calculated for variable temperatures, $\delta^{34}S$ of seawater sulfate and fractionation percentages of parent sulfate to sulfide at the time of formation. The methods and equations outlined below are after Ohmoto and Rye (1979) and Ohmoto and Goldhaber (1997), and have been tailored to fit the conditions of Lemarchant deposit genesis. These conditions consist of:

- Temperature (T) in Kelvin (K): 472.15°C and 572.15°C
- $\delta^{34}S$ of seawater sulfate ($SO_{4\ (parent,\ t=0)}$) = 35‰ (Kampschulte and Strauss, 2004; Paytan and Grey, 2012)
- Fractionation percentages of parent sulfate to sulfide at the time of formation (f) = 1.0

(1) The equation for the difference between the $\delta^{34}S$ values of sulfide (H_2S) and seawater sulfate (SO_4) is simplified to solve for $(\alpha_{(H_2S-SO_4)})$, considering constants: B, C = 0.

$$\delta^{34}S_{H_2S} - \delta^{34}S_{SO_4} = 1000 ln\alpha_{(H_2S-SO_4)} = A * \frac{10^6}{T^2} + B * \frac{10^3}{T} + C$$

(2) The simplified equation (2) is calculated from the temperature (T) with the following constants: A = -5.26.

$$\alpha_{(H_2S-SO_4)} = e^{(A*\frac{10^6}{T^2})/1000}$$

(3) The $\delta^{34}S$ value for the amount of unfractionated parent sulfate relative to reduced sulfide present at the time of formation ($SO_{4\ (parent,\ t)}$) is calculated from the original amount of parent sulfate ($SO_{4\ (parent,\ t=0)}$), fractionation percentage (f) and simplified equation (2).

$$\delta^{34}S_{SO_4(parent,t)} = \left(\delta^{34}S_{SO_4(parent,t=0)} + 1000\right) * f^{(\alpha_{(H_2S-SO_4)}-1)} - 1000$$

(4) The $\delta^{34}S$ value of sulfide produced by TSR ($\delta^{34}S_{H_2S}$) from unfractionated parent sulfide (3) is calculated also by using simplified equation (2).

$$\delta^{34}S_{H_2S} = \delta^{34}S_{SO_4(parent,t)} + 1000(\alpha_{(H_2S-SO_4)} - 1)$$

(5) The $\delta^{34}S$ value of sulfide phases formed with H_2S derived from TSR ($\delta^{34}S_{i\,TSR}$) is calculated using $\delta^{34}S_{H_2S}$ (4), temperature (T) and constant X_i, where i =pyrite, galena and chalcopyrite ($X_{pyrite} = 0.4 \pm 0.08$; $X_{galena} = 0.63 \pm 0.05$; and $X_{chalcopyrie} = 0.05 \pm 0.08$). Calculations for both upper and lower limits of uncertainty were made.

$$\delta^{34}S_{i\,TSR} = A * \frac{10^6}{T^2} + \delta^{34}S_{H_2S}$$

Table F.3.1 – TSR-derived $\delta^{34}S$ calculation for pyrite, galena and chacopyrite

Step:		**1,2**			**3**	**4**	**5$_{py, lower}$**	**5$_{py, upper}$**	**5$_{gn, lower}$**	**5$_{gn, upper}$**	**5$_{ccp, lower}$**	**5$_{ccp, upper}$**
T (°C)	T (K)	$\alpha_{H2S\text{-}SO4}$	*f*	$\delta^{34}S_{Late\ Cambrian}$	$\delta^{34}S_{SO4\ (parent,\ t)}$	$\delta^{34}S_{H2S}$	$\delta^{34}S_{TSR,\ py}$ lower	$\delta^{34}S_{TSR,\ py}$ upper	$\delta^{34}S_{TSR,\ gn}$ lower	$\delta^{34}S_{TSR,\ gn}$ upper	$\delta^{34}S_{TSR,\ ccp}$ lower	$\delta^{34}S_{TSR,\ ccp}$ upper
200	472.15	0.977	1	35	35.0	11.7	13.1	13.8	14.3	14.7	11.1	11.8
300	572.15	0.984	1	35	35.0	19.1	20.0	20.5	20.8	21.1	18.7	19.2

F.4 – Methods for Temperature Calculations from $\delta^{34}S$ in sulfide mineral pairs

Geothermometry calculations are be made from the analyzed $\delta^{34}S$ values of sulfide pairs that were deposited under equilibrium conditions. The methods and equations outlined below are after Kajiwara and Krouse (1971) and Ohmoto and Rye (1979).

(1) All $\delta^{34}S$ values of sulfide mineral pairs in contact (preferred) or proximal (≤1000 μm) were chosen from available analyzed data. Sulfide pairs included pyrite-chalcopyrite (py-ccp), pyrite-galena (py-gn) and chalcopyrite-galena (ccp-gn).
(2) If two analyses were performed on the same grain, the $\delta^{34}S$ value was averaged.
(3) Proximity of sulfides indicated by markers (yes).
(4) Temperatures of formation (T) in degrees Celsius (°C) were calculated using the two $\delta^{34}S$ values and the following equations, depending on sulfide pairing. Calculations for both upper and lower limits of uncertainty were made.

$$T_{py-ccp} = ((0.67 \pm 0.04) * 10^3) / \sqrt{\delta^{34}S_{py} - \delta^{34}S_{ccp}}$$

$$T_{py-gn} = ((1.01 \pm 0.04) * 10^3) / \sqrt{\delta^{34}S_{py} - \delta^{34}S_{gn}}$$

$$T_{ccp-gn} = \left[\frac{(2.25 \pm 0.25) * 10^{2.5}}{\sqrt{\delta^{34}S_{ccp} - \delta^{34}S_{gn}}}\right] - 272.15$$

Table F.4.1 – Geothermometry calculations with S-isotoptes for pyrite, galena and chalcopyrite mineral pairs

Pyrite	Mineral Assemb*	$\delta^{34}S$	Av* $\delta^{34}S$	in contact?	Chalcopyrite	Mineral Assemb.	$\delta^{34}S$	Av. $\delta^{34}S$	in contact?	Galena	Mineral Assemb.	$\delta^{34}S$	Av. $\delta^{34}S$	T (°C, lower)	T (°C, upper)
CNF29957 py5	Type 2B	2.88	3.44		CNF29957 ccp1	Type 2A	5.824367736	6.14						383	432
CNF29957 py6	Type 2B	4.00			CNF29957 ccp2	Type 2A	6.464981966								
CNF29957 py3	Type 2B	3.90	4.00	yes	CNF29957 ccp3	Type 2A	5.431798453	5.71						481	542
CNF29957 py4	Type 2B	4.10		yes	CNF29957 ccp4	Type 2A	5.997079814								
CNF29957 py1	Type 2B	4.24	4.00	yes	CNF29957 ccp5	Type 2A	5.145558854	5.66						489	551
CNF29957 py2	Type 2B	3.76			CNF29957 ccp6	Type 2A	6.168784591								
CNF29962 py1	Type 2B	6.38	6.47		CNF29962 ccp1	Type 2B	4.262650973	4.03						403	455
CNF29962 py2	Type 2B	6.55			CNF29962 ccp2	Type 2B	3.791259492								
CNF14291 py5	Type 3	6.86	7.19							CNF14291 gn5	Type 2B	12.63	12.81	409	443
CNF14291 py6	Type 3	7.53								CNF14291 gn6	Type 2B	12.99			
CNF14291 py1	Type 3	8.28	7.82						yes	CNF14291 gn1	Type 2B	6.80	5.85	692	749
CNF14291 py2	Type 3	7.35							yes	CNF14291 gn2	Type 2B	4.91			
CNF14291 py3	Type 3	7.65	7.33							CNF14291 gn3	Type 2B	7.95	6.71	1234	1336
CNF14291 py4	Type 3	7.01								CNF14291 gn4	Type 2B	5.47			
CNF29972 py5	Type 3	6.16	5.78						yes	CNF29972 gn5	Type 4	11.95		281	304
CNF29972 py6	Type 3	5.41								CNF29972 gn2	Type 4	5.42		417	451
CNF29972										CNF29972 gn3	Type 4	2.18		657	712
CNF29972										CNF29972 gn4	Type 4	11.03		292	316

CNF29986 py1	Type 2B	5.46	6.00							CNF29986 gn1	Type 2B	-1.73	-0.87	370	401
CNF29986 py2	Type 2B	6.54								CNF29986 gn2	Type 2B	0.00			
CNF29960 py1	Type 1	0.30	0.98						yes	CNF29960 gn1	Type 3	4.16	3.59	600	650
CNF29960 py2	Type 1	1.66							yes	CNF29960 gn2	Type 3	3.02			
CNF14259 py1	Type 2B	6.09	6.21							CNF14259 gn1	Type 2A	-1.62	-1.58	348	376
CNF14259 py2	Type 2B	6.34								CNF14259 gn2	Type 2A	-1.54			
CNF14259 py3	Type 2B	4.79	5.30						yes	CNF14259 gn3	Type 2A	11.78		283	306
CNF14259 py4	Type 2B	5.81							yes	CNF14259 gn4	Type 2A	0.35		1630	1764
CNF14259 py5	Type 2B	5.14	4.97							CNF14259 gn5	Type 2A	1.15	0.48	458	495
CNF14259 py6	Type 2B	4.81								CNF14259 gn6	Type 2A	-0.18			
					CNF29986 Ccp5	Type 2B	5.051654224	5.02		CNF29986 gn5	Type 2B	2.53	1.99	146	237
					CNF29986 Ccp6	Type 2B	4.984866697			CNF29986 gn6	Type 2B	1.46			
					CNF29962 ccp3	Type 2B	3.463242601	3.20		CNF29962 gn1	Type 2B	5.34	4.18	464	624
					CNF29962 ccp4	Type 2B	2.945182079			CNF29962 gn2	Type 2B	3.03			

*Where Assemb. = Assemblage; Av. = Averag